Stony Brook University

OFFICIAL COPY

The official electronic file of this thesis or dissertation is maintained by the University Libraries on behalf of The Graduate School at Stony Brook University.

© All Rights Reserved by Author.

Study of long-range azimuthal and longitudinal correlations in high energy nuclear collisions at the LHC using the ATLAS detector

A Dissertation presented

by

Sooraj Krishnan Radhakrishnan

to

The Graduate School

in Partial Fulfillment of the

Requirements

for the Degree of

Doctor of Philosophy

in

Physics

Stony Brook University

August 2016

Stony Brook University
The Graduate School

Sooraj Krishnan Radhakrishnan

We, the dissertation committe for the above candidate for the Doctor of Philosophy degree, hereby recommend acceptance of this dissertation acceptance of this dissertation

Jiangyong Jia - Dissertation Advisor
Associate Professor, Department of Chemistry

Derek Teaney - Chairperson of Defense
Assistant Professor, Department of Physics and Astronomy

Roy A. Lacey
Professor, Department of Chemistry

Axel Drees
Department Chair & Professor, Department of Physics and Astronomy

Xu Du
Associate Professor, Department of Physics and Astronomy

David Morrison
Physicist, Physics Department
Brookhaven National Lab

This dissertation is accepted by the Graduate School

Nancy Goroff
Interim Dean of the Graduate School

Abstract of the Dissertation

Study of long-range azimuthal and longitudinal correlations in high energy nuclear collisions at the LHC using the ATLAS detector

by

Sooraj Krishnan Radhakrishnan

Doctor of Philosophy

in

Physics

Stony Brook University

2016

Azimuthal correlations between particle pairs having large pseudorapidity separation (commonly called the "ridge") have been observed in p+p and p+Pb collisions. Different interpretations towards its origin, including collective transverse expansion of produced partons, and initial state correlations enhanced by gluon saturation have been proposed. We present a detailed measurement of the ridge and associated Fourier harmonics (v_n) in p+Pb collisions at $\sqrt{s_{NN}} = 5.02$ TeV at the LHC using the ATLAS detector. The ridge correlations are found to persist to high p_{T} ($\sim$10 GeV). Fourier harmonics up to order 5 are measured and found to be non-zero. The first order harmonic v_1 shows a p_{T} dependence characteristic of an origin due to collective expansion. Results are also compared to Pb+Pb collisions at similar multiplicity. The measured harmonics from the two systems are found to agree with expectations from a conformally invariant collective expansion model for the origin of these correlations. Multi-particle azimuthal correlations and cumulants are often used to study global correlations from collective expansion in nuclear collisions. We also investigate the limitations of this approach in studying collectivity in small systems.

Long range correlations had also been measured in nuclear collisions, between total multiplicity produced at different pseudorapidities. We present a new method to measure these "longitudinal correlations", using two particle correlations in pseudorapidity. The performance of the method is studied using the Monte-Carlo models, HIJING and AMPT. Measurements of the longitudinal correlations in $\sqrt{s} = 13$ TeV p+p, $\sqrt{s_{NN}} = 5.02$ TeV p+Pb and $\sqrt{s_{NN}} = 2.76$ TeV Pb+Pb collisions at the LHC using the ATLAS detector are presented. A data driven approach is used to separate the short-range correlations (SRC) arising during later stages of the system evolution and the long-range correlations (LRC) sensitive to the initial conditions. The SRC show a strong

system size dependence, largest in small collision systems. The correlation functions are expanded in an orthonormal basis of Legendre polynomials to study different shape components. We find the LRC is dominated by a linear anticorrelation between the forward and backward rapidities, and that the magnitude of this anticorrelation is similar between the three systems. The implications of these measurements in constraining the initial conditions along the longitudinal direction are discussed.

Dedication Page

To my parents and my sister.

Contents

List of Figures

List of Tables

Acknowledgements

I take this opportunity to express my sincere gratitude to Prof. Jiangyong Jia for being an excellent advisor and guiding me through the Ph.D research. I appreciate the patience and attention he has shown as an advisor. His passion to the field and in exploring new areas of research has been an inspiration to me throughout my Ph.D research.

I would also like to thank the collaborators at ATLAS experiment, whose dedicated efforts have ensured excellent detector performance and high quality data available for the studies. I also thank members of the Heavy Ion group at ATLAS for the many valuable discussions and for the collaborative effort in providing calibrations, under taking performance studies and recommending standard quality requirements for the data. My thanks also goes to the editorial board members in ATLAS for careful internal reviews of the analyses.

I thank my fellow graduate students Mingliang Zhou and Peng Huo with whom I have collaborated on the studies of multiplicity correlations, that is included in this thesis work. Many thanks also to my group members at the Nuclear Chemistry group, particularly Prof. Roy Lacey and Soumya Mohapatra, for their help and suggestions and support during the past years. Thanks and regards also to my friends during the years at Stony Brook, Visruth, Jinais, Ajay, Heli, Rohit and Vaishak, who have made the life here enjoyable.

Also, many thanks to my committee members for taking time out of their busy schedules and coming to my defense, and also for going through my thesis and suggesting improvements.

Last but not least, thanks to my family, my parents and my sister for their continued support and enouragement through out my life and during my Ph.D years. Thanks dad and mom, for the many small sacrifices you have made, that has made it possible for me to pursue this carrer path and be where I am today!

Part I

Introduction

Relativistic heavy ion collisions at the RHIC and LHC attempt to create and study the properties of the deconfined matter of quarks and gluons, sometimes referred to as the Quark Gluon Plasma (QGP) [1, 2]. The correlations between bulk particles produced in the medium, particularly the azimuthal correlations between transverse momenta (p_{T}) of particles, have been studied extensively in heavy ion collisions to understand the properties of the medium produced. The azimuthal correlations show up as an excess of pairs along relative azimuthal angle differences, $\Delta\phi \sim 0$ and $\Delta\phi \sim \pi$ and extend to pairs with large pseudorapidity (η) difference ($|\Delta\eta| \geq 5$), and are referred to as the "ridge" [3, 4]. Relativistic hydrodynamics is usually used to model the expansion of the QGP medium produced in heavy ion collisions, and the hydrodynamic calculations have been very successful in reproducing the ridge correlations and the Fourier harmonics (v_n) associated with them [5, 6]. The measurements of the azimuthal correlations combined with the hydrodynamic calculations have been extensively used to characterize the properties of the QGP medium like specific viscosity, equation of state and other transport parameters [5, 7, 8].

Recently, near side ($\Delta\phi \sim 0$) ridge in two particle correlations have been observed in smaller collision systems like p+p and p+Pb (and d+Au), in events of high multiplicity [9, 10, 11] The magnitudes of the ridge are smaller than that in A+A collisions, but features like p_{T} dependence were found to be qualitatively similar between the two systems [12, 13]. Hydrodynamic calculations can reproduce the ridge in p+Pb collisions [14, 15], however the validity of applying hydrodynamics in small systems is debated [16]. Another class of models attempt to explain the ridge in small systems as arising from initial state correlations that are enhanced by gluon saturation at the center of mass energies studied at LHC and top energy RHIC [17, 18]. One of the focuses of this thesis is the study of the ridge in small collision systems in more detail to provide further insights into the origin of these correlations. We present detailed measurements of the ridge and associated Fourier harmonics v_n in p+Pb collisions at $\sqrt{s_{NN}} = 5.02$ TeV at the LHC using the ATLAS detectors. We also study the limitations of multi-particle cumulants in studying collectivity in small systems and propose an alternate method to measure the cumulants in high energy nuclear collisions.

Long-range correlations also exist between total multiplicity produced at different pseudorapidities [19, 20]. These correlations are referred to as "longitudinal correlations" in this work. The origin of these correlations, unlike the ridge, are not attributed to the QGP or its expansion, but to the initial conditions along the η direction and to the correlations in early time entropy production [19]. We present a two particle correlation method to study the longitudinal correlations, with a focus on the study of the long-range longitudinal correlations in small collision systems. We isolate the different shape components associated with these correlations and also provide a separation of the contributions from short-range correlations (arising during later stages of the medium evolution, mainly from resonance decays, jet fragmentation, local charge conservation etc) and long-range correlations (related to the initial conditions along η). We present measurements of the longitudinal correlations using the ATLAS detector in $\sqrt{s_{NN}} = 2.76$ TeV Pb+Pb, $\sqrt{s_{NN}} = 5.02$ TeV p+Pb and $\sqrt{s} = 13$ TeV p+p collisions. The measurements are an improvement over the existing results [19, 20, 21] and is of importance in constraining initial conditions along the longitudinal direction and models for initial entropy production in high energy nuclear collisions.

The thesis is organized as follows. Part II provides a detailed introduction to the research presented in this thesis. The two topics of study in this work, the ridge and the longitudinal

correlations, are introduced and the scope and focus of the studies presented in this work are laid out. Part III presents a discussion on the Large Hadron Collider (LHC) and the ATLAS detector. Part IV presents the study of the ridge in small systems and the measurement of the ridge in p+Pb collisions at $\sqrt{s_{NN}} = 5.02$ TeV. Part V presents studies on the longitudinal correlations and the measurements of the correlations in $\sqrt{s_{NN}} = 2.76$ TeV Pb+Pb, $\sqrt{s_{NN}} = 5.02$ TeV p+Pb and $\sqrt{s}$ = 13 TeV p+p collisions. The main conclusions and outlook on further exploration are presented in Part VI. Appendix A and B presents complementary details to the measurements presented in Part IV and Part V, respectively, including a discussion of the evaluation of the systematic uncertainties in the measurements.

Part II

Background and Outline of the research

Chapter II.1

Heavy Ion collisions and the Quark Gluon Plasma

Relativistic heavy ion collisions attempt to create and study the properties of the state of nuclear matter referred to as the Quark Gluon Plasma (QGP) in which the quarks and gluons are the degrees of freedom. This state of matter is theorised to have existed a few microseconds after the Big Bang as well as in the core of neutron stars at extremely high densities. The current collider experiments at the Relativistic Heavy Ion Collider (RHIC) at Brookhaven and the Large Hadron Collider (LHC) at CERN collide heavy nuclei at nucleon nucleon center of mass energies of up to 200 GeV and 5.5 TeV respectively, which are expected to lead to the formation of the QGP [22]. The experiments at both RHIC and LHC have claimed discoveries of the state of matter consistent with the properties of the QGP [23, 2]. This chapter gives a brief introduction to the phenomenology of heavy ion collisions, the QGP and some of its most studied experimental signatures.

II.1.1 QCD phase diagram and the QGP

The nuclear matter is composed of the fundamental particles quarks, and the gluons which act as the mediators of the strong interactions between the quarks. The quarks come in six flavors, *up*(u), *down*(d), *charm*(c), *strange*(s), *top*(t) and *bottom*(b). The masses, charge and spin of the different quark species (along with other fundamental particles) are shown in figure II.1.1. Most of the observed matter is comprised of bound states of the three lightest quarks. The quarks and gluons carry color charge, which are responsible for the strong interactions, and come in three types: *red*, *blue*, and *green*, and their corresponding complementary types, *antired*, *antiblue*, and *antigreen*. A quark can have any one of the three color charges and an antiquark (the antiparticles of quarks) can have any one of the three complementary charges. The quarks interact with each other by the exchange of gluons which carry one color and an anticolor charge. The theory describing the strong interactions of the color charged particles is called *Quantumchromodynamics* (QCD) [24].

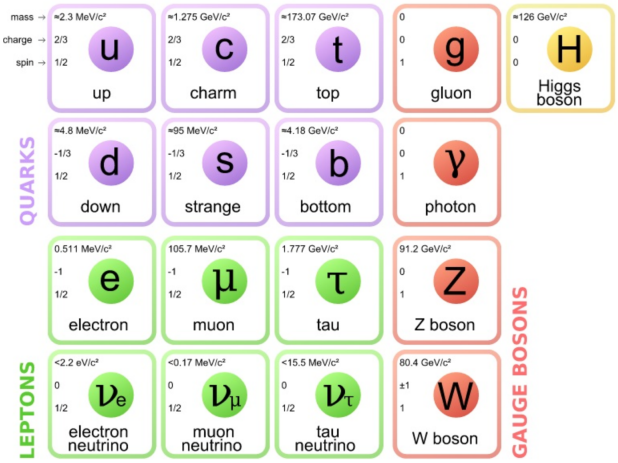

Figure II.1.1: The fundamental particles in the Standard Model of particle physics including quarks (top left), leptons, gauge bosons and the Higgs boson. Leptons don't have color charge, but interact via weak and electromagnetic interactions. The gauge bosons act as the mediators of the fundamental forces and the Higgs boson gives rise to the mass of the quarks and leptons by the Higgs mechanism [25]. Figure taken from [26].

One fundamental feature in QCD is *confinement* [27], which relates to the observation that the quarks and antiquarks do not exist isolated in the nature, but only in bound states of *color neutral* hadrons. Hadrons can be mesons, which are bound states of a quark of one color and an antiquark of the corresponding anticolor, or baryons, which are bound states of three quarks each with a different color. The phenomenon of color confinement is closely related to the feature of *asymptotic freedom* in QCD, where by the force between two quarks becomes asymptotically weaker as the energy increases or as the distance decreases. As the distance between two quarks in a hadron are increased, their interaction energy also increases and at some point it becomes energetically favorable to produce a new quark antiqurak pair from the vacuum which combine with the existing quarks and antiquarks to form mesons or baryons. The quarks are thus confined to distances of the order of the size of a hadron at normal temperatures ($T \sim 0$) and densities (of the order of densities inside nuclei).

As the density of the nuclear matter is increased, or as the temperature is increased which leads to the production of many low mass hadrons, the concept of hadronic matter starts to loose its meaning as each quark will find in its vicinity, at distances smaller than the hadronic radius, a number of quarks. This can lead to screening of the color charge and *deconfinement* whereby the nuclear matter exists in a state of deconfined quarks and gluons which are free to move in a larger volume than the size of a hadron. Such a state of deconfined quarks and gluons is sometimes called the Quark Gluon Plasma (QGP) [28, 29, 30]. Lattice QCD calculations at baryochemical potential (μ_B) of zero indicate that the transition from hadronic matter to the deconfined QGP state occurs around temperatures of ~ 170 MeV [31, 32]. In lattice QCD calculations this change

of state appears as a smooth crossover than a first order phase transition, but it is conjectured that at finite μ_B, the crossover changes into a first order phase transition thereby the suggesting the existence of a QCD critical point [33]. A schematic of the QCD phase diagram is shown in figure II.1.2.

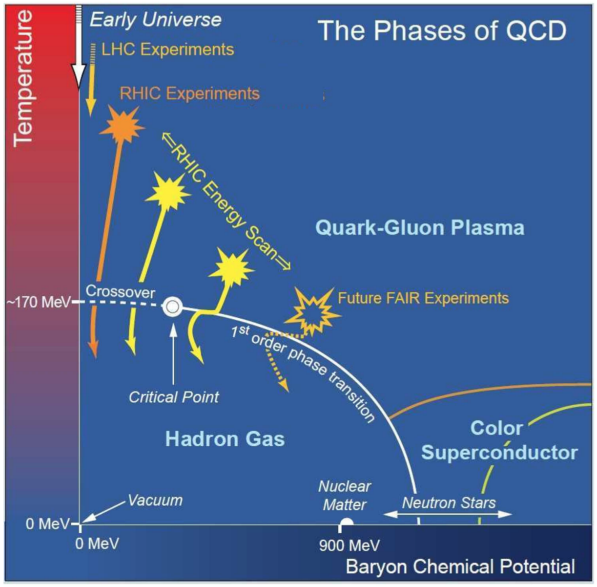

Figure II.1.2: The schematic of QCD phase diagram showing the different phases of QCD matter. The solid lines and the solid circles indicate the hypothesized phase transition curves and critical point respectively. Figure taken from [34].

The nuclear matter in the QGP state is also expected to show *chiral symmetry restoration* [35, 36]. *Chiral symmetry* is an exact symmetry of the QCD in the limit of vanishing quark masses, but is broken at low temperatures by the interaction with the QCD vacuum. In the deconfined QGP phase, as the quark masses are reduced to their small bare masses and the chiral symmetry is approximately restored.

The study of the properties of the QCD matter in the QGP phase, the phenomenon arising from deconfinement and chiral symmetry restoration, and the nature of the phase transition from the state of hadronic matter to deconfined QGP phase are the major focus of the relativistic heavy ion research. As matter is believed to have existed in the QGP state in the very early universe (within first few microseconds after big bang), the study of QGP helps to understand the matter as it existed in the very early universe. Relativistic heavy ion collisions at the RHIC and LHC are expected to produce matter with temperatures high enough for the existence of the QGP phase. The matter exists in the QGP phase only for a short duration of time and will freezeout into hadrons when the system cools down and the temperature falls below a critical value. Therefore, the properties of the QGP need to be understood from the distribution and correlations of the final hadrons observed in the detectors. The next two sections present an outline of the evolution of the

matter in relativistic nuclear collisions and some of the most studied observables to understand the QGP phase, respectively.

II.1.2 Time evolution of relativistic heavy ion collisions

The two Lorentz contracted nuclei travelling at nearly the speed of light collide at $t = 0$, $z = 0$ (z being the beam direction), forming a hot and dense fireball. The fireball evolves through various stages before the final hadrons are produced and they freezeout. The lines indicate the $t = \pm z$ directions. The various stages of the evolution of the fireball (see [37] for a discussion) are indicated in the figure and are described below.

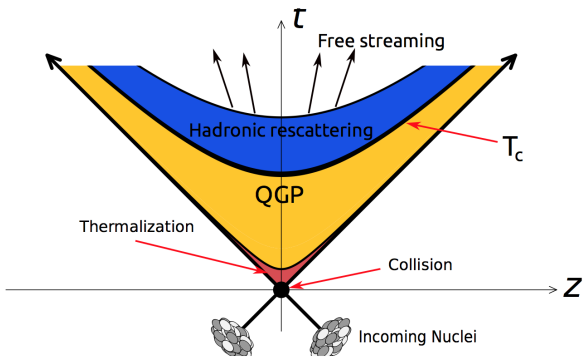

Figure II.1.3: The schematic of the time evolution of a relativistic heavy ion collision. The horizontal axis represents the beam direction and the vertical axis the time. Figure taken from [38]

(i)**Collision of the nuclei and the centrality variable** : The two relativistic nuclei travelling towards each other are Lorentz contracted along the beam direction. At the relativistic energies, the nucleus doesn't collide as one composite object, but the nucleons or the partons inside the nuclei from the two nuclei interact with each other. The time scales of the collisions are related to the inverse of the momentum transfer Q in the collisions. Thus the hard scatterings that produce hight p_{T} particles, jets, heavy quarks and gauge bosons happen in the very early stages of the collisions, followed by the production of lower p_{T} partons ($\mathcal{O}(1)$ GeV) by times ~ 0.2 fm. Most of the entropy in the system is produced in this stage. If the interactions between the produced partons (quarks and gluons) were negligible, the partons would evolve independently into the final state hadrons, as in the case of p+p collisions. However, multiple interactions between the partons lead to establishment of local thermal equilibrium in the produced matter. From model calculations using experimental data, a rapid thermalization is expected to occur, by times ~ 1 fm [37, 39].

The area of overlap of the two nuclei during the collision is characterized by the *centrality* variable [40]. Centrality is quoted in percentile, from 0–100, with the 0% corresponding to the case where the two nuclei overlap completely (or collide head on, referred to as *central* collisions),

while higher values of centrality correspond to cases where the two nuclei overlap partially with increasing separation between their centers (the distance between the centers of the two colliding nuclei is called the *impact parameter*). The collisions with values of centrality close to 100 are called *peripheral* collisions. The centrality is an important variable in characterizing heavy ion collisions, as the geometry and size of the produced system changes with centrality.

In experiments centrality is defined using the distribution of multiplicity or total transverse energy from events which are triggered/selected to come from inelastic collisions, and dividing it into percentile bins [40, 41, 42]. The centrality of a collision is related to the number of nucleons from either nuclei participating in the collision (number or participants, $N_{\rm part}$) and also to the number of binary nucleon nucleon collisions the participants undergo ($N_{\rm bin}$) using models for initial conditions. Usually the standard Glauber model (see Subsection II.2.1.3), which samples the distribution of nucleons participating in a collision to determine $N_{\rm part}$ and $N_{\rm bin}$, and a simple model for particle production that depends on both these variables, is used [43]. Figure II.1.4 shows a schematic of the mapping of the experimental observables to centrality and to the Glauber quantities.

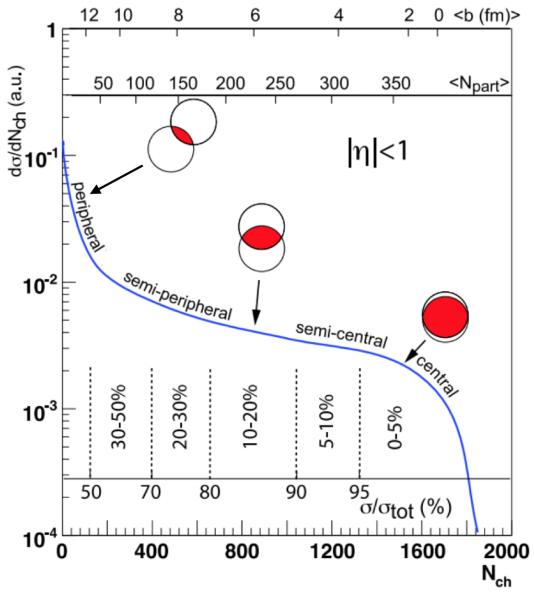

Figure II.1.4: The schematic of the mapping of the experimental observables to centrality variable and to Glauber quantities [43].

(**ii**)**Thermal equillibrium and expansion** : The thermalized system has pressure which acts against the surrounding vacuum, causing it to expand. The expansion phase of the QGP is usually modelled using relativistic hydrodynamics. In fact, the features of the experimental data have shown very good agreement to calculations from a relativistic hydrodynamic expansion of the medium with a very small medium viscosity (specific viscosity, $\eta/s \sim \hbar/4\pi$, near the conjectured lower bound for viscosity) [7, 8, 44]. This has led to the declaration of the discovery of "perfect-

liquid" at RHIC and LHC. The hydrodynamic calculations have been widely used to study the properties of the thermalized QGP. The expansion phase of the medium is also modelled sometimes using partonic transport models [45], which in the limit of zero mean free path approaches hydrodynamics. The partonic transport models have also been successful in describing many features of the data from heavy ion collisions [46]. The high p_{T} partons produced in the initial hard scattering don't thermalize with the bulk medium, but interact with it and loose energy and are modified as they traverse the medium. Studying these 'hard probes' and how they are modified by the medium also reveal valuable insights to the nature of the QGP medium produced.

(**iii**)**Chemical and kinetic freeze out** : As the system expands and the temperature decreases to where the phase transition (or crossover) occurs, the partons start to combine into hadrons. The hadrons still interact with themselves and may maintain local thermal equilibrium. As the system continues to expand, a stage will reach where the inelastic collisions that change the hadron identity become insignificant. This stage is called *chemical freezeout*. The relative abundances of hadrons will remain fixed after the chemical freeze-out. As the system further expands and continues to cool the interactions become too weak to alter the momenta of the particles. This stage is called *kinetic freezeout*. Particles from the kinetic freeze-out hyper surface are observed by the detectors.

II.1.3 Experimental features of QGP

The QGP phase is a transient phase and so any information about it can only be inferred through the study of final state hadrons coming from the collisions. We give a brief overview of some of the experimental observables and features most commonly attributed to the QGP phase and used to study its properties.

Anisotropic flow : One striking observation in heavy ion collisions has been the large anisotropy, in the momentum space, for the azimuthal ($\phi = \tan^{-1}(\mathrm{p_y}/\mathrm{p_x})$) distribution of produced particles [47, 48, 49, 4]. This azimuthal anisotropy in events is often characterized by a Fourier expansion of the particle distribution in azimuth [50, 51]:

$$\frac{dN}{d\phi} \propto 1 + \sum_{n=1}^{\infty} 2v_n \cos\left(n(\phi - \Psi_n)\right), \tag{II.1.1}$$

where the coefficients v_n, sometimes called "flow harmonics", characterize the magnitude of the n^{th} order azimuthal modulations and the phases Φ_n, called the "event plane" angles, reflect the direction of maximum anisotropy for the n^{th} order modulation in the event. The second order coefficient v_2 is called the elliptic flow and is the most studied. The origin of azimuthal anisotropy finds a natural explanation in hydrodynamic evolution of the system. The QGP under local thermal equilibrium expands under the pressure gradients acting on the system. This generates a flow velocity directed radially outwards (*radial flow*). But the pressure gradients acting on the system are not isotropic, as the initial spatial distribution of the energy density in collisions can be azimuthally anisotropic. This is particularly true in the case of mid-central collisions, where the overlap region has a large elliptic anisotropy in the transverse plane. This spatial anisotropy

translates into a momentum space anisotropy under the pressure driven expansion, with the largest values for the elliptic flow v_2 in mid-central collisions. [52, 53]

Figure II.1.5 shows an example of the comparison of anisotropic flow measurements from Pb+Pb collisions compared to hydrodynamic calculations. Excellent agreement is obtained with small values for η/s. The large values for the flow coefficients and excellent agreement with hydrodynamics with a small viscosity are both taken to indicate that the flow develops early in system [39, 37], during the quark-gluon (partonic) phase, and that the system is strongly interacting [54, 55]. The anisotropic flow has been one of the most extensively studied observables at RHIC and LHC as it is an important tool to characterize the properties of the medium including η/s and equation of state and also to constrain the models for initial conditions. And since part of the work in this thesis relates to the flow phenomenon, a more detailed discussion on flow is provided in the next chapter.

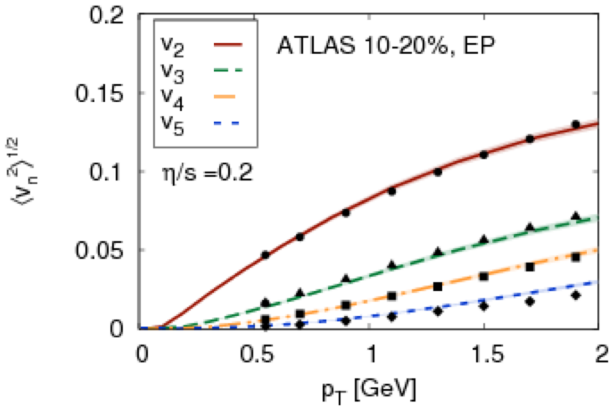

Figure II.1.5: The v_n values from Pb+Pb collisions at LHC by ATLAS (solid points) compared to values from hydrodynamic calculations using $\eta/s = 0.2$ (solid curves) [56].

Jet quenching : The matter produced in heavy ion collisions, particularly in central and mid-central collisions, is observed to be highly opaque to colored particles. This is particularly evidenced by the observation of "jet quenching" [57, 58, 59]. The high p_{T} partons produced from the initial hard scatterings have a large virtuality, which they reduce by radiating gluons or splitting into quark antiquark pairs [60]. The final collimated stream of hadrons resulting from an outgoing parton is called a *jet*. It is observed that the jet yield in central heavy ion collisions is much suppressed relative to the yield expected from a simple superposition of proton-proton collisions. The ratio of the measured to expected yield is denoted by R_{AA} [58]. In central heavy ion collisions jet R_{AA} values close to 0.5 are observed implying that the jets are heavily quenched in the produced medium. The extend of jet quenching is related to the energy lost by the parton in the medium and depends on the properties of the QGP medium through which it is traversing and is a useful tool to access parameters like mean free path λ, opacity ($N = L/\lambda$) or number of scattering centers in medium of length L, Debye mass m_D or inverse of the color screening length in the plasma, the transport coefficient $\hat{q} = m_D^2/\lambda$ or the average transverse momentum square

transferred to the traversing particle per unit path length etc.

Closely related to this effect is the suppression of high p_{T} hadrons, relative to the expected yield from a simple superposition of p+p collisions [61, 62, 63]. The hadron which carries the largest fraction of energy from a fragmenting parton is called the *leading hadron*. If the parent hadron loses energy in the medium, the energy available to the leading hadron will also be reduced and as a result their spectra will show a depletion relative to superposition from p+p collisions. The suppression of high p_{T} hadrons is observed at both RHIC and LHC and is regarded as a strong signature of the QGP phase. Figure II.1.6 shows an example of the R_{AA} for high p_{T} hadrons from RHIC and R_{AA} for inclusive jet production at LHC. It can be seen from the hadron R_{AA} plot that the direct photons (photons from initial hard scatterings or thermal photons from the medium, as opposed to photons from decays), which do not carry a color charge are not suppressed by the medium. Jet quenching and high p_{T} suppression are also widely studied in heavy-ion collisions, but a more detailed discussion is not attempted here.

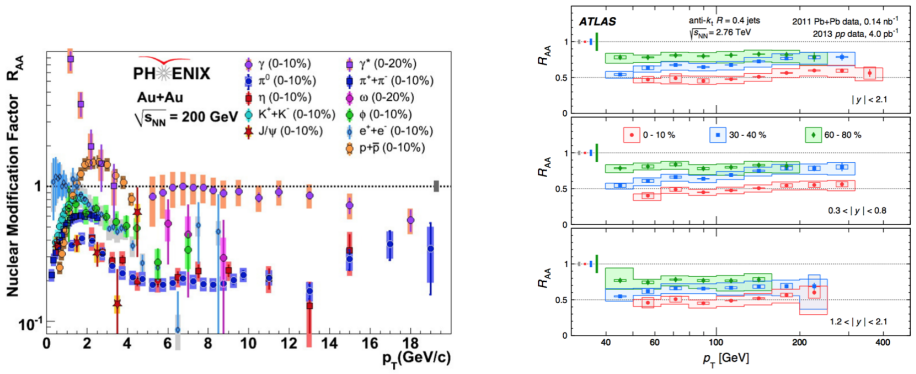

Figure II.1.6: (Left) The R_{AA} for different hadron species and direct photons (purple circles) measured in 200 GeV Au+Au collisions at RHIC by PHENIX Collaboration [64]. (Right) The jet R_{AA} as a function of p_{T} in different rapidity intervals for three different centrality ranges, measured in P+Pb collisions at 2.76 TeV at LHC by ATLAS Collaboration [58].

Strangeness enhancement is another phenomenon commonly attributed to the QGP phase [65]. Thermal production of strange quark antiquark pair production would be enhanced at the QGP temperatures and the yield of strange baryons would also be enhanced relative to p+p collisions. Enhancement of strange baryon production have been observed in the experimental data [66].

Study of the flow and yield of *heavy flavor* hadrons (hadrons containing heavy quarks, charm or bottom) is used as an important tool to study the degree of thermalization and nature of interactions in the medium [67]. Since the heavy quarks have masses higher than the QGP temperature, most of the heavy quark production happens at the initial hard scatterings. This allows for calculations of yields using pQCD and thus allow a clean comparison to the observed modifications in the yield from the presence of the medium. Also, because of their heavier mass, the heavy flavor quarks won't be in equilibrium with the bulk medium and so the flow coefficients measured for heavy flavor hadrons can provide insights into the interactions of heavy quarks with the medium.

Experiments at both RHIC and LHC have observed a significant suppression for heavy flavor yields and values for heavy flavor flow, indicating substantial coupling of the heavy flavor quarks to the QGP medium [68, 69]. More discussion on experimental signatures of QGP can be found elsewhere [70].

Chapter II.2

Flow in heavy ion collisions

The anisotropic flow arises from the initial spatial anisotropy of the fireball in the azimuthal direction and the collective expansion that converts these spatial anisotropies into momentum space anisotropies. The initial spatial geometry in non central heavy ion collisions is dominated by an elliptic shape, leading to large values of v_2. However, there can be other shape components in the initial geometry, like triangularity or dipole asymmetry, that arise from the event by event initial density fluctuations in the collisions [71, 72]. These shape components lead to different order harmonics v_n, and harmonics up to $n = 6$ have been measured in heavy ion collisions at LHC [4]. The magnitudes of the different shape components in the initial geometry are often quantified using the different order eccentricities, ϵ_n, defined as [72]:

$$\epsilon_n e^{in\Phi_n} = \frac{\langle r^n e^{in\phi} \rangle}{\langle r^n \rangle} \tag{II.2.1}$$

where the angular brackets denote the average over the transverse plane in a event and r and ϕ are the radial and azimuthal co-ordinates, and Φ_n represents the phase of the eccentricity plane (sometimes called "participant plane"). The observed flow harmonics v_n, defined by Eq. II.1.1, are related to ϵ_n. For lower order harmonics (v_2 and v_3) the correlation between the two is linear, however for higher orders there can be nonlinear correlations involving ϵ_n of more than one order for a given v_n.

The event by event orientation of the event plane, Ψ_n, is not known in experiments. Also there can be correlations between final produced particles that arise from sources other than flow, including resonance decays, jet fragmentation, local charge conservation etc. Several analysis techniques have been developed, with different sensitivities to the non flow correlations, to measure the flow harmonics (v_n) in experiments. The measured v_n values are compared to values from hydrodynamic calculations to infer the medium properties as well as information regarding the initial state of the system. This chapter presents a brief discussion of relativistic hydrodynamics in the context of heavy ion collisions, in Section II.2.1. Section II.2.2 presents a brief overview of few methods used to measure flow in heavy ion collisions, and that are also relevant to this work.

II.2.1 Relativistic hydrodynamics and anisotropic flow

This section presents only a brief overview to the formalism of relativistic hydrodynamics and its application to heavy ion collisions. The discussion mostly follows the presentation in [73]. The interested reader may refer there for more details. We use the natural units $c = \hbar = k_B = 1$ and the $g^{\mu\nu} = diag(1, -1, -1, -1)$, the Minkowiski metric, in this discussion.

II.2.1.1 Ideal hydrodynamics

The basic equations of ideal (zero viscosity) or viscous hydrodynamics for the system follows from the local conservation laws for the energy-momentum tensor and conserved charges.

$$\partial_\mu T^{\mu\nu} = 0, \quad \partial_\mu N_j^\mu = 0, \tag{II.2.2}$$

where, $T^{\mu\nu}$ is the energy-momentum tensor and N_j^μ is the j^{th} conserved current. For simplicity only the baryon number current need be considered. Also the system has to satisfy the constraint from the second law of thermodynamics,

$$\partial_\mu S^\mu \geq 0, \tag{II.2.3}$$

where S^μ is the entropy current. The currents and the energy-momentum tensor can be written in terms of the *distribution function*, $f(x, p)$, where $f(x, p)d^3xd^3p$ is defined as the average number of particles in a volume d^3x at x and with momenta between $\mathbf{p}$ and $\mathbf{p} + \mathbf{dp}$. The number current and $T^{\mu\nu}$ are then defined as the moments of $f(x, p)$,

$$N^\mu(x) = \frac{1}{(2\pi)^3} \sum_i n_i \int \frac{d^3p}{E} p^\mu f_i(x, p) \tag{II.2.4}$$

$$T^{\mu\nu}(x) = \frac{1}{(2\pi)^3} \sum_i \int \frac{d^3p}{E} p^\mu p^\nu f_i(x, p) \tag{II.2.5}$$

and the entropy current is given by,

$$S^\mu(x) = -\frac{1}{(2\pi)^3} \sum_i \int \frac{d^3p}{E} p^\mu \left[f_i(x, p) \ln(f_i(x, p)) \pm (1 \mp f_i(x + p)) \ln(1 \mp f_i(x, p)) \right], \tag{II.2.6}$$

where the sum is over all particle species and n_i is the amount of conserved charge N_i, carried by the species i (upper signs in the expression are for fermions and lower signs for bosons). The equations of ideal fluid dynamics follows from the condition of local thermal equilibrium, i.e. the time scale for microscopic collisions are much shorter than the time scales of macroscopic evolution of the system and after the collisions the distribution function relaxes instantaneously to the equilibrium form. The equilibrium phase space distribution function can be written as [73]

$$f_{eq}(x, p) = \frac{1}{e^{[p.u(x)+\mu(x)]/T(x)} \pm 1}, \tag{II.2.7}$$

where $u^\mu(x)$ is the local fluid four velocity and $\mu(x)$, the local chemical potential associated with the conserved charge and $T(x)$ is the local temperature of the system. $u^\mu(x)$ is a time like vector with $u^\mu(x)u_\mu(x) = 1$. Substituting II.2.7 into the definitions for particle current, energy density and entropy current, the equilibrium values of these quantities can be obtained.

$$N^\mu_{eq}(x) = n(x)u^\mu(x), \tag{II.2.8}$$

$$T^{\mu\nu}_{eq}(x) = e(x)u^\mu(x)u^\nu(x) - p(x)\Delta^{\mu\nu}(x), \tag{II.2.9}$$

$$S^\mu_{eq}(x) = s(x)u^\mu(x), \tag{II.2.10}$$

where $n(x) = N^0(x)$ is the local net charge density, $e(x) = T^{00}(x)$ is the local energy density and $s(x) = S^0(x)$ is the local entropy density in the fluid local rest frame. $\Delta^{\mu\nu}(x)$ is the projector defined as $\Delta^{\mu\nu}(x) = g^{\mu\nu} - u^\mu(x)u^\nu(x)$ and satisfies $\Delta^{\mu\nu}u_\nu = 0$. $p(x)$ is the hydrostatic pressure in the local fluid rest frame. Substituting Eqs II.2.8–II.2.10 into equation II.2.2, gives the relativistic *ideal fluid equations*:

$$\dot{n} = -n\partial.u \tag{II.2.11}$$

$$\dot{e} = -(e+p)\partial.u \tag{II.2.12}$$

$$\dot{u}^\mu = \frac{\nabla^\mu p}{e+p} = \frac{c_s^2}{1+c_s^2}\frac{\nabla^\mu e}{e}, \tag{II.2.13}$$

where $c_s^2 = \partial p/\partial e$ is the squared speed of sound and $\partial.u$ gives the local expansion rate. $\nabla^\mu = \Delta^{\mu\nu}\partial_\nu$, which in the local rest frame reduces to the time derivative, $\dot{f}$, and the spatial gradient $\nabla\mathbf{f}$.

Equations II.2.11 and II.2.12 describe the dilution of the local net charge and energy density by the expansion, while Eq. II.2.13 describes the acceleration of the fluid arising from the local pressure gradients. The quantity $h = e + p$ is the enthalpy of the system and acts as the inertia to the expansion. Thus anisotropic pressure gradients will give rise to anisotropic expansion rates in the fluid. Together with the equation of state (EOS), $p = p(e, n)$, that relates the three state variables, the ideal fluid equations given in Eqs. II.2.11–II.2.13 form a closed set, which can be solved to determine the fields n, e, p and u^μ.

II.2.1.2 Dissipative hydrodynamics

In reality the system is not ideal and there will be deviations from local thermal equilibrium. The distribution function will be deviated from its equilibrium value, $f(x,p) = f_{eq}(x+p) + \delta f(x,p)$. The expressions for particle current, energy-momentum tensor and the entropy current will be modified from their equilibrium form (Eq. II.2.8–II.2.10). The new expressions will have more terms than the equilibrium case and can be written (under the Landau matching conditions for readjusting the equilibrium temperature and chemical potential) as [73],

$$N^\mu = N^\mu_{eq} + \delta N^\mu = nu^\mu + V^\mu, \tag{II.2.14}$$

$$T^{\mu\nu} = T^{\mu\nu}_{eq} + \delta T^{\mu\nu}_{eq} = eu^\mu u^\nu - (p+\Pi)\Delta^{\mu\nu} + \pi^{\mu\nu} + W^\mu u^\nu + W^\nu u^\mu, \tag{II.2.15}$$

$$S^\mu = S^\mu_{eq} + \delta S^\mu = s u^\mu + \Phi^\mu, \tag{II.2.16}$$

where $V^\mu = \Delta^{\mu\nu} N_\nu$ describe a baryon flow in the local rest frame and $W^\mu = \frac{e+p}{n} V^\mu + q^\mu$, with $q^\mu = (u_\nu T^{\mu\sigma} - h N^\sigma)\Delta^\mu_\sigma$, is the energy flow in the local rest frame. q^μ is called the heat flow vector. $\Pi = -\frac{1}{3}\Delta_{\mu\nu} T^{\mu\nu} - p$ is the viscous bulk pressure and $\pi^{\mu\nu} = \left[\frac{1}{2}\left(\Delta^{\mu\sigma}\Delta^{\nu\tau} + \Delta^{\nu\sigma}\Delta^{\mu\tau}\right) - \frac{1}{3}\Delta^{\mu\nu}\Delta^{\sigma\tau}\right] T_{\tau\sigma}$ is the viscous shear pressure. Φ^μ is an entropy flow vector in the local rest frame. (The Landau matching condition leaves the velocity in the local rest frame u^μ ambiguous. There are two choices, used commonly, the "Eckart frame" where $u^\mu = N^\mu/n$, where there is no baryon flow in the local rest frame, and the "Landau frame", where $u^\mu = T^{\mu\nu} u_\nu / e$, in which there is no energy flow in the local rest frame. For systems with vanishing net baryon number, as in relativistic heavy ion collisions, the Eckart frame is ill defined and so Landau frame will be used here).

The conservation equations (Eq. II.2.2), with the definitions in Eq. II.2.14–II.2.16, gives the "non ideal fluid equations" (in the case of baryon free systems in Landau frame),

$$\dot{e} = -(e + p + \Pi)\partial . u + \pi_{\mu\nu}\langle \nabla^\mu u^\nu \rangle \tag{II.2.17}$$

$$(e + p + \Pi)\dot{u}^\mu = \nabla^\mu (p + \Pi) - \Delta^{\mu\nu}\nabla^\sigma \pi_{\nu\sigma} + \pi^{\mu\nu}\dot{u}_\nu, \tag{II.2.18}$$

where, $\langle A^{\mu\nu} \rangle = \left[\frac{1}{2}\left(\Delta^\mu_\alpha \Delta^\nu_\beta + \Delta^\mu_\beta \Delta^\nu_\alpha\right) - \frac{1}{3}\Delta^{\mu\nu}\Delta_{\alpha\beta}\right] A^{\alpha\beta}$. The viscous shear pressure couples the rate of change of flow velocities along different directions and the viscous bulk pressure adds an isotropic pressure contribution. The non equilibrium decompositions (Eq. II.2.14–II.2.16) involve 9 additional dynamical quantities. The equations II.2.17–II.2.18, in the case of baryon free systems, give three equations. The additional required equations are provided by the second law of thermodynamics ($\partial_\mu S^\mu \geq 0$), by expanding the entropy flow in powers of δN^μ and $\delta T^{\mu\nu}$, along with phenomenological "constitutive relations" between the different physical quantities. The first order expansion in δN^μ and $\delta T^{\mu\nu}$ of the entropy flow gives the Navier-Stokes equations. But these equations are acausal. The problem of causality is removed if the terms up to second order in δN^μ and $\delta T^{\mu\nu}$ are kept in the expansion. These give the Israel - Stewart formalism. The constitutive relations for the case of second order expansion (with additional relaxation terms for the heat conductivity and bulk and shear viscous pressure) can be written as [30],

$$\Pi = -\zeta \nabla^\mu u_\mu - \tau_\Pi D\Pi, \tag{II.2.19}$$

$$q^\mu = \kappa\left(\nabla^\mu T - \frac{T}{e+p}\nabla^\mu p\right) - \tau_q D q^\mu, \tag{II.2.20}$$

$$\pi^{\mu\nu} = 2\eta\langle \nabla^\mu u^\nu \rangle - \tau_\pi D\pi^{\mu\nu}, \tag{II.2.21}$$

where ζ is the bulk viscosity, κ is the heat conductivity and η is the shear viscosity. τ_Π, τ_q and τ_π are relaxation times for the bulk viscous pressure, heat conductivity and shear stress tensor, respectively and $D = u^\mu \partial_\mu$ is the convective time derivative. Together with these relations, the equations for dissipative hydrodynamics can be solved.

The viscosity of a fluid relates to its ability to return to local equilibrium after being driven away from it. Small viscosities are therefore related to small relaxation times and to strong interactions among the microscopic constituents. The bulk viscosity causes locally isotropic deviations

from equilibrium and adds a diagonal contribution which is negative (Eq. II.2.19) to the energy momentum-tensor. Therefore in an isotropically expanding fireball, the bulk viscosity (or the bulk viscous pressure, Π) contributes to reducing the build up of radial flow. Non zero shear viscosity (or the shear pressure tensor) contributes to locally anisotropic deviations from equilibrium to the energy-momentum tensor. The main effect of shear viscosity is that it tries to equalize the expansion rates along different directions. Therefore shear viscosity acts to reduce anisotropies in the transverse flow and thus limits the ability of the medium in converting the initial spatial anisotropies to final momentum anisotropies [5].

II.2.1.3 Initial conditions and freeze-out

The fireball after the collision, evolves hydrodynamically from an initial density profile after local thermal equilibrium is attained. Usually in hydrodynamic calculations, the density profile after thermalization is specified using models, with the model parameters adjusted to reproduce the final state observables from the collisions. Models widely used to specify the transverse initial density profile include the *Glauber* model [74, 43] and models based on the *Color Glass Condensate* theory (CGC) [75], including the Kharzeev-Levin-Nardy (KLN) model [76] and the impact parameter dependent saturation model, IP-Glasma [77]. Historically hydrodynamic calculations have assumed boost invariance along the longitudinal direction and the calculations were restricted to (2+1)-d [78, 79]. (3+1)-d calculations are now available, with different assumptions for the initial density distributions along the longitudinal direction [80, 81]. The initial density distributions along the longitudinal direction and its fluctuations are among the topics of interest in Part V of this thesis. The initial transverse flow velocity is usually taken to be zero in the calculations and usually, an initial longitudinal expansion velocity profile that is boost invariant is assumed [73].

The **Glauber model** assumes a simple model for the initial entropy production, the initial particle production is assumed to depend on the number of wounded nucleons (participants), n_{WN} that take part in the collision and number of binary nucleon-nucleon collisions n_{bin} [73],

$$s(\mathbf{x}_\perp, b) = K\left(x n_{\mathrm{WN}}(\mathbf{x}_\perp, b) + (1-x) n_{\mathrm{bin}}(\mathbf{x}_\perp, b)\right), \tag{II.2.22}$$

where $\mathbf{x}_\perp$ is the transverse coordinate and b is the impact parameter. The parameter x and the overall normalization constant K are adjusted to match the measured multiplicity distribution from the data. The number of wounded nucleons and binary collisions are calculated from a geometric model. The density distributions inside the colliding nuclei are assumed to follow the Woods-Saxon profile,

$$\rho(r) = \frac{\rho_0}{e^{r-R/\xi}+1} \tag{II.2.23}$$

The distribution is usually normalized to unity. ρ_0 is the nucleon density, R is the nuclear radius and ξ is the surface diffusiveness [82]. The nuclear thickness function is the probability to find a nucleon in the nucleus at transverse position $r = (x, y)$, and is given by

$$T(x,y) = \int_{-\infty}^{\infty} \rho(x,y,z)dz \tag{II.2.24}$$

For two nuclei, A and B, colliding with an impact parameter b along the horizontal direction, the number of binary nucleon-nucleon collisions at (x, y) is proportional to the product of the nuclear thickness functions of the two nuclei, at the point

$$n_{\rm bin}(x, y, b) = \sigma_0 T_A(x + b/2, y) T_B(x - b/2, y), \tag{II.2.25}$$

σ_0 is the total inelastic nucleon nucleon cross-section. It enters only as a normalization constant in Eq II.2.25 and is later absorbed into the normalization to determine the entropy production, Eq. II.2.22. The total number of binary nucleon nucleon collisions is given by integrating over the transverse plane,

$$N_{\rm bin}(b) = \int n_{\rm bin}(x, y, b) dx dy, \tag{II.2.26}$$

The number of wounded nucleons is the total number of nucleons from either nucleus which undergo at least one collision. The number of wounded nucleons in the Glauber model can be calculated as,

$$\begin{aligned} n_{\rm WN}(x, y, b) = T_A(x + b/2, y) \left(1 - \left(1 - \frac{\sigma_0 T_B(x - b/2, y)}{B}\right)^B\right) \\ + T_B(x - b/2, y) \left(1 - \left(1 - \frac{\sigma_0 T_A(x - b/2, y)}{A}\right)^A\right) \end{aligned} \tag{II.2.27}$$

where A and B are the mass numbers of the two nuclei. The total number of wounded nucleons is obtained by integrating over the transverse plane.

The color glass condensate theory treats the nuclei as dense gluon systems with a saturation scale, $Q_{\rm sat}$, above which the low x (longitudinal momentum fraction) gluon density saturates. The small x gluons are approximated as static classical fields in this theory. CGC can be used to calculate the cross sections in high energy collisions, distribution of produced particles in the collisions and also the initial conditions for heavy-ion and high energy collisions. A detailed description of the CGC theory and the different models based on it can be found in the references listed above.

The hydrodynamic equations give the evolution of the system till a 'freeze out condition', where the system deviates far from local equilibrium. The particle current and energy density fields at the end of hydrodynamic evolution needs to be converted into a particle spectra. This is done through the *Cooper − Frye* formalism [83]. The momentum distribution of particles from the Cooper-Frye formalism is given as,

$$E\frac{dN_i}{d^3p} = \frac{g_i}{2\pi^3} \int_\Sigma p.d^3\sigma(x) f_i(x, p), \tag{II.2.28}$$

where $\Sigma(x)$ is the three dimensional surface at which the freeze-out happens, $d^3\sigma(x)$ is an outward normal vector to the freeze-out surface and $p.d^3\sigma(x) f_i(x, p)$ gives the flux of particles of type i and momentum p through this surface. g_i is the degeneracy of the particle and $f_i(x, p)$ is the phase space distribution function just before the freeze-out. In the case of ideal hydrodynamics, the distribution function is given by Eq II.2.7, with the velocity, temperature and chemical potential fields taking values just before the freeze-out.

II.2.2 Methods for studying flow in heavy ion collisions

The anisotropic flow have been studied at RHIC and LHC quite extensively. Different experimental methods, with different sensitivities to non flow and event-by-event fluctuations in flow magnitude, are used to measure the v_n harmonics. One of the more common methods used to measure v_n is the "Event Plane (EP) method" [51, 4], in which the event plane angle Ψ_n is determined event by event using particles in a subset of the detector, usually in a specific region in η, and then the v_n are measured using particles in another region of the detector, as the correlation relative to this observed event plane. This method requires detector regions extend over η and also the measured values need to be corrected for "event plane resolution" arising from the statistical smearing in determining the event plane angle. Also the non-flow correlations between the regions used for event plane determination and v_n measurement contribute to the measured values. A modification of the EP method called the Scalar Product method is also used in flow measurements [84].

Another frequently used technique is the Two Particle Correlation (2PC) method [3, 4]. In this, the flow correlations are calculated from pair distributions averaged over many events. This has the advantage that the determination of the event plane is not required. But the 2PC method also is biased by contributions from non-flow, as pair correlation can arise from other sources like resonance decays, jets etc. Most of these non flow correlations are localized in small $|\Delta\eta|, |\Delta\phi|$ and hence can be suppressed by requiring a minimum $|\Delta\eta|$ cut. Alternatively, correlations involving higher number of particles, 4, 6 and 8 particles, and cumulants constructed from these multi-particle correlations have been proposed and used to measure flow [85, 86, 87]. These multi particle cumulants are expected to suppress non flow correlations, by excluding correlations involving lesser number of particles. For example in the 4 particle cumulants, the non-flow contributions from pair correlations get subtracted out [85]. A method involving correlations between all particles using Lee-Yang zeros is also used [88]. A detailed discussion of each of these methods can be found in the references quoted. Here we summarize the 2PC and the multi-particle cumulant methods, as they are used for the studies presented in Part IV.

II.2.2.1 'Ridge' and the two particle correlation method

The anisotropic flow causes all particles in the event to be correlated with the direction of the event plane, Ψ_n. Since any two particles are correlated with the event plane, they are also correlated with each other and this correlation can be used to measure the magnitude of the flow harmonics v_n. The two particle correlation functions, $C(\Delta\eta, \Delta\phi)$, are constructed as pair distributions in the relative azimuthal angle $\Delta\phi = \phi^a - \phi^b$ and the pseudorapidity difference $\Delta\eta = \eta^a - \eta^b$ between the two particles in the pair, averaged over many events. The two particles in the pair a and b and sometimes referred to as "trigger" particle and "associated" particle respectively. The overall normalization is usually set to make the average of the correlation function in the $\Delta\eta, \Delta\phi$ phase space 1. In experiments, the two particle correlation functions are constructed as the pair distribution using pairs from the same event ($S(\Delta\eta, \Delta\phi)$), averaged over many events, divided by the pair distribution using pairs from different events ($B(\Delta\eta, \Delta\phi)$), averaged over many different

event pairs [3, 4].

$$C(\Delta\eta, \Delta\phi) = \frac{S(\Delta\eta, \Delta\phi)}{B(\Delta\eta, \Delta\phi)} \tag{II.2.29}$$

The normalization of $B(\Delta\eta, \Delta\phi)$ is chosen appropriately to have the same total number of pairs as in $S(\Delta\eta, \Delta\phi)$. The overall normalization is not so important for the extraction of v_n as they are defined as modulations relative to the average (Eq. II.1.1). The division by $B(\Delta\eta, \Delta\phi)$ (often called "mixed-event distribution") helps to remove any correlations that arise from detector features in the correlation function [38]. The non-flow correlations have the largest contribution to the correlation function at small $|\Delta\eta|$. Therefore the azimuthal analysis is performed on the projected 1D correlation function $C(\Delta\phi)$, defined by averaging over the large $|\Delta\eta|$ region, usually with $|\Delta\eta| > 1$.

In the ideal case, where $B(\Delta\eta, \Delta\phi) = 1$ everywhere, the correlation function can be thought of as the convolution of the single particle distribution, $\frac{dN(\phi)}{d\phi}$ [38].

$$C(\Delta\phi) \propto \int \frac{dN^a(\phi_1)}{d\phi_1} \frac{dN^b(\phi_2)}{d\phi_2} \delta(\phi_1 - \phi_2 - \Delta\phi) d\phi_1 d\phi_2 \tag{II.2.30}$$

The superscripts a and b are to indicate that the single particle distributions can be from different p_{T} ranges or different kind of particles etc. Using Eq. II.1.1,

$$\begin{aligned}
C(\Delta\phi) &\propto \int \left(1 + \sum_{n=1}^{\infty} 2v_n^a \cos\left(n(\phi_1 - \Psi_n)\right)\right) \\
&\times \left(1 + \sum_{m=1}^{\infty} 2v_m^b \cos\left(m(\phi_2 - \Psi_m)\right)\right) \delta(\phi_1 - \phi_2 - \Delta\phi) d\phi_1 d\phi_2 \\
&= \int \left(1 + \sum_{n=1}^{\infty} 2v_n^a \cos\left(n(\phi_1 - \Psi_n)\right)\right) \\
&\times \left(1 + \sum_{m=1}^{\infty} 2v_m^b \cos\left(m\phi_1 - m\Delta\phi - m\Psi_m\right)\right) d\phi_1 \\
&= \int \left(1 + 4 \sum_{n,m=1}^{\infty} v_n^a v_m^b \cos\left(n\phi_1 - n\Psi_n\right) \cos\left(m\phi_1 - m\Delta\phi - m\Psi_m\right)\right),
\end{aligned} \tag{II.2.31}$$

where we have used the fact that $\int \cos(k\phi + const) d\phi = 0$ when integrated over the full azimuth. The product in the sum can be recast using the sum rule for cosines, $2\cos A \cos B = \cos(A + B) + \cos(A - B)$. The term with the sum of the angles goes to zero on integration and for the term with the difference of angles, the only non zero contribution comes from the case with $n = m$. This leads to

$$C(\Delta\phi) \propto \int 1 + 2 \sum_{n=1}^{\infty} v_n^a v_n^b \cos\left(-n\Delta\phi\right) d\phi_1 \tag{II.2.32}$$

The integration gives an overall normalization constant, and expanding the left hand side also in a Fourier series, we have,

$$1 + 2\sum_{n=1}^{\infty} v_{n,n}^{a,b} \cos\left(n\Delta\phi\right) = 1 + 2\sum_{n=1}^{\infty} v_n^a v_n^b \cos\left(n\Delta\phi\right), \tag{II.2.33}$$

where $v_{n,n}^{a,b}$ are the coefficients in the expansion of $C(\Delta\phi)$. This relates the coefficients in the expansion of the two particle correlation function as the product of the coefficients in the expansion of the single particle distribution.

$$v_{n,n}^{a,b} = v_n^a v_n^b, \tag{II.2.34}$$

and the single particle coefficients can be obtained from $v_{n,n}$ using the *factorization relation*,

$$v_n^a = \frac{v_{n,n}^{a,b}}{\sqrt{v_{n,n}^{b,b}}}. \tag{II.2.35}$$

The above derivation assumes that the event plane angles, $\Psi_{n(m)}$, both particles see are the same. This in general is not true, as the event plane angle is can depend of the pseudorapidity, η, or p_{T} value used [89, 90]. As a result, the factorization relation II.2.35 has been shown to give slightly different values for v_n^a depending on the choice of v_n^b [90].

Figure II.2.1 (left panel) shows an example of the 2PC function, $C(\Delta\eta, \Delta\phi)$, measured in central Pb+Pb collisions at the LHC. The correlation function shows a dominant "ridge-like" peak around $|\Delta\phi| \sim 0$ and $|\Delta\phi| \sim \pi$, that extends over the entire measured $\Delta\eta$ range. These long-range (extending to large pseudorapidity differences) correlations in the 2PC are sometimes referred to as the "ridge" and reflects the contribution to the correlation function from the flow harmonics (Eq. II.2.32). The correlation function also shows a peak at small $(|\Delta\phi|, |\Delta\eta|)$ values. This peak arises from short-range correlations like resonance decays, jets, fragmentation etc. The contribution from this peak to the flow analysis can be avoided by using only the region with large $|\Delta\eta|$, outside the short-range peak, to construct the 1D correlation $C(\Delta\phi)$. The 1D projection in the large $|\Delta\eta|$ region is shown in the right panel of the figure, overlaid with contributions from the individual $v_{n,n}, n \leq 6$ components and their sum. The azimuthal structure can be quite well described by including modulations up to order 6.

The non-flow correlations cannot be completely removed by the $|\Delta\eta|$ cut in the 2PC. For example, back to back decay pairs and dijets can contribute to the peak near $|\Delta\phi| \sim \pi$, even at large $|\Delta\eta|$ values. This is because the dijets or decay pairs are emitted back to back in azimuth to conserve transverse momentum, but their longitudinal momenta are not constrained. This leads to a much broader peak on the away side from these non-flow sources. The contribution to the 2PC from the non-flow sources grow with centrality, towards more peripheral collisions, roughly as $1/N$, N being the number of produced particles [91]. Thus the 2PC method will have large bias in measuring the v_n values from the global correlations as one goes to more peripheral event classes or small collision systems, where the produced multiplicity is small.

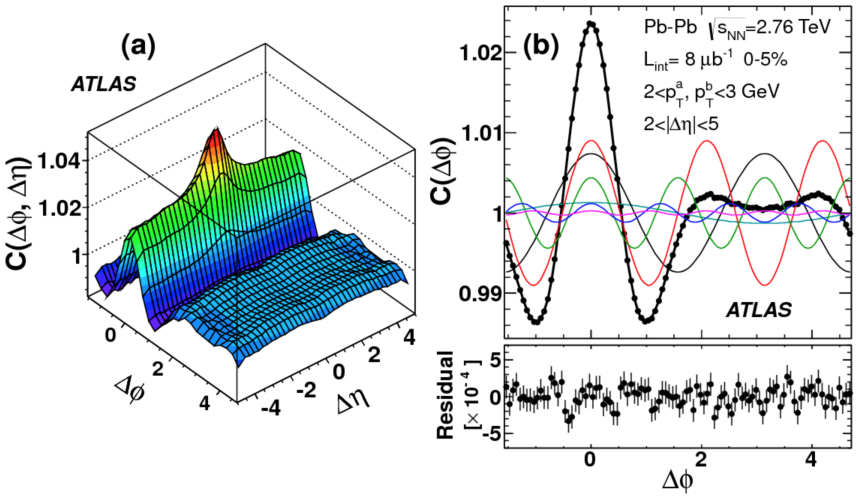

Figure II.2.1: (Left) The two particle correlation function measured in 0-5% central Pb+Pb collisions at the LHC using the ATLAS detector. (Right) The 1D correlation function $C(\Delta\phi)$ for the region with $|\Delta\eta| > 2.0$, overlaid with contributions from the individual $v_{n,n}, n \leq 6$ components and their sum. The smaller panel on the right show the deviation of the data points from the Fourier sum [4].

II.2.2.2 Multi-particle correlations and cumulants

Multi-particle cumulants using correlations between two and more particles are proposed to suppress the contributions of non flow to the flow measurements. The m particle correlations are defined by correlating m particles at a time and averaging over the set of all m particle combinations in the event, and then averaging over the events. For e.g. the 2 and 4 particle correlations in a single event for the n^{th} order harmonic, are defined as [86],

$$\langle 2_n \rangle \equiv \frac{1}{P_{N,2}} \sum_{i \neq j} e^{in(\phi_i - \phi_j)}, \tag{II.2.36}$$

$$\langle 4_n \rangle \equiv \frac{1}{P_{N,4}} \sum_{i \neq j \neq k \neq l} e^{in(\phi_i + \phi_j - \phi_k - \phi_l)}, \tag{II.2.37}$$

where $P_{N,m} = N!/(N-m)!$ and the sums are over combinations in which no indices are the same. The event averaged correlations are defined by averaging over many events, and optimally the averaging is done by weighting each event by the number of 2 particle or 4 particle combinations in the event, in order to minimize contributions from multiplicity fluctuations [86].

$$\langle\langle 2_n \rangle\rangle \equiv \frac{\sum_{events} W_{\langle 2 \rangle i} \langle 2 \rangle_i}{\sum_{events} W_{\langle 2_n \rangle i}}, \tag{II.2.38}$$

$$\langle\langle 4_n\rangle\rangle \equiv \frac{\sum_{events} W_{\langle 4\rangle i}\langle 4\rangle_i}{\sum_{events} W_{\langle 4_n\rangle i}}, \tag{II.2.39}$$

where the weights $W_{\langle m\rangle}$ are given as

$$W_{\langle 2\rangle} = N(N-1), \quad W_{\langle 4\rangle} = N(N-1)(N-2)(N-3) \tag{II.2.40}$$

Six and eight particle correlations, $\langle\langle 6_n\rangle\rangle$ and $\langle\langle 8_n\rangle\rangle$ can also be defined in a similar manner [92]. Using the event averaged multi particle correlations, the multi-particle cumulants are then defined as,

$$c_n\{2\} = \langle\langle 2_n\rangle\rangle \tag{II.2.41}$$

$$c_n\{4\} = \langle\langle 4_n\rangle\rangle - 2\langle\langle 2_n\rangle\rangle^2 \tag{II.2.42}$$

$$c_n\{6\} = \langle\langle 6_n\rangle\rangle - 9\langle\langle 4_n\rangle\rangle\langle\langle 2_n\rangle\rangle + 12\langle\langle 2_n\rangle\rangle^3 \tag{II.2.43}$$

$$c_n\{8\} = \langle\langle 8_n\rangle\rangle - 16\langle\langle 6_n\rangle\rangle\langle\langle 2_n\rangle\rangle + 18\langle\langle 4_n\rangle\rangle^2 + 144\langle\langle 4_n\rangle\rangle\langle\langle 2_n\rangle\rangle^2 - 144\langle\langle 2_n\rangle\rangle^4 \tag{II.2.44}$$

The above definitions for m particle cumulants are proposed to contain only the correlations involving m particles or higher. For example, in the definition of the 4 particle cumulants, the contributions from 2 particle combinations are subtracted out and thus contain correlations from flow (which produces correlations between all particles) and non flow contributions in which 4 (or more) particles are correlated with each other. The latter contribution varies with multiplicity as $1/N^3$, where N is the multiplicity. In general, the contribution from non flow sources to the $2k^{\text{th}}$ order cumulant is of the order of $1/N^{2k-1}$ [85].

The two particle cumulant (and the two particle correlator) just compute the average of $\cos(n(\phi_i - \phi_j))$ and from the definition of Fourier expansion, is equivalent to the $v_{n,n}$ coefficient calculated from two particle correlations. In the case where there is correlations only from flow, and if the magnitude of flow is same across events, then the two particle correlator $\langle\langle 2_n\rangle\rangle$ is equal to v_n^2 (from the factorization relation). Similar consideration shows that in the case of constant flow and no other correlation in the system, $\langle\langle 4_n\rangle\rangle$ gives $-v_n^4$, $\langle\langle 6_n\rangle\rangle$ gives v_n^6 and so on [85]. Therefore, from the cumulants $c_n\{2k\}$, the magnitude of the flow harmonics v_n may be approximated as

$$v_n\{2\} = \sqrt{c_n\{2\}}, \;\; v_n\{4\} = \sqrt[4]{-c_n\{4\}}, \;\; v_n\{6\} = \sqrt[6]{c_n\{6\}/4}, \;\; v_n\{8\} = \sqrt[8]{-c_n\{8\}/33}, \tag{II.2.45}$$

where $v_n\{2k\}$ denote the value of v_n calculated using the $2k^{\text{th}}$ order cumulant. Since the non flow is progressively suppressed in the higher order cumulants, the $v_n\{2k\}$ from the higher order cumulants are expected to converge as the value of k is increased.

This convergence is also expected if the flow is not constant, and fluctuating from event to event, but the fluctuations are Gaussian. In the case of Gaussian fluctuations the probability distribution for the event-by-event flow vector, $\vec{v_n} = (v_n\cos(n\Psi_n)), v_n\sin(n\Psi_n)$, would be given by,

$$p(\vec{v_n}) = \frac{1}{2\pi\delta_{v_n}^2} e^{-(\vec{v_n} - \vec{v_n^{RP}})^2/2\delta_{v_n}^2}, \tag{II.2.46}$$

where $\vec{v_n}^{RP}$ is the average flow vector in the event class, usually associated with the flow arising from the average geometry or relative to the "reaction plane" (reaction plane (RP) is the plane

defined by the impact parameter and the beam axis), and δ_{v_n} characterize the width of the fluctuations. The magnitude of flow v_n then has a Bessel Gaussian distribution, after averaging over the azimuthal direction.

$$p(v_n) = \frac{v_n}{\delta^2_{v_n}} e^{-\frac{(v_n)^2+\left(v_n^{RP}\right)^2}{2\delta^2_{v_n}}} I_0\left(\frac{v_n^{RP} v_n}{\delta^2_{v_n}}\right), \tag{II.2.47}$$

where $I_0(x)$ is the modified Bessel function of the first kind. If the distribution of v_n follows a Bessel Gaussian distribution, then the moments, $\langle v_n^{2k}\rangle$ (the multi-particle correlators $\langle\langle 2k_n\rangle\rangle$ in the case of zero non flow and statistical fluctuations) are as follows [93],

$$\langle v_n^2\rangle = (v_n^{RP})^2 + 2\delta^2_{v_n}, \tag{II.2.48}$$

$$\langle v_n^4\rangle = (v_n^{RP})^4 + 8(v_n^{RP})^2\delta^2_{v_n} + 8\delta^4_{v_n}, \tag{II.2.49}$$

$$\langle v_n^6\rangle = (v_n^{RP})^6 + 18(v_n^{RP})^4\delta^2_{v_n} + 72(v_n^{RP})^2\delta^4_{v_n} + 48\delta^6_{v_n} \tag{II.2.50}$$

Substituting these in the definition of the cumulants, $c_n\{2k\}$, it can be seen that,

$$c_n\{2\} = (v_n^{RP})^2 + 2\delta^2_{v_n}, \quad c_n\{4\} = -(v_n^{RP})^4, \quad c_n\{6\} = 4(v_n^{RP})^6 \tag{II.2.51}$$

The $v_n\{2k\}$ from the higher order cumulants thus converge to v_n^{RP}. This convergence of the higher order cumulants is often considered as evidence for the existence of collective flow in the system.

Figure II.2.2 shows the $v_n\{2k\}$ calculated from different order cumulants measured in Pb+Pb collisions at the LHC. The $v_n\{2\}$ values are larger than that calculated from the higher order cumulants through out the p_{T} range, while the higher order cumulants give consistent results.

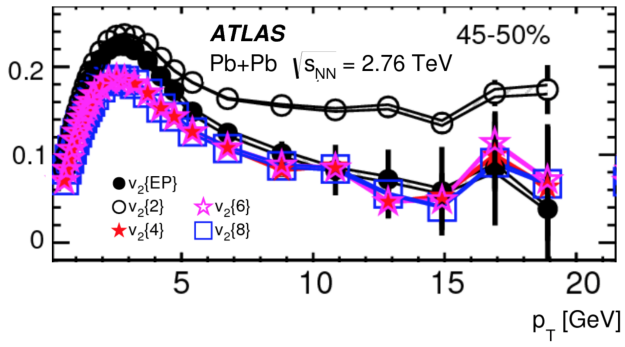

Figure II.2.2: The $v_n\{2k\}$ from 2 particle, 4 particle, 6 particle and 8 particle cumulants as a function of p_{T} measured in 40-45% Pb+Pb collisions at the LHC using ATLAS detector [87].

In practice, in doing experimental data analysis, calculating $\langle\langle 2k\rangle\rangle$ directly from the particle combinations is computationally costly. Instead these correlators are calculated using the magnitude of the flow vector Q_n [86], defined as,

$$Q_n = \sum_{i=1}^{N} e^{in\phi}, \tag{II.2.52}$$

where the sum runs over all or a subset of the particles in an event. From the definition of Q_n, it can be seen that $\langle\langle 2k\rangle\rangle$ can be obtained from the powers of Q_n, provided the terms where more than one index are the same are subtracted out. This can be calculated in a straight forward way and the cumulants calculated in this manner are some times called $Q-$ *cumulants* or *direct cumulants*. The expressions, for example, for the 2 and 4 particle correlators using Q_n are given below [86].

$$\langle\langle 2\rangle\rangle = \frac{|Q_n|^2 - N}{N(N-1)} \tag{II.2.53}$$

$$\begin{aligned}\langle\langle 4\rangle\rangle = &\frac{|Q_n|^4 + |Q_{qn}^2| - 2\Re(Q_{2n}Q_n^*Q_n^*)}{N(N-1)(N-2)(N-3)} \\ &- 2\frac{2(N-2)|Q_n|^2 - N(N-3)}{N(N-1)(N-2)(N-3)}\end{aligned} \tag{II.2.54}$$

Chapter II.3

Ridge in small systems and longitudinal correlations in heavy ion collisions

We are concerned in this thesis with two topics, that are some what beyond the general picture of heavy ion collisions presented in the last two chapters, but are intimately connected with and of importance to augment our understanding of the production and evolution of matter in heavy ion collisions. Both these topics concern with the existence of long-range correlations in high energy nuclear collisions. The first topic concerns with the observation of long-range "ridge" (see Subsection II.2.2.1) in two particle correlations in small collisions systems, particularly in high multiplicity p+Pb collisions [10, 9]. The multiplicities produced in the highest multiplicity p+Pb collisions can reach comparable values as ∼60% central Pb+Pb collisions, where ridge correlations are observed and usually attributed to collective flow. However, it is unclear and debated, if a thermalized QGP medium and hydrodynamic like collective expansion can happen in p+Pb collisions owing to the small size of the system produced [14]. Also the observation of the ridge in small system has inspired calculations in which the ridge arise from correlations in initial state, which do not require thermalization or hydrodynamic expansion [94]. Basic results on the observation of the ridge correlations in p+Pb system were existing before this thesis work was undertaken. In this work, we attempt to further the study of the two particle ridge correlations in p+Pb with a view to provide insights into the origin of these correlations. We also look into the effectiveness of using multi-particle cumulants to search for evidence of global collective flow (or "collectivity") in small collision systems.

The second topic is the study of the correlations between the total multiplicity produced at different pseudorapidity intervals. These correlations can arise from early time density fluctuations in the pseudorapidity direction which produce correlations between particles separated by large η difference (long-range correlations (LRC)) or from later stages of the system evolution including resonance decays, jet fragmentation, hadronization etc, producing correlations between particles closer to each other in η (typically within $|\Delta\eta| < 1.0$, and are called short-range correlations

(SRC)) [95]. The multiplicity correlations between pesudorapidities are sometimes referred to as "longitudinal correlations", as unlike the ridge correlations, these correlations are not very sensitive to the transverse expansion dynamics of the medium, or correlations in particle production along the transverse direction.

Measurements of such multiplicity correlations in pseudorapidity have been carried out since the early days of heavy ion collisions and results for top energy Au+Au collisions at RHIC and also for collisions at LHC exist [96, 95, 19, 97]. But these measurements have usually been carried out in a limited region in the two particle η_1, η_2 phase space, typically in symmetric pseudorapidity windows around $\eta = 0$ (and hence are also referred to as "forward-backward correlations"). The usually measured quantities do not separate the contributions from the SRC and LRC and also have contributions from statistical fluctuations from finite multiplicity effects which makes it difficult to interpret the results. Motivated by some recent suggestions from the theory side, we develop a new method to measure the longitudinal correlations in the full two particle phase space and without biases from statistical fluctuations. We also separate the correlations arising from SRC and LRC, in a data driven way. These measurements can help clarify the nature and origin of the longitudinal correlations in heavy ion collisions. The measurements are also of importance in providing constraints to the initial density distributions along the pseudorapidity direction and contributing towards more realistic (3+1)d simulations of heavy ion collisions.

In this chapter we provide an introduction to these two topics. We present a brief overview of the existing observation and results, briefly discuss the theoretical interpretations or models that are current on these topics and then present an overview of the focus and scope of the research carried out in this thesis work. Section II.3.1 will present the introduction to the topic of ridge in small systems while the research into the longitudinal correlations in heavy ion collisions are introduced in Section II.3.2.

II.3.1 Ridge in small collision systems

II.3.1.1 The observation: ridge in p+p and p+Pb collisions

The first observation of the ridge in small collision systems was made in 2010, by the CMS Collaboration. The two-particle correlation functions in high-multiplicity proton-proton collisions (for events that produces around (or more than) 60 charged particles), were shown to have a small but qualitatively similar ridge on the near-side ($|\Delta\phi| \sim 0$), as the ridge seen in 2PC in heavy ion collisions [9]. The ridge on the near side extends to at least 4 units of pesudorapidity difference, as shown in figure II.3.1, and cannot be attributed to mini-jets or correlations from fragmentation and decays. The ridge correlations were also found to be absent in the PYTHIA MC event generator, widely used to model the p+p collisions at the LHC. It was also shown that the per-trigger-yield (number of pairs per "trigger" particle, see Subsection II.2.2.1) on the near side increases with increase in number of charged particles produced in the collision (figure II.3.1). The signal was observed to be maximum in the p_{T} range $1 < p_{\mathrm{T}} < 3$ GeV and also found to be the same for like and unlike sign charged pairs. The ridge correlations were not expected in such small systems and came as a rather surprising observation [14].

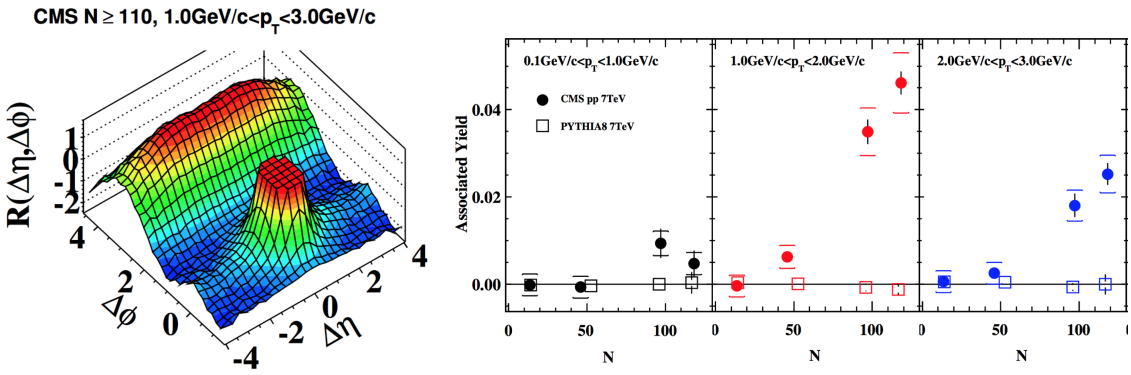

Figure II.3.1: (Left) The two-particle correlation function in $\Delta\eta, \Delta\phi$ for events with $N_{\rm trk}^{\rm offline} \geq 110$ and (right) Associated yield on the near-side for the correlation function integrated over the region of $2.0 < |\Delta\eta| < 4.8$, as a function of event multiplicity in bins of $p_{\rm T}$, for p+p collisions at $\sqrt{s} = 7$ TeV [9].

A proton - lead pilot run was conducted at the LHC in late 2012 (a small run with limited statistics, $L_{\rm int} \sim 1\mu{\rm b}^{-1}$). Analysis of the data from the proton-lead pilot run revealed a similar near-side ridge in two particle correlations, but with larger magnitude than that observed in p+p collisions and comparable to that in heavy ions. The ridge was most prominent in events with high multiplicity [10]. It was also shown that, if one subtracted the per-trigger-yield from a low multiplicity event class, the two particle correlations showed a "double ridge", with an away-side component with similar magnitude and transverse momentum ($p_{\rm T}$) and multiplicity dependence as the near-side (figure II.3.2) [13, 12]. This was a striking observation as the double ridge is a familiar feature in heavy ion collisions (particularly mid-central collisions), where it reflects the contribution from the product, $v_2^a v_2^b$ [4].

The second and third order Fourier coefficients (v_2 and v_3) associated with the particle distribution in azimuth were also measured from the two-particle correlations, after doing the peripheral yield subtraction. The values were measured up to $p_{\rm T}$ of $5 - 6$ GeV for the trigger particle, and were found to have a qualitatively similar $p_{\rm T}$ dependence as was observed in A+A collisions [12]. Initial measurements from four particle cumulants also showed non-zero values of v_2, suggesting a global correlation event-by-event [98]. Following the observations at LHC, similar long-range azimuthal correlations were also observed in high multiplicity d+Au collisions at RHIC [11].

Following the pilot run, a high statistics p+Pb run ($L_{int} \sim 28n{\rm b}^{-1}$) was conducted at the LHC in early 2013. The high statistics data allowed the measurements to be extended to higher multiplicities and also to get more detailed measurements of v_2 and v_3. A few measurements that showed further similarities with the ridge in A+A collisions were published along the course of this research. These include similar particle species dependence for the v_2 harmonic as in A+A collisions and also a higher precision measurement of the $v_2\{4\}$ values from the four particle cumulants [99, 100]. It was also observed by the CMS collaboration that the v_3 values had similar magnitudes between the p+Pb and Pb+Pb systems at a given multiplicity [100]. These were

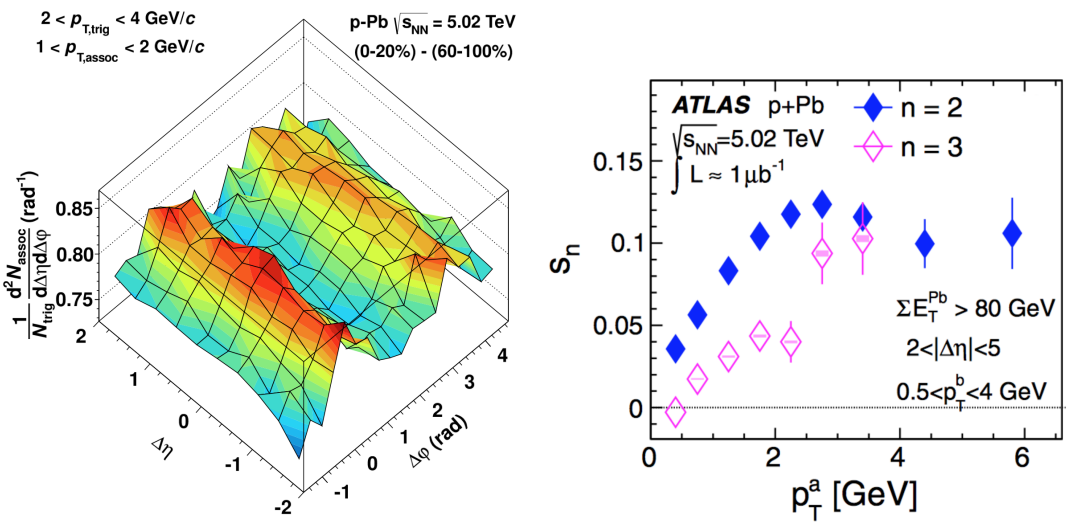

Figure II.3.2: (Left) ALICE measurement of the associated yield per trigger particle in $\Delta\phi$ and $\Delta\eta$ for pairs of charged particles in pPb collisions at $\sqrt{s_{NN}} = 5.02$ TeV for the 020% multiplicity class, after subtraction of the associated yield obtained in the 60-100% event class [13]. (Right) ATLAS measurement of the p_{T} dependence of the v_2 and v_3 (denoted as s_n in figure) harmonics from the associated yield in a high multiplicity event class, obtained after subtracting the associated yield in a low-multiplicity event class [12].

argued to point towards a similar origin for the ridge in the two collision systems.

II.3.1.2 Theoretical interpretations

Different theoretical origins have been proposed for the correlations observed in high multiplicity p+p and p+Pb collisions. One set of models attribute these correlations to a mechanism similar to that in heavy ion collisions: i.e. it is associated with initial state density fluctuations arising from the fluctuations of the sub-nucleonic structures in the transverse plane and the scatterings of partons or hydrodynamic expansion in the final state [101, 102, 14, 15]. The latter may be correlated to the requirement of high multiplicity. The p+Pb (and d+Au) collisions are also found to have non zero values for second and third order eccentricities, using the standard Glauber model [103]. It was also shown in the same work ([103]) that the Glauber eccentricities along with a viscous hydrodynamic expansion (starting at an early time, ~ 0.6 fm) can produce elliptic and triangular azimuthal anisotropies in the momentum space for the final particle distribution in p+Pb and d+Pb collisions.

The major problem with the hydro models is that because of the small system size and the resulting large pressure gradients, the viscous corrections would be larger in small collision systems (viscous corrections grow as $\sim 1/R$, R quantifying the transverse system size) and a hydrodynamic expansion may not be viable [14]. The expansion can be violent and thermalization may not take

place. There are arguments that this may not be the case, and that if the temperature, T, of the system increases as system size decreases (i.e if TR is held fixed) the dynamics of the system evolution, at least in the QGP phase, can be insensitive to the change of system size [14, 104]. The observation of similar v_3 in p+Pb and Pb+Pb systems at similar multiplicity has been pointed out as support to this conformal scaling picture.

Regardless of the validity of applying hydrodynamic evolution in the case of small systems, hydrodynamic calculations have been somewhat successful (at least in the low p_{T} region, $\lesssim 3$ GeV) in reproducing the ridge as well as the magnitude and p_{T} dependence of the observed v_n harmonics in p+A (d+A) collisions [15, 105]. Figure II.3.3 shows an example, in which the yield above uncorrelated background and the v_2 harmonic from p+Pb collisions are compared with hydrodynamic calculations with different initial conditions. It should be pointed out that models with a partonic transport during the system evolution, particularly the AMPT model, which has been quite successful in reproducing the flow measurements in heavy ion collisions, have also been able to reproduce the ridge correlations and their p_{T} dependence in p+Pb (and d+Au) collisions. The AMPT results also argue for a collective origin from final state interactions for the ridge in p+Pb collisions [106].

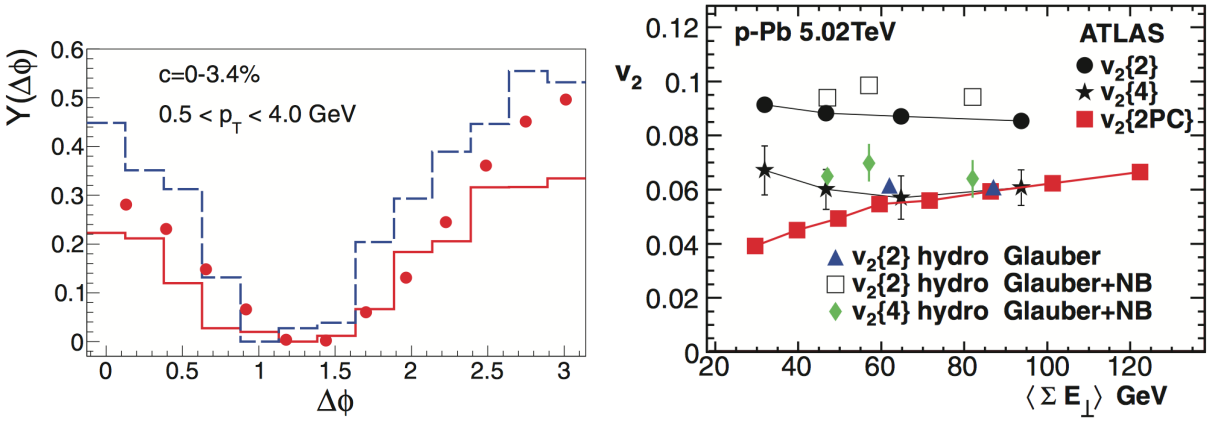

Figure II.3.3: (Left) The associated yield above combinatorial background, projected in $\Delta\phi$, for p+Pb collisions at $\sqrt{s_{NN}} = 5.02$ TeV from hydrodynamic calculations with a standard (solid line) and compact source (dashed line), compared to data from ATLAS (solid points). (Right) The second order harmonic coefficient, v_2, from ATLAS data compared with values from hydrodynamic calculations with different initial conditions. [15]

Another class of calculations associate the long-range ridge correlations to initial state effects, e.g. multi-parton processes that color connect partons across a large η range [107, 17, 108, 18]. These processes can be enhanced due to gluon saturation effects in central proton-proton and proton-lead collisions where the gluon density is high. These CGC based initial state models, have also been successful in reproducing some of the observed features of the correlation, including the magnitude and p_{T} dependence of the ridge correlations in p+p collisions (figure II.3.4). It has

been shown that azimuthal harmonics of similar qualitative p_{T} dependence as in A+A collisions can arise purely from initial state correlations, and arguments for non zero values for $v_2\{4\}$ in p+A collisions from initial state correlations were also presented [109, 110].

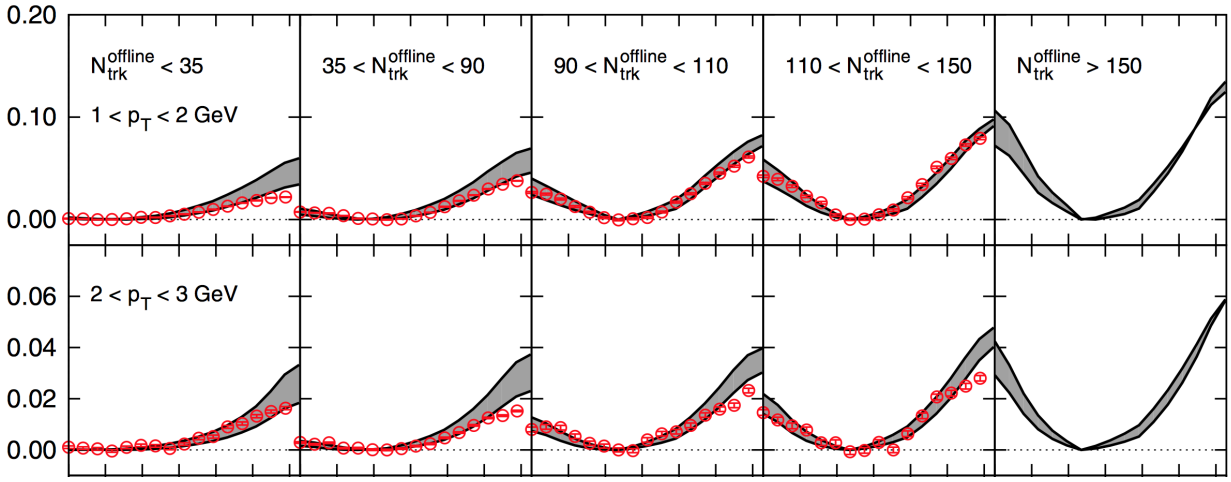

Figure II.3.4: The associated yield above combinatorial background, projected in $\Delta\phi$, for p+Pb collisions at $\sqrt{s_{NN}} = 5.02$ TeV calculated from initial state model with gluon saturation (lines) compared with data from CMS (open circles), for different multiplicity intervals and for pairs (with $p_{\mathrm{T}}^{\mathrm{trig}} = p_{\mathrm{T}}^{\mathrm{asso}}$) in two p_{T} ranges [17].

II.3.1.3 Focus and scope of the study in this work

The measurement presented in this work (in Part IV) is based on the p+Pb run conducted at the LHC in early 2013, using the data recorded by the ATLAS detector. ATLAS recorded an integrated luminosity of 28 nb^1 during the run. The high statistics run allows the extension of the study of the ridge correlations to higher multiplicities and higher p_{T} values. In order to enhance the rate of high-multiplicity events collected, specific triggers were enabled during the run that select events based on their total multiplicity and/or total transverse energy in the Forward Calorimeter (FCal, see Subsection III.2.2.2).

We use the two particle correlation method to study the ridge and the associated Fourier harmonics. The two particle correlations are studied as a function of two variables that serve to capture the overall multiplicity or "activity" in the event, the total number of reconstructed charged particle tracks at mid-rapidity ($|\eta| < 2.5$) and the total transverse energy in the FCal (situated between $3.1 < |\eta| < 4.9$). The study attempts to further the understanding of the ridge correlations along three directions: by extending the measurements to higher p_{T}, measuring other Fourier harmonics than v_2 and v_3, and comparing the results from the p+Pb collisions to that from similar multiplicity Pb+Pb events.

The current measurements measure the ridge and v_n only up to $p_{\mathrm{T}} < 6$ GeV. We extend the measurements up to $p_{\mathrm{T}} < 12$ GeV in the highest multiplicity classes. These measurements

are important since no evidence of high p_{T} suppression, which is also usually attributed to the interactions with the QGP medium, has been observed in p+Pb collisions so far [111, 112]. The ridge is observed to high p_{T} ($\gtrsim$ 10 GeV) in A+A collisions but at high p_{T}, in A+A collisions, it is attributed to the path length dependent energy loss of the particles in the QGP medium [113]. If a ridge correlation is observed up to $p_{\mathrm{T}} \gtrsim 10$ GeV, it could argue towards such a mechanism in p+Pb collisions as well.

The effects of viscous damping are larger for higher order harmonics, also measuring harmonics of different orders would allow constraining models for initial conditions and medium evolution better [56]. Current measurements of v_n exist for $n = 2, 3$ in the p+Pb system. In this study we measure the first five Fourier harmonics, v_1–v_5. The first order harmonic v_1 is particularly interesting since hydrodynamic (or collective expansion/transport) models predict a specific p_{T} dependence for it (see Chapter IV.1 for a discussion on the v_1 harmonic). Observation of such a signal can provide support to the hydrodynamic/final state models for the origin of the ridge in p+Pb collisions.

The highest multiplicity p+Pb collisions have comparable multiplicity as 55–60% central Pb+Pb collisions. The conformal scaling hypothesis argues that the medium response is similar in similar multiplicity p+Pb and Pb+Pb collisions which should result in simple scaling patterns for the v_n harmonics in the two systems [14, 104]. We compare the v_2, v_3 and v_4 as a function of p_{T} between similar multiplicity p+Pb and Pb+Pb. The p_{T} dependence is expected to overlap up to scalings to account for change in mean p_{T} and average geometry between the systems, if the final state origin picture for the ridge in p+Pb and the conformal scaling hypothesis hold.

The analysis uses a peripheral subtraction procedure, previously used in [12, 13, 100], to reduce contributions from non flow correlations. A better understanding of the performance of the recoil subtraction procedure is also an interest in this analysis.

Separately, a study into multi-particle cumulants with a focus on their behavior in small systems is also undertaken. The multi-particle cumulants are expected to show a specific pattern, shown by equations II.2.45 and II.2.51, if the underlying flow (or global correlation) is constant or has a Bessel-Gaussian distribution. We investigate the behavior of the cumulants for arbitrary distributions for the underlying flow and the limitations of using them to search for collectivity in small systems. We also present a new method to study the cumulants in heavy ion collisions, and evaluate its performance in small collision systems using toy simulations and HIJING events.

II.3.2 Longitudinal multiplicity correlations

II.3.2.1 An overview of existing results

The correlation between particle production at different pseudorapidities have been studied from the early days of high energy collisions. One of the major emphases of these studies is to evaluate and understand the origin and nature of the long-range correlations (correlations that exist to $|\Delta\eta| > 2$) in the collisions systems. The multiplicity correlations have been measured in e^+e^-, p+p and A+A collisions at different center of mass energies [114, 96, 95, 19, 21, 97, 20]. No significant long-range correlations have been observed in the e^+e^- collisions [114], while the p+p and A+A

collisions have shown significant values for the LRC [95, 19]. Most of these measurements use the Pearson correlation coefficient $b_{\rm corr}$, constructed using multiplicities in two symmetric rapidity windows around $\eta = 0$, defined as,

$$b_{\rm corr} = \frac{\langle N_F N_B \rangle - \langle N_F \rangle \langle N_B \rangle}{\langle N_F^2 \rangle - \langle N_F \rangle^2}, \tag{II.3.1}$$

where N_F and N_B are the number of particles produced in a rapidity bin in the forward and backward directions, respectively. Early measurements include the measurements of the multiplicity correlation between different pseudorapidities in p+p collisions at ISR energies and in $\bar{\rm p}$+p collisions at different center of mass energies from 200 to 900 GeV from the UA5 collaboration at CERN [96, 95]. Both these studies have identified significant long-range correlations in the system, which differ from expectations from pure Poisson (statistical) fluctuations.

Similar measurements have also been performed at RHIC and LHC experiments more recently. Figure II.3.5 shows examples of the correlation coefficient $b_{\rm corr}$ measured in Au+Au collisions at RHIC [19] and p+p collisions at the LHC [20]. The figure shows the correlation coefficient $b_{\rm corr}$, plot as a function of the pseudorapidity separation ($\Delta\eta$ or η_{gap}) between the two symmetric rapidity windows chosen, for Au+Au collisions at 200 GeV on the left and for p+p collisions at different center of mass energies on the right. For Au+Au collisions, $b_{\rm corr}$ values are found to be relatively independent of the pseudorapidity separation, $\Delta\eta$, in the more central event classes, but show a sharp decrease with $\Delta\eta$ towards more peripheral event classes. Also the magnitude of $b_{\rm corr}$ was found to decrease from more central to peripheral collisions. The $b_{\rm corr}$ values in the p+p collisions also decrease with increase in the pseudorapidity separation, η_{gap}, as in peripheral Au+Au collisions, at all energies. The differences in the $\Delta\eta$ dependence between the results in central and peripheral (or p+p) collisions might argue towards a difference in the nature of the multiplicity correlations in the two event classes. Measurements of $b_{\rm corr}$ in p+p collisions were also made by the ATLAS experiment [97].

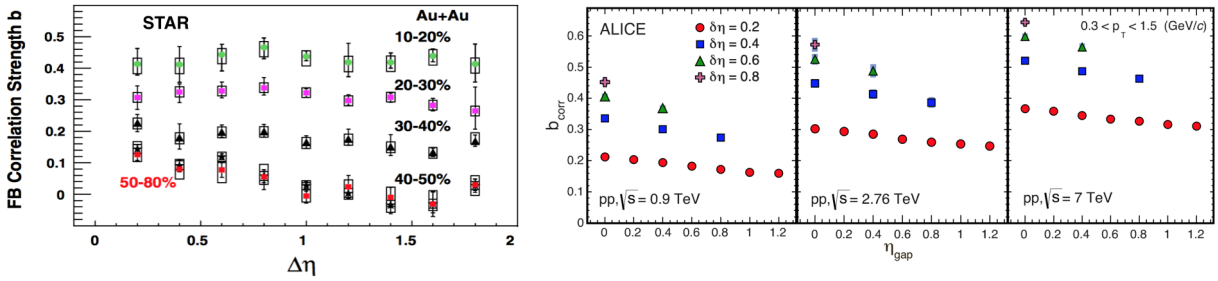

Figure II.3.5: The correlation coefficient $b_{\rm corr}$ as a function of the pseudorapidity separation ($\Delta\eta$ or η_{gap}) between the two symmetric rapidity windows chosen, for Au+Au collisions at 200 GeV at RHIC (left) [19] and for p+p collisions at different center of mass energies at the LHC (right) [20]. The different markers in the left panel indicates different centrality intervals and in the right panels they denote different widths for the symmetric pseudorapidity windows used.

The measurements by ALICE in p+p collisions were also performed by correlating the multiplicities in different $\eta - \phi$ windows [20]. Figure II.3.6 shows the $b_{\rm corr}$ values as a function of the pseudorapidity separation, $\eta_{sep}(\equiv \eta_{gap})$, for different choices of azimuthal separation between the windows. The magnitude of $b_{\rm corr}$ was found to decrease with increase in η_{sep} when the azimuthal separation was small, while the $b_{\rm corr}$ values were relatively independent of η_{sep} when the azimuthal windows were maximally separated (back to back). This dependence reflects the contribution of short-range correlations to $b_{\rm corr}$ which are largest at small ($|\Delta\eta|$, $|\Delta\phi|$) values, and decrease with increase in separation in the η and ϕ directions.

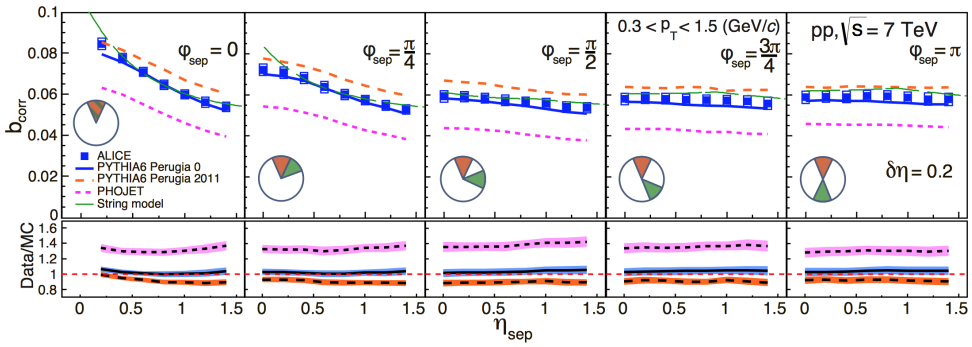

Figure II.3.6: The correlation coefficient $b_{\rm corr}$ as a function of the pseudorapidity separation (η_{gap}) between the two symmetric rapidity windows chosen, for p+p collisions at $\sqrt{s} = 7$ TeV, for different choices of azimuthal separation between the forward and backward rapidity regions [20].

One disadvantage of the correlation coefficient $b_{\rm corr}$ though, is that it is affected by the contribution from statistical fluctuations. The numerator in Eq II.3.1 is insensitive to statistical fluctuations while the variance in the denominator would be large in peripheral collisions or small collision systems where the number of sampled particles is smaller. This would contribute to smaller values of $b_{\rm corr}$ when the sampled multiplicity is smaller. The decrease of $b_{\rm corr}$ towards peripheral event classes could at least partially be from this. This effect can also be seen in the results from p+p collisions in figure II.3.5, where the $b_{\rm corr}$ values increase when the width of the pseudorapidity bins ($\delta\eta$) on both sides are increased (shown as different colored markers in the plot). This makes it difficult to make direct conclusions from these measurements and have to rely on model comparisons with similar number fluctuations built in to understand the underlying physics.

An alternative choice is to use a two particle correlation method to study the longitudinal multiplicity correlations. The two particle correlations can be constructed as the ratio of the average pair distribution, $\langle N(\eta_1)N(\eta_2)\rangle$ to the product of single particle distributions, $\langle N(\eta_1)\rangle\langle N(\eta_2)\rangle$. In this case, the value of the correlation function at two different η_1 and η_2 values are unaffected by contributions from statistical fluctuations, and offers a more direct measure of the multiplicity correlation. Some early results for such a correlation function exist [95], however is not explored in much detail. Also, as the correlation function measures the mean of the relative fluctuations from the average distribution, it is strongly sensitive to the multiplicity range of events used to construct

the averages. This can introduce a contribution to the correlation function if the shape of the single particle distribution, $\langle N(\eta_1)\rangle$, is changing with multiplicity, even if there are no correlations in the system. This bias and methods to correct for it will be discussed in detail in Part V. The variance of a somewhat related measure, $C = (N_F - N_B)/\sqrt{N_F + N_B}$ defined event-by-event, has been used to study the forward-backward correlations by the PHOBOS Collaboration in Au+Au collisions [21].

II.3.2.2 Early time density fluctuations and long-range correlations

The longitudinal multiplicity correlations observed in the data, and not accounted for by the estimated statistical fluctuations, are usually interpreted using a cluster model [95]. In this model, the produced particles are assumed to be emitted from independent clusters that exist as an intermediate step in the particle production. These clusters could be initial particle producing sources or final state resonances or fragmenting partons. The fluctuations in the early time rapidity distribution of the particle producing sources can give rise to long-range longitudinal correlations in the system. The nature of these sources depend on the models considered. Long-range correlations can also arise in CGC based models, where the initial produced particles have intrinsic long-range correlations [115].

A simple multiple source model in the case of heavy ion collisions would be wounded nucleon model, where the wounded nucleons (or participants) are considered as the initial particle producing sources in the system [116]. Each of these sources is assumed to emit particles asymmetrically in η, with more particles emitted in the forward rapidity direction if the source is moving in the forward direction and vice-versa. The fluctuations in the initial distribution of forward going and backward going participants would then result in long-range correlations in the system. We will discuss this model in bit more detail further below (the discussion doesn't have to assume the sources are wounded nucleons, but any source with the prescribed behavior).

The assumption that the particle production from the individual wounded nucleons are asymmetric in η is supported by the pseudorapidity distribution of produced particles in asymmetric collisions like p+Pb or d+Au [117, 118]. In these systems, the number of participants in the deuteron (proton) going rapidity is less than the number of participants in the ion going direction. If the particle production from each source were symmetric, the rapidity distribution of particles from these collisions would still be symmetric. But clear asymmetry can be seen in the particle distributions in central d+Au and p+Pb collisions with more particles produced in the ion going direction, along which there are more participants (see figure II.3.7). This asymmetry grows with increase in centrality and points to the asymmetric nature of particle production in rapidity from sources going in forward and backward directions. Such an asymmetry also holds in symmetric collision systems on an event by event basis, as the number of forward and backward going participants fluctuate event to event.

We discuss a simple picture of asymmetric sources in rapidity here (following [116]). For simplicity consider the sources to be wounded nucleons and that the particle distribution in rapidity ($\rho(y)$) from a single wounded nucleon being a linear function of rapidity, i.e. $\rho = a + by$, where y is the rapidity and a and b are constants. The sign of b depends on whether the nucleon is

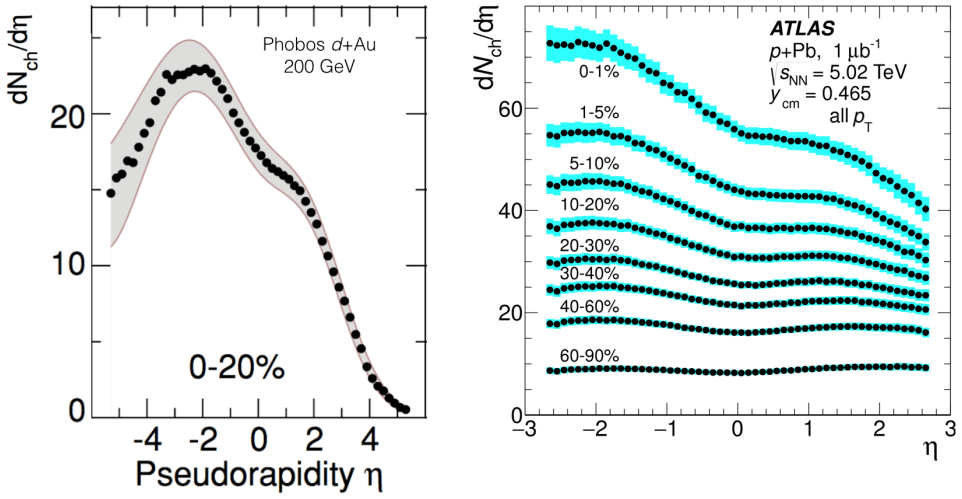

Figure II.3.7: The $dN/d\eta$ distributions, for 0-20% most central d+Au collisions at $\sqrt{s_{NN}} = 200$ GeV at RHIC (left) [117] and for different centrality intervals in $\sqrt{s_{NN}} = 5.02$ TeV p+Pb collisions at the LHC (right) [118].

forward or backward going. The linear profile is a reasonable approximation at mid-rapidity given the nearly linearly asymmetric particle distribution in central p+Pb (or d+Au) collisions [118]. If there are w_L wounded nucleons moving to the left and w_R moving to the right (and left taken as the negative rapidity direction), the single particle distribution from all the sources is given by,

$$\rho(y; w_L, w_R) = w_R(a + by) + w_L(a - by) = a(w_L + w_R) - by(w_L - w_R). \tag{II.3.2}$$

The two particle distribution is given by,

$$\begin{aligned} \rho_2(y_1, y_2; w_L, w_R) &= \rho(y_1; w_L, w_R)\rho(y_2; w_L, w_R) \\ &= a^2(w_L + w_R)^2 - ab(w_L^2 - w_R^2)(y_1 + y_2) + y_1 y_2 b^2 (w_L - w_R)^2 \end{aligned} \tag{II.3.3}$$

A two particle correlation function can be defined after averaging over many events, as:

$$\begin{aligned} C(y_1, y_2) &= \langle \rho_2(y_1, y_2) \rangle - \langle \rho(y_1) \rangle \langle \rho(y_2) \rangle \\ &= a^2 \left(\langle w_+^2 \rangle - \langle w_+ \rangle^2 \right) + y_1 y_2 b^2 \langle w_-^2 \rangle, \end{aligned} \tag{II.3.4}$$

where the angular brackets denote average over many events and $w_+ = w_L + w_R$ and $w_- = w_L - w_R$. It is assumed that the system is symmetric so that that after averaging over many events, $\langle w_L \rangle = \langle w_R \rangle$. Thus the asymmetry in the particle production from the initial sources is reflected in the two particle correlation function as a bilinear term in $y_1 y_2$. In reality, depending on the particle emission from the individual sources and also other effects like difference in "stopping" between the sources, additional structures can arise in the correlation function. These features can in general be

analysed by expanding the two particle correlation function in an orthonormal set of polynomials and studying the magnitude of the coefficients.

The distribution $\rho(y)$ will fluctuate event-by-event depending on the number of forward and backward going sources. If the event-by-event shape fluctuations in the single particle rapidity distribution relative to the average distribution, is expanded as [116],

$$\rho(y)/\langle\rho(y)\rangle = \left(1 + \sum_{i=0} a_i T_i(y/Y)\right), \tag{II.3.5}$$

where $\langle\rho(y)\rangle$ is the average particle distribution over all the events in the event class under consideration and T_i are a set of orthonormal polynomials (eg. Legendre, Tschebychev, etc) and Y is the maximum rapidity value considered in analysis. Then the two particle rapidity correlation function expands as,

$$C(y_1, y_2) = \langle\rho(y_1)\rangle\langle\rho(y_2)\rangle \left(1 + \sum_{i,j=0} \langle a_i a_j\rangle T_i(y_1/Y) T_j(y_2/Y)\right), \tag{II.3.6}$$

Thus in the expansion of the two particle correlation function in an orthonormal set of polynomials, the coefficients give the variance and covariance of the coefficients characterizing the event-by-event shape fluctuations. By choosing a set of orthonormal polynomial basis, the different components of event-by-event shape fluctuations and their magnitudes can be studied. The discussion above is valid regardless of the nature of the event-by-event shape fluctuations and if more complicated sources of fluctuations than that given by Eq. II.3.4 are present. The correlation function also has the advantage that statistical fluctuations average out (see Chapter V.1 for more details). The discussion of the expansion of the correlation function into orthonormal polynomials is equally valid if the pseudorapidity is used instead of the rapidity.

Most previous measurements of longitudinal correlations were limited to a small region of the phase space, mostly restricting to symmetric rapidity windows around zero. The correlation function allows one to study the features of longitudinal correlations across the full two particle pseudorapidity phase space. Also the expansion method allows for characterizing the nature and magnitude of the event-by-event fluctuations and provide insights into the nature of particle production in high energy collisions. It has to be pointed out that presence of short-range correlations will also contribute to the coefficients in the expansion of two particle correlations. These contributions have to be removed in order to understand the shape fluctuations associated with the LRC. This will be further discussed in Chapter V.3.

II.3.2.3 Focus and scope of the study in this work

We present a detailed study of the longitudinal correlations in high energy nuclear collisions in Part V. A new method, using a two particle pseudorapidity correlation function closely related to that defined in Eq. II.3.4, to study the longitudinal correlations is presented. In this method, the contributions arising from change of the average shape of the single particle distribution, $\langle N(\eta)\rangle$, with multiplicity, are removed. This also makes the correlation function a robust observable against

systematics from varying the "event-mixing" criteria used to construct them. The correlation functions are then expanded in an orthonormal set of Legendre polynomials [119] to quantify the shape fluctuations in the system.

The performance of the method is investigated using Monte-Carlo event generators HIJING [120] and AMPT [45]. In the model studies the initial source asymmetry and the final state asymmetry in the particle distribution can be directly related. The two models studied have different final state interactions, but similar initial conditions and thus help understand the contributions of the initial and final state effects to the correlation function.

The method is applied to measure the two particle correlation functions and associated Legendre coefficients, a_n, in $\sqrt{s_{NN}} = 2.76$ TeV Pb+Pb collisions. The r.m.s values of a_n are extracted as function of centrality. The first order coefficient a_1 corresponds to a bilinear contribution in $\eta_1\eta_2$ to the correlation function and is related to the forward-backward asymmetry in the number of initial particle producing sources (Eq. II.3.4). The r.m.s values of the coefficients are measured as function of centrality and compared to values from HIJING. These measurements reveal the general features of the correlation function in heavy-ion collisions. However, SRC also contribute to the correlation function and the a_n values and their contribution has to be estimated to properly understand the LRC in the system.

A separate analysis, using the same method, studying the two particle pseudorapidity correlation functions in $\sqrt{s} = 13$ TeV p+p, $\sqrt{s_{NN}} = 5.02$ TeV p+Pb and $\sqrt{s_{NN}} = 2.76$ TeV peripheral Pb+Pb collisions are presented with a focus to understand the long-range correlations in the systems. A data driven method is developed to separate the short- and long-range contributions to the pseudorapidity correlation function. Both the SRC and LRC are studied as a function of the multiplicity and compared across the different collision systems. The shape components in the LRC is quantified by the expansion into orthogonal Legendre polynomials. The collision system dependence of the SRC and LRC can provide insights into the early particle production and final state interactions in high energy nuclear collisions.

Part III

Large Hadron collider and ATLAS detector

Chapter III.1

Collider experiments

The major advantage of collider experiments where beams with equal energy travelling in opposite directions are collided, as opposed to fixed target experiments, where the high energy beam is made to collide with a stationary target, is that in collider experiments almost all the energy of beams are available for particle production while in fixed target experiments a significant fraction of the energy is lost in the motion of the center of mass. For a collider with beams having energy E, the center of mass energy,

$$\sqrt{s} = 2E, \tag{III.1.1}$$

while for a fixed target experiment with energy E, the center of mass energy is given by (for simplicity let us assume both the beam and target particles have the same mass m),

$$\sqrt{s} = \sqrt{(p_1^\mu + p_2^\mu)^2} = \sqrt{\left((E, \vec{p_1}) + (m, 0)\right)^2} = \sqrt{2m^2 + 2mE} \approx \sqrt{2mE}. \tag{III.1.2}$$

Besides the energy, another important parameter determining the physics discovery potential of a collider is the luminosity. The instantaneous luminosity is defined as the proportionality constant between the collision cross-section σ and the rate of collisions $\frac{dN}{dt}$,

$$\frac{dN}{dt} = \mathcal{L}\sigma, \tag{III.1.3}$$

Higher luminosity would mean higher number of rare processes that have a small cross-section, like Higgs production. Modern particle colliders aim to achieve the highest energy collisions possible while also ensuring the luminosity is high enough to produce enough number of rare events of interest.

Early circular particle accelerators were *cyclotrons*, first developed by Ernest Lawrence [121] in 1934. The cyclotron design involves two D shaped hollow metal electrodes kept facing each other with a narrow gap between them, inside a vacuum chamber. The two electrodes are kept in a constant magnetic field perpendicular to the plane of the Ds and a high frequency alternating voltage is applied between the two electrodes. Charged particles injected into the center of the apparatus get accelerated by the potential in the gap while the perpendicular magnetic field causes

the particles to move along a circular trajectory. If the period of the alternating potential is equal to the time taken by the charged particles to complete one full circle, then the particles keep getting accelerated every time they cross the gap between the electrodes. This requires that, for particles with speeds much less than the speed of light, the frequency of the alternating potential (called the cyclotron resonance frequency) be given by

$$f = qB/2\pi m, \tag{III.1.4}$$

where q is the charge and m is mass of the particles and B is the magnetic field strength. The velocity and thus the radius ($R = mv/qB$) of the particles increase each time they cross the gap between the electrodes un till they reach the maximum radius supported by the apparatus, where upon they are deflected and redirected to the desired target. The schematic of a cyclotron design and particle acceleration are shown in Fig. III.1.1

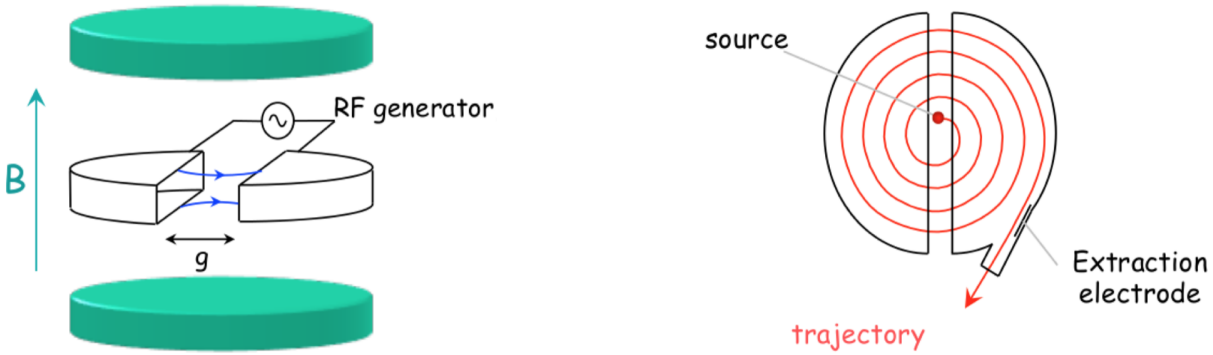

Figure III.1.1: Schematic of a cyclotron design (left) and particle acceleration inside the cyclotron (right). [122]

The relation $III.1.4$ for resonance frequency does not hold when the particle velocity approach the speed of light, the revolution frequency become velocity dependant and is given by

$$f = qB/2\pi\gamma m, \tag{III.1.5}$$

where γ is the relativistic Lorentz factor. There are variations of the cyclotron that can accelerate particles to very high energies, with velocities comparable to that of light, by either varying the frequency of the alternating potential to remain in sync with the revolution frequency (called *synchrocyclotrons*) or keeping the frequency of revolution constant by changing the magnetic field as a function of the radius (*isochronus cyclotron*).

Modern hadron colliders like the LHC and Tevatron are *synchrotrons* (proposed first in 1945, [123, 124]) in which the magnetic field is varied as a function of time (rather than in space, as in the case of isochronous cyclotron) as the particles are accelerated to higher energies, so that the radius of the circular path remains constant. Particles are accelerated by alternating potentials (radio

frequency, RF) applied across RF cavities located along the path. The frequency of the RF potential may also be changed to follow the non-constant circulation time of the particles. This allows for a more compact design and the vacuum chamber to be restricted along a large thin torus than a disk as in the case of cyclotrons.

III.1.1 Hadron Synchrotrons

Particles are accelerated in synchrotrons by RF cavities that generate a longitudinal (along the beam directions) alternating voltage across an isolated gap in the vacuum chamber. In order for the particle to see an accelerating voltage at the gap, the RF frequency, f_{RF}, must be an integral multiple of the revolution frequency, f_{rev}.

$$f_{RF} = h f_{rev}, \tag{III.1.6}$$

where h is an integer. A particle that is in sync with the RF frequency is called a synchronous particle. The segments of the circumference that is centered around the synchronous points are called *RF buckets*. Because of the RF system, particles will be clustered around the synchronous point within the RF buckets and are called *bunches*. Each bunch contains many particles (typically $10^8 - 10^{11}$). Particles in a bunch arriving earlier than the synchronous particle will see a decelerating voltage and loose energy. But particles with lower energies will have a shorter orbit and a higher revolution frequency. As a result, once the particle looses enough energy to have higher revolution frequency than the synchronous particle, it will arrive earlier at the gap and would see an accelerating voltage and start to gain energy. And with higher energy it will have a longer orbit and smaller revolution frequency. The process repeats once the energy increases enough to have the frequency fall behind that of the synchronous particle and thus arrive later than it. Thus particles remain confined to bunches and these oscillations are called *synchrotron oscillations*.

Figure III.1.2 shows the schematic of an RF bucket and bunch and the synchrotron oscillation. The bucket area is called the *longitudinal acceptance* and the bunch area in the longitudinal plane is called the *longitudinal emittance* and they have units of energy.

A series of *dipole magnets* are used to keep the bunches circulating in a closed path. Dipole magnets are electro-magnets with a single North/South pole pair that produce an uniform magnetic field between them. The dipole magnets are arranged to create an uniform magnetic field in a plane perpendicular to the beam direction, pointing vertically, causing it to curve in the horizontal direction. The radius of curvature of the path ρ is given by,

$$qvB = \frac{mv^2}{\rho} \Rightarrow B\rho = \frac{p}{q}, \tag{III.1.7}$$

where p is the momentum and q is the charge of the particle. The quantity $B\rho$ is called the *magnetic rigidity*. Since the ρ has to be kept constant in synchrotrons, the magnetic filed must be increased with increase in momentum to keep the particles moving in the same trajectory. The high magnetic fields required at very high particle energies cannot be produced by conventional metals and so modern high energy colliders rely on superconducting magnets for producing the required magnetic fields.

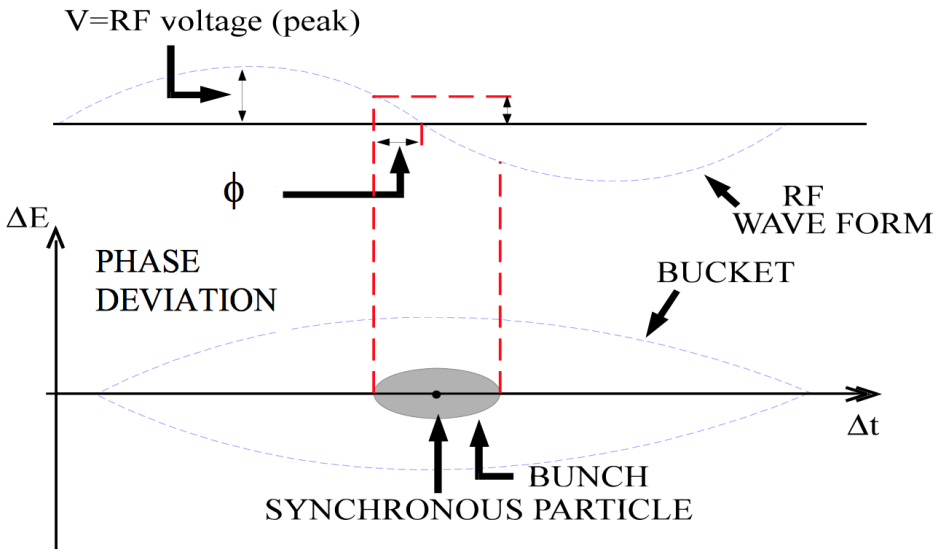

Figure III.1.2: Schematic of a bunch and synchrotron oscillation. The actual shapes of the RF bucket and bunches will depend of the RF voltage magnitude. [125]

The deviations of the particles, in the horizontal plane from the nominal orbit is constrained by the magnetic field. The magnetic field exerts a restoring force causing the particles to oscillate around the nominal orbit. This is called *weak focusing*. But the deviations in the vertical directions are un constrained. For strong focusing in both the horizontal and vertical directions, quadrapole magnets are used. A quadrapole magnet has two north and two south poles each, arranged symmetrically around the beam. In the transverse (perpendicular to the beam direction) plane, the field along the vertical (Y) axis is proportional to the horizontal distance from the center of the magnet system, $B_y \propto x$ and similarly, $B_x \propto y$. Therefore, as shown in figure III.1.3, a particle deviating from the central line in the horizontal direction experiences a restoring force towards the center of the magnet. Thus magnet acts as a focusing lens in the horizontal direction. But in the vertical direction, the force is away from the center and causes the beam to defocus in that direction. If the quadrapole arrangement is rotated by 90^0, it will act as a focusing lens in the vertical direction and defocusing lens in the horizontal direction. By alternating focusing and defocusing lens, net focussing can be achieved in both horizontal and vertical directions. The focusing and defocusing quadrupoles are normally arranged in a focusing-orbit-defocusing-orbit ($FODO$) pattern, separated by non focusing drift regions [126]. This focusing with the quadrapole magnets is called *strong focusing* or *alternating gradient* focusing. The schematic of a FODO half cell is shown in figure III.1.4

Since the restoring forces in the transverse directions are linear, the equation of motion of the particle relative to the beam bunch center can be written as

$$x'' + K(s)x = 0 \tag{III.1.8}$$

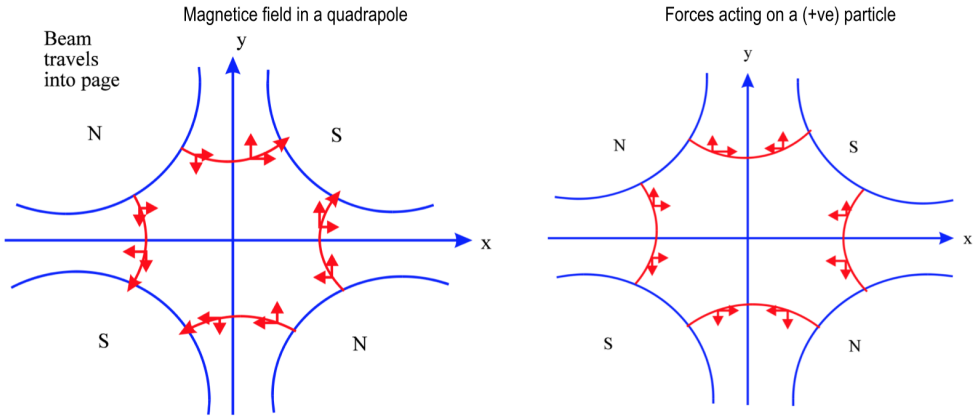

Figure III.1.3: Magnetic fields in a quadrapole magnet (left) and the forces acting on a beam of positive particle in the quadrapole magnet (right). [125]

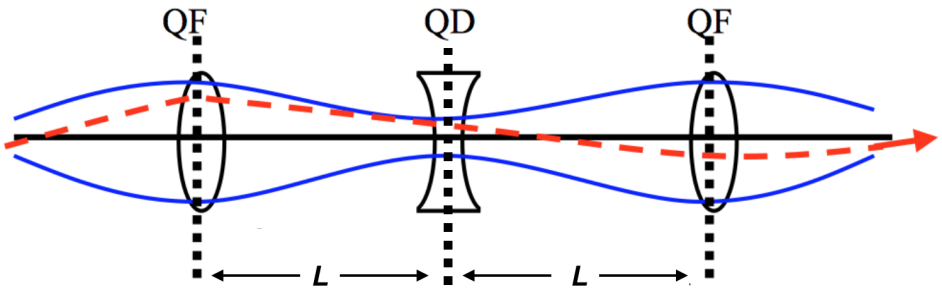

Figure III.1.4: Schematic of a symmetric FODO cell. The beam envelope is marked in blue and a single particle trajectory in red. [127]

, where s is the longitudinal coordinate along the orbit and K is periodic in s. Eq. III.1.8 is called the Hill's equation [128] and the solution to it is of the form

$$x(s) = \sqrt{\epsilon\beta(s)}cos(\mu(s) + \delta) \tag{III.1.9}$$

ϵ and δ are constants. $\pi\epsilon$ gives the area of the phase space ellipse (in the x-x' space) and is called the *transverse emittance*. The β function characterizes the transverse dimension of the beam and $\mu(s)$, the phase advance at position s. By plugging Eq. III.1.8 to the Hill's equation, it can be shown that

$$\mu(s) = \int_0^s ds_1/\beta(s_1), \tag{III.1.10}$$

and $\beta(s)$ is given by

$$\beta''(s) + 4K(s)\beta(s) = const. \tag{III.1.11}$$

Thus for regions with $K = 0$ (regions without focusing, 'drift regions') $\beta(s)$ is parabolic and for regions with focusing ($K \neq 0$), is given by the solution to a driven harmonic oscillator with a constant force term. The oscillations of the particles (Eq.III.1.9) in the transverse direction are called *betatron oscillations*. A large value of β means a large transverse size for the beam and a small phase advance. The integral of Eq. III.1.10 around the full orbit gives the total number of betatron oscillations per revolution and is called the tune, Q, of the synchrotron. The phase advance, μ, through a FODO cell must be real for stable trajectories. For focusing and defocusing quadrupoles of equal focal lengths f and separation between adjacent magnets equal to L, it can be shown that, under a thin lens approximation, this requires that $L < 2f$ [127].

Eq. III.1.8, in general, does not hold for particles that are longitudinally displaced from the bunch center. Such differences would cause additional dispersion and slightly altered trajectories to particles. Additional sextupole and octupole magnets are used to minimize such chromatic aberrations and keep the longitudinal extent of the bunches small.

The instantaneous luminosity of the collider is inversely proportional to the transverse extent of the beam (see next subsection), i.e $\mathcal{L} \propto 1/\sigma_x\sigma_y$ with $\sigma_x(y) = \sqrt{\epsilon\beta(s)}$. Therefore, in order to have high luminosity at the interaction points (IP), the beta function has to be minimized. The beta function at IP is denoted by β^*. Specialized sets of magnets are used to squeeze the beams to decrease the β^* by a factor of ten or more.

III.1.1.1 Luminosity

The instantaneous luminosity $\mathcal{L}$ (Eq.III.1.3) is one of the important measures of the performance of a collider. It has the units of $\mathrm{cm}^{-2}\mathrm{s}^{-1}$. The luminosity, $\mathcal{L}$, for a collider with revolution frequency f, can also be written as

$$\mathcal{L} = \frac{\mu N_b f}{\sigma}, \tag{III.1.12}$$

where N_b is the number of bunches crossing at the interaction point and μ is the number of interactions per bunch crossing and σ is the scattering cross-section. If the number of particles per bunch for the two beams are N_1 and N_2 respectively, then for head on collisions, the above expression can be written as,

$$\mathcal{L} = \frac{N_1 N_2 f N_b}{A_{\text{eff}}}, \tag{III.1.13}$$

where A_{eff} is the effective transverse area of the collision region. For beams with bunches having Gaussian distributions in the transverse directions, the effective area is given by,

$$A_{eff} = 2\pi\sqrt{\sigma_{1x}^2 + \sigma_{2x}^2}\sqrt{\sigma_{1y}^2 + \sigma_{2y}^2}, \tag{III.1.14}$$

where $\sigma_{1(2)x}$ and $\sigma_{1(2)y}$ are the r.m.s widths in the x and y directions respectively, in the two beams.

In experiments, the revolution frequency is known and the number of particles per bunch (or beam intensity) is continuously measured and can be known with very good accuracy (within 1% for LHC). So for head on collisions (Eq. III.1.13), the only unknown parameter is the effective overlap area, A_{eff}. If the horizontal and vertical energy distributions are uncorrelated, The effective

overlap area can be measured by *Van Der Meer* scans [129]. In Van Der Meer scans, the beams are displaced against each other in the horizontal and vertical directions separately and the interaction rates R_x and R_y are measured as a function of the relative separation δ_x and δ_y. The effective area, independent of the beam shape, can then be calculated as [130],

$$A_{eff} = \frac{\int R_x(\delta_x)d\delta_x}{R_x(0)} \frac{\int R_y(\delta_y)d\delta_y}{R_y(0)} \tag{III.1.15}$$

Figure III.1.5 shows an example of the interaction rate measurements in Van Der Meer scans in ATLAS [131]. Since the intensity of the beams decrease with time during the length of the scan, the rates normalized to the peak intensities, referred to as *specific rates* are used. $R_{x,sp} = \frac{(N_1N_2)_{MAX}}{N_1N_2} R_x$, where N_1N_2 is the product of the number of particles in the two colliding bunches at an instant and $(N_1N_2)_{MAX}$ is the maximum value of the product during the scan.

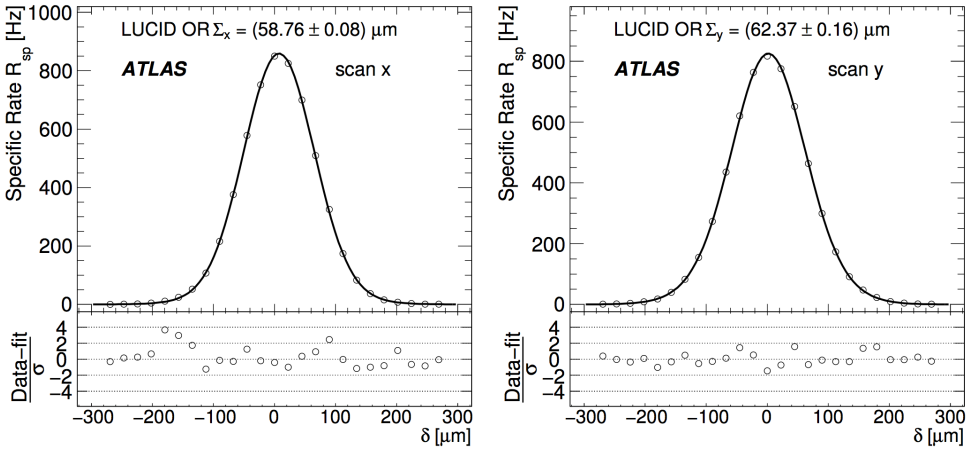

Figure III.1.5: Example of interaction rate measurements in the horizontal (left) and vertical (right) directions in ATLAS VdM scans. [131]

In high luminosity collisions, since there are many closely spaced bunches in the beam, head on collisions are not conducted to avoid unwanted extra collisions. Instead, the beams are collided at a small crossing angle. With a crossing angle, the luminosity gets decreased by a factor and is given as [130],

$$\mathcal{L} = \mathcal{L}_0 S = \frac{\mathcal{L}_0}{\sqrt{1 + \frac{\sigma_{1s}^2+\sigma_{2s}^2}{\sigma_{1x}^2+\sigma_{2x}^2}\left(\tan(\frac{\phi_x}{2})\right)^2 + \frac{\sigma_{1s}^2+\sigma_{2s}^2}{\sigma_{1y}^2+\sigma_{2y}^2}\left(\tan(\frac{\phi_y}{2})\right)^2}}, \tag{III.1.16}$$

where $\mathcal{L}_0$ is the luminosity for head-on collisions, as given by Eq. III.1.14, and $\sigma_{1(2)s}$ is the r.m.s length of the bunches in the longitudinal direction in the beams. ϕ_x and ϕ_y are projections of the crossing angle in the transverse plane. The decrease in luminosity means an increase in the effective area of the beam size in the crossing plane.

The above expressions assume that the transverse widths are independent of the distance to the interaction point. But as discussed in the previous subsection, the beta function is a function of the longitudinal coordinate s and so are the widths ($\sigma_x(s) = \sigma_y(s) = \sqrt{\epsilon\beta(s)}$). Near the interaction point (drift region), β is parabolic in the distance, s, to the minimum,

$$\beta(s) = \beta*(s)\left(1 + \left(\frac{s}{\beta*}\right)^2\right). \tag{III.1.17}$$

Thus the r.m.s widths increase linearly with the distance from the interaction point. This leads to a decrease in luminosity and an additional correction factor, H, to the luminosity expression given by,

$$H = \frac{1}{\sqrt{\pi}}\int_{-\infty}^{\infty}\frac{e^{-t^2}}{\sqrt{(1 + t^2/t_x^2)(1 + t^2/t_y^2)}}dt, \tag{III.1.18}$$

where

$$t_i^2 = \frac{2(\sigma *_{1i}^2 + \sigma *_{2i}^2)}{(\sigma_{1s}^2 + \sigma_{2s}^2)(\sigma *_{1i}^2/\beta *_{1i}^2 + \sigma *_{2i}^2/\beta *_{2i}^2)} \tag{III.1.19}$$

This effect is termed the *Hour glass effect* because of the shape of the β function. The luminosity in presence of a crossing angle and hour glass effect is given by $\mathcal{L} = \mathcal{L}_0 SH$. In actual collisions there are other effects that affect the luminosity. The colliding bunches could have a transverse offset between their bunch centers. There could also be, in practice, coupling between the betatron oscillations in the two transverse directions, even though by design they should be decoupled. At high intensities, there can also be beam-beam effects which can affect the orbit or emittance and can couple the transverse oscillations. These and other effects need to be taken into account when calculating the luminosity in experiments. More detailed discussion on the luminosity measurements in experiments can be found in these references. [130, 131]

The integrated luminosity over a period of time is defined as

$$L = \int_0^T \mathcal{L}dt \tag{III.1.20}$$

It has the units of inverse area and is usually expressed in units of μb^{-1}, $n\text{b}^{-1}$ etc. It is related to the total number of events, N_{ev}, and the collision cross-section σ as, $N_{ev} = L\sigma$.

In colliders, the luminosity decreases with time. Maximising the average luminosity $\langle\mathcal{L}\rangle$ is one of the important design concerns in collider experiments.

III.1.2 Large Hadron Collider

The Large Hadron Collider (LHC) [132, 133, 134] is a hadron synchrotron located at the European Organization for Nuclear Research (CERN) in Geneva, Switzerland. The LHC is built with a focus to find evidence for the Higgs mechanism that generate particle masses, search for physics beyond the Standard Model and to perform precision measurements within the Standard Model

by colliding proton beams at very high center of mass energies and to study the properties of strongly interacting matter created in heavy-ion collisions. It is the largest and most powerful particle accelerator currently in existence and can accelerate protons up to center of mass energies of 14 TeV and ions up to center of mass energies of 5.5 TeV per nucleon.

The LHC accelerator ring has a circumference of 26.7 km and has beams circulating in opposite directions in two separate magnetic channels. The shape of the ring is of a rounded octagon with eight arc sections with strong dipole magnetic fields and eight straight sections in between. The octants are labelled by eight interaction regions (IR), located at the middle of each straight segment. IR1 is the southern most and the remaining IR's are numbered clockwise. Hadrons are injected into ring 1 (clockwise circulating beam) at IR1 and ring 2 (counter-clockwise circulating) at IR8 and beam dumps happen in IR6. The rings switch between inner and outer positions at IR1, 2, 5 and 8 so that both the beams travel the same distance. The layout of the LHC ring is shown in figure III.1.6

The beams are made to collide at four interaction points (IP) located along the ring in the straight segments. There are seven experimental detectors located around the IPs. The two largest are the ATLAS (A Torroidal LHC ApparatuS) [135], located at IR1 and the CMS (Compact Muon Solenoid) [136], located at IR5. Both ATLAS and CMS are general purpose detectors designed for precision measurements of QCD and electroweak physics and also exploring new physics that could be reached at LHC energies. ALICE (A Large Hadron Collider Experiment) [137], located at IR2, is designed with a focus to study the strongly interacting matter produced in heavy ion collisions. A dedicated experiment to study the CP violation in the bottom quark sector, LHCb (Large Hadron Collider Beauty) [138] is located at IR8. There are three smaller detectors that share an IP with the larger experiments. LHCf (Large Hadron Collider Forward) [139] shares an interaction point with ATLAS and is dedicated to cosmic ray astroparticle physics. The experiment, TOTEM (TOTal Elastic and diffractive cross-section Measurement) [140] shares IR5 and measures the total, elastic and diffractive cross-sections in proton - proton collisions. Search for magnetic monopoles and other highly ionizing stable massive particles is the focus of MoEDAL (Monopoles and Exotic Detector at the LHC) [141] and shares IR8 with LHCb.

The LHC uses superconducting magnets kept at 1.8 K to produce the 8.3 T fields required to guide the beams in the rings and involves a total of 1232 main dipole magnets, 392 main quadrupoles and over 6000 smaller multipole corrector magnets. The cross section of an LHC dipole is shown in fig III.1.8. The particles are accelerated in eight radio frequency cavities operating at 400 MHz. The beams collide at a crossing angle of ≈ 280 μrad at the ATLAS IP. The value of β at injection is ≈ 10 m, but the beams are squeezed to $\beta*$ values of 0.55 m (0.4 m in high-luminosity Run2 operations), corresponding to transverse widths of $\sigma = 17$ μm (7 μm).

III.1.2.1 LHC accelerator chain

The LHC injection chain [142] involves the lower energy synchrotrons at CERN, the Proton Synchrotron (PS) and Super Protron Synchrotron (SPS), where the hadrons are accelerated and brought to LHC injection energy. Protons are injected into the LHC in the following sequence. Protons, produced form ionized hydrogen source, are accelerated to 50 MeV in the Linac2. The

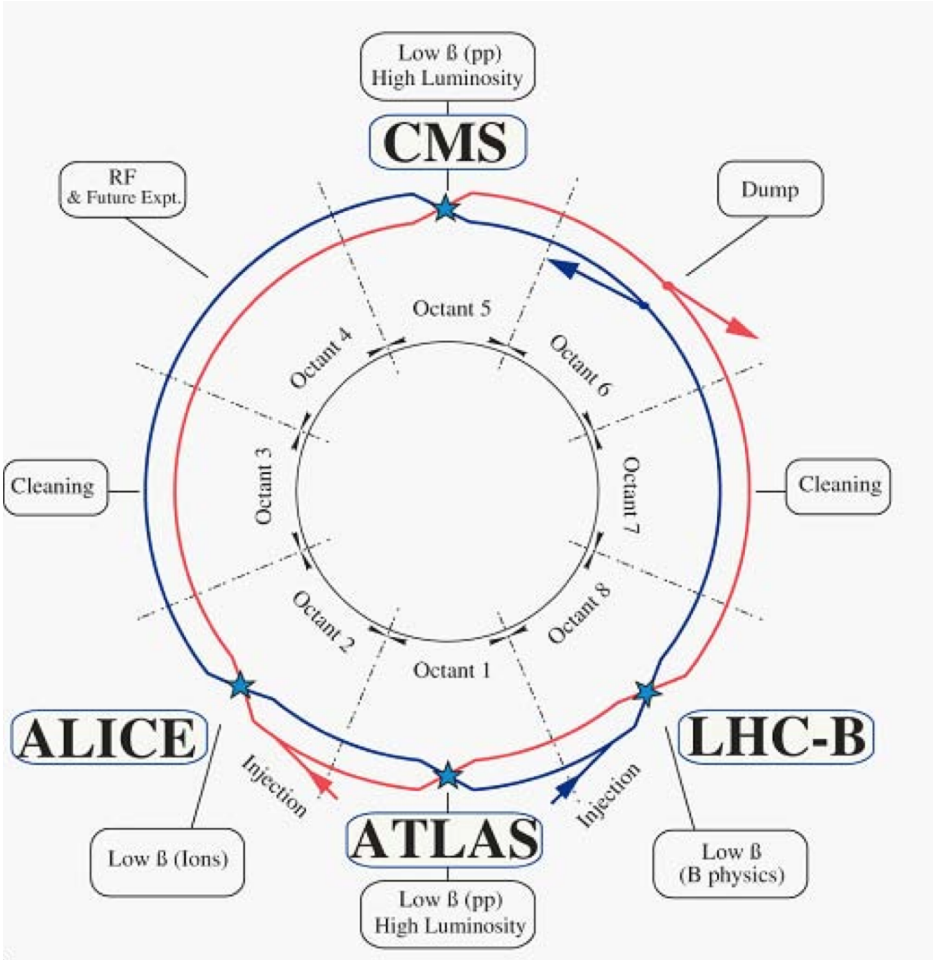

Figure III.1.6: Schematic layout of the LHC (Beam 1- clockwise, Beam 2 anticlockwise). [132]

protons are then accelerated to 1.4 GeV in the Proton Synchrotron Booster (PSB) and transferred to the Proton Synchrotron (PS), where they are accelerated to 26 GeV and from there to the Super Proton Synchrotron (SPS), where they are brought to the LHC injection energy of 450 GeV. The proton bunches, once injected into the LHC, are further accelerated and brought to the desired collision energy of few TeVs.

The injection of lead ions proceeds in a slightly different sequence. Lead ions with charge state Pb^{27+} are stripped to Pb^{54+} and are accelerated to 4.2 MeV/nucleon in Linac3. The ions are further accelerated in the Low Energy Ion Ring (LEIR) to 72 MeV/nucleon and then to 6 GeV/nucleon in the PS. The ions are fully stripped to Pb^{82+} before entering the SPS and are accelerated to the LHC injection energy of 177 GeV/nucleon in the SPS. The schematic of the proton and ion injection chains at the LHC are shown in figure III.1.9.

In the LHC ring, there are eight radio frequency (RF) cavities per beam operating at 400 MHz.

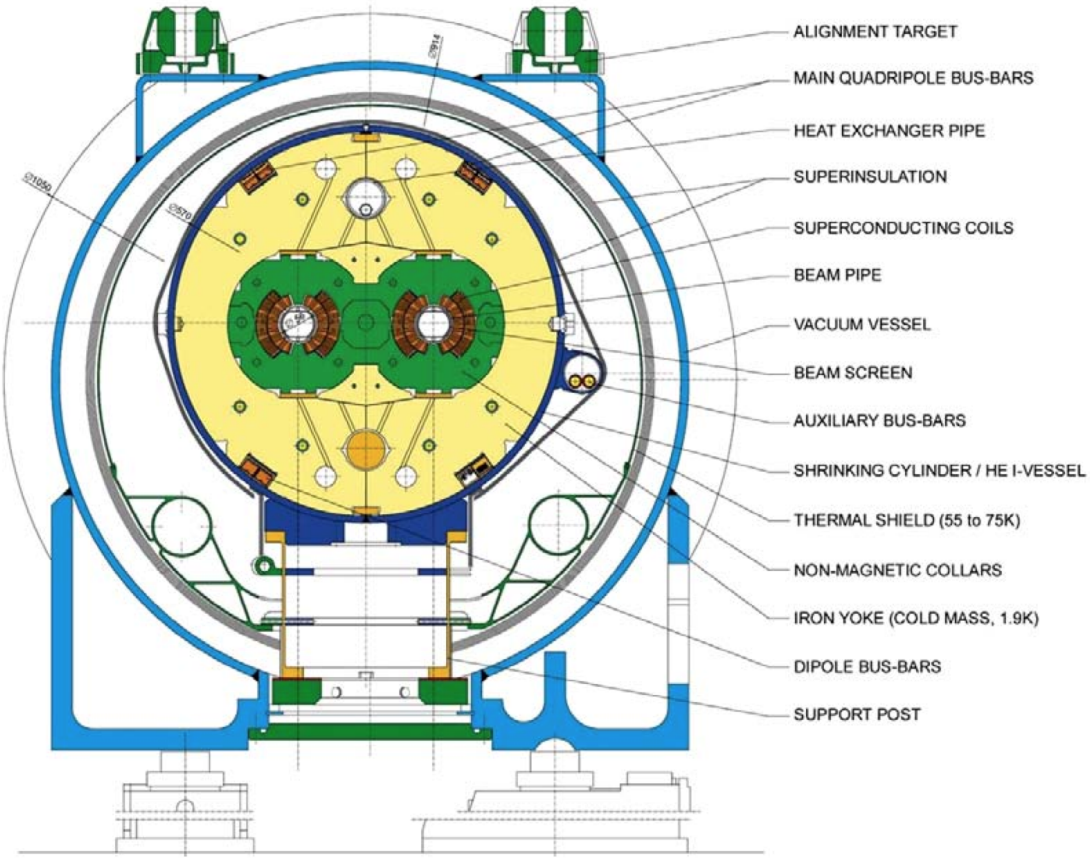

Figure III.1.7: Cross-section of an LHC dipole magnet. [132]

This sets the RF bucket size to 2.5 ns. However, the fill structure in SPS limits the spacing between bunches to 25 ns. This corresponds to a maximum of (26.7 km/3$x10^8$ m/s)25 ns = 3564 buckets that can be filled. These are enumerated with a bunch crossing identifier (BCID).The nominal bunch filling scheme in LHC for high luminosity operation consists of 39 batches of 72 bunches (with bunch spacing of 25 ns), with variable spacing between the batches to allow for the rise times of injection and extraction 'kickers' (fast pulsing dipole magnets used to deflect the beams), giving a total of 2808 filled bunches [132]. This filling scheme is illustrated in figure III.1.9. In Run1 though, other filling schemes with less number of bunches were used for lower luminosity operations [144]. The nominal filling scheme for ions consists of a maximum of 891 buckets that can be filled with spacing of 100 ns. The actual filling scheme is shown in figure III.1.10 and has a total of 592 buckets with bunches. The design luminosity for 14 TeV p+p collisions is 10^{34} $cm^{-2}s^{-1}$ and for ions at 5.5 TeV per nucleon is 10^{27} $cm^{-2}s^{-1}$

The LHC machine cycle consists of an injection phase, where bunches are injected into the LHC rings, an energy ramp to accelerator the beams to collision energies and then beam squeeze

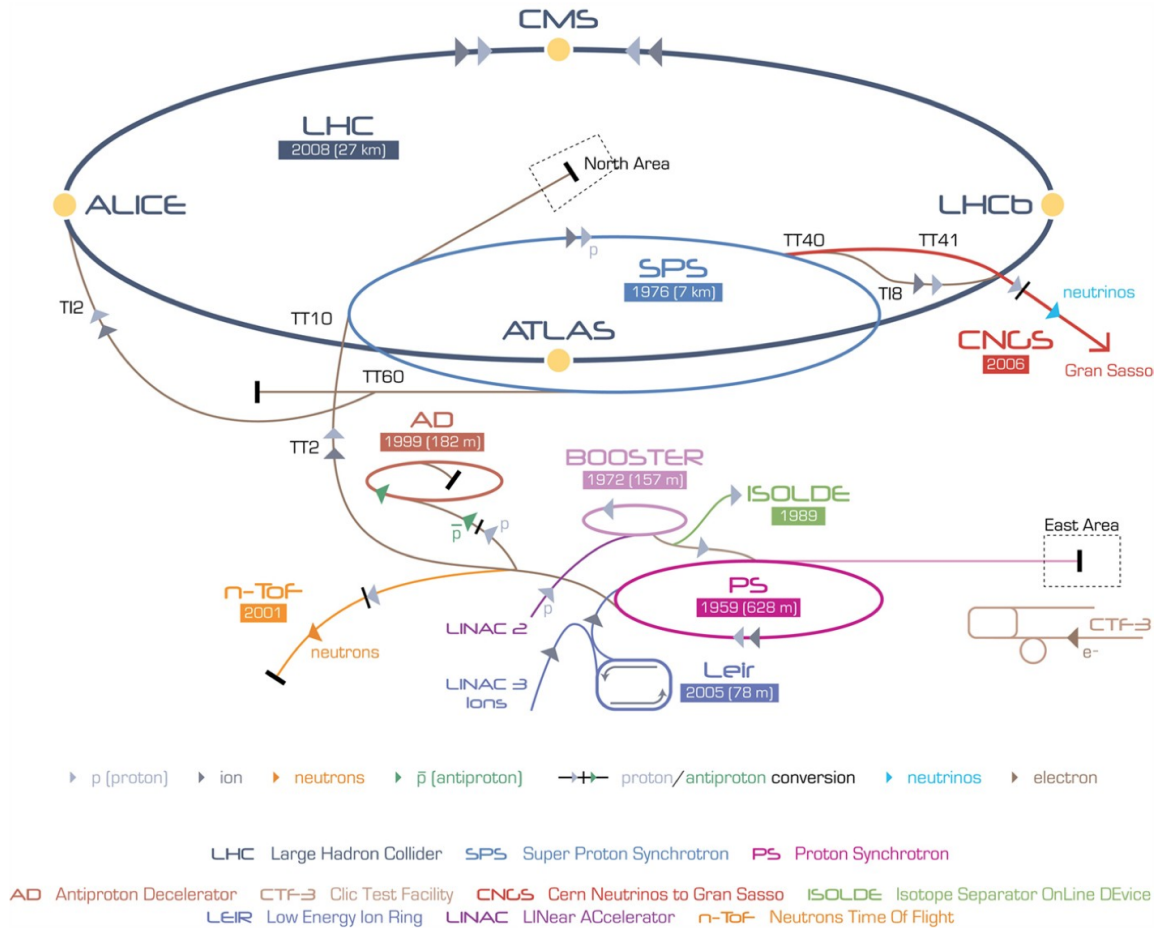

Figure III.1.8: Schematic representation of the LHC's injection chain. [143]

to bring down the $\beta*$ values and a stable beam phase with collisions at the experiments. At the end of the cycle, the beams are dumped using septum dipole magnets which redirect the beams into two dump blocks of 8 m deep graphite absorber.

III.1.2.2 Datasets used in analysis

In this work, three different datasets have been used, Pb+Pb data at $\sqrt{s_{NN}} = 2.76$ TeV from the heavy-ion run in 2010, p+Pb data at $\sqrt{s_{NN}} = 5.02$ TeV from 2013 heavy-ion run and p+p data at $\sqrt{s} = 13$ TeV from the two low μ runs in 2015.

The 2010 Pb+Pb data used in the analysis corresponds to an integrated luminosity of 7 μb^{-1}. The 2013 p+Pb run collected an integrated luminosity of 29.85 nb^{-1} of data. The machine conditions required that the proton and Pb beams have different momentum and resulted in a center of mass shift of 0.465 in rapidity in the proton going direction relative to the lab frame.

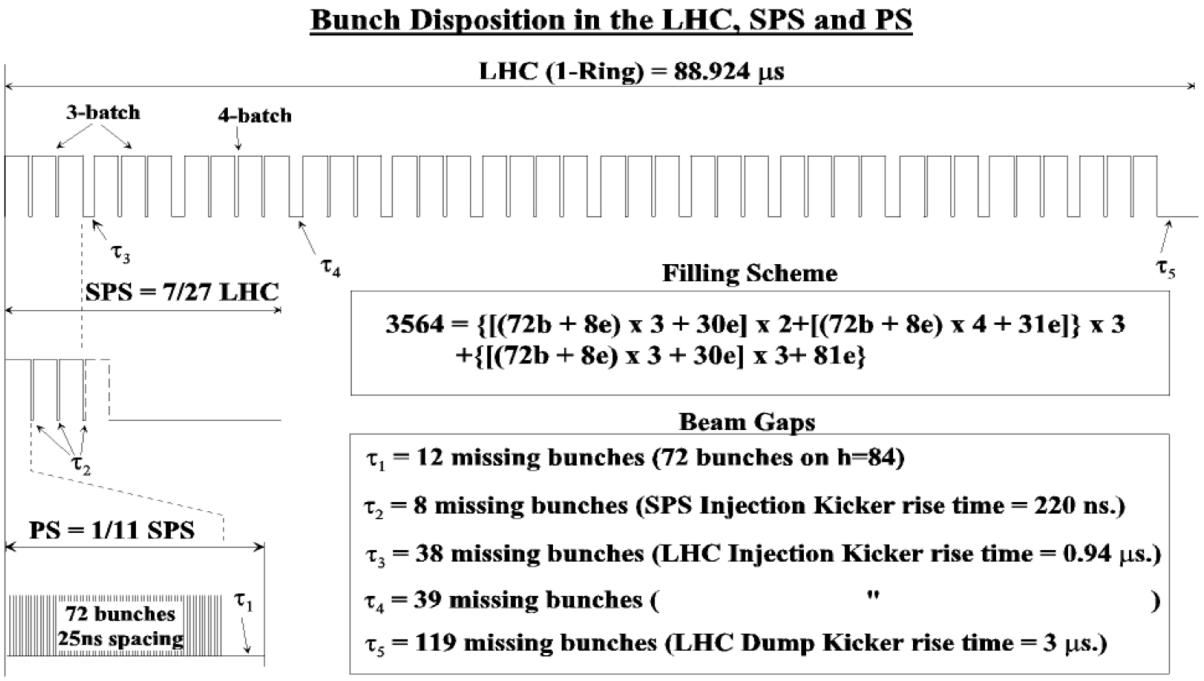

Figure III.1.9: Nominal bunch filling scheme for proton bunches in the PS, SPS and one LHC ring. [132]

The pile up (more than one collision during bunch crossing) rate was low, with an average μ value of 0.03. The 2015 p+p data used comes from a low μ run with average μ between 0.002 and 0.04 conducted in June and a moderate μ run with average μ between 0.05 and 0.6 from August 2015. The total integrated luminosity for the p+p data used in the analysis is 65 $n\text{b}^{-1}$

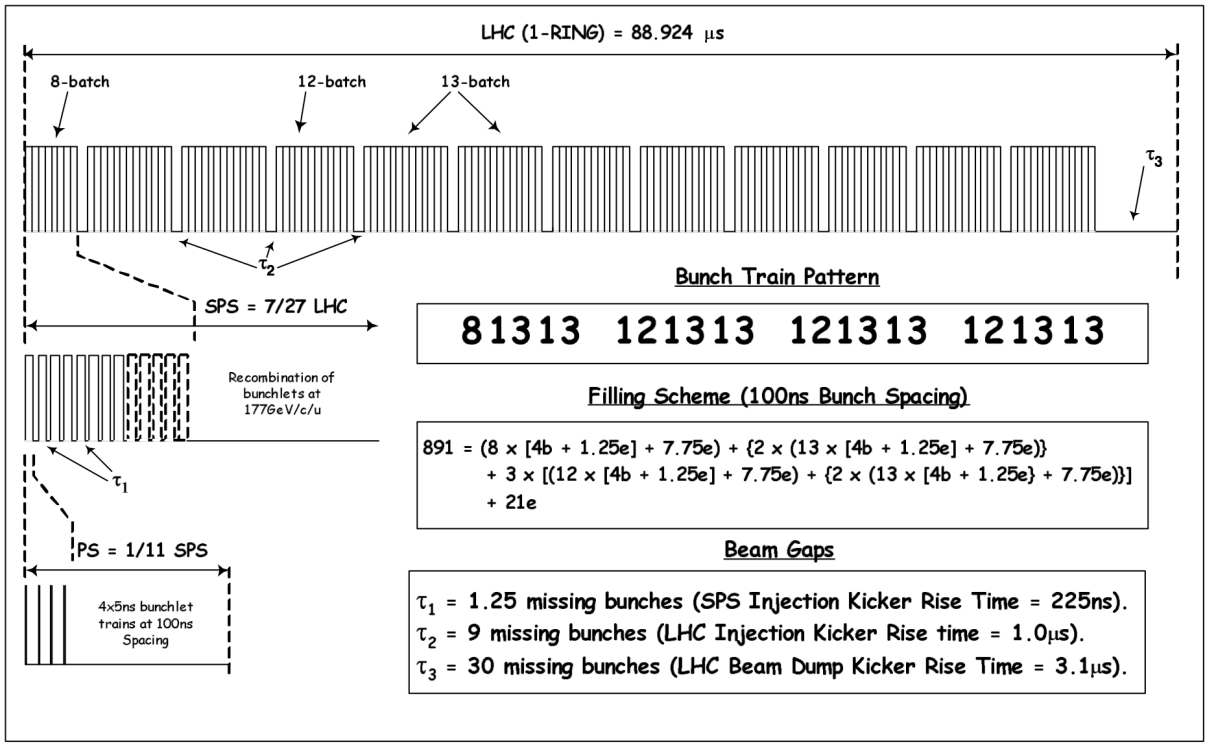

Figure III.1.10: Nominal bunch filling scheme for ion bunches in the PS, SPS and one LHC ring. [144]

Chapter III.2

ATLAS detector

The ATLAS detector is one of the two large general purpose detectors at LHC, the other being CMS. The ATLAS detector design requirements [145] was determined by the major physics objectives of the experiment, including search for the Standard Model Higgs boson, search for new heavy gauge bosons and supersymmetric particles and other new and exotic physics at the TeV scale, like signatures for extra dimensions and gravitons. To enable these measurements the detector should be able to efficiently reconstruct charged particles, jets, photons, leptons, collision vertices and secondary vertices and measure missing transverse energy with good resolution in high luminosity and radiation environments. For these purposes the ATLAS detector has been built with a large acceptance in "pseudorapdity" (see below) with full azimuthal coverage, good charged particle tracking and momentum resolution, very good electromagnetic calorimetry for electron and photon identification and hermetic hadronic calorimetry for jet and missing transverse energy measurements. The detector also provides good muon identification and momentum resolution. The experimental conditions at the LHC also require fast, radiation-hard electronics and sensor elements and high detector granularity to handle the particle fluxes.

The ATLAS detector is nominally forward-backward symmetric in the longitudinal direction about the interaction point. The detector has three main regions, an Inner Detector (ID), calorimeters and muon spectrometers. A thin superconducting solenoid magnet surrounds the inner-detector cavity, and three large superconducting toroid magnets (one barrel and two end-caps) are arranged around the calorimeters with an eight-fold symmetry. The different components of the detector are discussed in detail in the next sub sections. The layout of the detector is shown in figure III.2.1.

ATLAS uses a right-handed coordinate system. The origin of the coordinate system is taken to be the nominal interaction point. The beam direction defines the z-axis and the x-y plane is transverse to the beam direction. The positive z direction is defined as pointing towards the 'A' side of the detector (towards the counter-clockwise direction, when the LHC ring is viewed from above) and negative z direction as pointing towards the 'C' side of the detector (clockwise direction when viewed from above). The positive x direction points from the interaction point to the center of the LHC ring and positive y axis points upwards, perpendicular to the other two directions. The azimuthal angle ϕ is the angle measured around the beam axis and the polar angle θ is measured

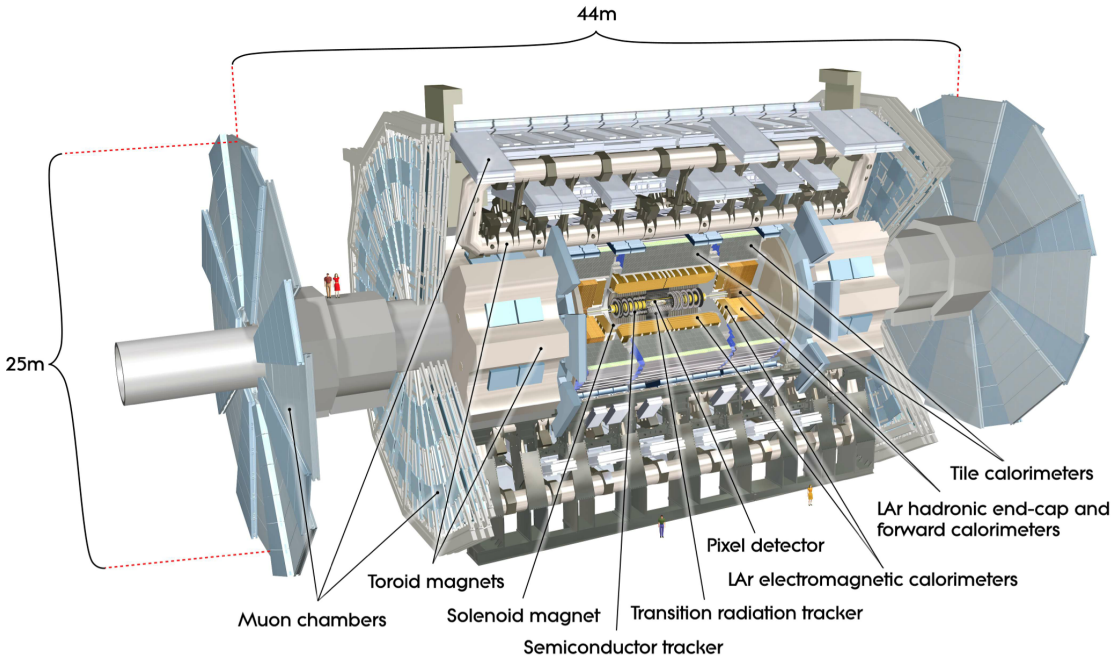

Figure III.2.1: Cut-away view of the ATLAS detector. [135]

from the beam axis. The pseudorapidity, η, defined as

$$\eta = -\ln\left(\tan(\theta/2)\right) = \frac{1}{2}\ln\left(\frac{|\vec{\mathrm{p}}| + p_z}{|\vec{\mathrm{p}}| - p_z}\right), \tag{III.2.1}$$

is often used as the longitudinal co-ordinate. For massive particles such as jets and leptons, the rapidity, $y = \frac{1}{2}\ln\left(\frac{E+p_z}{E-p_z}\right)$, is used, when the mass of the particle producing the tracks or energy deposition is known. For particles with momentum much larger than their mass, the momentum is approximately equal to the energy and $\eta \approx y$. The transverse momentum p_{T} and transverse energy E_T are measured in the $x-y$ plane unless specified otherwise.

III.2.1 Inner Detector

The ATLAS Inner Detector (ID) [146] is the component situated closest to the beam pipe and is designed to provide hermetic and robust pattern recognition, excellent momentum resolution and reconstruction of both primary and secondary vertices for charged particles tracks with $p_{\mathrm{T}} > 0.5$ GeV (nominally, but down to 0.1 GeV in ongoing studies). The design goal is a p_{T} resolution of $\frac{\sigma p_{\mathrm{T}}}{p_{\mathrm{T}}} = 0.05\% \times p_{\mathrm{T}}\,[\mathrm{GeV}] \oplus 1\%$. The detector covers the pseudorapidity range of $|\eta| < 2.5$ and has 2π azimuthal acceptance. It also provides electron identification over $\eta < 2.0$ and over energies

ranging from 0.5 GeV to 150 GeV. The ID is situated within a magnetic field of 2T of the central solenoid and has a length of ± 3512 mm in the z direction and extends to a radius of 1150 mm.

The ID has three independent but complementary sub-detectors. The innermost is the silicon pixel layers followed by the silicon microstrip layer (SCT). These provide high resolution pattern recognition at the inner radii. The Transition Radiation Tracker (TRT), situated at larger radii, with an average of 36 hits per track, provide continuous tracking to enhance the pattern recognition. It also provides electron identification over a wide range of energies. In order to maintain low noise levels in the high radiation environment, the silicon detectors are kept at low temperatures (between -5 to -10^0 C). The TRT is designed to operate at room temperature. Each of the sub-detectors have "barrel" and "endcap" regions, where the detector modules are arranged in concentric cylinders and disks along the z axis respectively. Figure III.2.2 shows the layout and dimensions of major detector elements. Details of the individual sub-detectors in the ID are given below.

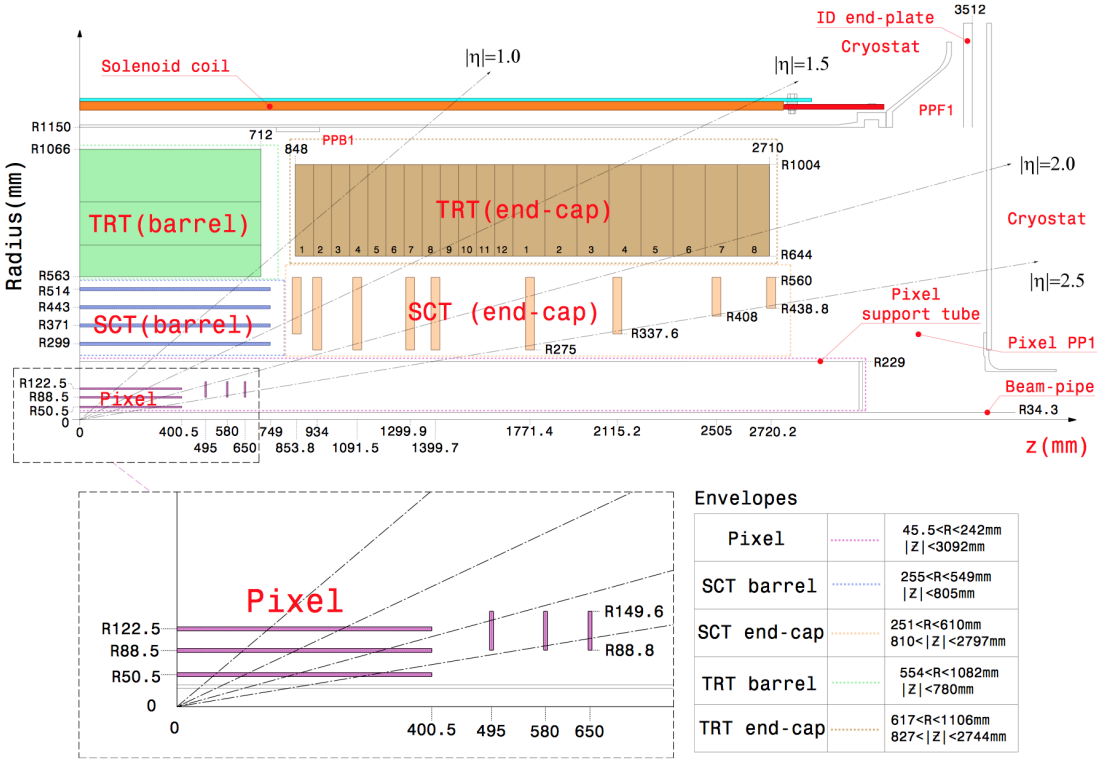

Figure III.2.2: Plan view of a quarter-section of the ATLAS inner detector showing the major detector elements (excluding IBL) with its active dimensions and envelopes. (Labels PP1, PPB1 and PPF1 indicate the patch-panels for the ID services.) [135]

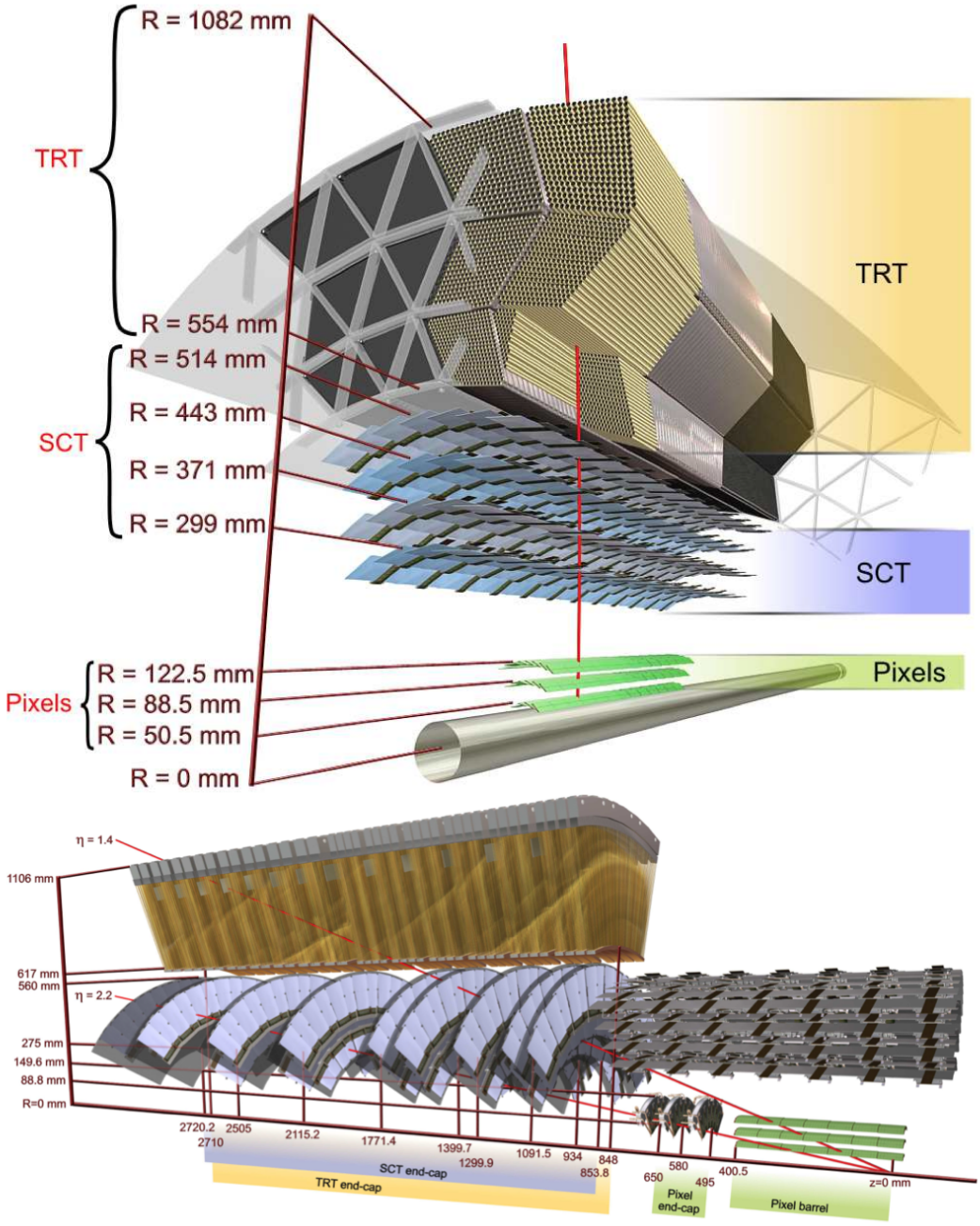

Figure III.2.3: Drawing showing the sensors and structural elements traversed by a charged track of $p_{\mathrm{T}} = 10$ GeV in the barrel inner detector at $\eta = 0.3$ (top) and by two charged tracks of $p_{\mathrm{T}} = 10$ GeV in the end-cap inner detector at $\eta = 1.4$ and $\eta = 2.2$ (bottom) [135]

III.2.1.1 Silicon Pixel Layer

The Pixel detector [147, 148] consists of three concentric cylindrical detectors in the barrel region and three endcap disks each in the forward and backward regions. The barrel cylinders are situated at radial distances $r = 5.05$, 8.85 and 12.25 cm and within $|z| = 40$ cm. The end cap disks (actually, annulus coaxial with the beam pipe) have a radial extend, 8.88 cm $< r <$ 14.96 cm and are situated at $z = \pm 49.5$, 50.0 and 65.0 cm. The pixel layers typically provide three measurements (four, including the IBL layer (see next sub-section) present in Run2 data taking) for a particle originating from the interaction point.

A pixel module consists of a stack made of front-end electronic chips, bump bonds which connect the electronic channels to the pixel sensor elements, the actual sensor tile and a printed circuit board with module-control chip (MCC) and a connector (barrel modules) or a wire micro-cable (endcap modules) bonded to the circuit board. The structure of a barrel pixel module is shown in figure III.2.4. The sensor tiles are 63.4×24.4 mm^2 in area and 250 μm thick and are oxygenated n-type semiconductor wafers with the readout on the n^+ implants (n-in-n type detectors). The particular choice is made because of its good charge collection efficiency and increased radiation tolerance. The sensors operate at a bias voltage of $\sim$ 150 V, but this could increase to up to 600 V, depending of the radiation damage over time. Each sensor tile contains a 328×144 array of pixel cells. The pixel cells have a nominal area of 50×400 μm^2, for 90% of the pixels, rest are 50×600 μm^2, near the regions of front end chips. Of the 47232 pixel cells in each sensor, some near the front end chips are ganged into groups of four, leading to a total of 46080 readout channels per pixel module and a total of $\sim$80.4 million readout channels in the pixel detector. The modules are arranged in 112 barrel staves (22, 38 and 52 staves respectively in the first, second and third layers), with 13 modules per stave and 48 endcap sectors (8 sectors per disk), with 6 modules each. The cross-sectional view of the arrangement of barrel staves are shown in figure III.2.4.

The pixel detector position resolution is 10 μm in $R - \phi$ plane and 115 μm in z direction for the barrel detectors and 10 μm in $R - \phi$ plane and 115 μm in R for the endcap disks.

III.2.1.2 Insertable B-Layer (IBL)

An additional pixel layer, called the Insertable B-Layer [149] was installed closer to the beam pipe than the first layer of the Pixel detector, in the long shut down after Run1 ended in 2013. The IBL will improve b-hadron tagging efficiency and tracking and vertexing performances by introducing a fourth, high granularity, pixel layer. The IBL consists of 14 staves arranged around the beam pipe with a tilt of 14^0 allowing for an azimuthal overlap of the staves and ensuring full azimuthal coverage. The average distance of the staves from the center of the beam pipe is 33.25 mm and each stave is 64 cm long covering a pseudorapidity of $|\eta| < 2.9$.

The IBL modules use planar sensors, like the Pixel sensors, for the inner parts of the detector for about 75% of the active area and innovative 3D sensors, in which the electrodes pass through the bulk and are not only on the surface of the silicon sensor, for the large $|\eta|$ region, covering the remaining 25%. The planar sensors use the n-in-in technology as the Pixel sensors and are 200 μm thick and 4×2 cm^2 in area. Each planar sensor has 26880 pixels arranged in 80 columns and 336 rows. The 3D sensors use n-in-p silicon sensors (readout on n^+ implants in p-type semiconductor),

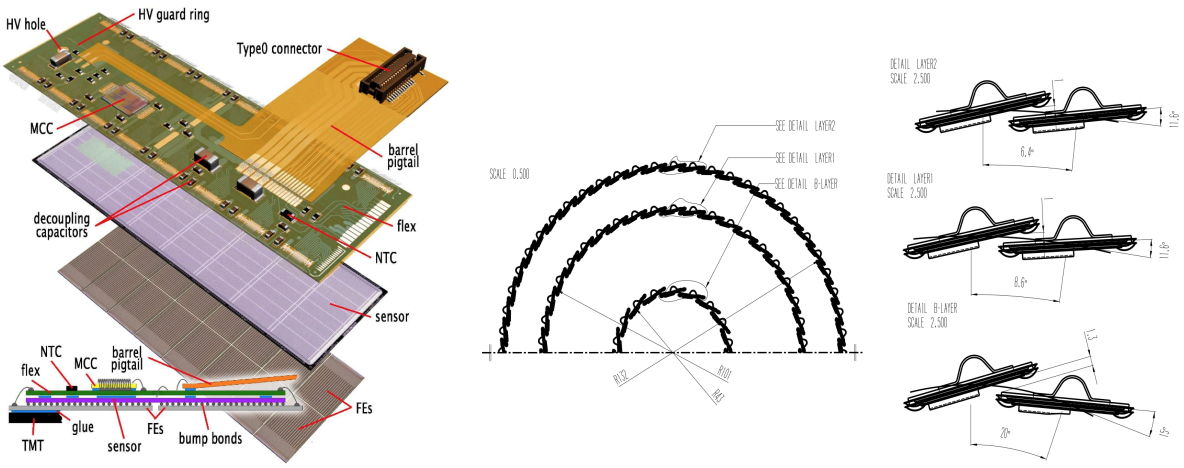

Figure III.2.4: Schematic view of a barrel pixel module illustrating the constitutive elements and a plan view of the module layout [135]. (Right) Schematic view of the barrel cross-section showing the arrangement of barrel staves in three layers [147].

230 μm thick and 2×2 cm^2 in area. Both the planar and 3D sensors are tested to have high radiation tolerance. The layout of the structure of a planar module and a cross-sectional view of the IBL staves are shown in figure III.2.5.

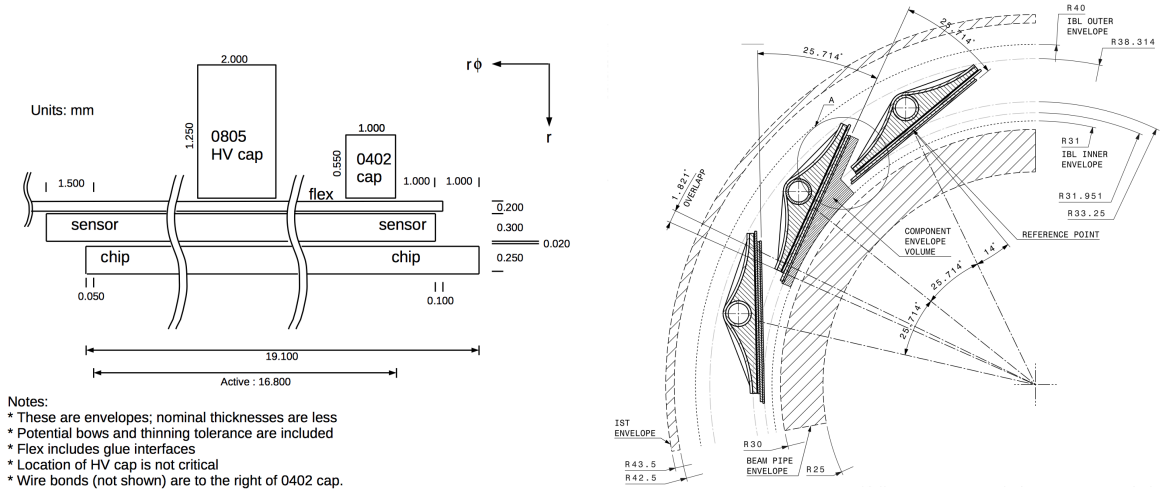

Figure III.2.5: (Left) Cross section view of a planar module assembly. (Right) A cross-sectional view of the layout of IBL staves [149].

III.2.1.3 Silicon Microstrip Detector (SCT)

The SCT detector [150, 151] consists of four cylindrical barrels and two endcaps with nine disk layers each. The average radii of the four barrel layers are 29.9, 37.1, 44.3 and 51.4 cm respectively and have a length of 149.8 cm each. The endcap disks are of varying annular size, with the largest having an inner radius of 27.5 cm and outer radius of 56 cm, and are located within $83.9 < |z| < 273.5$ cm. The inner radius of the outermost four disks increase such that a high momentum particle with $|\eta| = 2.5$ from the nominal interaction point just touches their inner radius. The SCT detector provides full azimuthal coverage and generally provides four space point measurements (or eight hits) for a track.

The SCT sensors are semi conductor sensors that use single sided p in n technology with AC coupled readout strips. The operating bias voltage for the sensors is $\sim$ 150 V initially, but could increase to between 250 and 350 V after ten years of operation depending on the radiation damage. The sensors have a thickness of 285$\pm$15 μm and have 768 active strips per sensor. Each strip has a binary readout. The rectangular barrel sensors have a strip pitch of 80 μm while the endcap sensors are trapezoidal with radial strips of constant azimuth with mean pitch of $\sim$ 80 μm.

The SCT has a total of 4088 modules with 2112 in the barrel layers and 1976 in the endcap disks. The modules are rectangular in barrel and arranged in rows with 12 modules per row. The disk modules are trapezoidal and are arranged in one, two or three rings (named Outer, Middle and Inner), depending on the disk. Each module consists of two planes of sensors glued back to back around a central spine with a relative angular rotation of 40 μrad between the planes. In the barrel modules and Outer and Middle ring modules of the endcap disks, each plane has two sensors daisy chained together while the Inner ring modules have one. In the barrel, the modules are arranged with the strips nearly parallel to the beam axis, while in the endcap modules, the strips are radial. Two hits on the back to back sensors with the relative stereo angle gives one space point with the desired position resolution. The layout of a barrel and an endcap SCT module is shown in figure III.2.6. The SCT position resolution is 17 μm in $r - \phi$ and 580 μm in z directions for the barrel modules and 16 μm in $r - \phi$ and 500 μm in r for the endcap modules.

III.2.1.4 Transition Radiation Tracker (TRT)

The TRT [152, 135] uses drift tubes (straws) to detect the transition radiation from the traversing particles. The TRT, like the Pixel and SCT detectors, has cylindrical barrel layers and endcap disks. The barrel cylinders extend to $|z| < 71.2$ cm in the longitudinal direction and are situated within 56.3 cm $< r <$ 106.6 cm. The end cap disks are situated within 64.4 cm $< r <$ 100.4 cm and within $\pm$84.8 cm $< z < \pm$271 cm.

The TRT straws are 4 mm diameter polyimide tubes with a tube wall thickness of 70 μm. The straw tube walls are made of two 35 μm thick multi-layer films, consisting of a 25 μm thick polyimide layer coated on one side with a 0.2 μm layer of Al and protected by a graphite-polyimide layer and on the other side with a polyurethane layer to heat-seal the two films back-to-back. The Al coating acts as the cathode and a 31 μm diameter W wire, coated with 0.5-0.7 μm of Au, running through the center of the straw serves as the anode. The anodes are directly connected to the front-end electronics and are kept at ground potential. The cathodes are operated typically

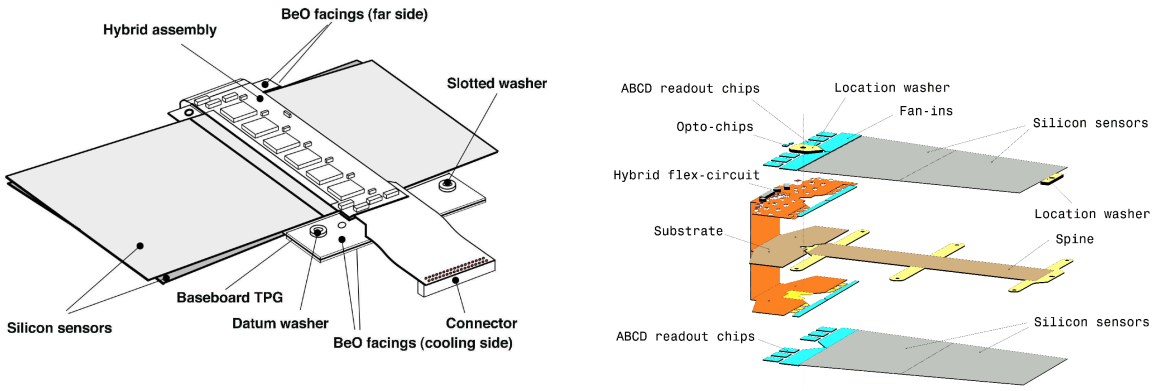

Figure III.2.6: Schematic drawing of a barrel SCT module (left) and a schematic showing the different components of an endcap module in the Middle ring (right) [135].

at -1530 V. A gas mixture of 70% Xe, 27% CO_2 and 3% O_2 fills the straws. The straws are mechanically stabilised using carbon fibres. Low energy transition radiation photons are absorbed in the Xe gas mixture and give much larger signal amplitudes than the signals from ionising charged particles. The front-end electronics is provided with separate low and high thresholds to distinguish between transition radiation and ionising particles.

The barrel TRT is made up of three rings with 32 modules each and is contained within a carbon fibre laminate shell. The straws are arranged in a uniform axial array with a mean spacing of ~ 7 μm and the arrays are stacked in layers with a total of 73 layers from all three rings. Each module has a total of 52544 straws. The straws are embedded in a matrix of 19 μm diameter polypropylene fibres which serve as the transition radiation material. The module shells are filled with $C0_2$ which circulate outside the straws and prevent accumulation of xenon from possible gas leakage and also help dissipate the heat from the straws to the module shells.

The TRT endcaps each consist of two sets of independent wheels. The first 12 wheels closer to the interaction point each has eight successive layers of straws spaced 8 mm apart and the outer eight wheels, eight layers spaced 15 mm apart. Each layer contains 768 radially arranged straws of 37 cm length with uniform azimuthal spacing. The space between the straw layers is filled with layers of 15 μm thick polypropylene foils separated by a polypropylene net. The successive straw layers are rotated from one layer to the next by 3/8 of the azimuthal straw spacing in the layer to have uniformity in the number of crossed tracks for high p_{T} tracks.

All charged tracks with $p_{\mathrm{T}} > 0.5$ GeV and $|\eta| < 2.0$ will traverse at least 36 straws, except in the barrel-end-cap transition region ($0.8 < |\eta| < 1.0$) where they traverse a minimum of 22 straws. Electrons with energies above 2 GeV typically give from seven to ten high threshold hits from transition radiation. The intrinsic position resolution of the TRT straws is 130 μm in the $r - \phi$ direction and gives essentially no position discrimination information in the z direction.

III.2.2 Calorimeters

The ATLAS calorimeters are sampling calorimeters with full azimuthal symmetry and coverage. The calorimeters closer to the beam are housed in one barrel and two endcap cryostats. The barrel cryostat houses the electromagnetic barrel calorimeter (EMB) and the two endcaps on each side contain an electromagnetic endcap calorimeter (EMEC), a hadronic endcap calorimeter (HEC) and a forward calorimeter (FCal). Liquid argon is used as the active medium in all these calorimeters. The outer calorimeters are hadronic calorimeters and consists of a central barrel and two extended barrels. The hadronic calorimeters uses scintillator tiles as the active medium. The different calorimeters together cover the range $|\eta| < 4.9$. A schematic view of the different calorimeter elements are shown in III.2.7.

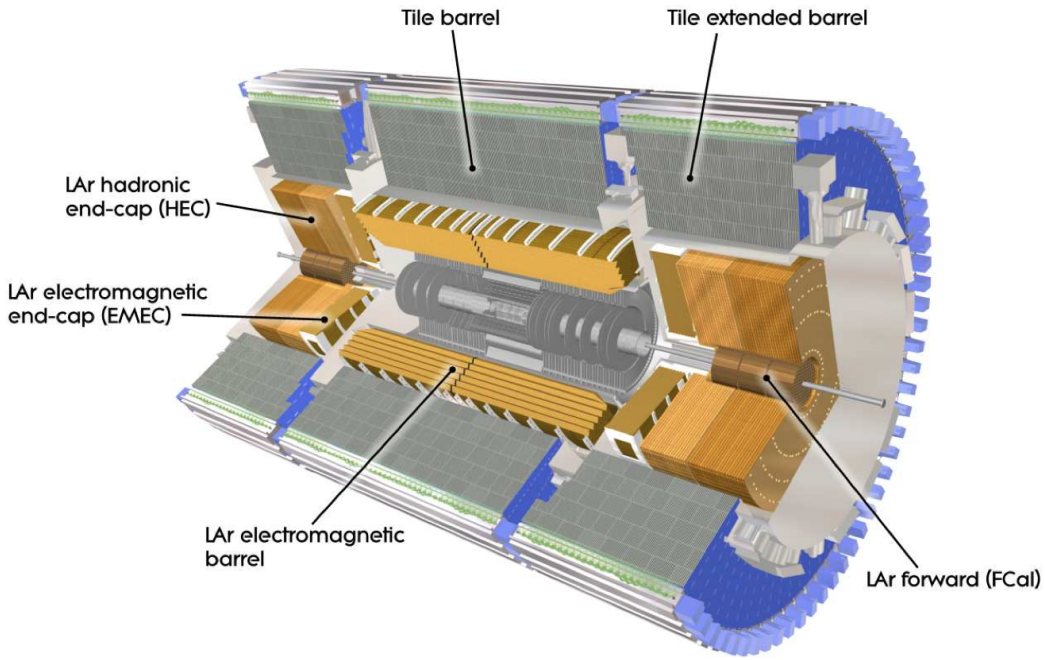

Figure III.2.7: Cut-away view of the ATLAS calorimeter system. [135].

The calorimeters are designed to satisfy the requirements of various physics processes of interest taking into account the radiation environment in which they are located. Over the pseudorapidity range where they overlap with the Inner Detector, the electromagnetic calorimeters have fine granularity for precision measurements of electrons and photons. The rest of the calorimeters have a coarser granularity sufficient to satisfy the requirements of jet reconstruction and missing energy measurements. The calorimeters also provide good containment for electromagnetic and hadronic showers and limit the punch-through to the muon detectors to levels well below that of the irreducible noise. The total thickness of the electromagnetic calorimeter is > 22 radiation

lengths (X_0) in the barrel and > 24 X_0 in the endcaps. The active barrel calorimeter has an approximate interaction length (λ) of 9.7 and the endcaps, of 10. The large η and full azimuthal coverage along with the large thickness of the calorimeters also allow for a good measurement of the missing transverse energy, E_T^{miss}.

The next subsections discuss the electromagnetic, hadronic and forward calorimeters in more detail.

III.2.2.1 Electromagnetic calorimeter

The electromagnetic (EM) calorimeter [135] consists of a barrel part situated in $|\eta| < 1.475$ and two endcaps at $1.375 < |\eta| < 3.2$. The barrel calorimeter in turn is divided into two identical half-barrels, separated by a small gap at $z = 0$. The half-barrels are 3.2 m in length and have inner and outer diameters of 2.8 m and 4.0 m respectively. Each endcap also consists of two coaxial wheels, an outer wheel covering the region $1.375 < |\eta| < 2.5$ and an inner wheel covering $2.5 < |\eta| < 3.2$. The wheels are 63 cm thick and have an external and internal radii of 2098 mm and 330 mm respectively. The EM calorimeter uses liquid argon (LAr) as the active medium with lead plates as absorbers arranged in an accordion geometry. The accordion geometry provides full coverage in ϕ and fast extraction of the signal. In the barrel region, the accordion waves are axial and run in ϕ, while in the endcaps the waves are radial and run axially. Three conducting copper layers separated by insulating polyimide sheets function as the electrodes and are located in the gap between the absorbers. The two outer copper layers are kept at high voltage and the inner layer is used to readout the signal.

The half-barrel consists of 1024 accordion shaped absorbers with electrodes in between them, held in position by honey comb spacers. The barrel is divided into three layers in depth (radially). The readout granularity in $\eta - \phi$ is finer in the first and second layers and coarser in the third layer. Most of the energy of the electromagnetic shower is collected by the second layer while the third layer sees only the tail of the shower. The endcap consists of two coaxial wheels on each side. In the region for precision physics ($1.5 < |\eta| < 2.5$), the endcap wheels, like the barrel calorimeters, are divided into three longitudinal layers. The first two layers have finer granularity than the third layer. The inner end cap wheel ($2.5 < |\eta| < 3.2$), only has two longitudinal layers and coarser readout granularity. The readout granularity for the different calorimeter layers are shown in figure III.2.8. The EM calorimeter also has a presampler detector in the region $|\eta| < 1.8$ in front of the first calorimeter layer used to correct for the energy lost by the electrons and photons before reaching the detector.

III.2.2.2 Hadronic Calorimeters

Tile Calorimeter

The Tile calorimeter [135] is located directly outside the EM calorimeter envelope and covers a pseudorapidity range $|\eta| < 1.8$. It consists of a central barrel, 5.8 m in length and two extended barrels of 2.6 m in length each. The Tile calorimeters extend radially from an inner radius of 2.28 m to an outer radius of 4.25 m. The central barrel extends to $|\eta| < 1.0$ and the extended barrels lie

	Barrel		End-cap	
EM calorimeter				
Number of layers and $\|\eta\|$ coverage				
Presampler	1	$\|\eta\| < 1.52$	1	$1.5 < \|\eta\| < 1.8$
Calorimeter	3	$\|\eta\| < 1.35$	2	$1.375 < \|\eta\| < 1.5$
	2	$1.35 < \|\eta\| < 1.475$	3	$1.5 < \|\eta\| < 2.5$
			2	$2.5 < \|\eta\| < 3.2$
Granularity $\Delta\eta \times \Delta\phi$ versus $\|\eta\|$				
Presampler	0.025×0.1	$\|\eta\| < 1.52$	0.025×0.1	$1.5 < \|\eta\| < 1.8$
Calorimeter 1st layer	$0.025/8 \times 0.1$	$\|\eta\| < 1.40$	0.050×0.1	$1.375 < \|\eta\| < 1.425$
	0.025×0.025	$1.40 < \|\eta\| < 1.475$	0.025×0.1	$1.425 < \|\eta\| < 1.5$
			$0.025/8 \times 0.1$	$1.5 < \|\eta\| < 1.8$
			$0.025/6 \times 0.1$	$1.8 < \|\eta\| < 2.0$
			$0.025/4 \times 0.1$	$2.0 < \|\eta\| < 2.4$
			0.025×0.1	$2.4 < \|\eta\| < 2.5$
			0.1×0.1	$2.5 < \|\eta\| < 3.2$
Calorimeter 2nd layer	0.025×0.025	$\|\eta\| < 1.40$	0.050×0.025	$1.375 < \|\eta\| < 1.425$
	0.075×0.025	$1.40 < \|\eta\| < 1.475$	0.025×0.025	$1.425 < \|\eta\| < 2.5$
			0.1×0.1	$2.5 < \|\eta\| < 3.2$
Calorimeter 3rd layer	0.050×0.025	$\|\eta\| < 1.35$	0.050×0.025	$1.5 < \|\eta\| < 2.5$
Number of readout channels				
Presampler	7808		1536 (both sides)	
Calorimeter	101760		62208 (both sides)	
LAr hadronic end-cap				
$\|\eta\|$ coverage			$1.5 < \|\eta\| < 3.2$	
Number of layers			4	
Granularity $\Delta\eta \times \Delta\phi$			0.1×0.1	$1.5 < \|\eta\| < 2.5$
			0.2×0.2	$2.5 < \|\eta\| < 3.2$
Readout channels			5632 (both sides)	
LAr forward calorimeter				
$\|\eta\|$ coverage			$3.1 < \|\eta\| < 4.9$	
Number of layers			3	
Granularity $\Delta x \times \Delta y$ (cm)			FCal1: 3.0×2.6	$3.15 < \|\eta\| < 4.30$
			FCal1: $\sim$ four times finer	$3.10 < \|\eta\| < 3.15$, $4.30 < \|\eta\| < 4.83$
			FCal2: 3.3×4.2	$3.24 < \|\eta\| < 4.50$
			FCal2: $\sim$ four times finer	$3.20 < \|\eta\| < 3.24$, $4.50 < \|\eta\| < 4.81$
			FCal3: 5.4×4.7	$3.32 < \|\eta\| < 4.60$
			FCal3: $\sim$ four times finer	$3.29 < \|\eta\| < 3.32$, $4.60 < \|\eta\| < 4.75$
Readout channels			3524 (both sides)	
Scintillator tile calorimeter				
	Barrel		Extended barrel	
$\|\eta\|$ coverage	$\|\eta\| < 1.0$		$0.8 < \|\eta\| < 1.7$	
Number of layers	3		3	
Granularity $\Delta\eta \times \Delta\phi$	0.1×0.1		0.1×0.1	
Last layer	0.2×0.1		0.2×0.1	
Readout channels	5760		4092 (both sides)	

Figure III.2.8: Main parameters of the ATLAS calorimeter system. [135].

between $0.8 < |\eta| < 1.7$. Tile calorimeter is a sampling calorimeter with steel as the absorber and polysterene plastic scintillator tiles as the active medium. The calorimeter is segmented in depth in three layers with 1.5, 4.1 and 1.8 interaction lengths (λ). The central and extended barrels are divided into 64 azimuthal modules and provides full coverage in ϕ. The scintillator tiles are arranged radially and normal to the beam line and are read out from two edges of the tiles using wavelength shifting fibres. The readout fibres are grouped into readout photomultiplier tubes to provide an approximate projective geometry.

Hadronic EndCap Calorimeter (HEC)

The hadronic endcap calorimeter [135] is located directly behind the EM endcap calorimeter and shares the same LAr cryostat with the EM endcap and Forward calorimeters. It covers a pseudo-rapidity range of $1.5 < |\eta| < 3.2$ and consists of two wheels in each end cap cryostat. Each wheel has two longitudinal sections and are constructed of 32 identical wedge shape modules arranged azimuthally. The wheels have an outer radius of 2.03 m and an inner radius of 0.475 m (except for $|\eta| > 3.1$ where it overlaps with the FCal, the inner radius is 0.372 m). The HEC uses LAr as the active medium and copper plates as absorbers. The modules of the front wheels consist of 24 copper plates of 25 mm thick, plus a 12.5 mm thick front plate, arranged longitudinally. The rear wheels are made of 16 copper plates, each 50 mm thick along with a front plate 25 mm thick. The LAr gaps in between the plates all have the same thickness of 8.5 mm. Three electrodes divide the space between the plates into four drift zones of 1.8 mm thickness each. The middle electrode carries a pad structure covered by a high resistivity layer and serves as the readout electrode and defines the lateral segmentation of the calorimeter. The size of the read out cells in $\Delta\eta \times \Delta\phi = 0.1 \times 0.1$ for $|\eta| < 2.5$ and 0.2×0.2 for larger η.

Forward Calorimeter (FCal)

The Forward calorimeter [135] covers $3.1 < |\eta| < 4.9$ in pseudorapidity and is situated in the LAr endcap cryostat. The FCal has a depth of approximately 10 interaction lengths and consists of three longitudinal modules 45 cm long on each side. The first module (FCal1) is optimised for electromagnetic measurements and the other two (FCal2 and FCal3) for measurement of hadronic showers. The arrangement of the FCal layers within the endcap cryostat is shown in figure III.2.9.

The location of FCal at large η means it is exposed to large particle fluxes and hence requires a design with very small LAr gaps to avoid problems due to ion buildup. This is achieved by using an electrode structure of small diameter rods centered in tubes with a small gap in between them filled with LAr, which acts as the active medium. Copper was chosen as the absorber for FCal1 to optimize resolution and heat removal while tungsten was used in FCal2 and FCal3 to contain and minimise the lateral spread of hadronic showers. FCal1 is made of stacked copper plates with 12260 holes drilled through them through which the electrodes are inserted. The electrodes are arranged parallel to the beam axis and consists of rods and tubes made of copper. FCal2 and FCal3 have a similar structure, except for the use of tungsten rods instead of copper rods. Figure III.2.10 shows the electrode structure in FCal1. Signals are read out from the side of FCal1 near the interaction point and from the side further from the interaction point in the case of FCal2 and FCal3. FCal1

has a total of 1008 readout channels and FCal2 and FCal3 500 and 254 respectively. The readout granularity of the different FCal layers are given in figure III.2.8.

III.2.3 Muon Spectrometers

Muon spectrometers [135] are located outside the calorimeters and measure the charged particles (muons) exiting the barrel and endcap calorimeters. The muon tracks are deflected by the superconducting air core toroid magnets and are detected in the precision tracking and trigger chambers. Precision tracking and momentum measurement are provided by Monitored Drift Tube chambers (MDT) in the range $|\eta| < 2.7$. The MDT in the barrel region are arranged in three concentric cylindrical shells around the beam axis at radial distances of approximately 5 m, 7.5 m and 10 m. The muon chambers in the endcap region are large wheels located perpendicular to the beam axis at $z = \pm 7.4$ m, 10.8 m, 14 m and 21.5 m from the interaction point. The barrel chambers are located between and on the coils of the barrel toroid magnet while the endcap wheels are in front and behind the two endcap torroid magnets. The MDT chambers consist of three to eight layers of drift tubes and achieve an average resolution of 80 μm per tube. The muon system also consists of fast trigger chambers, Resistive Plate Chambers (RPC), in the barrel region ($|\eta| < 1.05$) and Thin Gap Chambers (TGC), in the endcap region ($1.05 < |\eta| < 2.4$), that can provide track information within few tens of nanoseconds of passing of the particle.

III.2.4 Minimum Bias Trigger Scintillator and Forward Detectors

The minimum bias trigger scintillator (MBTS) [153] is used primarily to trigger on minimum bias (non diffractive inelastic collisions) events in p+p, p+Pb and Pb+Pb collisions. It is made of polystyrene scintillators and is located just in front of the electromagnetic endcap at $z = \pm 3.56$ m. The forward region of ATLAS has three small detector systems. Two of these, the LUCID (LUminosity measurement using Cerenkov Integrating Detector) [154], located at $z = \pm 17$ m from the interaction point, and the ALFA (Absolute Luminosity For ATLAS) [155], located at $z = \pm 240$ m, are used to determine the luminosity delivered to ATLAS. The LUCID detects inelastic p+p scattering in the forward region and is used as the primary online relative-luminosity monitor for ATLAS. ALFA measures elastic scattering at small angles and is used for absolute luminosity measurement. It consists of scintillating fiber trackers located inside Roman pots which are designed to approach as close as 1 mm to the beam. The third detector is the Zero Degree Calorimeter [156], located at $z = \pm 140$ m, and detects neutral particles from the collisions. The ZDC can be used to determine centrality the in heavy-ion collisions and is also used to trigger on minimum bias events in heavy-ion collisions. The MBTS and ZDC detectors are discussed in a bit more detail in the next subsections.

III.2.4.1 Minimum Bias Trigger Scintillator (MBTS)

The MBTS consists of two sets of eight polystyrene scintillators located at $|z| = 3.56$ m on each side of the interaction point. Each scintillator has a trapezoidal shape covering an angle of $2\pi/8$

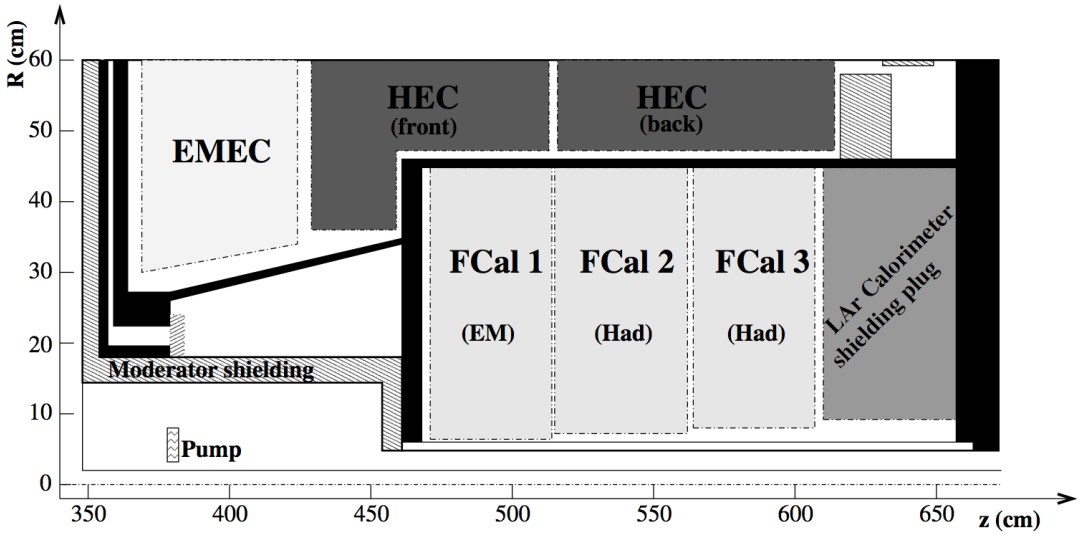

Figure III.2.9: Schematic diagram showing the three FCal modules located in the end-cap cryostat.. [135].

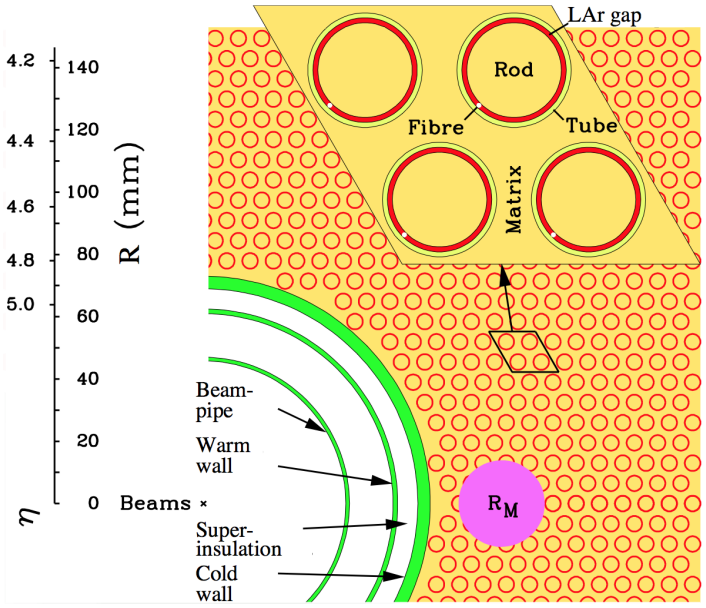

Figure III.2.10: Electrode structure of FCal1 showing the matrix of copper plates and the copper tubes and rods with the LAr gaps. The solid disk represents the Moliere radius, R_M. [135].

in azimuth and is 2 cm thick. The two sets are arranged radially with the inner set having 15.3 cm $< r <$ 42.6 cm ($3.84 < |\eta| < 2.82$) and the outer set, 42.6 cm $< r <$ 89.0 cm ($2.82 < |\eta| < 2.09$). Light collected from each wedge using wavelength shifting optical fibres are read out using a photomultiplier tube. The number of MBTS wedges with hits above a threshold are used to create Level 1 (L1) triggers of the form `MBTS_N`, triggering on hits on single side, and `MBTS_N_N`, triggering on hits on both side (N can have maximum value 16). The MBTS wedges are also timing capable. The average of the times (relative to the LHC clock) from the MBTS wedges having a hit above threshold can be calculated for each side of the detector. The difference between these times from the two sides can be used to reject non collision background in the offline analysis.

III.2.4.2 Zero Degree Calorimeter (ZDC)

The ZDC consists of four modules, one electromagnetic (about 29 radiation lengths deep) and three hadronic (each 1.14 interaction lengths deep), located on each side at $|z| = 140$ m ($|\eta| > 8.3$), where the straight section of the beam-pipe gets divided back into two separate beam-pipes. They are placed in a slot in the TAN (Tanget Absorder Neutral) absorber. The primary objective of the ZDC is to measure spectator neutrons from heavy ion collisions. Since minimum bias heavy ion collisions produce fragmenting neutrons from both participating ions, a coincidence of the two ZDC detectors on either side can be used as an efficient trigger for minimum bias events with very little background from beam-gas and beam halo effects. ZDC can also be used to detect and reconstruct π^0 and η decaying into two photons, in the forward region, in low luminosity p+p collisions.

The ZDC modules consist of 11 tungsten plates of 10 mm thick and 91.4 mm wide and 180 mm high, with steel plates extending above for 290 m, stacked perpendicular to the beam axis. Between the plates, 1.5 mm quarts strips (actually quartz rods, but called strips to distinguish from position sensing rods discussed below) run vertically and collect the Cherenkov light produced by the incident particles and is read out by photomultiplier tubes (PMT). The strips provide a measurement of the total incident energy on the modules. In addition to the strips, the EM module on C side and the first hadronic module on each side are equipped with quartz rods for transverse position measurement. Quartz rods of 1.0 mm diameter penetrate the tungsten plates parallel to the beam axis in an 8×12 matrix in the transverse plane. At the rear end of the module, the rods are bent 90^0 vertically and is read out from above using multi-anode phototubes (MAPMTs). In the EM module, each of the 96 position sensing rods is mapped onto one pixel of the MAPMT, while in the hadronic modules, clusters of four rods are mapped into one pixel. In heavy-ion collisions, the transverse position information can be used to determine the orientation of the reaction plane in the collision. A schematic of the arrangement of the ZDC modules are shown in figure III.2.11

III.2.5 ATLAS Trigger and Data Acquisition (TDAQ)

The high luminosity and rate of collisions at the LHC require that fast decisions be made to identify and select interesting events and the data from various sub-detectors for these events

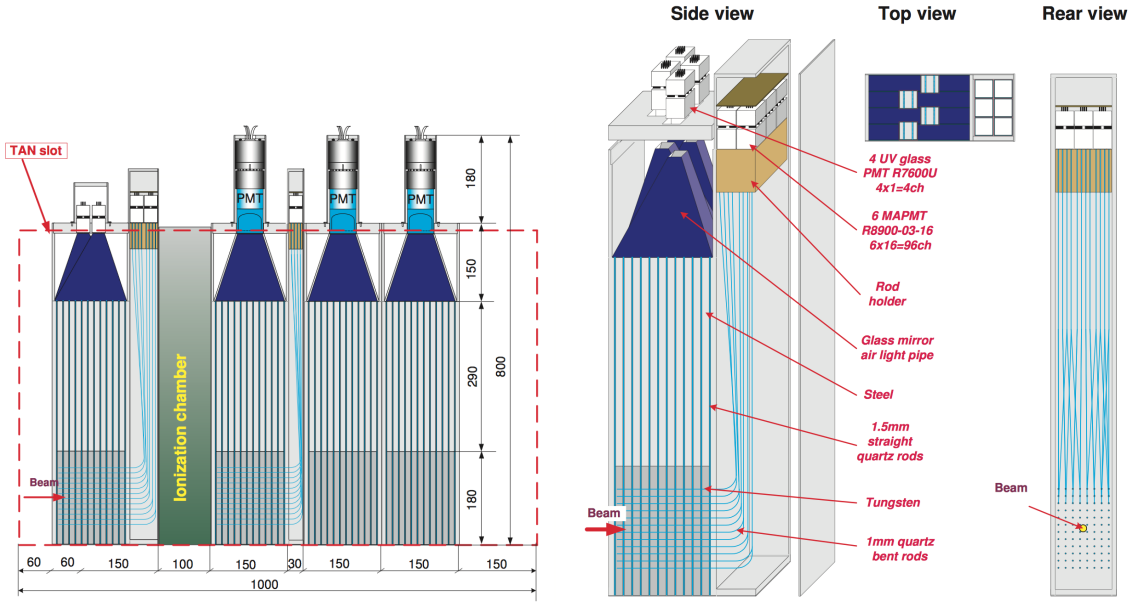

Figure III.2.11: (Left) Arrangement of ZDC modules on the side with position sensing EM module. (Right)Configuration of the EM module with position sensing rods [156].

be formatted and transferred for storage in a timely manner. This is done through the TDAQ system [157, 135]. The trigger system consists of Level 1 (L1) triggers, implemented using custom made electronics and uses limited granularity information from the detectors to provide the first level of event selection and Hight Level Triggers (HLT), using more detailed information from the detectors to further refine the selection and is implemented almost entirely on commercially available computers and networks. During Run1, the HLT trigger consisted of two separate levels, Level 2 (L2) triggers, which makes decision using the full granularity and precision data from the detectors, within the Regions of Interest defined by the L1 trigger and Event Filter (EF) triggers, which uses offline analysis procedures on fully built events to further refine the selection. In Run2, the L2 and EF triggers were combined into a single step HLT trigger. The 40 MHz event rate is reduced to 75 kHz (100 kHz in Run2) after the L1 selection and the HLT triggers do a further rate reduction to have a final rate of up to 200 Hz (1 kHz in Run2) with an event size of approximately 1.3 Mbyte.

The L1 triggers search for high transverse momentum muons, electrons, photons, jets, τ leptons decaying into hadrons, large missing energy and total energy in events. It only uses the information from a subset of detectors and with limited granularity. High p_{T} muons are identified using signatures from Resistive Plate Chambers (RPC) and Thin-Gap Chambers (TGC) in the muon system. The logic provides six independently programmable p_{T} thresholds. The detectors have a timing accuracy sufficient to provide unambiguous bunch cross identification of the event containing the muon candidate. All the calorimeter subsystems are used to identify jets, τ-leptons, electromagnetic clusters, missing and total energy. The calorimeter triggers are implemented using

the L1Calo system. It receives the analogue signals from 7000 trigger towers of reduced granularity from the electromagnetic and hadronic calorimeters. The L1Calo consists of three modules, a preprocessor module (PPM) which digitizes the input signals and perform bunch crossing identification, the Cluster Processor (CP) which identifies electrons, photons and *tau*-leptons with E_T above programmable thresholds and a Jet/Energy-sum processor (JEP) which identify jets and check for large missing and total E_T. The L1 triggers send the multiplicities of trigger objects passing the thresholds to the central trigger processor. The L1 triggers also identify Regions of Interest (RoI) where the signatures of the trigger candidates were identified, which is later used by L2 triggers.

The overall L1 accept decision is made by the Central Trigger Processor (CTP) [158]. The CTP receives trigger informations from the calorimeter and muon triggers. Additional trigger information for minimum bias event selection is provided from MBTS, and in the case of heavy-ion collisions from ZDC, and filled bunch triggers from the beam pick up monitors. These trigger information are then used to define trigger conditions (a trigger condition, for example, could be that the number of muons above a certain threshold be 2). A total of 256 trigger conditions can be defined. The CTP then combines these trigger conditions into trigger items, which could require one or more of the trigger conditions are true. The maximum number of trigger items that can be defined is 256. Each trigger item also has a prescale factor (if prescale factor is N, the trigger item is true for 1 of every N events that pass the trigger conditions of the item) that can be assigned to limit the number of events from that item. The CTP generates the L1 accept (L1A) signal as the logical OR of all the trigger items. Once the decision is made, the L1A signal is sent to the L2 trigger and the data acquisition. The CTP also sends the L1A decision, along with the clock signals from the CTP to the sub-detector Local Trigger Processors (LTP) via LTP links and from there to the front end electronics via the Trigger and Timing Control (TTC). The high rate of collisions require that the L1 trigger decision reaches the front end electronics within 2.5 μs of the bunch crossing with which it is associated. The CTP also assigns a "lumi block number" to the event, which is the shortest interval of time in which the integrated luminosity can be determined.

The data acquisition/high level trigger system (DAQ/HLT) consists of readout, L2 trigger, event building, event filter, and configuration, control and monitoring systems. Upon reception of a L1 trigger selection, the event data stored in detector specific front-end electronics is transferred to the DAQ/HLT through Read Out Links (ROL). These are temporarily stored in the Read Out Buffers (ROB) which is part of the Read Out System (ROS). For every event accepted at L1, the CTP also sends the RoI information from the L1 to the L2 trigger's RoI builder. Using the RoI information requests for the required event data (typically 2% of the entire event data) are made to the ROS for analysis by L2 algorithms. Once a L2 decision is made, it is forwarded to the Data Flow Manager (DFM). If the event is rejected the DFM informs the ROS to remove the event data from the buffers. The accepted events are then assigned to be built into a single event and once completed are sent to event filter for further selection. The event filter, in addition to performing the required selections also classifies the event according to a predefined set of event streams. Selected events from the EF are then sent to the output nodes of the DAQ/HLT and from there to CERN's central data-recording facility. A block diagram of the ATLAS trigger and data acquisition system is shown in figure III.2.12.

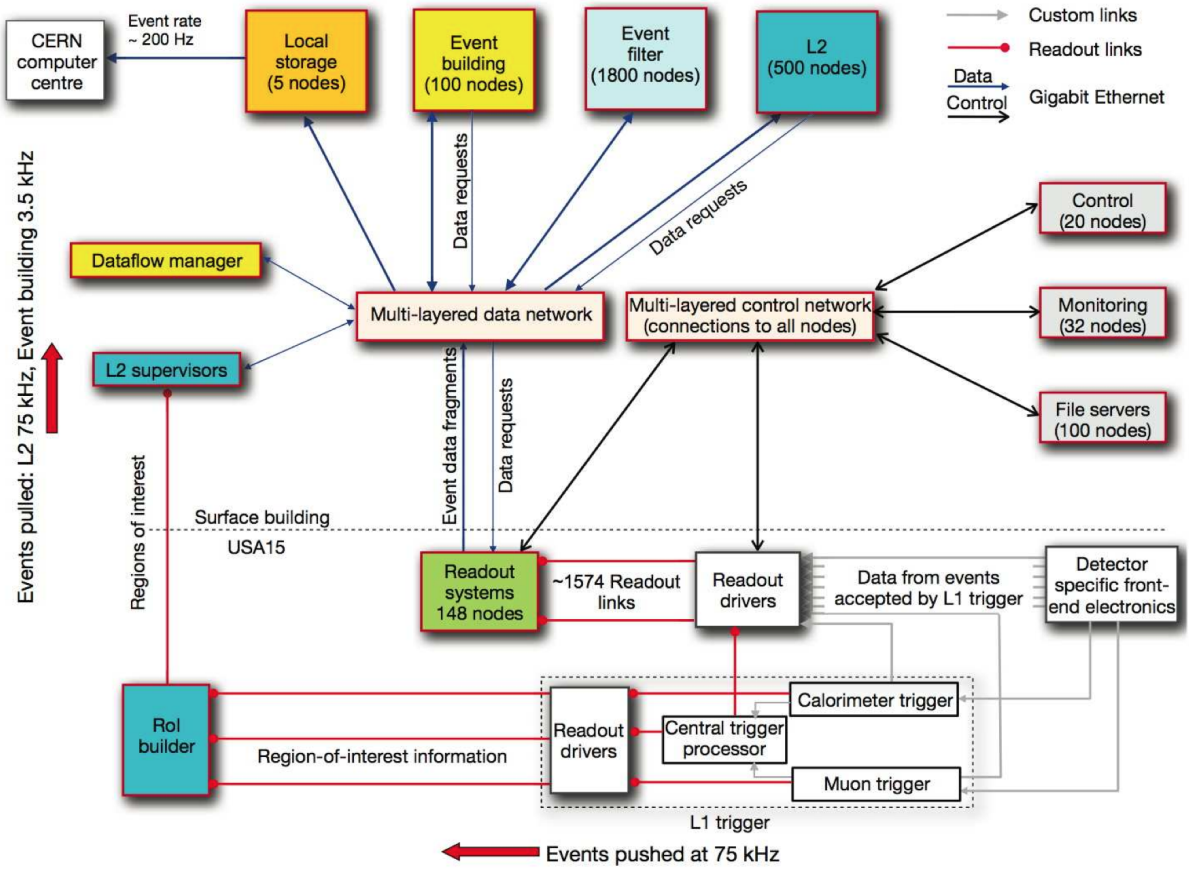

Figure III.2.12: Block diagram of the ATLAS trigger and data acquisition systems [135].

Chapter III.3

Track reconstruction in ATLAS Inner Detector

The charged particle tracks and their momenta are reconstructed in ATLAS using hits in the Inner Detector [159, 160, 161]. In ATLAS, the collisions at high luminosity and also heavy-ion collisions produce a large number of hits in the Inner Detector. The track reconstruction algorithm has to identify the different charged particle tracks that can be associated to these hits and also reconstruct the collision vertices from where the tracks originate. There are different strategies used in ATLAS for track reconstruction, the most commonly used is the *inside out* strategy where the reconstruction starts from the track seeds identified in the silicon detectors (Pixel and SCT detectors) and are then extended into the TRT. A complementary strategy called *outside in* is also employed occasionally where the track seeds are found in the TRT and the reconstruction extends the tracks inward into the silicon detectors.

The **inside-out tracking** proceeds in the following steps:

Space point formation: In the first step of the track reconstruction, clusters are identified in the silicon detectors and drift circles in the TRT and then silicon clusters are used to form *space points*. Clusters in Pixel detector are formed from connected cells and in the SCT from connected strips. Space points are precision points in 3D formed from pixel clusters or from strips in the front and back-side sensors of the SCT modules and are built taking into account the module surface and then transforming from the local coordinate system to the global coordinate system. Some times two close together tracks will produce merged clusters. A neural network based cluster splitting algorithm is used to identify and resolve merged pixel clusters.

Track finding from space point seeds: The space points are used to form track seeds. Track seeds are usually formed from three space point measurements that are consistent with a track with minimum p_{T} threshold (usually 0.5 GeV). The seeds can be formed either from only pixel space points (denoted PPP) or only from space points in SCT (SSS) or from both pixel and SCT space points (PSS and PPS). A z-vertex constraint can be imposed in the track seed finding. A fast primary vertex search is performed using space point pairs from the pixel detector and track seeds with three space points and consistent with the primary vertex are selected. With z-vertex

constraint, the total number of tracks will be smaller and thus the reconstruction faster compared to without the constraint while the seed finding without z-vertex constraint has the advantage that it is more efficient in finding the tracks. To reduce the total number of seeds, additional cuts can be applied to the seed properties. The seeds passing the selection cuts are input to a track finding algorithm that uses a Kalman filter technique[162] to associate additional silicon hits to the track to form track candidates. Individual hits are used in this step as opposed to space points. Usually a minimum number of 7 silicon hits are required on the track candidate.

Ambiguity solving: The track candidates may include random combination of hits that are not from an actual particle (called *fakes*) or track duplicates. The ambiguity solving attempts to remove such track candidates by assigning a score to each track candidate as a measure indicating the likelihood of it being from a real particle trajectory. Unique hits associated with the track with good fit quality get a high score while the tracks are penalised for having *holes* (not having a hit on a detector module where one is expected). Hits that are shared between more than one track candidate are associated to the track with the highest score. Track candidates not having a minimum number of hits, or having more holes than a maximum number, after the ambiguity solving are excluded from further processing.

TRT extension: The track candidates passing ambiguity solving are extended into the TRT by finding compatible measurements in the TRT detector. The extension is done by finding a road through the TRT from extrapolating the silicon track from the silicon hit closest to the TRT, and then either by doing a line fit to estimate if the TRT hit is compatible with the silicon track or by doing a extension using a modified Kalman filter. The silicon only track is not to be modified with the TRT hits association and so is a pure extension. If the track can be extended into the TRT, that significantly improves the momentum resolution.

The **outside-in** strategy for track finding is sometimes employed after finding tracks using the inside-out sequence. The inside-out strategy will fail to reconstruct some of the tracks which can be recovered using the outside-in strategy. Some tracks may have shared or ambiguous hits in the silicon detectors causing the score for the track candidate to be low and thus rejected in the ambiguity solving process. Tracks from secondary decays, from further inside the ID, may fail to have the required number of silicon hits to be selected in the inside-out sequence. In the outside-in sequence, the track seeds are formed from drift circles in the TRT and the tracks are extended into the silicon detectors using standard Hough transform mechanism. The hits that were already assigned to tracks in the inside-out sequence are prevented from being added or used in the outside-in sequence.

In ATLAS, a track is parametrized by five perigee parameters at the point of closest approach with the z-axis III.3.1. These are

- $\frac{\mathbf{q}}{\mathbf{p}}$: the charge of the particle divided by the momentum
- ϕ_0: the angle with x-axis in the $x-y$ plane at the perigee point
- θ_0: the angle with z-axis in the $r-z$ plane
- d_0: the signed distance to the z-axis.

- z_0: the z-coordinate of the track at the point of closest approach to the z-axis.

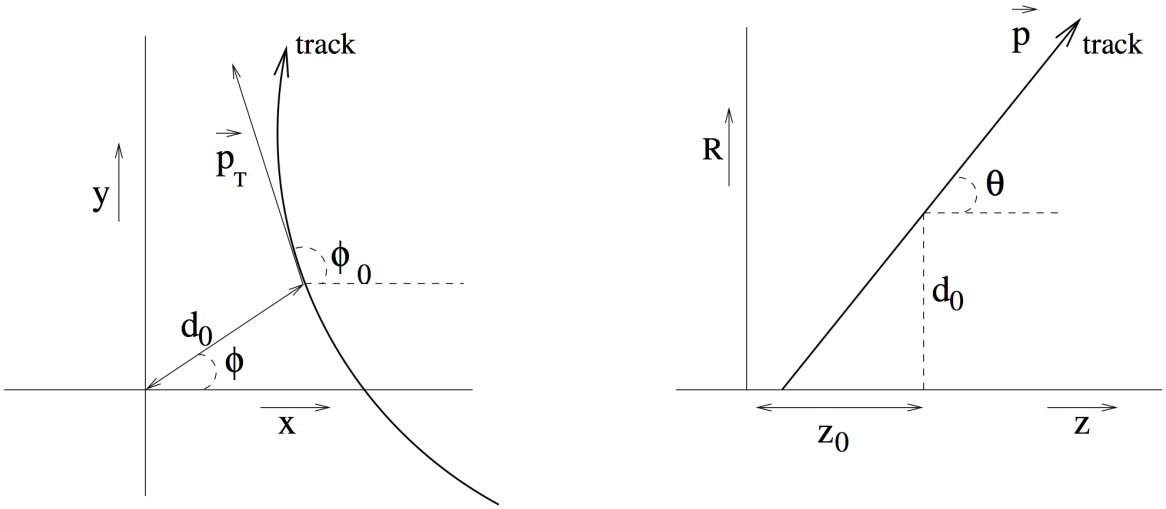

Figure III.3.1: Track perigee parameters in the transverse (left) and RZ plane (right) [161].

The track candidates provide a list of measurements along the track trajectory. Track fitting algorithms are used to evaluate the best possible estimate of the track parameters. Two approaches are used in ATLAS, a global chi squared minimization and also an estimation using a Kalman filter algorithm [163]. The chi squared minimization scales with the number of measurements on the track (M) as M^2 and so consumes more CPU for tracks with more measurements. The Kalman filter proceeds iteratively and uses only one measurement at a time. At each measurement, the track parameters at the next measurement position is calculated by extrapolation from the track parameters and their covariance matrices at the current measurement. Extrapolation involves propagating through the magnetic fields as well as material layers. The estimate and actual measurement at that point and the agreement between the two is used to evaluate the position at the next point. The filtering process can proceed bidirectionally and can give precise measurements of the track parameters at the perigee point.

Vertex fitting: The tracks in a collision could come from different collision (primary) vertices or from secondary vertices of particle decays. It is very important to identify with good accuracy the collision vertices with which the tracks are associated. Vertex reconstruction proceeds in three steps, vertex seed finding, track assignment and fitting. Several different vertex finding algorithms are implemented in the ATLAS reconstruction framework [164].

The most commonly used and the default strategy in ATLAS for finding primary vertices is the *AdaptiveMultiVertexFinder* (AMVF) strategy. It proceeds via the "finding-through-fitting" approach. The reconstruction starts by selecting tracks that are likely to have originated from the interaction region and a single primary vertex candidate is then formed from the selected

tracks. The tracks are then fitted with an adaptive multi-vertex fitter. The tracks that are marked outliers are then used to create a new vertex seed and in the next iteration of vertex fitting, a simultaneous adaptive fit of two vertices is performed. The procedure is iterated with the number of vertices fitted increasing at each step. An alternate strategy using the "fitting-after-finding" approach is employed in the ATLAS *InDetPriVxFinder* algorithm, where all the primary vertex seeds are determined at the beginning by searching for clusters of selected tracks in the longitudinal projection. The clusters are then iteratively fitted with a vertex fitter, rejecting outliers at each iteration, to determine the primary vertices. Unlike the previous algorithm, the tracks that are rejected as outliers from one cluster is not used in fitting of any other clusters.

The vertex fitting is usually done using fast or full versions of the fitter proposed by P.Billoir [165]. An alternate fitting approach using kinematic constraints, based on χ^2 minimization with Lagrange multipliers, is implemented in the *VertexKinematicFitter* tool. Vertex fitting with kinematic constraints need to be employed when reconstructing secondary vertices from the decay of an unstable particle.

Part IV

Ridge in small systems and measurement of long-range azimuthal correlations in p+Pb collisions at $\sqrt{s_{NN}} = 5.02$ TeV

Chapter IV.1

First order flow in A+A collisions

This chapter describes a study of the first order flow harmonic from density fluctuations using model simulations, carried out as a part of this doctoral research. The first order flow from density fluctuations has a characteristic p_{T} dependence, arising from its origin during the hydrodynamic/collective expansion phase of the medium evolution [72]. It has been measured in A+A collisions at RHIC and LHC [166, 4], and if presented in the p+Pb system as well, could provide support for the collective expansion origin of the ridge correlations. This chapter will familiarize with the basic features of the first order harmonic from density fluctuations. A study using model simulations is also presented, establishing the role of final state interactions in the development of this flow component. The chapter is organized as follows: Section IV.1.1 discusses the first order flow harmonic from density fluctuations and describes its basic features. Section IV.1.2 presents the details of the study and the analysis method. The results from the study on model simulations are presented in Section IV.1.3 and finally Section IV.1.4 summarizes the discussion in this chapter.

IV.1.1 First order flow from density fluctuations

The flow harmonic coefficients from v_2 to v_4 (and to v_6, with the results from LHC experiments) have been studied extensively at RHIC and LHC [167]. The third and higher order eccentricities (ϵ_n) arise mostly from density fluctuations in the initial state and can contribute to significant values for the v_n harmonics [168, 71, 169, 170]. In fact, in the most central collisions, where all ϵ_n arise from density fluctuations, the third and fourth order harmonics are comparable to the second order harmonic [4, 171]. One could expect a similar first order eccentricity from density fluctuations to be present in the initial density distribution, and a corresponding first order flow harmonic in the particle distribution. However, un till recently, the first order flow from density fluctuations was mostly neglected in the study of azimuthal anisotropies.

The hydrodynamic model predictions for a first order harmonic from density fluctuations in heavy-ion collisions were made in a recent paper [72]. The initial first order asymmetry followed by collective expansion gives rise to a specific flow pattern [72, 166]. Consider the case of an initial

density profile with only a first order anisotropy, characterized by the first order eccentricity ϵ_1 and the first order participant plane Φ_1:

$$\epsilon_1 e^{i\Phi_1} = \langle \frac{r^3 e^{i\phi}}{r^3} \rangle, \tag{IV.1.1}$$

where the angular brackets denote the average over the initial density distribution. In a pressure driven hydrodynamic expansion, the fluid velocity will be largest along the direction with the steepest gradient, i.e. along the direction of Φ_1. The particles with larger transverse momentum are emitted from regions where the fluid velocity is largest and the direction of their momentum is parallel to the fluid velocity [172]. As a result, in the presence of a first order asymmetry in the initial state, there will be a preferential emission of higher p_T particles along the direction of the first order event plane. Since the overall transverse momentum has to be conserved, i.e $\langle v_1 p_T \rangle = 0$, this requires that the particles with smaller transverse momentum flow in the opposite direction. This leads to a characteristic p_T dependence for the first order harmonic v_1, where the v_1 values are negative at low p_T, but becomes zero at a higher p_T and then increases further with p_T till reaching a maximum [166, 72]. This predicted p_T dependence of v_1 is shown in figure IV.1.1. Similar to the higher order harmonics that arise from anisotropies in the initial state, the first order flow from density fluctuations is expected to be even in pseudorapidity.

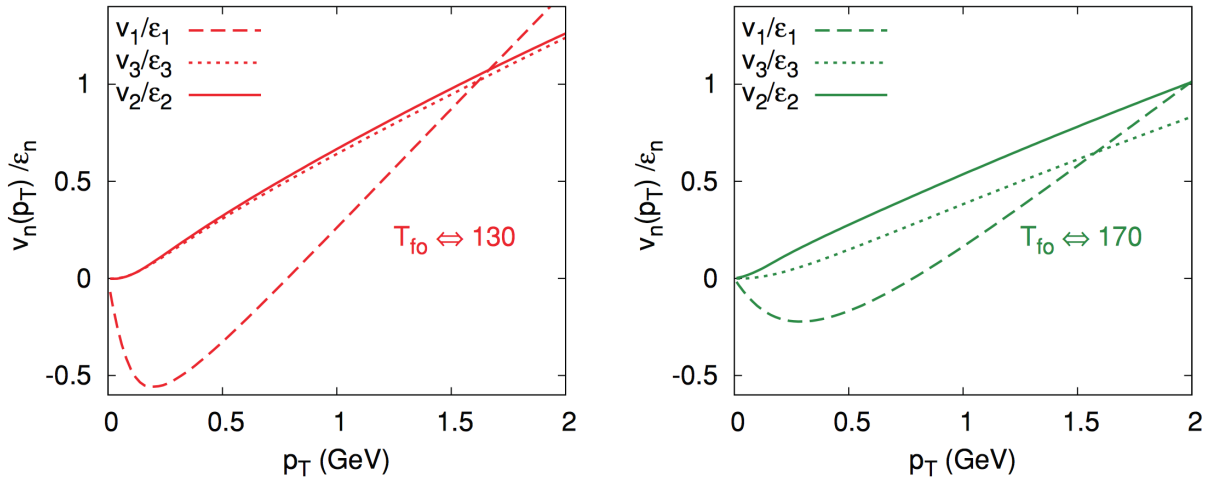

Figure IV.1.1: The transverse momentum dependence of the first order flow harmonic from density fluctuations (dashed line) predicted by hydrodynamic calculations, for two difference freeze out temperatures, from [72]

The first order flow, like the higher order harmonics, will also contribute to the two particle correlations. But unlike the higher order harmonics, for which the factorization $v_{n,n}(p_T^a, p_T^b) = v_n(p_T^a) v_n(p_T^b)$ is found to hold approximately, the first order coefficient $v_{1,1}(p_T^a, p_T^b)$ from the two particle correlations is found not to factorize into a product of single particle anisotropies, $v_1(p_T^a)$ and $v_1(p_T^b)$ [4]. This is understood to be from the contribution from global momentum conservation

which creates correlation between particle pairs even in the absence of any collective flow [91]. It has been shown recently, in an analysis of the published $v_{1,1}$ data from ALICE measurements [173] and in measurements of the first order flow by ATLAS collaboration [4], that accounting for the contribution from momentum conservation does allow the factorization of the $v_{1,1}$ coefficients into single particle harmonics. The study presented in this chapter uses a similar procedure to extract the first order flow harmonic from model simulation studies, and is presented in more detail in the next section.

It should be pointed out that a first order harmonic that is odd in rapidity also arises in heavy-ion collisions. This component arises from the "sideward" deflection of the created matter and can provide important information on the early stages of the medium evolution [167, 174]. This component is usually called "directed flow" and has been studied quite extensively from the early days of heavy-ion collisions. However, this rapidity odd component is expected to be very small for the rapidity range and the collision energies considered here [175, 176], and is not considered in this analysis. Also, the analysis uses particles from a symmetric pseudorapidity window thereby making the contribution from the odd component negligible.

IV.1.2 Outline of analysis and analysis method

The analysis uses the standard two particle correlation method to extract the $v_{1,1}$ coefficients from the simulation data [4]. Two particle correlation function is constructed from all particles as a function of $\Delta\phi$, for particle pairs with transverse momenta $p_{\rm T}^{\rm a}$ and $p_{\rm T}^{\rm b}$, and having a pseudorapidity separation, $|\Delta\eta|$. A value of $|\Delta\eta| > 1.5$ is chosen as default to suppress contribution from short-range correlations, but is varied for some systematic studies. The two particle correlation function is then expanded in a Fourier series to determine the coefficient $v_{1,1}(p_{\rm T}^{\rm a}, p_{\rm T}^{\rm b})$.

The first order coefficient $v_{1,1}$ gets a contribution from global momentum conservation. It can be shown, quite generally, using the central limit theorem that, in a system of M particles, the contribution to the two particle correlation from global momentum conservation is given by [91]

$$C^{\sum p_{\rm T}}(\mathbf{p}_{\rm T}^{a}, \mathbf{p}_{\rm T}^{b}) = -\frac{2\mathbf{p}_{\rm T}^{a}\cdot\mathbf{p}_{\rm T}^{b}}{M\langle {p_{\rm T}}^2\rangle} = -2\frac{p_{\rm T}^{\rm a}p_{\rm T}^{\rm b}cos(\Delta\phi)}{M\langle {p_{\rm T}}^2\rangle}, \tag{IV.1.2}$$

where $\Delta\phi = \phi_a - \phi_b$ is the azimuthal angle difference between the transverse momentum vectors $\mathbf{p}_{\rm T}^{a}$ and $\mathbf{p}_{\rm T}^{b}$ and the angular brackets in the denominator denote average over all particles in the system. The correlation from momentum conservation contributes (only) to the first order coefficient and therefore, in the presence of a first order flow, $v_{1,1}$ may be written as,

$$v_{1,1}(p_{\rm T}^{\rm a}, p_{\rm T}^{\rm b}) = v_1(p_{\rm T}^{\rm a})v_1(p_{\rm T}^{\rm b}) - \frac{p_{\rm T}^{\rm a}p_{\rm T}^{\rm b}}{M\langle {p_{\rm T}}^2\rangle}, \quad c = \frac{1}{KM\langle {p_{\rm T}}^2\rangle} \tag{IV.1.3}$$

Thus, for a fixed value of $p_{\rm T}^{\rm b}$, the magnitude of the contribution from momentum conservation to $v_{1,1}$ increases linearly with increase in $p_{\rm T}^{\rm a}$.

The first order flow harmonic is extracted as a function of $p_{\rm T}$ from the $v_{1,1}(p_{\rm T}^{\rm a}, p_{\rm T}^{\rm b})$ values using a least square minimisation with the parametrization,

$$v_{1,1}(p_{\rm T}^{\rm a}, p_{\rm T}^{\rm b}) = v_1^{Fit}(p_{\rm T}^{\rm a})v_1^{Fit}(p_{\rm T}^{\rm b}) - cp_{\rm T}^{\rm a}p_{\rm T}^{\rm b}, \tag{IV.1.4}$$

where $v_1^{Fit}(p_T)$ at 9 values of p_T (0.5,0.7,0.9,1.1,1.5,2.0,3.0,3.8,4.6 GeV) and c are used as the fit parameters. K in Eq. IV.1.3 represent the fraction of particles that are correlated via momentum conservation. It is kept as a free parameter in the fit since due to the presence of dijets and resonance decays, the transverse momentum could be conserved within a smaller subset of particles, and also in experiments, the values of M and $\langle {p_T}^2 \rangle$ are not known precisely. The $v_1^{Fit}(p_T)$ values at other values of p_T than the 9 points are obtained using a cubic spline interpolation with ROOT [177], using the values at the 9 points. A similar fitting procedure was used to extract the $v_1(p_T)$ values from the ALICE data in [173] and also by ATLAS collaboration in their measurement [4]. Figure IV.1.2 shows the $v_{1,1}(p_T^a, p_T^b)$ values and the fit using a function similar to Eq IV.1.4 and also the extracted momentum conservation term, $cp_T^a p_T^b$, from ATLAS measurements in Pb+Pb.

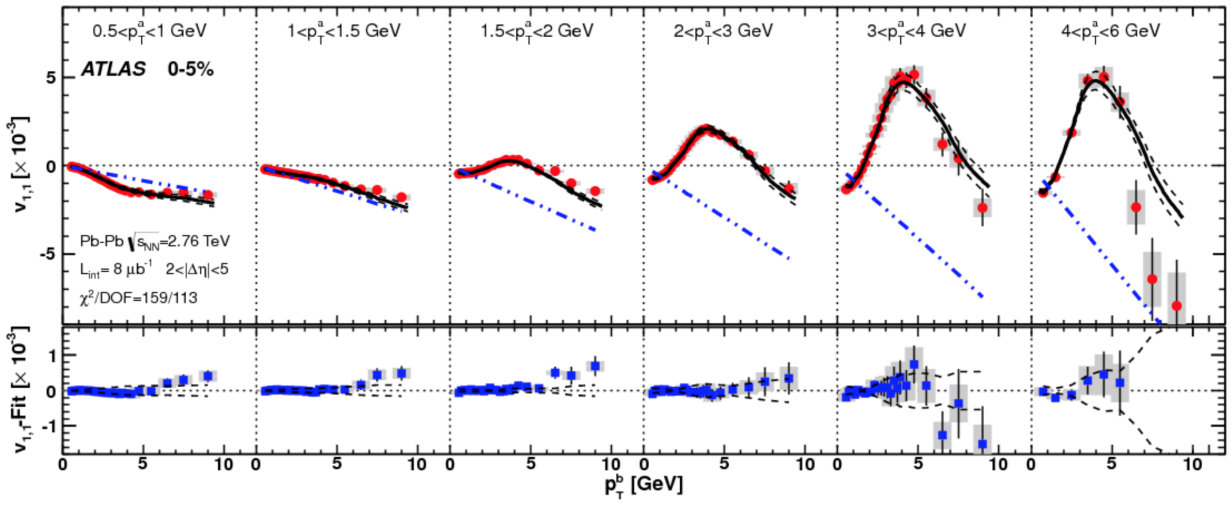

Figure IV.1.2: (Top panels) The $v_{1,1}(p_T^a, p_T^b)$ values as a function of p_T^b for different p_T^a windows (solid circles), fit using a function similar to Eq IV.1.4 (black solid lines), systematic uncertainties on the fit (broken black lines) and the extracted momentum conservation component (broken blue lines), for 0-5% central Pb+Pb collisions. (Bottom panels) The difference of the data points from the fit as function of p_T^b for different p_T^a windows. [4]

The study presented here (mostly following the work published in [178]) is done using events generated with the AMPT (A Multi Phase Transport) model [45]. The AMPT model has HIJING [120] as the initial particle generator which produces minijet partons for hard scattering and strings for soft coherent interactions. The strings are then converted into soft partons via a string melting scheme. The partons are then allowed to interact via a parton transport model. At freezeout partons are recombined into hadrons and are further allowed to interact using a hadron transport model. The initial conditions in AMPT is seeded by a Glauber model and thus the fluctuations that generate the event-by-event anisotropies in the initial density profile are naturally included in the model. The outputs from the AMPT event generator are complete Monte-Carlo events that contains various flow and non-flow effects, including the global momentum conserva-

tion. It shall be shown that the $v_{1,1}$ from AMPT has similar features as the experimental data, and can be well described by Eq. IV.1.4. The extracted v_1 values are studied as a function of $p_{\rm T}$, η, centrality, collision energy and parameters in the partonic transport, and also compared to the values from ATLAS data.

The parton and hadron transport is responsible for transforming the initial asymmetries into the momentum space anisotropy. The parton transport in AMPT include only elastic scattering whose cross-sections are controlled by the values of the strong coupling constant (α_s) and the Debye screening mass (μ) [45]:

$$\frac{d\sigma}{dt} \approx \frac{9\pi\alpha_s^2}{2(t-\mu^2)^2}, \quad \sigma = 9\pi\alpha_s^2/(2\mu^2) \tag{IV.1.5}$$

where t is the Mandelstam variable for four momentum transfer. The total cross-section can be increased either with a larger α_s or a smaller value of μ. However changing α_s is more effective for momentum dissipation than changing μ, as decreasing μ includes only softer scattering (Eq. IV.1.5).

AMPT events are generated for two different α_s values for parton transport: set-A with α_s = 0.47 and set-B with α_s = 0.33 from [46] (set-A and set-B also uses different parameterization of the Lund fragmentations in HIJING, which affect mainly the total multiplicity but not v_1). We vary the total cross-section from 1.5 mb to 10 mb by adjusting μ according to [45], separately for set-A and set- B. Varying α_s and μ allows us to study how v_1 depends on the strength of final state interactions. The events are generated for collisions at RHIC energy (Au+Au at $\sqrt{s_{NN}}$ = 0.2 TeV) and/or LHC energy (Pb+Pb at $\sqrt{s_{NN}}$ = 2.76 TeV) for the impact parameters b = 4 fm and b = 8 fm, corresponding to approximately 0-10% and 30-40% most centralevents, respectively. In addition, HIJING events generated at the same energies are used to demonstrate the flow component from density fluctuations are not observed in HIJING which does not include a parton or hadron transport phase.

IV.1.3 Results from study on model simulations

The $v_{1,1}$ values from AMPT events at RHIC energy using the parameter set-A with a parton scattering cross-section of 10 mb is shown in figure IV.1.3(a) and IV.1.3(c), as a function of ${p_{\rm T}}^b$, for different $p_{\rm T}^{\rm a}$ bins. In calculating the $v_{1,1}$ values, the pairs of particles are required to have a minimum pseudorapidity gap, $|\Delta\eta|, > 1.5$ to suppress short-range correlations. The $v_{1,1}$ values from AMPT model show qualitatively similar features as seen in the ATLAS and ALICE data [173, 4], the $v_{1,1}$ values for different $p_{\rm T}^{\rm a}$ selections cross each other and is positive when both ${p_{\rm T}}^a$ and $p_{\rm T}^{\rm b}$ are large and negative when one of the particles is at high $p_{\rm T}$ and the other at low $p_{\rm T}$, in the region with $p_T^{a,b} < 3$ GeV. Also shown in the figures are the fit to the $v_{1,1}$ values using Eq. IV.1.4. The fit describes the $p_T^{a,b}$ dependence of the data, particularly in the region with small $p_T^{a,b}$ values.

Figure IV.1.3(b) and IV.1.3(d) show similar plots for $v_{1,1}$ values from HIJING that does not include the parton and hadron transports. The $v_{1,1}$ values from HIJING in a given ${p_{\rm T}}^a$ window shows a nearly linear dependence on $p_{\rm T}^{\rm b}$, consistent with the behaviour expected from global

momentum conservation (Eq IV.1.2). This suggests that the complex $p_T^{a,b}$ dependence of the $v_{1,1}$ values from AMPT is a consequence of the final state interactions in that model. The $v_{1,1}$ values for the case with $0.5 < p_{\mathrm{T}}^{\mathrm{a}} < 1.0$ GeV is similar between AMPT and HIJING. This is because the $v_1(p_{\mathrm{T}}^{\mathrm{a}})$ is very close to zero in that $p_{\mathrm{T}}^{\mathrm{a}}$ bin (see figure IV.1.4), and thus the $v_{1,1}$ values as given by Eq. IV.1.3 is dominated by the momentum conservation component.

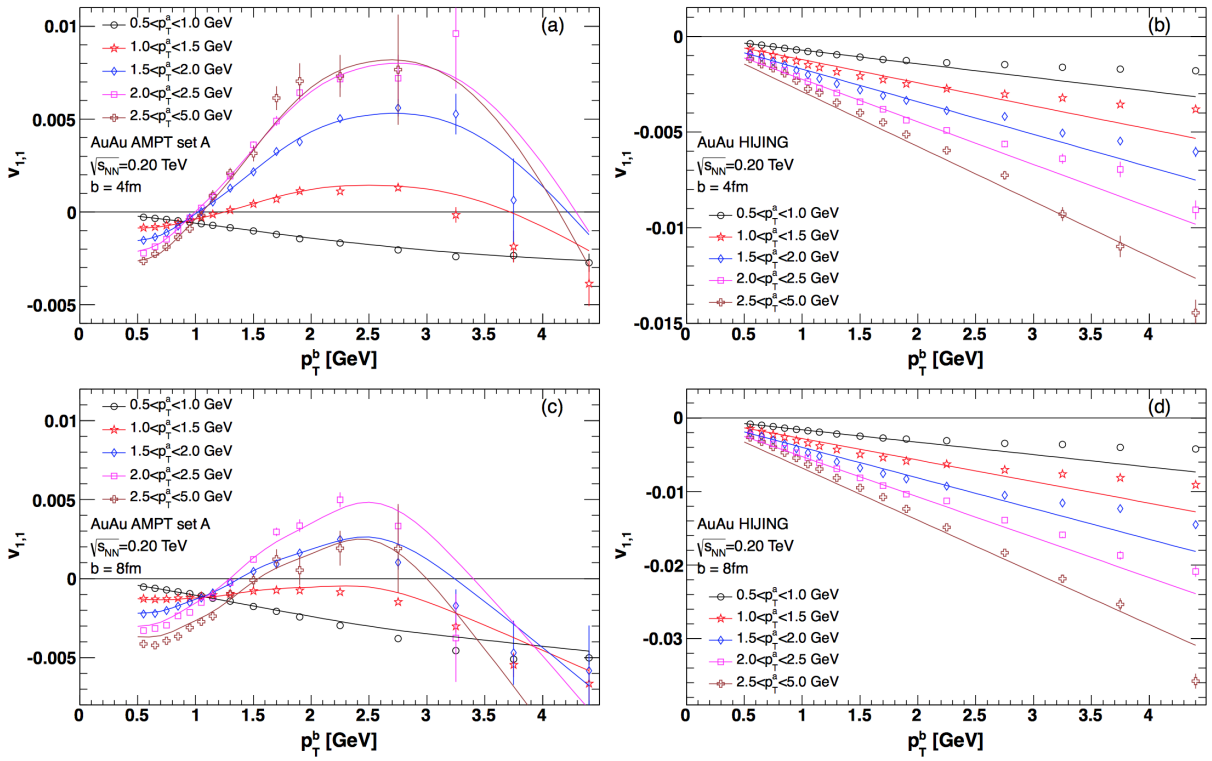

Figure IV.1.3: The $v_{1,1}$ values as a function of $p_{\mathrm{T}}^{\mathrm{b}}$ for different $p_{\mathrm{T}}^{\mathrm{a}}$ ranges for (a)AMPT events with $b = 4$ fm, (b)HIJING events with $b = 4$ fm (c)AMPT events with $b = 8$ fm and (d)HIJING events with $b = 8$ fm, for Au+Au events at $\sqrt{s_{NN}} = 200$ GeV. [178]

Figure IV.1.4 shows the $v_1^{Fit}(p_{\mathrm{T}})$ extracted from the fit to the $v_{1,1}$ values. The shaded bands show the systematic uncertainties from repeating the fit by varying all the points up or down by the statistical uncertainties on each point, accounting for the correlation between uncertainties between points with $p_{\mathrm{T}}^{\mathrm{a}} > p_{\mathrm{T}}^{\mathrm{b}}$ and $p_{\mathrm{T}}^{\mathrm{a}} \leq p_{\mathrm{T}}^{\mathrm{b}}$, following the procedure in [4]. The v_1^{Fit} values are negative at low p_{T}, crosses zero with the crossing point $p_{T,0} \sim 0.7 - 0.8$ GeV at RHIC energy and around 0.9 GeV at LHC energy. This dependence on p_{T} is qualitatively similar to that observed in the ATLAS data. The v_1^{Fit} values are consistent between $b = 4$ fm and $b = 8$ fm. This is consistent with weak centrality dependence of the first order asymmetry in the initial density profile [170, 72]. The v_1^{Fit} values at LHC energy is moderately larger than at RHIC energy. The conservation of total transverse momentum requires that $\int dp_{\mathrm{T}} p_{\mathrm{T}} v_1(p_{\mathrm{T}}) = 0$. It can be shown that, if $v_1(p_{\mathrm{T}})$ is

a linear function of $p_{\rm T}$, then the crossing point is given by $p_{T,0} = \langle p_T^2 \rangle / \langle p_{\rm T} \rangle$ and so the change in $p_{T,0}$ mainly reflects the change of $\langle p_{\rm T} \rangle$ and $\langle {p_{\rm T}}^2 \rangle$ between the two energies.

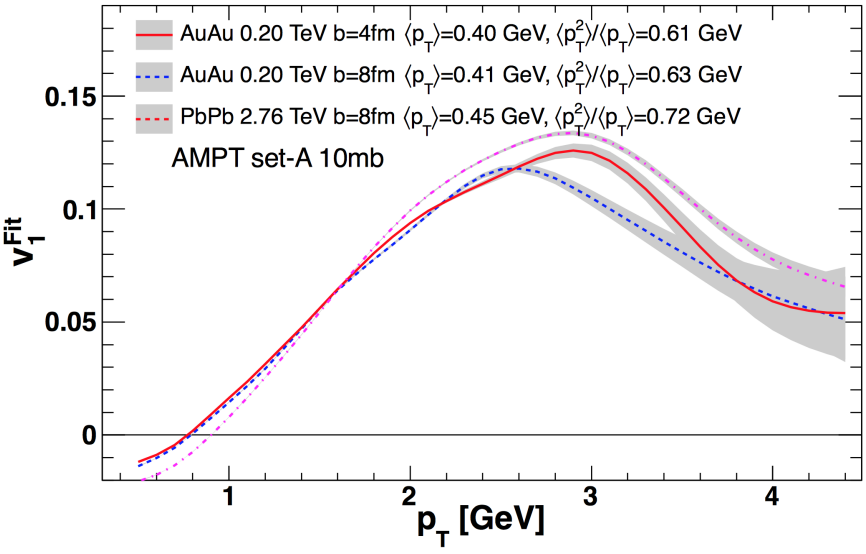

Figure IV.1.4: The v_1^{Fit} values as a function of $p_{\rm T}$ extracted from fit to $v_{1,1}$ values at RHIC and LHC energies. The sign of v_1^{Fit} is chosen to be positive at high $p_{\rm T}$. The shaded bands indicate the systematic uncertainties. [178]

The v_1^{Fit} values for the two parameter sets, set-A and set-B, for different parton scattering cross sections are shown in figure IV.1.5. The magnitude of v_1^{Fit} increases with increase in the scattering cross-section, as expected in a collective interaction picture for the origin of this component. For the same parton scattering cross-section, the v_1^{Fit} values are smaller for a smaller value of the coupling constant α_s. Changing from set-A with $\alpha_s = 0.47$ to set-B with $\alpha_s = 0.33$ reduces the peak value of v_1^{Fit} by about 40%. For a given cross section, larger value of α_s implies larger value for μ as well (Eq. IV.1.5) and thus less dominance from softer scattering, which could enhance the collective behaviour during the expansion. The plots also show the $v_1(p_{\rm T})$ values from ATLAS measurement. The AMPT values for set-B with a cross-section of 1.5 mb agree better with the data at low $p_{\rm T}$ (< 2 GeV). However, both sets fail to describe the $p_{\rm T}$ dependence in the data for $p_{\rm T} >$ 3 GeV, where the values from AMPT begin to show a decreasing trend, while the data continues to increase with $p_{\rm T}$. This could be from the increasing contribution from non flow correlations in AMPT. Similar studies of v_2 have also found that the set-B with 1.5 mb cross section has the best agreement with data, and for $p_{\rm T} < 2$ GeV [46].

A generalization of the fitting method used above can be used to study the pseudorapidity dependence of v_1 in the AMPT model. First, the two particle correlation functions are calculated in bins of $p_{\rm T}^{\rm a}$, $p_{\rm T}^{\rm b}$, η^a and η^b and the 4-D dataset $v_{1,1}(p_{\rm T}^{\rm a}, p_{\rm T}^{\rm b}, \eta^a, \eta^b)$ are calculated. These values are then fit to a function of the form:

$$v_{1,1}(p_{\rm T}^{\rm a}, p_{\rm T}^{\rm b}, \eta^a, \eta^b) = v_1^{Fit}(p_{\rm T}^{\rm a}, \eta^a) v_1^{Fit}(p_{\rm T}^{\rm b}, \eta^b) - c(\eta^a, \eta^b) p_{\rm T}^{\rm a} p_{\rm T}^{\rm b} \qquad \text{(IV.1.6)}$$

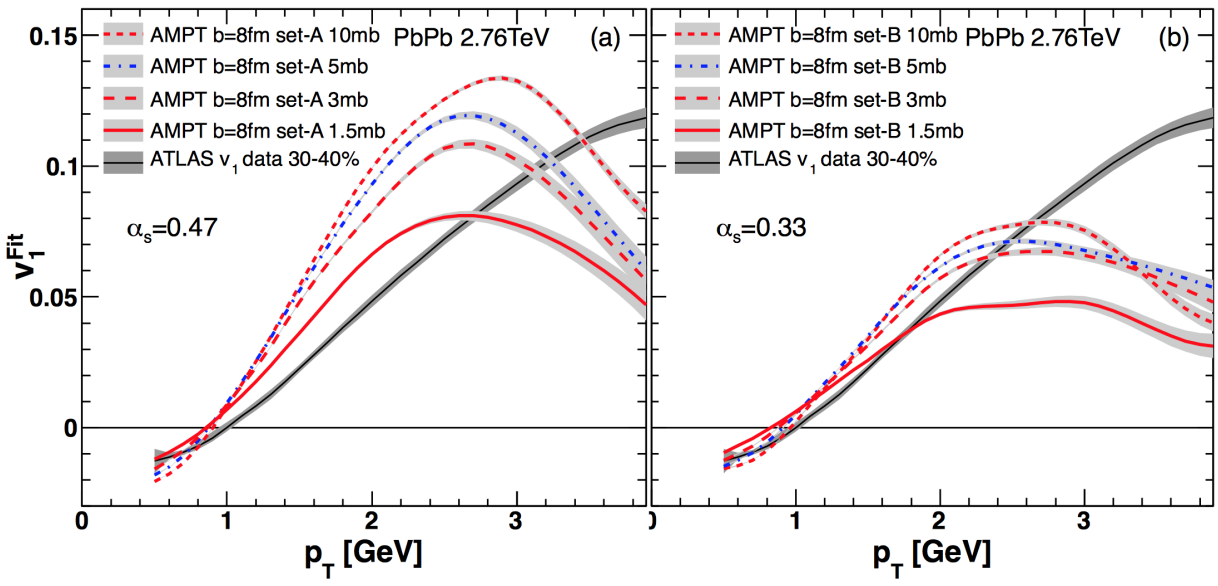

Figure IV.1.5: The v_1^{Fit} values as a function of p_{T} for four different values of the parton scattering cross-section for set-A (left) and set-B (right) for Pb+Pb collisions at 2.76 TeV at $b = 8$ fm from the AMPT model. The $v_1(p_{\mathrm{T}})$ values from ATLAS measurements in Pb+Pb collisions at 2.76 TeV are also shown. [178]

to extract the $v_1^{Fit}(p_{\mathrm{T}}, \eta)$ values. A minimum $\Delta\eta$ gap is required between the pairs to suppress non-flow correlations and so the total number of data points used in the fit depends on this gap requirement. The v_1^{Fit} is still parametrized using the values at the 9 p_{T} values as in the case of figure IV.1.3, but these values are now allowed to depend on η. Both the v_1^{Fit} and c functions are assumed to be symmetric in η, i.e. $v_1^{Fit}(\eta) = v_1^{Fit}(-\eta)$ and $c(\eta^a, \eta^b) = c(-\eta^a, -\eta^b)$. In addition we also have the condition $c(\eta^a, \eta^b) = c(\eta^b, \eta^a)$. The analysis is done in the region with $|\eta| < 3$, dividing it into 12 equally spaced bins. This leads to a total of 54 independent parameters for v_1^{Fit} and 24 parameters for c, resulting in a total of 78 fitting parameters. The quality of the fit is generally comparable to those shown in figure IV.1.3

Figure IV.1.6 shows the v_1^{Fit} values as a function of η, obtained using the procedure described above, for two p_{T} bins at the RHIC and LHC energies. The error bands include the statistical uncertainty and the variation of the fit results from changing the minimum $|\Delta\eta|$ gap for points used in the global fit from 0.5 to 2.5. The v_1^{Fit} shows a weak η dependence at RHIC energies and show a gradual decrease towards large $|\eta|$ values, similar to the η dependence seen for higher order harmonics [179]. The values at both $b = 4$ fm and $b = 8$ fm show similar η dependence at the RHIC energy. The v_1^{Fit} values at the LHC however shows a small dip at midrapidity, for both p_{T} bins. The origin of this dip is not clearly understood. Figure IV.1.7 shows the $c(\eta^a, \eta^b)$ values for different η^a, η^b choices, plot as a function of $|\eta^a - \eta^b|$ for $b = 8$ fm collisions at RHIC and LHC energies. The $c(\eta^a, \eta^b)$ values fall approximately on the same curve for $|\eta^a - \eta^b| > 2$, particularly

at the LHC energy. This suggests that the value of c depends mostly only on $|\eta^a - \eta^b|$ for pairs with large pseudorapidity difference. The c values are also independent of the minimum $|\Delta\eta|$ gap required for points used in the global fit, as shown by the black and open red circles. The values of c at large pseudorapidity difference are generally larger than that predicted by Eq. IV.1.3 with $K = 1$, but of the same order of magnitude, with the values at RHIC energy being closer to the predicted value than those at the LHC energies.

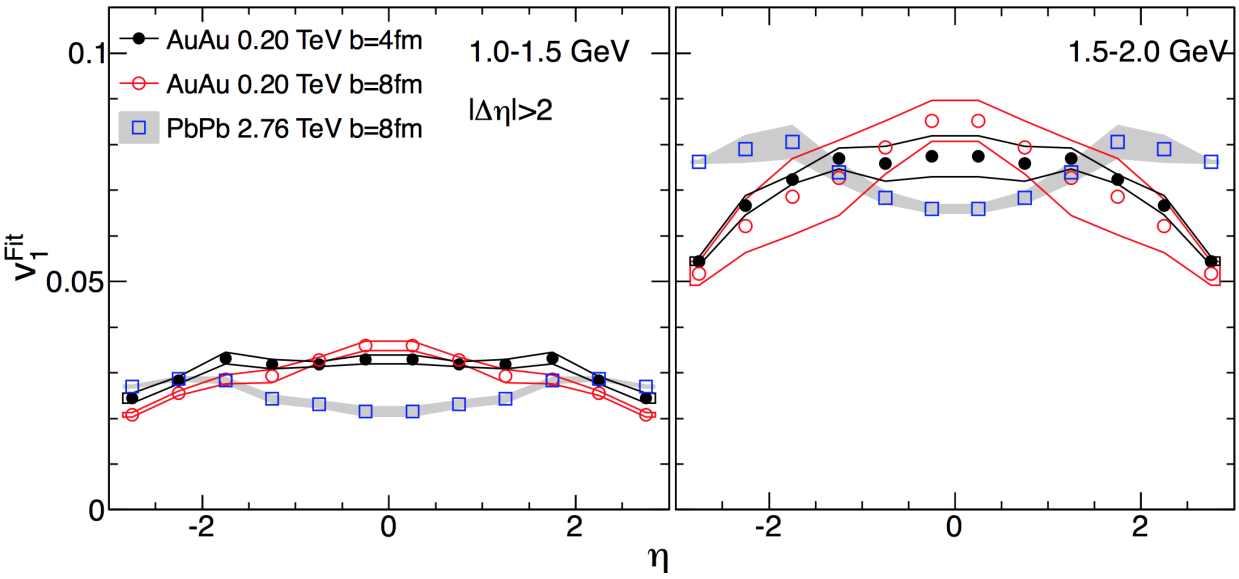

Figure IV.1.6: The v_1^{Fit} values as function of η for two $p_{\rm T}$ bins, obtained using the global fit described in Eq. IV.1.6, for $b = 8$ fm and $b = 4$ fm collisions at RHIC energy and $b = 8$ fm collisions at LHC energy. The values are from using points with a minimum separation of $|\Delta\eta| > 2$ in the global fit. The contours and shaded bands represent systematic uncertainties. [178]

In the original fitting function Eq. IV.1.4, the parameter c is assumed to be a constant. But Figure IV.1.7 shows this is clearly not the case in AMPT and the value of c depends on the pseudorapidity separation between the pairs. Some of this dependence, particularly at small values of $|\eta^a - \eta^b|$, could be from the presence of short-range correlations like jet fragmentation and resonance decay which seem to be giving a negative contribution to the c values in that region. However, the values of c change with $|\eta^a - \eta^b|$ up to $|\eta^a - \eta^b| = 3$ and then seem to flatten out at higher $|\eta^a - \eta^b|$, but at a larger value than that predicted by Eq. IV.1.3 with $K = 1$. This would suggest that calculating c using all the particles produced in the collision might be incorrect and in particular should be taken into account in an event plane calculation, where the first order event plane angle is to be corrected for the bias from global momentum conservation [166].

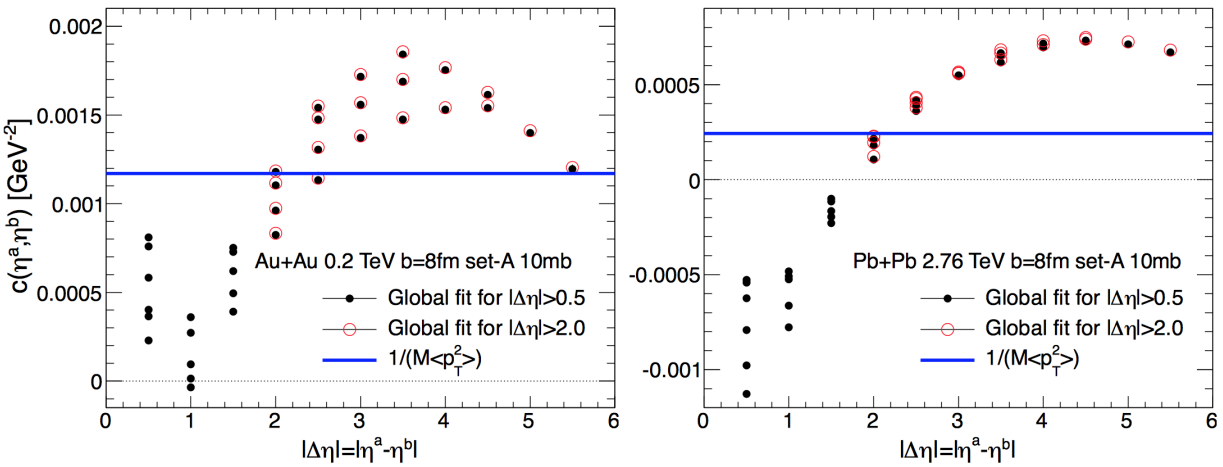

Figure IV.1.7: $c(\eta^a, \eta^b)$ values as a function of $|\eta^a - \eta^b|$ for global fits using points with $|\Delta\eta| > 0.5$ (open circles) and $|\Delta\eta| > 2.0$ (solid circles) obtained for the global fit for $b = 8$ fm collisions at RHIC (left) and LHC (right) energies. Points at a given $|\eta^a - \eta^b|$ correspond to different η^a, η^b combinations

IV.1.4 Summary

The study of the first order flow using the AMPT model at RHIC and LHC energies are presented. The $v_{1,1}$ values are calculated for AMPT events using two particle correlations. A global fit of the $v_{1,1}$ values using the fitting procedure [173, 4] allows the simultaneous extraction of $v_1(p_{\rm T})$ and the global momentum conservation component. The $v_{1,1}(p_{\rm T}^{\rm a}, p_{\rm T}^{\rm b})$ values in AMPT show similar features as seen in the ATLAS data while the $v_{1,1}(p_{\rm T}^{\rm a}, p_{\rm T}^{\rm b})$ values from HIJING reflect mostly only a momentum conservation component, suggesting that the complex features seen in data and the AMPT model arise from final state interactions during the system evolution. The extracted $v_1(p_{\rm T})$ values from the fit is negative at low $p_{\rm T}$, crosses zero and further increases with $p_{\rm T}$ until 2−3 GeV, qualitatively agreeing with the behavior predicted by the hydrodynamic models and also with the dependence seen in the data. The v_1 function shows very little centrality dependence but increases with collision energy. The $p_{\rm T}$ value where v_1 crosses zero also increases with collision energy. The magnitude of v_1 increases with parton scattering cross-section, suggesting that its magnitude increases with the strength of the final state interactions. By choosing the parameters in AMPT model carefully, reasonable agreement with the ATLAS data can be achieved for $p_{\rm T} < 2$ GeV, but not at higher $p_{\rm T}$. The fitting method is extended to extract the η dependence of v_1 and the global momentum conservation component. The extracted v_1 shows a weak dependence on η. The coefficient of global momentum conservation component is found to depend on $|\eta^a - \eta^b|$ and differs from that given by Eq. IV.1.3 with $K = 1$. This suggests that an estimation of the momentum conservation component should not be done using all the particles produced in the collision.

Chapter IV.2

Measurement of long-range azimuthal correlations in p+Pb collisions at $\sqrt{s_{NN}} = 5.02$ TeV using ATLAS detector at the LHC

This chapter discusses the measurement of the long-range azimuthal correlations ("ridge") and the associated Fourier harmonics in p+Pb collisions at $\sqrt{s_{NN}} = 5.02$ TeV at the LHC using the ATLAS detector. The analysis is based on the 28^{-1} nb data from the proton - lead run at the LHC in 2013. The measurements presented in this chapter are performed using the ATLAS inner detector (ID), forward calorimeters (FCals), minimum-bias trigger scintillators (MBTSs), zero-degree calorimeter (ZDC), and the trigger and data acquisition systems. Two particle correlation functions are constructed using tracks reconstructed in the ID. The analysis is performed in different "event activity" classes defined using the total number of reconstructed tracks (track selection criteria are defined in Section IV.2.2) with $p_{\mathrm{T}} > 0.4$ GeV within $|\eta| < 2.5$, $N_{\mathrm{ch}}^{\mathrm{rec}}$, or the total transverse energy in forward calorimeter on the Pb-going side, $E_{\mathrm{T}}^{\mathrm{Pb}}$. Data from the ZDC, MBTS and TDAQ are used for event selection and to reject non collision background and "pileup" (events with more than one collision) events. This chapter aims to present a summary of the analysis and results, presented in more detail in [180] and [181].

The organization of the chapter is as follows: Section IV.2.1 presents the details of the event selection and trigger selections used in the analysis. Track selection cuts and tracking efficiency are discussed in Section IV.2.2. Section IV.2.3 summarizes the analysis procedure and the details of the analysis. A summary of the systematic uncertainties in the measurement are provided in Section IV.2.4, detailed descriptions of the determination of the systematic uncertainties are relegated to Appendix A. Section IV.2.5 presents and discusses the results from the measurement. The chapter ends with a summary in Section IV.2.6.

IV.2.1 Event selection

The data for this analysis comes from the 2013 proton - lead run at the LHC from January 7 to February 10, 2013. LHC operated in two configurations during the run period, each contributing to roughly half of the total integrated luminosity. During the first half (period A), LHC was setup to have protons traveling towards the "C"-side ("beam 1") with beam energy of 4 TeV, while the Pb ions were traveling towards "A"-side ("beam 2") with a beam energy of $4 \times 82/208$ = 1.57 TeV per-nucleon. This leads to $\sqrt{s_{NN}}$ = 5.02 TeV in the nucleon-nucleon center-of-mass frame, which is shifted from the lab frame by 0.47 in η towards the proton-going side. The second half (period B) had protons in beam 2 and Pb ions in beam 1. In the ATLAS coordinate system this corresponds to positive pseudorapidity for particles on the Pb going side during period A and negative during period B, but following the conventions used before [112], the Pb-fragmenting side is always taken as the negative pseudorapidity direction in the analysis. The analysis is limited to the runs included in the Good Run List which can be found here: https://twiki.cern.ch/twiki/bin/viewauth/Atlas/HeavyIonRunList.

In addition to the trigger requirements discussed below, the events are required to belong to good luminosity block, and to have a reconstructed vertex with z coordinate within 150 mm of the nominal collision center. The events are also required to have a time difference of less than 10 ns between the two sides of the MBTS detector to minimize contribution from non collision background. For the two-particle correlation analysis, it is also required that events are not contaminated by pileup (see Subsection IV.2.1.3), and contain at least 2 reconstructed tracks with $p_{\mathrm{T}} > 0.4$ GeV.

IV.2.1.1 Minimum Bias Trigger Selection

The primary minimum bias (MB) trigger for the run period was `EF_mbMBTS_1_1`, which requires at least one hit on both sides of the MBTS detector, along with a timing cut to reject non collision background applied at L2. About 46 million events selected by the primary MB trigger are used in the analysis. The performance of this trigger selection relative to the MB trigger selection in 2012 p+Pb run [182] is shown in figure IV.2.1. Also, (about 10 million) events selected by the `L1_ZDC` trigger on the Pb-going side (`L1_ZDC(Pb)`), which selects events with at least one neutron on the Pb-fragmenting side of the ZDC, are also included in the MB sample. The ratio of the normalized distributions of events selected by the ZDC trigger to that from the primary MB trigger is shown in figure IV.2.2, as a function of $N_{\mathrm{ch}}^{\mathrm{rec}}$ and $E_{\mathrm{T}}^{\mathrm{Pb}}$. The `L1_ZDC(Pb)` trigger has $\approx 90\%$ of its maximum efficiency at $E_{\mathrm{T}}^{\mathrm{Pb}}$ =0 and at $N_{\mathrm{ch}}^{\mathrm{rec}}$ =2, and becomes 100% by $E_{\mathrm{T}}^{\mathrm{Pb}}$ =20 GeV and $N_{\mathrm{ch}}^{\mathrm{rec}}$ =40. This loss of efficiency at low $N_{\mathrm{ch}}^{\mathrm{rec}}$ and $E_{\mathrm{T}}^{\mathrm{Pb}}$ values is found to have no impact on the measured quantities, as will be shown in Section IV.2.4.

IV.2.1.2 High Multiplicity Trigger Selection

The high rate of collisions during the run meant that only a small fraction ($\sim 1/1000$, determined by the prescale values for the trigger during the run) of the events passing the MB trigger conditions could be selected. In order to enhance the selection of high multiplicity events, in which the ridge

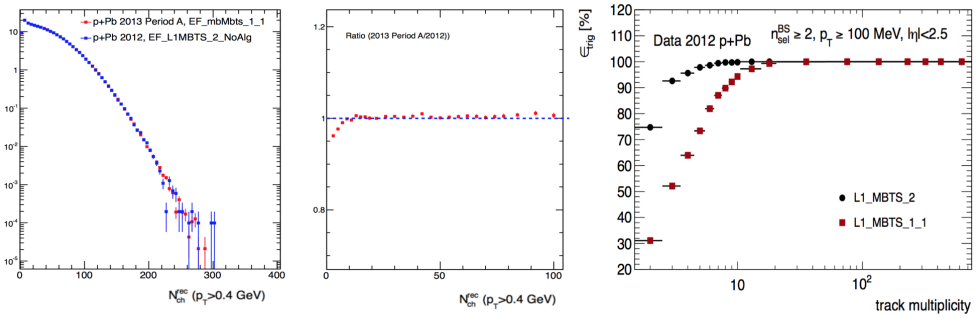

Figure IV.2.1: (Left) Distribution of events (normalized to have the same integrated counts) as a function of $N_{\mathrm{ch}}^{\mathrm{rec}}$ from p+Pb run in 2012 selected using `EF_L1_MBTS2_NoAlg` and from p+Pb run in 2013 selected by `EF_mbMBTS_1_1`. (Middle) Ratio of the distribution from 2013 to that from 2012. (Right) Efficiency of the `EF_L1_MBTS2_NoAlg` trigger in 2012 p+Pb run as a function of number of charged tracks with $p_{\mathrm{T}} > 0.1$ GeV, taken from [182].

correlations are most prominent, several triggers were implemented using the ATLAS L1 and HLT systems [183]. These triggers will be collectively referred to as High Multiplicity Triggers (HMT). The HMT is implemented to select events with large transverse energy in the FCal rapidity interval and/or large number of tracks in the ID. The transverse energy selection is made by L1 triggers, by requiring the total transverse energy in the FCal at L1, ($E_{\mathrm{T}}^{\mathrm{L1}}$) to be above a tunable threshold. The number of tracks are determined by an online reconstruction at the HLT. In the HLT, the charged-particle tracks are reconstructed by requiring at least two hits in the pixel detector and three hits in the SCT. The collision vertex with the highest number of online tracks is determined and the number of tracks associated with this vertex with $p_{\mathrm{T}} > 0.4$ GeV and a distance of closest

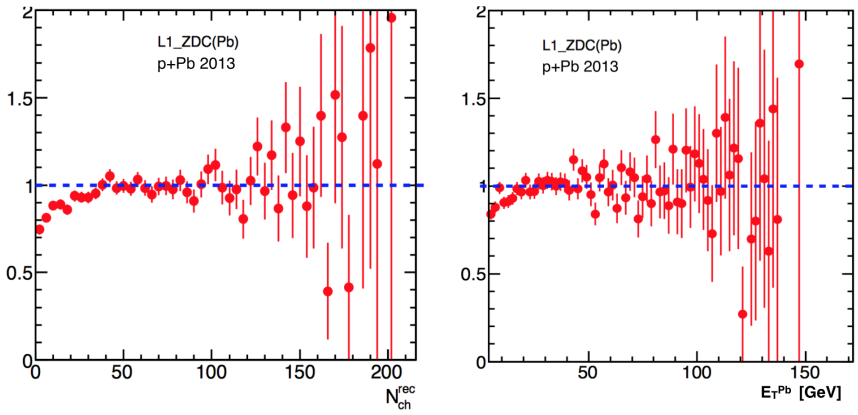

Figure IV.2.2: Ratio of the normalized distribution of events from `L1_ZDC(Pb)` trigger to that from the primary MB trigger, as a function of $N_{\mathrm{ch}}^{\mathrm{rec}}$ (left) and as a function of $E_{\mathrm{T}}^{\mathrm{Pb}}$ (right).

approach of less than 4 mm ($N_{\rm trk}^{\rm HLT}$) is calculated. The HLT selection is made by requiring $N_{\rm trk}^{\rm HLT}$ to be above different tunable thresholds.

We include in the analysis events triggered by four triggers (primary HMT triggers) that were enabled during most of the runs: `EF_mbSpTrkVtxMh_hip_trk150_L1TE50`, `EF_mbSpTrkVtxMh_hip_trk180_L1TE50`, `EF_mbSpTrkVtxMh_hip_trk200_L1TE65`, `EF_mbSpTrkVtxMh_hhip_trk225_L1TE65`, and also those triggered by `EF_mbSpTrkVtxMh_hip_trk100_L1TE10` and `EF_mbSpTrkVtxMh_hip_trk130_L1TE10`, which were enabled towards the second half of the run period and has good statistics. These triggers have the $E_{\rm T}^{\rm L1}$ thresholds ≥ 50, ≥ 50, ≥ 65, ≥ 65, ≥ 10 and ≥ 10 respectively and $N_{\rm trk}^{\rm HLT}$ thresholds of ≥ 150, ≥ 180, ≥ 200, ≥ 225, ≥ 100 and ≥ 130 respectively. `EF_mbSpTrkVtxMh_hip_trk225_L1TE65` is an unprescaled trigger throughout the run, and the rest are prescaled.

The efficiencies (or turn or curves) for the HMT triggers relative to the primary MB trigger, as function of $N_{\rm ch}^{\rm rec}$ are shown in figure A.3 (Appendix A.1). In general, the turn on curves for these triggers are very sharp, the efficiencies increase from zero to >90% within a range of ∼10 tracks. The increase of statistics from the different HMT, as function of $N_{\rm ch}^{\rm rec}$ and $E_{\rm T}^{\rm Pb}$ are shown in the top panels of figure IV.2.3. The enhancement of statistics from the HMT, owing to their different thresholds and prescale values, causes the $N_{\rm ch}^{\rm rec}$ and $E_{\rm T}^{\rm Pb}$ distributions to be different from that with the MB selection, as can be seen from the same figure (IV.2.3). Also the HMT selection causes mean and r.m.s $N_{\rm ch}^{\rm rec}$ in a given $E_{\rm T}^{\rm Pb}$ class (and vice versa) to be very different from that from the MB selection (see figures A.3, A.4, in Appendix A.1).

In order to properly include the HMT events in the sample, the events are weighted by the inverse probability for selecting an event at the $N_{\rm ch}^{\rm rec}$ and $E_{\rm T}^{\rm Pb}$ values for the event. For a finite number, N, of triggers active during a particular run, each with its own prescale factor and trigger efficiency, the total probability, P, for an event to be selected is given by,

$$P = \sum_{i=1}^{N} P_{trig}^{i} - \sum_{i=1}^{N}\sum_{j=i+1}^{N} P_{trig}^{i}P_{trig}^{j} + \sum_{i=1}^{N}\sum_{j=i+1}^{N}\sum_{k=1}^{N} P_{trig}^{i}P_{trig}^{j}P_{trig}^{k} - ..., \tag{IV.2.1}$$

where P_{trig}^{i} denotes the probability for the $i^{\rm th}$ trigger to select an event and depends on the trigger efficiency and prescale values for that trigger. The second, third and higher terms are to ensure events in which more than one trigger fired are not counted more than once. The probabilities for the individual triggers and also the total probability are functions of the $N_{\rm ch}^{\rm rec}$ and $E_{\rm T}^{\rm Pb}$, as the trigger efficiencies depend on those variables. The details of evaluation of the probabilities and the event by event weight are provided in Appendix A.1. The lower panels in figure IV.2.3 shows the $N_{\rm ch}^{\rm rec}$ and $E_{\rm T}^{\rm Pb}$ distributions from the combined MB and HMT (MB+HMT) sample after the "reweighting" by applying the event-by-event weights discussed above. The reweighted distribution is consistent with the MB distribution in both $N_{\rm ch}^{\rm rec}$ and $E_{\rm T}^{\rm Pb}$. This can be further seen if one compares the mean $N_{\rm ch}^{\rm rec}$ and its standard deviation in different $E_{\rm T}^{\rm Pb}$ classes (and vice-versa) (figures A.3, A.4 in Appendix A.1), which were very different before the reweighting but consistent within a few percent, after. The final results shown in this chapter are obtained with this reweighting procedure applied. Comparison of the results for the default case (MB+HMT with reweighting) with those from purely MB selection are shown in Subsection IV.2.3.2.

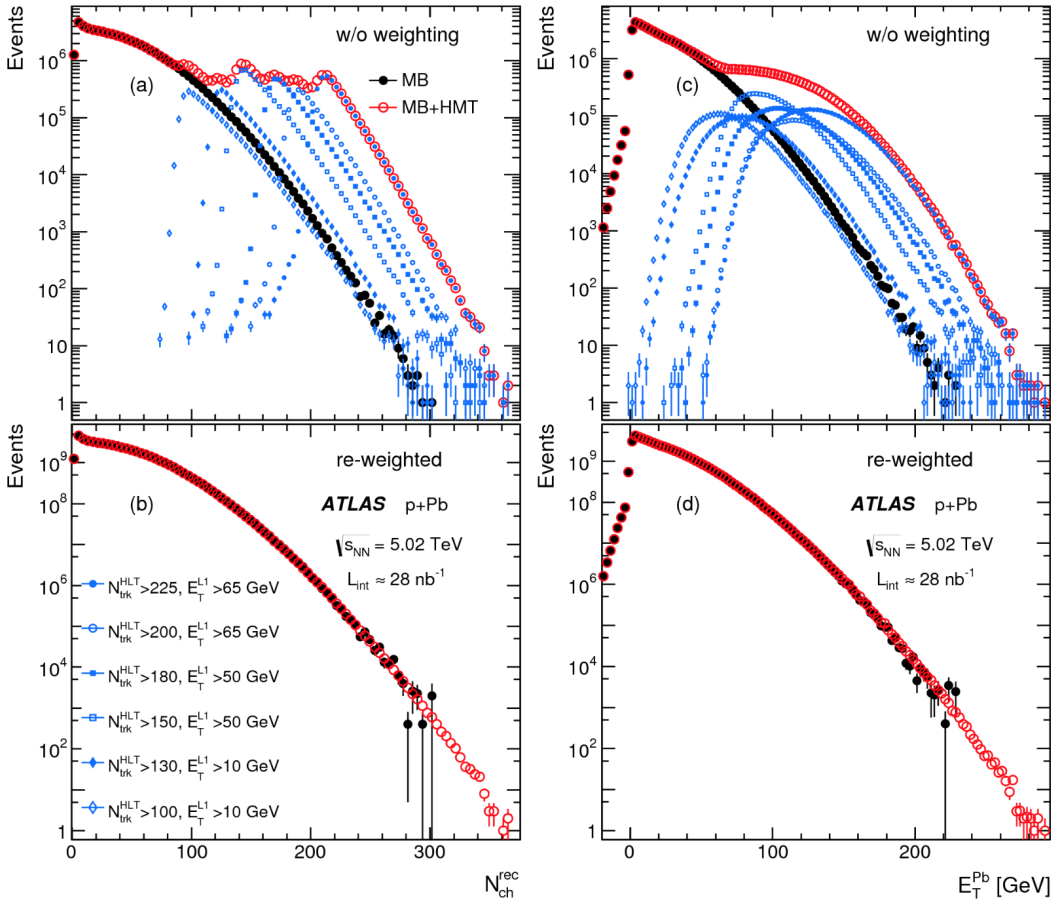

Figure IV.2.3: The distributions of $N_{\mathrm{ch}}^{\mathrm{rec}}$ (left panels) and $E_{\mathrm{T}}^{\mathrm{Pb}}$ (right panels) for MB and MB + HMT events before (top panels) and after (bottom panels) applying an event-by-event weight (see text for details). The smaller symbols in the top panels show the distributions from the six individual HMT triggers.

IV.2.1.3 Pileup estimation and rejection

In the 2013 p+Pb run, the luminosity conditions provided by the LHC result in an average probability of 3% that an event contains two or more p + Pb collisions (pileup). The pileup events are suppressed by rejecting events containing more than one good reconstructed vertex. A vertex is considered a good vertex if the total transverse momentum from all the tracks associated with the vertex, $\sum p_{\mathrm{T}}$, is greater than 5 GeV. The remaining pileup events are further suppressed based on the signal in the ZDC on the Pb-fragmentation side. ZDC detects neutral particles at large forward rapidity, mostly the neutrons fragmenting from the Pb nucleus which have approximately the nucleon beam energy [156]. Since the maximum number of participants in p+Pb collisions saturates at some impact parameter, the energy distribution in ZDC also saturates. Events with

two collisions will show up around a second peak at twice the energy of the first saturation peak, and so on. Therefore, pileup can be suppressed by a simple cut on the high tail end of the ZDC signal distribution. The ZDC distribution is also used to estimated the residual pileup in the event sample. The details of the performance of the pileup rejection using the ZDC energy and the estimation of the residual pileup fraction can be found in Appendix A.2.

Figure IV.2.4 shows the estimated pileup fraction in the event sample remaining after the pileup rejection cut, including the cut on ZDC energy, used in the analysis (shown as open star markers), as a function of $E_{\mathrm{T}}^{\mathrm{Pb}}$. The pileup fraction increases towards the higher energy classes. This is because, even though the pileup rate is small, the probability of a very high $E_{\mathrm{T}}^{\mathrm{Pb}}$ event happening is also small. After the default pileup rejection cut, the residual pileup fraction is less than 1% in all the $E_{\mathrm{T}}^{\mathrm{Pb}}$ classes in MB events and less than 1.5% in the HMT events. The impact of the residual pileup events on the measured quantities is evaluated and is included as a source of systematic uncertainty in the measurements.

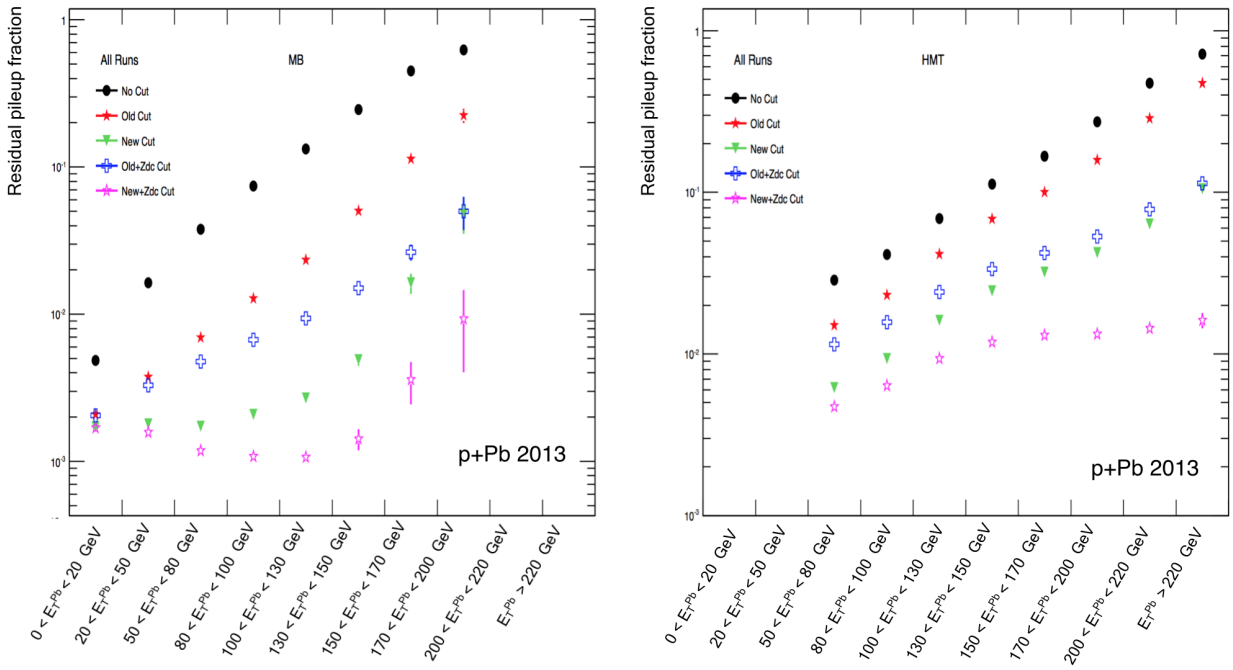

Figure IV.2.4: Estimated residual pileup fraction remaining after the default pileup rejection cut (open stars) and other cuts used for systematic studies (see Appendix A.2) in increasing $E_{\mathrm{T}}^{\mathrm{Pb}}$ bins for MB triggered events (left) and HMT triggered events (right).

After all the event selection cuts, about 57 million MB triggered events and about 15 million HMT events are included in the analysis.

IV.2.1.4 Event activity variable

The two particle correlation analysis is performed in events divided into different event activity classes. The event activity bins are defined using $N_{\rm ch}^{\rm rec}$ or $E_{\rm T}^{\rm Pb}$. These quantities were used to define event-activity in previous p+Pb analyses [12, 10]. Events with larger event activity have on average a larger number of participating nucleons in the Pb nucleus and a smaller impact parameter (and in general larger total multiplicity in events). Hence, the terms "central" and "peripheral", commonly used in descriptions of A+A collisions, are sometimes used to refer to event classes with high and low event activities respectively.

The left panel of figure IV.2.5 shows the correlation between $N_{\rm ch}^{\rm rec}$ and $E_{\rm T}^{\rm Pb}$ from MB+HMT (after reweighting) p+Pb events. The $E_{\rm T}^{\rm Pb}$, in general, increase with increase in $N_{\rm ch}^{\rm rec}$, suggesting that, on average, $E_{\rm T}^{\rm Pb}$ on the nucleus going direction correlates with the particle production at mid-rapidity. However, the broad distribution of $E_{\rm T}^{\rm Pb}$ at fixed $N_{\rm ch}^{\rm rec}$ also implies significant fluctuations. The mean and r.m.s values of $E_{\rm T}^{\rm Pb}$ calculated in narrow $N_{\rm ch}^{\rm rec}$ bins is shown in the right panel of figure IV.2.5, as a function of the (mean) $N_{\rm ch}^{\rm rec}$ in those bins. A nearly linear increase on the $\langle E_{\rm T}^{\rm Pb}\rangle$ with $N_{\rm ch}^{\rm rec}$ is observed. This linear relationship is used to match an $N_{\rm ch}^{\rm rec}$ class to a corresponding $E_{\rm T}^{\rm Pb}$ class for some comparisons. The approximately linear relationship can be parameterized as

$$\langle E_{\rm T}^{\rm Pb}\rangle/{\rm GeV} \approx 0.60 N_{\rm ch}^{\rm rec} \tag{IV.2.2}$$

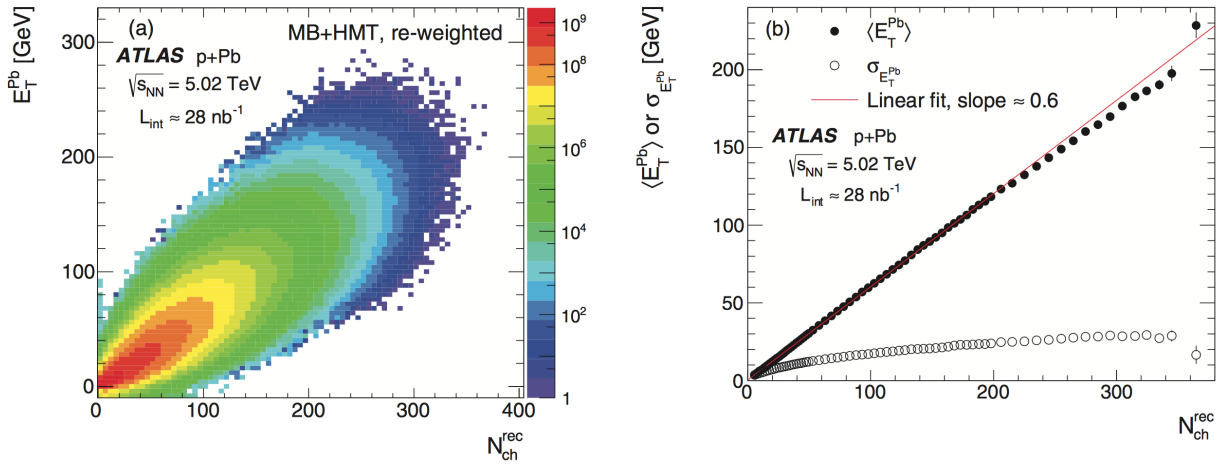

Figure IV.2.5: (Left) Correlation between $E_{\rm T}^{\rm Pb}$ and $N_{\rm ch}^{\rm rec}$ in MB + HMT events. (Right) The mean ($\langle E_{\rm T}^{\rm Pb}\rangle$) and root-mean-square ($\sigma_{E_{\rm T}^{\rm Pb}}$) values of $E_{\rm T}^{\rm Pb}$ distributions in slices of narrow $N_{\rm ch}^{\rm rec}$, as a function of the $N_{\rm ch}^{\rm rec}$. The line is a linear fit to the $N_{\rm ch}^{\rm rec}$ dependence of $\langle E_{\rm T}^{\rm Pb}\rangle$ values.

Table IV.2.1 shows a list of event activity classes used in the analysis, along with the fraction of the MB + HMT (after reweighting) events contained in each event class. The average $N_{\rm ch}^{\rm rec}$ and $E_{\rm T}^{\rm Pb}$ values as well as the efficiency corrected average number of tracks within $|\eta| < 2.5$ and $p_{\rm T} >$

0.4 GeV, $\langle N_{\rm ch}\rangle$, are also shown. The event classes defined in narrow intervals of $N_{\rm ch}^{\rm rec}$ or $E_{\rm T}^{\rm Pb}$ are used for detailed studies of the centrality dependence while the broader bins in $N_{\rm ch}^{\rm rec}$ and $E_{\rm T}^{\rm Pb}$ were used for studies of the $p_{\rm T}$ dependence of the correlations. Most of the HMT triggers had higher thresholds in $N_{\rm ch}^{\rm rec}$ and relatively lower thresholds for $E_{\rm T}^{\rm L1}$, and so the increase in statistics in the large $E_{\rm T}^{\rm Pb}$ region is much smaller than the increase in the large $N_{\rm ch}^{\rm rec}$ region. As a result, the main results presented in this study are using event classes defined in $N_{\rm ch}^{\rm rec}$.

Event activity classes based on $N_{\rm ch}^{\rm rec}$					Event activity classes based on $E_{\rm T}^{\rm Pb}$				
$N_{\rm ch}^{\rm rec}$ range	fraction	$\langle E_{\rm T}^{\rm Pb}\rangle$ [GeV]	$\langle N_{\rm ch}^{\rm rec}\rangle$	$\langle N_{\rm ch}\rangle$	$E_{\rm T}^{\rm Pb}$ range [GeV]	fraction	$\langle E_{\rm T}^{\rm Pb}\rangle$ [GeV]	$\langle N_{\rm ch}^{\rm rec}\rangle$	$\langle N_{\rm ch}\rangle$
$[0, 20)$	0.31	7.3	10.3	12.6 ± 0.6	< 10	0.28	4.8	12.4	15.4 ± 0.7
$[20, 40)$	0.27	18.6	29.1	37.9 ± 1.7	$[10, 23)$	0.26	16.1	29.2	38.1 ± 1.7
$[40, 60)$	0.19	30.8	48.8	64 ± 2.9	$[23, 37)$	0.19	29.5	47.3	62 ± 2.8
$[60, 80)$	0.12	42.8	68.6	90 ± 4.1	$[37, 52)$	0.12	43.8	64.0	84 ± 3.8
$[80, 100)$	0.064	54.9	88.3	117 ± 5.3	$[52, 68)$	0.067	58.8	80.4	106 ± 4.8
$[100, 120)$	0.029	66.4	108.1	143 ± 6.5	$[68, 83)$	0.028	74.2	96.1	127 ± 5.7
$[120, 140)$	0.011	78.4	127.9	170 ± 7.6	$[83, 99)$	0.012	89.7	110.9	147 ± 6.6
$[140, 160)$	0.0040	90.3	147.7	196 ± 8.8	$[99, 116)$	0.0043	105.7	126.1	167 ± 7.5
$[160, 180)$	0.0013	101.8	167.5	222 ± 10.0	$[116, 132)$	0.0012	122.0	141.0	187 ± 8.4
$[180, 200)$	3.6×10^{-4}	113.2	187.4	249 ± 11.2	$[132, 148)$	3.6×10^{-4}	138.0	154.7	205 ± 9.3
$[200, 220)$	9.4×10^{-5}	124.7	207.3	275 ± 12.4	$[148, 165)$	1.0×10^{-4}	154.5	169.4	225 ± 10.1
$[220, 240)$	2.1×10^{-5}	134.3	227.1	302 ± 13.6	$[165, 182)$	2.2×10^{-5}	171.3	183.8	244 ± 11.0
$[240, 260)$	4.6×10^{-6}	145.2	247.0	329 ± 14.8	$[182, 198)$	4.6×10^{-6}	187.6	196.3	261 ± 11.8
$[260, 290)$	1.1×10^{-6}	157.2	268.9	357 ± 16.1	$[198, 223)$	1.1×10^{-6}	205.9	210.7	280 ± 12.6
$[290, 370)$	8.9×10^{-8}	174.1	300.6	393 ± 17.7	$[223, 300)$	9.6×10^{-8}	232.2	230.0	306 ± 13.8
$[0, 40)$	0.58	12.5	19.0	24 ± 1.1	< 25	0.59	10.2	21.7	28 ± 1.3
$[40, 80)$	0.32	35.3	56.4	74 ± 3.3	$[25, 50)$	0.27	35.1	54.7	72 ± 3.3
$[80, 110)$	0.081	56.8	91.7	121 ± 5.5	$[50, 75)$	0.096	61.5	81.4	107 ± 4.9
$[110, 140)$	0.023	74.2	121.0	160 ± 7.2	$[75, 100)$	0.025	84.5	105.9	140 ± 6.3
$[140, 180)$	0.0053	93.0	152.5	202 ± 9.1	$[100, 130)$	0.0051	109.5	130.0	172 ± 7.8
$[180, 220)$	4.6×10^{-4}	115.5	191.5	254 ± 11.5	$[130, 165)$	5.6×10^{-4}	141.4	156.4	208 ± 9.4
$[220, 260)$	2.6×10^{-5}	136.1	230.6	307 ± 13.8	$[165, 200)$	2.7×10^{-5}	174.2	186.2	247 ± 11.1
$[260, 370)$	1.2×10^{-6}	158.4	271.3	361 ± 16.2	$[200, 300)$	1.0×10^{-6}	207.9	213.6	284 ± 12.8

Table IV.2.1: A list of the event activity classes defined in $N_{\rm ch}^{\rm rec}$ (left part) and $E_{\rm T}^{\rm Pb}$ (right part) ranges. For each event class, the faction of MB+HMT events after reweighting, the average values of $E_{\rm T}^{\rm Pb}$ and $N_{\rm ch}^{\rm rec}$, and the efficiency corrected average number of charged particles within $|\eta| < 2.5$ and $p_{\rm T} > 0.4$ GeV, $\langle N_{\rm ch}\rangle$ are also shown.

IV.2.2 Track selection and tracking efficiency

Charged particle tracks are reconstructed in the ID using a combination of "doLowMuRunSetup" flag and "doMinBias" flag, both of which are also used for reconstructing the low pileup p+p data [184]. The "doLowMuRunSetup" flag enables the track reconstructions above 400 MeV using inside out tracking, while tracks below 400 MeV are reconstructed by the "doMinBias" flag. Tracks reconstructed with $p_{\rm T} > 0.3$ GeV are included in the 2PC analysis. The track selection cuts follow those from the minimum bias p+p analysis [184], and are listed below:

- Track author requirement: trk_patternReco1 & 1 or trk_patternReco2 & 16;
- $|\eta| < 2.5$
- SCT hits:
  nSCTHits ≥ 2 for$p_{\rm T} \in [0.1, 0.2]$ GeV,

nSCTHits ≥ 4 for$p_{\mathrm{T}} \in [0.2, 0.3]$ GeV,
nSCTHits ≥ 6 for$p_{\mathrm{T}} > 0.3$ GeV

- nPixHits ≥ 1
- nBLHits ≥ 1 if expected (i.e., expectBLayerHit > 0)
- $|d_0| < 1.5$ mm, $|z_0 \times \sin(\theta)| < 1.5$mm,
- significance cuts: $|\frac{d_0}{err\_d_0}| < 3$ and $|\frac{z_0 \sin\theta}{err\_z_0 \sin\theta}| < 3$

Three other cuts, similar to those used for cross-checks in [182], are defined for cross-checks and systematic studies. These are:

Weak cut: Same as default cut except without the significance cuts

Strong cut: Same as default cut plus requiring: nPixHits ≥ 1, nSCTHoles≤ 1, nSCTHits > 7, and $\chi^2/ndf < 6.0$.

Strong cut+: Same as strong cut plus $|d_0| < 1$ mm, $|z_0 \times \sin(\theta)| < 1$mm. These are the cuts used for the Pb+Pb analysis [4].

The efficiency, $\epsilon(p_{\mathrm{T}}, \eta)$, for track reconstruction, for different selection cuts, is obtained using p + Pb Monte Carlo events produced with version 1.38b of the HIJING event generator [120] with a center-of-mass boost matching the beam conditions. The response of the detector is simulated using GEANT4 [185, 186] and the resulting events are reconstructed with the same algorithms as applied to the data. The tracking efficiency used in this analysis is taken from the 2012 ridge analysis [12, 182], since the detector conditions were very similar between the two runs. This can be seen from figure IV.2.6 and figure IV.2.7. Figure IV.2.6 compares the uncorrected p_{T} spectra from tracks in the mid-rapidity region with the default track selection cuts, between the 2012 and 2013 p+Pb runs. The shapes of the raw spectra are very consistent (within 1%) between the two runs suggesting the tracking efficiencies are not too different between them. Figure IV.2.7 shows the ratio of the uncorrected p_{T} spectra from the 2013 run to that from the 2012 run in different pseudorapidity bins of 0.5 unit width from η = -2.5 to 2.5. The raw spectra are largely consistent over the entire pseudorapidity range between the two runs, except in the most negative η slice, where about a 2% difference at low p_{T} (< 1.0 GeV) is seen.

The tracking efficiency as a function of p_{T} (for the inclusive mid-rapidity region, $|\eta| < 2.5$) and η (for the integrated p_{T} bin, $0.5 < p_{\mathrm{T}} < 5.0$ GeV) are shown in figure IV.2.8 for different multiplicity intervals. The tracking efficiency shows very weak variation with multiplicity. The efficiency increases with p_{T} by 6% from $p_{\mathrm{T}} = 0.3$ GeV to 0.5 GeV, but varies only weakly with increase in p_{T} above 0.5 GeV. The tracking efficiency for $p_{\mathrm{T}} > 0.5$ GeV ranges from 82% at $\eta = 0$ to 70% at $|\eta| = 2$ and 60% at $|\eta| > 2.4$. The tracking efficiency is evaluated in 10 pseudorapidity bins from -2.5 to 2.5 as a function of p_{T} and parametrized as function of p_{T} and η [182].

The uncertainty in tracking efficiency is evaluated by varying the track selection cuts and studying the closure, i.e consistency between the efficiency corrected spectra for different track

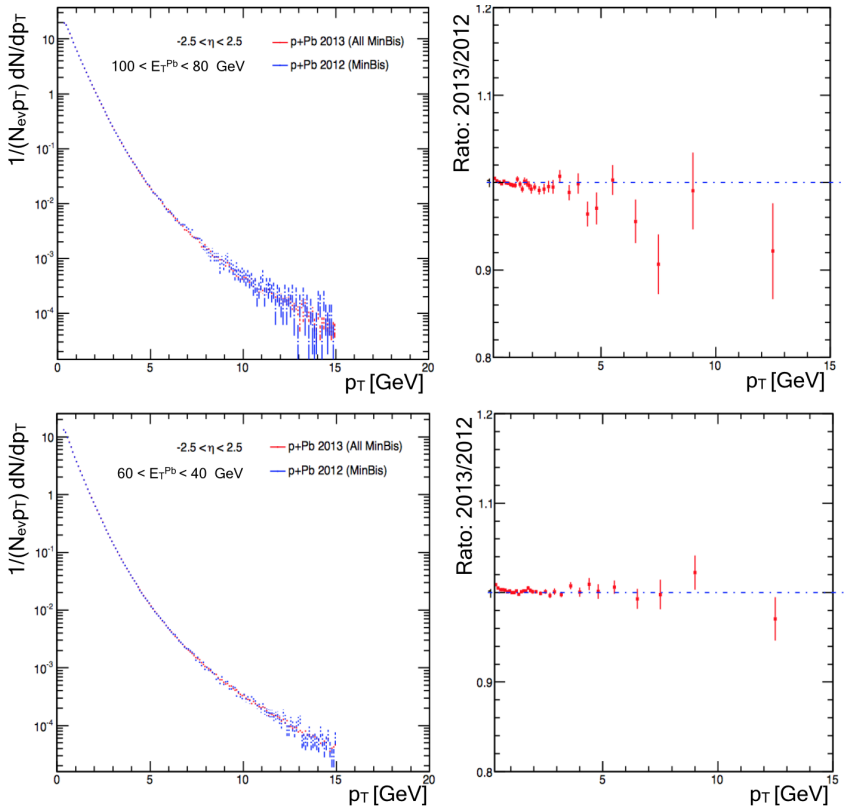

Figure IV.2.6: Comparison of the uncorrected p_{T} spectra from 2012 and 2013 p+Pb runs and the ratio of the spectra from 2013 to that from 2012, for events in two $E_{\mathrm{T}}^{\mathrm{Pb}}$ ranges. The tracks are using the default track selection cuts and with $|\eta| < 2.5$.

selection cuts, as a function of p_{T}, η and multiplicity, and also from the variation of efficiency as function of multiplicity. Figure IV.2.9 shows an example of the comparison between efficiency corrected spectra for different track selection cuts and their ratios. Except for the case of weak cuts, where a non closure of about 2% can be seen, the efficiency corrected spectra from different cuts is consistent with each other. Similar levels of agreement were observed as function of η and multiplicity. The efficiency was found to vary by 3% between the lowest and highest multiplicity bins for $p_{\mathrm{T}} < 0.5$ and by 1% for $p_{\mathrm{T}} > 0.5$ GeV. To account for the fact that, even the multiplicity in the highest multiplicity bin in HIJING is smaller than that in the data, an additional uncertainty is quoted by comparing the variation of tracking efficiency in Pb+Pb analyses from peripheral bin to 55-60% bin, which has comparable multiplicity as highest multiplicity p+Pb collisions. This variation was found to be 2% independent of p_{T}. The combined uncertainty quoted from non closure and multiplicity dependence of the efficiency is 4.8% for $p_{\mathrm{T}} < 0.5$ GeV and 3.6% for $p_{\mathrm{T}} > 0.5$ GeV.

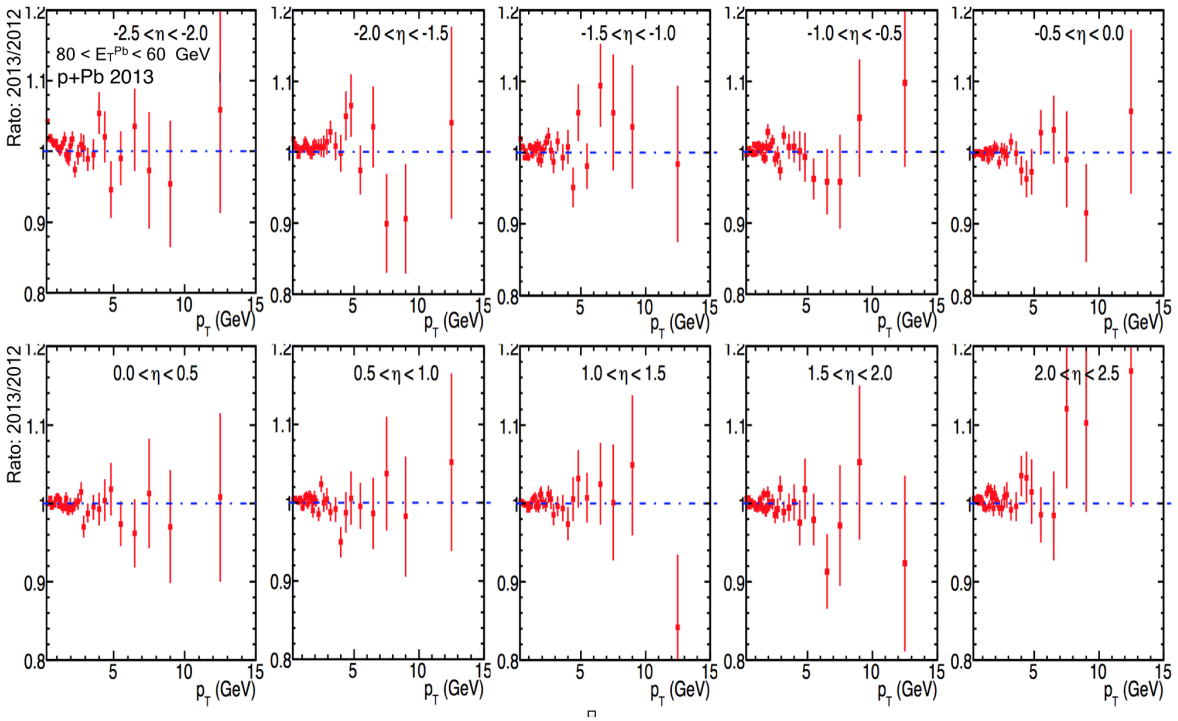

Figure IV.2.7: Ratio of the uncorrected p_{T} spectra from 2013 p + Pb run to that from the 2012 p+Pb run in pseudorapidity bins of 0.5 units from η = -2.5 to η = 2.5, for events with $80 > E_{\mathrm{T}}^{\mathrm{Pb}} > 60$ GeV.

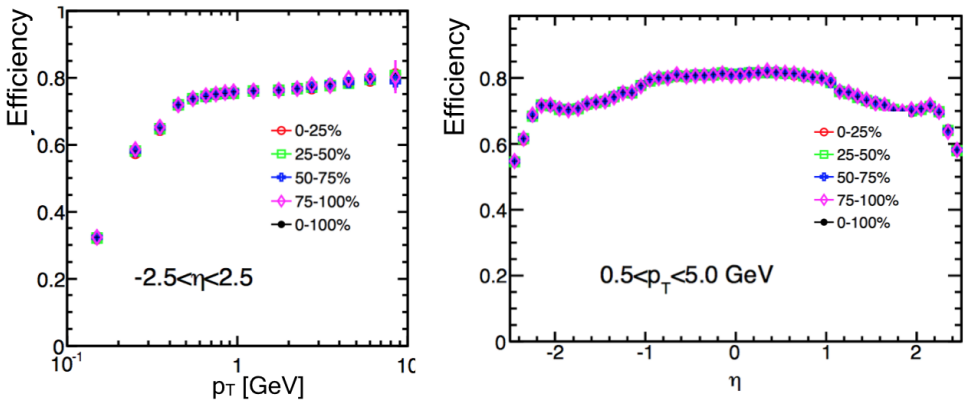

Figure IV.2.8: Tracking efficiency as a function of p_{T} for tracks with $|\eta| < 2.5$ (left) and as a function of η for tracks in $0.5 < p_{\mathrm{T}} < 5.0$ GeV (right) for the default track selection cuts, in increasing multiplicity bins, each containing 25% of the total statistics [182].

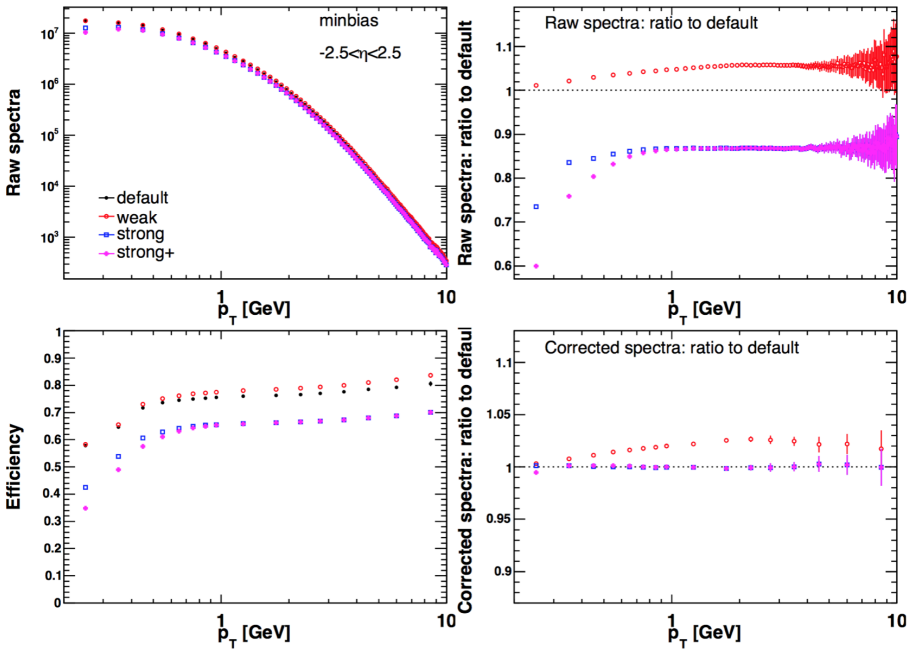

Figure IV.2.9: The raw spectra (top-left), ratio of the raw spectra (top-right), efficiency from HIJING (bottom left) and ratios of efficiency corrected spectra (bottom right) for the four different types of cuts [182].

IV.2.3 Data analysis

IV.2.3.1 Analysis procedure

Two particle correlation

The analysis uses the two particle correlation method (Subsection II.2.2.1) to study the correlations in the system. The two particle correlation functions are measured in each event activity class as a function of the relative azimuthal angle $\Delta\phi = \phi^a - \phi^b$ and relative pseudorapidity $\Delta\eta = \eta^a - \eta^b$, with $|\Delta\eta| < \eta_\Delta^{max} = 5$. The labels a and b denote the two particles in the pair and is conventionally referred to as the "trigger" and "associated" particle, respectively. The two particles may be selected from different $p_{\rm T}$ intervals. The correlation function is constructed as the ratio of the pair distribution from "same" events ($S(\Delta\eta, \Delta\phi)$), where both the particles in a pair are taken from the same event, to the distribution from "mixed" events ($B(\Delta\eta, \Delta\phi)$), where the two particles in the pair are taken from two different events. Figure IV.2.10 shows an example of the $S(\Delta\eta, \Delta\phi)$ and $B(\Delta\eta, \Delta\phi)$ distributions and their ratio, for one of the high multiplicity event classes. The $S(\Delta\eta, \Delta\phi)$ and $B(\Delta\eta, \Delta\phi)$ distributions are dominated by the triangular shape along the $\Delta\eta$ direction, arising from the finite detector acceptance, but most of these features cancel in the ratio, where the familiar features, viz the ridge and the near-side jet and away-side peaks can

be seen. In this analysis, we are interested mainly in the modulation along the $\Delta\phi$ direction. The detector features along this direction are much smaller compared to the magnitude of the signal. This can be seen clearly in figure IV.2.11, where the (normalized) projections of S and B distributions along $\Delta\phi$ for the region with $2 < |\Delta\eta| < 5$ are shown. For all event classes, the background (projection from B) is negligible to the signal distribution (projection from S).

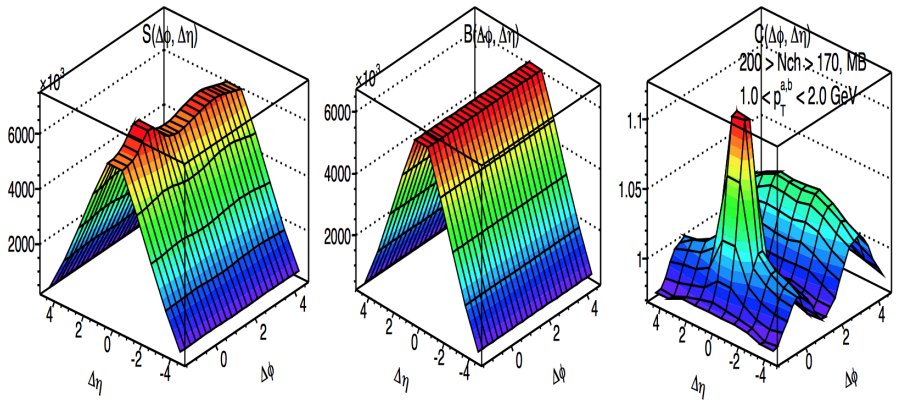

Figure IV.2.10: The same event distribution, $S(\Delta\eta, \Delta\phi)$, mixed event distribution $B(\Delta\eta, \Delta\phi)$, and the ratio $C(\Delta\eta, \Delta\phi) = S(\Delta\eta, \Delta\phi)/B(\Delta\eta, \Delta\phi)$ for events with $170 < N_{\rm ch}^{\rm rec} < 200$ ($N_{\rm ch}^{\rm rec}$ denoted as $\rm N_{ch}$ in figure).

In the ridge analysis, the yield or number of associated particles produced per trigger particle is a quantity of interest. The normalization of the correlation function in this analysis is therefore set to give the "per trigger yield". The correlation strength expressed in terms of yield per trigger particle is defined as [3, 187]:

$$Y(\Delta\phi, \Delta\eta) = \frac{\int B'(\Delta\phi, \Delta\eta) d\Delta\eta\Delta\phi}{\pi\eta_{\Delta}^{max}} \left[\frac{S'(\Delta\phi, \Delta\eta)}{B'(\Delta\phi, \Delta\eta)}\right], \tag{IV.2.3}$$

where, S' and B' represent the pair distributions from the same event and mixed events respectively, which are normalized by the efficiency corrected average number of trigger particles in the event class.

The mixed-event distribution, $B(\Delta\phi, \Delta\eta)$, measures the distribution of uncorrelated pairs and is used to divide out the structures in the pair distribution arising purely from detector and acceptance effects. The $B(\Delta\phi, \Delta\eta)$ distribution is constructed by choosing the two particles in the pair from different events of similar $N_{\rm ch}^{\rm rec}$ (matched to within 10 tracks), $E_{\rm T}^{\rm Pb}$ (matched to with 10 GeV) and z_{vtx} (matched to within 10 mm), so that $B(\Delta\phi, \Delta\eta)$ properly reflects the detector effects in $S(\Delta\phi, \Delta\eta)$. When measuring S and B, pairs are filled in one quadrant of the $(\Delta\phi, \Delta\eta)$ space and then reflected to the other quadrants [12]. The normalization factor in front of the S'/B' ratio is chosen such that the $(\Delta\phi, \Delta\eta)$-averaged value of $B'(\Delta\phi, \Delta\eta)$ is unity. While constructing the pair distributions, in order to correct $S(\Delta\phi, \Delta\eta)$ and $B(\Delta\phi, \Delta\eta)$ for detector inefficiencies,

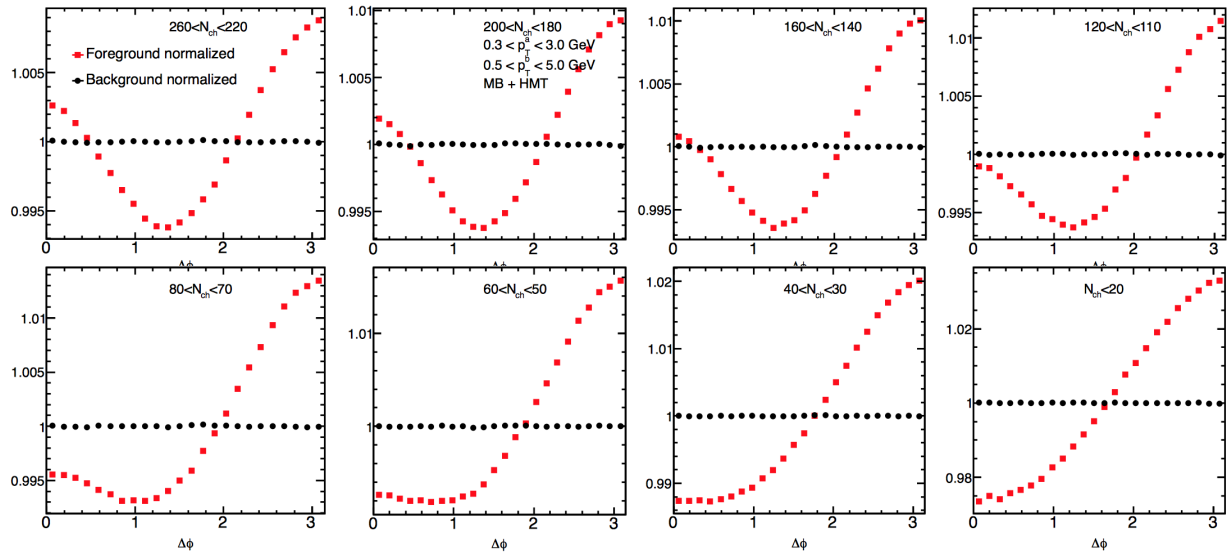

Figure IV.2.11: The projections of $S(\Delta\eta, \Delta\phi)$ (red squares) and $B(\Delta\eta, \Delta\phi)$ (black circles) along $\Delta\phi$ for the region with $2 < |\Delta\eta| < 5.0$, for different event activity classes defined using $N_{\mathrm{ch}}^{\mathrm{rec}}$ (denoted as $\mathrm{N_{ch}}$ in figure).

the pairs are weighted by the inverse product of their tracking efficiencies $1/(\epsilon_a \epsilon_b)$. Remaining detector distortions not accounted for in the efficiency largely cancel in the S'/B' ratio.

The one-dimensional (1D) distribution ($Y(\Delta\phi)$) is defined in a similar manner as:

$$Y(\Delta\phi) = \frac{\int B'(\Delta\phi) d\Delta\phi}{\pi} \left[\frac{S'(\Delta\phi)}{B(\Delta\phi)}\right], \tag{IV.2.4}$$

where the 1D distributions $S'(\Delta\phi)$ and $B'(\Delta\phi)$ are obtained by integrating $S'(\Delta\phi, \Delta\eta)$ and $B'(\Delta\phi, \Delta\eta)$, respectively, over a $\Delta\eta$ range. The range for integration, $|\Delta\eta| < 1$, is used to focus on the features of the short-range correlations, while the region $|\Delta\eta| > 2$ is chosen to study the features of the long-range correlations. These two regions are hence referred to as the "short-range region" and the "long-range region", respectively, in this chapter. The normalization factor in front of the S'/B' ratio is again chosen such that the $\Delta\phi$ averaged value of $B'(\Delta\phi)$ is unity.

Figure IV.2.12 shows the two dimensional (2D) correlation functions for charged particles with $1 < p_{\mathrm{T}}^{\mathrm{a,b}} < 3$ GeV for events in a class with low event activity, $E_{\mathrm{T}}^{\mathrm{Pb}} < 10$ GeV, and in a class with high event activity, $E_{\mathrm{T}}^{\mathrm{Pb}} > 100$ GeV. The correlation function in the low-activity event class shows a sharp peak centered at $(\Delta\phi, \Delta\eta) = (0,0)$, owing to short-range correlations for pairs resulting from jets, resonance decays, and Bose-Einstein correlations. The correlation function also shows a broad structure around $\Delta\phi \sim \pi$ (the "away-side") from back to back resonances, dijets, and momentum conservation that is collectively referred to as "recoil" [12] in the remainder of this chapter. In the high event activity class, in addition to peak around $(\Delta\phi, \Delta\eta) = (0,0)$, the correlation function

shows a ridge like structure at $\Delta\phi \sim 0$ (the "near-side"), that extends over the full measured $\Delta\eta$ range. This long-range component has a very weak $\Delta\eta$ dependence.

The distribution at $\Delta\phi \sim \pi$ is also broadened in $\Delta\eta$ in the high-activity event class, consistent with the presence of a long-range ridge component, like the ridge on the near-side, in addition to the recoil component [12]. In order to study the long-range ridge component, the recoil component in the high event activity classes need to be estimated. In this analysis the recoil component in the high event activity class is estimated from the yield in a low activity event class, where there is no long-range ridge component present on the near-side, and subtracted out. This recoil subtraction procedure is further explained below.

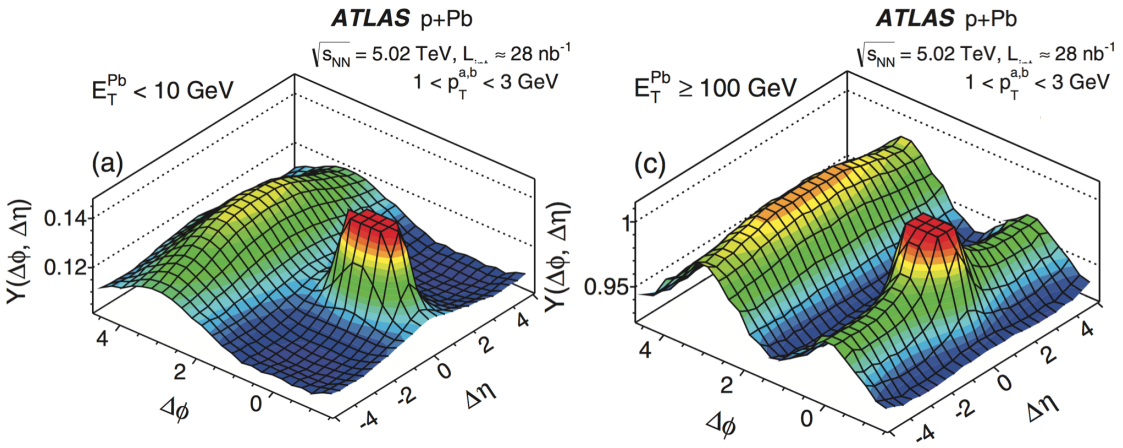

Figure IV.2.12: The 2D correlation function in $(\Delta\phi, \Delta\eta)$ for particle pairs with $1 < p_{\mathrm{T}}^{\mathrm{a,b}} < 3$ GeV for events in a low event activity class (left) and for events in a high event activity class (right).

Recoil subtraction

The 2D per trigger yield distributions are constituted of uncorrelated pairs from combinatorial background which is flat in $(\Delta\phi, \Delta\eta)$ and correlated pairs coming from short-range correlations, recoil and, in higher event activity classes, from the long-range ridge modulation. The number of correlated pairs above the flat pedestal from uncorrelated pairs is defined, following previous analyses [10, 13, 12], as

$$Y^{corr}(\Delta\phi, \Delta\eta) = \frac{\int B'(\Delta\phi, \Delta\eta) d\Delta\eta\Delta\phi}{\pi\eta_{\Delta}^{max}} \left[\frac{S'(\Delta\phi, \Delta\eta)}{B'(\Delta\phi, \Delta\eta)} - b_{ZYAM}\right],$$
$$Y^{corr}(\Delta\phi) = \frac{\int B'(\Delta\phi) d\Delta\phi}{\pi} \left[\frac{S'(\Delta\phi)}{B'(\Delta\phi)} - b_{ZYAM}\right], \tag{IV.2.5}$$

where b_{ZYAM} denotes the pedestal from uncorrelated pairs and is determined using a zero-yield-at-minimum (ZYAM) method [188, 189]. The value of b_{ZYAM} is evaluated by fitting a second order polynomial function around $\Delta\phi \sim \pi/2$ to the 1D $Y(\Delta\phi)$ distribution in the long-range region.

The point of minimum yield, $\Delta\phi_{ZYAM}$, is determined from the fit and b_{ZYAM} is determined as the yield at this value. The stability of this evaluation is checked by varying the $\Delta\phi$ window around $\Delta\phi \sim \pi/2$ used for fitting with the polynomial function and the resulting differences are propagated into the systematic uncertainties.

The correlated yield in the low event activity classes, $Y^{corr}_{peri}(\Delta\phi)$, contains mainly the short-range correlation component and the recoil component. The short-range and the recoil component in a higher event-activity class is estimated as $\alpha Y^{corr}_{peri}(\Delta\phi)$, where α is a scale factor used to match the integrated yield from the short-range correlation between the central and peripheral event classes. The scale factor α is determined for each $p_{\rm T}^{\rm a}$ and $p_{\rm T}^{\rm b}$ combination in the event class and is obtained as $\alpha = Y^{n-peak}/Y^{n-peak}_{peri}$, where Y^{n-peak} quantifies the magnitude of the short-range yield in the higher event activity class and is defined using $Y(\Delta\eta) = \int_{|\Delta\phi|<1} Y(\Delta\phi,\Delta\eta)d\Delta\phi$ as:

$$Y^{n-peak} = \int_{|\Delta\eta|<1} Y(\Delta\eta)\Delta\eta - \frac{1}{5-\eta^{min}_{\Delta}} \int_{\eta^{min}_{\Delta}<|\Delta\eta|<5} Y(\Delta\eta)\Delta\eta, \tag{IV.2.6}$$

and Y^{n-peak}_{peri} is the same quantity evaluated in the low event activity class. The default value of α is obtained using $\eta^{min}_{\Delta} = 2$, but the value of η^{min}_{Δ} is varied from 2 to 4 to check the stability of the determined value and the differences are propagated to systematic uncertainties. The scale factor α accounts for the enhancement in the higher event activity classes, relative to the peripheral event class, of the short-range correlation and also the recoil contribution, under the assumption that the magnitude of the away-side recoil component scales with the magnitude of the near-side short-range component. A similar rescaling procedure was also used by CMS in [100]. The default peripheral event class is chosen to be one with $E_{\rm T}^{\rm Pb} < E_{\rm T}^{0} = 10$ GeV. However, the results have also been checked with other $E_{\rm T}^{0}$ values, as well as with a peripheral event class defined by $N_{\rm ch}^{\rm rec} < 20$, the details of which are discussed in Subsection IV.2.4.

Figure IV.2.13 shows the $N_{\rm ch}^{\rm rec}$ dependence of the estimated short-range yield, Y^{n-peak}, and the scale factor α, for particles with $0.5 < p_{\rm T}^{\rm a,b} < 3.0$ GeV. The α values are calculated using the default peripheral event class ($E_{\rm T}^{\rm Pb} < 10$ GeV). The yield and the value of α show a strong increase with $N_{\rm ch}^{\rm rec}$ in the low $N_{\rm ch}^{\rm rec}$ region (< 60 tracks) and a much slower increase with $N_{\rm ch}^{\rm rec}$ in the higher $N_{\rm ch}^{\rm rec}$ region. The increase in the high $N_{\rm ch}^{\rm rec}$ region is expected since the selection requiring large number of tracks induces a small autocorrelation bias by increasing the probability of selecting events with more jets and short-range contributions. The Y^{n-peak} and α values were found to have a similar $N_{\rm ch}^{\rm rec}$ dependence in other $p_{\rm T}^{\rm a,b}$ regions as well. Figure IV.2.14 shows the $p_{\rm T}$ dependence of the short-range yield and α. The Y^{n-peak} values show a nearly linear increase with the $p_{\rm T}$ of the trigger particle for a given value of the associated particle $p_{\rm T}$. The short-range yield is expected to increase with $p_{\rm T}$ as the number of pairs from jets increase with $p_{\rm T}$ [100]. The scale factor α is nearly constant and close to 1 in the higher $p_{\rm T}^{\rm a}$ region, with $p_{\rm T}^{\rm a} > 3$ GeV, but shows a strong dependence on $p_{\rm T}^{\rm a}$ in the low $p_{\rm T}^{\rm a}$ region.

The effectiveness of the estimation of the recoil component in different event activity classes is shown in figure IV.2.15. The figure shows the integrated yields, $Y_{\rm int}$, on the near-side and away-side (solid black points), obtained by integrating $Y^{corr}(\Delta\phi)$ over $|\Delta\phi| < \pi/3$ and $|\Delta\phi| < 2\pi/3$, respectively, as function of $N_{\rm ch}^{\rm rec}$ and $E_{\rm T}^{\rm Pb}$. Also shown is the difference between the yield on the

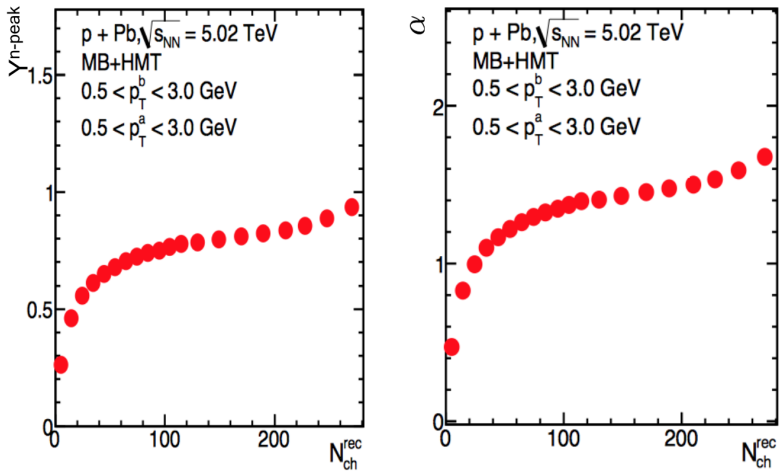

Figure IV.2.13: The estimated per trigger yield from the short-range correlation, Y^{n-peak}, (left) and the scale factor α, as a function of $N_{\rm ch}^{\rm rec}$ for particles with $0.5 < p_{\rm T}^{\rm a,b} < 3.0$ GeV.

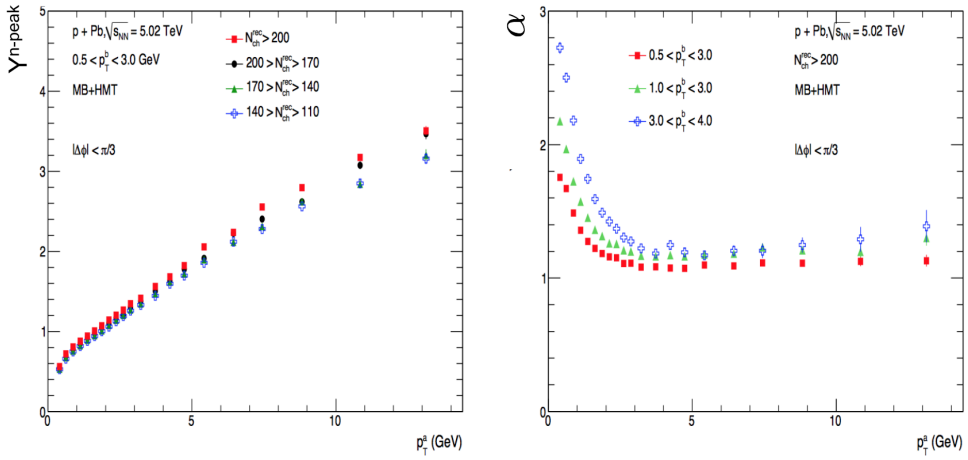

Figure IV.2.14: (Left) The estimated per trigger yield from the short-range correlation, Y^{n-peak}, as a function of the trigger particle $p_{\rm T}$ for associated particles with $0.5 < p_{\rm T}^{\rm a,b} < 3.0$ GeV in different high multiplicity event classes. (Right) The scale factor α, as a function of the trigger particle $p_{\rm T}$ for events in a high multiplicity event class with $N_{\rm ch}^{\rm rec} > 200$ for different associated particle selections.

away-side and the near-side ($Y_{\rm int}^{\rm diff}$, solid red points). Since the integration windows on the near-side and away-side are symmetric and has a length of $\pi/3$, any contributions from second, third, fourth and higher even order modulations cancel in the difference. Since the long-range ridge correlation is found to be dominated by second and third order modulations, the difference between the yields

is a measure of the recoil component in the event class. The figure also shows the integrated yield on the away-side from the estimated recoil component, $\alpha Y^{corr}(\Delta\phi)$, shown as solid lines. For the $p_{\rm T}^{\rm a,b}$ bin chosen ($1 < p_{\rm T}^{\rm a,b} < 3$ GeV), the estimated recoil component agrees quite well with the recoil component ($Y_{\rm int}^{\rm diff}$) in the different event activity classes, both as function of $N_{\rm ch}^{\rm rec}$ and $E_{\rm T}^{\rm Pb}$.

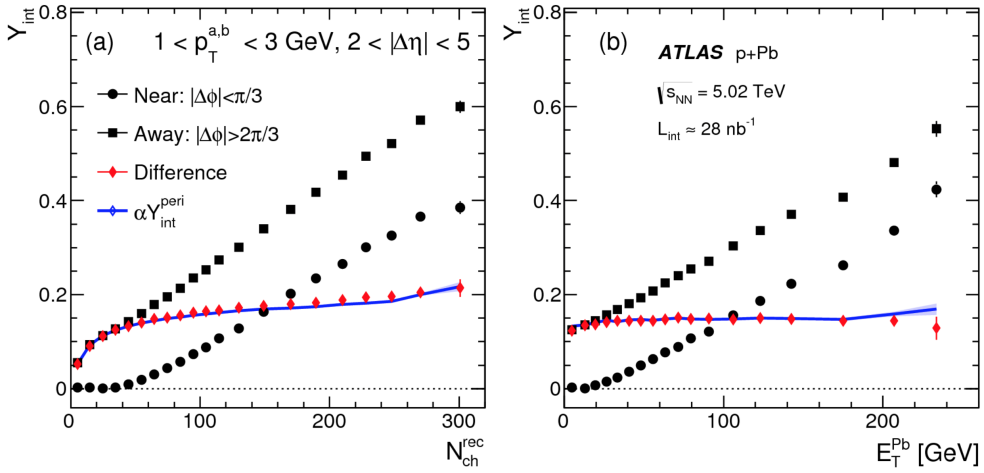

Figure IV.2.15: The integrated per-trigger yield above ZYAM pedestal, $Y_{\rm int}$, on the near-side (solid circles), the away-side (solid squares), and their difference (solid diamonds) as functions of $N_{\rm ch}^{\rm rec}$ and $E_{\rm T}^{\rm Pb}$ for pairs in $2 < |\Delta\eta| < 5$ and 1 ¡ $p_{\rm T}^{\rm a,b} < 3$ GeV. The yield difference is compared to the estimated recoil contribution in the away-side (blue solid lines). The error bars or the shaded bands represent the combined statistical and systematic (discussed in the next section) uncertainties.

The agreement holds quite well for other choices of $p_{\rm T}$ bins also, as long as one of the particles in the pair is from $1 < p_{\rm T} < 3$ GeV (or a bin with similar mean value), but shows some deviations if both particles are from a different $p_{\rm T}$ bin. Such deviations can arise if a long-range first order harmonic, similar to the v_1 component present in A+A collisions (Section IV.1) is also present in p+Pb collisions. Figure IV.2.16 shows the integrated yields on the away- and near-sides and the difference between the two, as well as the integrated yield on the away-side from the estimated recoil component, as a function of $N_{\rm ch}^{\rm rec}$. There are systematic deviations, the estimated component is larger than $Y_{\rm int}^{\rm diff}$ if both particles are at lower $p_{\rm T}$ or both are at higher $p_{\rm T}$ (relative to the 1−3 GeV bin), and is smaller when one of the particles is in a lower $p_{\rm T}$ bin and the other higher. Figure IV.2.17 shows the difference between $Y_{\rm int}^{\rm diff}$ and the estimated recoil component as a function of $p_{\rm T}^{\rm a}$ for different $p_{\rm T}^{\rm b}$ windows in a high multiplicity event class (the quantity is normalized to have same definition as a Fourier coefficient, $v_{1,1}$). The $p_{\rm T}^{\rm a,b}$ dependence shows a very similar $p_{\rm T}^{\rm a,b}$ dependence as in figure IV.1.3, characteristic of the $v_{1,1}$ component from density fluctuations and is of a similar magnitude as the $v_{1,1}$ component in Pb+Pb collisions. This suggests that, up to deviations from a possible small v_1 component in p+Pb collisions, the estimated recoil component correctly reproduces the recoil contribution in the event classes.

In the analysis, for most of the results, the default choice for associated particles is taken as

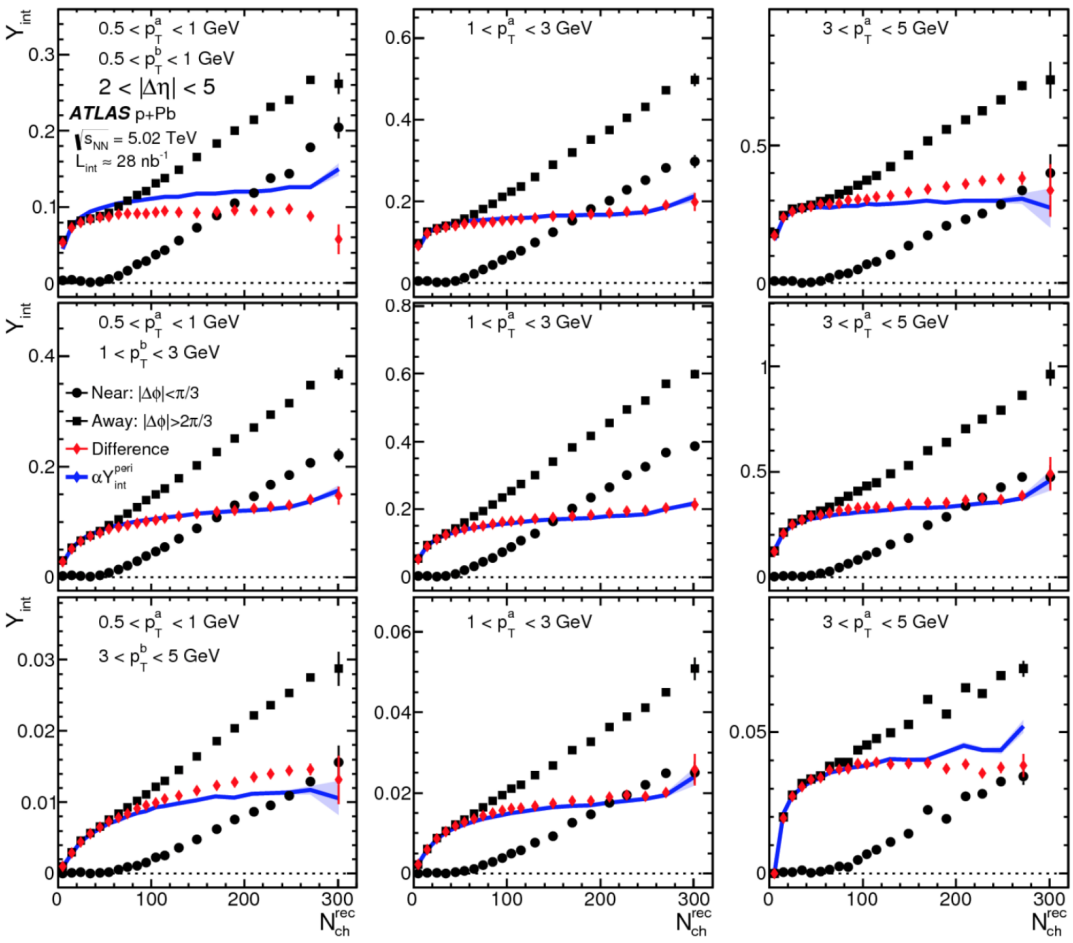

Figure IV.2.16: The integrated per-trigger yield above ZYAM pedestal, $Y_{\rm int}$, on the near-side (solid circles), the away-side (solid squares), and their difference (solid diamonds) as functions of $N_{\rm ch}^{\rm rec}$ and $E_{\rm T}^{\rm Pb}$ for pairs in $2 < |\Delta\eta| < 5$. Each panel is for a different combination of $p_{\rm T}^{\rm a}$ and $p_{\rm T}^{\rm b}$ range. The yield difference is compared to the estimated recoil contribution in the away-side (blue solid lines). The error bars or the shaded bands represent the combined statistical and systematic (discussed in section) uncertainties.

$1 < p_{\rm T}^{\rm b} < 3$ GeV, although other choices of $p_{\rm T}^{\rm b}$ are used for cross-checks and comparisons. Using the estimated recoil component, the recoil subtracted yield in different event activity classes is obtained as

$$\begin{aligned} Y^{sub}(\Delta\phi,\Delta\eta) &= Y(\Delta\phi,\Delta\eta) - \alpha Y^{corr}(\Delta\phi,\Delta\eta), \\ Y^{sub}(\Delta\phi) &= Y(\Delta\phi) - \alpha Y^{corr}(\Delta\phi) \end{aligned} \tag{IV.2.7}$$

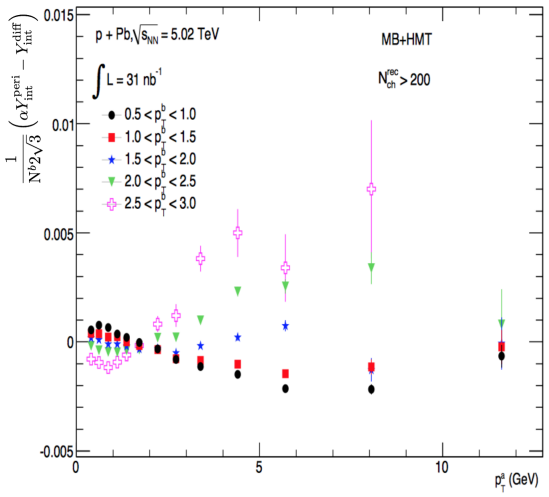

Figure IV.2.17: The difference between the estimated recoil contribution in the away-side and the yield difference in a high multiplicity event class with $N_{\rm ch}^{\rm rec} > 200$, as a function of $p_{\rm T}^{\rm a}$ for different $p_{\rm T}^{\rm b}$ selections. The values are normalized to have the same definition as the Fourier coefficient $v_{1,1}$.

Figure IV.2.18 shows an example of the recoil subtraction. The left panel shows the correlated yield, $Y^{corr}(\Delta\phi)$ from a high multiplicity event class and the estimated recoil component and the right panel shows the 1D yield $Y(\Delta\phi)$ and recoil subtracted 1D yield, $Y^{sub}(\Delta\phi)$. After subtracting the recoil component, a nearly symmetric "double ridge" similar to that observed in A+A collisions can be seen.

Fourier harmonics

The azimuthal structure of the long-range ridge correlation is studied using a Fourier decomposition, similar to the approach followed in A+A collisions [190, 4]. $Y^{sub}(\Delta\phi)$ is expanded in a Fourier series as:

$$Y^{sub}(\Delta\phi) = \frac{\int Y^{sub}(\Delta\phi)d\Delta\phi}{\pi}\left[1 + \sum_n 2v_{n,n}cos(n\Delta\phi)\right], \tag{IV.2.8}$$

where $v_{n,n}$ are the discrete Fourier coefficients calculated using a discrete Fourier transform,

$$v_{n,n} = \frac{\sum_{m=1}^{N} cos(n\Delta\phi_m)Y^{sub}(\Delta\phi_m)}{\sum_{m=1}^{N} Y^{sub}(\Delta\phi_m)}, \tag{IV.2.9}$$

where $N = 24$ is the number of $\Delta\phi$ bins used from 0 to π. The first fiver Fourier coefficients are obtained for the different event activity classes for different $p_{\rm T}^{\rm a}, p_{\rm T}^{\rm b}$ combinations.

The coefficients characterizing the azimuthal anisotropy in the single particle distribution, v_n,

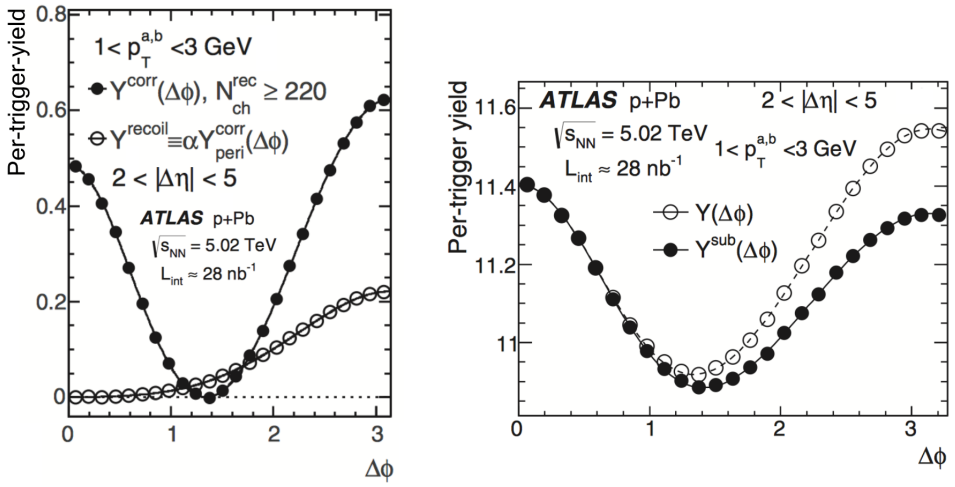

Figure IV.2.18: (Left) The correlated yield above ZYAM pedestal, $Y^{corr}(\Delta\phi)$, and the estimated recoil component, $\alpha Y^{corr}_{peri}(\Delta\phi)$, and (right) the yield, $Y(\Delta\phi)$ and the recoil subtracted yield $Y^{sub}(\Delta\phi)$, for pairs with $2 < |\Delta\eta| < 5$ and $1 < p_{\rm T}^{\rm a,b} < 3$ GeV for events with $N_{\rm ch}^{\rm rec} > 220$.

may be obtained using the familiar factorization relation [190, 4, 11]

$$v_{n,n}(p_{\rm T}^{\rm a}, p_{\rm T}^{\rm b}) = v_n(p_{\rm T}^{\rm a}) v_n(p_{\rm T}^{\rm b}), \tag{IV.2.10}$$

for the cases with $n = 2$ to 5. The case of the first order harmonic is slightly different and is discussed in Section IV.2.5. The v_n coefficients are obtained as

$$v_n(p_{\rm T}^{\rm a}) = v_{n,n}(p_{\rm T}^{\rm a}, p_{\rm T}^{\rm b}) / \sqrt{v_{n,n}(p_{\rm T}^{\rm b}, p_{\rm T}^{\rm b})}. \tag{IV.2.11}$$

The results presented in this chapter uses the default transverse momentum range for associated particles, $1 < p_{\rm T}^{\rm b} < 3$ GeV, for calculating $v_n(p_{\rm T}^{\rm a})$ in Eq. IV.2.11. But the factorization behaviour is checked using different ranges for $p_{\rm T}^{\rm b}$. The v_n values as a function of the trigger particle transverse momentum is denoted as $v_n(p_{\rm T}^{\rm a})$ or simply by $v_n(p_{\rm T})$ where appropriate. The two particle and single particle Fourier coefficients are calculated also for the yields without recoil subtraction, $Y(\Delta\phi)$, and are denoted as $v_{n,n}^{unsub}$ and v_n^{unsub} respectively.

Figure IV.2.19 shows a comparison of the v_2, v_3 and v_4 values obtained from the yield before and after the recoil subtraction, as a function of the $|\Delta\eta|$ range used for integration to define the 1D yields (Eq.IV.2.4). The values after subtraction, v_n, show a weak dependence on $|\Delta\eta|$, as expected from the long-range nature of the correlations observed. The v_n values are much smaller than v_n^{unsub} for $|\Delta\eta| < 1$, reflecting the removal of the short-range correlations on the near-side. For $|\Delta\eta| > 1$, the v_n values are systematically smaller than v_n^{unsub} for $n = 2$ and 4 and larger for $n = 3$, reflecting the removal of the away-side recoil contribution.

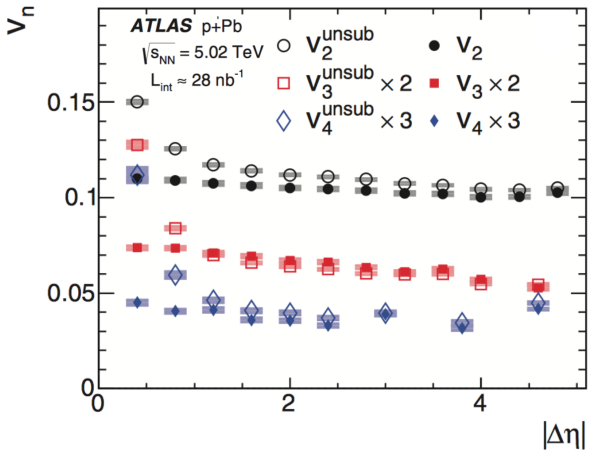

Figure IV.2.19: The v_2, v_3 and v_4 values obtained from the yield before and after the recoil subtraction, as a function of the $|\Delta\eta|$ range used for integration to define the 1D yields for pairs with $1 < p_{\mathrm{T}}^{\mathrm{a,b}} < 3$ GeV in the event class with $N_{\mathrm{ch}}^{\mathrm{rec}} > 220$. The error bars and shaded boxes are statistical and systematic (discussed in section) uncertainties, respectively.

IV.2.3.2 Comparison of results using different trigger selections

The v_n values obtained using MB events and using MB+HMT events after applying the reweighting procedure as discussed in Subsection IV.2.1.2 are compared with each other. In the region where the MB selection has good statistics, the results from the two trigger selections show good agreement with each other. Figure IV.2.20 shows the v_2 values as a function of $N_{\mathrm{ch}}^{\mathrm{rec}}$ and $E_{\mathrm{T}}^{\mathrm{Pb}}$ compared between the two trigger selections. The values are consistent with each other across the measured $N_{\mathrm{ch}}^{\mathrm{rec}}$ and $E_{\mathrm{T}}^{\mathrm{Pb}}$ range within systematic uncertainties.

Figure IV.2.21 shows a comparison of the v_2 values differentially in p_{T}, for a few high multiplicity event classes, between the two trigger selections. The agreement between the two selections holds independent of the $p_{\mathrm{T}}^{\mathrm{a}}$ value considered. Similar agreement was found to hold for higher order harmonics for both event activity and p_{T} dependence, but with larger statistical uncertainties.

As discussed in section IV.2.1.1, the `L1_ZDC(Pb)` trigger has a lower trigger efficiency than the primary MB trigger in low event activity region. One might wonder if this lower trigger efficiency affects the event selection in peripheral event classes which can influence the results through the recoil subtraction. The left panels of figure IV.2.22, shows the integrated yield on the near-side and away-side separately, as a function of $E_{\mathrm{T}}^{\mathrm{Pb}}$. The values from the `L1_ZDC(Pb)` and the primary MB trigger overlaps with each other and shows very good consistency, particularly in the low $E_{\mathrm{T}}^{\mathrm{Pb}}$ region. The right panel of figure IV.2.22 shows a comparison between the v_2 values obtained using events selected by the primary MB trigger and using those selected by the `L1_ZDC(Pb)` trigger (open circles), as a function of $N_{\mathrm{ch}}^{\mathrm{rec}}$. The values from the two selections agree within statistical uncertainties throughout the range.

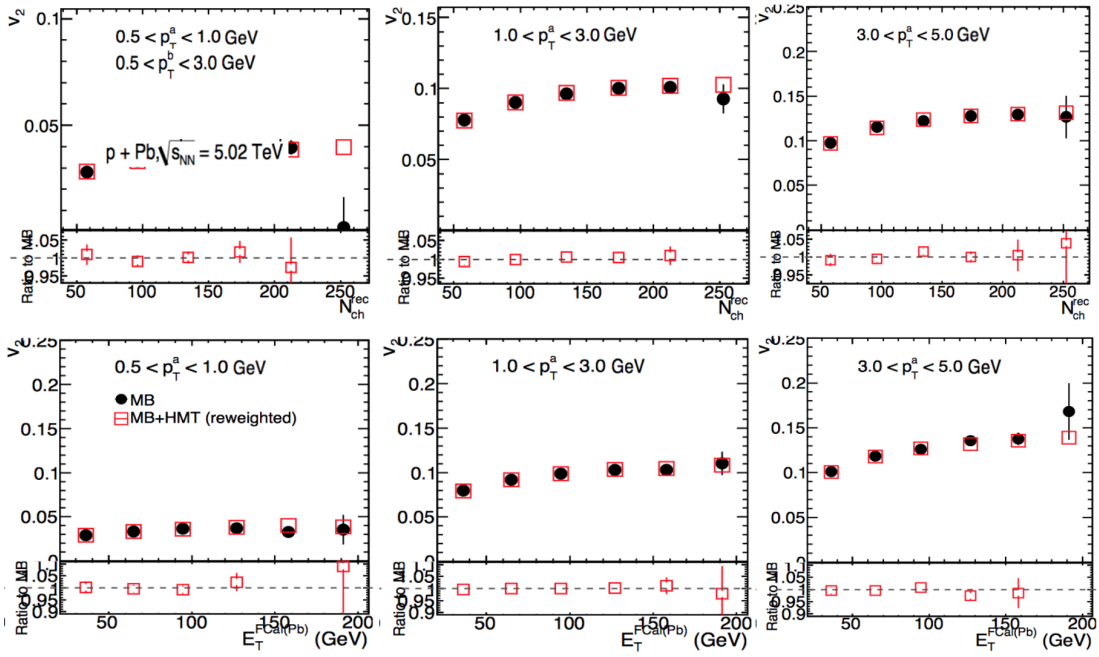

Figure IV.2.20: The v_2 values from MB and MB+HMT events with reweighting as a function of $N_{\rm ch}^{\rm rec}$ (top set of panels) and $E_{\rm T}^{\rm Pb}$ (bottom set of panels) for different $p_{\rm T}^{\rm a}$ bins for associated particles in $0.5 < p_{\rm T}^{\rm b} < 3$ GeV. The smaller panels show the ratio of values from MB+HMT to that from MB

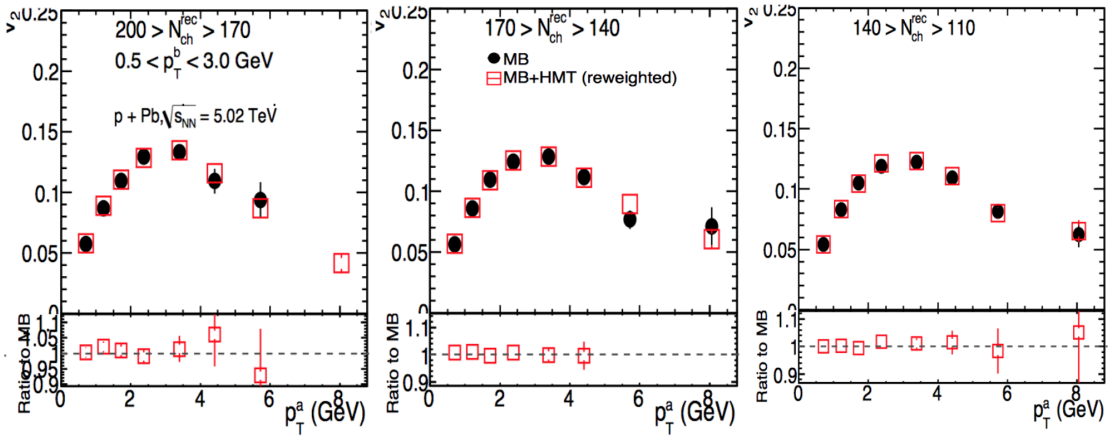

Figure IV.2.21: The v_2 values from MB and MB+HMT events with reweighting as a function of $p_{\rm T}^{\rm a}$ for events in different $N_{\rm ch}^{\rm rec}$ ranges where HMT triggers are active. The smaller panels show the ratio of values from MB+HMT to that from MB.

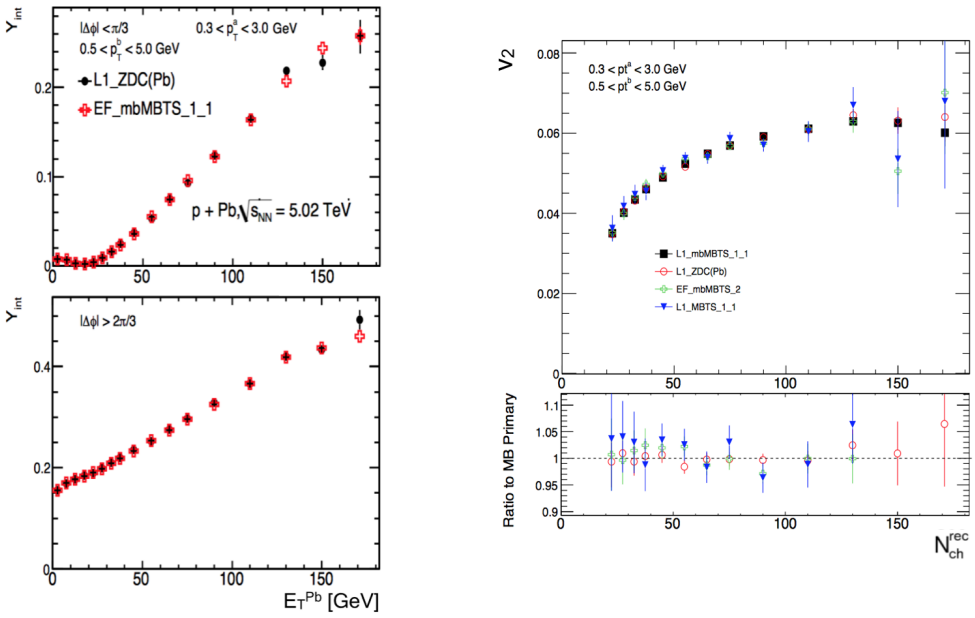

Figure IV.2.22: (Left panels) The integrated yield above the ZYAM pedestal on the near-side (top) and the away-side (bottom) as a function of $E_{\mathrm{T}}^{\mathrm{Pb}}$ for events selected by `L1_ZDC` and the primary MB trigger, `EF_mbMBTS_1_1`. (Right panel) The v_2 values from events selected by the primary MB trigger (solid squares) and `L1_ZDC(Pb)` (open circles) as a function of $N_{\mathrm{ch}}^{\mathrm{rec}}$, for pairs with $0.5 < p_{\mathrm{T}}^{\mathrm{a,b}} < 3$ GeV. The smaller panel shows the ratio of values relative to that from the primary MB trigger.

IV.2.3.3 Cross checks with different peripheral bins for recoil subtraction

As given in Table IV.2.1, the low-activity event class used for the peripheral subtraction, $E_{\mathrm{T}}^{\mathrm{Pb}} < {E_{\mathrm{T}}}^{0} = 10$ GeV, corresponds to lowest 28% of the MB triggered events. The pair distributions in this event class might contain a small long-range ridge component, leading to a slightly reduced estimation of the long-range signal in a high activity event class via the recoil subtraction procedure. The influence of this potential over subtraction is evaluated by varying the definition of the peripheral event class used for recoil subtraction, ${E_{\mathrm{T}}}^{0}$, in the range of ${E_{\mathrm{T}}}^{0} = 5$ GeV to ${E_{\mathrm{T}}}^{0} = 20$ GeV. For each variation, $Y^{\mathrm{sub}}(\Delta\phi)$ is calculated and the Fourier analysis is repeated to obtain v_n. The v_n values are found to decrease approximately linearly with increasing ${E_{\mathrm{T}}}^{0}$. The amount of over subtraction can be estimated by extrapolating ${E_{\mathrm{T}}}^{0}$ to zero and is included in the systematic uncertainties. As a cross check, the analysis is repeated by using the event class with $N_{\mathrm{ch}}^{\mathrm{rec}} < 20$ as the peripheral event class. The variation of v_n values from the default in this case is found to be within the variation from varying ${E_{\mathrm{T}}}^{0}$.

Figure IV.2.23 shows the v_2 values as a function of $N_{\mathrm{ch}}^{\mathrm{rec}}$ from using different choices of ${E_{\mathrm{T}}}^{0}$ for defining the peripheral event class. The v_2 values are quite stable in the more central event classes

with variations of about 4% for $N_{\mathrm{ch}}^{\mathrm{rec}} > 150$, from varying ${E_{\mathrm{T}}}^{0}$ over the range from 5 to 20 GeV. At lower $N_{\mathrm{ch}}^{\mathrm{rec}}$ values, the deviations are larger and increase approximately as $1.5/N_{\mathrm{ch}}^{\mathrm{rec}}$. Similar results were observed for the $E_{\mathrm{T}}^{\mathrm{Pb}}$ dependence as well, with variations of about 4% beyond $E_{\mathrm{T}}^{\mathrm{Pb}} > 100$ GeV and increasing in a similar way towards lower $E_{\mathrm{T}}^{\mathrm{Pb}}$ values.

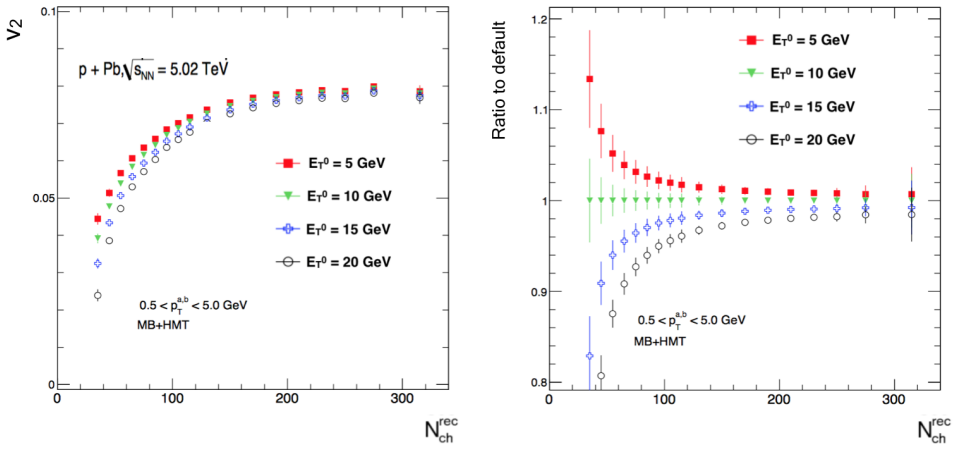

Figure IV.2.23: The v_2 values (left) from using different peripheral bins for recoil subtraction and their ratios relative to the default values (right) as a function of $N_{\mathrm{ch}}^{\mathrm{rec}}$.

Figure IV.2.24 shows the v_2 values as a function of p_{T} from using the different ${E_{\mathrm{T}}}^{0}$ values, and the ratio of the different cases to the default choice. The p_{T} dependence is relatively stable with changing the recoil bin, only a few percent difference can be seen. In the region where the statistics is good, this is nearly independent of p_{T}. This suggests that the deviations are not from jet contributions with increase strongly with p_{T}. In the higher p_{T} region, the differences are consistent within statistical uncertainties. Figure IV.2.25 shows the cross-check using the peripheral event class with $N_{\mathrm{ch}}^{\mathrm{rec}} < 20$ for recoil subtraction, compared with the values from the default choice. Even though the yield in the peripheral event class with $N_{\mathrm{ch}}^{\mathrm{rec}} < 20$ can be about 2 times smaller than that in the event class with $E_{\mathrm{T}}^{\mathrm{Pb}} < 10$ GeV (Figure. IV.2.15), the v_n values obtained after recoil subtraction is consistent with each other over the entire p_{T} range. This is because the differences in magnitude of the yield is accounted for the large part, by the scale factor α.

IV.2.3.4 Dependence of $|\Delta\eta|$ cut

The contributions from the short-range peak on the near-side is suppressed by using a $|\Delta\eta|$ range outside this peak to determine the 1D correlation function. The near-side ridge modulation is a long-range phenomenon, i.e. it extends to large pseudorapidity differences. Figure IV.2.26 shows the v_n values for $n = 2$–4, as a function of p_{T} for different choices of lower limit for the $|\Delta\eta|$ cut. The lower limit is varied from 1.2 to 3.2. As can be seen from the ratio plots, the v_n values are

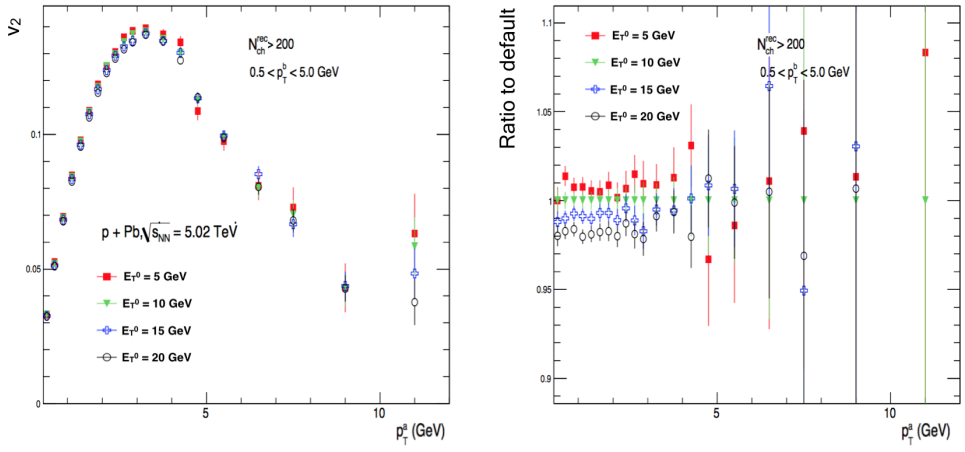

Figure IV.2.24: The v_2 values from using different peripheral bins for recoil subtraction and their ratios relative to the default values as a function of p_{T} for events in a high multiplicity event class.

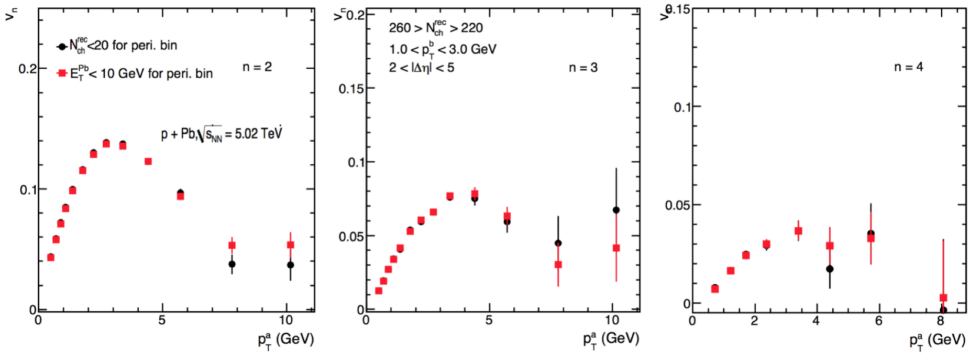

Figure IV.2.25: The v_2 (left), v_3 (middle) and v_4 values from using the peripheral class with $N_{\mathrm{ch}}^{\mathrm{rec}} < 20$ and $E_{\mathrm{T}}^{\mathrm{Pb}} < 10$ GeV for recoil subtraction, as a function of p_{T} for a high multiplicity event class.

quite stable against the variations in the $|\Delta\eta|$ cut, with the maximum variations in the case of v_2 being $\sim 2\%$. These variations show the long-range nature of the ridge correlations. However, these variations are not quoted as systematic uncertainties in the analysis.

IV.2.4 Systematic uncertainties

A summary of the systematic uncertainties in the measured quantities are presented in this section. Detailed discussion of the different sources of systematic uncertainties can be found in Appendix A.3. The systematic uncertainties in this analysis arise from pair acceptance, the ZYAM procedure, tracking efficiency, Monte Carlo consistency, residual pileup, and the recoil subtrac-

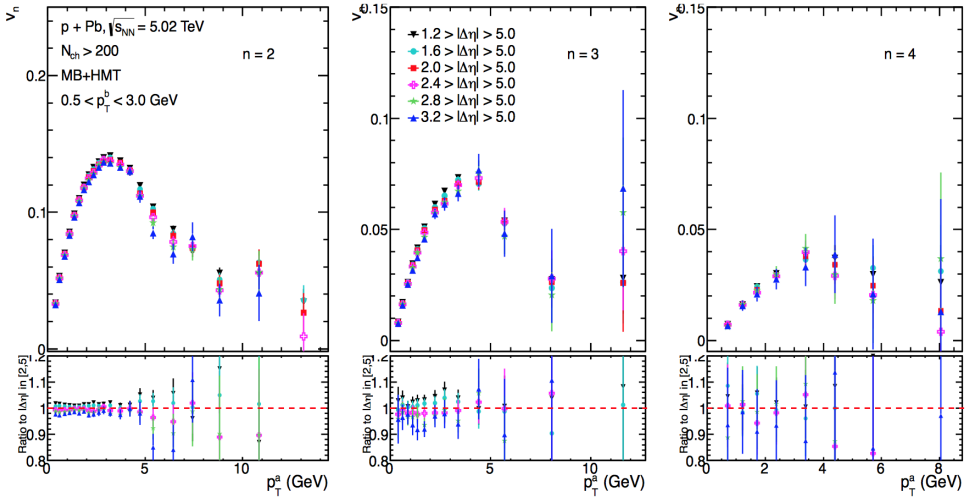

Figure IV.2.26: The v_2 (left), v_3 (middle) and v_4 values as a function of ${p_{\rm T}}^b$ for different choices for the lower limit of the $|\Delta\eta|$ cut, in one of the high multiplicity event classes. The lower panels show the ratios relative to the default case with the cut $2 < |\Delta\eta| < 5.0$

tion. The systematic uncertainty from each source is evaluated for the per-trigger yields ($Y(\Delta\phi)$, $Y^{\rm corr}(\Delta\phi)$ and $Y^{\rm sub}(\Delta\phi)$) and then propagated to Fourier harmonics coefficients $v_{n,n}$ and v_n. Each of the different source is discussed below.

Residual pair acceptance: The analysis uses the distributions from mixed events, $B(\Delta\eta, \Delta\phi)$ and $B(\Delta\phi)$, to reproduce the pair acceptance effects from detector features in the signal distribution. The pair acceptance function, in general, is quite flat in $\Delta\phi$. The maximum fractional variation from its average value is observed to be less than 0.001 for pairs integrated in $2 < |\Delta\eta| < 5$. The extend of influence the pair acceptance effects can have on the measured $v_{n,n}$ and v_n signals can be quantified by expanding the pair acceptance function in a Fourier series similar to Eq. IV.2.8. The resulting $v^{det}_{n,n}$ values are quite small, with $|v^{det}_{n,n}|$ values less than 2×10^{-4} for pairs in $2 < |\Delta\eta| < 5$. The $v^{det}_{n,n}$ values are expected to cancel mostly in the correlation function and only a small fraction contributes to the uncertainty from pair acceptance effects. This possible residual effects from the pair acceptance are evaluated following [4] by varying the criteria for matching events in $N^{\rm rec}_{\rm ch}$, $E^{\rm Pb}_{\rm T}$ and z_{vtx} position. In each case, the residual $v^{det}_{n,n}$ values are evaluated from the ratio of the pair acceptance function from the cross-check to that from the default criteria. The residual $v^{det}_{n,n}$ values vary in the range from $((5-8) \times 10^{-6}$. This uncertainty is small for v_2 and v_3, but becomes significant for higher order harmonics, particularly in the low $p_{\rm T}$ region, where the magnitude of the signal is small.

ZYAM procedure: The value of b_{ZYAM} is evaluated by fitting a second order polynomial function to the 1D $Y(\Delta\phi)$, as discussed in Section IV.2.3, and the uncertainties in this evaluation are estimated by varying the range for fitting the quadratic function. This uncertainty depends on the local curvature around $\Delta\phi_{ZYAM}$ and is between $0.0003 - 0.001$ of the value of b_{ZYAM}. This

uncertainty contributes directly to the correlated yield, $Y^{corr}(\Delta\phi)$, but indirectly to $Y^{sub}(\Delta\phi)$ and the v_n values through peripheral subtraction. The uncertainty on v_n from this source is found to be less than 2% for all n.

Tracking efficiency and material The uncertainty from the tracking efficiency correction contributes directly to the uncertainties in the per-trigger yields, $Y(\Delta\phi)$, $Y^{corr}(\Delta\phi)$, and $Y^{sub}(\Delta\phi)$, from the normalization by number or trigger particles. This uncertainty is estimated by varying the track selection cuts (see Section IV.2.2) and the detector material in the simulation, re-analyzing the data using corresponding Monte Carlo efficiencies, and evaluating the change in the extracted yields. The resulting uncertainty is estimated to be 2.5% from the track selection and 2% 3% from our limited knowledge of the detector material. The v_n and $v_{n,n}$ values depend only on the shape of the $Y^{sub}(\Delta\phi)$ distribution and hence are not sensitive to the tracking efficiency, and the uncertainties from the above variations are within 1% for $n < 4$ and up to 2.5% for $n = 5$.

Monte-Carlo consistency: Monte-Carlo HIJING [120] sample, reconstructed using the same algorithm and conditions as in data, is used to evaluate the stability of the analysis procedure, by comparing the results between the truth level and the reconstructed level. Small systematic deviations are seen between the results at truth and reconstructed levels and are included in the final systematic uncertainties. This uncertainty is relatively larger and varies from $1 - 8\%$, depending on the value on n.

Residual pileup The estimated pileup fraction in the events used in the analysis is quite small, as discussed in Subsection IV.2.1.3. The influence of the residual pileup on the results is evaluated by relaxing the cuts for pileup rejection, which increases the pileup fraction by more than two times the residual pileup, and then calculating the change in the per-trigger yields and v_n values. The differences are taken as systematic uncertainties and are found to be negligible in low event activity classes, and increase up to 2% for events event classes with $N_{\rm ch}^{\rm rec} > 300$ or $E_{\rm T}^{\rm Pb} > 200$ GeV.

Uncertainty on scale factor α: The uncertainties on the scale factor α, used in the recoil subtraction, is evaluated by varying the $\Delta\eta$ range used to subtract the long-range component in Eq. IV.2.6. A systematic uncertainty of $3-5\%$ for α is quoted for these variations. The resulting uncertainty on v_n from this, for $n = 2-5$ is within 1% for $p_{\rm T} < 4$ GeV and increases to about 10% at the highest $p_{\rm T}$. The v_1 component is more sensitive to the variation of the value of α and the uncertainties on v_1 from this source is $8-12\%$ for $p_{\rm T} < 1$ GeV and up to $20-30\%$ for $p_{\rm T} > 3$ GeV.

Choice of peripheral events: As discussed in Section IV.2.3.4, the peripheral bin used for recoil subtraction can have a small long-range ridge component present. To estimate the possible over subtraction of the signal from this, the maximum $E_{\rm T}^{\rm Pb}$ to define peripheral event class, ${E_{\rm T}}^0$, is varied from from ${E_{\rm T}}^0 = 5$ GeV to ${E_{\rm T}}^0 = 20$ GeV. The yields $Y^{sub}(\Delta\phi)$ and the Fourier harmonics v_n are recalculated for each case. The v_n values are found to decrease approximately linearly with increase in ${E_{\rm T}}^0$. The amount of over subtraction can be estimated by extrapolating ${E_{\rm T}}^0$ to zero. The estimated changes of v_n and $Y^{sub}(\Delta\phi)$ are less than 1% for $E_{\rm T}^{\rm Pb} > 100$ GeV or $N_{\rm ch}^{\rm rec} > 150$, and increase for lower event-activity classes approximately as $1.5/N_{\rm ch}^{\rm rec}$. The relative change of v_n as a function of $p_{\rm T}$ is found to be independent of $p_{\rm T}$. The results are also cross-checked by using an event class with $N_{\rm ch}^{\rm rec} < 20$ for recoil subtraction and were found to be within the range of systematic uncertainties quoted from varying ${E_{\rm T}}^0$.

The systematic uncertainties from the different sources for the per-trigger-yield and v_n measurements are shown in Tables. IV.2.2 and IV.2.3 respectively. Since $v_1(p_{\mathrm{T}})$ becomes close to zero around $1-2$ GeV, the relative uncertainties quoted for v_1 are for $p_{\mathrm{T}} < 1$ GeV and $p_{\mathrm{T}} > 3$ GeV.

Residual pair acceptance	$0.1-0.9$
ZYAM procedure	$0.2-1.5$
Tracking efficiency due to cuts and due to material	4.2
pileup effects	$0-2$

Table IV.2.2: Summary of relative systematic uncertainties for per trigger yield.

	n = 1	n = 2	n = 3	n = 4	n = 5
Residual pair acceptance[%]	1.0−5.0	<0.5	1.0−4.0	7.0−12	7.0−20
ZYAM procedure[%]	0.6	0.3	0.3	0.5	0.6
Tracking efficiency due to cuts and material uncertainty[%]	1.0	0.4	0.8	1.2	2.4
Monte-Carlo consistency [%]	4.0	1.0	2.0	4.0	8.0
Residual pileup [%]	0−2.0	0−2	0−2	0−2	0−2
Uncertainty on scale factor α[%]	8.0−30	0.2−10	0.2−12	0.2−14	1.0−14
Choice of peripheral events, for $N_{\mathrm{ch}}^{\mathrm{rec}} > 160$ or $E_{\mathrm{T}}^{\mathrm{Pb}} > 100$ GeV [%]	4.0	1.0	1.0	2.0	4.0

Table IV.2.3: Summary of relative uncertainties on v_n.

IV.2.5 Results

IV.2.5.1 Correlation functions and integrated yields

Figure IV.2.27 shows the per-trigger-yield in 2D before and after the recoil subtraction, in on of the high multiplicity event classes with $N_{\mathrm{ch}}^{\mathrm{rec}} > 220$ (the event class has approximately 3 $\times 10^{-5}$ of the MB p+Pb events). A clear long-range ridge on the near-side can be seen before the recoil subtraction, as well as a peak around small $(\Delta\eta, \Delta\phi)$ from the short-range correlations and an away-side ridge which also includes contribution from the recoil component. The away-side ridge is larger in magnitude than the near-side ridge. After the recoil subtraction both the short-range component and the recoil component on the away-side are removed and the correlation function shows a nearly symmetric ridge between the near-side and away-side. The magnitude of the ridge on the away-side also remains approximately constant with $\Delta\eta$ after the recoil subtraction.

Figure IV.2.28 shows the per-trigger-yield in 1D with the ZYAM background subtracted, $Y^{corr}(\Delta\phi)$, in different $p_{\mathrm{T}}^{\mathrm{a}}$ ranges for events with $N_{\mathrm{ch}}^{\mathrm{rec}} > 220$. The associated particles are chosen to be in the range $1 < p_{\mathrm{T}}^{\mathrm{b}} < 3$ GeV. The 1D projections are made in the region with $2 < |\Delta\eta| < 5$.

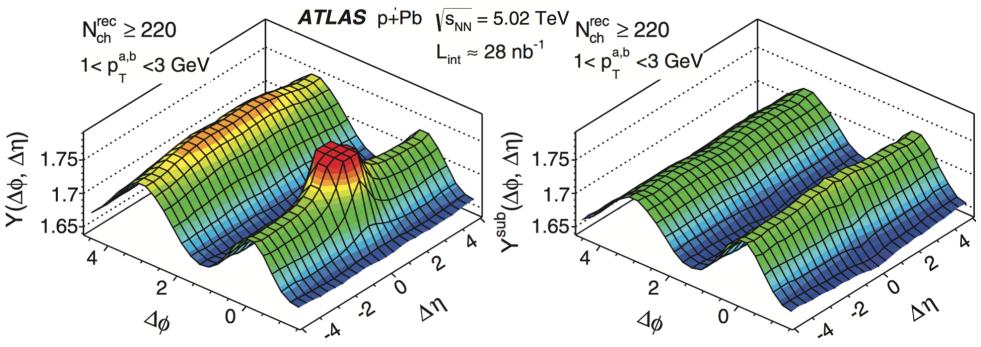

Figure IV.2.27: (Left) The per-trigger-yield in 2D, $Y(\Delta\phi, \Delta\eta)$, in an event class with $N_{\rm ch}^{\rm rec} > 220$ for particles with $1 < p_{\rm T}^{\rm a,b} < 3$ GeV. (Right) The per-trigger-yield after recoil subtraction in 2D, $Y^{sub}(\Delta\phi, \Delta\eta)$, in an event class with $N_{\rm ch}^{\rm rec} > 220$ for particles with $1 < p_{\rm T}^{\rm a,b} < 3$ GeV.

Also shown is the estimated recoil component, $\alpha Y_{peri}^{corr}(\Delta\phi)$, for the corresponding $p_{\rm T}^{\rm a,b}$ ranges. The yield from the estimated recoil component is consistent with zero at $\Delta\phi \sim 0$ in all the $p_{\rm T}^{\rm a}$ ranges. In the central event class, a clear near-side ridge can be seen, the magnitude of which increases with $p_{\rm T}^{\rm a}$, reaches a maximum and then decrease further with further increase in $p_{\rm T}^{\rm a}$. A non-zero ridge yield on the near-side can be seen even in the highest $p_{\rm T}^{\rm a}$ bins studied, $9 < p_{\rm T}^{\rm a} < 12$ GeV. An excess above the estimated recoil is also observed on the away-side in all the $p_{\rm T}^{\rm a}$ ranges considered. The non-zero near-side ridge yield at high $p_{\rm T}$ in A+A collisions is commonly attributed to path length dependent energy loss [113]. But no evidence for path length dependent energy loss has been observed in spectra or jet measurements in p+Pb [112, 111] and so is unclear if the high $p_{\rm T}$ ridge in p+Pb collisions are also of similar origin.

Figure IV.2.29 shows the integrated yields, $Y_{\rm int}$, on the near-side and away-side, from integrating $Y^{corr}(\Delta\phi)$ over $|\Delta\phi| < \pi/3$ and $|\Delta\phi| > 2\pi/3$ respectively, as function of $p_{\rm T}^{\rm a}$ in different $N_{\rm ch}^{\rm rec}$ classes. The integrated yields on the near-side increase with $p_{\rm T}^{\rm a}$, reach a maximum around $p_{\rm T}^{\rm a} \sim 3$ GeV and then decrease to values close to zero for $p_{\rm T}^{\rm a} \sim 10$ GeV. This trend is similar to the $p_{\rm T}$ dependence of the ridge yield in A+A collisions [100]. The away-side yields however shows a continuous increase with $p_{\rm T}^{\rm a}$ since the away-side yield is dominated by the contribution from the recoil component, mostly from dijets, which increase with $p_{\rm T}$.

IV.2.5.2 Fourier coefficients: $v_2 - v_5$

Figure IV.2.30 shows the Fourier coefficients, v_2, v_3 and v_4, calculated from the 1D yields $Y(\Delta\phi)$ and $Y^{sub}(\Delta\phi)$, as a function of $p_{\rm T}^{\rm a}$ in the event class with $N_{\rm ch}^{\rm rec} > 220$. The v_n^{unsub} and v_n values, calculated from the yields without subtraction and with subtraction, respectively, differ slightly for $p_{\rm T}^{\rm a} < 3$ GeV, but becomes increasingly important for higher trigger $p_{\rm T}$ values. This can be expected, as the dijet contributions, that are the dominant contribution to the recoil component, increase rapidly with $p_{\rm T}$ [4, 100]. At high $p_{\rm T}$, the contribution of dijets appear as a narrow peak

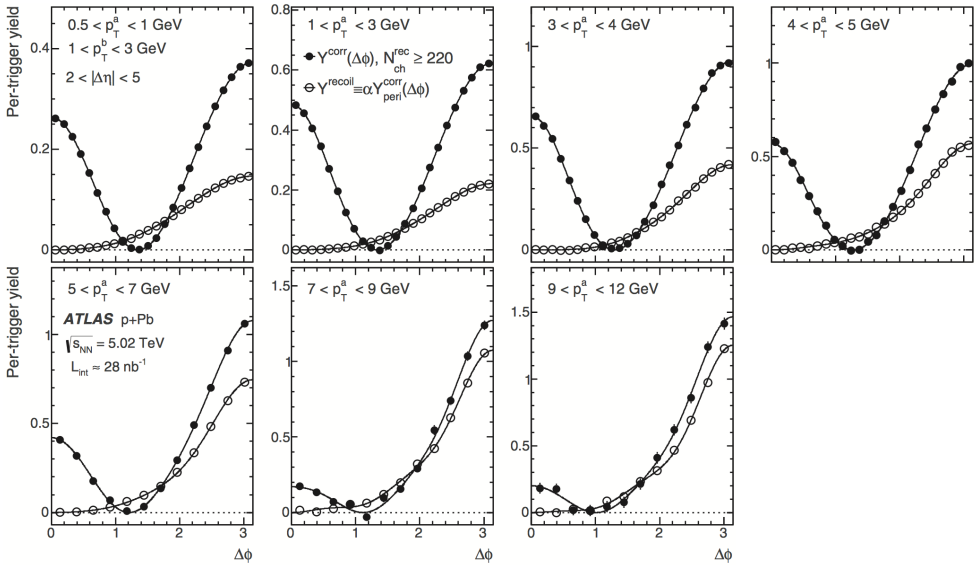

Figure IV.2.28: (Solid circles) The per-trigger-yield above ZYAM background, $Y^{corr}(\Delta\phi)$, for different $p_{\mathrm{T}}^{\mathrm{a}}$ selections for associated particles with $1 < p_{\mathrm{T}}^{\mathrm{b}} < 3$ GeV, in the event class with $N_{\mathrm{ch}}^{\mathrm{rec}} > 220$. (Open circles) The estimated recoil component, $\alpha Y_{peri}^{corr}(\Delta\phi)$, for the same $p_{\mathrm{T}}^{\mathrm{a,b}}$ ranges in the event class with $N_{\mathrm{ch}}^{\mathrm{rec}} > 220$. The error bars represent combined statistical and systematic uncertainties.

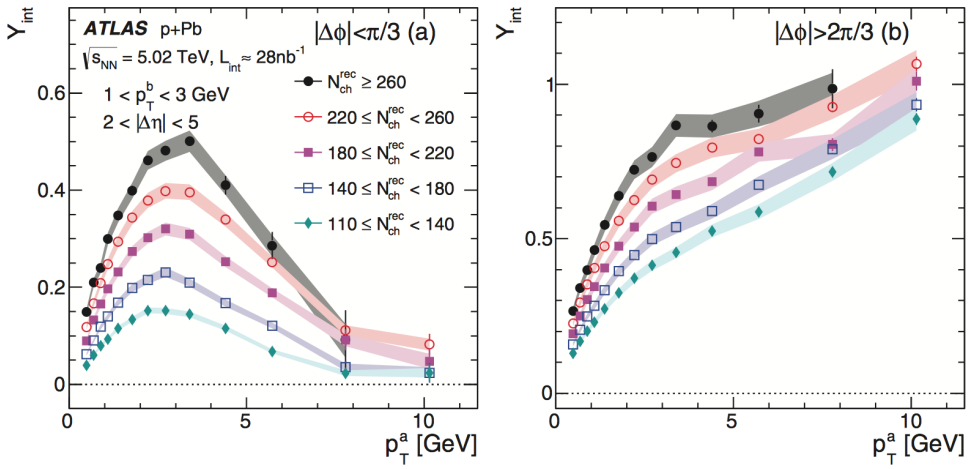

Figure IV.2.29: The integrated yield on the near-side (left) and away-side (right), as a function of $p_{\mathrm{T}}^{\mathrm{a}}$ for associated particles with $1 < p_{\mathrm{T}}^{\mathrm{b}} < 3$ GeV, in different $N_{\mathrm{ch}}^{\mathrm{rec}}$ classes. The shaded band represents systematic uncertainties.

at the away-side, leading to increasing contribution to v_n^{unsub} coefficients with alternating sign: (-1^n) [4]. The values after subtraction on the other hand, decrease with increase in p_T after reaching a maximum around $p_T^a \sim 3-4$ GeV and remains positive throughout the measured p_T^a range. The p_T dependence of the v_n values after recoil subtraction is qualitatively similar to the p_T dependence of the v_n coefficients measured in A+A collisions at RHIC and LHC [4, 3].

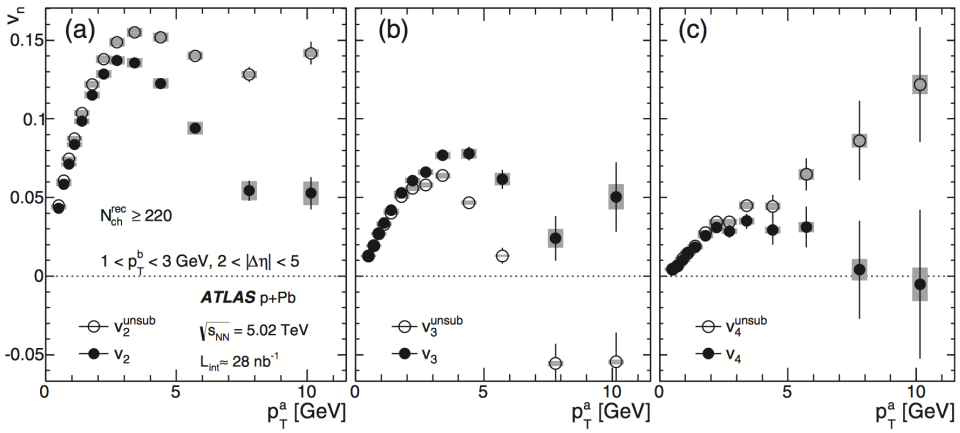

Figure IV.2.30: The v_n^{unsub} and v_n values as a function of p_T^a for $n = 2$ (left), 3 (middle) and 4 (right), for events with $N_{ch}^{rec} > 220$ and the associated particles in the range $1 < p_T^b < 3$ GeV. The error bars and shaded boxes represent systematic uncertainties, respectively.

The v_n coefficients for $n = 2-5$ are shown as a function of p_T^a for different event activity classes in figure IV.2.31. The v_5 could be measured only in three high multiplicity event classes, due to statistical limitations. All the v_n coefficients show similar behavior in p_T, increases at low p_T and decreases after a maximum at higher p_T. The magnitude of the coefficients decrease with increase in harmonic number n. This is also very similar to the behavior observed in A+A collisions, where the higher order harmonics are damped more by viscous corrections. The comparison with the v_2 and v_3 values from CMS [100] in a comparable multiplicity class as the event class with $220 < N_{ch}^{rec} < 260$, is also shown. The CMS results compared also use a recoil subtraction, similar to that used in this analysis, and good consistency can be seen between the two measurements.

The extraction of v_n coefficients from $v_{n,n}$ assumes the factorization behavior as given by Eq. IV.2.10. This can be checked by varying the associated p_T range used for calculating the $v_n(p_T^a)$ in Eq. IV.2.11. Figure IV.2.32 shows the comparison of $v_n(p_T^a)$ calculated using different choices for p_T^b, for one of the high multiplicity event classes. The v_n values at a given p_T^a is consistent within statistical uncertainties for the different choices of associated p_T bins from $0.5 < p_T^b < 1$ GeV to $3 < p_T^b < 4$ GeV (except for the case of v_3 for $p_T^a < 2$ and $3 < p_T^b < 4$ GeV). This shows that the factorization relation holds in general, for the associated particles in the low p_T region ($< 3-4$ GeV), and that the ridge correlations can be attributed to an anisotropy in the single particle azimuthal distribution.

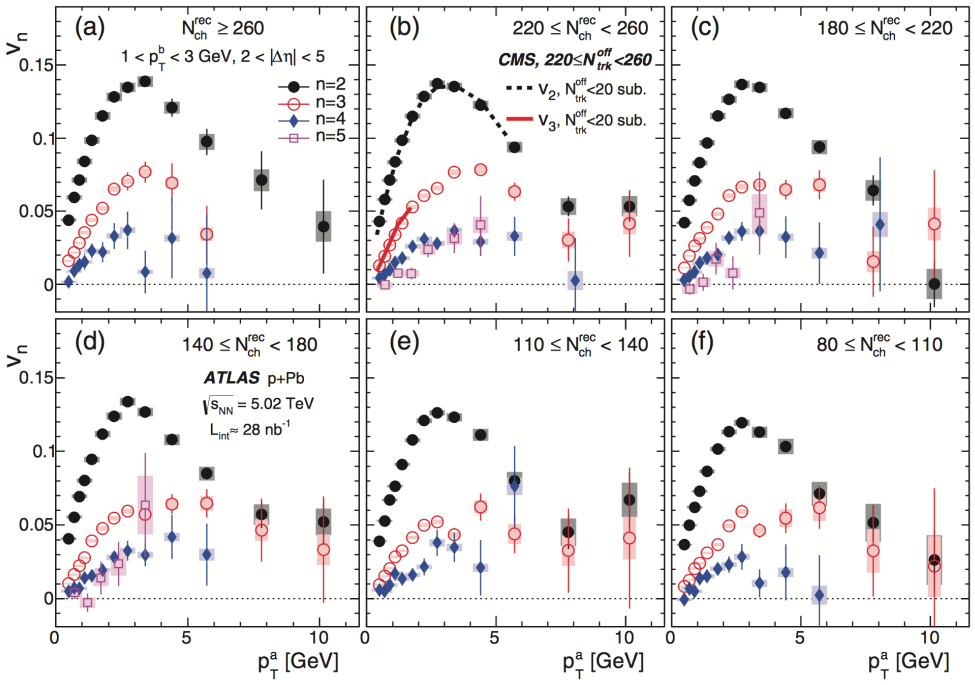

Figure IV.2.31: The v_n coefficients for $n = 2{-}5$ as a function of $p_{\mathrm{T}}^{\mathrm{a}}$ for events in different high multiplicity classes. The associated p_{T} bin used is $1 < p_{\mathrm{T}}^{\mathrm{b}} < 3$ GeV. The error bars and shaded boxes represent statistical and systematic uncertainties, respectively. The second panel in first row also shows comparison with results CMS, indicated by dashed lines.

The extent to which factorization holds can also be quantified using the ratio [89, 191]

$$r_n(p_{\mathrm{T}}^{\mathrm{a}}, p_{\mathrm{T}}^{\mathrm{b}}) = \frac{v_{n,n}(p_{\mathrm{T}}^{\mathrm{a}}, p_{\mathrm{T}}^{\mathrm{b}})}{\sqrt{v_{n,n}(p_{\mathrm{T}}^{\mathrm{a}}, p_{\mathrm{T}}^{\mathrm{a}}) v_{n,n}(p_{\mathrm{T}}^{\mathrm{b}}, p_{\mathrm{T}}^{\mathrm{b}})}}. \tag{IV.2.12}$$

The value of r_n should be 1 for perfect factorization. The values r_n^{unsub} and r_n for the cases without and with recoil subtraction, respectively, are shown in figure IV.2.33 for $n = 2$ and 3. The values are shown as a function of $p_{\mathrm{T}}^{\mathrm{b}} - p_{\mathrm{T}}^{\mathrm{a}}$, for different choices of $p_{\mathrm{T}}^{\mathrm{b}}$ from $1.5 < p_{\mathrm{T}}^{\mathrm{b}} < 4$ GeV. The deviations of r_n^{unsub} and r_n from 1 are quite small, within $5 - 10\%$ where statistics is good, and is also comparable to the r_n values from a theoretical calculation using viscous hydrodynamic model [192]. In most cases, the data are consistent with the prediction within uncertainties. The level of factorization breaking seen is similar to that observed in peripheral Pb+Pb collisions [90].

Figure IV.2.34 shows the event activity dependence of the v_2, v_3 and v_4 values, as functions of $N_{\mathrm{ch}}^{\mathrm{rec}}$ and $E_{\mathrm{T}}^{\mathrm{Pb}}$. The results are shown for $0.4 < p_{\mathrm{T}}^{\mathrm{a,b}} < 3$ GeV, both before and after the recoil subtraction. The difference between v_n^{unsub} and v_n values are quite small, within $3 - 4\%$, in the high event activity classes, but increases towards the more peripheral event classes. The difference reaches $20 - 30\%$ for $N_{\mathrm{ch}}^{\mathrm{rec}} \sim 40$ or $E_{\mathrm{T}}^{\mathrm{Pb}} \sim 30$ GeV. The sign of the difference also alternates with

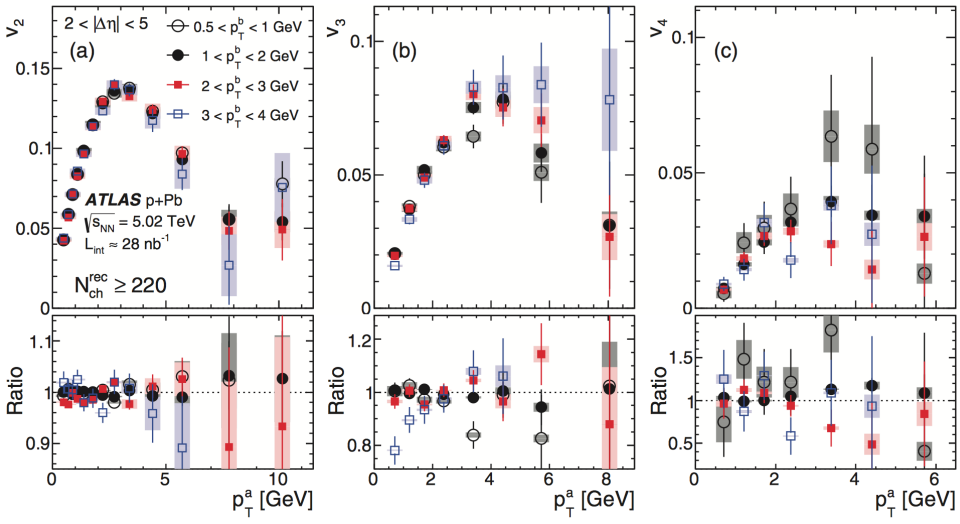

Figure IV.2.32: The $v_n(p_{\mathrm{T}}^{\mathrm{a}})$ values for $n = 2$ (left), 3 (middle) and 4 (right) for different choices of associated p_{T} bins for events with $N_{\mathrm{ch}}^{\mathrm{rec}} > 220$. The error bars and shaded boxes represent statistical and systematic uncertainties, respectively.

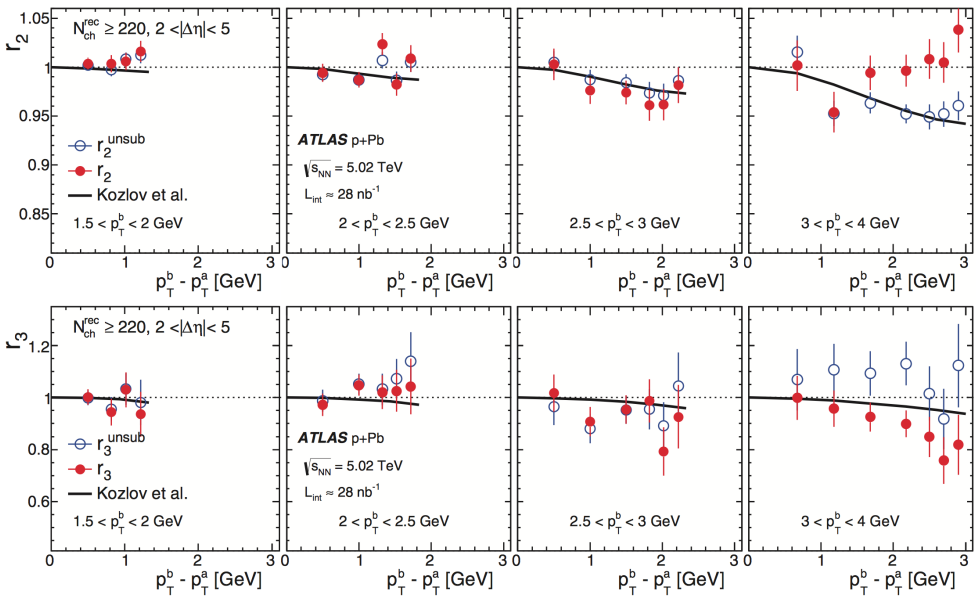

Figure IV.2.33: The $r_n(p_{\mathrm{T}}^{\mathrm{a}}, p_{\mathrm{T}}^{\mathrm{b}})$ values shown as a function of $p_{\mathrm{T}}^{\mathrm{b}} - p_{\mathrm{T}}^{\mathrm{a}}$ for different choices of the associated particle p_{T}, for $n = 2$ (top) and $n = 3$ (bottom). The error bars represent the combined statistical and systematic uncertainties.

n, with $v_n^{unsub} > v_n$ when n is even and $v_n^{unsub} < v_n$ when n is odd. The v_2 values show a modest event activity dependence, increasing by about 30% from $N_{\rm ch}^{\rm rec}$ values of 40 to 100, and a relatively weaker dependence thereafter, increasing by less than 10%. The behavior is similar as function of $E_{\rm T}^{\rm Pb}$. The v_3 values show stronger event activity dependence, showing a continuous increase over the measured $N_{\rm ch}^{\rm rec}$ and $E_{\rm T}^{\rm Pb}$ range.

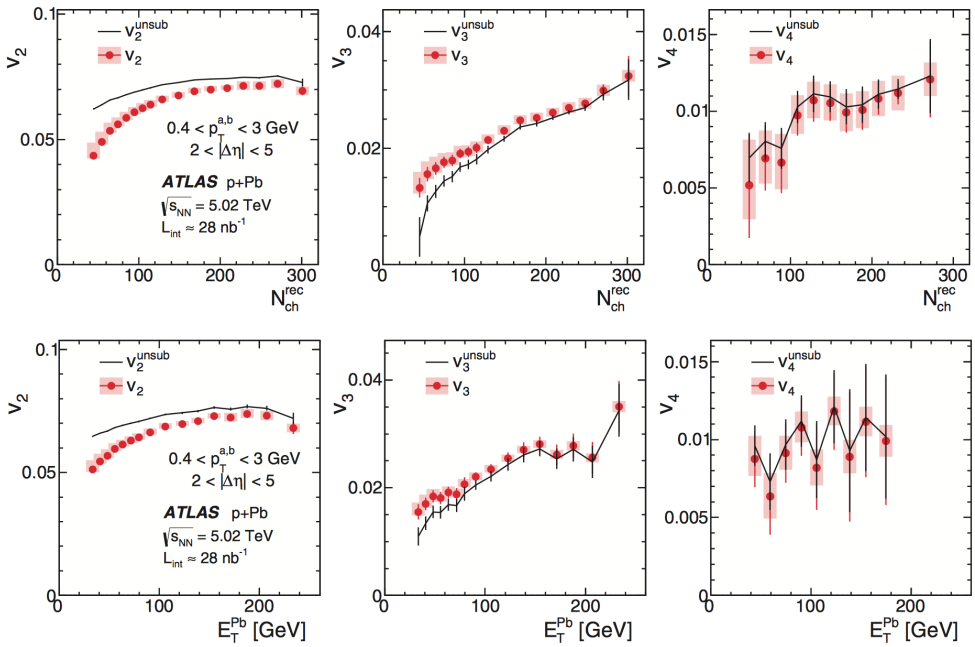

Figure IV.2.34: The v_n (solid circles) and v_n^{unsub} (solid line) values as a function of $N_{\rm ch}^{\rm rec}$ (top) and as a function of $E_{\rm T}^{\rm Pb}$ (bottom) for particles with $0.4 < p_{\rm T}^{\rm a,b} < 3$ GeV, for $n = 2$ (left panels), 3 (middle panels) and 4 (right panels). The error bars and shaded boxes on the v_n values indicate the statistical and systematic uncertainties respectively while the error bars for v_n^{unsub} values indicate the combined statistical and systematic uncertainties.

Figure IV.2.35 compares the event activity dependence measured using the two variables, $N_{\rm ch}^{\rm rec}$ and $E_{\rm T}^{\rm Pb}$. The correlation data [not the fit] in figure IV.2.5 are used to map the $N_{\rm ch}^{\rm rec}$ dependence in the top row of figure IV.2.34 to a corresponding $E_{\rm T}^{\rm Pb}$ dependence. The $E_{\rm T}^{\rm Pb}$ dependence of v_n mapped from the $N_{\rm ch}^{\rm rec}$ dependence is then compared to the directly measured $E_{\rm T}^{\rm Pb}$ dependence in figure IV.2.34. Good agreement is seen between the two for both v_2 and v_3.

IV.2.5.3 First order harmonic, v_1

The first order flow harmonic from density fluctuations measured in A+A collisions, and its $p_{\rm T}$ dependence, can be explained quite successfully using hydrodynamic model calculations or transport model calculations, pointing towards a collective origin for it and its characteristic $p_{\rm T}$ dependence

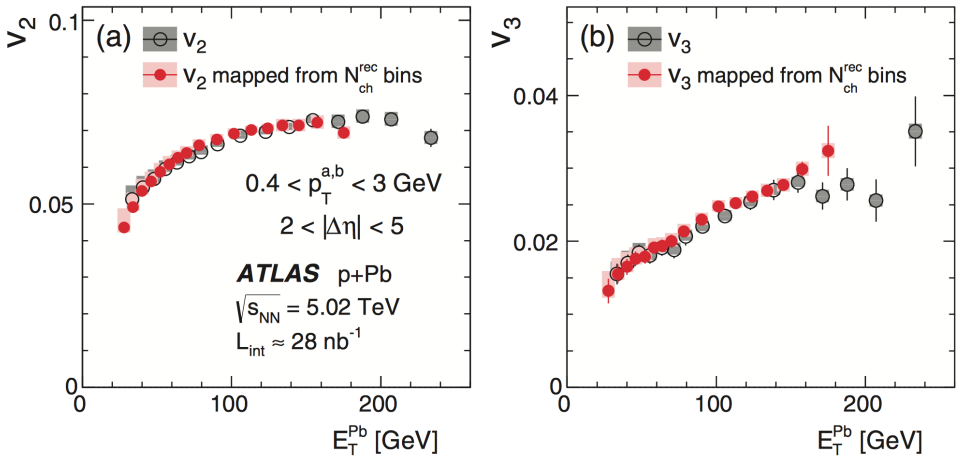

Figure IV.2.35: The v_2 (left panel) and v_3 (right panel) as a function of $E_{\mathrm{T}}^{\mathrm{Pb}}$ calculated directly for narrow ranges in $E_{\mathrm{T}}^{\mathrm{Pb}}$ (open circles) and obtained indirectly by mapping from the $N_{\mathrm{ch}}^{\mathrm{rec}}$ dependence of v_n using the correlation data shown in figure IV.2.5 (solid circles). The error bars and shaded boxes represent the statistical and systematic uncertainties, respectively.

(see Chapter IV.1). The first order coefficient $v_{1,1}$ can also be measured in p+Pb collisions, following the same procedures as in the measurement of higher order coefficients. The left panel of figure IV.2.36 shows the $v_{1,1}^{unsub}$ values, obtained before doing any recoil subtraction, in p+Pb collisions in the event class with $N_{\mathrm{ch}}^{\mathrm{rec}} \geq 220$ as a function of the trigger p_{T} for different associated p_{T} selections. The $v_{1,1}^{unsub}$ values are negative for all $p_{\mathrm{T}}^{\mathrm{a,b}}$ selections and show mostly a linear decrease with increase in $p_{\mathrm{T}}^{\mathrm{a}}$, except for the region around 3−4 GeV, where a shoulder like structure can be seen. This shoulder is very similar to that observed in A+A collisions [4], where it can be attributed to the product $v_1(p_{\mathrm{T}}^{\mathrm{a}})v_1(p_{\mathrm{T}}^{\mathrm{b}})$ of the first order flow harmonics from density fluctuations. The linear decrease reflects the contribution from momentum conservation, the magnitude of which increase nearly linearly with $p_{\mathrm{T}}^{\mathrm{a}}$ (Eq. IV.1.3).

The right panel of figure IV.2.36 shows the $v_{1,1}$ coefficients after recoil subtraction. The contribution from momentum conservation is largely removed by the recoil subtraction and the $v_{1,1}$ values show a very similar $p_{\mathrm{T}}^{\mathrm{a,b}}$ dependence as the $v_{1,1}$ coefficients measured in central Pb+Pb collisions, where the momentum conservation component is small (figure IV.1.2), and AMPT events for A+A collisions (figure IV.1.3). The $v_{1,1}$ values cross each other at around $p_{\mathrm{T}}^{\mathrm{a}} \sim 1.5$−$2.0$ GeV, also the $v_{1,1}(p_{\mathrm{T}}^{\mathrm{a}}, p_{\mathrm{T}}^{\mathrm{b}})$ values for $1.5 < p_{\mathrm{T}}^{\mathrm{b}} < 2.0$ GeV is consistent with zero for different $p_{\mathrm{T}}^{\mathrm{a}}$ values. Both these observations are consistent with a $v_1(p_{\mathrm{T}})$ that crosses zero at $p_{\mathrm{T}} \sim 1 - 2$ GeV, a feature also observed in A+A collisions.

The single particle $v_1(p_{\mathrm{T}}^{\mathrm{a}})$ coefficients can be calculated using a similar factorization as in the case of the higher order v_n.

$$v_1(p_{\mathrm{T}}^{\mathrm{a}}) = \frac{v_{1,1}(p_{\mathrm{T}}^{\mathrm{a}}, p_{\mathrm{T}}^{\mathrm{b}})}{v_1(p_{\mathrm{T}}^{\mathrm{b}})}, \tag{IV.2.13}$$

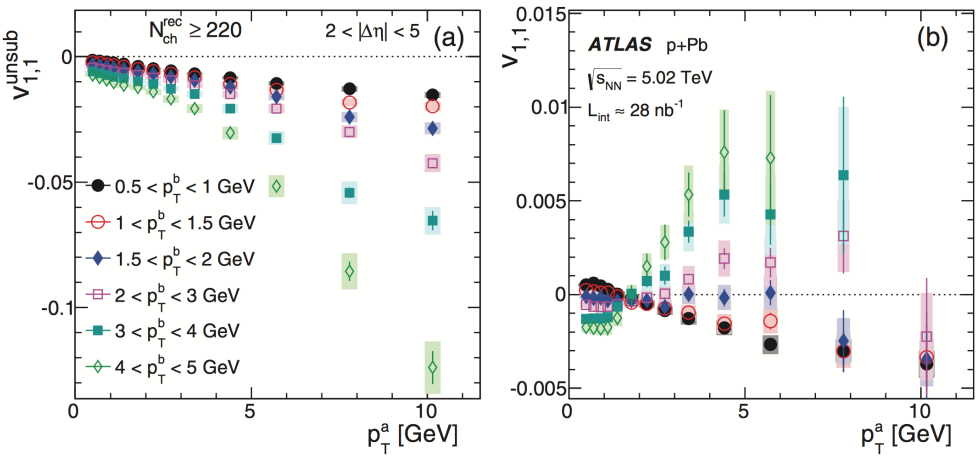

Figure IV.2.36: The $v_{1,1}^{unsub}$ (left panel) and $v_{1,1}$ (right panel) values as a function of $p_{\mathrm{T}}^{\mathrm{a}}$ for different choices of associated p_{T} bins for events with $N_{\mathrm{ch}}^{\mathrm{rec}} \geq 220$. The error bars and shaded boxes represent statistical and systematic uncertainties, respectively.

where the v_1 in the associated p_{T} bin, $v_1(p_{\mathrm{T}}^{\mathrm{b}})$, is defined as

$$v_1(p_{\mathrm{T}}^{\mathrm{b}}) = \mathrm{sign}(p_{\mathrm{T}}^{\mathrm{b}} - p_{\mathrm{T}}^{\mathrm{a}})\sqrt{|v_{1,1}(p_{\mathrm{T}}^{\mathrm{b}}, p_{\mathrm{T}}^{\mathrm{b}})|}, \tag{IV.2.14}$$

where $\mathrm{sign}(p_{\mathrm{T}}^{\mathrm{b}} - p_{\mathrm{T}}^{\mathrm{a}})$ is the sign of the v_1, defined to be negative for $p_{\mathrm{T}}^{\mathrm{b}} < {p_{\mathrm{T}}}^0 = 1.5$ GeV and positive otherwise. This factor is necessary to account for the change in sign of v_1 at low p_{T}. The $v_1(p_{\mathrm{T}}^{\mathrm{a}})$ values are extracted for three $p_{\mathrm{T}}^{\mathrm{b}}$ ranges, $0.5 < p_{\mathrm{T}}^{\mathrm{b}} < 1.0$ GeV, $3.0 < p_{\mathrm{T}}^{\mathrm{b}} < 4$ GeV and $4.0 < p_{\mathrm{T}}^{\mathrm{b}} < 5.0$ GeV. The calculation is not possible in the range $1.0 < p_{\mathrm{T}}^{\mathrm{b}} < 3.0$ GeV, where the v_1 values are small and hence, the resulting $v_1(p_{\mathrm{T}}^{\mathrm{a}})$ values have large statistical uncertainties.

The calculated v_1 values are shown as a function of $p_{\mathrm{T}}^{\mathrm{a}}$ for the different $p_{\mathrm{T}}^{\mathrm{b}}$ ranges in figure IV.2.37. The $v_1(p_{\mathrm{T}}^{\mathrm{a}})$ values are consistent between the different associated p_{T} selections. The v_1 values change sign around $p_{\mathrm{T}} \sim 1.5$ GeV and reaches a maximum value of about 0.1 at $4 - 6$ GeV. This p_{T} dependence is very similar to the p_{T} dependence of the v_1 measured in Pb+Pb collisions, although the value at which v_1 crosses zero is smaller in Pb+Pb (~ 1.1 GeV) [4]. The increase in the p_{T} at which v_1 crosses zero can be expected in p+Pb collisions where the $\langle p_{\mathrm{T}} \rangle$ is larger (see Section IV.1.3). The magnitude of the v_1 is also similar to that of the v_1 measured in Pb+Pb collisions.

IV.2.5.4 Comparison with similar multiplicity Pb+Pb results

The multiplicity in the highest multiplicity p+Pb collisions are comparable to that in semi-peripheral Pb+Pb collisions. For example the 55-60% centrality class in Pb+Pb collisions ($\sqrt{s_{NN}}$ = 2.76 TeV) has approximately the same efficiency corrected multiplicity as the p+Pb event class with $220 < N_{\mathrm{ch}}^{\mathrm{rec}} < 260$. In these Pb+Pb event classes, the long-range ridge correlations are expected to arise from the collective expansion of the produced medium, as the system size is large to

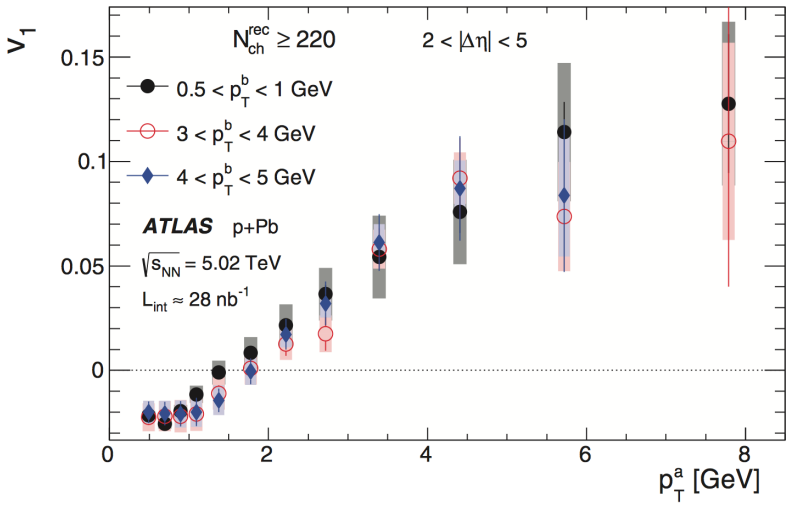

Figure IV.2.37: The v_1 values, calculated using Eq. IV.2.13, as a function of $p_{\mathrm{T}}^{\mathrm{a}}$ for different choices of associated p_{T} bins for events with $N_{\mathrm{ch}}^{\mathrm{rec}} \geq 220$. The error bars and shaded boxes represent statistical and systematic uncertainties, respectively.

have an hydrodynamic expansion [14, 71]. The similar multiplicity p+Pb event class has a much smaller system size. Therefore comparing the magnitudes of the long-range ridge correlations in p+Pb and Pb+Pb collisions could provide further insights into the origin of these correlations.

The left column of figure IV.2.38 shows the comparison of the v_2, v_3 and v_4 between the p+Pb collisions at $\sqrt{s_{NN}} = 5.02$ TeV and Pb+Pb collisions at $\sqrt{s_{NN}} = 2.76$ TeV, for event classes with comparable multiplicity. The event classes compared are those with $220 < N_{\mathrm{ch}}^{\mathrm{rec}} < 260$ for p+Pb and the 55-60% centrality class in the case of Pb+Pb. The efficiency corrected charged particle multiplicity for particles with $p_{\mathrm{T}} > 0.5$ GeV and $|\eta| < 2.5$, N_{ch}, and its standard deviation, σ, for the Pb+Pb event class are $\langle N_{\mathrm{ch}} \rangle \pm \sigma = 241 \pm 43$, while for the p+Pb class they are 259 ± 13. The results for the Pb+Pb system are taken from [180], and were obtained via an event plane method by correlating tracks in $\eta > 0$ ($\eta < 0$) with the event plane determined in the FCal in the opposite side.

The v_2 and v_4 values in the Pb+Pb system are larger than those in the p+Pb system while the v_3 values are of comparable magnitudes between the two collision systems. Within the hydrodynamic model, the larger v_2 values in the Pb+Pb system could be from the larger elliptic eccentricity (ϵ_2) in the initial state in the Pb+Pb system than in the p+Pb system [193, 194]. The v_4 gets a non-linear contribution from ϵ_2 [195] and hence could also be larger in the Pb+Pb system. The v_3 on the other hand is driven by ϵ_3 which arise from density fluctuations in both systems, and if the medium response is similar, could be of similar magnitudes. However, even though the magnitudes are similar, the p_{T} dependence of v_3 shows some difference between the two collision systems. Similar observations were also made by CMS, in the case of v_2 and v_3 between the two collision systems [100].

These observations, along with the other similarities observed between the ridge correlations in the two collision systems, point to a similar origin for these correlations in the two collision systems. Recently, it was argued that, hydrodynamic expansion can happen in small collision systems like the p+Pb system, provided the temperature increases so that the expansion dynamics in the QGP phase remain invariant under a change of the system size [14, 104]. A smaller system like p+Pb can still be expected to undergo an hydrodynamic expansion, if its temperature is appropriately larger. Using such a conformal scaling hypothesis, it is argued in [104], that since the mean free path to system size ratio, and thus the expansion dynamics, remain the same between the p+Pb and Pb+Pb systems, the average values $\langle v_n \rangle$ measured in the two systems should also be similar provided the initial eccentricities $\langle \epsilon_n \rangle$ are similar. It was shown that, scaling the $\langle v_2 \rangle$ values in the Pb+Pb system down to account for the increase in $\langle \epsilon_2 \rangle$ in Pb+Pb, good agreement can be obtained between the $\langle v_2 \rangle$ values between the p+Pb and Pb+Pb systems. The $\langle \epsilon_3 \rangle$ values are argued to be similar in the two collision systems [104] and thus similar values for $\langle v_3 \rangle$ as well. It is further argued that the p_{T} differential values $v_n(p_{\mathrm{T}})$ in p+Pb and $v_n(p_{\mathrm{T}}/K)$ in Pb+Pb should be comparable between the two collision systems, up to vertical scale factors to account for the differences in the initial eccentricities (This is the case, provided the average v_n are consistent up to scaling for geometry, if the p_{T} spectra in the two systems differ only by a scaling along the x-axis by a factor K). Here K is a constant equal to the ratio of the mean p_{T} in the two collision systems, $K = \frac{\langle p_{\mathrm{T}} \rangle_{p+Pb}}{\langle p_{\mathrm{T}} \rangle_{Pb+Pb}} \approx 1.25$.

The right panels of figure IV.2.38 show the comparison between v_n in the two collision systems after the scaling of the p_{T} axis, and a vertical scaling scaling in the cases of v_2 and v_4 are applied. Excellent agreement can be seen for v_2 up to $5 - 6$ GeV, with a vertical scale factor ≈ 0.66. The v_3 values also overlap better after the scaling of the p_{T} axis. The v_4 values are also found to agree after the scaling and with a similar value for the vertical scale factor as in the case of v_2. The magnitude of the scale factor in the case of v_4 can be explained as arising from an interplay of the linear and non-linear contributions to v_4 [196]. This observation of the scaling of the v_n harmonics between the two collision systems provides support to the conformal scaling hypothesis and to a similar origin for the ridge in the two collision systems.

IV.2.6 Summary

The measurement of the 2PC and the first five Fourier coefficients associated with the long-range ridge correlations, $v_1 - v_5$, for p+Pb collisions at $\sqrt{s_{NN}} = 5.02$ TeV at the LHC, using data recorded by the ATLAS experiment with an integrated luminosity of approximately 28 nb^{-1}, has been presented in this chapter. The ridge yields and v_n are measured as a function of p_{T} for pairs with $|\Delta\eta| > 2.0$ for events in different event activity classes, defined using the total number of reconstructed charged particle tracks with $p_{\mathrm{T}} > 0.4$ GeV and $|\eta| < 2.5$, $N_{\mathrm{ch}}^{\mathrm{rec}}$ or the total transverse energy in the forward calorimeter in the FCal on the Pb-going side, $E_{\mathrm{T}}^{\mathrm{Pb}}$. A recoil subtraction procedure, similar to that used in previous studies, is employed to remove the contributions to the correlation function from the away-side recoil.

The 2PC show significant long-range "ridge-like" correlations on the near-side ($|\Delta\phi| < \pi/3$)

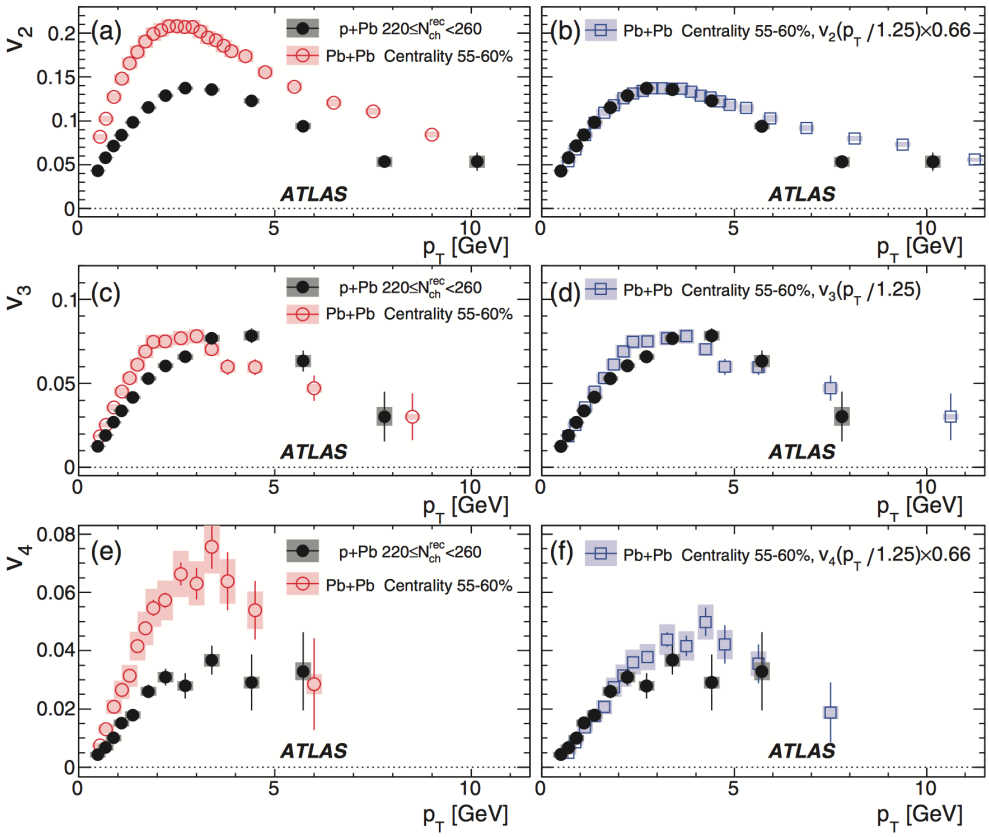

Figure IV.2.38: (Left) The v_n values as a function of p_{T} for $n = 2$ (top), 3 (middle) and 4 (bottom), compared between the p+Pb event class with $220 < N_{\mathrm{ch}}^{\mathrm{rec}} < 260$ and the 55-60% centrality class in Pb+Pb. (Right) The same data, but with the p_{T} axis for the Pb+Pb data points scaled by $K = 1.25$ and the v_2 and v_4 values in Pb+Pb being scaled down by a p_{T} independent constant factor. The error bars and shaded boxes represent statistical and systematic uncertainties, respectively.

extending to $|\Delta\eta| = 5$ in the high event activity classes. The subtraction of the recoil contribution reveals a "double ridge", approximately symmetric between the near and away ($|\Delta\phi| > 2\pi/3$) sides. The magnitude of the ridge yield on the near-side is found to increase with p_{T}, reach a maximum around $3 - 4$ GeV and then decrease, similar to the behavior of the ridge correlations measured in A+A collisions. Non zero ridge yields on the near-side are observed over the entire p_{T} range studied, including the highest bin with $9 < p_{\mathrm{T}} < 12$ GeV, in the highest multiplicity event classes.

The Fourier harmonic coefficients $v_2 - v_5$ associated with the long-range ridge correlations are measured as a function of p_{T} and event activity. The v_n values for $n = 2 - 5$, increase approximately linearly with p_{T} in the low p_{T} region, reaches a maximum around $3 - 4$ GeV and then decrease with further increase in p_{T}, but remains positive over the entire measured p_{T} range.

This p_{T} dependence is qualitatively similar to the p_{T} dependence of v_n harmonics measured in A+A collisions. The overall magnitude of $v_n(p_{\mathrm{T}})$ is found to decrease with increasing n. The $v_n(p_{\mathrm{T}}^{\mathrm{a}})$ values are also found to be independent of the associated p_{T} range used to calculate them via the factorization relation (Eq. IV.2.10) for $p_{\mathrm{T}}^{\mathrm{b}} < 4$ GeV. The magnitude of v_n increase with increase in event activity, as a function of both $N_{\mathrm{ch}}^{\mathrm{rec}}$ and $E_{\mathrm{T}}^{\mathrm{Pb}}$. The v_2 values tend to saturate at high event activity values, while the v_3 values are found to increase approximately linearly with increase in $N_{\mathrm{ch}}^{\mathrm{rec}}$ and $E_{\mathrm{T}}^{\mathrm{Pb}}$ over the measured range.

The first order coefficient $v_{1,1}(p_{\mathrm{T}}^{\mathrm{a}}, p_{\mathrm{T}}^{\mathrm{b}})$, obtained after the recoil subtraction, shows a characteristic $p_{\mathrm{T}}^{\mathrm{a}}, p_{\mathrm{T}}^{\mathrm{b}}$ dependence which is consistent with the $v_{1,1}(p_{\mathrm{T}}^{\mathrm{a}}, p_{\mathrm{T}}^{\mathrm{b}})$ dependence arising from first order flow harmonic from density fluctuations. The $v_{1,1}(p_{\mathrm{T}}^{\mathrm{a}}, p_{\mathrm{T}}^{\mathrm{b}})$ values factorize into a single $v_1(p_{\mathrm{T}})$ function, using a similar factorization relation as Eq. IV.2.10. The measured $v_1(p_{\mathrm{T}})$ values are negative at low p_{T}, increases and crosses zero ≈ 1.5 GeV and continues to increase to about 0.1 at $p_{\mathrm{T}} \sim 4$ GeV. The magnitude and p_{T} dependence of the $v_1(p_{\mathrm{T}})$ in p+Pb collisions is similar to that measured in Pb+Pb collisions.

The v_2, v_3 and v_4 values as a function of p_{T} from the p+Pb collisions are compared with those from the Pb+Pb collisions at $\sqrt{s_{NN}} = 2.76$ TeV, in event classes with similar multiplicity. After applying a scaling along the p_{T} axis to account for the difference in $\langle p_{\mathrm{T}} \rangle$ in the two systems, and a constant vertical scale factor in the case of v_2 and v_4 to account for the difference in initial eccentricities, the $v_n(p_{\mathrm{T}})$ values in p+Pb are found to be consistent with the $v_n(p_{\mathrm{T}}/K)$ values from Pb+Pb over a wide transverse momentum range (up to $p_{\mathrm{T}} \sim 5 - 6$ GeV). This observation is consistent with the predictions from a conformal scaling hypothesis and suggest the v_n coefficients in the two systems have similar origins.

The similar p_{T} dependence and decrease in magnitude with n of the v_n harmonics in p+Pb and Pb+Pb collisions, observation of a first order harmonic, v_1, similar to that in A+A collisions and the agreement of the $v_n(p_{\mathrm{T}})$ values in the two systems under a conformal scaling hypothesis all provide further support to models that argue for a similar origin of the ridge correlations in the p+A and A+A systems. However, more studies are required to fully understand the nature of these correlations and to answer the question if a thermalized QGP medium is indeed formed in the small collision systems. The high p_{T} near-side ridge measured in high multiplicity p+Pb events remains unexplained by current models and is particularly surprising given the fact that no evidence of suppression of high p_{T} particle production or jet quenching have been observed in the p+Pb system so far [112, 111]. Further measurements on high p_{T} suppression and also measurements of heavy flavor flow in p+Pb collisions could help understand the nature of the medium produced in p+Pb collisions and if (and how much of) a thermalized state is formed during the system evolution.

Chapter IV.3

Multi-particle cumulants and collectivity in small systems

The non-zero values measured for $v_n\{2k\}$ using multi-particle cumulants (see Subsection II.2.2.2 for an overview on multi-particle cumulants) and their convergence for $k >= 4$ is often taken to indicate the evidence of collective flow, which introduces correlations between all particles, in the system [197, 100, 87]. The $v_n\{2k\}$ have been measured for p+Pb collisions for $k \leq 4$ [100]. Figure IV.3.1 shows, on the left panel, the $c_2\{4\}$ values as a function of multiplicity for p+Pb collisions at $\sqrt{s_{NN}} = 5.02$ TeV at the LHC, and the right panel, shows the $v_n\{2k\}$ values for $k =$ 1–4, measured by the CMS collaboration. The $c_2\{4\}$ values are negative for $N_{trk}^{offline} \gtrsim 50$. The $c_2\{4\}$ is expected to be negative (Eq. II.2.45) if there is a global collective flow that is constant or if the 2D flow vector $\vec{v_n}$ follows a Gaussian distribution. The $v_n\{2k\}$ values converge for $k >$ 2 and suggests that in high multiplicity p+Pb collisions, there is a global v_2 modulation in these collisions. However, the fact that $c_2\{4\}$ has the wrong sign for $N_{trk}^{offline} < 50$ cannot be taken to indicate that the global or collective correlations are onset beyond a minimum multiplicity. The underlying distribution of the $\vec{v_n}$ is *a priori* unknown, particularly in small collision systems and cumulants from an arbitrary distribution need not show the behavior expected from Eq. II.2.45. In this chapter we investigate the sensitivity of the cumulants to the underlying distribution and the limitations of using the cumulants to investigate collectivity in small systems. We also propose an alternative method to measure multi-particle cumulants, directly from the distributions, which can be useful in the case of small systems. The study presented in Section IV.3.1 of this chapter can be found here [198]; the reader may refer to it for more detailed descriptions and results.

IV.3.1 Cumulants for arbitrary distributions of v_n

It was pointed out in Subsection II.2.2.2 that, if the v_n is constant across events or if the fluctuations in $\vec{v_n}$ follow a Gaussian distribution, then the cumulants $c_n\{2k\}$ alternate signs with k, with $c_n\{2\} > 0$, $c_n\{4\} < 0$ and so on, and that the magnitudes of $v_n\{2k\}$ converge with higher values of k. This behaviour is further investigated in two cases below, which study narrow and broad (the

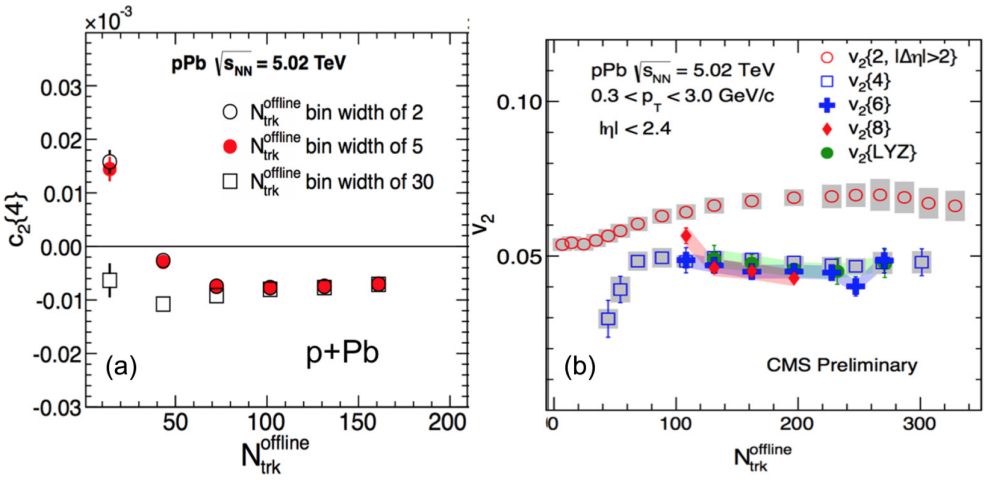

Figure IV.3.1: (Left) The $c_2\{4\}$ values and (right) the $v_n\{2k\}$ values as a function of the number or charged tracks reconstructed offline, $N_{trk}^{offline}$, for p+Pb collisions at $\sqrt{s_{NN}} = 5.02$ TeV at the LHC.

average magnitude of fluctuations in v_n being much smaller than or comparable to v_n, respectively) distributions. The first case looks at arbitrary narrow distributions for v_n and the second case considers two distributions that can be broad. It will be shown that the behaviour of cumulants as given by Eq. II.2.45 and II.2.51 are more general and valid for arbitrary distributions, as long as the distributions are narrow, but not valid for arbitrary broad distributions.

IV.3.1.1 Behavior of cumulants for narrow distributions

The cumulants in the limit of large multiplicity (or no statistical fluctuations) and no non flow correlations are related to the moments of the underlying v_n distribution. The quantities $C_n\{2k\}$ are defined from the cumulants, as follows,

$$C_n\{2\} \equiv c_n\{2\} = \langle v_n^2 \rangle, \tag{IV.3.1}$$

$$-C_n\{4\} \equiv c_n\{4\} = \langle v_n^4 \rangle - 2\langle v_2^2 \rangle^2, \tag{IV.3.2}$$

$$4C_n\{6\} \equiv c_n\{6\} = \langle v_n^6 \rangle - 9\langle v_n^4 \rangle \langle v_n^2 \rangle + 12\langle v_n^2 \rangle^3, \tag{IV.3.3}$$

$$-33C_n\{8\} \equiv c_n\{8\} = \langle v_n^8 \rangle - 16\langle v_n^6 \rangle \langle v_n^2 \rangle + 18\langle v_n^4 \rangle^2 + 144\langle v_n^4 \rangle \langle v_n^2 \rangle^2 - 144\langle v_n^2 \rangle^4, \tag{IV.3.4}$$

where the angular brackets denote the averages over the distribution.

The $v_n\{2k\}$ are now defined using $C_n\{2k\}$ as,

$$v_n\{2k\} \equiv sign\left(C_n\{2k\}\right) \sqrt[2k]{|C_n\{2k\}|}\,. \tag{IV.3.5}$$

The $v_n\{2k\}$ with this definition can take negative values, but has the traditional meaning when the distributions are constant or Bessel Gaussian.

The moments $\langle v_n^{2k}\rangle$ of the distribution can be expanded in terms of the central moments,

$$\begin{aligned}\langle v_n^{2k}\rangle &= \langle v_n\rangle^{2k}\int\left(1+\frac{v_n-\langle v_n\rangle}{\langle v_n\rangle}\right)^{2k}p(v_n)dv_n \\ &= \langle v_n\rangle^{2k}\left(\sum_{j=2}^{2k}\mathrm{C}_{2k}^{j}\theta_j\right),\end{aligned} \tag{IV.3.6}$$

where $p(v_n)$ is the underlying probability distribution and $\theta_j = \int\left(\frac{v_n-\langle v_n\rangle}{\langle v_n\rangle}\right)^j p(v_n)dv_n$ are the central moments normalized by the j^{th} power of the mean (or reduced central moments). C_{2k}^{j} are the standard binomial expansion coefficients. It should be noted that $\theta_1 = 0$ by definition and $\theta_{2n}\theta_{2m} \leq \theta_{2n+2m}$, by the Cauchy-Schwarz inequality.

The value of θ_j is determined by the characteristic variable $\epsilon \equiv \frac{v_n-\langle v_n\rangle}{\langle v_n\rangle}$. If the distribution is narrow, with the probability for v_n values with $|\epsilon| > 1$ small, i.e $\int_{|\epsilon|>1}p(v_n)dv_n \ll 1$, and the value of j is not too large, it can be expected that $|\theta_j| \ll 1$ and that the magnitude of θ_j decrease with increasing values of j. Using Eq. IV.3.6, the equations IV.3.1– IV.3.4 can be written, keeping terms up to fourth order, as

$$\begin{aligned}&C_n\{2\}/\langle v_n\rangle^2 \approx 1+\theta_2, \\ &C_n\{4\}/\langle v_n\rangle^4 \approx 1-2\theta_2-4\theta_3-\theta_4+2\theta_2^2, \\ &,C_n\{6\}/\langle v_n\rangle^6 \approx 1-3\theta_2-4\theta_3+\frac{3}{2}\theta_4-\frac{9}{2}\theta_2^2,, \\ &C_n\{8\}/\langle v_n\rangle^8 \approx 1-4\theta_2-\frac{56}{11}\theta_3+\frac{62}{33}\theta_4-\frac{40}{11}\theta_2^2,\end{aligned} \tag{IV.3.7}$$

and the corresponding approximation for the $v_n\{2k\}$ values as,

$$\begin{aligned}&v_n\{2\}/\langle v_n\rangle \approx 1+\frac{1}{2}\theta_2-\frac{3}{8}\theta_2^2, \\ &v_n\{4\}/\langle v_n\rangle \approx 1-\frac{1}{2}\theta_2-\theta_3-\frac{1}{4}\theta_4+\frac{1}{8}\theta_2^2, \\ &,v_n\{6\}/\langle v_n\rangle \approx 1-\frac{1}{2}\theta_2-\frac{2}{3}\theta_3+\frac{1}{4}\theta_4-\frac{11}{8}\theta_2^2,, \\ &v_n\{8\}/\langle v_n\rangle \approx 1-\frac{1}{2}\theta_2-\frac{7}{11}\theta_3+\frac{131}{132}\theta_4-\frac{177}{88}\theta_2^2,\end{aligned} \tag{IV.3.8}$$

Hence the $v_n\{2k\}$ values from the higher order cumulants, for $k > 1$, are approximately the same when the distribution is narrow,

$$v_n\{2k\} \approx \langle v_n\rangle\left(1-\frac{1}{2}\theta_2\right), \quad k>1 \tag{IV.3.9}$$

and the root mean square width σ_n of the distribution approximates as,

$$\frac{\sigma_n}{\langle v_n\rangle} \equiv \theta_2 \approx \sqrt{\frac{v_n^2\{2\}-v_n^2\{4\}}{v_n^2\{2\}+v_n^2\{4\}}} \tag{IV.3.10}$$

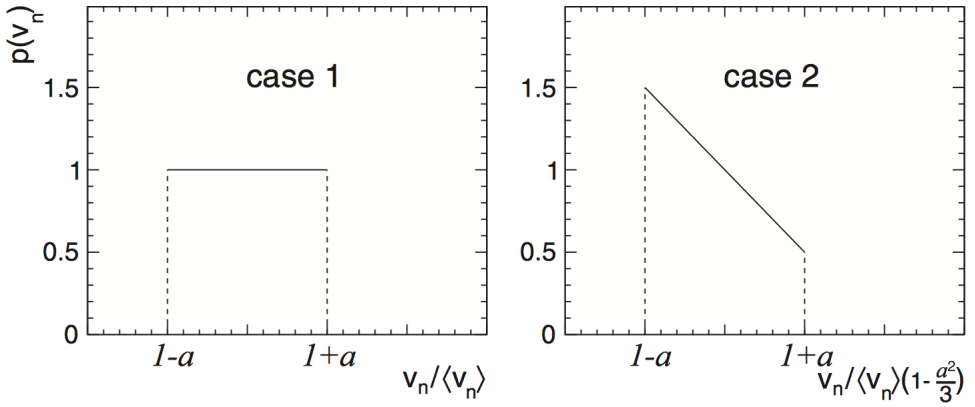

Figure IV.3.2: The illustration of $p(v_n)$ distributions defined by equations IV.3.11 (left) and IV.3.12 (right).

IV.3.1.2 Behavior of cumulants for broad distributions

The expansions in Eq. IV.3.7 are not valid when the distributions are broad (when the probabilities for events with $\epsilon \sim 1$ is large) as θ_j for larger values of j will also be significant. Depending on the distribution $p(v_n)$, the values of $v_n\{2k\}$ may differ significantly. We say "may" because for Bessel-Gaussian distribution, regardless of how broad the distribution is, the $v_n\{2k\}$ values will converge. On the other hand, it is easy to construct distributions for which $v_n\{2k\}$ won't converge or have the expected signs. This point is important since the underlying distributions are unknown in many cases, particularly in the case of small systems or in the case of collisions of deformed nuclei. We discuss two distributions here to illustrate the non-convergence for arbitrary broad distributions.

We consider two distributions as given below,

$$p(x;a) = \begin{cases} 1, & |x-1| \le a \\ 0, & |x-1| > a \end{cases} \quad x \equiv \frac{v_n}{\langle v_n \rangle} \tag{IV.3.11}$$

$$p(x;a) = \begin{cases} 2-x, & |x-1| \le a \\ 0, & |x-1| > a \end{cases} \quad x \equiv \frac{v_n}{\langle v_n \rangle}\left(1 - a^2/3\right) \tag{IV.3.12}$$

These distributions are illustrated in figure IV.3.2. The parameter a determines how broad the distributions are. The widths of the distributions increase with a, but their mean values remain either same (Eq. IV.3.11) or decrease with increase in a (Eq IV.3.12). Hence these distributions are suitable to study the behaviour of cumulants in going from a case with the average fluctuations in v_n much less than the mean value, $\sigma_n \ll \langle v_n \rangle$, to the case where fluctuations dominate, $\sigma_n > \langle v_n \rangle$.

Figure IV.3.3 shows the $v_n\{2k\}$ values from the above two distributions as a function of the parameter a. In both cases, it can be seen than $v_n\{6\}$ and $v_n\{8\}$ have the wrong signs for large values of a. For the second case (Eq. IV.3.12), the $v_n\{4\}$ values also change sign for large values of a.

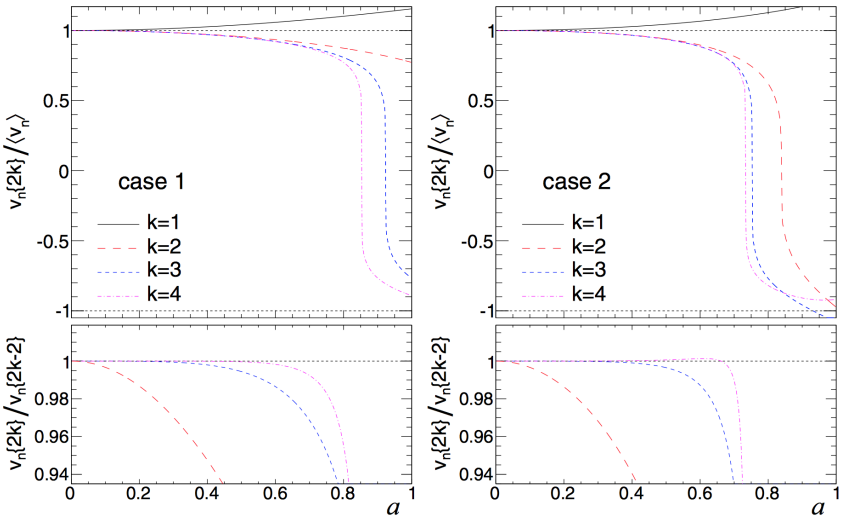

Figure IV.3.3: The $v_n\{2k\}$ values as a function of a for the distributions given by Eq IV.3.11 (left) and Eq. IV.3.12 (right). The smaller panels below show the ratios $v_n\{2k\}/v_n\{2k-2\}$ as a function of a for the corresponding distributions.

The transition from positive to negative values happen rather abruptly due to the large exponential powers that relate $C_n\{2k\}$ and $v_n\{2k\}$. The convergence (or divergence) between $v_n\{2k\}$ from successive values of k are shown in the lower panels, which plot the ratios, $v_n\{2k\}/v_n\{2k-2\}$ as a function of a. As discussed before, when the value of a is small ($a < 0.5$), all the four $v_n\{2k\}$ values are close to each other. The higher cumulants start to deviate from each other for values of $a > 0.7$, and eventually change to have signs contrary to that expected in Eq. II.2.45. Thus for arbitrary broad distributions, the ratios in Eq. II.2.45 relating v_n (or v_n^{RP}) and $c_n\{2k\}$ cease to be valid and the $v_n\{2k\}$ values for $k > 1$ won't exhibit convergence.

IV.3.2 Alternate method for measuring cumulants using the flow distribution

The discussion in the last Subsection shows that the behaviour of cumulants, in general, depends on the nature of the underlying v_n distribution. However, it should be also noted that the distributions measured in experiments are not the true underlying distribution, but the true distribution convoluted with distributions of the same quantity arising from purely non flow sources and statistical fluctuations. Let $\vec{q_n}$ denote the flow vector observed in an event. This differs from the true flow vector, $\vec{v_n}$, in that event by contributions from statistical noise (arising from finite number of particles in the event) and non flow contributions (arising from sources of correlation other than global flow, like decays, jets etc). We can write,

$$\vec{q_n} = \vec{v_n} + \vec{s_n}, \tag{IV.3.13}$$

where $\vec{s_n}$ denotes the contribution to $\vec{v_n}$ from the non flow correlations and statistical fluctuations. Here the vector $\vec{q_n}$ is defined as the per particle observed flow vector in the event,

$$\vec{q_n} = (q_n \cos(n\psi_n), q_n \sin(n\psi_n)), \quad q_n e^{in\psi_n} = \frac{1}{N}\sum_{i=1}^{N} e^{in\phi_i}, \tag{IV.3.14}$$

where the sum is over all the particles in the event used in the analysis and ϕ_i is the azimuthal angle of the i^{th} particle. The distribution of $\vec{q_n}$ will therefore be a convolution of the distributions for $\vec{v_n}$ and $\vec{s_n}$. It is possible that the distribution of $\vec{s_n}$ is non Gaussian, particularly in small systems and event classes with small number of tracks, thus making the distribution of $\vec{q_n}$ also, non Gaussian. As a result, even if the underlying true flow ($|\vec{v_n}|$) distribution is constant or Bessel-Gaussian, the distribution of $|\vec{q_n}|$ might not be, and the cumulants won't exhibit the expected behaviours as in equations II.2.45 and II.2.51. This again points to the observation that wrong sign for the cumulants (from those expected in Eq. II.2.45) or lack of convergence for higher order cumulants, cannot be taken as evidence for lack of collectivity or a global v_n signal in the system.

IV.3.2.1 The method

We present the theory behind the method here. A discussion and preliminary results on this method can be found at [199]. The cumulants of distributions, by definition, are additive under convolution. This can be seen quite easily in the case of the flow harmonics. Let $f(v_{n,x}, v_{n,y})$ denote the probability distribution for the random variable $\vec{v_n}$ and $g(s_{n,x}, s_{n,y})$ be the distribution for $\vec{s_n}$. Then the distribution, $h(q_{n,x}, q_{n,y})$, for $\vec{q_n}$, will be a convolution of the two distributions f and g. We are interested in the moments $\langle q_n^2 \rangle \equiv \langle q_{n,x}^2 + q_{n,y}^2 \rangle$, $\langle q_n^4 \rangle$, $\langle q_n^6 \rangle$ etc.

$$\begin{aligned}
\langle q_n^2 \rangle &= \int\int (q_{n,x}^2 + q_{n,y}^2) h(q_{n,x}, q_{n,y}) dq_{n,x} dq_{n,y} \\
&= \int\int\int\int (q_{n,x}^2 + q_{n,y}^2) f(v_{n,x}, v_{n,y}) g(q_{n,x} - v_{n,x}, q_{n,y} - v_{n,y}) dq_{n,x} dq_{n,y} dv_{n,x} dv_{n,y} \\
&= \int\int\int\int ((s_{n,x} + v_{n,x})^2 + (s_{n,y} + v_{n,y})^2) f(v_{n,x}, v_{n,y}) g(s_{n,x}, s_{n,y}) dv_{n,x} dv_{n,y} ds_{n,x} ds_{n,y} \\
&= \int\int \langle s_{n,x}^2 + s_{n,y}^2 \rangle + 2\langle s_{n,x} \rangle v_{n,x} + 2\langle s_{n,y} \rangle v_{n,y} + (v_{n,x}^2 + v_{n,y}^2) f(v_{n,x}, v_{n,y}) dv_{n,x} dv_{n,y} \\
&= \langle v_{n,x}^2 + v_{n,y}^2 \rangle + \langle s_{n,x}^2 + s_{n,y}^2 \rangle + 2\langle v_{n,x} \rangle \langle s_{n,x} \rangle + 2\langle v_{n,y} \rangle \langle s_{n,y} \rangle
\end{aligned} \tag{IV.3.15}$$

The system is isotropic when averaged over many events as there is no preference for the direction of the flow event plane. Also the smearing distribution, g, in particular can be expected to be isotropic, implying $\langle s_{n,x} \rangle = \langle s_{n,y} \rangle = 0$. And using the notations $\langle v_n^2 \rangle \equiv \langle v_{n,x}^2 + v_{n,y}^2 \rangle$ and $\langle s_n^2 \rangle \equiv \langle s_{n,x}^2 + s_{n,y}^2 \rangle$, we see that,

$$\langle q_n^2 \rangle = \langle v_n^2 \rangle + \langle s_n^2 \rangle, \tag{IV.3.16}$$

or in terms of the cumulants,

$$c_n^q\{2\} = c_n^v\{2\} + c_n^s\{2\} \tag{IV.3.17}$$

Similarly, for $\langle q_n^4 \rangle$, it can be seen that,

$$\begin{aligned}
\langle q_n^4 \rangle &= \int\int (q_{n,x}^2 + q_{n,y}^2)^2 h(q_{n,x}, q_{n,y}) dq_{n,x} dq_{n,y} \\
&= \int\int\int\int ((s_{n,x} + v_{n,x})^2 + (s_{n,y} + v_{n,y})^2)^2 f(v_{n,x}, v_{n,y}) g(s_{n,x}, s_{n,y}) dv_{n,x} dv_{n,y} ds_{n,x} ds_{n,y} \\
&= \langle (v_{n,x}^2 + v_{n,y}^2)^2 \rangle + \langle (s_{n,x}^2 + s_{n,y}^2)^2 \rangle + 4\left(\langle v_{n,x}^2 \rangle \langle s_{n,x}^2 \rangle + \langle v_{n,y}^2 \rangle \langle s_{n,y}^2 \rangle + 2\langle v_{n,x} v_{n,y} \rangle \langle s_{n,x} s_{n,y} \rangle\right) \\
&+ 2\langle v_{n,x}^2 + v_{n,y}^2 \rangle \langle s_{n,x}^2 + s_{n,y}^2 \rangle + 4\left(\langle s_{n,x}^3 \rangle \langle v_{n,x} \rangle + \langle s_{n,x}^2 s_{n,y} \rangle \langle v_{n,y} \rangle + \langle s_{n,x} s_{n,y}^2 \rangle \langle v_{n,x} \rangle + \langle s_{n,y}^3 \rangle \langle v_{n,y} \rangle\right) \\
&+ 4\left(\langle v_{n,x}^3 \rangle \langle s_{n,x} \rangle + \langle v_{n,x}^2 v_{n,y} \rangle \langle s_{n,y} \rangle + \langle v_{n,x} v_{n,y}^2 \rangle \langle s_{n,x} \rangle + \langle v_{n,y}^3 \rangle \langle s_{n,y} \rangle\right)
\end{aligned} \tag{IV.3.18}$$

Again, if the distributions are isotropic, $\langle s_{n,x} \rangle = \langle s_{n,y} \rangle = \langle v_{n,x} \rangle = \langle v_{n,y} \rangle = 0$, and also $\langle v_{n,x} v_{n,y} \rangle \langle s_{n,x} s_{n,y} \rangle = 0$, and the above expression reduces to,

$$\begin{aligned}
\langle q_n^4 \rangle &= \langle (v_{n,x}^2 + v_{n,y}^2)^2 \rangle + \langle (s_{n,x}^2 + s_{n,y}^2)^2 \rangle \\
&\quad + 4\left(\langle v_{n,x}^2 \rangle \langle s_{n,x}^2 \rangle + \langle v_{n,y}^2 \rangle \langle s_{n,y}^2 \rangle\right) + 2\langle v_{n,x}^2 + v_{n,y}^2 \rangle \langle s_{n,x}^2 + s_{n,y}^2 \rangle \\
&= \langle v_n^4 \rangle + \langle s_n^4 \rangle + 4\langle v_n^2 \rangle \langle s_n^2 \rangle,
\end{aligned} \tag{IV.3.19}$$

where in the last step we have used the fact that $2\langle s_{n,x}^2 \rangle = 2\langle s_{n,y}^2 \rangle = \langle s_n^2 \rangle$. Defining $c_n^q\{4\} = \langle q_n^4 \rangle - 2\langle q_n^2 \rangle^2$, $c_n^v\{4\} = \langle v_n^4 \rangle - 2\langle v_n^2 \rangle^2$, $c_n^s\{4\} = \langle s_n^4 \rangle - 2\langle s_n^2 \rangle^2$ and substituting in Eq. IV.3.19, it can be found that,

$$c_n^q\{4\} = c_n^v\{4\} + c_n^s\{4\} \tag{IV.3.20}$$

In general, it can be shown that, the $2k^{\text{th}}$ order cumulant for the observed distribution is given by the sum of the $2k^{\text{th}}$ order cumulants for the true and smearing distributions,

$$c_n^q\{2k\} = c_n^v\{2k\} + c_n^s\{2k\} \tag{IV.3.21}$$

However, it should be noted that there is an implicit assumption in the derivation of equations. IV.3.17 and IV.3.20, that the variables $\vec{v_n}$ and $\vec{s_n}$ are uncorrelated with each other, so that the averages can be calculated separately. Eq. IV.3.21 is valid only in this case where $\vec{v_n}$ and $\vec{s_n}$ are uncorrelated. It is reasonable to assume that the global flow signal and the non flow correlation from jets, resonances etc are uncorrelated with each other in small collision systems. However, the statistical noise contribution is correlated with the flow signal and should be taken into account.

The contributions from the correlation between statistical fluctuations and the flow signal can be evaluated in a straightforward way. Consider for now that there is no non flow correlations in the system and $\vec{s_n}$ arise purely from statistical fluctuations. To simplify the discussion, let us choose the x-axis to coincide with the direction of the event plane and that only the second order harmonic is non-zero. In this case $\langle v_{n,y} \rangle = \langle s_{n,x} \rangle = \langle s_{n,y} \rangle = 0$ and $\langle v_{n,x} \rangle = v$. Therefore from Eq. IV.3.15, it can be seen that the cross terms in the integral, $\langle s_{n,x} v_{n,x} \rangle = \langle s_{n,x} v \rangle$ and $\langle s_{n,x} v_{n,y} \rangle$ go to zero. And the relation, Eq. IV.3.17, holds for the second order cumulants, even when the correlation between the v_n and statistical fluctuations are taken into account.

For the four-particle case, it can be seen quite easily that the only cross terms that don't vanish in the case of non-zero correlation between $\vec{v_n}$ and $\vec{s_n}$ are $4\langle s_{n,x}^3 v_{n,x}\rangle$ and $4\langle s_{n,x}s_{n,y}^2 v_{n,x}\rangle$. These can be evaluated as discussed below,

For events with magnitude of flow v, a finite number (N) of tracks are drawn every event from a 'true distribution' given by,

$$f(\phi) = \frac{1}{2\pi}\left(1 + 2vcos(2\phi)\right) \tag{IV.3.22}$$

For the true distribution, the moments and covariances of the x and y coefficients (denoted x_t and y_t) can be calculated by integrating over the distribution function. The first several moments and covariances can be found to be.

$$\begin{aligned}&\langle x_t\rangle = v, \langle y_t\rangle = 0, \langle x_t^2\rangle = \frac{1}{2}, \langle y_t^2\rangle = \frac{1}{2}, \langle x_t^3\rangle = \frac{3v}{4}, \langle y_t^3\rangle = 0\\ &\langle x_t y_t\rangle = 0, \langle x_t^2 y_t\rangle = 0, \langle x_t y_t^2\rangle = \frac{k}{4}\end{aligned} \tag{IV.3.23}$$

The components of the observed q vector, x_q and y_q, are sample means from several independent samplings of the true distribution. The variables $x_s = s_{n,x} = x_q - v$ and $y_s = s_{n,y} = y_q$ and the non-zero terms in the cumulant relation (Eq. IV.3.18) above can be rewritten in terms of x_q, y_q and v. The moments of the sample means, $\langle x_q^k y_q^l\rangle$ (for integer k and l) can be related to the true moments $\langle x_t^i y_t^j\rangle$ (with integer values for i and j) using standard expressions [200] (A derivation of the results and general formulae are given in [200]. These can also be evaluated using the *mathStatica* package [201] in the software *Mathematica*. In *mathStatica*, one can first express the sample means in terms of the power sums [200] using the function `RawMomentsToPowerSum` and then use the function `RawMomentsToRaw` with the power sum as the argument to obtain the relation between the moments of sample mean and the true moments). Using this procedure, and the values for the true moments and covariances in Eq. IV.3.23, the first term evaluates as $4\langle s_{n,x}^3\rangle\langle v_{n,x}\rangle = 4\left(\frac{2v^4}{N^2} - \frac{3v^2}{4N^2}\right)$ and the second term evaluates as $4\langle s_{n,x}s_{n,y}^2 v_{n,x}\rangle = -\frac{v^2}{N^2}$. The corrections are both very small, suppressed by N^2 and significant mainly for small collision systems with small values for N. Note that the first term has power v^2 while the cumulant, $c_n\{4\}$ is of order v^4, and so can be significant when $v \sim N$. The relation between the cumulants for the fourth order can now be written as,

$$c_n^q\{4\} = c_n^v\{4\} + c_n^s\{4\} - \frac{4v^2}{N^2} + \frac{8v^4}{N^2} \tag{IV.3.24}$$

Similar expressions can be derived for the higher order cumulants, but we don't attempt them here. Since the value of v are not constant in an event class, the correction terms should be averaged over the flow distribution. As an approximation the value of v for Eq. IV.3.23 can be taken as the values from 2PC or an Event Plane method. Equations IV.3.17 and IV.3.24 can be used as an alternative method to evaluate the second and fourth order cumulants in heavy-ion and p+p collisions, provided an estimation of the smearing distribution $g(s_{n,x}, s_{n,y})$ (sometime also referred to as the "response function" (RF)) be made (for an example see [202]).

IV.3.2.2 Study using toy and HIJING simulations

We present studies on the cumulants in a toy and HIJING models, using the method discussed above. The toy model used just includes flow correlations and smearing from statistical fluctuations. The ϕ distribution of the particles is sampled N_{trk} times from a distribution of the form in Eq. IV.3.22, with constant magnitude for flow, $v = 0.06$. The sampled 'events' are grouped in bins of N_{trk}, and a range of N_{trk} values similar to that in p+Pb collisions is studied.

For each event, the magnitude of the flow vector q_2 and its even powers are calculated and then averaged over the events within the same N_{trk} bin, and from these values, the cumulants of the distribution ($c_n^q\{2k\}$, here we consider only the cases with $k = 1$ and 2) are calculated. The smearing distribution in this case is taken as the distribution of q_2 from events sampled in the same N_{trk} class, but with $v = 0$. The $c_n^s\{2k\}$ are obtained from the events sampled with zero flow in the same way as for the case with flow. From these two values, the $c_n^v\{2k\}$ are calculated via equations IV.3.17 and IV.3.24 respectively, for $k = 1$ and $k = 2$. While doing the calculation, bin widths of 1 in N_{trk} are used, which are combined after the cumulants $c_n^v\{2k\}$ are calculated into larger bins. While averaging over events, q_2^{2k} values are weighted by an event-by-event weight equal to the total number of pairs (including self pairs), $w_i = N_{trk}^{2k}$ i.e the average values in event classes of 1 N_{trk} bin width are calculated as, $\langle q_2^{2k} \rangle = \frac{w_i q_2^{2k}}{w_i}$ (Results without this weighting are consistent with the case with weighting, as there are no multiplicity fluctuations in the case considered here). From the final $c_n^v\{2k\}$ values, the $v_n\{2k\}$ are determined.

The $v_n\{2k\}$ values were also calculated following the 'multi-particle cumulant' procedure described in II.2.2.1 [86]. Again, the calculation of the cumulants were done in widths of 1 N_{trk} and then averaged. Event-by-weights are applied while averaging, following the equations II.2.38 and II.2.39. Figure IV.3.4 shows the $v_2\{2k\}$ values for $k = 1$ and 2, as a function of N_{trk} from the toy model study. The $v_2\{2k\}$ values calculated for different cases are shown. The values calculated directly using the moments of $c_n^q\{2k\}$ or the observed values (black solid circles), the values obtained after cumulants from the smearing distribution are subtracted, $c_n^q\{2k\} - c_n^s\{2k\}$ (blue open squares), and the $c_n^v\{2k\}$ values from equations IV.3.17 and IV.3.24 (open green crosses) are shown. Also the values calculated from the multi-particle cumulant method are shown (open red circles). The truth v_2 value is indicated by the dashed line.

The $v_2\{2k\}$ from $c_n^q\{2k\}$ have contributions from autocorrelations, where the same particle is correlated with itself. This causes the values to be much larger in the case of $k = 1$. For $k = 2$, at higher values of N_{trk}, $N_{trk} \gtrsim 100$, the cumulants calculated directly from $c_n^q\{2k\}$ agree with the truth values. This is because the autocorrelations in the large N_{trk} region introduces Gaussian smearing and thus get removed in the four particle cumulants. Both the multi-particle cumulant method and the new cumulant method can correctly reproduce the truth level v_2 for $k = 1$ and 2, down to very low multiplicities. This is not very surprising, as the statistical contributions get subtracted in the multi-particle cumulant method as the autocorrelations are excluded in the definition of $\langle\langle 2k \rangle\rangle$ (Eqs. II.2.53 and II.2.54). For the new method, the statistical fluctuations are almost entirely captured by the smearing function and thus are subtracted out. The correction terms for $c_2^v\{4\}$ become important in the case of $k = 2$, for $N_{trk} \lesssim 100$.

The toy model considered above has no non flow, from jets, decays, local charge conservation

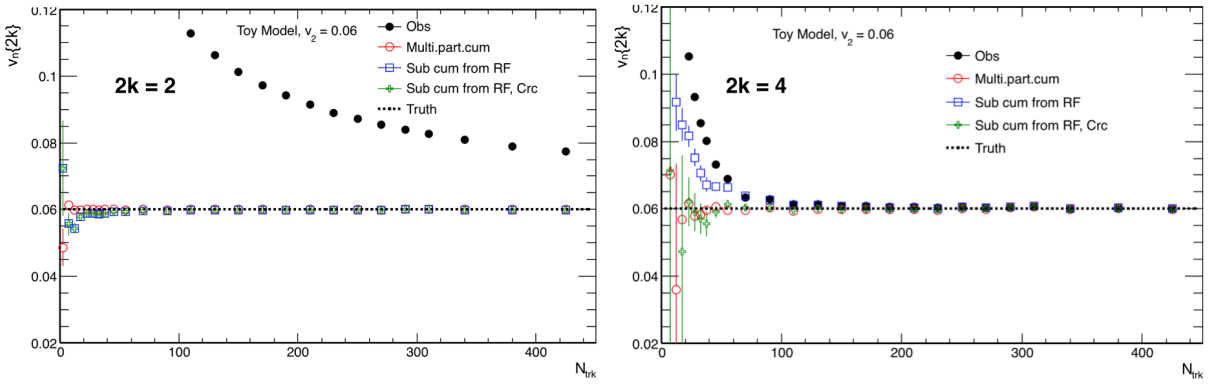

Figure IV.3.4: The $v_n\{2k\}$ values as a function of N_{trk} for toy model simulations, calculated using $c_n^q\{2k\}$ (solid black circles), $c_n^q\{2k\} - c_n^s\{2k\}$ (open blue squares), $c_n^v\{2k\}$ (open green crosses) and from the multi-particle cumulant method (open red circles), for k=1 (left) and k = 2(right). The true value is indicated by dashed lines.

etc. To study the impact of the non flow on the methods, HIJING events for p+Pb collisions at $\sqrt{s_{NN}}$ = 5.02 TeV where generated. HIJING does not have global flow like correlations. The flow correlations are implemented through a "Flow Afterburner" algorithm, following [203]. The Afterburner introduces small modulations to the final azimuthal particle distribution to artificially have an azimuthal anisotropy. Implementing the flow via the Afterburner largely preserves the non flow correlations in the system [204]. A p_{T} and η independent constant flow of $v_2 = 0.06$ and $v_3 = 0.03$ was implemented.

The analysis procedure follows that discussed above for the toy model study. The analysis is limited to using all truth level particles with $0.3 < p_{\mathrm{T}} < 3$ GeV and $|\eta| < 2.5$. The events are binned into event classes based on the value of N_{trk}, defined to be the total number of particles with $0.3 < p_{\mathrm{T}} < 3$ GeV and $|\eta| < 2.5$. The cumulants are calculated, as in the case of the toy model, in bins of 1 N_{trk} width, and the averaging over events within the 1 N_{trk} width classes are done applying the same weights as those used in the case of toy study (The weighting doesn't affect the results in this case either, as there are no multiplicity fluctuations within the event classes). The final results are combined into larger N_{trk} bins. The smearing distribution is taken to be the q_n distribution from the HIJING events before adding the flow modulations via the Afterburner. This is an approximation. Even though the non flow correlations are largely preserved by the Afterburner, small deviations can be seen in the q_n distribution from non flow (calculated from the event by event difference vector $\vec{q_n}^A - \vec{q_n}^B$, where A and B denote two "sub events" defined using tracks with $\eta > 0$ or $\eta < 0$ of the same event), before and after implementing the flow via the Afterburner, particularly in the large q_n tail of the distribution [204]. This can make the estimation of the $c_n^s\{2k\}$ values, particularly for higher order cumulants slightly incorrect.

The presence of non flow causes the cumulants from the multi-particle cumulant method to deviate from the true values. This can be seen from figure IV.3.5 which shows the $c_2\{4\}$ calculated

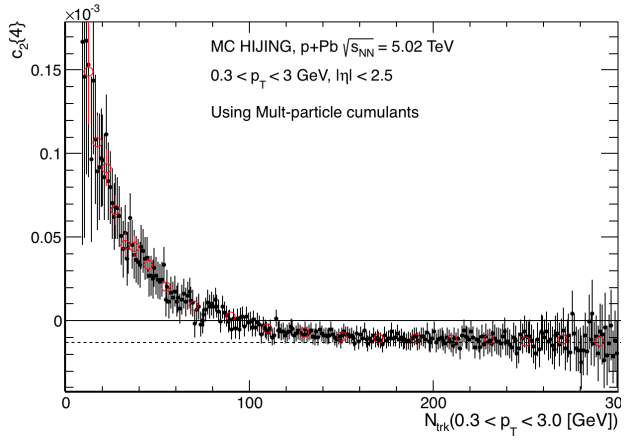

Figure IV.3.5: The $c_2\{4\}$ values as a function of N_{trk} from HIJING simulations with flow, calculated using the multi-particle cumulant method. The values calculated using bins of width 1 N_{trk} (solid black) and the values after combining into larger N_{trk} bins (open red circles) are shown. The dashed line indicates the true value.

from the mult-particle cumulant method as a function of N_{trk}. The values calculated in bins of width 1 N_{trk} (solid black) and the values combined into larger N_{trk} bins are shown (open red circles). The $c_2\{4\}$ values deviate much from the true value below $N_{trk} \sim 100$, and becomes positive below that N_{trk}. In the data also, the $c_2\{4\}$ values become positive at low multiplicity values. This could purely be from the presence of non flow correlations and not from absence of collectivity.

Figure IV.3.6 compares the $v_2\{2k\}$ and $v_3\{2k\}$ values for $k = 1$ and $k = 2$, between the multi-particle cumulant method and the new cumulant method with the distribution from HIJING without flow used as the RF. The values for both harmonics for $k = 1$ shows large deviation from the true values with the multi-particle cumulant method. For $k = 2$, also the values change sign around $N_{trk} \sim 100$ for $v_2\{4\}$ and ~ 200 for $v_3\{4\}$. The new cumulant method (open green crosses) gives almost perfect closure for both harmonics in the case of $k = 1$. For $k = 2$ also, the performance is better. The $c_2\{4\}$ remain negative throughout the N_{trk} range and within $\sim 6\%$ of the true value at $N_{trk} = 100$ and within 30% for $N_{trk} \sim 20$, for v_2. This residual non closure could be from the small modifications to the non flow in events introduced by the Afterburner. A better simulation can be constructed by superimposing tracks drawn from a $f(\phi)$ distribution with the true flow modulations, with the tracks from HIJING, to demonstrate the 'proof of principle' validity for the new method. However, this not attempted here and left for future studies. The $v_3\{4\}$ values also show similar or better level of closure with the new method.

In data, the true RF or the RF for the case without flow is not known. It has to be approximated from the data itself. A common choice used is to use the RF from the "two sub event" (2SE) method, where an event-by-event difference vector, defined as $\vec{q_n}^A - \vec{q_n}^B$ are constructed using the per particle flow vectors (Eq.IV.3.14) in the two sub events. The two sub events, denoted A and

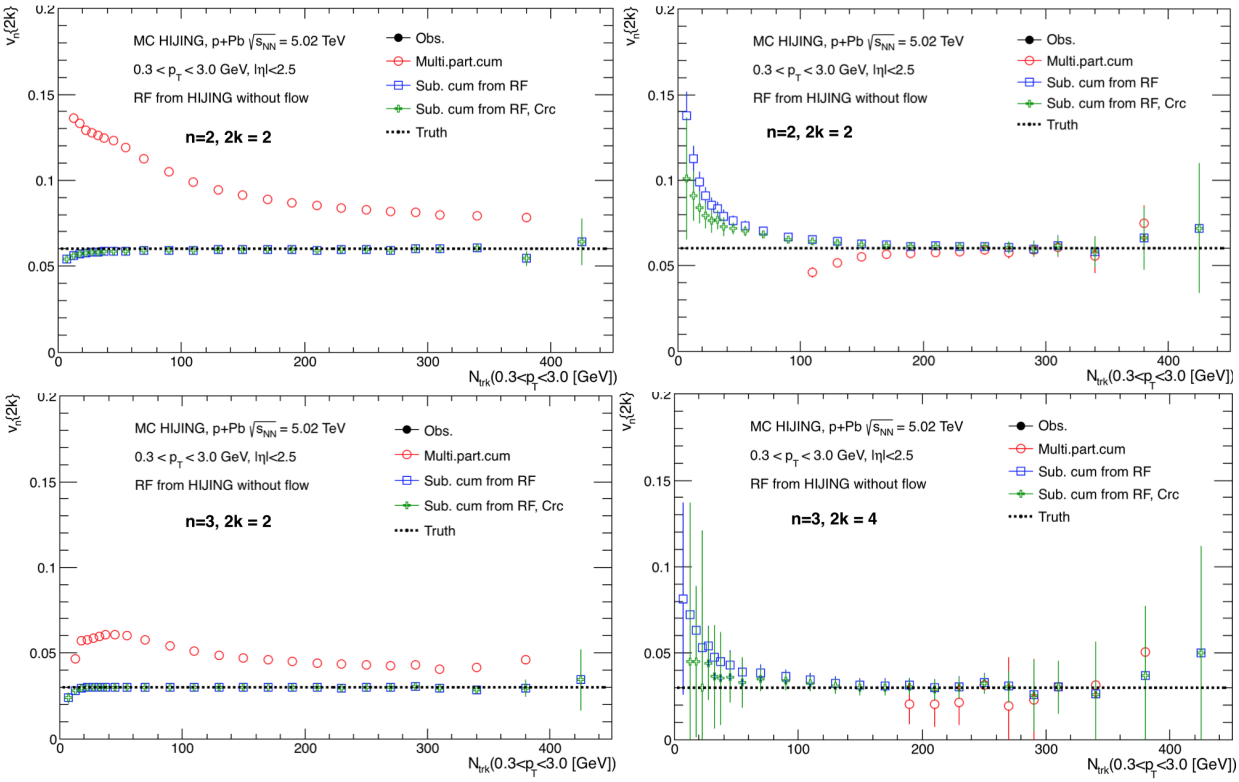

Figure IV.3.6: The $v_n\{2k\}$ values as a function of N_{trk} for MC HIJING simulations with flow, calculated using $c_n^q\{2k\} - c_n^s\{2k\}$ (open blue squares), $c_n^v\{2k\}$ (open green crosses) and from the multi-particle cumulant method (open red circles), for k=1 (left) and k = 2(right). The RF are obtained from HIJING events without flow. The true value is indicated by dashed lines.

B are constructed using tracks from the same event [202, 204]. The sub events can be constructed using tracks divided into those with $\eta < 0$ and $\eta > 0$ or randomly into two halves. The true flow cancels out in the difference vector (the v_n have weak η dependence [4], and the magnitude of longitudinal fluctuations are also small [90]). The RF estimated this way is an approximation, as non flow can cause correlations between the two sub events and thus under estimate (or over estimate, depending on the nature of the correlations) the cumulants $c_n^s\{2k\}$ from the smearing. The 2SE method with the η sub events works better than the case with random sub events [204]. This can be expected as the non flow correlations in the two η sub events are more uncorrelated than that in the random sub events.

Figure IV.3.7 shows the comparison of the $v_2\{2k\}$ and $v_3\{2k\}$ values for $k = 1$ and $k = 2$, between the multi-particle cumulant method and the new cumulant method with the RF calculated using the η 2SE method. The new cumulant method still shows better performance than the multi-particle cumulant method. The $v_2\{2\}$ have large non closure now for the new cumulant method. The $v_3\{2\}$ values show better closure, within 10% throughout the N_{trk} range. The non flow correlations seem to have a bigger impact on v_2 values than v_3 values. The $v_n\{4\}$ values show good closure, for values down to ~ 50 tracks, for both harmonics. The closure for $v_3\{4\}$ is better at very low multiplicities ($N_{trk} <$) 50. The multi-particle cumulant method fails to give $c_3\{4\}$ of the correct sign for N_{trk} values as high as 200 (for the 3% v_3 values), while the new method works significantly better down to much lower multiplicities.

The new method works better, at least in model simulations, compared to the multi-particle cumulant method in low multiplicity systems. However, the performance of this method in data and also in model simulations for different distributions for flow and longitudinal fluctuations in flow need to be evaluated. Studies can also be done to optimize the approximation for RF in data, in which the correlations from non flow between the two sub events are minimized. Introducing a gap in η between the two η sub events would reduce non flow correlations, or the tracks can be classed to minimize correlation between jets in an event. Another approach could be to construct the response function using pseudo mixed events that are constructed to capture non flow correlations but the flow correlations to drop out from the random orientation of the event plane. These improvements and further validation require more studies and are left for future work.

IV.3.3 Summary

In this chapter, investigations into the limitations of using multi-particle cumulants to study collectivity in small systems were presented. The v_n values calculated from higher order cumulants, $v_n\{2k\}$ for $k >1$, were found to converge for arbitrary distributions, as long as the distributions are narrow, thus showing that the expressions given in equations II.2.45 and II.2.51 are bit more general. However, the $v_n\{2k\}$ values were found not to converge for $k >1$ or have the correct sign as in equations II.2.45 and II.2.51, for arbitrary broad distributions. Since the underlying distributions of v_n in small collision systems are not *a priori* known and also since non flow smearing can cause modifications to the distributions, the wrong sign or lack of convergence of $v_n\{2k\}$ cannot be used to infer lack of collectivity (or global correlations) in small collision systems.

An alternate method to study cumulants using the distributions of the magnitude of the flow

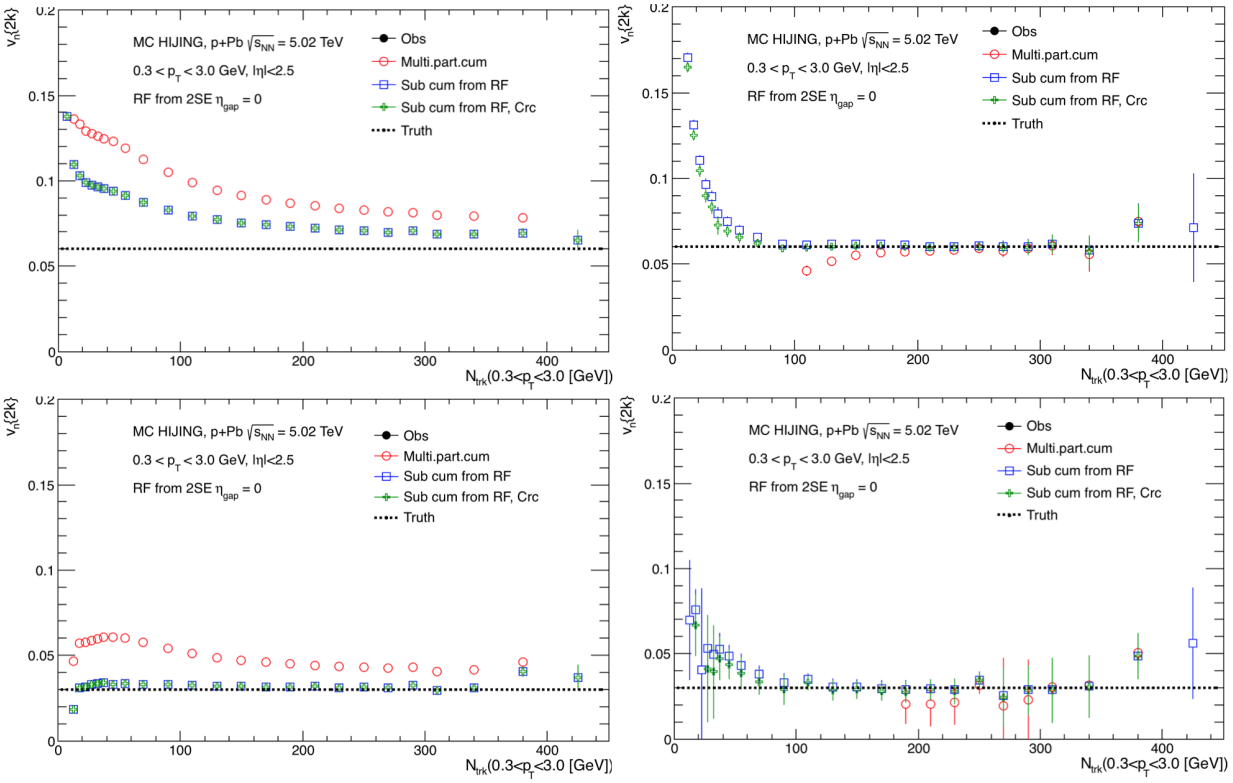

Figure IV.3.7: The $v_n\{2k\}$ values as a function of N_{trk} for MC HIJING simulations with flow, calculated using $c_n^q\{2k\} - c_n^s\{2k\}$ (open blue squares), $c_n^v\{2k\}$ (open green crosses) and from the multi-particle cumulant method (open red circles), for k=1 (left) and k = 2(right). The RF in the case are obtained from the η 2SE method. The true value is indicated by dashed lines.

vector, q_n, was presented. The method follows from the property that the cumulants of distributions are additive under convolution. The performance of the method was compared to the multi-particle cumulant method using toy model and MC HIJING simulations with Flow Afterburner. In the toy model, both methods could reproduce the true flow values down to very low multiplicities. In the case of HIJING, the multi-particle cumulants were found to deviate from the true value and give wrong sign for $c_n\{4\}$ for $N_{trk} \lesssim 100$ for a 6% v_2 signal and for $N_{trk} \lesssim 200$ for a 3% v_3 signal. The new method, using a response function from the 2SE method using η sub events was found to perform better, with $c_n\{4\}$ values remaining within 10% of the true signal down to $N_{trk} \sim 50$, for the cases of both harmonics. The new method can be used as an alternate method to measure the cumulants in small collision systems and may improve the measurements at low multiplicities. However, further studies are required to better evaluate and improve the performance of the new method presented.

Part V

Longitudinal correlations and measurement of longitudinal correlations in Pb+Pb, p+Pb and p+p collisions

Chapter V.1

Method to study longitudinal fluctuations and results from model simulations

This chapter presents in detail, the method to expand the event-by-event shape fluctuations in the longitudinal particle distribution and presents two methods two measure them. One, a single particle method which attempts to unfold for statistical fluctuations and another, a two particle correlation method, similar to that discussed in Subsection II.3.2.2. The methods are applied to study the longitudinal correlations in the HIJING and AMPT models. The equivalence of the single particle and two particle methods are shown and possible further directions of exploration are discussed. The results presented in this chapter have been published here [205] and can be referenced for further details. The chapter is organized as follows. Section V.1.1 presents the single particle and two particle methods to study the longitudinal correlations. The study of longitudinal correlations in HIJING and AMPT models are discussed in Section V.1.2. The relationship of the measured quantities to the initial conditions within the context of the event generator models are discussed. The equivalence between the single particle and two particle methods are also shown. The chapter ends with a summary in Section V.1.3.

V.1.1 Analysis method

The particle distribution in the pseudorapidity direction can fluctuate event-by-event depending on the number and nature of particle producing sources in each event. Let $N(\eta)$ denote the number of particles at a given pseudorapidity in an event. The fluctuations in $N(\eta)$ can be studied relative to the average pseudorapidity distribution, $\langle N(\eta)\rangle$, from many events in an event class. Let

$$R(\eta) = \frac{N(\eta)}{\langle N(\eta)\rangle} \tag{V.1.1}$$

The event-by-event modulations in $R(\eta)$ can be expanded quite generally into a set of orthonormal polynomials as (here we use Legendre polynomials),

$$R(\eta) = 1 + \sum_{n=0}^{\infty} a_n^{obs} T_n(\eta), \;\; T_n(\eta) = \sqrt{n + \frac{1}{2}} P_n(\eta/Y), \tag{V.1.2}$$

where the $P_0(x) = 1$, $P_1(x) = x$, $P_0(x) = 1/2(3x^2 - 1)$, ... are the Legendre polynomials and Y is the maximum value of the pseudorapidity range considered in the analysis. In the current model study $Y = 6$ is chosen, but in experimental studies the value of Y will be limited by the acceptance of the detector. The new bases $T_n(x)$ are chosen such that their orthogonality and completeness relations are normalized as

$$1/Y \int_{-Y}^{Y} T_n(\eta) T_m(\eta) d\eta = \delta_{nm}, \qquad 1/Y \sum_{n=0}^{\infty} T_n(\eta_1) T_m(\eta_2) = \delta(\eta_1 - \eta_2) \tag{V.1.3}$$

The superscript *obs* is to denote that the coefficients characterize the observed fluctuations in an event. In an event, since the total number of particles are finite, $R(\eta)$ can be different from 1 just from statistical noise. The observed fluctuations thus include both the genuine shape fluctuations and the fluctuations from statistical noise. The statistical fluctuations have to be estimated and subtracted to get the genuine shape fluctuations, and is discussed further below. The Legendre polynomials are chosen as the basis since the first few polynomials correspond to some of the expected shape fluctuations in the pseudorapidity distribution. $T_0(x)$ is constant in pseudorapidity and characterize an overall change in the multiplicity in an event, while the first order term, $T_1(x)$, capture the linear forward-backward fluctuations that could arise from linearly asymmetric sources in pseudorapidity, as in the simple wounded nucleon model presented in II.3.2.2. The second order term $T_2(x)$ reflects modulations with more particles at mid-rapidity and less at forward rapidity, or vice-versa, relative to the average and could arise for example from difference in nuclear stopping event-by-event. All these modulations can get contributions from short-range correlations, which are localized in η and would contribute to all order modulations in the expansion. The bases chosen here differ from that used in [116], where Tschebychev polynomials were used, which have a weight factor of $1/\sqrt{1 - (\eta/Y)^2}$ in the normalization relation that diverges at $\eta = \pm Y$.

In the analysis, the events are first divided into narrow multiplicity classes based on the total multiplicity M in $|\eta| < Y$. The multiplicity of all the events in an event class is required to differ from the average multiplicity in the event class by at most 1%. For each event class, the distributions $\langle N(\eta) \rangle$ are determined which are then used to calculate $R(\eta)$ event-by-event. The coefficients of T_n and their statistical uncertainty are evaluated as

$$a_n^{obs} = \sum_i w_i^n - \delta_n, \quad \delta a_n^{obs} = \sqrt{\sum_i (w_i^n)^2}, \quad w_i^n = \frac{T_n(\eta_i)}{\langle N(\eta_i) \rangle}, \tag{V.1.4}$$

where the sum is over all particles in the event and $\delta_n = 1$ for $n = 0$ and 0 otherwise.

The δa_n^{obs} characterize the statistical fluctuations due to the finite number of particles in the event and can be in principle used to unfold for statistical noise. But a more robust procedure

is used in this study to estimate the statistical fluctuations. For each event with multiplicity M, a random event is generated by sampling from the $\langle N(\eta)\rangle$ distribution M times and the a_n^{ran} values are calculated in a similar way as in Eq. V.1.4. The a_n^{ran} contain only effects from statistical fluctuations. The non-statistical components of the shape fluctuations can be obtained after averaging over many events as

$$\langle a_n a_m\rangle = \langle a_n^{obs} a_m^{obs}\rangle - \langle a_n^{ran} a_m^{ran}\rangle \tag{V.1.5}$$

and particularly for the diagonal terms, the r.m.s values of the coefficients can be obtained as

$$\langle a_n^2\rangle = \left(\langle a_n^{obs}\rangle\right)^2 - \left(\langle a_n^{ran}\rangle\right)^2 \tag{V.1.6}$$

The $\langle a_n a_m\rangle$ values can also be calculated from a two particle correlation function. The two particle correlation function is defined as

$$\begin{aligned} C(\eta_1,\eta_2) &= \frac{\langle N(\eta_1)N(\eta_2)\rangle - \langle N(\eta_1)\rangle\delta(\eta_1-\eta_2)}{\langle N(\eta_1)\rangle\langle N(\eta_2)\rangle} \\ &= \langle R(\eta_1)R(\eta_2)\rangle - \frac{\delta(\eta_1-\eta_2)}{\langle N(\eta_2)\rangle} \end{aligned} \tag{V.1.7}$$

The statistical fluctuations in the particle production at two different pseudorapidity intervals are uncorrelated with each other. The contribution from statistical fluctuations will enter the correlation function only when $\eta_1 = \eta_2$. This contribution is reflected by the second term in Eq. V.1.7, which takes into account the Poisson fluctuations in the case when $\eta_1 = \eta_2$. This statistical contribution can be explicitly evaluated using the random events introduced above, but these are found to be identical to the second term in Eq. V.1.7. The correlation function above can be expanded into an orthonormal basis of 2D Legendre polynomials. Since the $R(\eta)$ from random events contain only statistical fluctuations,

$$\langle R^{ran}(\eta_1)R^{ran}(\eta_2)\rangle = 1 + \frac{\delta(\eta_1-\eta_2)}{\langle N(\eta_2)\rangle} \tag{V.1.8}$$

Using this, Eq. V.1.7 becomes

$$\begin{aligned} C(\eta_1,\eta_2) &= \langle R(\eta_1)R(\eta_2)\rangle + \langle R^{ran}(\eta_1)R^{ran}(\eta_2)\rangle - 1 \\ &= 1 + \sum_{n,m=0}^{\infty}\left(\langle a_n^{obs}a_m^{obs}\rangle - \langle a_n^{ran}a_m^{ran}\rangle\right) T_n(\eta_1)T_m(\eta_2) \\ &= 1 + \sum_{n,m=0}^{\infty}\langle a_n a_m\rangle T_n(\eta_1)T_m(\eta_2) \\ &= 1 + \sum_{n,m=0}^{\infty}\langle a_n a_m\rangle \frac{T_n(\eta_1)T_m(\eta_2) + T_n(\eta_2)T_m(\eta_1)}{2} \end{aligned} \tag{V.1.9}$$

Thus the correlations between the different a_n coefficients in the single particle expansion of the event-by-event (genuine) shape fluctuations can be obtained directly from the two particle correlation function. The last line in Eq. V.1.9 follows from the fact that the correlation function is symmetric under interchange of η_1 and η_2 by construction, i.e $C(\eta_1, \eta_2) = C(\eta_2, \eta_1)$. Also in symmetric collision systems, like Pb+Pb, one also has $C(\eta_1, \eta_2) = C(-\eta_1, -\eta_2)$, leading to $\langle a_n a_{n+1} \rangle = 0$. The other $\langle a_n a_m \rangle$ coefficients can be obtained as

$$\langle a_n a_m \rangle = \frac{1}{Y^2} \int [C(\eta_1, \eta_2) - 1] \frac{T_n(\eta_1) T_m(\eta_2) + T_n(\eta_2) T_m(\eta_1)}{2} d\eta_1 d\eta_2 \tag{V.1.10}$$

The shapes of the first few Legendre bases in 2D are shown in figure V.1.1. They are plot assuming $\langle a_n a_m \rangle = 0.01$.

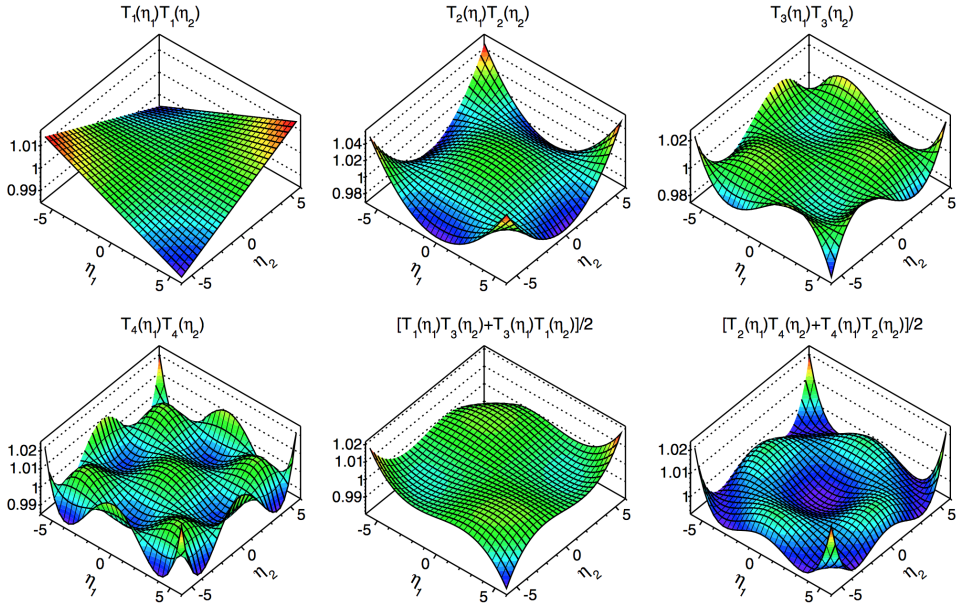

Figure V.1.1: The shapes of the first few bases $T_n(\eta_1)T_m(\eta_2)$, plot assuming $\langle a_n a_m \rangle = 0.01$.

The single particle method can be useful to study the properties of the a_n distributions themselves and also to correlate with other event level observables, particularly initial state parameters in model simulations. But to get the $\langle a_n a_m \rangle$ values, the distributions have to be unfolded for statistical noise. The two particle correlation method on the other hand, can give the $\langle a_n a_m \rangle$ values directly and is also better suited to control the systematic effects from detector acceptance in experiments, as the quantity in the denominator of Eq. V.1.7 can be calculated from mixed events. The two methods are mathematically equivalent and give identical results for $\langle a_n a_m \rangle$ values (see Section V.1.2).

In the expansion of the two particle correlation function, two different contributions can be distinguished. One contribution is from the change in average shape ($\langle N(\eta) \rangle$) with multiplicity

and contributes to non-zero values to the $\langle a_0 a_n \rangle$ coefficients in the expansion. The other set of terms, $\langle a_n a_m \rangle$ with $n, m > 0$, arise from genuine shape fluctuations at a given multiplicity. The $\langle a_0 a_n \rangle$ terms are sensitive to the width of the multiplicity interval used to calculate $\langle N(\eta) \rangle$ in the denominators of Eq. V.1.1 and V.1.7, as a large range for multiplicity fluctuations within an event class will contribute to large values for $\langle a_0 a_n \rangle$. The change in the overall shape of particle distributions in pseudorapidity with multiplicity (or centrality) can be studied separately and measurements of it exist for different systems [42, 118], and it is useful to separate these contributions from the study of the longitudinal correlations. In this study, the focus is on the $\langle a_n a_m \rangle$ terms with $n, m > 0$ that characterize the genuine shape fluctuations at a given multiplicity.

In the analysis, the $\langle a_0 a_n \rangle$ terms can be removed from the correlation function by a simple renormalization, as discussed below. Eq. V.1.9 can be written as

$$C(\eta_1, \eta_2) = 1 + \frac{1}{2}\langle a_0 a_0 \rangle + \frac{1}{\sqrt{2}} \sum_{n=1}^{\infty} \langle a_0 a_n \rangle \left[T_n(\eta_1) + T_n(\eta_2) \right] + \sum_{n,m=1}^{\infty} \langle a_n a_m \rangle \frac{T_n(\eta_1) T_m(\eta_2) + T_n(\eta_2) T_m(\eta_1)}{2}. \tag{V.1.11}$$

The first term, $\langle a_0 a_0 \rangle$, reflects the overall multiplicity fluctuation in the event class and drops out if the correlation function is normalized to have mean value 1. The projections of the correlation function along the η_1 and η_2 directions,

$$C_P(\eta_1) = \frac{\int C(\eta_1, \eta_2) d\eta_2}{2Y}, \quad C_P(\eta_2) = \frac{\int C(\eta_1, \eta_2) d\eta_1}{2Y}, \tag{V.1.12}$$

have contributions only from the $\langle a_0 a_n \rangle T_n(\eta_1)$ term and $\langle a_0 a_n \rangle T_n(\eta_2)$ respectively because of the orthogonality of the T_n. So, to leading order, the $\langle a_0 a_n \rangle$ term in Eq. V.1.11 can be removed by renormalizing the correlation function by the product of projections,

$$C_N(\eta_1, \eta_2) = \frac{C(\eta_1, \eta_2)}{C_P(\eta_1) C_P(\eta_2)}. \tag{V.1.13}$$

$C_N(\eta_1, \eta_2)$ will have contributions only from the genuine shape fluctuations.

$$C_N(\eta_1, \eta_2) = 1 + \sum_{n,m=1}^{\infty} \langle a'_n a'_m \rangle \frac{T_n(\eta_1) T_m(\eta_2) + T_n(\eta_2) T_m(\eta_1)}{2}, \tag{V.1.14}$$

where the new coefficients $\langle a'_n a'_m \rangle$ are given by

$$\langle a'_n a'_m \rangle \approx \langle a_n a_m \rangle - \langle a_0 a_n \rangle \langle a_0 a_m \rangle, \tag{V.1.15}$$

and differ only by a small term, $\langle a_0 a_n \rangle \langle a_0 a_m \rangle$, from the $\langle a_n a_m \rangle$ values.

In practice, if short-range correlations are present, the renormalization as done via Eq. V.1.12, introduces a small bias. The SRC being localized in η, contribute to a peak with finite width in $|\Delta\eta|$ (usually $|\Delta\eta| \sim 1$) along $\eta_1 = \eta_2$, in the correlation function. As a result, near the edges of the acceptance ($\eta \sim \pm Y$) only a fraction (half the $|\Delta\eta|$ width at $\eta = \pm Y$) of the short-range peak is visible and therefore induces an η dependence to the projections (Eq. V.1.12). So the projections

should be defined excluding the contribution from the short-range peak. The bias from this is usually small and depends on the magnitude of the SRC. We don't discuss the details on removing this bias here, but is presented in detail in Subsection V.3.2.2, Chapter V.3 of the thesis.

Figure V.1.2 shows an example of the renormalization procedure. The left panel of the figure shows the correlation function obtained with $\langle N(\eta)\rangle$ defined in narrow multiplicity bins (multiplicity of events vary by at most 1% from the average multiplicity in the event class) while calculating the correlation function, for AMPT events with impact parameter, $b = 8$ fm. The second panel of the figure shows the correlation function for the same events, but using one inclusive bin in multiplicity to calculate $\langle N(\eta)\rangle$. The two correlation functions look markedly different. The third panel shows the contribution from the $a_0 a_n$ terms ($C_P(\eta_1 C_P(\eta_2))$ to the correlation function in the second panel. The fourth panel shows the correlation function from panel two, after the renormalization via Eq. V.1.13. After the renormalization, the correlation function is largely consistent with the case where narrow bin widths were used. Experimentally, this procedure gives a correlation function that is stable against the variations of bin widths used in the analysis.

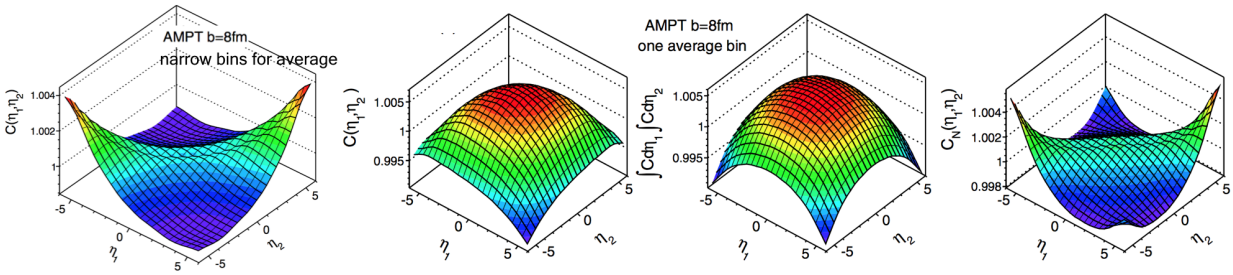

Figure V.1.2: (First panel from left) The $C(\eta_1, \eta_2)$ for AMPT events with $b = 8$ fm calculated using narrow multiplicity bins to define $\langle N(\eta)\rangle$ in Eq. V.1.7. The $C(\eta_1, \eta_2)$ (second panel), the $C_P(\eta_1)C_P(\eta_2)$ (third panel) and the $C_N(\eta_1, \eta_2)$ (fourth panel) for AMPT events with $b = 8$ fm, calculated using one inclusive multiplicity bin to define $\langle N(\eta)\rangle$ in Eq. V.1.7.

V.1.2 Results from study using HIJING and AMPT simulations

The analysis method is utilized to study the longitudinal correlations in the HIJING and AMPT models. HIJING uses a pQCD inspired model for jet production, along with multiple minijets (typically less than transverse energy of 5 GeV) production and a Lund-type model for soft interactions [120]. The hadronization is implemented through a Lund string fragmentation model. The HIJING model thus naturally contains many sources for short and long-range correlations. The AMPT model [45] starts from the partons produced from HIJING, and runs them through a parton transport model. The partons are recombined into hadrons at freezeout and further evolved through a hadronic transport model. The AMPT model has been particularly successful in describing the v_n coefficients associated with the azimuthal anisotropy in A+A and also in p+A collisions, which are usually attributed to final state interactions. Comparing the magnitudes of

the a_n coefficients between HIJING and AMPT models could provide insight into how the longitudinal correlations are influenced by final state interactions and hadronization. (The AMPT events used in this study are generated with the string-melting mode for initial parton production and with a total partonic cross section of 1.5 mb and strong coupling constant $\alpha_s = 0.33$. The setup has been previously used to reproduce the $p_{\rm T}$ spectra and v_n data at RHIC and LHC [46]).

The HIJING and AMPT events are generated for Pb+Pb collisions at $\sqrt{s_{NN}} = 2.76$ TeV. All stable particles with $p_{\rm T} > 0.1$ GeV and $|\eta| < Y = 6$ are used in the analysis. In the default case, narrow bins in multiplicity (with multiplicity of events varying by at most 1% from the average multiplicity in the event class) are used to define $\langle N(\eta)\rangle$ in calculating $R(\eta)$ and the two particle correlation function, $C(\eta_1, \eta_2)$. The analysis is performed using both the single particle and two particle correlation methods, although most results included in this section are from the single particle method.

Figure V.1.3 shows the distributions of a_n^{obs} and a_n^{ran} for n up to 5 for HIJING and AMPT events with $b = 8$ fm. The a_n^{obs} distributions are in general broader than the a_n^{ran} distributions, reflecting the contribution from non statistical a_n from the shape fluctuations. The difference between the two distributions decreases with increase in n. The rate of decrease is faster for AMPT events in which the a_n^{obs} distribution becomes consistent with pure statistical fluctuations for $n = 5$. The r.m.s values of a_n^{obs} and a_n^{ran} along with the r.m.s values of a_n calculated via Eq. V.1.6 are shown in figure V.1.4 as a function of n. The $\sqrt{\langle a_n^2\rangle}$ values decrease with increase in n for both HIJING and AMPT events, and the first order component is the dominant shape fluctuation in both models. Significant values of $\sqrt{\langle a_n^2\rangle}$ are seen for HIJING for all n, while for AMPT, the values become consistent with zero for $n > 5$. The AMPT values are also smaller than the HIJING values. The difference between HIJING and AMPT values could mainly be due to the difference in short-range correlations between HIJING and AMPT. HIJING has much larger short-range correlation than in AMPT (see figure V.1.9). The decrease in a_n and the strength of correlations, particularly SRC, in AMPT could be from the final state interactions (and details of hadronization) in AMPT.

Figure V.1.5 shows the centrality dependence (as a function of $N_{\rm part}$) of the r.m.s a_n values for $n = 1$ to 3 compared between the HIJING and AMPT events. The $\sqrt{\langle a_n\rangle^2}$ values from HIJING are larger than those from AMPT for all the centrality range and for all values of n. The magnitude of the $\sqrt{\langle a_n\rangle^2}$ values decrease towards more central events. The larger values in peripheral events could be expected as the number of sources in peripheral events are small and thus the relative shape fluctuations, larger.

The first order coefficient a_1 is found to be strongly correlated with the asymmetry between the number of forward and backward going participants, $A_{\rm part}$, defined as:

$$A_{\rm part} = \frac{N^F_{\rm part} - N^B_{\rm part}}{N^F_{\rm part} + N^B_{\rm part}}, \tag{V.1.16}$$

where $N^F_{\rm part}$ is the number of participants in the forward going direction and $N^B_{\rm part}$ is the number of participants in the backward going direction. Figure V.1.6 shows the correlation between the event-by-event a_1^{obs} and $A_{\rm part}$ values (left panel). The correlation between higher order a_n^{obs} and

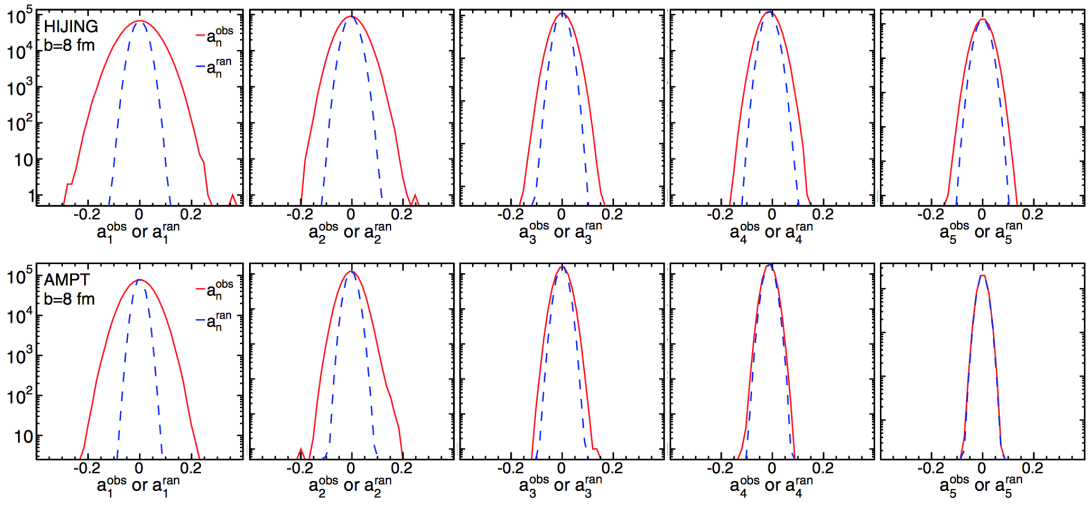

Figure V.1.3: The a_n^{obs} and a_n^{ran} distributions for $n = 1$ to 5 for HIJING events (top panels) and AMPT events (lower panels) with impact parameter $b = 8$ fm.

$A_{\rm part}$ are also shown. The results are shown for HIJING events with fixed impact parameter $b = 8$ fm. The first order coefficient is strongly correlated with the participant asymmetry, a behaviour similar to that predicted by a wounded nucleon model (Subsection II.3.2.2). A small positive correlation is also observed between the third order coefficient and $A_{\rm part}$, suggesting that the multiplicity asymmetry caused by $A_{\rm part}$ has a small nonlinear odd component. On the other hand, no correlation is observed between a_2^{obs}, a rapidity event component, and $A_{\rm part}$, a rapidity odd component, as expected. The width of these distributions are partly from the statistical fluctuations in a_n^{obs}, which in principle can be unfolded, but is not attempted here.

Figure V.1.7 compares the centrality dependence of $\sqrt{\langle a_1^2 \rangle}$ from HIJING and AMPT and $\sqrt{\langle A_{\rm part}^2 \rangle}$. A constant scale factor of 0.7 is applied to the $\sqrt{\langle A_{\rm part}^2 \rangle}$ values to have comparable magnitude with the AMPT values. The similar centrality dependence between the two variables suggest the (linear component of) FB asymmetry in $N(\eta)$ is mostly driven by the asymmetry in number of forward and backward going participants.

The asymmetry in the number of forward and backward going spectators is anti correlated with the participant asymmetry, since, $N_{\rm part}^F - N_{\rm part}^B = -(N_{spec}^F - N_{spec}^B)$, where N_{spec}^F and N_{spec}^B are the number of spectator nucleons in the forward and backward going directions respectively. Therefore, the a_1^{obs} values should be anti-correlated with the spectator asymmetry. The event-by-event number of spectators in the forward and backward going directions is accessible in heavy-ion experiments. Most experiments at RHIC and LHC have a dedicated Zero Degree Calorimeter (ZDC or similar modules) that can detect the spectator neutrons from the collision. However the measured number of neutrons in ZDC constitutes only a fraction of the total number of spectators and so the correlation would be more smeared out and weaker. Taking into account the efficiency of the ZDC in detecting the number of neutrons (and thus the spectators) and

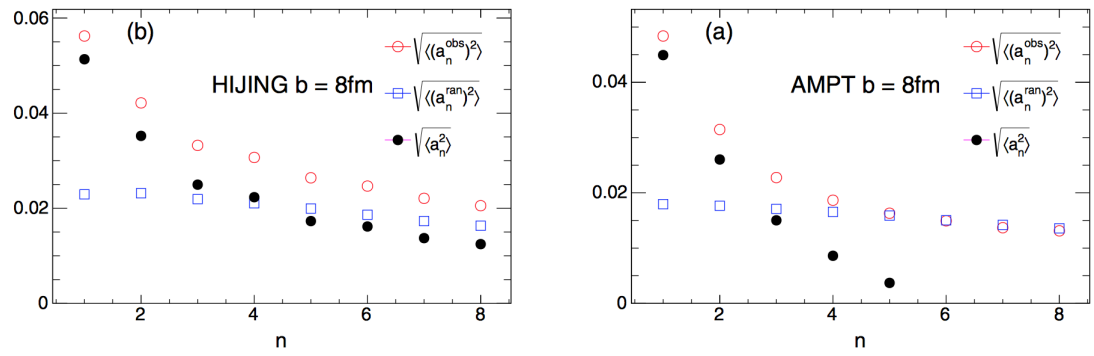

Figure V.1.4: The $\sqrt{\langle a_n^{obs}\rangle^2}$, $\sqrt{\langle a_n^{ran}\rangle^2}$ and $\sqrt{\langle a_n\rangle^2}$ values as a function of n for HIJING events (left) and AMPT events (right) with $b = 8$ fm.

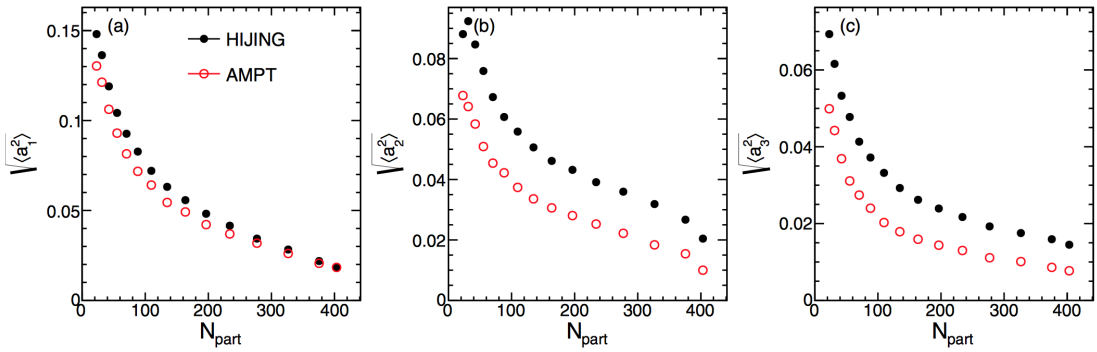

Figure V.1.5: The $\sqrt{\langle a_n\rangle^2}$ values as a function of the number of participants, $N_{\rm part}$ for $n = 1$, 2, 3 for HIJING and AMPT events.

assuming similar magnitude of FB asymmetry signal in data as in the AMPT model, it has been argued that the correlation between a_1^{obs} and spectator asymmetry can be measured in heavy-ion collisions [205], and if so, could provide a data-driven way to understand the origin of the FB multiplicity fluctuations.

Figure V.1.8 shows the two particle correlation function $C(\eta_1, \eta_2)$ from AMPT events at b = 8 fm. The correlation function shows a depletion when the pseudorapidity difference between the two particles, $|\Delta\eta| = |\eta_1 - \eta_2|$, is large. This is expected since the shape fluctuations are dominated by an a_1 modulation (see figure V.1.1). As the pseudorapidity difference $|\Delta\eta|$ decreases the correlation function starts to show a sharp increase for $|\Delta\eta| \lesssim 1.5$ that extends along the diagonal region with $\eta_1 = \eta_2$. This reflects the contribution from short-range correlations like resonance decays, fragmentation, correlations during hadronization etc. A small dip can also be seen on top of the short-range peak, suggesting a depletion of pairs with very small $\Delta\eta$. But this could be a feature of the specific final state correlations that are present in AMPT as such a dip is not seen in two particle correlations from HIJING events.

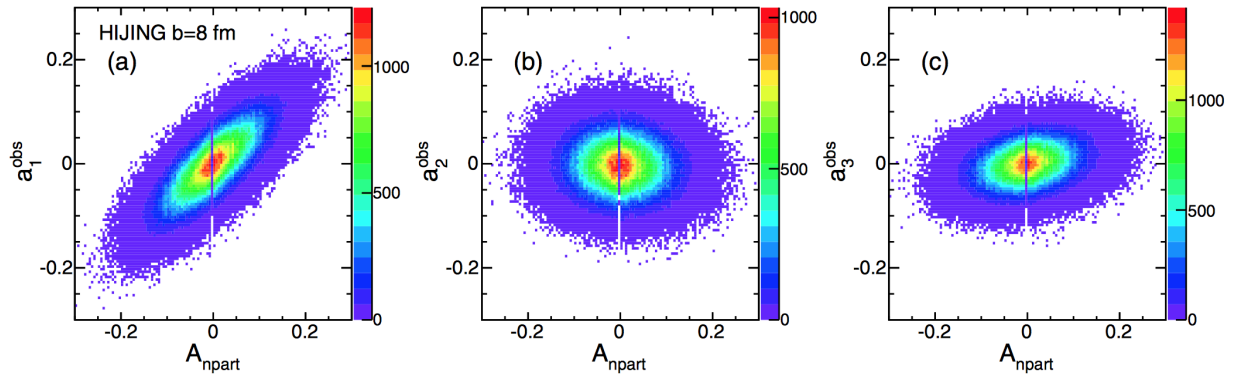

Figure V.1.6: The correlation between a_n^{obs} and the participant asymmetry, $A_{\rm part}$ for $n = 1$, 2 and 3 for HIJING events with impact parameter $b = 8$ fm.

The figure also shows a comparison between the $\langle a_n a_m \rangle$ values obtained using the two particle correlation method (Eq. V.1.9) and the single particle method (Eq. V.1.5). The first 9 diagonal terms and terms of the form $\langle a_n a_{n+2} \rangle$ and $\langle a_n a_{n+4} \rangle$ are shown for $n \leq 9$. TH values from the two methods are almost identical with each other, as expected, since the two methods are mathematically consistent.

Figure V.1.9 compares the renormalized correlation function, $C_N(\eta_1, \eta_2)$, between the AMPT and HIJING models. The correlation strength is much larger in HIJING than in the AMPT model. Most of the difference in strength is in fact in the small $|\Delta\eta|$ region where contribution from SRC is large. The short-range correlation in HIJING is much larger than in AMPT, which could suggest that the final state interactions reduce the short-range correlations in the system. The difference could also be due to the differences in the ways by which the freeze-out and hadronization are implemented in the models. The small dip in the very small $|\Delta\eta|$ region seen in AMPT events is not present in HIJING events, which again could reflect the difference in final state effects implemented in the models.

The two particle correlations can also be used to study the charge correlations in the system. The correlation function cane be constructed by requiring the two particles in the pair to have opposite charges or same charges. Due to local charge conservation, the short-range correlation between positive and negative charges is expected to be larger than the correlation between same charged pairs or inclusive charged particle correlation. Indeed, it was found in AMPT and HIJING models that $\langle a_n^+ a_n^- \rangle > \langle a_n^2 \rangle > \langle a_n^+ a_n^+ \rangle = \langle a_n^- a_n^- \rangle$. Figure V.1.10 shows the two particle correlation function, $C_N(\eta_1, \eta_2)$, from AMPT events for opposite charged pairs and same charged pairs. The correlation strength, particularly in small $|\Delta\eta|$ region is larger in opposite charged pairs than in same charged pairs. Also the small dip around $|\Delta\eta| \sim 0$ is more prominent in the same charged combination. Similar results were observed for HIJING, the correlation in small $|\Delta\eta|$ region is larger for opposite than same charged pairs, although the dip around $|\Delta\eta| \sim 0$ is not seen for either charge combination. This suggests that the final state interactions and hadronization mechanism play a significant role in determining the correlation in the small $|\Delta\eta|$ region. Since the long-range

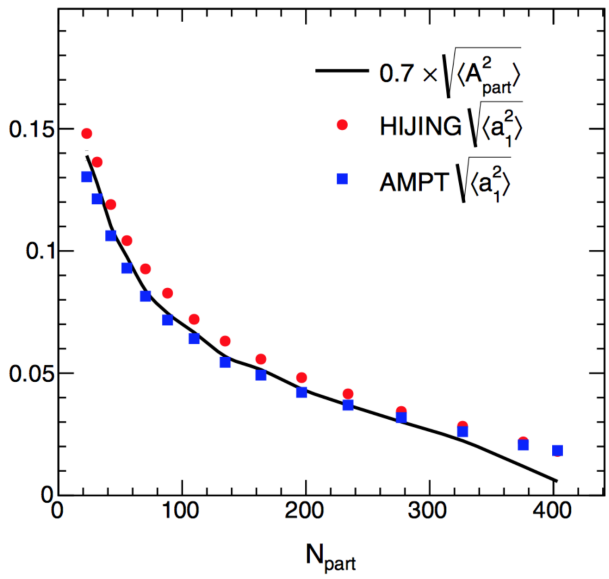

Figure V.1.7: The centrality dependence (as function of $N_{\rm part}$) of $\sqrt{\langle a_1^2\rangle}$ from HIJING and AMPT events compared with the centrality dependence of $\sqrt{\langle A_{\rm part}^2\rangle}$. The $\sqrt{\langle A_{\rm part}^2\rangle}$ values are scaled down by a constant factor of 0.7 to be comparable to the values from AMPT.

correlations are independent of charge combination, as they arise from initial state effects, studying the ratio of opposite to same charged correlation functions can help isolate and understand the features of the SRC (see Chapter V.3) for more details).

V.1.3 Summary

This chapter has presented a systematic way to study the longitudinal correlations and event-by-event shape fluctuations in the longitudinal particle distributions in high energy nuclear collisions. The correlations can arise from the fluctuations in the initial particle producing sources and the non-uniform particle emission profile in pseudorapidity from the individual sources as well as final state correlations from resonance decays, fragmentation and hadronization etc. The event-by-event particle distributions relative to the average distribution in an event class is expanded in an orthonormal basis (a basis of slightly modified Legendre polynomials are chosen in this study) and the coefficients in the expansion, a_n are studied. The r.m.s values of a_n and the correlations between the coefficients, $\langle a_n a_m\rangle$ can be studied using a single particle method or a two particle correlation method, both of which give equivalent results. The methods are utilized to study the correlations in HIJING and AMPT models.

The AMPT and HIJING models show non-zero values for $\langle\sqrt{a_n^2}\rangle$ for first several values of n. In both models, the first order coefficient $\langle\sqrt{a_1^2}\rangle$ is the largest in magnitude and the magnitude of the higher order coefficients decrease with increase in n. The rate of decrease in AMPT is

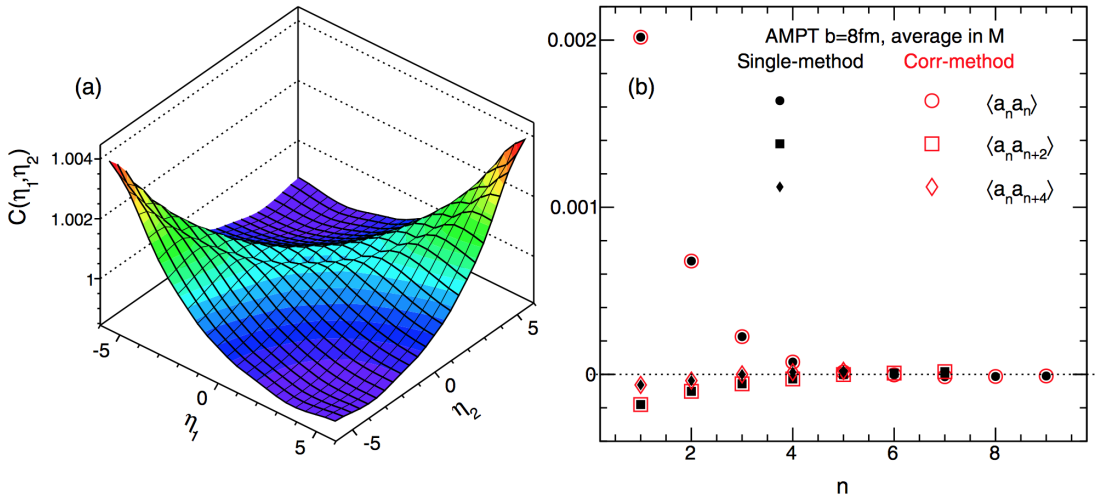

Figure V.1.8: (Left) The two particle correlation function $C(\eta_1, \eta_2)$, and (right) comparison between the $\langle a_n a_m \rangle$ values from the two particle correlation method (Eq. V.1.9) and the single particle method (Eq. V.1.5), for AMPT events with $b = 8$ fm.

faster than in HIJING and the values become consistent with zero for $n > 5$ for AMPT, while they remain non-zero in the case of HIJING. The $\langle\sqrt{a_1^2}\rangle$ values are found to be larger in HIJING than in AMPT, possibly due to the final state interactions present in AMPT, and the values are found to increase from peripheral to central collisions in both models. Event-by-event, the first order coefficient, a_1^{obs}, is found to be strongly correlated with the asymmetry in the number of forward and backward going participants, $A_{\rm part}$, suggesting that the forward-backward asymmetry in particle production is driven by the asymmetry in the number of participants. In heavy-ion collisions, studying the correlation between a_1^{obs} and the asymmetry in the number of spectator neutrons measured in ZDC can help understand and test for a similar model of origin for the FB fluctuations in $N(\eta)$. The centrality dependence of $\langle\sqrt{a_1^2}\rangle$ is also found to be similar to the centrality dependence of $\langle\sqrt{A_{\rm part}^2}\rangle$, up to a constant scale factor. The two-particle correlations in the large $|\Delta\eta|$ region shows a depletion consistent with the presence of a dominant a_1 component, while in the small $|\Delta\eta|$ region, shows a sharp enhancement from the short-range correlations. The correlation strength in the short-range region is much larger in HIJING than in the AMPT model.

The two particle correlation method is particularly suited for experimental studies. The correlations in the entire two particle pseudorpaidity phase space can be studied and also the detector non uniformities and acceptance effects can be removed using the familiar mixed event technique. Two particle correlations can also be constructed using the two particles in the pair belonging to opposite or same charges and can help understand the features of the short-range correlations. The two-particle correlations can also be constructed using particles from different $p_{\rm T}$ ranges or from different species, which can further help to understand particle production and hadronization mechanisms in heavy-ion collisions. The study of the longitudinal correlations thus promises to be

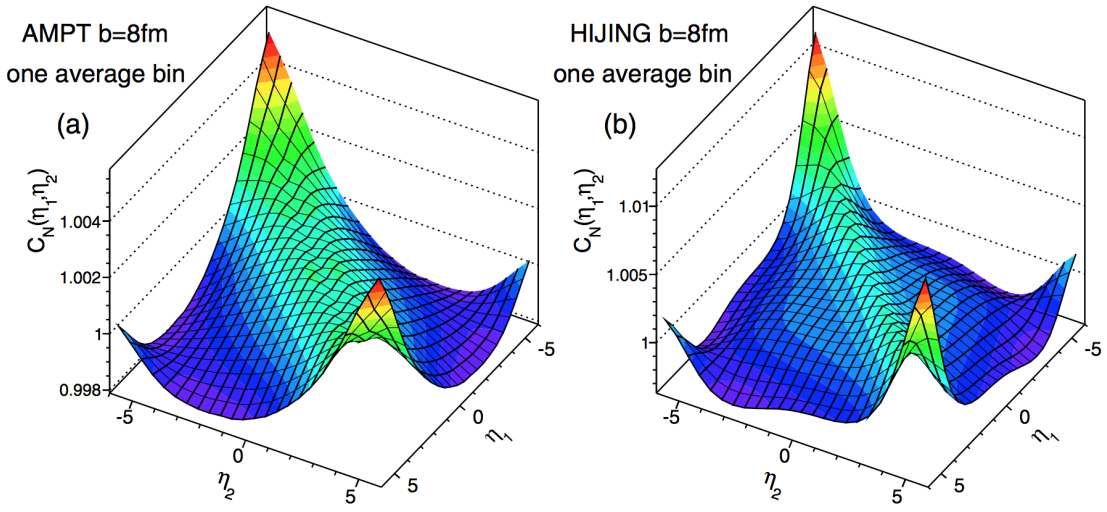

Figure V.1.9: The two particle correlation function, $C_N(\eta_1, \eta_2)$, from the AMPT (left) and HIJING (right) events with impact parameter $b =$ fm.

of much potential in understanding the early time and late time dynamics in heavy-ion collisions.

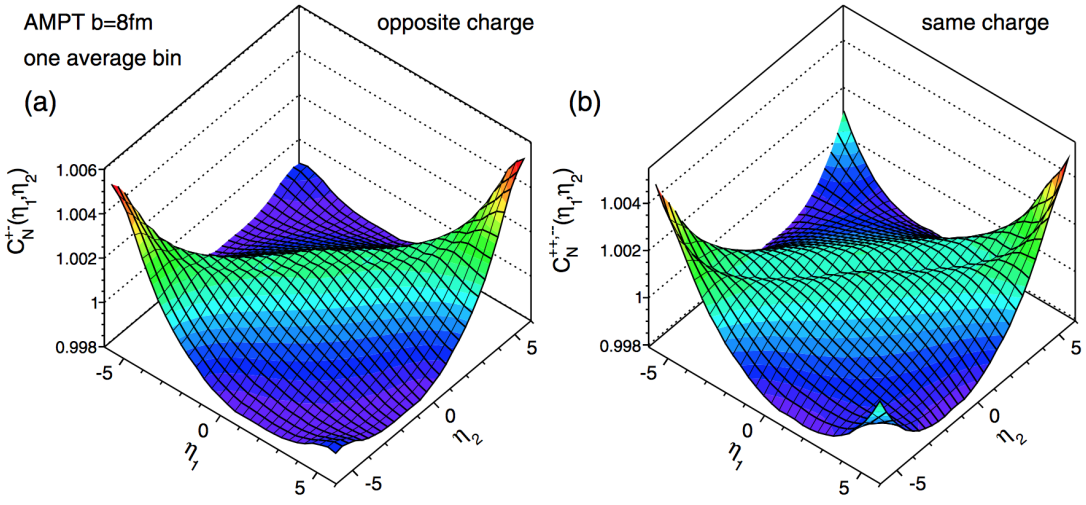

Figure V.1.10: The two particle correlation function, $C_N(\eta_1, \eta_2)$, for opposite charged pairs (left) and same charged pairs (right) from AMPT events with $b = 8$ fm.

Chapter V.2

Measurement of longitudinal correlations in $\sqrt{s_{NN}} = 2.76$ TeV Pb+Pb collisions at the LHC using ATLAS detector

The two particle correlation method presented in Chapter V.1 are applied to study the longitudinal correlations in Pb+Pb collisions at $\sqrt{s_{NN}} = 2.76$ TeV at the LHC, using the ATLAS detector. The two particle correlation functions $C_N(\eta_1, \eta_2)$ are constructed using charged particle tracks reconstructed in the Inner Detector. The correlation functions are constructed for different centrality intervals and their features are studied in detail using the projections of the correlation function. The first several Legendre coefficients, a_n, associated with the two particle correlations are calculated and the values are compared to the centrality dependence of $A_{\rm part}$ values from Glauber model and also to the a_n values from the HIJING model. The detailed set of results corresponding to the study presented in this Chapter can be found at [206].

This chapter presents the details of this measurement. The chapter is organized as follows. The details of event and track selection are presented in Section V.2.1. Section V.2.2 discusses the construction of the two particle correlations and the extraction of the Legendre coefficients from it. A summary of the systematic uncertainties in the measurement are presented in Section V.2.3, while details of the evaluation of systematic uncertainties are relegated to Appendix B.1. The results from the analysis are summarized in Section V.2.4. The chapter ends with a summary in Section V.2.5.

V.2.1 Event and track selections

The analysis is based on approximately 7 μb^{-1} of Pb+Pb data at $\sqrt{s_{NN}} = 2.76$ TeV collected by the ATLAS during the Pb+Pb run in 2010 at the LHC. The analysis uses the reconstructed charged particle tracks from the ATLAS Inner Detector to construct the correlation functions.

The total energy measured in the forward calorimeters is used to class the events into different centrality classes and the information from the ZDC, MBTS and the trigger systems are used to do event selection and to reject non-collision backgrounds.

Event selection

The offline event selection requires the events to have a reconstructed primary vertex with z-coordinate, $|z_{vtx}| < 100$ mm, from the nominal center of the ATLAS detector. The events are required to pass the triggers which require at least one hit on either side of the MBTS detector. A time difference of $\Delta t < 3$ ns between the MBTS trigger counters on either side of the interaction point is required to suppress non-collision backgrounds. The events are also required to have signal above the single neutron detection threshold on the ZDCs on either side which helps reject a variety of background process while maintaining high efficiency for inelastic processes.

The events are divided into the different centrality classes [42] based on the total transverse energy ($\sum E_T$) measured in the ATLAS FCal over the pseudorapidity range $3.2 < |\eta| < 4.9$ at the electromagnetic scale [207]. After all the trigger and event selection requirements, the fraction of the total inelastic cross section sampled is estimated to be 98±2%. The uncertainties in the centrality determination is evaluated by varying the effects of trigger and event selection efficiencies and varying the background rejection requirements for the most peripheral events [42]. The analysis uses events divided into a set of 5% percentile bins. The 0-5% bin is the most central bin where the collisions are nearly head on. The average number of participants, $N_{\rm part}$, in each centrality bin is evaluated from a Monte Carlo Glauber analysis [42, 43]. These $N_{\rm part}$ values for the different centrality bins are summarized in Table V.2.1

Table V.2.1: The list of centrality intervals and associated values of the average number of participating nucleons $N_{\rm part}$ and the associated systematic uncertainties used in this analysis, taken from Ref.

Centrality	0–5%	5–10%	10–15%	15–20%	20–25%	25–30%	30–35%	35–40%	40–45%
$N_{\rm part}$	382 ± 2	330 ± 3	282 ± 4	240 ± 4	203 ± 4	170 ± 4	142 ± 4	117 ± 4	95 ± 4
Centrality	45–50%	50–55%	55–60%	60–65%	65–70%	70–75%	75–80%	80–85%	85–90%
$N_{\rm part}$	76 ± 4	60 ± 3	46 ± 3	35 ± 3	25 ± 2	18 ± 2	12 ± 2	8.2 ± 1.2	5.4 ± 0.8

Track selection and tracking efficiency

The tracks used in the analysis to construct correlation functions are required to have $p_{\rm T} > 0.4$ GeV and $|\eta| < 2.4$. The track selection requirements used are same as those used in previous flow analyses using the same Pb+Pb data [4, 195]. The tracks are required to have at least nine hits in the silicon detectors with no missing Pixel hit and a maximum of one missing hit in the SCT. The point of closest approach of the tracks to the position of primary vertex is required to be within 1 mm of the primary vertex in both transverse and longitudinal directions. The track reconstruction efficiency and the performance of the track reconstruction for different track selection cuts are evaluated using HIJING (version 1.38b) events. The response of the detector is simulated using

GEANT4 and the resulting events are reconstructed using the same algorithm as that used for the data.

The tracking efficiency is defined as the fraction of the primary charged particles in the HIJING events, reconstructed after evolving through the detector simulation and selected by the track selection requirements. The tracking efficiency as a function of p_{T} increases by ∼7% between 0.5 and 0.8 GeV and varies only weakly for $pT > 0.8$ GeV. The efficiency shows a stronger dependence on the pseudorapidity and multiplicity. In peripheral events, for $p_{\mathrm{T}} > 0.8$ GeV, it ranges from 72% at $\eta \approx 0$ to about 57% for $|\eta| > 2$. This variation in central event classes is from 72% at $\eta \approx 0$ to about 42% for $|\eta| > 2$. As the position of the collision z_{vtx} changes, the regions of the detector the tracks with a given η sees and thus the tracking efficiency varies slightly. So the tracking efficiencies are evaluated separately for events in different z_{vtx} intervals, in steps of 10 mm. Figure V.2.1 shows the tracking efficiency evaluated in 0-5% most central events, as a function of η and z_{vtx} in few different p_{T} selections.

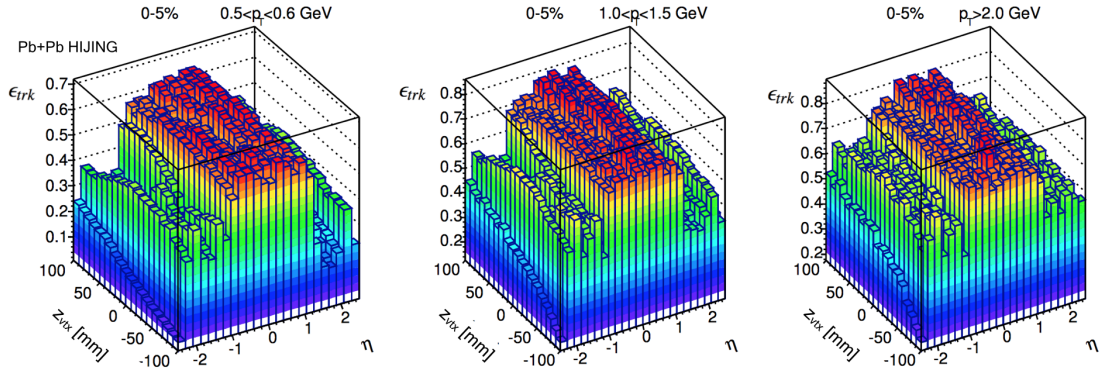

Figure V.2.1: The tracking efficiency ϵ_{trk} for 0-5% most central Pb+Pb events at $\sqrt{s_{NN}} = 2.76$ TeV at the ATLAS detector as a function of η and the z_{vtx} position in few different p_{T} bins.

V.2.2 Analysis procedure

V.2.2.1 Two particle correlation function

The analysis uses the two particle correlation method presented in Chapter V.2.1 and [205]. The maximum range for η_1 and η_2 values used in the analysis is $Y = 2.4$. The two particle correlation functions (Eq. V.1.7) are calculated for each 5% centrality interval using charged particle tracks with $p_{\mathrm{T}} > 0.5$ GeV. The two particle correlations are constructed as the ratio of the pair distribution from the same events (foreground), $S(\eta_1, \eta_2) = \langle N(\eta_1, \eta_2)\rangle - \delta(\eta_1 - \eta_2)\langle N(\eta_2)\rangle$, where the two tracks in the pair comes from the same event, to that of the pair distribution from mixed events (background), $B(\eta_1, \eta_2) = \langle N(\eta_1)\rangle\langle N(\eta_2)\rangle$, where the two tracks in the pair are taken from two

different events:

$$C(\eta_1, \eta_2) = \frac{S(\eta_1, \eta_2)}{B(\eta_1, \eta_2)} \tag{V.2.1}$$

The mixed event distributions are constructed by selecting for each foreground event, another event with similar centrality, by requiring them to have FCal $\sum E_{\mathrm{T}}$ matched within 0.5% and matched in z_{vtx} (within 2.5 mm), so that the detector features in the same event distributions are properly accounted for in the mixed event distributions. The events also also required to be close together in time to avoid possible time dependent fluctuations in the detector conditions. The mixed event distributions capture most of the contributions from detector inefficiencies and acceptance effects. Nevertheless, the pairs are weighted by the inverse of their tracking efficiencies, $1/\epsilon_1\epsilon_2$, while filling the $S(\eta_1, \eta_2)$ and $B(\eta_1, \eta_2)$ distributions, in order to correct for individual inefficiencies of the particles in the pair. The correlation function, $C(\eta_1, \eta_2)$, is normalized to have a value of 1 when averaged over the (η_1, η_2) phase space. By construction, the correlation function has the symmetry, $C(\eta_1, \eta_2) = C(\eta_2, \eta_1)$. Also since the collision system is symmetric, there also the symmetry requirement that, $C(\eta_1, \eta_2) = C(-\eta_1, -\eta_2)$. As a result, to enhance the statistics, all pairs are filled into one quadrant defined with $\eta_1 - \eta_2 > 0$ and $\eta_1 + \eta_2 > 0$, and then reflected to the other quadrants.

The shape of the single particle distribution, $\langle N(\eta) \rangle$, varies with multiplicity (or centrality) in Pb+Pb collisions [42]. Therefore, if bins with large range in multiplicity are used to match the events used for mixing, it can lead to non zero values for terms of the form $\langle a_0 a_n \rangle$ in the correlation function, in a similar way as explained in Section V.1.1. These modulations are sometimes referred to as "residual centrality dependence" in this chapter, and can be removed by renormalizing the correlation functions by the product of projections along η_1 and η_2 via Eq. V.1.13. The renormalized correlation function, $C_N(\eta_1, \eta_2)$, is also normalized to have value of 1 when averaged over the (η_1, η_2) phase space. $C_N(\eta_1, \eta_2)$ also satisfies the two symmetry conditions,

$$C_N(\eta_1, \eta_2) = C_N(\eta_2, \eta_1), \quad C_N(\eta_1, \eta_2) = C_N(-\eta_1, -\eta_2) \tag{V.2.2}$$

The $C_N(\eta_1, \eta_2)$ function does not contain terms from residual centrality dependence and should be stable regardless of the extend of multiplicity fluctuations in the bins used to do the event-mixing. To illustrate this, mixed event distributions are constructed using events matched in the charged particle multiplicity, $N_{\mathrm{ch}}^{\mathrm{rec}}$ (instead of FCal$\sum E_{\mathrm{T}}$), defined as the total number of charged particle tracks in the ID with $p_{\mathrm{T}} > 0.5$ GeV. The events used for mixing are required to be from the same $N_{\mathrm{ch}}^{\mathrm{rec}}$ bin, where each bin is defined to contain 0.5% of the total statistics. The other matching requirements on z_{vtx} and time are kept the same. The events in the same $N_{\mathrm{ch}}^{\mathrm{rec}}$ class have much smaller range of multiplicity fluctuations than the events in the FCal$\sum E_{\mathrm{T}}$ class (from the smearing between the two variables [58]). As a result the terms from the residual centrality dependence should be much smaller in the correlation function defined using the mixed events from $N_{\mathrm{ch}}^{\mathrm{rec}}$ mixing. The left panels of figure V.2.2 show the correlation functions $C(\eta_1, \eta_2)$, constructed using the two mixing schemes. The shapes of the two correlation functions show marked difference, due to the presence of the $\langle a_0 a_n \rangle$ terms. The renormalized correlation function, $C_N(\eta_1, \eta_2)$, are shown in the right panels of the same figure and it can be seen that after renormalization, the two correlation functions are consistent with each other. The renormalized correlation functions are

closer to the $C(\eta_1, \eta_2)$ from the case with $N_{\rm ch}^{\rm rec}$ mixing. The differences in the correlation function and results from using these two different mixing schemes are included as a systematic uncertainty in the measurements.

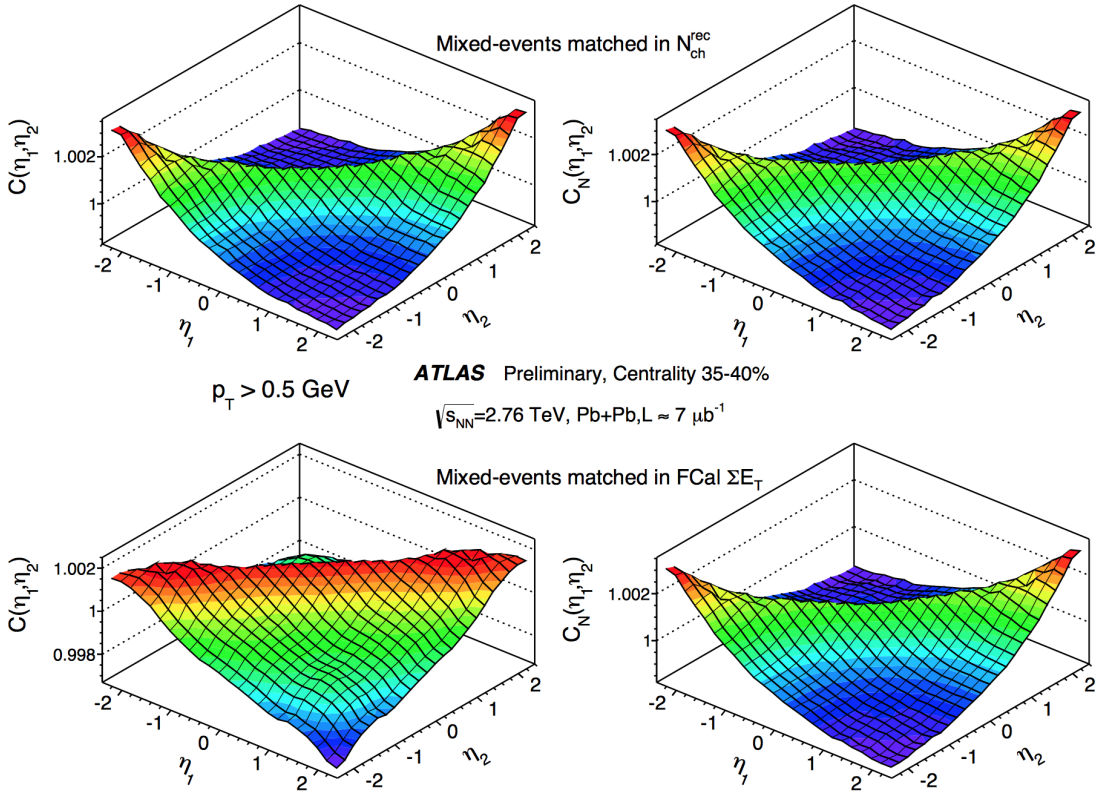

Figure V.2.2: The correlation functions $C(\eta_1, \eta_2)$ (left panels) and the renormalized correlation functions $C_N(\eta_1, \eta_2)$, constructed using mixed events matched in narrow FCal$\sum E_{\rm T}$ bins (lower panels) and narrow $N_{\rm ch}^{\rm rec}$ bins (top panels)

As discussed in Section V.1.1, the $C_N(\eta_1, \eta_2)$ defined using Eq. V.1.13 carries a small bias from the presence of short-range correlations. This induces a small bias in the shape in the long-range region (see Subsection V.3.2.2), but does not affect the values of the $\sqrt{\langle a_n \rangle^2}$ calculated (the short-range correlations themselves do contribute to $\sqrt{\langle a_n \rangle^2}$ though). The analysis presented in this chapter does not correct for this bias. However, a method to correct for it can be found in Subsection V.3.2.2.

V.2.2.2 Extraction of Legendre coefficients

The two particle correlations can directly give the r.m.s values and the correlations between the a_n coefficients by expanding the $C_N(\eta_1, \eta_2)$ in a 2D orthonormal basis of (slightly modified) Legendre polynomials, $T_i(\eta/Y)$. The $\langle a_n a_m \rangle$ values are calculated from $C_N(\eta_1, \eta_2)$ using Eq. V.1.10. The

results are presented after taking the square root, as $\sqrt{\langle a_n a_m \rangle}$, since for $n = m$, this gives the r.m.s value of the different order fluctuations. Because of the symmetry conditions (Eq. V.2.2), the correlation between the even and odd coefficients in the expansion should be zero, i.e $\langle a_n a_{n+1} \rangle = 0$. The other coefficients are studied as function of the centrality. The shapes of the base functions in 2D are shown in figure V.1.1. The first base function is proportional to $\eta_1 \eta_2$ and characterizes the linear asymmetry in FB multiplicity production.

The correlation function can be approximated, in the case where the first order term a_1 is dominating, as

$$C_N(\eta_1, \eta_2) \approx 1 + \langle a_1^2 \rangle \frac{3}{2Y^2} \eta_1 \eta_2 \tag{V.2.3}$$

This expression can be written in terms of two new variables, $\eta_+ = \eta_1 + \eta_2$ and $\eta_- = \eta_+ - \eta_- = \Delta\eta$,

$$C_N(\eta_+, \eta_-) \approx 1 + \langle a_1^2 \rangle \frac{3}{8Y^2} (\eta_+^2 - \eta_-^2) = 1 + 0.065 \langle a_1^2 \rangle (\eta_+^2 - \eta_-^2) \tag{V.2.4}$$

As a function of the η_+ and η_- variables, the correlation function is expected to show a quadratic shape, a positive quadratic dependence along η_+ and a negative quadratic dependence along η_-. Therefore, if a_1 is dominating, the magnitude of $\langle a_1^2 \rangle$ can be obtained by projecting the correlation function along the η_+ at different slices of η_- and fitting with a quadratic function. In principle, a similar projection and a negative quadratic fit can be done along the η_- direction, but due to strong dependence of the short-range correlations of the η_- variable, the long-range quadratic dependence may not be apparent. In this analysis, the $\langle a_1^2 \rangle$ values are also extracted using projections along the η_+ direction and compared with the values from the Legendre expansion.

V.2.3 Systematic uncertainties

The systematic uncertainties in this analysis come from varying the criteria for event mixing, uncertainties from track reconstruction efficiency, pair acceptance effects and consistency of correlation function at the generated and reconstructed levels using MC events reconstructed with the detector geometry. A natural way to quantify the systematic uncertainties is to calculate the correlation function, $C_N(\eta_1, \eta_2)$, for each systematic variation and then construct the ratio of this to the $C_N(\eta_1, \eta_2)$ from the default case. The ratio is denoted by $d(\eta_1, \eta_2)$. Since both $C_N(\eta_1, \eta_2)$ and $d(\eta_1, \eta_2)$ are small modulations around 1, the deviations from unity of $d(\eta_1, \eta_2)$ can be directly compared to the magnitude of the correlation signal to estimate the systematic uncertainty. The $d(\eta_1, \eta_2)$ may also be expanded in a Legendre basis and the coefficients $\langle a_m^r a_n^r \rangle$ can be used to determine the systematic uncertainties for the Legendre coefficients. The summary of the systematic uncertainties from each of the different sources are described below. A detailed presentation of the evaluation of systematic uncertainties from the different sources can be found in Appendix B.1.

The mixed event distributions are used to remove the contributions from detector geometry to the correlation functions. The stability of this procedure can be evaluated by varying the criteria for matching events used for constructing the mixed event distributions. The stability of the results from varying the event matching requirement on centrality is studied by comparing the results from matching events using FCal$\sum E_{\mathrm{T}}$ and $N_{\mathrm{ch}}^{\mathrm{rec}}$. In both cases, the bin size in $N_{\mathrm{ch}}^{\mathrm{rec}}$ or Fcal$\sum E_{\mathrm{T}}$ are

varied such that the fraction of the total statistics in each bin varies from 0.3% to 1%. Most of the variation from changing the event matching criteria appear as $\langle a_0 a_n \rangle$ ("residual centrality dependence") terms and are removed by the renormalization and the $C_N(\eta_1, \eta_2)$ functions remain quite stable. The maximum variation in $C_N(\eta_1, \eta_2)$ from varying the bin widths and from varying the variable used for centrality matching is found to be 2% of the correlation signal and the $\sqrt{\langle a_n^2 \rangle}$ values are found to vary between 0.5-8%. The impact of z_{vtx} matching is evaluated by doubling the bin width in z_{vtx} used for selecting matched events. The maximum variation from this is on the correlation function is found to be less than 3% of the signal and $1-7$% variation for the $\sqrt{\langle a_n^2 \rangle}$ values.

The stability of the correlation function against time dependent fluctuations of detector conditions is evaluated by dividing the dataset into 17 subgroups, ordered in time, and calculating the correlation function and Legendre coefficients for each case. The results are found to be consistent within 2-3% for the correlation signal and within $0.5-7$% for the first few largest Legendre coefficients. The correlation functions are also evaluated separately for events with $|z_{vtx}| < 50$ mm and for events with $50 < |z_{vtx}| < 100$ mm, as events with different z_{vtx} positions would see slightly different parts of the detector for the same η. Good consistency, within 3% is seen for the correlation signal and variations of about $1-9$% for the first few largest Legendre coefficients.

The results are not very sensitive to the tracking efficiency correction, as the corrections are applied to both the numerator and denominator in Eq. V.2.1. However, both the signal and efficiency are found to increase slightly with $p_{\rm T}$ and so the correlation signal is expected to be slightly smaller when efficiency correction is applied. Indeed, applying the efficiency correction is found to reduce the $\sqrt{\langle a_n^2 \rangle}$ values by a few percentage. But this entire variation is not quoted as the systematic uncertainty. The systematic uncertainty associated with tracking efficiency correction is evaluated by varying the track selection cuts, determining the efficiency for these cuts using MC, and then recalculating the correlation functions with the new cuts and tracking efficiency. This uncertainty is found to be less than 4% for $\sqrt{\langle a_1^2 \rangle}$ and 7% for $\sqrt{\langle a_2^2 \rangle}$ and $\sqrt{\langle a_3^2 \rangle}$ in central collisions, and less than 2% in mid-central and peripheral collisions.

The tracking efficiency is also found to depend slightly on the relative position of the two tracks due to track splitting (one particle incorrectly reconstructed as two tracks) and track merging (reconstructing tracks from two particle as one). These effects happen at small $\Delta\eta, \Delta\phi$, ($|\Delta\eta| \lesssim 0.02$, $|\Delta\phi| \lesssim 0.1$) and are reasonably described in HIJING reconstructed with the detector simulation. The uncertainty from this is evaluated by calculating the correlation functions by excluding pairs with $|\Delta\eta| < 0.02$ in the same event and mixed event distributions. The variation is less than 1% for $\sqrt{\langle a_n^2 \rangle}$ values in most cases, but increases to $1-7$% in most central collisions.

The magnitudes of the coefficients $\langle a_n a_m \rangle$ decrease with increasing values of n and m and the higher order coefficients capture more short-range correlations. The magnitudes of the coefficients with $n, m \geq 10$ are found to show non-statistical fluctuations around zero. As these fluctuating higher order coefficients could reflect some shorter range correlations from residual detector effects, their average spread is also included as a source of systematic uncertainty, and is quoted as the uncertainty from "pair acceptance" in the tables below.

The HIJING events show nonzero values for the correlation signal and the Legendre coefficients. The correlation functions and the coefficients can be calculated in the HIJING model using the

generated particle and also using the reconstructed tracks, after evolving the generated events through the detector geometry and reconstructing the tracks. Good consistency is seen in general between the values at the generated and reconstructed levels. The maximum difference observed was about 9% for $\sqrt{\langle a_1^2 \rangle}$ in mid-central collisions and 5% for $\sqrt{\langle a_2^2 \rangle}$ and $\sqrt{\langle a_3^2 \rangle}$.

Table V.2.2 and V.2.3 summarizes the systematic uncertainties from the different sources in the correlation function and the first few Legendre coefficients respectively, for a few centrality intervals. The ranges quotes usually covers the maximum uncertainty in a given centrality interval. The uncertainties from the different sources are added together in quadrature to give the combined systematic uncertainties for the measurements.

Centrality	0–20%	20-40%	40–60%	60–90%
Event-mixing [%]	2–4	1–2	0.5–1.0	0.7–1.4
Run-by-run stability [%]	2–3	1–2	0.9	1–1.5
z_{vtx} variation [%]	1.5–3	1–1.6	0.9	1.0
Track selection& efficiency [%]	1.4–2.8	0.5–1	0.4	0.4–0.8
Pair cuts [%]	0.8–2	0.4–0.8	<0.3	<0.2
Simulation consistency [%]	3–5	1.5–3	1–1.5	1–1.5
Total [%]	5.5–8.5	2.5–4	2	2–3.5

Table V.2.2: Summary of average systematic uncertainties for $C_N(\eta_1, \eta_2)$. The uncertainty is calculated as the variations (in $d(\eta_1, \eta_2)$), averaged over the entire η_1 and η_2 space relative to the observed strength of the correlation signal defined as the difference between the maximum and minimum.

V.2.4 Results

V.2.4.1 Two particle correlations

Figure V.2.3 shows the two particle correlation function, $C_N(\eta_1, \eta_2)$, for different centrality intervals. The overall features of the correlation function look qualitatively similar to that seen in HIJING and AMPT (figure V.1.9). The long-range (large $|\Delta\eta|$, $|\Delta\eta| > 2$) region shows a depletion, which is consistent with the shape resulting from a large a_1 modulation. The other dominant feature in the correlation function is the peak in the short-range (small $|\Delta\eta|$, $|\Delta\eta| < 1.5$) region arising from short-range correlations in the system. The magnitude of the correlation function, and of the short-range peak, increase from central to peripheral collisions.

The features of the correlation function can be better studied by projecting the correlation function along the two variables $\eta_- = \eta_1 - \eta_2$ and $\eta_+ = \eta_1 + \eta_2$, as discussed in Subsection V.2.2.1. The correlation function is expressed in terms of the new variables to give $C_N(\eta_+, \eta_-)$. Projections of the correlation function are then made along η_+ (η_-) in different narrow slices of η_- (η_+), to give the 1D functions $C_N(\eta_+)$ ($C_N(\eta_-)$). The traditional FB correlation analyses ([19, 20]) studies the $C_N(\eta_-)$ for a fixed η_+ slice with $\eta_+ = 0$. This analysis, on the other hand, provides a more detailed measurement in the full two particle (η_1, η_2) phase space.

	Uncertainty in $\sqrt{\langle a_1^2\rangle}$				$\sqrt{\langle a_2^2\rangle}$			
Centrality	0–20%	20-40%	40–60%	60–90%	0–20%	20-40%	40–60%	60–90%
Event-mixing [%]	1.5–3	1–1.5	1	1–4	4–7	2.5–3.7	1.6–2.3	1–4
Run-by-run stability [%]	0.7–1.6	0.7–1	0.5	0.5–1.5	2–3	1–2	1.0	1–3
z_{vtx} variation [%]	0.5–1.5	0.5–1.3	0.8	0.5–1.0	1–6	1–4	1–2.2	1
Track selec.& efficiency[%]	1.6–4.3	0.6–1.1	0.5	0.5	1–6	1	1	1–2
Pair cuts [%]	0.4–1	0.5	<0.2	<0.2	0.4–2	0.5	<0.2	<0.2
Pair acceptance [%]	1.4–1.8	0.7–1.2	0.5–0.7	0.2–0.5	4–5.5	2–3.5	1.3–2.0	0.4–1.3
Simulation consistency [%]	2–10	4–7	1–1.6	3–8	2–5	2–4	1–3	2–10
Total [%]	4–11	4–8	2	3–9	8.5–10	4–6	3–5	3–10
	Uncertainty in $\sqrt{\langle a_3^2\rangle}$				$\sqrt{-\langle a_1 a_3\rangle}$			
Centrality	0–20%	20-40%	40–60%	60–90%	0–20%	20-40%	40–60%	60–90%
Event-mixing [%]	8–12	4.3–7.6	2.4–3.4	1–4	1–1.6	1	0.7–1	1–4
Run-by-run stability [%]	4–7	3–5	2–2.5	2–5	3–6	2–4	3–4	3–6
z_{vtx} variation [%]	3–9	2–5	1–4	1–3	3–5	3–4	2–3	1–2
Track selec.& efficiency [%]	2–7	1–2	1	1	1.5–7	1–2	1–2	1–3
Pair cuts [%]	1–7	0.5–1	<0.5	<0.5	3–5	1–3	0.5 –1	<0.5
Pair acceptance [%]	8.5–12	3.5–7	2–3.6	0.6–2.1	7.3–10.5	5–8.5	3.5–5.5	1.4–4
Simulation consistency [%]	1.6–4	1–5	2–3	2–10	3–7	1–4	1–6	2–7
Total [%]	13–18	6–12	3.5–6.5	4–11	11–14	7–10	5–8	5–11

Table V.2.3: Summary of systematic uncertainties in percent for $\sqrt{\langle a_1^2\rangle}$, $\sqrt{\langle a_2^2\rangle}$, $\sqrt{\langle a_3^2\rangle}$ and $\sqrt{-\langle a_1 a_3\rangle}$.

Figure V.2.4 shows the projections of the correlation function along η_-, for different η_+ slices. The $C_N(\eta_-)$ values show a peak around $\eta_- \sim 0$ and the magnitude of the peak increase with increase in η_+. The $C_N(\eta_-)$ values show a sharp decrease with increase in η_- for $|\eta_-| < 1$ and a weaker decrease thereafter. The initial sharp decrease is due to the dominance of short-range correlations which are mostly centered around $|\eta_-| \sim 0$. The weaker decrease at large $\Delta\eta$ could be from the negative quadratic term ($\propto -\eta^2$) arising from a dominant a_1 modulation.

The projections of the correlation function along η_+, $C_N(\eta_+)$, are shown in figure V.2.5 for different narrow η_- slices. The $C_N(\eta_+)$ values show a clear quadratic dependence on η_+ for all the different η_- slices. This is consistent with the η_+^2 dependence in the case of dominating a_1 modulation (Eq. V.2.4). The values from different η_- slices seem to differ only by a constant pedestal, including in the short-range region. This could be expected if the short-range correlations have a weak dependence on η_+. Also shown in the figure are fits, motivated by Eq. V.2.4, to the $C_N(\eta_+)$ values with the function

$$C_N(\eta_+) = 1 + 0.065\sqrt{\langle a_1^2\rangle_{\rm Fit}}\eta_+^2 + b \qquad \text{(V.2.5)}$$

The fits using Eq. V.2.5 describes the $C_N(\eta_+)$ values quite well. The extracted $\sqrt{\langle a_1^2\rangle_{\rm Fit}}$ values from the fits, as a function of the η_- slice used are shown in figure V.2.6. The fits are performed

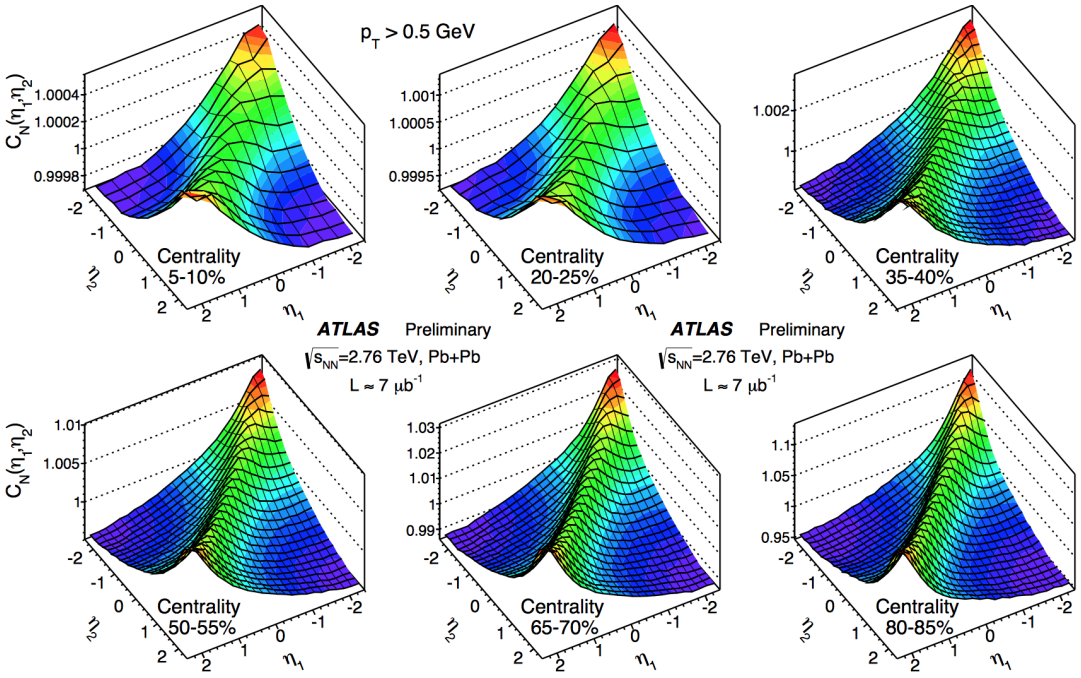

Figure V.2.3: The two particle correlation function, $C_N(\eta_1, \eta_2)$, for charged particle tracks with $p_{\rm T} > 0.5$ GeV, calculated in different 5% centrality intervals for Pb+Pb collisions at $\sqrt{s_{NN}} = 2.76$ TeV.

only in the slices with at least 5 points. For the 0-40% centrality range, the $\sqrt{\langle a_1^2 \rangle_{\rm Fit}}$ are found to increase slightly with $|\eta_-|$ for $|\eta_-| < 1.5$ and then remain consistent with each other. For the higher centrality ranges, the $\sqrt{\langle a_1^2 \rangle_{\rm Fit}}$ values are found to have a weak dependence on $|\eta_-|$. The general weak dependence of $\sqrt{\langle a_1^2 \rangle_{\rm Fit}}$ on $|\eta_-|$ suggests that most of the contribution to these values are from the a_1 modulation and that the values are relatively less sensitive to the short-range correlations. The magnitudes of the extracted $\sqrt{\langle a_1^2 \rangle_{\rm Fit}}$ values are also found to increase from central to peripheral event classes.

V.2.4.2 Coefficients from the Legendre expansion

Figure V.2.7 shows the first few largest Legendre coefficients extracted from the correlation function using Eq. V.1.15. The $\sqrt{\langle a_n^2 \rangle}$ values decrease with increase in n and is largest for $n = 1$. The rate of decrease with increase in n is faster than that seen in HIJING and smaller than that in AMPT (figure V.1.4), for comparable centrality interval. The magnitudes of the coefficients increase from central to peripheral collisions. Non zero values are seen also for mixed terms, $\sqrt{\langle a_n a_m \rangle}$. The most significant group of the mixed coefficients were found to be $\sqrt{\langle a_n a_{n+2} \rangle}$ and are also shown in the figure. The $\sqrt{\langle a_n a_{n+2} \rangle}$ values are found to be negative, or anticorrelated with each other.

The centrality dependence, as a function of $N_{\rm part}$, of $\sqrt{\langle a_1^2 \rangle}$, $\sqrt{\langle a_2^2 \rangle}$, $\sqrt{\langle a_3^2 \rangle}$ and $\sqrt{-\langle a_1 a_3 \rangle}$ are

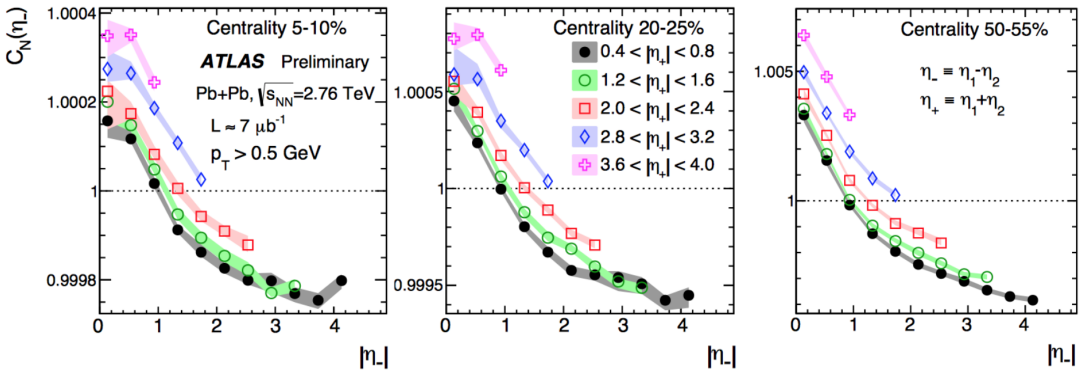

Figure V.2.4: The projections of the correlation function along η_-, $C_N(\eta_-)$, as a function of $|\eta_-|$ for different η_+ slices, for Pb+Pb events with $\sqrt{s_{NN}} = 2.76$ TeV, in a few centrality intervals. The shaded bands are total uncertainties.

shown in figure V.2.8. All coefficients increase towards peripheral collisions. The increase could be contributed by the increase in both short-range and long-range contributions, the magnitude of the short-range peak as well as the fluctuations in the initial particle producing sources increase towards peripheral collisions. The values are also compared to the corresponding coefficients from the HIJING model. The values from HIJING are larger than that from the data for all the coefficients.

Figure V.2.9 compares the $\sqrt{\langle a_1^2 \rangle}$ values obtained directly from the correlation function, using Eq. V.1.15, with the $\sqrt{\langle a_1^2 \rangle_{\rm Fit}}$ values from the fits to $C_N(\eta_+)$ in different $|\eta_-|$ slices. The values from the fit are 2−20% smaller than that from the calculation from the correlation function. This could be because the short-range correlations contribute directly in the Legendre expansion while the projections are less sensitive to it (except for a small bias introduced by the renormalization as discussed earlier, and in further detail in Subsection V.3.2.2). The $\sqrt{\langle a_1^2 \rangle}$ values are also compared to the r.m.s of the participant asymmetry, $A_{\rm part}$, from the Glauber model. The centrality dependence of $\sqrt{\langle A_{\rm part}^2 \rangle}$ shows similar qualitative behavior, larger in peripheral events and decreasing towards central events, as that of the $\sqrt{\langle a_1^2 \rangle}$ values. The centrality dependence of the two agree quite well over a broad range of centrality. Some deviations can be seen between the centrality dependence of $\sqrt{\langle a_1^2 \rangle}$ and $\sqrt{\langle A_{\rm part}^2 \rangle}$, in the peripheral and most central event classes. This could be from additional sources of fluctuations becoming important in these regions.

V.2.5 Summary

The measurement of the two particle pseudorapidity correlation function and the associated Legendre harmonics in $\sqrt{s_{NN}} = 2.76$ TeV Pb+Pb collisions have been presented. The correlation functions are constructed using charged particle pairs with $p_{\rm T} > 0.5$ GeV and with $|\eta| < 2.4$ in

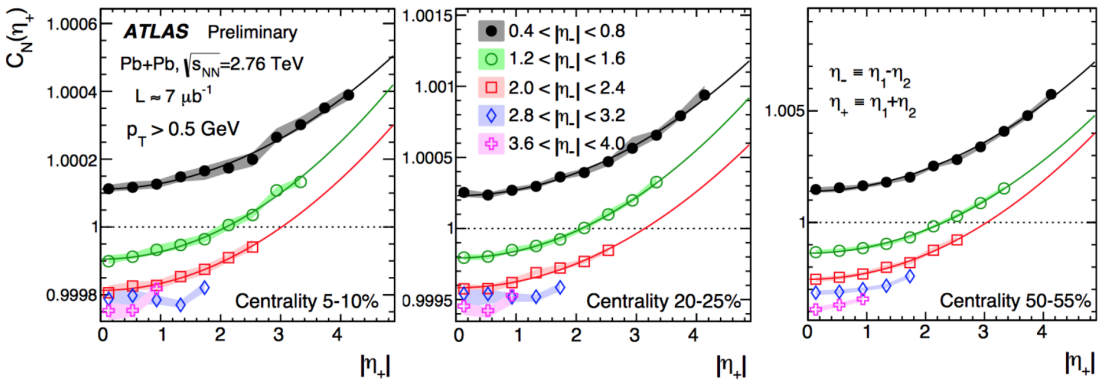

Figure V.2.5: The projections of the correlation function along η_+, $C_N(\eta_+)$, as a function of $|\eta_+|$ for different η_- slices, for Pb+Pb events with $\sqrt{s_{NN}} = 2.76$ TeV, in a few centrality intervals. The shaded bands are total uncertainties.

different 5% centrality intervals. The genuine shape fluctuations at a given multiplicity, captured by $C_N(\eta_1, \eta_2)$, are found to be quite stable against variations of tracking efficiency and event mixing requirements, thereby making the values viable for direct comparison with model calculations. The correlation functions show a depletion in the large $|\Delta\eta|$ region with $\eta_1 \sim -\eta 2$, and a strong quadratic dependence along the η_+ direction, both consistent with the contribution from a dominant a_1 modulation. The correlation function also shows a sharp peak along the $\eta_1 \sim \eta_2$ direction, which reflects the contribution from short-range correlations like jets, resonance decays, fragmentation etc.

The features of the correlation function are further studied by projecting the correlation function along the η_- and η_+ directions. A negative (positive) quadratic dependence is expected along the η_- (η_+) direction, if the a_1 component is dominating. Along the η_- direction, this dependence is not obvious, as the short-range correlations have a very strong dependence on the η_- variable. But the projections along the η_+ direction shows a clear positive quadratic dependence for all η_- slices used for projection, including in the short-range region. This quadratic dependence is fit with a second order polynomial function to extract the $\sqrt{\langle a_1^2 \rangle_{\rm Fit}}$ values as function of the η_- slice. The magnitude of the $\sqrt{\langle a_1^2 \rangle_{\rm Fit}}$ values is found to have weak dependence on η_-, suggesting the short-range correlations contribute mostly to the pedestal in the projections, and not to the quadratic term.

The Legendre coefficients are also obtained by expanding the $C_N(\eta_1, \eta_2)$ in the 2D Legendre basis. The first order coefficient, $\sqrt{\langle a_1^2 \rangle}$, is found to be the largest and the magnitude of the $\sqrt{\langle a_n^2 \rangle}$ terms are found to decrease with increase in n. The rate of decrease with n is found to be larger than in HIJING, but slower than in AMPT and since the higher order terms are more sensitive to the short-range correlations, suggest that the short-range correlations from final state effects are stronger in data than in AMPT, but smaller than that in HIJING. Non zero negative values or anticorrelation are observed for terms of the form $\langle a_n a_{n+2} \rangle$. The magnitude of the coefficients are found to decrease from peripheral to central collisions and the magnitudes of each coefficient are

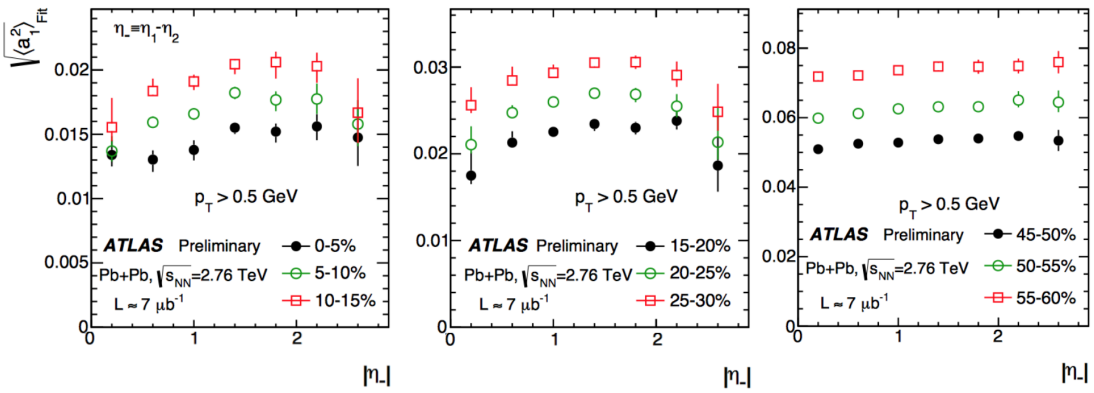

Figure V.2.6: The $\sqrt{\langle a_1^2\rangle_{\rm Fit}}$ values from fits using Eq. V.2.5 to the $C_N(\eta_+)$ values, shown as a function of the η_- slice used for projection, for Pb+Pb events at $\sqrt{s_{NN}} = 2.76$ TeV. The error bars are total uncertainties.

found to be smaller than that of the corresponding terms in HIJING.

The $\sqrt{\langle a_1^2\rangle}$ values and the $\sqrt{\langle a_1^2\rangle_{\rm Fit}}$ values are compared as a function of centrality. The $\sqrt{\langle a_1^2\rangle_{\rm Fit}}$ values are found to be 2−20% smaller than the $\sqrt{\langle a_1^2\rangle}$ values depending on centrality. This could be because the short-range correlations contribute directly to the values extracted from the Legendre expansion, while the values from the fits to projection are less sensitive to the short-range correlations. The overall centrality dependence of the $\sqrt{\langle a_1^2\rangle}$ values agree with the centrality dependence of the participant asymmetry, $\sqrt{\langle A_{\rm part}^2\rangle}$, particularly in the mid-central collisions. This could suggest that the participant asymmetry is driving the FB multiplicity fluctuations. However, as the $\sqrt{\langle a_n^2\rangle}$ also get contribution from short-range correlations, an estimation and subtraction of short-range correlations are required to have a clear understanding of the nature of the event-by-event shape fluctuations and the magnitudes of the long-range components.. It is not attempted for the measurements in Pb+Pb presented in this chapter and is left for future studies. However, the estimation of the SRC and separation of the SRC and LRC are performed for the analysis presented in the next chapter, which focuses on the correlations in small systems.

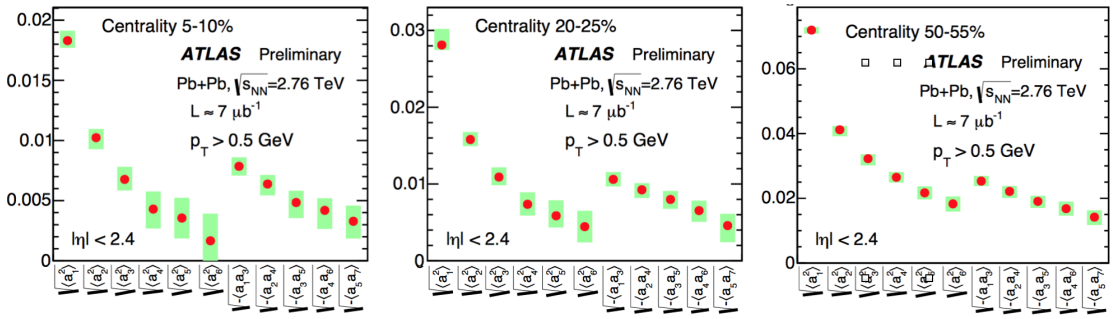

Figure V.2.7: The first few largest Legendre coefficients $\sqrt{\langle a_n a_m \rangle}$ for Pb+Pb events with $\sqrt{s_{NN}} = 2.76$ TeV, in different centrality intervals. The values for $\sqrt{\langle a_n^2 \rangle}$ for $n = 1{-}6$, and for $\sqrt{\langle a_n a_{n+2} \rangle}$ for $n = 1{-}5$ are shown. The shaded bands are total uncertainties.

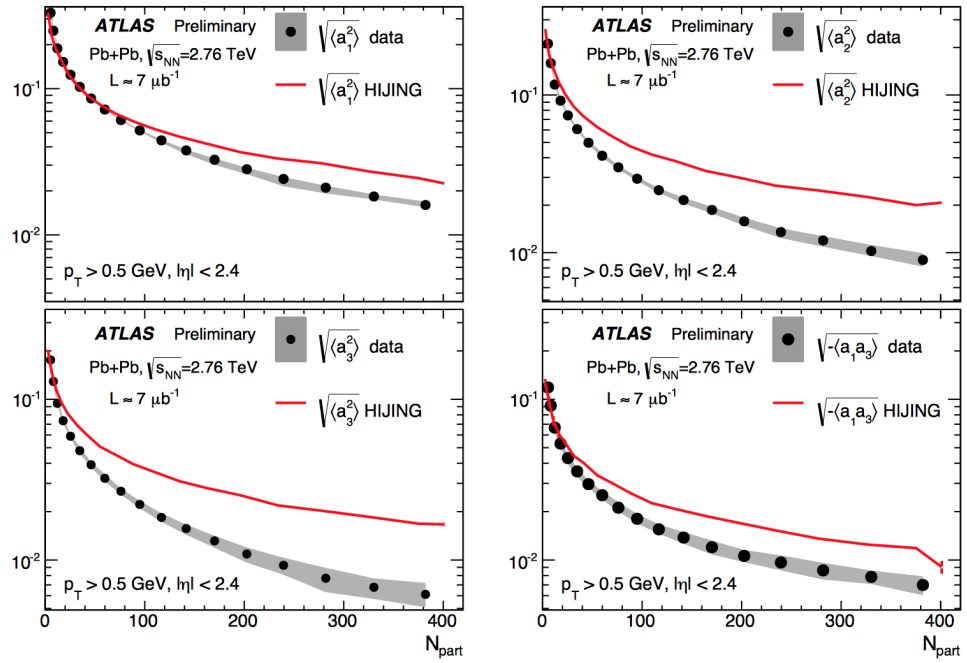

Figure V.2.8: The centrality dependence (as a function of N_{part}) of $\sqrt{\langle a_1^2 \rangle}$, $\sqrt{\langle a_2^2 \rangle}$, $\sqrt{\langle a_3^2 \rangle}$ and $\sqrt{-\langle a_1 a_3 \rangle}$ for Pb+Pb events with $\sqrt{s_{NN}} = 2.76$ TeV. The shaded bands are total uncertainties. The values are compared to the values of the corresponding terms from HIJING.

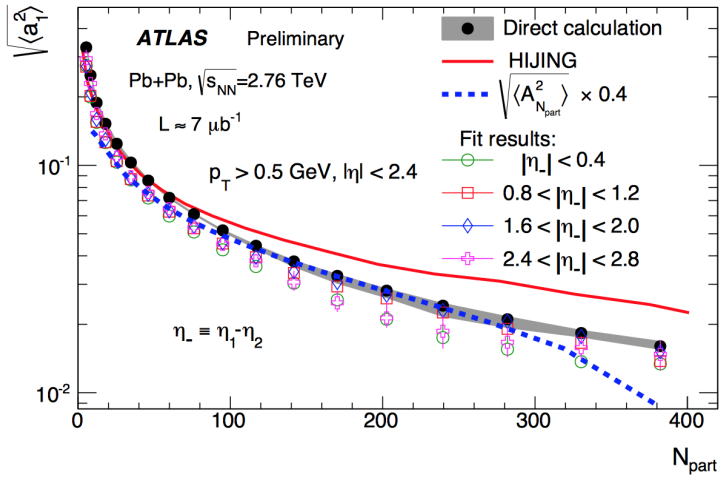

Figure V.2.9: The $\sqrt{\langle a_1^2 \rangle}$ values from Legendre expansion compared with the $\sqrt{\langle a_1^2 \rangle_{\rm Fit}}$ values from fits to $C_N(\eta+)$ in different η_- slices, as a function of the number of participants, $N_{\rm part}$. The $\sqrt{\langle A^2_{\rm part} \rangle}$ values from Glauber model and the $\sqrt{\langle a_1^2 \rangle}$ values from HIJING are also shown. The error bars or shaded bands are total uncertainties

Chapter V.3

Measurement of longitudinal correlations in p+p, p+Pb and peripheral Pb+Pb collisions at the LHC using ATLAS detector

The studies presented so far have looked at the two particle longitudinal correlations in the A+A collisions. In models, the event by event FB multiplicity asymmetry is strongly correlated with the participant asymmetry. The similar centrality dependence of the first order coefficient and the participant asymmetry in data may also suggest a similar correlation in the data. However, once you go to smaller collision systems like p+Pb or p+p, the wounded nucleon model may no longer be a useful model to describe the particle production or its fluctuations. The exact nature of particle production sources or their fluctuations, particularly in high multiplicity collisions still remain unclear. Studying the pseudorapidity correlations in the small systems like p+p and p+Pb and comparing them to the correlations in peripheral Pb+Pb can provide further understanding into the nature of particle production in the small collision systems.

Additionally, the high multiplicity events in p+Pb and p+p have shown azimuthal correlations that are long-range in pseudorapidity. The origin of these correlations, particularly in p+p collisions, are still a matter of debate [94]. The measurements of longitudinal correlations complement the ridge measurements by providing information on the long-range correlations in total multiplicity production. Also the multiplicity correlation measurements help understand the initial conditions and nature of particle production in the longitudinal direction. These can help provide further insights into the origin of the ridge correlations as well.

The two particle pseudorapidity correlation functions have contributions from both short-range and long-range components. The short-range correlations can be quite different for different collisions systems, it has been observed that similar multiplicity p+Pb events show a larger short-range correlation signal than Pb+Pb events with comparable multiplicity [100]. A meaningful comparison of the long-range multiplicity correlations in the three systems requires that an estimation

of the short-range correlation contributions to the correlation function be made. In this analysis, a data driven approach is attempted to separate the short- and long-range contributions to the correlation function and to study their multiplicity and collision system dependence.

This chapter will present the measurement of longitudinal multiplicity correlations in peripheral Pb+Pb collisions with $\sqrt{s_{NN}}$ = 2.76 TeV, p+Pb collisions with $\sqrt{s_{NN}}$ = 5.02 TeV and p+p collisions at $\sqrt{s_{NN}}$ = 13 TeV, using data recorded by the ATLAS detector. The two particle pseudorapidity correlations, the estimated SRC and LRC and the Legendre coefficients associated with the LRC will be compared across the three systems in bins of similar multiplicity. More details on the analysis and the results presented in the Chapter can be found here [208].

The chapter is organized as follows. Section V.3.1 describes the event and track selections used for the analysis. The details of the analysis procedure including the estimation and subtraction of the short-range contribution are presented in Section V.3.2. A summary of the systematic uncertainties are presented in Section V.3.3, while the detailed estimation of uncertainties are relegated to Appendix B.2. Section V.3.4 presents the major results from the analysis and the chapter concludes with a summary in Section V.3.5.

V.3.1 Event and track selection

V.3.1.1 Datasets and event selection

The datasets used in this analysis come from three different runs at the LHC. The Pb+Pb data at $\sqrt{s_{NN}}$ = 2.76 TeV comes from the 2010 Pb+Pb run at the LHC and has approximately 7μb^{-1} of data recorded by the ATLAS detector, and corresponds to the same dataset used in Chapter V.2. The p+Pb data corresponds to the same dataset used in the analysis in Chapter IV.2, from the 2013 p+Pb run at the LHC at $\sqrt{s_{NN}}$ = 5.02 TeV (proton beams were configured at 4 TeV and Pb beams at 1.57 TeV per-nucleon). The p+Pb dataset corresponds to an integrated luminosity of 28 nb^{-1}. The p+p data used were collected during a low-luminosity (low pileup) operation of the LHC in June and August of 2015 at $\sqrt{s_{NN}}$ = 13 TeV and has an integrated luminosity of 65 nb^{-1}.

The p+p and p+Pb runs listed above had several high multiplicity triggers (HMT) that enabled to enhance the statistics of events with large multiplicity. The HMT were implemented using the ATLAS L1 and High Level Trigger (HLT) systems. The HMT uses an algorithm similar to the offline track reconstruction algorithm to reconstruct the tracks in an event online, to calculate the total number of tracks ($N_{\rm trk}^{\rm HLT}$) with $p_{\rm T} > 0.4$ GeV associated to the primary vertex, and the events having $N_{\rm trk}^{\rm HLT}$ larger than predefined thresholds are selected. The Pb+Pb data used in the analysis are collected using a minimum bias (MB) trigger, while the p+Pb and p+p data use events collected by both MB and HMT triggers.

The MB trigger for the Pb+Pb collisions requires at least one hit on either side of the MBTS and also a coincidence (signal above threshold for single neutron peak) between the ZDCs on the two sides. The MB triggers for p+Pb data are same as those listed in Chapter IV.2, trigger that requires at least one hit on both sides of the MBTS along with a timing cut on the MBTS signals to reduce non collision background at HLT or trigger that requires a hit above threshold on the ZDC

on the Pb-fragmenting side. The MB trigger for p+p requires at least one hit on either side of the MBTS, along with a timing cut on the MBTS signals to reduce non collision background at HLT. The HMT triggers used for the p+Pb analysis are the same as those used for the ridge analysis in Chapter IV.2 (Subsection IV.2.1.2). They require the events to have a minimum threshold for the total transverse energy in the forward calorimeters and threshold on $N_{\rm trk}^{\rm HLT}$ at HLT. The p+p data used includes events triggered by two HMT triggers. The first trigger requires at least one hit on both sides of the MBTS at L1 and have at least 900 SCT space points hits and $N_{\rm trk}^{\rm HLT}$ greater than 60 at the HLT. The second trigger selects events with more than 10 GeV of total transverse energy at L1 and have at least 1400 SCT space point hits and $N_{\rm trk}^{\rm HLT}$ greater than 90 at the HLT. More details of the MB and HMT triggers in p+p and p+Pb can be found in references [209, 210] and [183, 180] respectively.

The offline event selection for Pb+Pb events require the events to have a reconstructed vertex and the z coordinate of the vertex to be within 100 mm. The events are also required to have a time difference of less than 3 ns between the signals on the two sides of the MBTS detector to minimize non-collision backgrounds. The p+Pb and p+p events are also required to have a reconstructed vertex with $|z_{vtx}| < 100$ mm. The p+Pb events are required to have a time difference of less than 10 ns between the signals on the two sides of the MBTS detector. The mean number of collisions per bunch crossing, μ, for the p+Pb data is around 0.03 and between 0.002 and 0.04 for p+p data from June 2015 and between 0.05 and 0.6 for the p+p data from August 2015. The pileup events in p+Pb data are rejected using the same cuts used for the ridge analysis, as given in Chapter IV.2. Events with more than one good reconstructed vertex or energy on the ZDC above a threshold beyond the saturation peak from neutrons are rejected. The pileup in the p+p data is minimized by rejecting events with at least two reconstructed vertices each having at least four tracks associated to them. The impact of the residual pileup in the p+p data sample is evaluated by comparing the results from the two different run periods from June and August, which have quite different μ values. The offline event selections for the three datasets used are same as those used in other correlation analyses done using these datasets [4, 180, 210].

V.3.1.2 Track selection and tracking efficiency

The track reconstruction algorithm and offline track selection cuts for the different datasets were optimized for the detector performance during RUN1 and RUN2 at the LHC. The offline track selection cuts used in the analysis for the p+Pb and p+p datasets are the same as those used for the ridge analyses in p+Pb and p+p [180, 210], respectively. The Pb+Pb data from 2010 for peripheral events (more than ∼50% centrality) were reconstructed using the same reconstruction algorithm as used for the reconstruction of the p+Pb data, in order to have better comparison between the two datasets for correlation analyses, including the study of the ridge. The same track selection cuts as used for the track selection in p+Pb are also used for the track selection in the peripheral Pb+Pb data sample.

The tracks used in the analysis are required to have at least $p_{\rm T} > 0.2$ GeV. The track selection cuts for the p+Pb and Pb+Pb analyses require the tracks to have at least one hit on the Pixel detector, with a hit in the B-Layer if expected, and at least 4 SCT hits for tracks with $0.2 < p_{\rm T} <$

0.3 GeV and at least 6 SCT hits for tracks with $p_{\mathrm{T}} > 0.3$ GeV. The tracks are also required to have a significance (ratio relative to the standard deviation) of less than 3 for the transverse (d_0) and longitudinal ($z_0 sin(\theta)$) impact parameters. The track selection cuts for the p+p data are optimized for the presence of the IBL in RUN2. For p+p data, the tracks are required to have a hit in the IBL, if expected, at least 1 hit on the Pixel detector, and at least 4 SCT hits for tracks with $0.2 < p_{\mathrm{T}} < 0.3$ GeV and at least 6 SCT hits for tracks with $p_{\mathrm{T}} > 0.3$ GeV. The transverse impact parameter of the track relative to the beam-spot (d_0^Z) and the longitudinal impact parameter, $z_0 sin(\theta)$ are required to be within 1.5 mm.

The two particle correlation functions are constructed using tracks with $p_{\mathrm{T}} > 0.2$ GeV and with $|\eta| < 2.4$. The analysis is performed in different event classes defined using $N_{\mathrm{ch}}^{\mathrm{rec}}$, the total number of charged particle tracks with $p_{\mathrm{T}} > 0.4$ GeV and $|\eta| < 2.5$ and satisfying the track selection requirements. The kinematic ranges used for defining $N_{\mathrm{ch}}^{\mathrm{rec}}$ is consistent with the ranges used in the p+Pb and p+p ridge analyses and is slightly different from that used to construct correlation functions in this analysis. One primary goal of the analysis is to compare th long-range pseudorapidity correlations between different collision systems in same $N_{\mathrm{ch}}^{\mathrm{rec}}$ bins. The $N_{\mathrm{ch}}^{\mathrm{rec}}$ distributions in the three systems are shown in figure V.3.1.

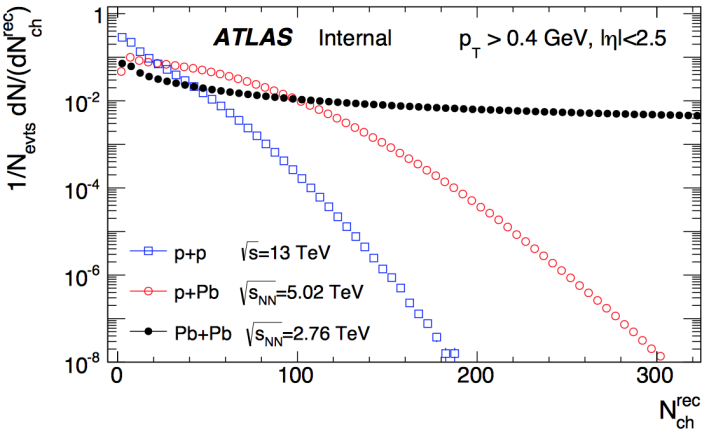

Figure V.3.1: The normalized $N_{\mathrm{ch}}^{\mathrm{rec}}$ distributions for the three collision systems, Pb+Pb, p+Pb and p+p.

The tracking efficiency for the p+Pb and Pb+Pb events are evaluated using HIJING events, and in the case of p+p using Pythia [211] events using parameter settings according to the "A2" tune [212], reconstructed with the detector simulation using GEANT4. The details of the evaluation of the tracking efficiency and uncertainties for the p+Pb data were presented in Section IV.2.2. The uncertainties in the tracking efficiency are evaluated by varying the track selection requirements, recalculating the efficiencies and comparing the efficiency corrected spectra from the different cases. The MC sample for the Pb+Pb events available was very small and so the reconstruction efficiency from the p+Pb events, having the same reconstruction settings, were used for the Pb+Pb case. However, the p+Pb efficiency was checked to be consistent with the efficiency from Pb+Pb

MC, but with higher precision. The efficiency for p+p data has been taken from the p+p ridge analysis. Figure V.3.2 shows the track reconstruction efficiency as a function of p_{T}, evaluated for the p+Pb and p+p datasets. The tracking efficiencies are similar between the datasets, although the p+p dataset shows slightly higher efficiency from the presence of the additional Pixel layer and improved track reconstruction algorithms in RUN2. The final results from the analysis are presented as a function of the efficiency corrected number of tracks N_{ch}. The N_{ch} values are found to differ by a constant scale factor from $N_{\mathrm{ch}}^{\mathrm{rec}}$, independent of the $N_{\mathrm{ch}}^{\mathrm{rec}}$ value, i.e. $N_{\mathrm{ch}} = bN_{\mathrm{ch}}^{\mathrm{rec}}$. The values and uncertainties in b were found to be 1.29±0.05 for the p+Pb and Pb+Pb data and 1.18±0.05 for the p+p case.

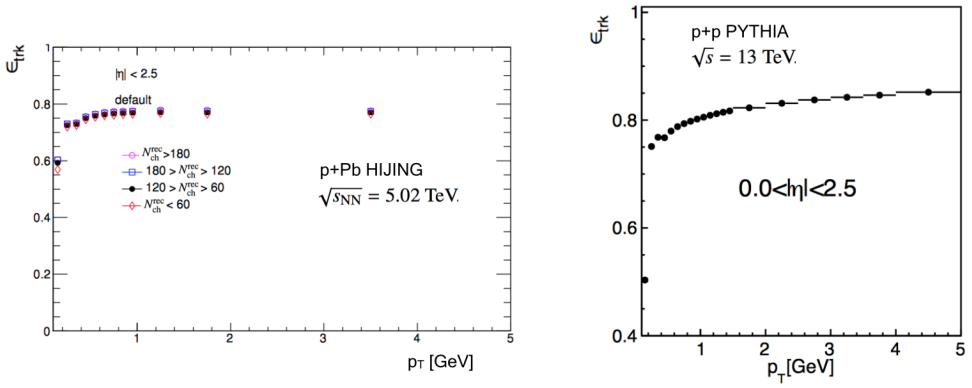

Figure V.3.2: The tracking efficiency ϵ_{trk}, as a function of p_{T} for p+Pb events evaluated using simulated HIJING events (left) and for p+p events evaluated using simulated Pythia events (right).

V.3.2 Data Analysis

V.3.2.1 Two particle correlation function

The correlation analysis is performed on events binned into different multiplicity classes defined using $N_{\mathrm{ch}}^{\mathrm{rec}}$. The two particle correlation functions are constructed for each multiplicity class, as the ratio of the pair distribution from the same events ($S(\eta_1,\eta_2) = \langle N(\eta_1,\eta_2)\rangle - \delta(\eta_1-\eta_2)\langle N(\eta_2)\rangle$) to the pair distribution from the mixed events ($B(\eta_1,\eta_2) = \langle N(\eta_1)\rangle\langle N(\eta_2)\rangle$), in the same manner as discussed in Subsection V.2.2.1:

$$C(\eta_1,\eta_2) = \frac{S(\eta_1,\eta_2)}{B(\eta_1,\eta_2)} \tag{V.3.1}$$

The event mixing is done by requiring the events to be matched in multiplicity (within $N_{\mathrm{ch}}^{\mathrm{rec}}$ of 2) and z_{vtx} (within 2.5 mm). The events are also required to be close together in time to account for possible time dependent variations of the detector conditions. The tracks are weighted by

the product of their tracking efficiencies, $1/(\epsilon_1\epsilon_2)$ while constructing the S and B distributions to account for detector inefficiencies. The remaining detector effects largely cancel in the ratio of same and mixed event distributions. The correlation function $C(\eta_1, \eta_2)$ is normalized by the product of projections to obtain $C_N(\eta_1, \eta_2)$, following equation V.1.13 to remove the contributions arising from residual centrality dependence. The $C_N(\eta_1, \eta_2)$ thus obtained is normalized to have a value of 1 when averaged over the η_1, η_2 phase space. The correlation functions and the projections of the correlation function are sometimes expressed in terms of the orthogonal variables $\eta_+ = \eta_1 + \eta_2$ and $\eta_- = \eta_1 - \eta_2$, as in Chapter V.2.

The correlation function $C_N(\eta_1, \eta_2)$ satisfies the symmetry condition $C_N(\eta_1, \eta_2) = C_N(\eta_2, \eta_1)$, and for the symmetric collision systems (p+p and Pb+Pb case) also satisfies the requirement that $C_N(\eta_1, \eta_2) = C_N(-\eta_1, -\eta_2)$. Therefore, for the p+p and Pb+Pb case, the pairs are filled into one quadrant defined with $\eta_1 - \eta_2 > 0$ and $\eta_1 + \eta_2 > 0$ and then reflected into the other quadrants. For the asymmetric case of p+Pb, the pairs are filled into one half of the phase space with $\eta_1 - \eta_2 > 0$ and then reflected. Separately, the analysis is also carried out on a symmetric p+Pb case, in which the correlation function is symmetrized by requiring $C_N(\eta_1, \eta_2) = C_N(-\eta_1, -\eta_2)$. This represents the case where the p+Pb and Pb+p collisions happen with equal probability in the data and the results from this can be compared with the results obtained for the symmetric systems. Most of the results for p+Pb, obtained in this chapter are using the correlation functions without symmetrizing, the results obtained otherwise, using the symmetrize case, are specified to be so when they are shown. For the p+Pb results without symmetrization, by convention, the proton going direction is taken as the positive η direction.

The short-range correlations (SRC) generally arise from final state effects, including resonance decays, fragmentation, local charge conservation etc. The short-range correlations tend to have a strong charge dependence, as charge conservation during decays and fragmentation increase the correlation between opposite charged pairs than between the same charged pairs. Studying the correlation functions separately for same and opposite charge combinations can provide insights into the nature of the short-range correlations and can help towards separating the short-range and long-range contributions in the correlation function.

Figure V.3.3 shows the correlation function, $C_N(\eta_1, \eta_2)$ from the opposite $(+-)$ and same $(++, --)$ charged pairs and the ratio between the two ($R(\eta_1, \eta_2) = C_N^{+-}(\eta_1, \eta_2)/C_N^{\pm\pm}(\eta_1, \eta_2)$) on the top row, for Pb+Pb events with $200 < N_{\rm ch}^{\rm rec} < 220$. The correlation function shows a peak along $\eta_1 \sim \eta_2$ (or $\eta_- \sim 0$). The magnitude of this peak is larger for the opposite charge pairs than for the same charge pairs, as can be expected from the contribution from SRC. The ratio, $R(\eta_1, \eta_2)$, is consistent with 1 in the large $|\eta_-|$ region, which shows that the long-range correlations in the system are independent of the charge combination. The small $|\eta_-|$ region, with $|\eta - | \lesssim 1.5$, on the other hand, shows a peak that extends over the entire η_+ range, reflecting the difference in the short-range correlations between the opposite and same charge combinations.

The lower panels of the figure show the width along η_- of $R(\eta_1, \eta_2)$, as a function of η_+, obtained by fitting a Gaussian to projections of $R(\eta_1, \eta_2)$ along narrow slices of η_+. The projections at different η_+ values fit well to a Gaussian and the width of the Gaussian fit is independent of the η_+ value, suggesting that the shape of the SRC along η_- in $R(\eta_1, \eta_2)$ is independent of η_+. The

bottom right panel of figure V.3.3 shows the ratio

$$f(\eta_+) = \frac{\int_{-0.4}^{0.4} R(\eta_+, \eta_-)/0.8 d\eta_- - 1}{\int_{-0.4}^{0.4} R(0, \eta_-)/0.8 d\eta_- - 1} \tag{V.3.2}$$

which quantifies the shape of the SR peak along η_+. For the Pb+Pb system, the $f(\eta_+)$ values are also found to be independent of η_+, showing that the magnitude of the SRC doesn't change as a function of η_+ in the Pb+Pb system.

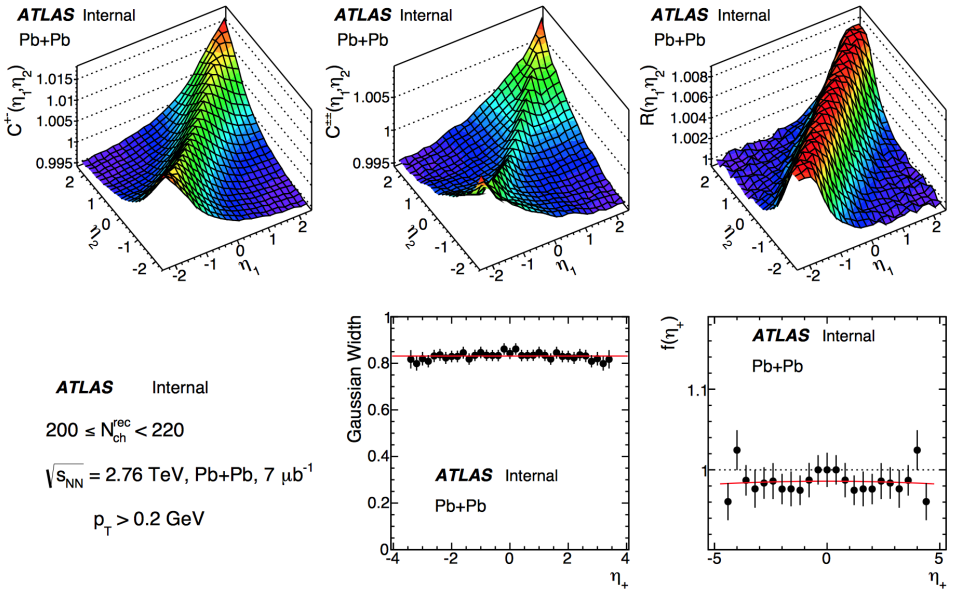

Figure V.3.3: The two particle correlation function $C_N(\eta_1, \eta_2)$ for opposite charged pairs (top left) and for same charged pairs (top middle) and the ratio $R(\eta_1, \eta_2)$ (top right) for Pb+Pb events with $200 < N_{\rm ch}^{\rm rec} < 220$. The lower middle panel shows, for the same events, the width of the Gaussian fits to projections of $R(\eta_+, \eta_-)$ along η_- as a function of the η_+ slice used for projection and the bottom right panel shows the $f(eta_+)$ values as a function of η_+.

Figure V.3.4 shows similar set of plots for the p+Pb system. Most of the observations from the Pb+Pb case hold for the p+Pb case as well, the major difference being the magnitude of the SRC increases towards the proton going direction. The magnitude of the short-range peak in the correlation functions as well as the ratio increase towards positive η_+ values where both particles in the pair are from the proton going direction. The increase in magnitude towards the proton going direction can also be seen from the η_+ dependence of $f(\eta_+)$, which increases towards large η_+ values. However, the width of the projections along η_- at different η_+ slices still remain independent of η_+ as in the Pb+Pb case. Similar observations were also made for the p+p data, with the width and shape of the SR peak in $R(\eta_1, \eta_2)$ remaining independent of η_+ while the $f(\eta_+)$ values show a dependence, increasing towards large η_+ values on the positive and the negative side.

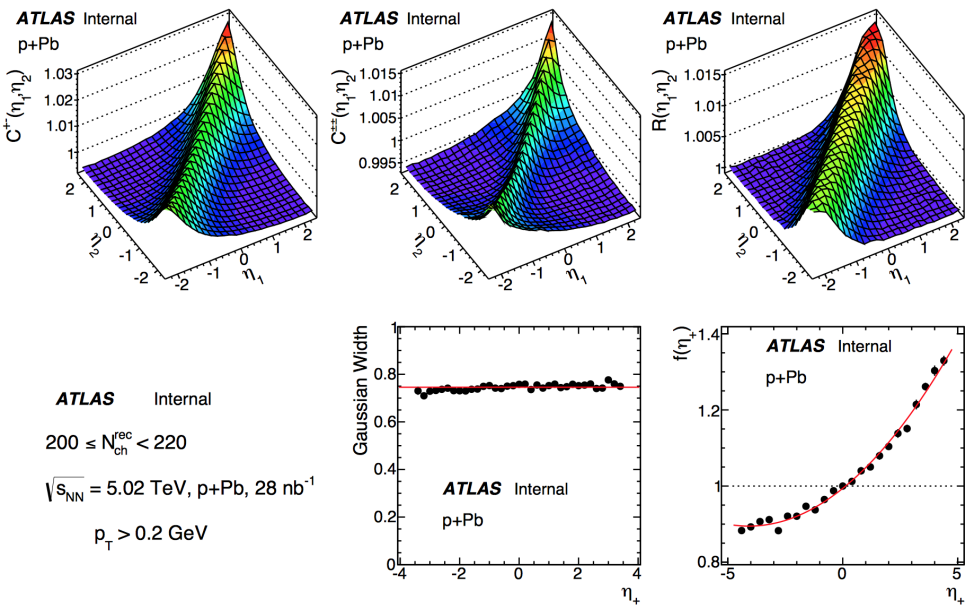

Figure V.3.4: The two particle correlation function $C_N(\eta_1, \eta_2)$ for opposite charged pairs (top left) and for same charged pairs (top middle) and the ratio $R(\eta_1, \eta_2)$ (top right) for Pb+Pb events with $200 < N_{\rm ch}^{\rm rec} < 220$. The lower middle panel shows, for the same events, the width of the Gaussian fits to projections of $R(\eta_+, \eta_-)$ along η_- as a function of the η_+ slice used for projection and the bottom right panel shows the $f(eta_+)$ values as a function of η_+.

V.3.2.2 Separation of short and long-range correlations

The ratio of the correlation function between opposite and same charges, $R(\eta_+, \eta_-)$, does not have contribution from long-range correlations and reflect mainly the difference between the short-range correlations between the two charge combinations. If the magnitude of the short-range correlations are small, $R(\eta_+, \eta_-)$ can be written as,

$$R(\eta_+, \eta_-) \approx 1 + \delta^{+-}_{SRC}(\eta_+, \eta_-) - \delta^{\pm\pm}_{SRC}(\eta_+, \eta_-), \tag{V.3.3}$$

where $\delta^{+-}_{SRC}(\eta_+, \eta_-)$ and $\delta^{\pm\pm}_{SRC}(\eta_+, \eta_-)$ denote the SRC for the opposite charge and same charge combinations respectively. From the discussion above, the shape of the SRC in $R(\eta_+, \eta_-)$ along η_- is observed to be independent of η_+. Assuming that the η_- and η_+ dependence of the SRC factorize for the individual charge combinations as well, and that the shape along η_+ for both charge combinations are given by $f(\eta_+)$, the SRC correlations and $R(\eta_+, \eta_-)$ can be written as

$$\begin{aligned} &\delta^{+-}_{SRC}(\eta_+, \eta_-) = f(\eta_+) g^{+-}(\eta-), \quad \delta^{\pm\pm}_{SRC}(\eta_+, \eta_-) = f(\eta_+) g^{\pm\pm}(\eta-), \\ &R(\eta_+, \eta_-) = 1 + f(\eta+) \left[g^{+-}(\eta_-) - g^{\pm\pm}(\eta_-) \right], \end{aligned} \tag{V.3.4}$$

where $g^{+-}(\eta_-)$ and $g^{\pm\pm}(\eta_-)$ characterize the η_- dependence of the SRC for the opposite and same charge combinations respectively, which can differ in both magnitude and shape and $f(\eta_+)$ is the

η_+ dependence calculated using Eq. V.3.2.

In order to evaluate the η_- dependence of SRC, the $g^{\pm\pm}(\eta_-)$ function for the same charge combination is first evaluated. The $C_N^{\pm\pm}(\eta_+, \eta_-)$ is projected along η_- over a narrow slice with $|\eta_+| < 0.4$. The top panels of figure V.3.5 shows the $C_N^{\pm\pm}(\eta_-, \eta_+)$ on the left panel and the projection along η_-, $C_N(\eta_-)$ on the second panel, for Pb+Pb events with $200 < N_{\rm ch}^{\rm rec} < 220$. The $C_N(\eta_-)$ shows a quadratic dependence in the long-range region (large $|\eta_-|$) along with a peak in the short-range region, on top of the long-range quadratic component. The quadratic dependence along η_- in the long-range region can be expected if the correlation signal is dominated by an a_1 modulation, as discussed in Section V.2.2.2. The short-range peak is estimated by fitting a quadratic function to the region with $|\eta_-| > 1.5$ and subtracting the fit from the data points in the short-range region with $|\eta_-| < 2.0$. The magnitude of the short-range peak is assumed to be zero for $|\eta_-| > 2.0$. The range in η_- used for doing the quadratic fit ($|\eta_-| > 1.5$) is about twice the width of the peak in $R(\eta_+, \eta_-)$ for the event class shown. The stability of the fit and results are evaluated by varying the range of fit from 1.0 to 2.0 in $|\eta_-|$. Once the $g^{\pm\pm}(\eta_-)$ function is obtained, the SRC in the full η_1, η_2 space is evaluated using Eq. V.3.4, and is shown in the third panel in figure V.3.5. This estimated SRC is then subtracted from the $C_N(\eta_1, \eta_2)$ function to get the first estimate of the LRC in the event class. The subtracted results are shown in the last panel of the figure. The lower panels of figure V.3.5 shows the same set of plots for the p+Pb system.

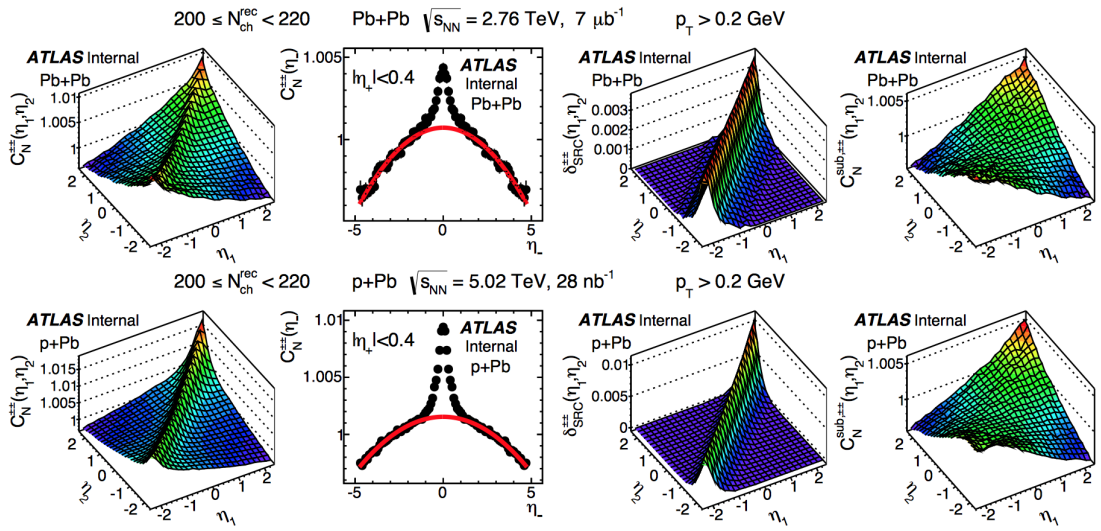

Figure V.3.5: The two particle correlation function $C_N(\eta_1, \eta_2)$ for same charged pairs (left), the projection of this correlation function, $C_N(\eta_-)$, along η_- over a narrow slice with $|\eta_+| < 0.4$ along with the quadratic fit in the long-range region (second panel), the estimated SRC in 2D (third panel) and the LRC obtained after subtracting out the SRC from $C_N(\eta_1, \eta_2)$ (right panel). The top set of plots are for Pb+Pb events with $200 < N_{\rm ch}^{\rm rec} < 220$ and the lower set of panels are for the p+Pb events with $200 < N_{\rm ch}^{\rm rec} < 220$.

The long-range and short-range components extracted as detailed above still contain a small bias from short-range correlations. This is because the in the definition of $C_N(\eta_1, \eta_2)$ (Eq. V.1.13), the SRC also contributes to the denominator, $C_P(\eta_1)C_P(\eta_2)$. This contribution arises from the fact that the entire short-range peak is not visible across the full acceptance, as shown in the left panel of figure V.3.6. The full short-range peak is visible in the region with $\eta_1, \eta_2 \sim 0$, but as one goes to the edges of the acceptance with η_1 or η_2 close to 2.4, part of the short-range peak falls outside the acceptance. Thus the projections along the η_1 or η_2 directions will get varying contributions from the SRC and is not uniform in η_1 or η_2, as shown in the middle panel of the figure. This causes the $C_P(\eta_1)C_P(\eta_2)$ to be different from 1, as shown in the last panel of the figure. The renormalization by the product of projections will thus introduce a bias that depends on the magnitude of the SRC.

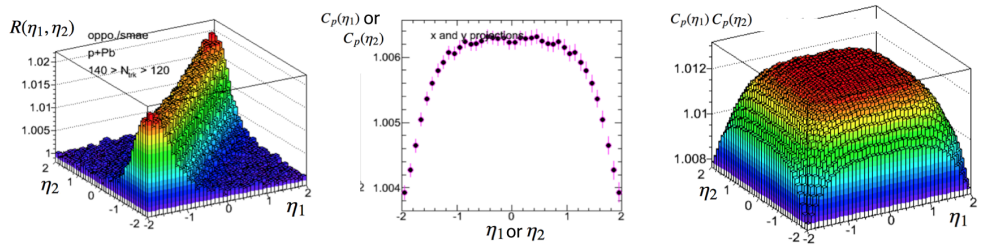

Figure V.3.6: Figure illustrating the bias on $C_P(\eta_1)C_P(\eta_2)$ from the presence of SRC. (Left) The $R(\eta_1, \eta_2)$ for p+Pb events with $120 < N_{\rm ch}^{\rm rec} < 140$, (middle) the projections $C_P(\eta_1)$ and $C_P(\eta_2)$ from $R(\eta_1, \eta_2)$ on the left panel, (right) the product $C_P(\eta_1)C_P(\eta_2)$ from the 1D functions in the middle panel.

This bias is removed by a simple iteration procedure. The SRC estimated from $C_N(\eta_1, \eta_2)$ as discussed above is used to redefine the projections as,

$$C_P^{sub}(\eta_1) = \frac{\int [C(\eta_1, \eta_2) - \delta_{SRC}(\eta_1, \eta_2)] d\eta_2}{2Y}, \quad C_P^{sub}(\eta_2) = \frac{\int [C(\eta_1, \eta_2) - \delta_{SRC}(\eta_1, \eta_2)] d\eta_1}{2Y} \tag{V.3.5}$$

which are then used to redefine the normalized correlation function as

$$C'_N(\eta_1, \eta_2) = \frac{C(\eta_1, \eta_2)}{C_P^{sub}(\eta_1) C_P^{sub}(\eta_2)}. \tag{V.3.6}$$

The estimation of the SRC is then repeated as discussed above using the $C'_N(\eta_1, \eta_2)$ function. The projection along η_-, $\delta_{SRC}(\eta_1, \eta_2)$ and the LRC shown in the second, third and fourth panels of figure V.3.5 are in fact obtained after doing the iterative correction. In most cases, the results are found to converge after one iteration. Figure V.3.7 shows an example, comparing the projections along η_- and the quadratic fits before (top panels) and after (lower panels) doing the iterative correction for one of the multiplicity classes for the three collision systems. The impact on the estimated SRC from doing the iterative correction is small. The results shown in this chapter are obtained after doing the iterative correction. In most cases the results from with and without

doing the iterative correction are consistent with each other. The difference between the two cases for p+Pb and Pb+Pb, where the SRC is small is about 2%, but is larger in p+p and reaches to about 4% for $N_{\rm ch}^{\rm rec} > 100$, where the SRC is larger.

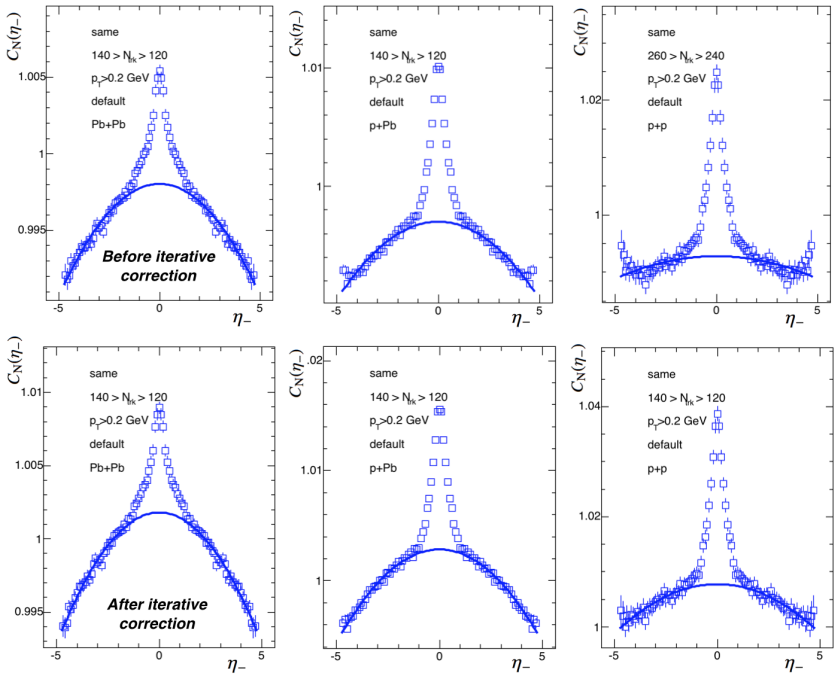

Figure V.3.7: The projections of the correlation functions $C_N(\eta_1, \eta_2)$ (top panels) and $C'_N(\eta_1, \eta_2)$ (lower panels) along η_- for Pb+Pb (left), p+Pb (middle) and p+p (right) collisions with $120 < N_{\rm ch}^{\rm rec} < 140$, for the same charge combination. The quadratic fit to the long-range region is also shown.

The same procedure could be used, in principle, to evaluate the SRC in all charge and opposite charge combinations. However, since the magnitude of the SRC is larger in all charge and opposite charge combinations, the systematic uncertainties from the SRC estimation are slightly larger. For opposite charge combination, the SRC is evaluated by employing Eq. V.3.3 and using the $\delta^{\pm\pm}_{SRC}(\eta_1, \eta_2)$ evaluated for the same charge combination,

$$\delta^{+-}_{SRC}(\eta_1, \eta_2) = R(\eta_1, \eta_2) - 1 + \delta^{\pm\pm}_{SRC}(\eta_1, \eta_2). \tag{V.3.7}$$

A similar ratio as the $R(\eta_1, \eta_2)$ is constructed using the correlation functions from all charge and same charge combinations which is then used to evaluate the δ_{SRC} for the all charge combination. The LRC is then obtained by subtracting the estimated SRC from $C'_N(\eta_1, \eta_2)$ as in the case of same charge combination.

V.3.2.3 Quantifying the long-range correlation

The features of the correlation function are quantified using the expansion of the correlation function into the Legendre basis, as presented in Chapters V.1 and V.2. This chapter uses a slightly different normalization for the polynomials, compared to the discussions in Chapters V.1 and V.2, so that the prefactor in front of the a_1 term in the expansion becomes 1. The modified Legendre polynomials $T_n(\eta)$, used in this chapter are defined as

$$T_n(\eta) = \sqrt{\frac{2n+1}{3}} Y P_n(\eta/Y), \tag{V.3.8}$$

where $P_n(x)$ are the Legendre polynomials and $Y = 2.4$. The Legendre coefficients $\langle a_n a_m \rangle$ can be obtained from the correlation function as

$$\langle a_n a_m \rangle = (\frac{3}{2Y^3})^2 \int C_N(\eta_1, \eta_2) \frac{T_n(\eta_1)T_m(\eta_2) + T_n(\eta_2)T_m(\eta_1)}{2} d\eta_1 d\eta_2 \tag{V.3.9}$$

The correlation function after the subtraction of SRC, as shown in figure V.3.5, is dominated by an $\langle a_1^2 \rangle$ modulation, as can be seen from the shapes of the different base functions in figure V.1.1. If the first order modulation is dominating, then the correlation function after subtraction of the SRC, denoted by $C_N^{sub}(\eta_1, \eta_2)$, can be written as

$$C_N^{sub}(\eta_1, \eta_2) \approx 1 + \langle a_1^2 \rangle \eta_1 \eta_2 = 1 + \frac{\langle a_1^2 \rangle}{4} (\eta_+^2 - \eta_-^2) \tag{V.3.10}$$

The correlation function, in the case of dominating first order modulation, is expected to have a positive quadratic dependence along η_+ and a negative quadratic dependence along η_- directions. The magnitude of $\langle a_1^2 \rangle$ can also be extracted from projections along the η_+ and η_- directions by fitting them with a quadratic function. The projections can be taken at different η_- and η_+ slices respectively and thus allows the study of the shape of the correlation function more differentially across the η_1, η_2 phase space.

An alternate way to study the correlation function is by using the ratio, $r_N^{sub}(\eta)$, defined as

$$r_N^{sub}(\eta) = \begin{cases} C_N^{sub}(-\eta, \eta_{ref})/C_N^{sub}(\eta, \eta_{ref}), & \eta_{ref} > 0 \\ C_N^{sub}(\eta, -\eta_{ref})/C_N^{sub}(-\eta, -\eta_{ref}), & \eta_{ref} < 0 \end{cases} \approx 1 - 2\langle a_1^2 \rangle \eta \eta_{ref}, \tag{V.3.11}$$

where η_{ref} is narrow η interval of width 0.2. The second line of the equation follows in the case when the first order modulation is dominating, and therefore $\langle a_1^2 \rangle$ can be extracted from a linear fit to $r_N^{sub}(\eta)$. The $r_N^{sub}(\eta)$ has the advantage that the residual centrality dependence term cancel in the ratio, as they are even functions in η. Therefore this ratio provides a robust consistency check of any potential bias introduced by the renormalization procedure (Eq. V.1.13). As with the case of the projections along η_+ and η_-, the $r_N^{sub}(\eta)$ can be evaluated for different values of η_{ref}, and thus also helps study the correlation function more differentially in the η_1, η_2 phase space. It also has the advantage that the η_{ref} in Eq. V.3.11 can be taken from a different detector, further forward or backward from the mid-rapidity detectors, and thus can be particularly useful in experiments where the detector is not continuous or only has a limited range at mid-rapidity.

The four methods discussed above, Legendre decomposition of the 2D correlation function, quadratic fits along η_+ and η_- projections and linear fits to $r_N^{sub}(\eta)$ are used to extract the magnitude of $\langle a_1^2 \rangle$ in this analysis. If the correlation function is dominated by an $\langle a_1^2 \rangle$ modulation, then all three methods are expected to give consistent results.

V.3.3 Summary of Systematic Uncertainties

The sources of systematic uncertainties for this measurement are similar to that for the measurement presented in Chapter V.2, except that in this measurement, an additional source of systematic uncertainty from the SRC subtraction is also present. Systematic uncertainties arising from event mixing criteria, track reconstruction efficiency, pair acceptance, run period variation and Monte-Carlo closure, where the signals at the truth and reconstructed level are compared for MC events, are evaluated. The systematic uncertainties from the different sources are quantified by calculating the ratio, $d(\eta_1, \eta_2)$, of the correlation function from doing the systematic variations to the correlation function from the default choice. The uncertainties on the Legendre coefficients can be evaluated by expanding $d(\eta_1, \eta_2)$ into the 2D Legendre basis. The uncertainties on the values extracted from the three fitting methods are evaluated by repeating the projections and fits on the correlation functions from each of the cross checks. The summary of the systematic uncertainties from the different sources in this measurement are discussed below, more detailed discussion of the evaluation of the systematic uncertainties from the different sources can be found in Appendix B.2.

The systematic uncertainty from the SRC subtraction procedure is one of the major sources of systematic uncertainties for the correlation function and the Legendre coefficients, after the SRC subtraction. Since the magnitude of the SRC is significantly different (by about a factor of two or more) between the opposite and same charged combinations, the difference between the C_N^{sub+-} and $C_N^{sub\pm\pm}$ is a conservative check on the robustness of the subtraction procedure. The difference is typically small, found to be within 0.2–2% of the correlation signal and 1–6% for the $\sqrt{\langle a_1^2 \rangle}$ coefficients, depending on the collision system. This difference is included as part of the systematic uncertainty. The stability of the SRC subtraction is also evaluated by varying the $|\eta_-|$ range used for doing the long-range fit and also the $|\eta_+|$ range used for the projection to evaluate $g(\eta_-)$ for the same charge combination. The uncertainties from these variations are propagated to the final results for the different charge combinations. This uncertainty is about 1–2% of the correlation signal and 1–5% for the $\sqrt{\langle a_1^2 \rangle}$ values and is smaller for Pb+Pb than for p+Pb and largest for p+p data.

The systematic uncertainties from event mixing is evaluated by varying the $N_{\rm ch}^{\rm rec}$ and z_{vtx} bin widths used for matching events used in the construction of mixed event distribution. The bin width in $N_{\rm ch}^{\rm rec}$ is varied to have twice the bin width from the default case and the bin width in z_{vtx} is varied from 2.5 mm to 5 mm and 10 mm to check the sensitivity of the event matching criteria on the results. The variations of event mixing bins contribute mostly to the terms characterizing the residual centrality dependence and thus are mostly removed by the renormalization and the $C_N(\eta_1, \eta_2)$ and $C_N^{sub}(\eta_1, \eta_2)$ values are quite stable against these variations. The uncertainty from

varying the $N_{\rm ch}^{\rm rec}$ mixing bin width is found to be about 2% of the correlation signal and for the $\sqrt{\langle a_1^2 \rangle}$ values. The uncertainty from the variation of the z_{vtx} matching is found to be smaller, about 0.5% of the correlation signal.

The analysis is repeated separately for events with $|z_{vtx}| < 50$ mm and $50 < |z_{vtx}| < 100$ mm to check for possible variations from tracks of same η from different z_{vtx} positions seeing slightly different parts of the detector. Good consistency is seen between the results from the two cases, with the variations being less than 2% of the correlation signal. To check for the stability of the correlation functions, the Pb+Pb events are divided into different run groups ordered in time and the analysis is repeated. The p+Pb events from the two run orientations are also grouped separately and analysed. The results are found to be quite stable across the different groups, the variations being less than 2% for the correlation signal and the $\sqrt{\langle a_1^2 \rangle}$ values. The p+p data from June and August of 2015 have different μ values (average number of collisions per bunch crossing) with the average μ in the August run being about 10 times larger than in the June run. The results calculated separately from the two runs can be used to evaluate the effects of residual pileup in the data. The results are found to be quite consistent and no significant systematic deviations were found.

The correlation functions are not very sensitive to the tracking efficiency correction, as the corrections are applied to both the numerator and denominator. Also most of the detector inefficiencies cancel in the ratio to the mixed event distribution. However, since both the signal and tracking efficiency are observed to increase slightly with $p_{\rm T}$, the tracking efficiency correction is expected to decrease the magnitude of the signal a bit. In fact, with the efficiency correction, the correlation signal and $\sqrt{\langle a_1^2 \rangle}$ values are found to decrease by about 1–2%. This difference is conservatively quoted as a systematic uncertainty.

The analysis is also repeated using MC HIJING events, in the cases of Pb+Pb and p+Pb, and MC Pythia events, in the case of p+p, using particles at the generated level and using reconstructed tracks after passing the events through the detector simulation using GEANT4. The ratio between the correlation functions at the generated and reconstructed levels are determined. The variations in this ratio is then added on to the correlation function from the data and the entire analysis, including the SRC subtraction, is repeated and the variations for the different quantities measured are determined. The differences in the correlation functions at the generated and reconstructed levels reflect the contributions from efficiency correction, pair effects, influence of secondary decays and fake tracks. In the ratio, the deviations from 1 are mostly in the short-range region and thus mostly affect the SRC measurements and have smaller impact on the measurement of the LRC from C_N^{sub}. The uncertainties from the MC study is found to be up to 5% for $\sqrt{\langle a_1^2 \rangle}$ calculated from C_N and between 0.2–3.5% for those calculated from C_N^{sub}.

The systematic uncertainties from the various sources are added in quadrature to get the total systematic uncertainties in the measured quantities. The summary of systematic uncertainties on the correlation function, $C_N^{sub}(\eta_1, \eta_2)$, are listed in table V.3.1and on the $\sqrt{\langle a_1^2 \rangle}$ values calculated using the four different methods are given in table V.3.2. The uncertainties in the SRC are found to be much smaller and are not listed here.

Collision system	Pb+Pb	p+Pb	p+p
Event-mixing [%]	0.7–1.0	0.4–2.5	0.2–1.8
Run-by-run stability [%]	0.4–0.8	0.3–1.7	0.2–1.6
z_{vtx} variation [%]	0.4–0.7	0.3–1.8	0.2–2.0
Track selection& efficiency [%]	0.7–1.4	0.2–0.3	0.3–0.6
MC consistency [%]	0.4–2.2	0.6–2.9	0.6–2.9
Charge dependence [%]	0.2–1.6	0.2–1.9	0.7–2.2
SRC subtraction [%]	1.0–2.2	1.2–5.7	1.1–3.9
Total [%]	1.6–3.6	1.6–7.2	2.0–5.9

Table V.3.1: Summary of average systematic uncertainties in percent for $C_N^{sub}(\eta_1, \eta_2)$ with $p_{\mathrm{T}} > 0.2$ GeV. The uncertainty is calculated as the variations (in $d(\eta_1, \eta_2)$), averaged over the entire η_1 and η_2 space relative to the observed strength of the correlation signal, defined as the difference between the maximum and minimum.

	Quadratic fit to $C_N^{sub}(\eta_-)\|_{\lvert\eta_+\rvert<0.1}$			Quadratic fit to $C_N^{sub}(\eta_+)\|_{0.9<\lvert\eta_-\rvert<1.1}$		
Collision system	Pb+Pb	p+Pb	p+p	Pb+Pb	p+Pb	p+p
Event-mixing [%]	0.5–2.5	0.2–2.8	0.2–4.2	0.4–1.8	0.4–3.2	0.3–3.4
Run-by-run stability [%]	0.3–2.1	0.2–1.8	0.2–3.0	0.2–2.4	0.2–2.1	0.2–1.5
z_{vtx} variation [%]	0.4–2.2	0.2–1.5	0.2–1.4	0.3–1.7	0.2–2.4	0.2–3.7
Track selec.& efficiency[%]	0.6–4.4	0.5–1.0	1.0–1.9	0.7–4.7	0.7–1.0	0.8–1.4
MC consistency [%]	0.5–4.5	0.4–4.9	1.8–7.2	0.8–5.1	0.2–5.8	0.4–8.1
Charge dependence [%]	0.1–2.7	0.4–2.5	1.1–3.4	0.2–5.5	0.5–7.0	1.2–7.3
SRC subtraction [%]	1.0–2.9	0.8–3.1	1.4–5.3	1.0–2.9	0.8–3.1	1.8–3.5
Total [%]	2.1–6.2	1.8–7.5	3.1–9.7	2.2–5.6	1.9–6.2	2.8–100
	Linear fit to $r_N^{sub}(\eta)\|_{2.2<\lvert\eta_{ref}\rvert<2.4}$			Global Legendre expansion of C_N^{sub}		
Centrality	Pb+Pb	p+Pb	p+p	Pb+Pb	p+Pb	p+p
Event-mixing [%]	0.4–2.2	0.4–1.2	0.3–2.6	0.2–1.7	0.2–1.6	0.2–0.4
Run-by-run stability [%]	0.2–1.9	0.1–2.2	0.2–3.0	0.2–0.6	0.1–1.8	0.2–2.2
z_{vtx} variation [%]	0.2–1.6	0.2–2.6	0.2–2.7	0.2–1.7	0.2–2.8	0.2–2.5
Track selec.& efficiency[%]	0.6–2.2	0.3–1.0	1.0–1.5	0.5–1.4	0.5–1.0	1.1–2.1
MC consistency [%]	0.6–4.4	0.2–4.8	0.8–3.4	0.5–4.3	0.8–4.6	0.2–4.0
Charge dependence [%]	0.3–3.4	0.4–3.5	0.9–4.3	0.3–4.5	0.4–5.2	1.5–6.3
SRC subtraction [%]	1.3–2.4	1.2–2.4	1.4–2.7	1.2–4.5	2.2–8.8	2.5–5.9
Total [%]	2.4–4.9	1.8–5.3	2.4–4.5	2.3–5.0	2.5–9.1	3.4–8.2

Table V.3.2: Summary of systematic uncertainties in percent for $\sqrt{\langle a_1^2 \rangle}$, calculated using the four methods. The uncertainties on the $\sqrt{\langle a_1^2 \rangle}$ values, shown for the cases of quadratic fits along η_- and quadratic fits along η_+ are those calculated in one of the slices used for projection. The uncertainties quoted for $r_N^{sub}(\eta)$ are also for a fixed η_{ref} range.

V.3.4 Results

V.3.4.1 Two particle correlations and Legendre spectra

Figure V.3.8 shows the two particle correlation function, $C_N(\eta_1, \eta_2)$, the estimated SRC, $\delta_{SRC}(\eta_1, \eta_2)$ and the correlation function with the SRC subtracted, $C_N^{sub}(\eta_1, \eta_2)$ for the three collision systems, in the multiplicity class with $100 < N_{\rm ch}^{\rm rec} < 120$. The overall magnitude of the correlation function $C_N(\eta_1, \eta_2)$ is larger in the p+p system than in the p+Pb or Pb+Pb systems. The peak in the short-range region along $\eta_- \sim 0$ is also more pronounced in the p+p data. The correlation function in the p+Pb system is asymmetric, particularly the peak in the short-range region, which increases towards the proton going side. The estimated SRC is largest in the p+p system than in the p+Pb system and is smallest in the Pb+Pb system. The asymmetry of the correlation function seen for the p+Pb case mostly reflects the asymmetry in the SRC, which is much larger in the proton going direction than the Pb going direction. Most of the differences between the $C_N(\eta_1, \eta_2)$ in the three systems arise from the difference in the SRC, as can be seen from the third row of the figure which shows the $C_N^{sub}(\eta_1, \eta_2)$ values for the three systems. The $C_N^{sub}(\eta_1, \eta_2)$, both in magnitude and shape, are very similar between the three collision systems and is dominated by an a_1 modulation.

Figure V.3.9 shows the Legendre coefficients, $\langle a_n^2 \rangle$ for n = 1–6 and $\langle a_n a_{n+2} \rangle$ for n = 1–5, calculated for the correlation functions $C_N(\eta_1, \eta_2)$, in the top row, and $C_N^{sub}(\eta_1, \eta_2)$, in the bottom row. The coefficients obtained from the correlation functions for all, same and opposite charge combinations are shown. The Legendre coefficients from C_N shows strong charge dependence, with the values being highest for the opposite charge combination and smallest for the same charge combination. The values also show a strong system size dependence, with $|\langle a_n a_m \rangle|_{p+p} > |\langle a_n a_m \rangle|_{p+Pb} > |\langle a_n a_m \rangle|_{Pb+Pb}$. These features are suggestive of a large contribution from the SRC to the $\langle a_n a_m \rangle$ coefficients. The first order coefficient is dominating, but non-zero values are seen for the higher order coefficients as well. The $\langle a_n a_m \rangle$ values after subtraction of the SRC show a very different picture. Only the $\langle a_1^2 \rangle$ modulation remains significantly larger than zero. The three charge combinations also give consistent results after the SRC subtraction. This shows that most of the contribution to the higher order coefficients arise from the peak in the short-range region. The magnitude of $\langle a_1^2 \rangle$ obtained from C_N^{sub} is very similar between the three collision systems, reflecting the fact that after SRC subtraction, the C_N^{sub} in the three collision systems have similar magnitudes. Since the higher order coefficients are much smaller than $\langle a_1^2 \rangle$ and close to zero, the rest of the discussion in this chapter focuses only on the $\langle a_1^2 \rangle$ coefficient.

V.3.4.2 Projections of correlation function

The projections of the correlation function, discussed in Subsection V.3.2.3, can be used to study the correlation function more differentially in the η_1, η_2 space and also to extract the $\langle a_1^2 \rangle$ coefficient. Figure V.3.10 (top panels) shows the projections of the correlation function $C_N^{sub}(\eta_1, \eta_2)$ along the η_- and η_+ directions for different η_+ and η_- slices respectively, and the $r_N^{sub}(\eta)$ for few different η_{ref} values for the Pb+Pb events. The quadratic fits to the η_- and η_+ projections are also shown, and the linear fits to $r_N^{sub}(\eta)$. The lower panels of the figure shows the $\sqrt{\langle a_1^2 \rangle}$ values obtained from

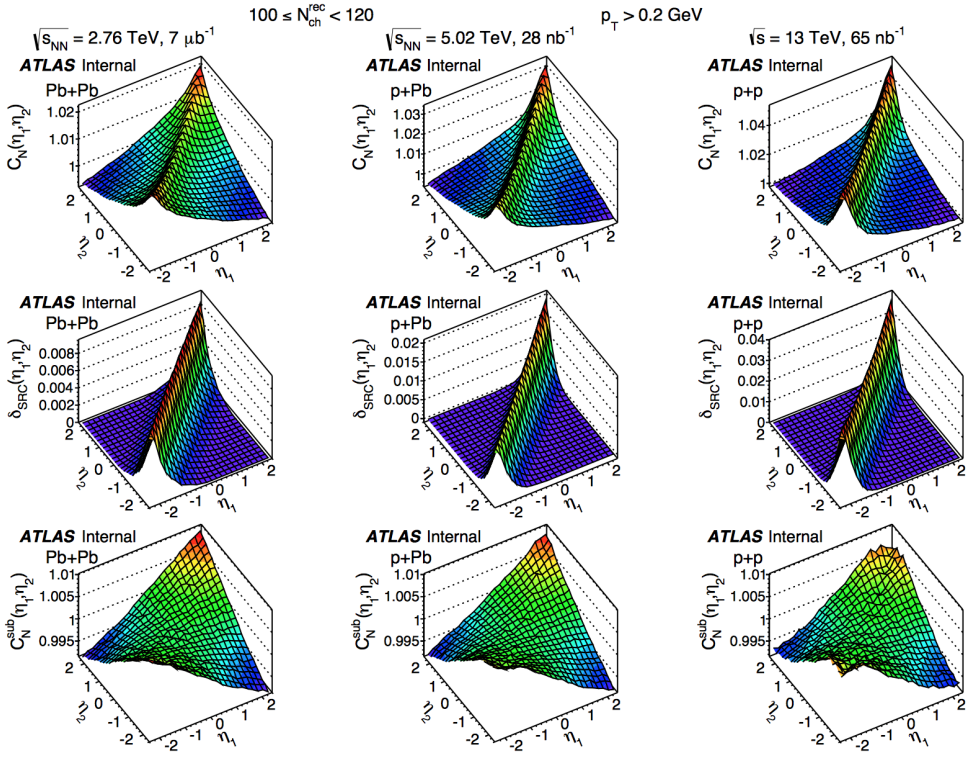

Figure V.3.8: The two particle correlation function $C_N(\eta_1, \eta_2)$ (top row), the estimated SRC, $\delta_{SRC}(\eta_1, \eta_2)$ (second row), and the correlation function with the SRC subtracted, $C_N^{sub}(\eta_1, \eta_2)$ (third row), for Pb+Pb (left column), p+Pb (middle column) and p+p (right column) events with $100 < N_{\rm ch}^{\rm rec} < 120$, for charged particle tracks with $p_{\rm T} > 0.2$ GeV and $|\eta| < 2.4$.

the fits as a function of the η_-, η_+ or η_{ref} values used for making the projections or the ratio. The $\sqrt{\langle a_1^2 \rangle}$ values from all the three cases are consistent with each other and also with the $\sqrt{\langle a_1^2 \rangle}$ value from the global Legendre expansion, irrespective of the η_-, η_+ or η_{ref} slice considered. This shows that the shape of $C_N^{sub}(\eta_1, \eta_2)$ is indeed characterized by a global $\langle a_1^2 \rangle$ modulation.

Figures V.3.11 and V.3.12 show similar plots for the p+Pb and p+p systems respectively. Results are quite similar to those in the case of Pb+Pb, albeit with larger systematic uncertainties from the subtraction of larger SRC in p+Pb and p+p. For the p+Pb case, the small residual asymmetry in C_N^{sub} between the proton and Pb going directions is responsible for the small differences in the $\sqrt{\langle a_1^2 \rangle}$ values between η_+ and $-\eta_+$ and also between η_{ref} and $-\eta_{ref}$. But the overall deviations from a global $\sqrt{\langle a_1^2 \rangle}$ modulation is quite small. The results from p+p also shows small deviations from the global $\langle a_1^2 \rangle$ modulation, but overall magnitude is quite close to that obtained from the Legendre expansion.

The comparison of the $\sqrt{\langle a_1^2 \rangle}$ values from the four different methods are shown in figure V.3.13 for the three collision systems. The η_- projection from the slice around $|\eta_+| < 0.1$ (which has the

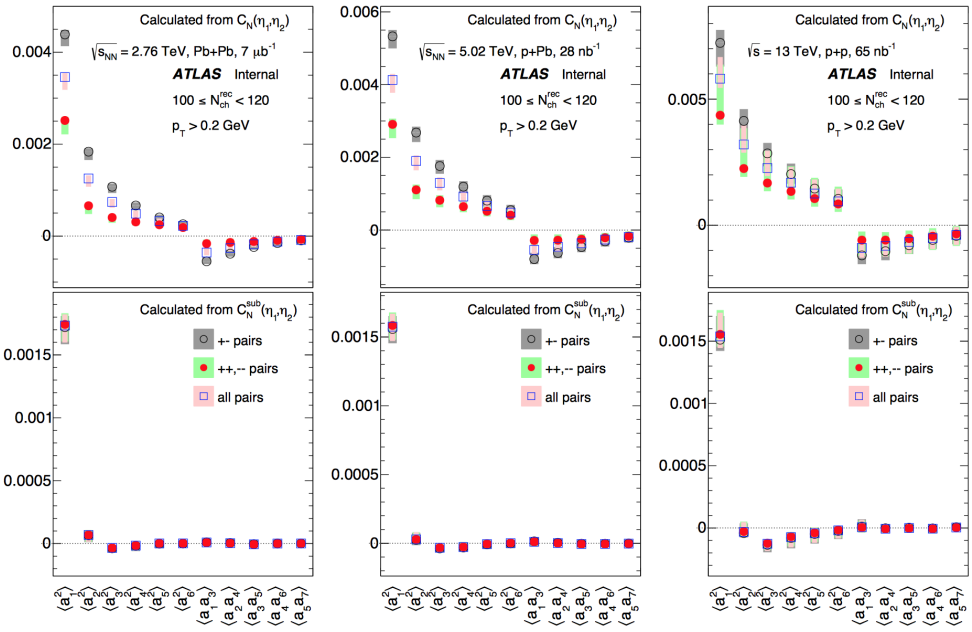

Figure V.3.9: The Legendre coefficients $\langle a_n^2 \rangle$ for n = 1–6 and $\langle a_n a_{n+2} \rangle$ for n = 1–5, calculated from $C_N(\eta_1, \eta_2)$ (top row) and from $C_N^{sub}(\eta_1, \eta_2)$ (bottom row), for Pb+Pb (left), p+Pb (middle) and p+p (right) collisions with $100 < N_{\rm ch}^{\rm rec} < 120$. The different markers show the values from the different charge combinations. The shaded boxes represent combined statistical and systematic uncertainties.

largest range in η_-), the η_+ projection at $0.9 < |\eta_-| < 1.1$ (which is outside the SRC region, but has enough points to constrain the fit), and the $r_N^{sub}(\eta)$ values for $2.2 < \eta_{ref} < 2.4$ (which also has the largest η range outside the SRC region or small $|\eta - \eta_{ref}|$ values), are used for showing the comparison. The values from all the four methods are consistent with each other across the full $N_{\rm ch}$ range studied and for all the three collision systems.

V.3.4.3 Collision system dependence of short and long-range correlations

The magnitude of the SRC averaged over the two particle η_1, η_2 phase space is defined as,

$$\Delta_{SRC} = \frac{\int \delta_{SRC}(\eta_1, \eta_2) d\eta_1 d\eta_2}{4Y^2}, \tag{V.3.12}$$

Since $\langle a_1^2 \rangle$ reflects the magnitude of the long-range FB modulation, $\sqrt{\Delta_{SRC}}$ can be used to compare with $\sqrt{\langle a_1^2 \rangle}$, which is used to characterize the magnitude of the LRC.

Figure V.3.14 shows the SRC, in terms of $\sqrt{\Delta_{SRC}}$, and LRC, in terms of $\sqrt{\langle a_1^2 \rangle}$, compared between the different charge combinations for the three different collision systems. As noted before, the SRC shows a strong dependence on the charge combination, with the magnitude of

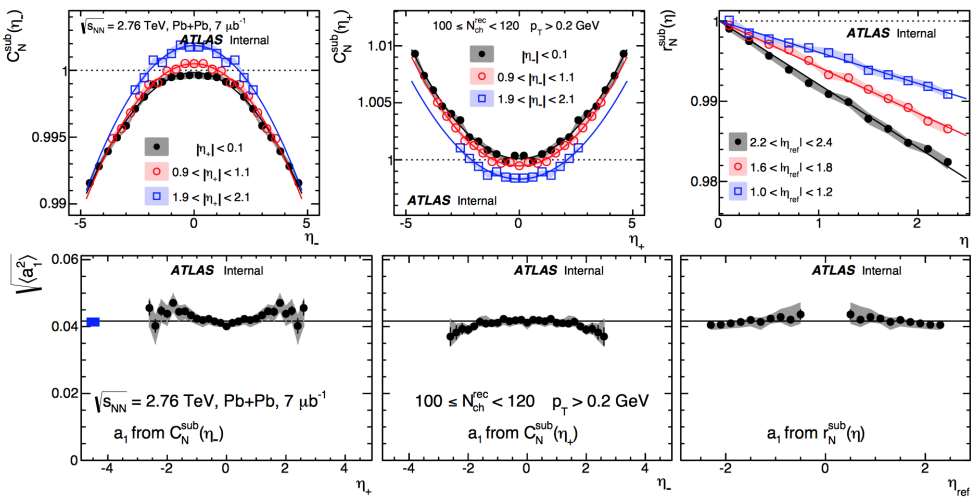

Figure V.3.10: (Top panels) The projections of the correlation function $C_N^{sub}(\eta_1, \eta_2)$ along η_- (left), along η_+ (middle) and the $r_N^{sub}(\eta)$ values, for three different ranges of η_+, η_- and η_{ref} respectively, for Pb+Pb events with $100 < N_{\rm ch}^{\rm rec} < 120$. The quadratic fits to the η_- and η_+ projections as well as the linear fits to $r_N^{sub}(\eta)$ are also indicated. (Lower panels) The $\sqrt{\langle a_1^2 \rangle}$ values obtained from the fit to projections along η_- and η_+ and fits to $r_N^{sub}(\eta)$ as a function of the η_+, η_- and η_{ref} ranges used for the projection and the ratio. The value of $\sqrt{\langle a_1^2 \rangle}$ from the Legendre expansion is indicated by the solid line in the lower panels and its total uncertainty by the shaded blue box. The error bars and shaded bands represent the statistical and systematic uncertainties respectively.

$\sqrt{\Delta_{SRC}}$ being factor of two or more larger in the opposite charge combination than for the same charge combination. The LRC on the other hand is independent of the charge combination. The magnitude of the SRC is also found to be larger for the smaller collision systems.

Figure V.3.15 compares the SRC and LRC as a function of $N_{\rm ch}$ between the three collision systems. The SRC shows a strong collision system dependence, with the values being the largest for p+p than for p+Pb which is larger than that in Pb+Pb at a given multiplicity. The LRC on the other hand are found to be consistent between the three collision systems across the entire multiplicity range studied. Both the $\sqrt{\Delta_{SRC}}$ and $\sqrt{\langle a_1^2 \rangle}$ values are found to fit to a power law function: c/N_{ch}^{α}. The fits to this function are also indicated in the figure. The values of α from the fit for the different cases are summarized in table V.3.4.3. For the $\sqrt{\langle a_1^2 \rangle}$ values the power law function is approximately $c/\sqrt{N_{ch}}$, as the value of α is close to 0.5 for all the three systems. The α values for the SRC on the other hand are found to be dependent on the collision system, with the value for p+p being much smaller than 0.5, suggesting a much slower drop with $N_{\rm ch}$ than for the larger collision systems. This could suggest that the nature of short-range correlation in high multiplicity p+p is much different from that in similar multiplicity p+Pb or Pb+Pb collisions.

In an independent source model, in which the forward (backward) going sources emit particles preferentially in the forward (backward) direction and the emission profile from the individual

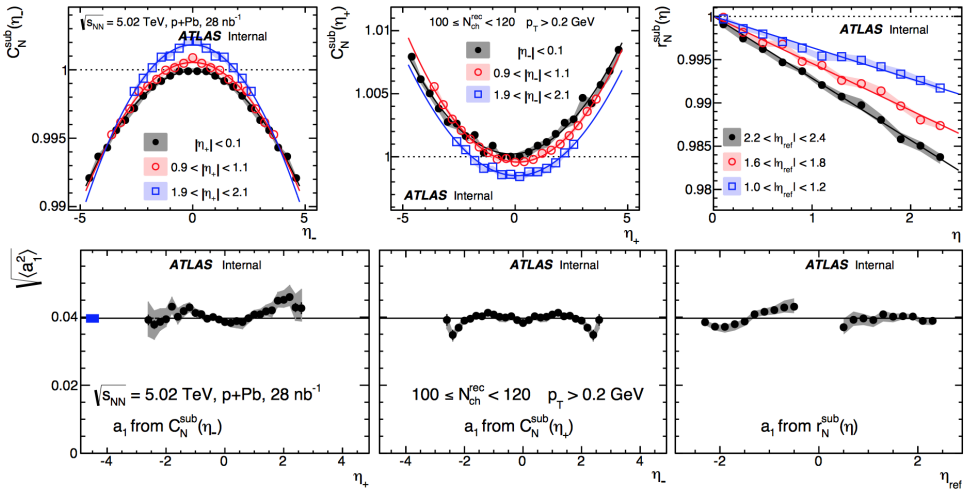

Figure V.3.11: (Top panels) The projections of the correlation function $C_N^{sub}(\eta_1, \eta_2)$ along η_- (left), along η_+ (middle) and the $r_N^{sub}(\eta)$ values, for three different ranges of η_+, η_- and η_{ref} respectively, for p+Pb events with $100 < N_{\rm ch}^{\rm rec} < 120$. The quadratic fits to the η_- and η_+ projections as well as the linear fits to $r_N^{sub}(\eta)$ are also indicated. (Lower panels) The $\sqrt{\langle a_1^2 \rangle}$ values obtained from the fit to projections along η_- and η_+ and fits to $r_N^{sub}(\eta)$ as a function of the η_+, η_- and η_{ref} ranges used for the projection and the ratio. The value of $\sqrt{\langle a_1^2 \rangle}$ from the Legendre expansion is indicated by the solid line in the lower panels and its total uncertainty by the shaded blue box. The error bars and shaded bands represent the statistical and systematic uncertainties respectively.

	Pb+Pb	p+Pb	p+p
α for $\sqrt{\Delta SRC}$	0.505 ± 0.011	0.450 ± 0.010	0.365 ± 0.014
α for $\sqrt{\langle a_1^2 \rangle}$	0.454 ± 0.011	0.433 ± 0.014	0.465 ± 0.018

Table V.3.3: The power index α and the associated total uncertainty from a power law fit to the $N_{\rm ch}$ dependence of the $\sqrt{\Delta_{SRC}}$ and $\sqrt{\langle a_1^2 \rangle}$ values.

sources being approximately linear at mid-rapidity, the magnitude of the long-range correlation depends on both the magnitude of the slope of the emission profile and on the fluctuations in the asymmetry between the number of forward and backward going sources (Eq. II.3.4). In such a model, $\langle a_1^2 \rangle \propto \langle A_n^2 \rangle$, where $A_n = (n_f - n_b)/(n_f + n_b)$, with n_f and n_b being the number forward and backward going sources. Similar values for $\langle a_1^2 \rangle$, in this picture, could suggest similar values not just of $\langle A_n^2 \rangle$, but also for the slope of the emission profile as well, between the three collision systems.

In an independent cluster model [213], each cluster emits the same number or particles and the number of clusters follow Poisson fluctuations. Assuming $N_{\rm ch}$ is proportional to the number

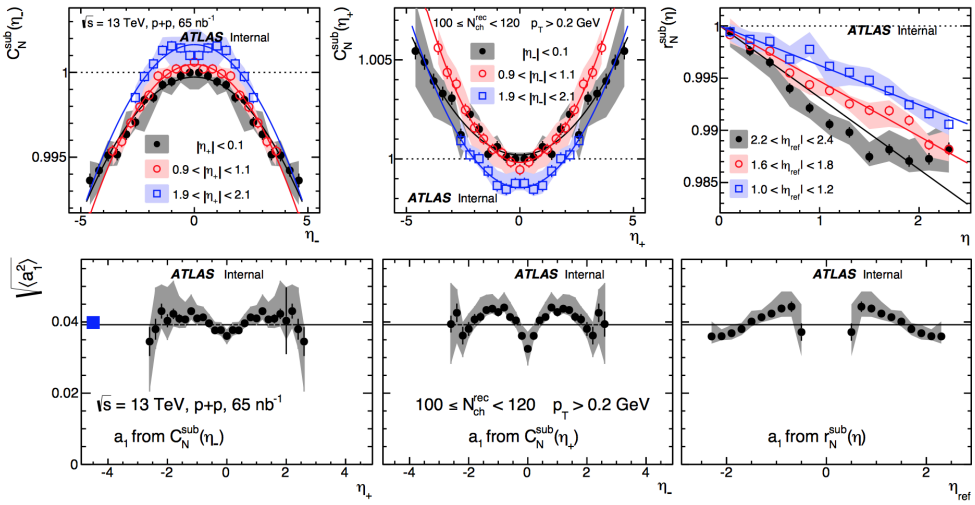

Figure V.3.12: (Top panels) The projections of the correlation function $C_N^{sub}(\eta_1, \eta_2)$ along η_- (left), along η_+ (middle) and the $r_N^{sub}(\eta)$ values, for three different ranges of η_+, η_- and η_{ref} respectively, for p+p events with $100 < N_{\rm ch}^{\rm rec} < 120$. The quadratic fits to the η_- and η_+ projections as well as the linear fits to $r_N^{sub}(\eta)$ are also indicated. (Lower panels) The $\sqrt{\langle a_1^2 \rangle}$ values obtained from the fit to projections along η_- and η_+ and fits to $r_N^{sub}(\eta)$ as a function of the η_+, η_- and η_{ref} ranges used for the projection and the ratio. The value of $\sqrt{\langle a_1^2 \rangle}$ from the Legendre expansion is indicated by the solid line in the lower panels and its total uncertainty by the shaded blue box. The error bars and shaded bands represent the statistical and systematic uncertainties respectively.

of clusters $n = n_f + n_b$, it follows that $\sqrt{\langle a_1^2 \rangle}$ scales with the inverse of the number of clusters, i.e.

$$\sqrt{\langle a_1^2 \rangle} \sim \frac{1}{n^\alpha} \sim \frac{1}{{N_{\rm ch}}^\alpha}, \quad \alpha \sim 0.5. \tag{V.3.13}$$

The observed value of $\alpha \approx 0.5$ for the LRC could be explained using the cluster model. This picture would suggest that the number of particle emitting clusters is similar between the three collision systems at a given value of $N_{\rm ch}$.

Figure V.3.16 shows a comparison of the $\sqrt{\Delta_{SRC}}$ and the $\sqrt{\langle a_1^2 \rangle}$ values from p+p data with the corresponding values obtained from p+p Pythia [211] and p+p EPOS [214] Monte-Carlo events. The MC samples are the same as those used in the minimum bias p+p analysis in [209]. The shaded bands indicate the total uncertainties for the data and the systematic uncertainties from SRC subtraction for the MC. The SRC values in the Pythia is much larger than in the data and shows a different dependence on the $N_{\rm ch}$, particularly in the high $N_{\rm ch}$ region. The $\sqrt{\Delta_{SRC}}$ values are slightly larger than in the data for EPOS, but it was seen that the short-range peak is broader in $|\eta_-|$ than in the data (not shown here). The LRC values from Pythia are slightly smaller than that in the data, but follows the same trend as data. The values from EPOS are much lower, and has a different $N_{\rm ch}$ dependence as well. However, the systematic uncertainties for the EPOS

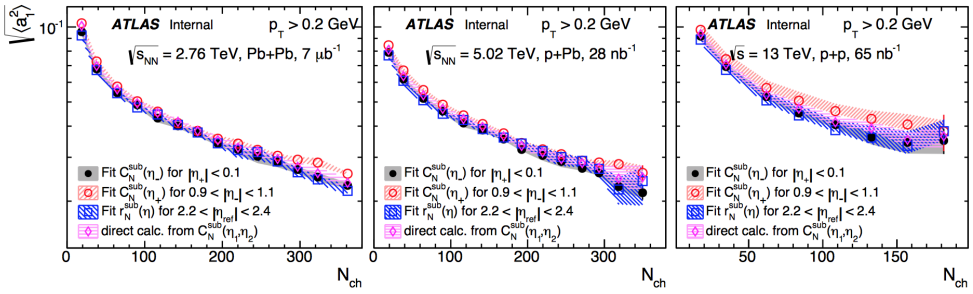

Figure V.3.13: The $\sqrt{\langle a_1^2 \rangle}$ values as a function of $N_{\rm ch}$ obtained from the global Legendre expansion, quadratic fits to projections along η_-, to projections along η_+ and from linear fits to $r_N^{sub}(\eta)$ for Pb+Pb (left), p+Pb (middle) and p+p (right) data. The error bars and shaded bands represent the statistical and systematic uncertainties, respectively.

results are much larger (resulting mainly from the broader short-range peak). The LRC values in data and Pythia are similar, but the SRC values are much different between the two. EPOS shows large difference in the case of the LRC. These suggest that the MC models need to be tuned appropriately to include the correct longitudinal correlations as observed in the data.

A striking feature of the short-range correlation in p+Pb collisions is that it increases towards the proton going side, as can be seen in figure V.3.8. This observation may also be interpreted in the context of a cluster model. If the number of clusters with pseudorapidity η are assumed to be proportional to the particle distribution in pseudorapidity, $dN/d\eta$, and if each cluster emits m particles, the magnitude of the short-range correlation, $\delta_{SRC}(\eta,\eta)$ can be written as,

$$\delta_{SRC}(\eta,\eta) \propto \frac{n\langle m(m-1)\rangle}{n\langle m\rangle^2} \approx \frac{1}{n} \propto \frac{1}{dN/d\eta} \tag{V.3.14}$$

The $dN/d\eta$ is lower on the proton going side than the Pb-going side in high multiplicity p+Pb collisions and can lead to an increase in the magnitude of the SRC. The increase of the SRC towards proton going direction can also be seen from the $f(\eta_+)$ function, which reflects the relative change in shape along η_+ from $\eta_+ = 0$. The relationship between $\delta_{SRC}(\eta,\eta)$ and $dN/d\eta$ can be checked in MC events. Figure V.3.17 shows the $dN/d\eta$ from Pythia and the ratio $(dN/d\eta(0))/(dN/d\eta(\eta))$ and the $f(eta_+)$ calculated from $R(\eta_1,\eta_2)$ for $\eta_+ = 2\eta$. The $f(\eta)$ values can be seen to reflect the shape of the $dN/d\eta$ in Pythia. Figure V.3.18 shows the $f(\eta_+)$ values as a function of η_+ for the three collision systems and for the symmetrized p+Pb case. Figure V.3.18 shows the $f(\eta_+)$ function in symmetrized p+Pb is more similar to the $f(\eta_+)$ from p+p than from the Pb+Pb collisions. Following the discussion above, this suggests that the $dN/d\eta$ in high multiplicity p+p and symmetrized p+Pb are similar to each other than to similar multiplicity Pb+Pb events.

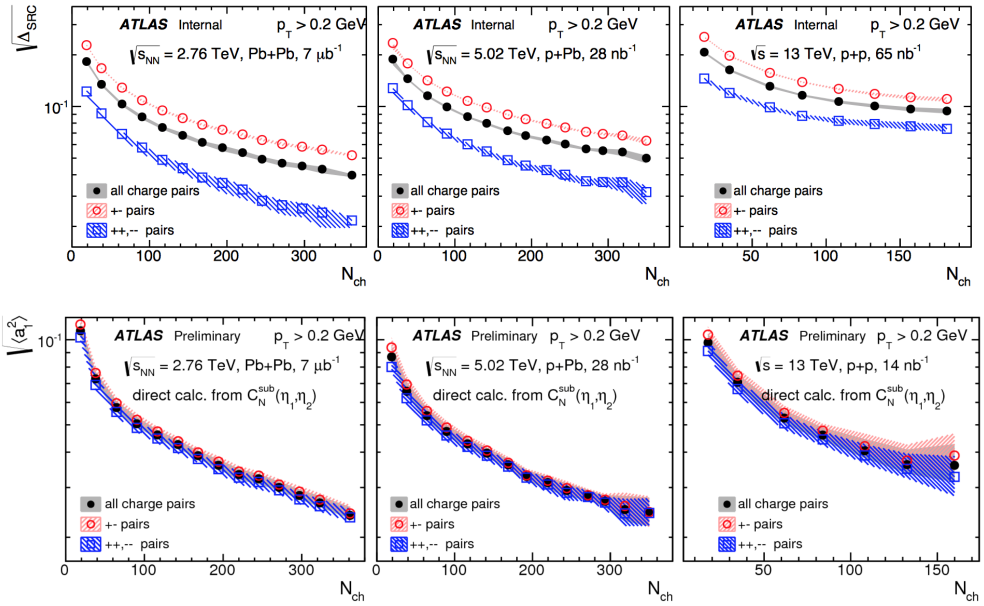

Figure V.3.14: The $\sqrt{\Delta_{SRC}}$ values (top panels) and the $\sqrt{\langle a_1^2 \rangle}$ values (lower panels) as a function of the $N_{\rm ch}$ compared between the different charge combinations, for Pb+Pb (left panels), p+Pb (middle panels) and p+p (right panels) collisions. The shaded bands represent the systematic uncertainties and the statistical uncertainties are smaller than the markers.

V.3.5 Summary

The two particle pseudorapidity correlation functions are measured for Pb+Pb collisions at $\sqrt{s_{NN}}$ = 2.76 TeV, p+Pb collisions at $\sqrt{s_{NN}} = 5.02$ TeV and p+p collisions at $\sqrt{s_{NN}} = 13$ TeV with total integrated luminosities of approximately 7 μb^1, 28 nb^1 and 65 nb^1, respectively. The correlation functions are measured using charged particle tracks with $p_{\rm T} > 0.2$ GeV and with $|\eta| < 2.4$ in event classes defined using the total number of reconstructed tracks with $p_{\rm T} > 0.4$ GeV and $|\eta| < 2.5$. The two particle correlation functions $C_N(\eta_1, \eta_2)$ show a depletion in the large $|\eta_-|$ region and a peak in the small $|\eta_-|$ region along $\eta_- \sim 0$. The peak along the small $|\eta_-|$ region is associated with the short-range correlation (SRC) and shows strong dependence on the charge combination and is much larger for the opposite charged pairs than for the same charged pairs. The short-range peak is observed to be larger along the proton going direction than the Pb-going direction in p+Pb collisions. Based on the features of the short-range peak in ratio of the correlation functions from opposite to same charge combination, $R(\eta_1, \eta_2)$, a data driven method is used to separate the contributions from SRC and the long-range correlations (LRC) in the correlation function. The magnitude of the first order coefficient $\langle a_1^2 \rangle$ is extracted from the correlation function after subtraction, $C_N^{sub}(\eta_1, \eta_2)$.

The Legendre coefficients, $\langle a_n a_m \rangle$ extracted from the correlation function without subtraction,

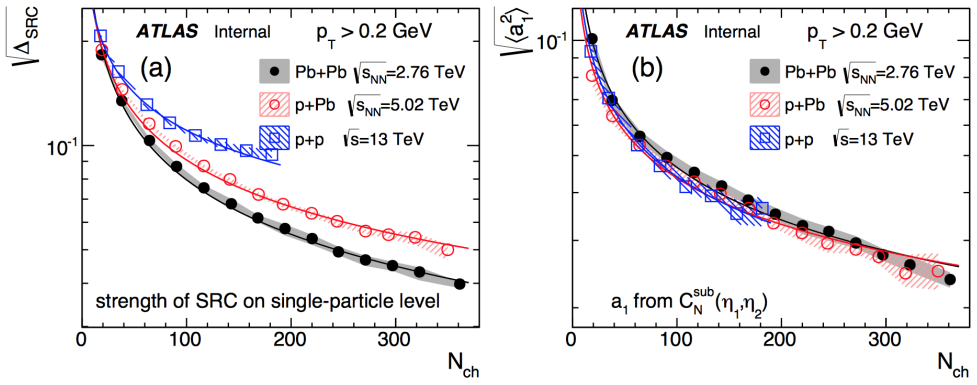

Figure V.3.15: The $\sqrt{\Delta_{SRC}}$ values (left) and the $\sqrt{\langle a_1^2 \rangle}$ values (right) as a function of the $N_{\rm ch}$ compared between the different collision systems. The shaded bands represent the systematic uncertainties and the statistical uncertainties are smaller than the markers.

$C_N(\eta_1, \eta_2)$, show strong dependence on charge combination and remains non-zero for n, m at least up to 10. After subtraction of the SRC, $\delta_{SRC}(\eta_1, \eta_2)$, the Legendre spectra is dominated by $\langle a_1^2 \rangle$ and the higher order coefficients with $n, m > 0$ become close to zero. The values after subtraction are also independent of charge combination, suggesting the higher order terms arise mainly from the structure along the short-range region. The correlation function after subtraction, $C_N^{sub}(\eta_1, \eta_2)$, is also studied more differentially in the η_1, η_2 phase space, using projections along the η_- and η_+ directions and also the ratio of $C_N^{sub}(\eta_1, \eta_2)$ between two points, $r_N^{sub}(\eta_1, \eta_{ref})$. The projections and the ratios are consistent with a global $\langle a_1^2 \rangle$ modulation and the magnitudes of $\langle a_1^2 \rangle$ obtained from the fits to the projections and the ratio are consistent with each other and with value obtained from the 2D Legendre expansion, suggesting that the shape of $C_N^{sub}(\eta_1, \eta_2)$ is characterized by a first order modulation associated with the forward-backward (FB) asymmetry.

The magnitudes of SRC, in terms of $\sqrt{\Delta_{SRC}}$, and of the LRC, in terms of $\sqrt{\langle a_1^2 \rangle}$, are studied as a function of the total number of charged tracks with $p_{\rm T} > 0.2$ GeV and $|\eta| < 2.5$, $N_{\rm ch}$, and is compared between the three collision systems. The SRC shows a strong dependence on the collision system with the values being largest in the smaller collision system of p+p than in p+Pb than in Pb+Pb. The LRC on the other hand shows a weak dependence on the collision system, with the values being approximately similar between the three systems at a given multiplicity. Both the $\sqrt{\Delta_{SRC}}$ and $\sqrt{\langle a_1^2 \rangle}$ values as a function of $N_{\rm ch}$ are found to fit to a power law function of the form $c/{N_{\rm ch}}^{\alpha}$. The value of α is found to be close to 0.5 for the LRC for the three collision systems, which may be explained in the context of an independent cluster model. This would suggest that the number or particle producing sources are similar between the three collision systems, at a given multiplicity. The α values for the SRC are found to depend of the collision system, with the value for p+p being much smaller than 0.5. Results are compared to calculations from MC Pythia and EPOS models. Both models were found to deviate from the measured results. These measurements can help constrain the longitudinal dynamics in Monte-Carlo models.

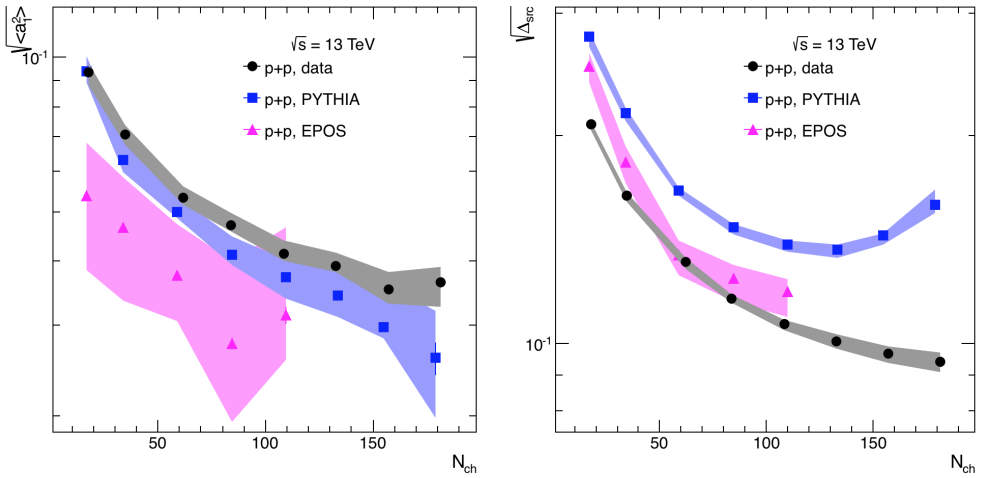

Figure V.3.16: The $\sqrt{\Delta_{SRC}}$ values (left) and the $\sqrt{\langle a_1^2 \rangle}$ values (right) as a function of the $N_{\rm ch}$ compared between the data and the MC models of Pythia and EPOS. The shaded bands show the total systematic uncertainties for the data and the systematic uncertainties from the SRC subtraction for the MC.

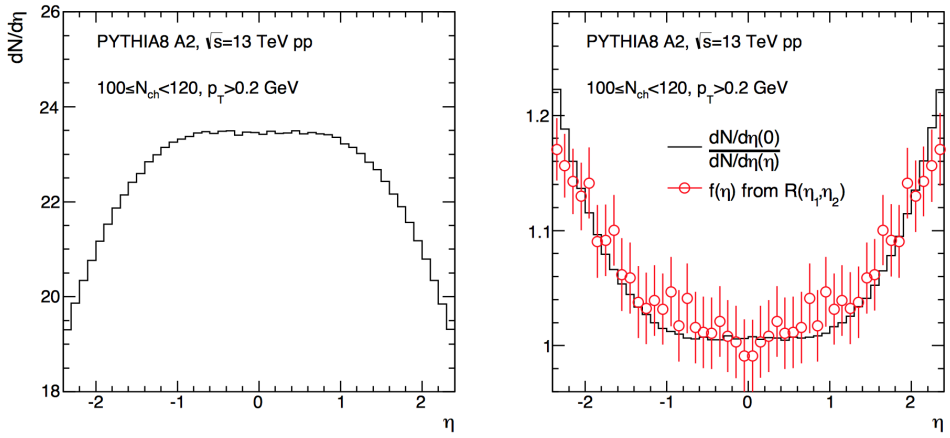

Figure V.3.17: The $dN/d\eta$ (left) and the $f(eta+)$ values for $\eta_+ = 2\eta$ compared with the ratio $(dN/d\eta(0))/(dN/d\eta(\eta))$ (right) from p+p Pythia events with $100 < N_{\rm ch} < 120$.

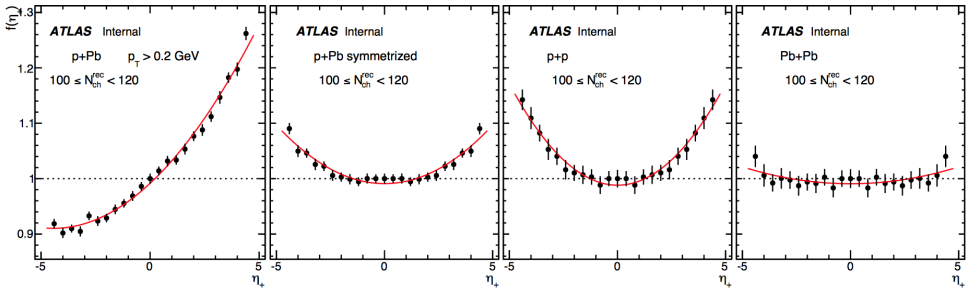

Figure V.3.18: The $f(eta+)$ values as a function of η_+ for p+Pb (left panel), symmetrized p+Pb (second panel), p+p (third panel) and Pb+Pb (right panel) events with $100 < N_{\mathrm{ch}} < 120$. The solid lines are fits to a quadratic function. The error bars represent total uncertainties.

Part VI

Conclusions and Outlook

The research into the long-range correlations, both the azimuthal correlations (the "ridge"), and the correlations between multiplicity produced at different pseudorapidities (the "longitudinal correlations"), in high energy nuclear collisions, carried out as part of this thesis work have been presented. The main conclusions and possible future directions are discussed below.

Conclusions:

The measurement of the ridge and the associated Fourier harmonics in two particle correlations in p+Pb collisions at $\sqrt{s_{NN}} = 5.02$ TeV at the LHC using ATLAS detector were presented in Chapter IV.2. The two particle correlations were measured over a wide range of "event activity" characterized by the $N_{\rm ch}^{\rm rec}$, the total number of charged particle tracks with $p_{\rm T} > 0.4$ GeV in $|\eta| < 2.5$, and/or $E_{\rm T}^{\rm Pb}$, the total transverse energy in the region, $3.2 < |\eta| < 4.9$. A recoil subtraction procedure, in which the per trigger yield in a lower activity (peripheral) event class is subtracted from that in a higher activity (central) event class, is used to subtract the contributions from the away side recoil (arising from dijets, decays etc) in the measured quantities. The yield in the peripheral event class is scaled so that the yield from the near-side jet matches between the peripheral and central event classes. In the $p_{\rm T}$ region where the first order harmonic from density fluctuation is expected to be zero, the recoil component in higher event activity classes is found to be well reproduced by the scaled yield from the peripheral event class. The first five Fourier harmonics, v_1–v_5 were extracted from the recoil subtracted yields in higher activity event classes.

The v_n harmonics measured in the p+Pb system show many similarities with the v_n harmonics measured in heavy ion collisions at RHIC and the LHC, and this is commonly attributed to the collective flow during the medium expansion. The v_n harmonics from $n = 2$–5, decrease with increase in harmonic number and rise with $p_{\rm T}$ in the low $p_{\rm T}$ region, reach maximum around 3–4 GeV and then decrease with further increase in $p_{\rm T}$. This $p_{\rm T}$ dependence is qualitatively similar to the $p_{\rm T}$ dependence of v_n measured in A+A collisions [4, 215]. The factorization relation (Eq. II.2.35) was found to hold within a few percent for the v_n harmonics in the low $p_{\rm T}$ region ($p_{\rm T}^{\rm a,b} < 3$–4 GeV), suggesting that the ridge in the two particle correlations can be attributed to a single particle anisotropy, another feature that is attributed to a global anisotropy from collective expansion [4].

The measured v_1 values in the p+Pb system are negative at low $p_{\rm T}$, cross zero around 1.5–2 GeV and then increase with $p_{\rm T}$ reaching a maximum value of about 0.1 at 3–4 GeV. The $p_{\rm T}$ dependence of v_1, being negative at low $p_{\rm T}$ and positive at higher $p_{\rm T}$, finds a natural explanation in hydrodynamic models and is also reproduced by models with partonic and hadronic transport during medium evolution [72, 178]. The observation of such a v_1 component provides further support to the models which attribute the ridge to final state interactions during the medium evolution. The measured v_n values were also compared to the v_n values measured in similar multiplicity Pb+Pb collisions at $\sqrt{s_{NN}} = 2.76$ TeV. It was argued that the medium produced in p+Pb collisions are smaller but hotter, such that the ratio of the system size to temperature remains constant and the medium evolution in both systems are conformal in the QGP phase [14, 104]. The $v_n(p_{\rm T})$ values in the two systems were found to overlap with each other after accounting for

the difference in mean $p_{\rm T}$ and average eccentricity in the collision systems, providing support to the conformal scaling picture [104]. Thus the results, in general, argue for a similar mechanism of origin for the ridge in p+Pb collisions as in A+A collisions.

A result for which a clear theoretical explanation is still lacking is the observation of non-zero values for the ridge and v_2 harmonic at high $p_{\rm T}$ ($p_{\rm T} \sim 10$ GeV) in high multiplicity p+Pb events. In A+A collisions, the high $p_{\rm T}$ ridge is typically attributed to the path length dependent energy loss of the high $p_{\rm T}$ particles in the medium [113]. However, no direct evidence of high $p_{\rm T}$ suppression or jet quenching in p+Pb collisions exist so far [112, 111]. It should be noted that the measurements of high $p_{\rm T}$ suppression and jet quenching have not been performed in the very high multiplicity p+Pb collisions ($N_{\rm ch}^{\rm rec} > 200$), where the near-side ridge at high $p_{\rm T}$ is observed. Other models that could explain a ridge at high $p_{\rm T}$, including the initial state models based on CGC[107, 17, 18] and models that predict azimuthal anisotropies from gluon bremsstrahlung of beam jets [16], do exist. But qualitative and quantitative description of the various features of the v_n observed [100, 180, 99] are still lacking from these models. More studies are required in this direction to understand the origin of the ridge at high $p_{\rm T}$.

Another aspect of the ridge in small systems that requires further studies, on both the experimental and theoretical fronts, is the question of collectivity in low multiplicity systems ($N_{\rm ch}^{\rm rec} < 60$). For the p+Pb system, the measurements of v_2 and v_3 from the two particle correlation (2PC) method exist down to $N_{\rm ch}^{\rm rec} \sim 40$ [180, 100], and to smaller values in the case of p+p recently [210, 216]. But the magnitude and $N_{\rm ch}^{\rm rec}$ dependence of the values obtained from the 2PC, in the low multiplicity region, depend on the assumptions used in the recoil subtraction procedure (mainly on the assumption whether the v_n are close to zero in peripheral events or have comparable values as in the central events) [210, 216]. The measurements using multi-particle cumulants are limited by the presence of non flow to values of $N_{\rm ch}^{\rm rec} \gtrsim 60$ [216, 100]. The four particle cumulants are found to have the 'wrong sign' (positive) below this $N_{\rm ch}^{\rm rec}$ value. In this work (in Chapter IV.3), it was shown that the wrong sign or lack of convergence of the $v_n\{2k\}$ values from higher order cumulants in small systems, need not indicate the absence of collectivity. This is because the cumulants are sensitive to the underlying distribution of v_n, whose functional form is *a priori* unknown in small collision systems. Also, the smearing from the non flow distribution can change the underlying distribution and cause the cumulants to behave differently from conventional expectations (as given by equations II.2.45 and II.2.51). It was shown that, in HIJING simulations, the presence of non-flow can indeed cause the cumulants to have the 'wrong sign'.

We presented an alternate method to study the cumulants, using the distributions of the flow vector in the collisions, in Chpater IV.3. The method follows from the known property that the cumulants of distributions are additive under convolution. In model studies, this new method has a better performance than the existing method in low multiplicity events. The method could potentially be applied in data to measure the cumulants in small systems. However, more studies including using more general distributions and pseudorapidity dependence for the v_n have to be investigated, before applying the method for data analysis.

The study of the correlations between multiplicities produced at different pseudorapidity bins were presented in Part V. We presented a two particle pseudorapidity correlation method to measure these longitudinal correlations in high energy nuclear collisions. The different shape fluctua-

tions, associated with the event-by-event fluctuation of the particle distribution in pseudorapidity, and their magnitudes (a_n), are obtained by expanding the correlation function in a basis of orthogonal Legendre polynomials. The method and measurements presented significantly improve our understanding of the nature of longitudinal correlations, by extending the measurements to the full two particle pseudorapidity phase space, excluding contributions from statistical fluctuations and estimating and separating the contributions from short-range correlations.

The method was applied to study the longitudinal correlations in HIJING and AMPT models, and the discussion was presented in Chapter V.1. The correlation between the shape modulations in the final particle distribution and initial state variables were studied. The value of the coefficient of the first order modulation, a_1, was found to be strongly correlated with the asymmetry in the number of forward and backward going participants in the model study. The correlation functions, particularly in the short-range region, were found to differ significantly between the HIJING and AMPT models, reflecting the sensitivity of the correlation function to the final state interactions and details of hadronization implemented in the two models. Preliminary measurements of the correlation function and Legendre coefficients in Pb+Pb collisions across the full centrality range was done, and the details of the measurement were presented in Chapter V.2. The shape fluctuations were found to be dominated by the a_1 component, suggesting that the particle production between forward and backward rapidities are anticorrelated event-by-event.

Chapter V.3 presented detailed measurements and comparisons of the longitudinal correlations in p+p, p+Pb and peripheral Pb+Pb collisions. A data driven method was used to determine the contributions from short-range correlations and thus isolate the genuine long-range correlations in the system. The magnitudes of the SRC and LRC were compared as a function of multiplicity between the three collision systems. The SRC was found to have a strong dependence on the collision system and charge combination, with values being larger for the smaller collision system and opposite charge combination, at a given multiplicity. The LRC on the other hand, were found to be similar between the three collision systems at a given multiplicity, and insensitive to the charge combination. The LRC is found to be composed almost entirely of a first order modulation (a_1), implying an event-by-event linear anticorrelation between the forward and backward rapidities. The r.m.s a_1 values are found to have a power law dependence, $\sqrt{\langle a_1^2 \rangle} \sim 1/{N_{\rm ch}}^{\alpha}$, with $\alpha \approx 0.5$. This can be expected in an independent source model [208]. In an independent source picture, the dominance of a_1 suggests that the emission profile from each source is linear in η in mid-rapidity [116]. The magnitude of $\sqrt{\langle a_1^2 \rangle}$ at a given $N_{\rm ch}$ depends also on the slope of the emission profile and the similar magnitudes between the three systems could also suggest that these slopes are also similar between the three collision systems [116].

Outlook:

The ridge and the v_n in the low $p_{\rm T}$ region show many features that are commonly attributed to hydrodynamic/collective expansion. However, measurements on the interaction of the high $p_{\rm T}$ partons and jets with the medium are still very limited, particularly in the very high multiplicity event classes. Measurements of high $p_{\rm T}$ spectra and hadron and jet nuclear modification factor R_{pPb} values in the very high multiplicity event classes can provide insights into how the high $p_{\rm T}$

particles interact with the medium produced in p+Pb collisions, and thus help understand the nature of the medium produced. However, a technical complication is determination of properly scaled yield from p+p collisions to use as reference, as centrality determination in p+Pb collisions is more difficult than in A+A collisions [217, 118]. An alternative way to look for potential jet quenching effects in high multiplicity p+Pb collisions would be to measure the dijet asymmetry (measurement of the energy imbalance between back to back jets) [58] in these collisions. Also comparisons of spectra and jet yield can be directly made between high multiplicity p+Pb and peripheral Pb+Pb collisions. A possible choice would be to match events with same underlying activity (or particle production) from the Pb nucleus, using a detector on the Pb-going side of the collision. A natural choice would be to use the ZDC on the Pb-going side. A detector in the forward rapidity, similar to FCal, on the Pb-going side, might also be used. In this case, the difference in contribution to the particle production from the proton on the other side in the p+Pb case and Pb nucleus on the other side in the case of Pb+Pb need to be taken into account. The longitudinal multiplicity correlation measurements could provide information about the nature of the particle emission profile from the individual sources and can potentially help estimate these contributions.

Measuring the ridge and v_n from heavy flavor hadrons in p+Pb collisions can provide further insights to if a thermalized medium is indeed produced in high multiplicity p+Pb (or d+Au) and p+p collisions and also to deduce the degree of thermalization of the medium. The heavy flavor flow measurements are used towards these purposes in A+A collisions [67, 68]. Because of their larger mass, heavy quarks require more interactions to thermalize and thus by comparing the magnitude of the ridge from the heavy flavor hadrons to that from charged particles (dominated by pions), the degree of thermalization in the medium can be calculated. Preliminary measurements do exist for two particle correlations from heavy flavor decay electrons (figure 19), from ALICE at LHC [218]. More detailed measurements could be possible with potentially more data from the upcoming p+Pb run at the LHC in 2016.

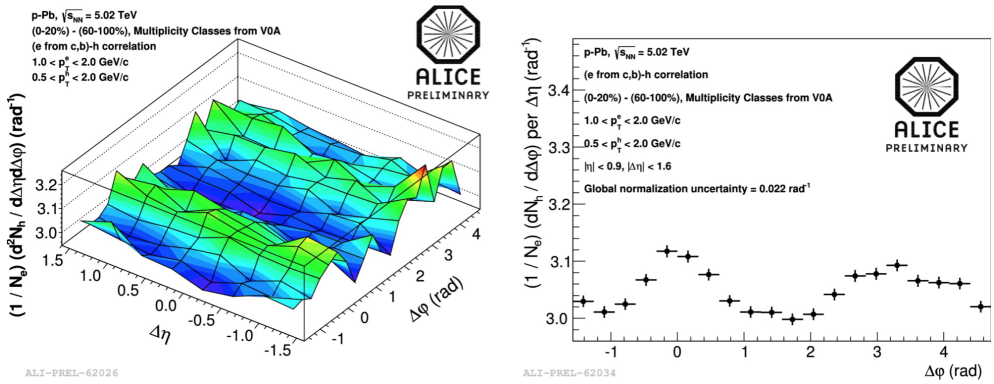

Figure 19: Difference between two-particle correlation distribution in high (0-20%) and low (60-100%) multiplicity p+Pb collisions, in the $(\Delta\phi, \Delta\eta)$ space (left panel) and the projection on the $\Delta\phi$ axis (right panel), for electrons from heavy flavor decay, from ALICE [218].

Another area where the experimental measurements can be improved, regarding the study of ridge and collectivity in small systems, is the measurement of the v_n associated with the global correlations in low multiplicity event classes. The current measurements of cumulants are limited by the presence of non-flow [100] in events with $\lesssim 60$ tracks. These measurements could be improved, more quantitative studies on the impact of the non flow correlations to cumulant measurements need to be done. We presented an alternate method to measure cumulants using the flow vector distributions from the collisions, which has a better performance than the multi-particle cumulant method in low multiplicity events. This method is limited by the approximation of the response function from the data. Better ways of constructing the response function, that minimize the non flow correlations between subevents has to be investigated. Further studies on optimization of the new method is left for future work.

The longitudinal multiplicity correlations in most models arise from the initial density fluctuations along the pseudorapidity direction, the wounded nucleon model [116] being one of the simplest cases. Following the preliminary results published on the measurements in Pb+Pb collisions, in [206], calculations were made from the theory side to describe the measured longitudinal correlations [219, 220, 221]. The calculations with fluctuating initial density distributions were able to reproduce the forward backward correlations seen in the data, with a dominating a_1 signal. An example of these calculations can be seen in the right panel of figure 20 [219]. The calculation shows that when the lengths of the initial particle producing sources in rapidity are allowed to fluctuate, the correlation function shows forward-backward asymmetry similar to that observed in the data, and are absent in the case where the source lengths are not allowed to fluctuate. The left panel shows a separate calculation with fluctuating initial density distributions along the longitudinal direction, and can also reproduce the measured correlations in the data [220]. Thus the measurements can be used to constrain the initial conditions along the η direction. The measurements in small systems, with the SRC and LRC separated, can provide important constraints for the initial conditions along the longitudinal direction in studies of the ridge in small systems.

The two particle pseudorapidity correlations can be extended to study the correlations in a larger η range. This could be possible at experiments like ATLAS and CMS, where the calorimeters in the detector span the η range $|\eta| \lesssim 5$. The fluctuations in the particle production may not be linear away from mid-rapidity ($|\eta| \lesssim 2$), and therefore such measurements are important in understanding the nature of early time particle production. Understanding the shape fluctuations can help to estimate the contribution to the multiplicity production at forward rapidity from the backward going projectile, and vice versa. This, as discussed above, can be of importance to match "event activities" between different collision systems.

The measurements of a_1 can be performed by experiments like STAR and ALICE with a limited $|\eta|$ range for tracking ($|\eta| \lesssim 1$), as well, using the ratio $r_N(\eta, \eta_{ref})$ defined in Eq. V.3.11, by correlating the mid-rapidity with a forward detector at η_{ref}. This method works as long as a_1 is dominating and the other higher order odd terms are small. With the beam energy scan data available at RHIC (STAR), this method can be used to study the evolution of the a_1 and the nature of the event by event fluctuations in particle production as a function of beam energy. Such measurements could also help constrain the initial conditions along the longitudinal direction for (3+1)d hydrodynamic calculations used to access the medium properties from the beam energy

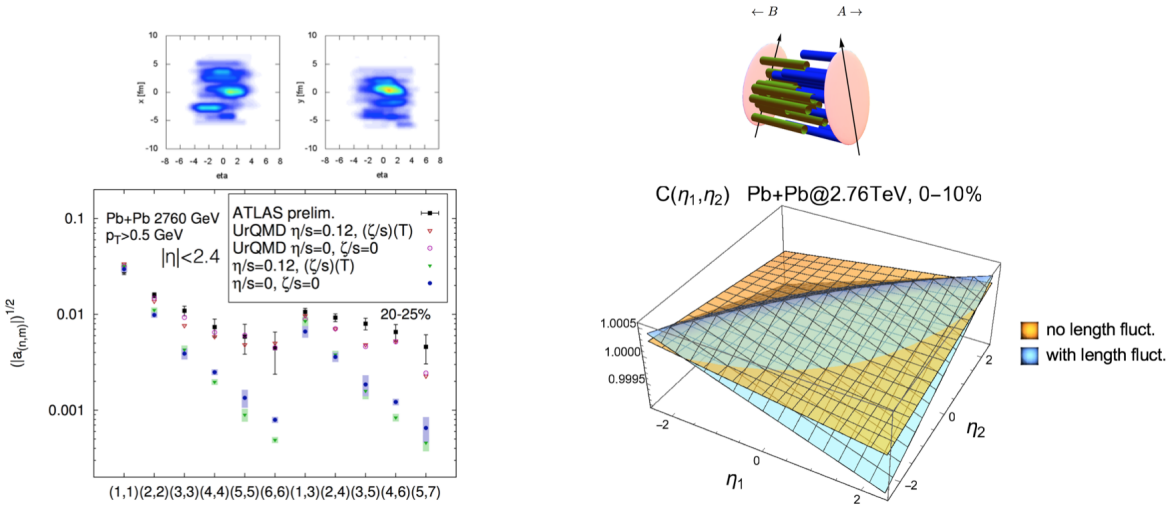

Figure 20: (Left) The $\sqrt{\langle a_n a_m \rangle}$ coefficients from hydrodynamic calculation with fluctuating initial conditions along the longitudinal direction compared to the ATLAS data [220]. (Right) The two particle correlation function $C(\eta_1, \eta_2)$ from a model with extended, initial particle producing sources in rapidity, for the cases without length fluctuations and with length fluctuations for the sources [219].

scan data.

The method developed to study the longitudinal multiplicity correlations can potentially be used to study the correlations in the pseudorapidity direction for other quantities also. For example, the correlations between the flow harmonics at different pseudorapidities can be studied. The flow harmonics are also argued to have different order shape fluctuations along the pseudorapidity direction [222]. Recently, measurements at the LHC have shown that the event plane angle, Ψ_n, could fluctuate or rotate as a function of pseudorapidity [90]. The magnitude of the flow harmonics can also vary along pseudorapidity, and it was shown in model calculations that this indeed happens depending on the eccentricities from wounded nucleons in the forward and backward going nuclei [223]. A similar two particle pseudorapidity correlation function, as the multiplicity correlation function $C(\eta_1, \eta_2)$, can be constructed using the observed magnitudes of flow harmonics q_n, and a similar analysis procedure can be carried out to identify the different shape components associated with the longitudinal flow fluctuations.

We hope our results will inspire more measurements and studies into the ridge correlations, collectivity and longitudinal correlations and along with the results presented here, will contribute to further our understanding of the matter created in p+A (p+p) and A+A collisions and also provide better constraints to models for early time entropy production and system evolution in high energy nuclear collisions.

Bibliography

[1] P. Braun-Munzinger and J. Stachel. The quest for the quarkgluon plasma. *Nature*, 448:302–309, 2007.

[2] E. Shuryak. Viewpoint: A Little Bang arrives at the LHC. *Physics*, 3:105, 2010.

[3] A. Adare et al. Dihadron azimuthal correlations in Au+Au collisions at $\sqrt{s_{NN}} = 200$ GeV. *Phys.Rev.C*, 78:014901, 2008.

[4] ATLAS Collaboration. Measurement of the azimuthal anisotropy for charged particle production in $\sqrt{s_{NN}} = 2.76$ TeV lead-lead collisions with the ATLAS detector. *Phys.Rev.C*, 86:014907, 2012.

[5] U. Heinz. Collective Flow and Viscosity in Relativistic Heavy-Ion Collisions. *Annu.Rev.Nucl.Part.Sci.*, 63:123, 2013.

[6] U. Heinz. Hydrodynamics at RHIC: how well does it work, where and how does it break down? *J.Phys.G: Nucl.Part.Phys.*, 31:S717, 2005.

[7] D. Teaney. The effects of viscosity on spectra, elliptic flow, and HBT radii. *Phys.Rev.C.*, 68:034913, 2003.

[8] P. Romatschke and U. Romatschke. Viscosity Information from Relativistic Nuclear Collisions: How Perfect is the Fluid Observed at RHIC? *Phys.Rev.Lett.*, 99:172301, 2007.

[9] CMS Collaboration. Observation of long-range, near-side angular correlations in proton-proton collisions at the LHC. *JHEP*, 09:091, 2010.

[10] CMS Collaboration. Observation of long-range, near-side angular correlations in pPb collisions at the LHC. *Phys.Lett.B*, 718:795814, 2013.

[11] A. Adare et al. Quadrupole Anisotropy in Dihadron Azimuthal Correlations in Central d +Au Collisions $\sqrt{s_{NN}} = 200$ GeV. *Phys.Rev.Lett*, 111:212301, 2013.

[12] ATLAS Collaboration. Observation of Associated Near-Side and Away-Side Long-Range Correlations in $\sqrt{s_{NN}} = 5.02$TeV Proton-Lead Collisions with the ATLAS Detector. *Phys.Rev.Lett.*, 110:182302, 2013.

[13] ALICE Collaboration. Long-range angular correlations on the near and away side in p-Pb collisions at $\sqrt{s_{NN}} = 5.02$ TeV. *Phys.Lett.B*, 719:29–41, 2013.

[14] E. Shuryak and I. Zahed. High-multiplicity pp and pA collisions: Hydrodynamics at its edge. *Phys.Rev.C*, 88:044915, 2013.

[15] P. Bozek and W. Broniowski. Collective dynamics in high energy proton nucleus collisions. *Phys.Rev.C*, 88:014903, 2013.

[16] M. Gyulassy, P. Levai, I Vitev, and T. Biro. Non-abelian bremsstrahlung and azimuthal asymmetries in high energy p + A reactions. *Phys.Rev.D*, 90:054025, 2014.

[17] K. Dusling and R. Venugopalan. Explanation of systematics of CMS p+Pb high multiplicity dihadron data at $\sqrt{s_{NN}}$=5.02TeV. *Phys.Rev.D*, 87:054014, 2013.

[18] L. McLerran, M. Praszalowiczd, and B. Schenke. Transverse momentum of protons, pions and kaons in high multiplicity pp and pA collisions: Evidence for the color glass condensate? *Nuc.Phys.A*, 916:210–218, 2013.

[19] B. Abelev et al. (STAR Collaboration). Growth of Long Range Forward-Backward Multiplicity Correlations with Centrality in Au+Au Collisions at $\sqrt{s_{NN}} = 200$ GeV. *Phys.Rev.Lett*, 103:172301, 2009.

[20] J. Adam et al. (ALICE Collaboration). Forward-backward multiplicity correlations in pp collisions at $\sqrt{s} = 0.9$, 2.76 and 7 TeV. *JHEP*, 05:097, 2015.

[21] B. Back et al. (PHOBOS Collaboration). Forward-backward multiplicity correlations in $\sqrt{s_{NN}} = 200$ GeV Au + Au collisions. *Phys.Rev.C*, 74:011901, 2006.

[22] A. Aprahamian, R Atcher, et al. Reaching for the horizon: The 2015 long range plan for nuclear science. 2015. http://science.energy.gov/np/nsac/reports/.

[23] S. Aronson and T. Ludlam. Hunting the Quark Gluon Plasma: Results from the First 3 Years at RHIC. 2005. rep. no. BNL-73847-2005, available at http://www.bnl.gov/npp/docs/Hunting the QGP.pdf.

[24] F. Wilzcek. QCD Made Simple. *Physics Today*, 2000. August 2000.

[25] P. Higgs. Broken symmetries, massless particles and gauge fields. *Phys.Lett.*, 12:132, 1964.

[26] http://www.animatedphysics.com/particle_zoo/particle_zoo.htm.

[27] T. Muta. Foundations of quantum chromodynamics: an introduction to perturbative methods in gauge theories. *World Scientific*, 78, 2010.

[28] E. Shuryak. Quantum chromodynamics and the theory of superdense matter. *Physics Reports*, 61(2):71–158, 1980.

[29] E. Shuryak. Quark-Gluon Plasma and Hadronic Production of Leptons, Photons and Pions. *Phys.Lett.B*, 78:150, 1978.

[30] A. Chaudhuri. A short course on Relativistic Heavy Ion Collisions. *arXiv*, 2012. 1207.7028.

[31] F. Karsch and E. Laermann. The Pressure in two flavor, (2+1)-flavor and three flavor QCD. *Phys.Lett.B*, 478:447–455, 2000.

[32] A. Bazavov, M Bhattacharya, N. Cheng, C. Christ, C. DeTar, et al. Equation of state and QCD transition at finite temperature. *Phys.Rev.D*, 80:014504, 2009.

[33] Z. Fodor and S. Katz. Critical point of QCD at finite T and μ, lattice results for physical quark masses. *JHEP*, 0404:050, 2004.

[34] R. Tribble et al. 2007 long range plan: The frontiers of nuclear science, report to the nuclear science advisory committee. 2007. arXiv:0809.3137.

[35] E. Shuryak. Chiral symmetry restoration in qcd. *Advances in Nuclear Dynamics 2*, 1996. 215-224.

[36] F. Karsch. Deconfinement and chiral symmetry restoration. 1999. arXiv:hep-lat/9903031.

[37] E. Iancu. Qcd in heavy ion collisions. 2012. arXiv:1205.0579.

[38] S. Mohapatra. Measurement of the azimuthal anisotropy for charged particle production in Pb+Pb collisions at $\sqrt{s_{NN}}$=2.76 tev and in p+pb collisions at $\sqrt{s_{NN}}$==5.02 tev with the atlas detector at the lhc. 2013. CERN-THESIS-2013-181.

[39] U. Heinz and P. Kolb. Early thermalization at RHIC. *Nuc.Phys.A*, 702:269, 2012.

[40] The ALICE Collaboration. Centrality determination of Pb-Pb collisions $\sqrt{s_{NN}}$ = 2.76 tev with ALICE. *Phys.Rev.C*, 88:044909, 2013.

[41] S. Esumi. Soft physics results from the PHENIX experiment. *Prog.Theor.Exp.Phys.*, 2015. ptu069.

[42] The ATLAS Collaboration. Measurement of the centrality dependence of the charged particle pseudorapidity distribution in leadlead collisions at $\sqrt{s_{NN}}$ = 2.76 TeV with the ATLAS detector. *Phys.Lett.B*, 710(3):363382, 2012.

[43] M. Miller, K. Reygers, J. Sanders, and P. Steinberg. Glauber Modeling in High-Energy Nuclear Collisions. *Ann.Rev.Nucl.Part.Sci.*, 57:205, 2007.

[44] H. Song, S. Bass, U. Heinz, T. Hirano, and C. Shen. Hadron spectra and elliptic flow for 200 A GeV Au+Au collisions from viscous hydrodynamics coupled to a boltzmann cascade. *Phys.Rev.C.*, 83:054910, 2011.

[45] Z. Lin, C. Ko, B. Li, B. Zhang, and S. Pal. Multiphase transport model for relativistic heavy ion collisions. *Phys.Rev.C*, 72:064901, 2005.

[46] J. Xu and C.M. Ko. Triangular flow in heavy ion collisions in a multiphase transport model. *Phys.Rev.C.*, 84:014903, 2011.

[47] K. Ackermann et al. (STAR Collaboration). Elliptic Flow in Au+Au Collisions at $\sqrt{s_{NN}}$=130 GeV. *Phys.Rev.Lett.*, 86:402, 2001.

[48] K. Adcox et al. (PHENIX Collaboration). Formation of dense partonic matter in relativistic nucleusnucleus collisions at RHIC: Experimental evaluation by the PHENIX Collaboration. *Nucl.Phys.A.*, 757:184, 2005.

[49] K. Aamodt et al. (ALICE Collaboration). Elliptic Flow of Charged Particles in Pb-Pb Collisions at $\sqrt{s_{NN}}$ = 2.76TeV. *Phys.Rev.Lett.*, 105:252302, 2010.

[50] S. Voloshin and Y. Zhang. Flow study in relativistic nuclear collisions by fourier expansion of azimuthal particle distributions. *Phys.Rev.C.*, 70:665, 1996.

[51] A. Poskanzer and S. Voloshin. Methods for analyzing anisotropic flow in relativistic nuclear collisions. *Phys.Rev.C.*, 58:1671, 1998.

[52] J. Ollitrault. Anisotropy as a signature of transverse collective flow. *Phys.Rev.D.*, 46:229, 1992.

[53] S. Voloshin, A. Poskanzer, and R Snellings. Collective Phenomena in Non-Central Nuclear Collisions. *in Landolt-Boernstein, Relativistic Heavy Ion Physics*, 1/23:5–54, 2010.

[54] E. Shuryak. Physics of Strongly coupled Quark-Gluon Plasma. *Prog.Nucl.Part.Phys.*, 62(1):48–101, 2009.

[55] P. Huovinen and P Ruuskanen. Hydrodynamic Models for Heavy Ion Collisions. *Ann.Rev.Nucl.Part.Sci.*, 56:163, 2006.

[56] C. Gale, S. Jeon, B. Schenke, P. Tribedy, and R. Venugopalan. Event-by-event anisotropic flow in heavy-ion collisions from combined Yang-Mills and viscous fluid dynamics. *Phys.Rev.Lett*, 110:012302, 2013.

[57] S. Adler et al. (PHENIX Collaboration). Dense-Medium Modifications to Jet-Induced Hadron Pair Distributions in Au+Au Collisions at $\sqrt{s_{NN}}$= 200 GeV. *Phys.Rev.Lett.*, 97:052301, 2006.

[58] The ATLAS Collaboration. Observation of a Centrality-Dependent Dijet Asymmetry in Lead-Lead Collisions at $\sqrt{s_{NN}}$ = 2.77 TeV with the ATLAS Detector at the LHC. *Phys.Rev.Lett.*, 105:252303, 2010.

[59] The CMS Collaboration. Observation and studies of jet quenching in PbPb collisions at nucleon-nucleon center-of-mass energy = 2.76 TeV. *Phys.Rev.C.*, 84:024906, 2011.

[60] A. Majumder. Jet modification in the next decade: A pedestrian outlook. *Pramana-J.Phys*, 84:821, 2015.

[61] J. Aamodt et al. (STAR Collaboration). Evidence from d + Au measurements for final state suppression of high p_t hadrons in Au+Au collisions at RHIC. *Phys.Rev.Lett.*, 91:072304, 2003.

[62] A. Adare et al. (PHENIX Collaboration). Suppression pattern of neutral pions at high transverse momentum in Au + Au collisions at $\sqrt{s_{NN}}$ = 200 GeV and constraints on medium transport coefficients. *Phys.Rev.Lett.*, 101:232301, 2008.

[63] K. Aamodt et al. (ALICE Collaboration). Suppression of charged particle production at large transverse momentum in central PbPb collisions at $\sqrt{s_{NN}}$ = 2.76 TeV. *Phys.Lett.B*, 696:30–39, 2011.

[64] M. Tannenbaum. Results from PHENIX at RHIC with implications for LHC. *Int.J.Mod.Phys.A*, 26:5299, 2011.

[65] P. Koch, B Muller, and J Rafelski. Strangeness in relativistic heavy ion collisions. *Phys.Rept.*, 142:167–262, 1986.

[66] G. Agakishiev et al. (STAR Collaboration). Strangeness Enhancement in Cu-Cu and Au-Au Collisions at $\sqrt{s_{NN}}$=200GeV. *Phys.Rev.Lett.*, 108:072301, 2012.

[67] H. Qiu for the STAR Collaboration. STAR heavy flavor tracker. *Nucl.Phys.A.*, 931:1141–1146, 2014.

[68] A. Adare et al. (PHENIX Collaboration). Energy Loss and Flow of Heavy Quarks in Au+Au Collisions at $\sqrt{s_{NN}}$=200GeV. *Phys.Rev.Lett.*, 98:172301, 2007.

[69] B. Abelev et al. (ALICE Collaboration). Suppression of high transverse momentum D mesons in central Pb–Pb collisions at $\sqrt{s_{NN}}$=2.76 TeV. *J.High.Energ.Phys.*, 2012. 2012,112.

[70] S. Bass, M. Gyulassy, H. Stoecker, and W. Greiner. Signatures of Quark-Gluon-Plasma formation in high energy heavy-ion collisions: A critical review. *J.Phys.G*, 25:R1–R57, 1999.

[71] B. Alver and G. Roland. Collision-geometry fluctuations and triangular flow in heavy-ion collisions. *Phys.Rev.C*, 81:054905, 2010.

[72] D. Teaney and L. Yan. Triangularity and dipole asymmetry in relativistic heavy ion collisions. *Phys.Rev.C*, 83:064904, 2011.

[73] U. Heinz. Early collective expansion: Relativistic hydrodynamics and the transport properties of QCD matter. *in Landolt-Boernstein, Relativistic Heavy Ion Physics*, 1/23, 2010. Chapter 5.

[74] R. Glauber. Lectures on Theoretical Physics. *W.E. Brittin, L.G. Dunham (eds.), (Interscience, NY, 1959)*, 1, 1959.

[75] F. Gelis. Color Glass Condensate and Glasma. *Int.J.Mod.Phys.A*, 28:1330001, 2013.

[76] D. Kharzeev, E. Levin, and M. Nardi. Color glass condensate at the LHC: hadron multiplicities in pp, pA and AA collisions. *Nucl.Phys.A*, 747:609, 2005.

[77] B. Schenke, P. Tribedy, and R. Venugopalan. Fluctuating Glasma Initial Conditions and Flow in Heavy Ion Collisions. *Phys.Rev.Lett.*, 108:252301, 2012.

[78] D. Teaney, J. Lauret, and E. Shuryak. Flow at the SPS and RHIC as a Quark-Gluon Plasma Signature. *Phys.Rev.Lett.*, 86:4783, 2001.

[79] H. Song and U. Heinz. Causal viscous hydrodynamics in 2 + 1 dimensions for relativistic heavy-ion collisions. *Phys.Rev.C.*, 77:064901, 2008.

[80] I. Karpenko, P. Huovinen, and M. Bleicher. A 3+13+1 dimensional viscous hydrodynamic code for relativistic heavy ion collisions. *Comp.Phys.Comm*, 185:30163027, 2014.

[81] L. Pang, H. Petersen, G. Qin, et al. Decorrelation of anisotropic flow along the longitudinal direction. *Eur.J.Phys.A*, 52:97, 2016.

[82] K. Hagiwara et al. (Particle Data Group). Review of particle properties. *Phys.Rev.D.*, 66:010001(R), 2002.

[83] F. Cooper and G. Frye. Single-particle distribution in the hydrodynamic and statistical thermodynamic models of multiparticle production. *Phys.Rev.D.*, 10:186, 1974.

[84] C. Adler et al. (STAR Collaboration). Elliptic flow from two- and four-particle correlations in Au+Au collisions at $\sqrt{s_{NN}}$=130 GeV. *Phys.Rev.C.*, 66:034904, 2002.

[85] N. Borghini, P. Dinh, and J. Ollitrault. Flow analysis from multiparticle azimuthal correlations. *Phys.Rev.C.*, 64:054901, 2001.

[86] A. Bilandzic, R. Snellings, and S. Voloshin. Flow analysis with cumulants: Direct calculations. *Phys.Rev.C.*, 83:044913, 2011.

[87] The ATLAS Collaboration. Measurement of flow harmonics with multi-particle cumulants in pb+pb collisions at $\sqrt{s_{NN}}$=2.76 tev with the atlas detector. *Eur.J.Phys.C.*, 74:3157, 2014.

[88] R. Bhalerao, N. Borghini, and J. Ollitrault. Analysis of anisotropic flow with LeeYang zeroes. *Nucl.Phys.A.*, 727:373–426, 2003.

[89] F. Gardim, F. Grassi, M. Luzum, and J Ollitrault. Breaking of factorization of two-particle correlations in hydrodynamics. *Phys.Rev.C.*, 87:031901, 2013.

[90] The CMS Collaboration. Evidence for transverse momentum and pseudorapidity dependent event plane fluctuations in PbPb and pPb collisions. *Phys.Rev.C*, 92:01692, 2015.

[91] N. Borghini, P. Dinh, and J. Ollitrault. Is the analysis of flow at the CERN Super Proton Synchrotron reliable? *Phys.Rev.C*, 62:034902, 2000.

[92] A. Bilandzic. Anisotropic Flow Measurements in ALICE at the Large Hadron Collider. 2012. PhD Thesis, http://www.nikhef.nl/pub/services/biblio/theses_pdf/thesis_A_Bilandzic.pdf.

[93] S. Voloshin, A. Poskanzer, A. Tang, and G. Wang. Elliptic flow in the gaussian model of eccentricity fluctuations. *Phys.Lett.B.*, 659:537541, 2008.

[94] W. Li. Observation of a ridge correlation structure in high multiplicity proton-proton collisions: A brief review. *Mod.Phys.Lett.*, 27:1230018, 2012.

[95] R. Ansorge et al. (UA5 Collaboration). Charged Particle Correlations in $\bar{p}p$ Collisions at c.m. Energies of 200 GeV, 546 GeV and 900 GeV. *Z.Phys.C.*, 37:191, 1988.

[96] S. Uhlig et al. Observation of Charged Particle Correlations Between the Forward and Backward Hemispheres in pp Collisions at ISR Energies. *Nucl.Phys.B.*, 132:15, 1978.

[97] The ATLAS Collaboration. Forward-backward correlations and charged-particle azimuthal distributions in pp interactions using the ATLAS detector. *JHEP*, 07:019, 2007.

[98] ATLAS Collaboration. Measurement with the ATLAS detector of multi-particle azimuthal correlations in p+Pb collisions at $\sqrt{s_{NN}} = 5.02$TeV. *Phys.Lett.B*, 725:6078, 2013.

[99] The ALICE Collaboration. Long-range angular correlations of π, K and p in pPb collisions at $\sqrt{s_{NN}} = 5.02$ TeV. *Phys.Lett.B.*, 726(1-3):164–177, 2013.

[100] The CMS Collaboration. Multiplicity and transverse momentum dependence of two- and four-particle correlations in pPb and PbPb collisions. *Phys.Lett.B.*, 724(4-5):213–440, 2013.

[101] E. Shuryak. Comments on the CMS discovery of the "Ridge" in High Multiplicity pp collisions at LHC. 2010. arXiv:1009.4635.

[102] K. Werner, I. Karpenko, and T. Pierog. Ridge in Proton-Proton Scattering at 7 TeV. *Phys.Rev.Lett*, 106:122004, 2011.

[103] P. Bozek. Collective flow in p-Pb and d-Pb collisions at TeV energies. *Phys.Rev.C*, 85:014911, 2012.

[104] D Basar, G aand Teaney. Scaling relation between pA and AA collisions. *Phys.Rev.C.*, 90:054903, 2014.

[105] A. Bzdak, B. Schenke, P. Tribedy, and R. Venugopalan. Initial-state geometry and the role of hydrodynamics in proton-proton, proton-nucleus, and deuteron-nucleus collisions. *Phys.Rev.C.*, 87:064906, 2013.

[106] G. Ma and P. Bozek. Long-range azimuthal correlations in protonproton and protonnucleus collisions from the incoherent scattering of partons. *Phys.Lett.B*, 739:209–213, 2014.

[107] K. Dusling and R. Venugopalan. Evidence for BFKL and saturation dynamics from dihadron spectra at the LHC. *Phys.Rev.D*, 87:051502, 2013.

[108] Y. Kovchegov and D. Wertepny. Long-range rapidity correlations in heavylight ion collisions. *Nuc.Phys.A.*, 906:50–83, 2013.

[109] A. Dumitru, L. McLerran, and V. Skokovf. Azimuthal asymmetries and the emergence of collectivity from multi-particle correlations in high-energy pA collisions. *Phys.Lett.B.*, 743:134, 2015.

[110] T. Lappi. Azimuthal harmonics of color fields in a high energy nucleus. *Phys.Lett.B.*, 744:315, 2015.

[111] The ALICE Collaboration. Transverse Momentum Distribution and Nuclear Modification Factor of Charged Particles in p+Pb collisions at $\sqrt{s_{NN}}$ =5.02 TeV. *Phys.Rev.Lett.*, 110:082302, 2013.

[112] The ATLAS Collaboration. Centrality and rapidity dependence of inclusive jet production in $\sqrt{s_{NN}}$ =5.02 TeV source protonlead collisions with the ATLAS detector. *Phys.Lett.B*, 748:392, 2014.

[113] The CMS Collaboration. Azimuthal anisotropy of charged particles at high transverse momenta in PbPb collisions at $\sqrt{s_{NN}}$ =2.76 TeV. *Phys.Rev.Lett*, 109:022301, 2012.

[114] W. Braunschweig et al. (TASSO Collaboration). Charged Multiplicity Distributions and correlations in e^+e^- Annihilation at PETRA Energies. *Z.Phys.C*, 45:193, 1989.

[115] Y. Kovchegov, E. Levin, and L. McLerran. Large scale rapidity correlations in heavy ion collisions. *Phys.Rev.C*, 63:024903, 2001.

[116] A. Bzdak and D. Teaney. Longitudinal fluctuations of the fireball density in heavy-ion collisions. *Phys.Rev.C*, 87:024906, 2013.

[117] B. Alver et al. (PHOBOS Collaboration). Charged-particle multiplicity and pseudorapidity distributions measured with the PHOBOS detector in Au+Au, Cu+Cu, d+Au, and p+p collisions at ultrarelativistic energies. *Phys.Rev.C*, 83:024913, 2011.

[118] The ATLAS Collaboration. Measurement of the centrality dependence of the charged-particle pseudorapidity distribution in protonlead collisions at $\sqrt{s_{NN}}$=5.02 TeV with the ATLAS detector. *Eur.J.Phys.C*, 76:199, 2016.

[119] M. Abramowitz, Stegun, and I. Ann. Handbook of mathematical functions with formulas, graphs, and mathematical tables. *Applied Mathematics Series 55*, 1964. Chapter 8.

[120] X Wang and M Gyulassy. HIJING 1.0: A Monte Carlo Program for Parton and Particle Production in High Energy Hadronic and Nuclear Collisions. *Comp.Phys.Comm.*, 83:307, 1994.

[121] E. O. Lawrence. Method and apparatus for the acceleration of ions. *US Patent No.1948384*, 1934.

[122] R. Tecker. Longitudinal beam dynamics. *CERN Accelerator School: Advanced Accelerator Physics Course*, 2014. doi: 10.5170/CERN-2014-009.1.

[123] E. M. McMillan. The Synchrotron - A Proposed High Energy Particle Accelerator. *Phys.Rev*, 68:143, 1945. doi: http://dx.doi.org/10.1103/PhysRev.68.143.

[124] V. I. Veksler. A new method of accelerating relativistic particles. *Comptes Rendus de l'Academie Sciences de l'URSS*, 43:329, 1944.

[125] S. Baird. Accelerators for pedestrians. 2007. CERN-AB-Note-2007-014.

[126] E. D. Courant, M. S Livingston, and H. S. Snyder. The Strong-Focusing Synchroton: A New High Energy Accelerator. *Phys.Rev.*, 88:1190–1196, 1952.

[127] B. J. Holzer. Beam optics and lattice design for particle accelerators. *CERN Accelerator School: Course on High Power Hadron Machines*, 2013. doi: 10.5170/CERN-2013-001.171.

[128] G. W. Hill. On the part of the motion of the lunar perigee which is a function of the mean motions of the sun and moon. *Acta Mathematica*, 8:1–36, 1886.

[129] S. Van der Meer. Calibration of the eective beam height in the ISR. 1968. internal report, CERN-ISR-PO/68-31.

[130] S. M. White. Determination of the Absolute Luminosity at the LHC. 2010. CERN-THESIS-2010-139.

[131] The ATLAS Collaboration. Luminosity determination in pp collisions at $\sqrt{s_{NN}} = 7$ TeV using the ATLAS detector at the LHC. *Eur.Phys.Jour.C*, 71:1–37, 2011.

[132] L. Evans and P. Bryant. LHC Machine. *JINST*, 3, 2008. S08001.

[133] O. S. Bruning, P. Collier, P. Lebrun, R. Ostojic, J. Poole and P. Proudlock. LHC Design Report v.1 : The LHC Main Ring. 2004. Tech. rep, CERN-2004-003-V-1.

[134] O. S. Bruning, P. Collier, P. Lebrun, R. Ostojic, J. Poole and P. Proudlock. LHC Design Report v.2 : The LHC Infrastructure and General Services. 2004. Tech. rep, CERN-2004-003-V-2.

[135] The ATLAS Collaboration. The ATLAS Experiment at the CERN Large Hadron Collider. *JINST*, 3, 2008. S08003.

[136] The CMS Collaboration. The CMS experiment at the CERN LHC. *JINST*, 3, 2008. S08004.

[137] K. Aamodt et al. The ALICE experiment at the CERN LHC. *JINST*, 3, 2008. S08002.

[138] A. Augusto et al. The LHCb Detector at the LHC. *JINST*, 3, 2008. S08005.

[139] O. Adriani et al. The LHCf detector at the CERN Large Hadron Collider. *JINST*, 3, 2008. S08006.

[140] G. Anelli et al. The TOTEM Experiment at the CERN Large Hadron Collider. *JINST*, 3, 2008. S08007.

[141] J. Pinfold et al. Technical Design Report of the MoEDAL Experiment. 2009. CERN-LHCC-2009-006, MoEDAL-TDR-001.

[142] M. Benedikt, P. Collier, V. Mertens, J. Poole, K. Schindl. LHC Design Report v.3 : The LHC injector chain. 2004. Tech. rep, CERN-2004-003-V-3.

[143] TE-EPC-LPC in LHC. http://te-epc-lpc.web.cern.ch/te-epc-lpc/machines/lhc/general.stm.

[144] P. Bailey, R. Collier. Standard Filling Schemes for Various LHC Operation Modes. 2003. LHC-PROJECT-NOTE-323.

[145] The ATLAS Collaboration. ATLAS detector and physics performance : Technical Design Report, 1. 1999. Tech. rep, CERN-LHCC-99-014, ATLAS-TDR-14.

[146] The ATLAS Collaboration. The ATLAS Inner Detector commissioning and calibration. *Eur.Phys.Jour.*, C70:787–821, 2010.

[147] The ATLAS Collaboration. ATLAS pixel detector: Technical Design Report. 1998. Tech. rep, CERN-LHCC-98-01, ATLAS-TDR-11.

[148] The ATLAS Collaboration. ATLAS pixel detector electronics and sensors. *JINST*, 3, 2008. P07007.

[149] The ATLAS Collaboration. ATLAS Insertable B-Layer: Technical Design Report. 2010. Tech. rep, CERN-LHCC-2010-013, ATLAS-TDR-19.

[150] J. Jackson (for the ATLAS SCT Collaboration). The ATLAS semiconductor tracker (SCT). *NIM*, A 541:89 – 95, 2005.

[151] A. Ahmad and other. The silicon microstrip sensors of the ATLAS semiconductor tracker. *NIM*, A 578:98 – 118, 2007.

[152] The ATLAS TRT collaboration et al. The ATLAS TRT Barrel Detector. *JINST*, 3, 2008. P02014.

[153] The ATLAS Collaboration. Performance of the Minimum Bias Trigger in pp collisions at $\sqrt{s} = 900$ GeV. 2010. ATLAS-CONF-2010-025, http://cds.cern.ch/record/1277657.

[154] The ATLAS Collaboration. ATLAS forward detectors for luminosity measurement and monitoring. 2004. CERN-LHCC-2004-010, LHCC-I-014, http://cdsweb.cern.ch/record/721908.

[155] The ATLAS Collaboration. ATLAS forward detectors for measurement of elastic scattering and luminosity. 2008. CERN-LHCC-2008-004, ATLAS-TDR-18, http://cdsweb.cern.ch/record/1095847.

[156] The ATLAS Collaboration. Zero degree calorimeters for ATLAS. 2007. CERN-LHCC-2007-01, LHCC-I-016, http://cdsweb.cern.ch/record/1009649.

[157] The ATLAS Collaboration. ATLAS high-level trigger, data-acquisition and controls : Technical Design Report.

[158] S. Ask et al. The ATLAS central level-1 trigger logic and TTC system. *JINST*, 3, 2008. P08002.

[159] T. Cornelissen et al. The new ATLAS Track Reconstruction (NEWT). *Journal of Physics: Conference Series*, 119, 2008. 032014.

[160] The ATLAS Collaboration. Track Reconstruction Performance of the ATLAS Inner Detector at $\sqrt{s} = 13$ TeV. 2015. ATLAS NOTE, ATL-PHYS-PUB-2015-018.

[161] M Limper. Track and vertex reconstruction in the ATLAS inner detector. 2009. CERN-THESIS-2009-061.

[162] R. Fruhwirth et al. Application of Kalman Filtering to Track and Vertex Fitting. *Nucl.Instrum.Meth.*, A262:444, 1987.

[163] I Gavrilenko. Description of Global Pattern Recognition Program (XKalman). 1997. ATLAS public note, ATL-INDET-97-165.

[164] E. Bouhova-Thacker et al. Vertex Reconstruction in the ATLAS Experiment at the LHC. 2008. ATLAS public note, ATL-INDET-PROC-2008-003.

[165] S. Billoir, P. Qian. Fast vertex fitting with a local parametrization of tracks. *Nucl.Instrum.Meth.*, A311:139–150, 1992.

[166] M. Luzum and J. Ollitrault. Directed Flow at Midrapidity in Heavy-Ion Collisions. *Phys.Rev.Lett*, 106:102301, 2011.

[167] S. Voloshin, A. Poskanzer, and R. Snellings. Collective phenomena in non-central nuclear collisions. 2009. arXiv:0809.2949.

[168] Miller and R. M. Snellings. Eccentricity fluctuations and its possible effect on elliptic flow measurements. 2003. arXiv:0312008.

[169] B. Alver, C. Gombeaud, M Luzum, and J. Ollitrault. Triangular flow in hydrodynamics and transport theory. *Phys.Rev.C*, 82:034913, 2010.

[170] P. Staig and E. Shuryak. Fate of the initial state perturbations in heavy ion collisions. II. Glauber fluctuations and sounds. *Phys.Rev.C*, 84:034908, 2011.

[171] The CMS Collaboration. Centrality dependence of dihadron correlations and azimuthal anisotropy harmonics in PbPb collisions at $\sqrt{s_{NN}}$ = 2.76 TeV. *Eur.Phys.Jour.C*, 72:2012, 2012.

[172] N. Borghini and J. Ollitrault. Momentum spectra, anisotropic flow, and ideal fluids. *Phys.Lett.B*, 642,3:227–231, 2006.

[173] E. Retinskaya, M. Luzum, and J. Ollitrault. Directed Flow at Midrapidity in $\sqrt{s_{NN}}$ = 2.76TeV Pb+Pb Collisions. *Phys.Rev.Lett*, 108:252302, 2012.

[174] R. Snellings, S. Voloshin, F. Wang, and N. Xu. Novel Rapidity Dependence of Directed Flow in High-Energy Heavy-Ion Collisions. *Phys.Rev.Lett*, 84:2803, 2000.

[175] B. Back et. al. (PHOBOS Collaboration). Energy Dependence of Directed Flow over a Wide Range of Pseudorapidity in Au+Au Collisions at the BNL Relativistic Heavy Ion Collider. *Phys.Rev.Lett*, 97:012301, 2006.

[176] I. Selyuzhenkov for the ALICE Collaboration. Charged particle directed flow in PbPb collisions at $\sqrt{s_{NN}}$ = 2.76 TeV measured with ALICE at the LHC. *J.Phys.G: Nucl.Part.Phys.*, 38:124167, 2011.

[177] R Brun and F Rademakers. ROOT - An Object Oriented Data Analysis Framework. *Nucl.Instrum.Meth.Phys.Res.Sect.A*, 389:81, 1996. See also http://root.cern.ch/.

[178] J. Jia, S. Radhakrishnan, and S. Mohapatra. A study of the anisotropy associated with dipole asymmetry in heavy ion collisions. *J.Phys.G: Nucl.Part.Phys.*, 40:105108, 2013.

[179] B. Alver et al. System Size, Energy, Pseudorapidity, and Centrality Dependence of Elliptic Flow. *Phys.Rev.Lett.*, 98:242302, 2007.

[180] The ATLAS Collaboration. Measurement of long-range pseudorapidity correlations and azimuthal harmonics in $\sqrt{s_{NN}}$ = 5.02 TeV proton-lead collisions with the ATLAS detector. *Phys.Rev.C.*, 90:044906, 2014.

[181] The ATLAS Collaboration. Measurement of the long-range pseudorapidity correlations and associated fourier harmonics in $\sqrt{s_{NN}}$ =5.02 TeV proton-lead collisions with the ATLAS detector. 2013. ATL-COM-PHYS-2013-1017.

[182] The ATLAS Collaboration. Observation and measurement of the long-range pseudorapidity correlations in $\sqrt{s_{NN}}$ =5.02 TeV proton-lead collisions with the ATLAS detector. 2012. ATL-COM-PHYS-2012-1606.

[183] The ATLAS Collaboration. Performance of the atlas minimum bias and forward detector triggers in ppb collisions. 2013. ATLAS-CONF-2013-104.

[184] The ATLAS Collaboration. Charged-particle multiplicities in pp interactions measured with the ATLAS detector at the LHC. *New.J.Phys.*, 13:053033, 2011. ATL-COM-PHYS-2010-682, https://cdsweb.cern.ch/record/1286839.

[185] S. Agostinelli et al. Geant4a simulation toolkit. *Nucl.Instrum.Meth.Phys.Res.Sect.A*, 506(3):250–303, 2003.

[186] S. Agostinelli et al. The atlas simulation infrastructure. *Eur.Phys.Jour.C*, 70:823–874, 2010.

[187] B. Alver et al. High Transverse Momentum Triggered Correlations over a Large Pseudorapidity Acceptance in Au+Au Collisions at $\sqrt{s_{NN}}$ = 200 GeV. *Phys.Rev.Lett*, 104:062301, 2010.

[188] N. Ajitanand, J. Alexander, et al. Decomposition of harmonic and jet contributions to particle-pair correlations at ultrarelativistic energies. *Phys.Rev.C*, 72:011902, 2005.

[189] J. Jia. Probing jet properties via the two-particle correlation method. *J.Phys.G: Nucl.Part.Phys.*, 31:S521, 2005.

[190] ALICE Collaboration. Harmonic decomposition of two particle angular correlations in PbPb collisions at $\sqrt{s_{NN}}$ = 2.76 TeV. *Phys.Lett.B*, 708:249, 2012.

[191] U. Heinz, Z. Qiu, and C. Shen. Fluctuating flow angles and anisotropic flow measurements. *Phys.Rev.C.*, 87:034913, 2013.

[192] I. Kozlov, M Luzum, G. Denicol, S. Jeon, and C. Gale. Transverse momentum structure of pair correlations as a signature of collective behavior in small collision systems. 2014. arXiv:1405.3976.

[193] P. Bozek and W. Broniowski. Hydrodynamic approach to p-Pb. *Nuc.Phys.A*, 926:16–23, 2014.

[194] Z. Qui, C. Shen, and W Heinz. Hydrodynamic elliptic and triangular flow in Pb-Pb collisions at $\sqrt{s_{NN}}$ =2.76ATeV. *Phys.Lett.B*, 12:041, 2011.

[195] The ATLAS Collaboration. Measurement of the correlation between flow harmonics of different order in lead-lead collisions at $\sqrt{s_{NN}}$ =2.76 TeV with the ATLAS detector. *Phys.Rev.C*, 92:034903, 2015.

[196] S.Radhakrishnan for The ATLAS Collaboration. Measurement of the correlation between flow harmonics of different order in lead-lead collisions at $\sqrt{s_{NN}}$ =2.76 TeV with ATLAS. 2015. QuarkMatter2015, Kobe: https://indico.cern.ch/event/355454/contributions/838763/.

[197] R. Snellings. Elliptic flow: a brief review. *New.J.Phys.*, 13:055008, 2011.

[198] J. Jia and S. Radhakrishnan. Limitation of multiparticle correlations for studying the event-by-event distribution. *Phys.Rev.C.*, 92:024911, 2015.

[199] J. Jia. Meanings of cumulant measurements.

[200] L. Shenton and K. Bowman. The Development of Techniques for the Evaluation of Sampling Moments. *Int.Stat.Rev.*, 3:317–334, 1975.

[201] mathStatica. mathstatica for mathematica. http://www.mathstatica.com/install/2.7/mac.html.

[202] The ATLAS Collaboration. Measurement of the distributions of event-by-event flow harmonics in Pb+Pb collisions at $\sqrt{s_{NN}}$=2.76 TeV with the ATLAS detector. *JHEP*, 11:183, 2013.

[203] M. Masera, G. Ortona, M. Poghosyan, and F.. Prino. Anisotropic transverse flow introduction in monte carlo generators for heavy ion collisions. *Phys.Rev.C*, 79:064909, 2009.

[204] J. Jia and S. Mohapatra. Disentangling flow and nonflow correlations via bayesian unfolding of the event-by-event distributions of harmonic coefficients in ultrarelativistic heavy-ion collisions. *Phys.Rev.C*, 75:031901, 2013.

[205] J. Jia, S. Radhakrishnan, and M. Zhou. Forward-backward multiplicity fluctuation and longitudinal harmonics in high-energy nuclear collisions. *Phys.Rev.C*, 93:044905, 2016.

[206] The ATLAS Collaboration. Measurement of two-particle pseudorapidity correlations in leadlead collisions at $\sqrt{s_{NN}}$ = 2.76 TeV with the ATLAS detector. 2016. ATLAS-CONF-2015-020.

[207] The ATLAS Collaboration. Jet energy measurement with the ATLAS detector in proton-proton collisions at $\sqrt{s}$=7 TeV. *Eur.J.Phys.C*, 73:2304, 2013.

[208] The ATLAS Collaboration. Measurement of forward-backward multiplicity correlations in lead-lead, proton-lead and proton-proton collisions with the ATLAS detector. 2016. arXiv:1606.08170.

[209] The ATLAS Collaboration. Charged-particle distributions in $\sqrt{s}$=13 TeV pp interactions measured with the ATLAS detector at the LHC. *Phys.Lett.B*, 758:67, 2016.

[210] The ATLAS Collaboration. Observation of Long-Range Elliptic Azimuthal Anisotropies in $\sqrt{s}$ = 13 and 2.76 TeV pp Collisions with the ATLAS Detector. *Phys.Rev.Lett.*, 116:172301, 2016.

[211] T. Sjstrand, S. Mrenna, and P. Skands. A brief introduction to PYTHIA 8.1. *Comput.Phys.Commun.*, 178:852, 2008.

[212] The ATLAS Collaboration. ATLAS tunes of PYTHIA 6 and Pythia 8 for MC11. 2011. ATLAS-PHYS-PUB-2011-009, url: http://cds.cern.ch/record/1363300.

[213] The ATLAS Collaboration. Rapidity correlations at fixed multiplicity in cluster emission models. *Nucl.Phys.B*, 85:61, 1975.

[214] T. Pierog and K. Werner. EPOS Model and Ultra High Energy Cosmic Rays. *Nucl.Phys.Proc.Suppl.*, 196:102–105, 2009.

[215] CMS Collaboration. Measurement of higher-order harmonic azimuthal anisotropy in PbPb collisions at $\sqrt{s_{NN}}$ = 2.76 TeV. *Phys.Rev.C*, 89:044906, 2014.

[216] The CMS Collaboration. Evidence for collectivity in pp collisions at the LHC. 2016. arXiv:1606.06198.

[217] J. Adam et al. (ALICE Collaboration). Centrality dependence of particle production in pPb collisions at $\sqrt{s_{NN}}$=5.02 TeV. *Phys.Rev.C*, 91:064905, 2015.

[218] E. Pereira (for the ALICE Collaboration). Measurements of electrons from heavy-flavour hadron decays in pp, p-Pb and Pb-Pb collisions with ALICE at the LHC. *Nucl.Phys.A*, 00:1–4, 2014.

[219] W. Broniowski and P. Boek. Simple model for rapidity fluctuations in the initial state of ultrarelativistic heavy-ion collisions. *Phys.Rev.C*, 93:064910, 2016.

[220] A. Monnaia and B. Schenke. Pseudorapidity correlations in heavy ion collisions from viscous fluid dynamics. *Phys.Lett.B*, 752:317321, 2016.

[221] P. Boek, W. Broniowski, and A. Olszewski. Two-particle correlations in pseudorapidity in a hydrodynamic model. *Phys.Rev.C*, 92:054913, 2015.

[222] R. Bhalerao, J. Ollitrault, S. Pal, and D. Teaney. Principal Component Analysis of Event-by-Event Fluctuations. *Phys.Rev.Lett.*, 114:152301, 2015.

[223] J. Jia and P. Huo. Forward-backward eccentricity and participant-plane angle fluctuations and their influences on longitudinal dynamics of collective flow. *Phys.Rev.C*, 90:034915, 2014.

Appendix A

Appendix to Part IV

The Chapter of the Appendix contains supplementray information to the analysis presented in Part IV of this thesis. Appendix A.1 discusses the reweighting procedure used to combine events from different trigger selections and shows plots detailing its performance. The estimation of pileup fraction in the p+Pb data sample and the procedures used to reject the pileup events are presented in Appendix A.2. The details of the evaluation of the systematic uncertainties in the measurement of the ridge and v_n harmonics are presented in Appendix A.3

A.1 Combining events from different triggers

The efficiencies for the four primary HMT, relative to the primary MB trigger, as function of $N_{\rm ch}^{\rm rec}$ are shown in figure A.1. The efficiencies are evaluated as the fraction of events selected by the primary MB trigger also selected by the given trigger, in lumi-blocks where the prescale for the trigger was 1. For the other two HMT triggers included in the analysis, the turn-on curves showing the fraction of events selected by the given trigger in all events selected the primary MB trigger are shown, in figure A.2. The flat part of the ratio is scaled to match 1. The HMT triggers in general have a sharp turn on curve, whereby the efficiency increases from 0 to 90% within a span of ~ 10 tracks.

The enhancement of statistics from the HMT, owing to their different thresholds and prescale values, causes the $N_{\rm ch}^{\rm rec}$ and $E_{\rm T}^{\rm Pb}$ distributions to be different from that with the MB selection, as can be seen from the top panels in figure IV.2.3. Also the HMT selection causes mean and r.m.s $N_{\rm ch}^{\rm rec}$ in a given $E_{\rm T}^{\rm Pb}$ class (and vice versa) to be very different from that from the MB selection (see figures A.3, A.4, discussed below). The prescale is a random reset for a passed trigger chain to fail. A prescaled trigger, with a prescale of α, passes $\frac{1}{\alpha}$ number of events passed by the unprescaled trigger. The trigger efficiency ϵ_{trig} gives the probability (relative to MB) for the trigger selecting the event, if the prescale was 1. So weighting the $N_{\rm ch}^{\rm rec}$ or $E_{\rm T}^{\rm Pb}$ distributions from a given trigger by the inverse probability to select an event, $\frac{\alpha}{\epsilon_{trig}(N_{\rm ch}^{\rm rec},E_{\rm T}^{\rm Pb})}$, would give the distribution if all events satisfying the trigger condition, were to be selected. The trigger efficiency for MB trigger is 1 in the HMT selection region, and so this will give a distribution consistent with MB. The trigger

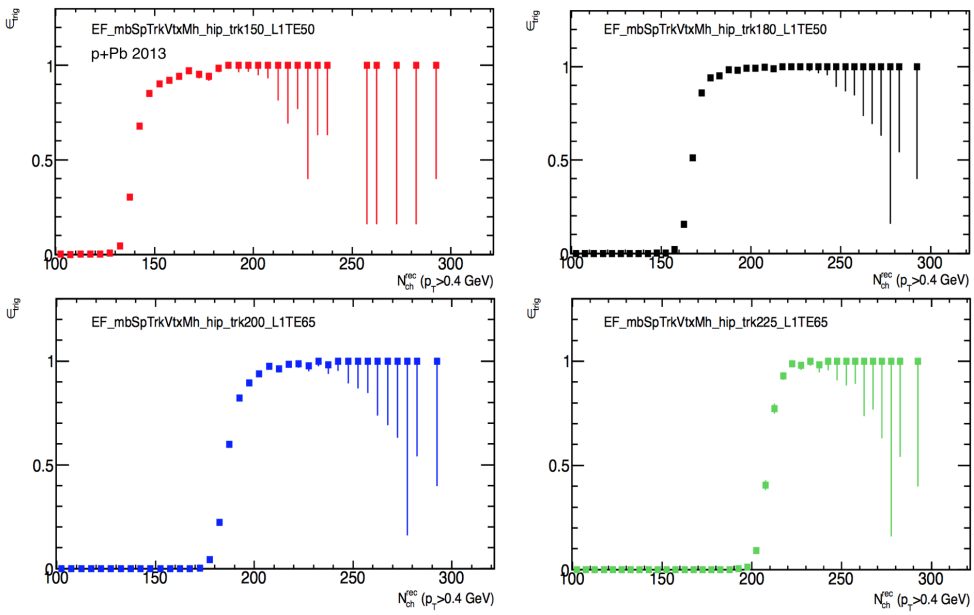

Figure A.1: Efficiencies of four primary triggers relative to the primary MB trigger, `EF_mbMBTS_1_1`, as a function of $N_{\mathrm{ch}}^{\mathrm{rec}}$.

efficiencies for the HMT triggers are function of both $N_{\mathrm{ch}}^{\mathrm{rec}}$ and $E_{\mathrm{T}}^{\mathrm{Pb}}$ as the trigger thresholds were determined using the two corresponding online quantities. In the present analysis the efficiency is applied as a function of $N_{\mathrm{ch}}^{\mathrm{rec}}$ and $E_{\mathrm{T}}^{\mathrm{L1}}$. This is due to the practical limitation from finite statistics in evaluating the efficiency simultaneously in the two variables. But this doesn't affect the performance of the procedure to combine the events, as can be seen below.

As each HMT trigger is selecting a subset of events selected by the L1 TE trigger it is seeded on, $\epsilon_{trig}(N_{\mathrm{ch}}^{\mathrm{rec}}, E_{\mathrm{T}}^{\mathrm{L1}}) = \epsilon_{trig}(N_{\mathrm{ch}}^{\mathrm{rec}})\epsilon_{trig}(E_{\mathrm{T}}^{\mathrm{L1}})$, where $\epsilon_{trig}(E_{\mathrm{T}}^{\mathrm{L1}}) = 0$ below the corresponding L1 TE threshold and 1 above it. For the four primary HMT triggers, the trigger efficiencies $\epsilon_{trig}(N_{\mathrm{ch}}^{\mathrm{rec}})$ are taken from the efficiency curves shown in figure A.1, while for the other two triggers, the turn on curves with the flat part normalized to 1 (figure A.2) are used to evaluate $\epsilon_{trig}(N_{\mathrm{ch}}^{\mathrm{rec}})$.

The data sample has multiple triggers selecting in the same regions, with appreciable statistics, as can be seen from figure IV.2.3. To combine the events selected from the different triggers, each event is weighted by the inverse of the combined probability of selecting an event at that $N_{\mathrm{ch}}^{\mathrm{rec}}$ and $E_{\mathrm{T}}^{\mathrm{Pb}}$. For a finite number, N, of triggers active during a particular run, each with its own prescale factor and trigger efficiency, the probability for an event to be selected is given by

$$P(N_{\mathrm{ch}}^{\mathrm{rec}}, E_{\mathrm{T}}^{\mathrm{L1}}) = \sum_{i=1}^{N} P_{trig}^{i} - \sum_{i=1}^{N}\sum_{j=i+1}^{N} P_{trig}^{i}P_{trig}^{j} + \sum_{i=1}^{N}\sum_{j=i+1}^{N}\sum_{k=1}^{N} P_{trig}^{i}P_{trig}^{j}P_{trig}^{k} - ..., \qquad \text{(A.1)}$$

where $P_{trig}^{i} = \epsilon(N_{\mathrm{ch}}^{\mathrm{rec}}, E_{\mathrm{T}}^{\mathrm{L1}})/\alpha^{i}$ denotes the probability for the i^{th} trigger to select an event at

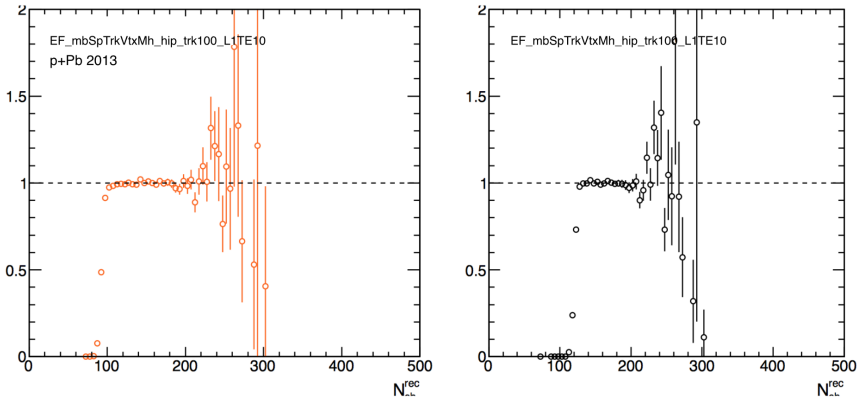

Figure A.2: Fraction of events selected by the HMT triggers `trk100_LITE10` and `trk130_LITE10` in events selected by `EF_mbMBTS_1_1`, as a function of $N_{\mathrm{ch}}^{\mathrm{rec}}$. The flat part of the ratio is scaled to 1.

that $N_{\mathrm{ch}}^{\mathrm{rec}}$ and $E_{\mathrm{T}}^{\mathrm{L1}}$) values. The second, third and higher terms are to ensure events in which more than one trigger fired are not counted more than once.

The distributions from the combined MB and HMT (MB+HMT) sample after the "reweighting" by applying the event-by-event weights were shown in figure IV.2.3. The reweighted distribution is consistent with the MB distribution in both $N_{\mathrm{ch}}^{\mathrm{rec}}$ and $E_{\mathrm{T}}^{\mathrm{Pb}}$. This can be further seen from figures A.3 and A.4, which show the mean and r.m.s $N_{\mathrm{ch}}^{\mathrm{rec}}$ in different $E_{\mathrm{T}}^{\mathrm{Pb}}$ bins of differing bin widths, and vice-versa, respectively. The values from the MB, MB+HMT and the reweighted MB+HMT distributions are shown. The mean and r.m.s $N_{\mathrm{ch}}^{\mathrm{rec}}$ values in $E_{\mathrm{T}}^{\mathrm{Pb}}$ bins are very different between the MB and MB+HMT samples before doing the reweighting, particularly when the bin width used is large. But with reweigting, consistent values within a few percentage are obtained for all bin width ranges and $E_{\mathrm{T}}^{\mathrm{Pb}}$ and $N_{\mathrm{ch}}^{\mathrm{rec}}$ values considered.

A.2 Pileup rejection and estimation of residual pileup

The performance of the pileup rejection cut with a cut on the high tail end of the ZDC energy distribution and the estimation of the residual pileup fraction in the event classes are presented in this section. To study the performance few different pileup rejection cuts are defined and used, these are discussed below.

Figure A.5 shows the ZDC energy distribution of events along with the distribution for events rejected by two pileup rejection cuts. The first cut rejects events with two good vertices that are more than 15 mm apart from each other. Secondary vertices lie mostly within 15 mm from the primary vertex and so the events rejected by this cut are more likely to be pileup events. This was the pileup rejection cut used in the 2012 ridge analysis [12] and is referred to as the "old cut". The second cut is one of the cuts used in this analysis, rejecting events with two good vertices, and is referred to as the "new cut". The ZDC energy distribution shows a broad saturation peak, and a second peak from pileup events around which the events rejected by the pileup rejection

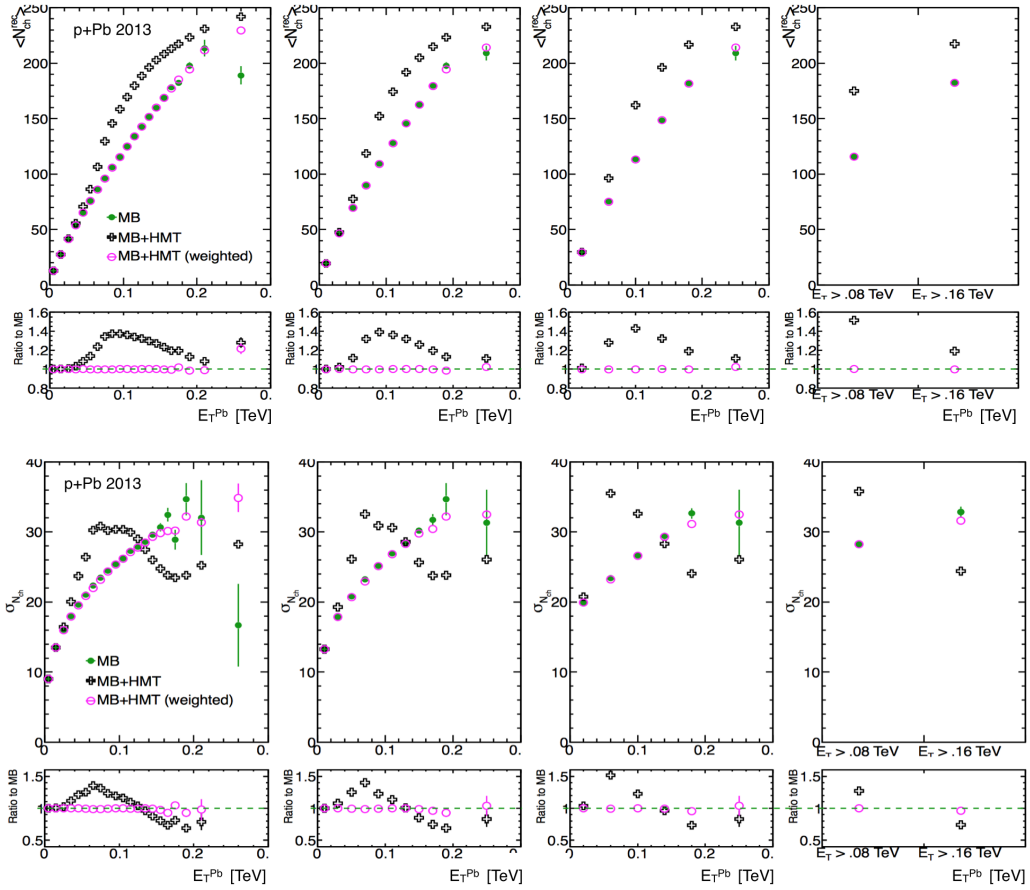

Figure A.3: The mean (top set of panels) and r.m.s (lower set of panels) $N_{\rm ch}^{\rm rec}$ values in different $E_{\rm T}^{\rm Pb}$ bins for different choices of bin widths in $E_{\rm T}^{\rm Pb}$ from the MB, MB+HMT and reweighted MB+HMT distributions. The smaller panels in both sets show the ratio from the MB+HMT and reweighted MB+HMT distributions to that from the MB distribution.

cuts are populated. The distribution from the "old cut" doesn't match the ZDC distribution from all events near the tail of the distribution, where the events are likely to be entirely from pileup, while the "new cut" shows better matching to the tail of the distribution and thus gives a better pileup rejection. But even after applying the "new cut", a small second peak towards the tail of the distribution remains, for example see figure A.6. An additional hard cut on the ZDC energy removes a large fraction of such events. The threshold for this cut is determined using the estimated residual pileup fraction in the sample and is discussed below. The cut on the ZDC energy doesn't reject many good events as can be seen from the distribution of events with only one vertex, in right panel of figure A.5. The ZDC cut keeps $\sim 98\%$ of the single vertex events.

The estimated distribution of pileup events is obtained by scaling the distribution of events

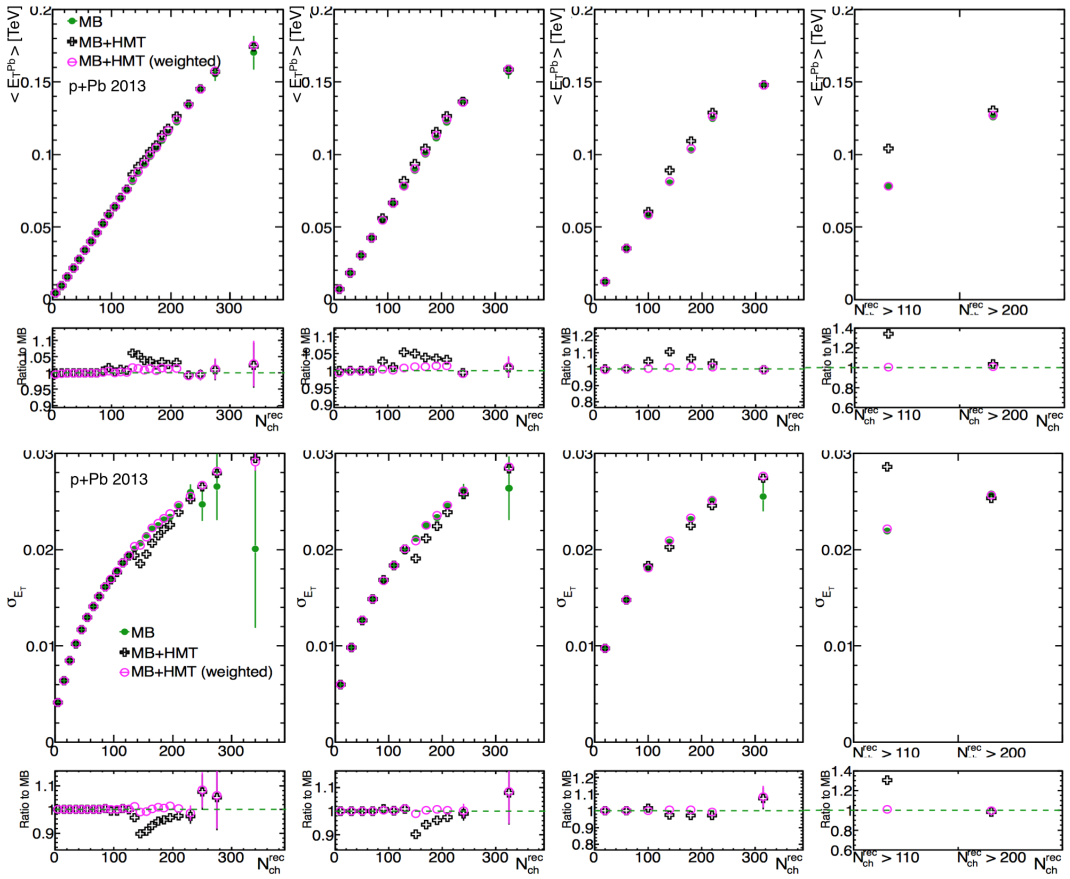

Figure A.4: The mean (top set of panels) and r.m.s (lower set of panels) $E_{\mathrm{T}}^{\mathrm{Pb}}$ values in different $N_{\mathrm{ch}}^{\mathrm{rec}}$ bins for different choices of bin widths in $N_{\mathrm{ch}}^{\mathrm{rec}}$ from the MB, MB+HMT and reweighted MB+HMT distributions. The smaller panels in both sets show the ratio from the MB+HMT and reweighted MB+HMT distributions to that from the MB distribution.

rejected by the "old cut" to match the ZDC energy distribution from all events in the tall (> two times the position of the first peak) of the distribution. This is illustrated in figure A.6. The estimated pileup distribution is shown in red. After the "old cut" and the "new cut" are applied, similar procedure is used to estimate the residual pileup distribution: by scaling the distribution of events rejected by the "old cut" to match the ZDC energy distribution of events remaining after the cuts are applied, in the tail region. These curves are also indicated in figure (blue and green curves). It can be seen that even after applying the "new cut", some pileup remains (green curve). The hard cut on the ZDC energy is determined using the distributions obtained after the "new cut" is applied. It is defined as the ZDC energy at which 80% (or more) of the events are (estimated) pileup events. The cut on ZDC energy is defined using the distributions in a high multiplicity event class with $150 < E_{\mathrm{T}}^{\mathrm{Pb}} < 170$ GeV, where the pileup is large, and the performance is studied

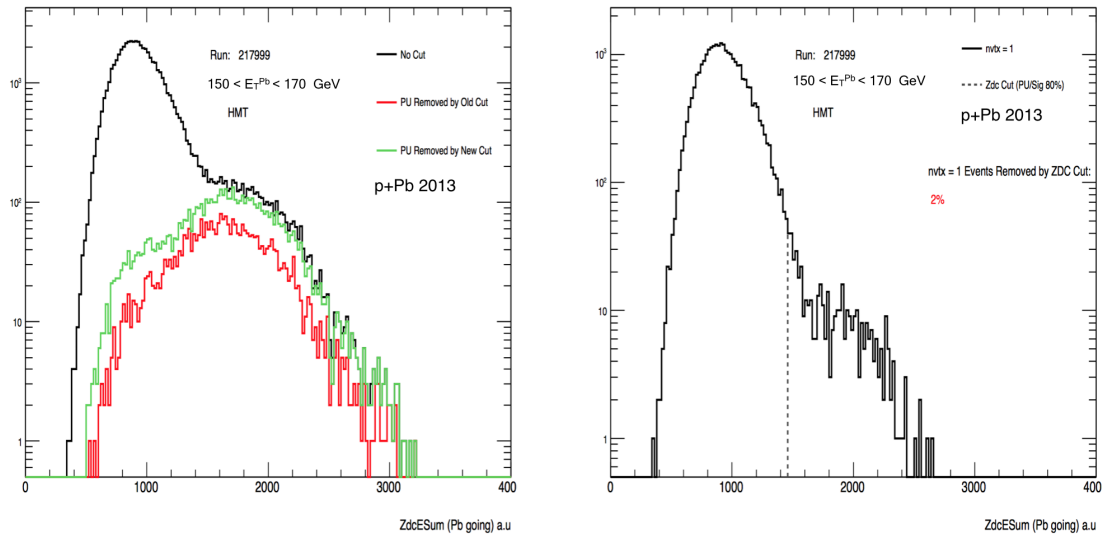

Figure A.5: (Left)The ZDC energy distributions of all events, events rejected by "old cut" and events rejected by "new cut", for events with $150 < E_{\mathrm{T}}^{\mathrm{Pb}} < 170$ GeV, for Run 217999. (Right) ZDC Energy distribution of events with only one good reconstructed vertex, for events with $150 < E_{\mathrm{T}}^{\mathrm{Pb}} < 170$ GeV, for Run 217999.

at all other energies. The cut is determined independently for different runs during the run period since the gain of the detector read out amplifier was changed in between the runs. Figure A.7 shows the cuts on ZDC energy for pileup rejection, along with the estimated pileup curves for few different runs.

Figure A.8 shows the estimated pileup fraction in the event sample remaining after the different pileup rejection cuts for different $E_{\mathrm{T}}^{\mathrm{Pb}}$ energy regions. The pileup fraction increases towards the higher energy classes. This is because, even though the pileup rate is small, the probability of a very high $E_{\mathrm{T}}^{\mathrm{Pb}}$ event happening is also small. The "new cut" significantly reduces the pileup, to about 6% in the highest $E_{\mathrm{T}}^{\mathrm{Pb}}$ class in MB events and to about 10% in the HMT events. Applying further the ZDC cut ("new + ZDC cut"), which is the default pileup rejection cut used in the analysis, the residual pileup fraction is less than 1% in all the $E_{\mathrm{T}}^{\mathrm{Pb}}$ classes in MB events and less than 1.5% in the HMT events.

A.3 Systematic Uncertainties

We discuss the evaluation of the systematic uncertainties summarized in Section IV.2.4. The different sources are discussed below.

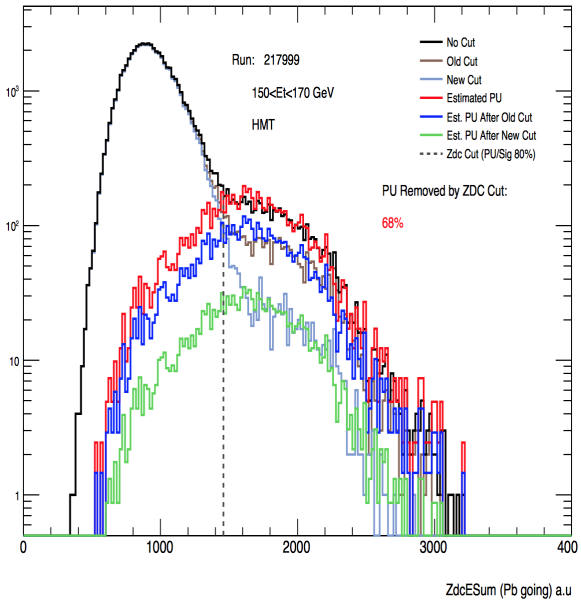

Figure A.6: ZDC energy distribution of events selected by the "old" and "new" cuts and estimated residual pileup after each cut for Run 217999 for events with $150 < E_{\mathrm{T}}^{\mathrm{Pb}} < 170$ GeV. The dotted line shows the cut on ZDC energy at which 80% of events are estimated pileup and the percentage indicates the fraction of the total estimated pileup rejected by the ZDC cut.

A.3.1 Detector acceptance and event mixing

The modulation along $\Delta\phi$ is quite small in the background (mixed event) distribution compared to the signal IV.2.11. And most of these small modulations are expected to cancel in the same to mixed event ratio. The mixed event distributions are constructed by requiring the events used for mixing to match within 10 tracks in $N_{\mathrm{ch}}^{\mathrm{rec}}$, 10 GeV in $E_{\mathrm{T}}^{\mathrm{Pb}}$ and z_{vtx} within 10 mm. These requirements are varied to evaluate for any dependence of the background and the measured quantities on the matching requirements.

The impact of multiplicity matching is checked by changing the bin width in $N_{\mathrm{ch}}^{\mathrm{rec}}$ to half and double the default value. Also the bin width in $E_{\mathrm{T}}^{\mathrm{Pb}}$ is also allowed to vary to have optimal statistics. In the low multiplicity region, where the statistics is good, the bin width in $E_{\mathrm{T}}^{\mathrm{Pb}}$ is allowed to be ass small as 5 GeV, but in the high multiplicity region, it is increased to 20 GeV. All mixing bins are selected to have approximately equal statistics, for a given choice of $N_{\mathrm{ch}}^{\mathrm{rec}}$ matching. The z_{vtx} matching requirement is relaxed to 20 mm and 30 mm to look for any potential variations.

The relative variations in $\Delta\phi$ of the background distribution projected in $2 < \Delta\eta < 5$, for the individual mixing choices, relative to the default choice, is shown in figure A.9, for one of the lowest p_{T} bins where the signal is the weakest. The relative fluctuations are 0.00005 of the background in central collisions, where statistics is large, and less than 0.0002 of the background, across the multiplicity range. No systematic deviations are seen with varying the multiplicity matching or

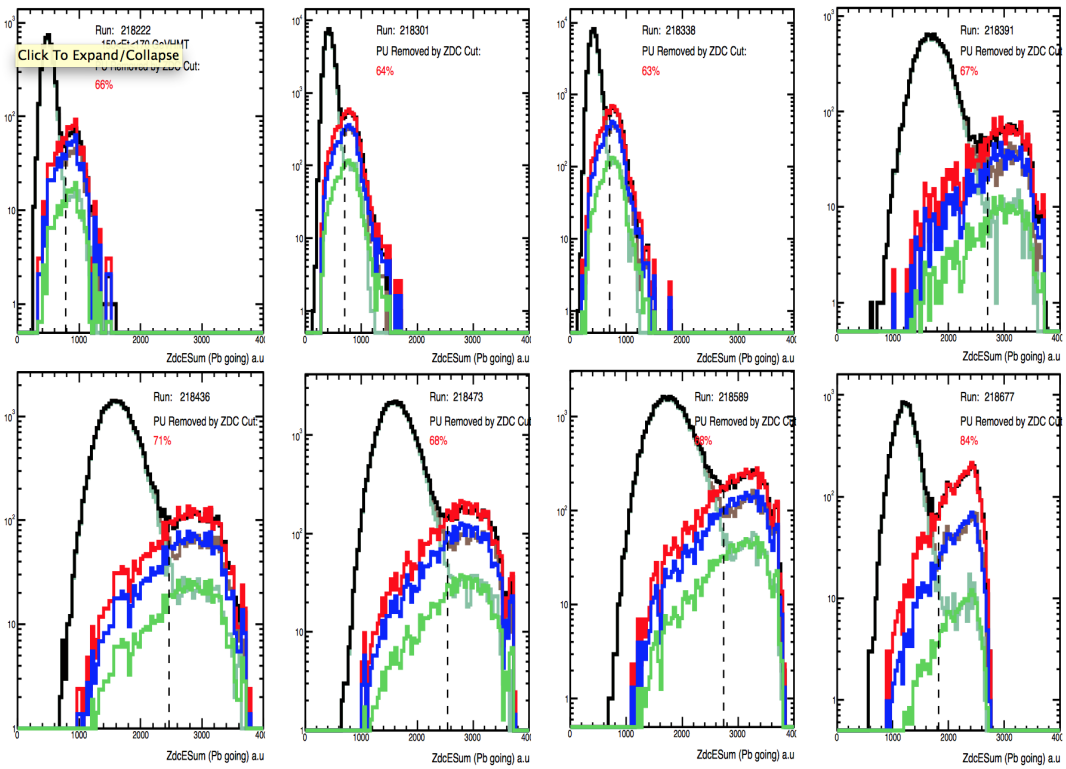

Figure A.7: ZDC energy distribution of events remaining after the different cuts and the estimated pileup distributions along with the cut on the ZDC energy (dashed vertical lines) for few different runs.

the z-vertex matching criteria. A systematic uncertainty of 0.0002 of the background is quoted as an uncertainty on the per trigger yield as coming from pair acceptance. The effect of residual background fluctuations in v_n are quantified in the same way as done in [4]. The relative variations in figure A.9 are decomposed into Fourier harmonics ($v_{n,n}^{det}$). Figure A.10 shows the $v_{n,n}^{det}$ values, for the different choice of multiplicity matching (left panel) and the different choices of z-vertex matching (right panel), for harmonics from 1 to 5. The values are shown for one of the highest multiplicity class. The $v_{n,n}^{det}$ values are quite small, 10^{-5} in most cases, and in most cases consistent with statistical uncertainties. No systematic deviations are seen either with multiplicity matching or z-vertex matching. An uncertainty of $1 - 2$ x 10^{-5}, reflecting the fluctuations in $v_{n,n}^{det}$ with the variation in mixing criteria is quoted as a systematic uncertainty on $v_{n,n}$, depending on the order n, and are propagated to the v_n values.

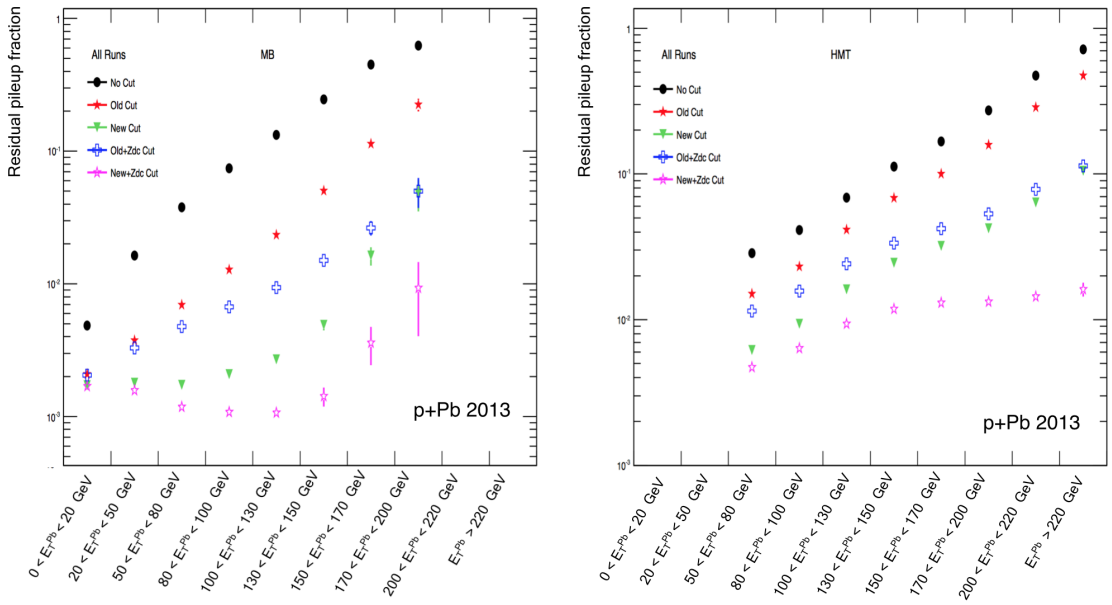

Figure A.8: Estimated residual pileup fraction remaining after different pileup rejection cuts in increasing $E_{\mathrm{T}}^{\mathrm{Pb}}$ bins for MB triggered events (left) and HMT triggered events (right).

A.3.2 Effect of residual pileup

As shown in figure A.8, the final residual pileup in the event samples are small, but non-zero in the highest $E_{\mathrm{T}}^{\mathrm{Pb}}$ classes. The pileup events can lower the event activity dependent ridge signal in a given $E_{\mathrm{T}}^{\mathrm{Pb}}$ class, as the pileup events each have a lower $E_{\mathrm{T}}^{\mathrm{Pb}}$ than the bin they are included in. This bias from residual pileup is significant mainly for the measurements in $E_{\mathrm{T}}^{\mathrm{Pb}}$ classes, as in the case of $N_{\mathrm{ch}}^{\mathrm{rec}}$ classes, the events are binned based on the number of tracks associated with the primary vertex.

The potential bias from the residual pileup is estimated by re-doing the analysis by changing the cut for pileup rejection to the "new cut" (see Section A.2) from the default. This variation of the pileup rejection cut changes the residual pileup by more than a factor of four of the estimated residual pileup in the event classes. Figure A.11 shows an example of the impact of doing this variation on the v_2 values. The ratio of the values from the default cut to that from the "new cut" are shown as a function of p_{T} for different event classes. Applying a tighter pileup rejection cut increases the values slightly. The systematic variations are of the order of 1–2% and independent of p_{T}. Similar level of variations are expected for the other harmonics as the pileup cut only impacts the event sampling in an event class. The actual residual pileup is much smaller than the increase in the pileup fraction introduced by this change of rejection cut, but the differences arising from this variation are quoted as a conservative estimate of the uncertainty from this source.

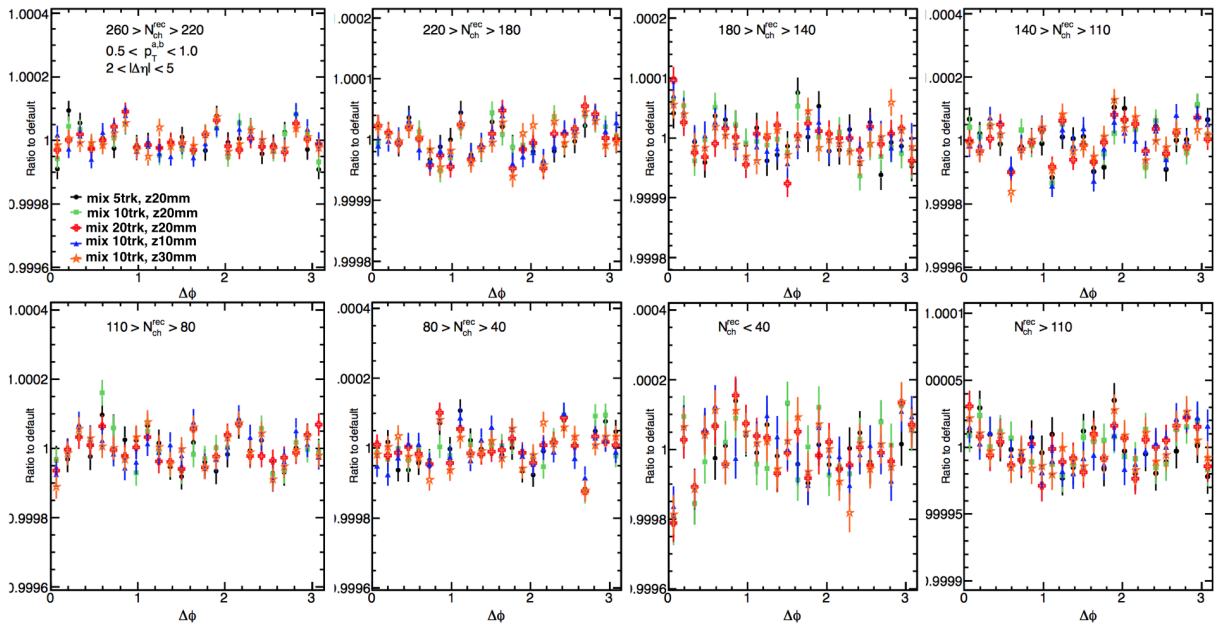

Figure A.9: The relative variation in $\Delta\phi$, of the background distribution projected in the region $2 < \Delta\eta < 5$, for the different mixing choices relative to the default choice. Each panel shows one multiplicity bin.

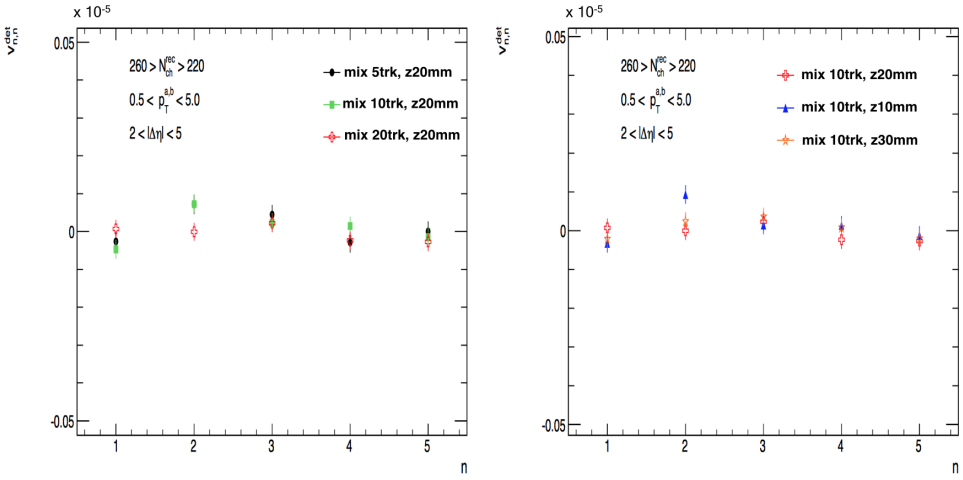

Figure A.10: The $v_{n,n}^{det}$ values as a function of n, for different choice of multiplicity matching (left) and z-vertex matching criteria (right), for an event class with $260 > N_{ch}^{rec} > 220$ tracks.

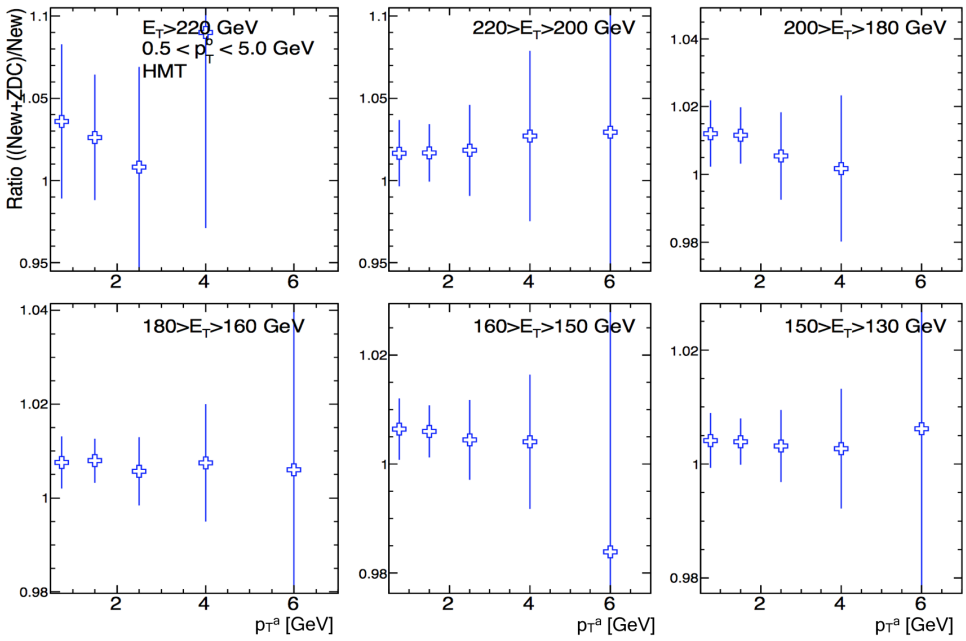

Figure A.11: Ratio of v_2 from "new+ZDC cut" (default) to that from "new cut" alone as a function $p_{\mathrm{T}}^{\mathrm{a}}$ in the highest $E_{\mathrm{T}}^{\mathrm{Pb}}$ (denoted as $\mathrm{E_T}$ bins.

A.3.3 Uncertainty from tracking efficiency and track selection cuts

The uncertainties in tracking efficiency contributes directly to the per-trigger-yield measurements (Eq. IV.2.4). The uncertainties quoted in Section IV.2.2 for the tracking efficiency is therefore quoted for the per-trigger-yield values as well. The v_n values on the other hand are less sensitive to variations in tracking efficiency as they are quantities defined relative to the average multiplicity in the event class. Regardless, here we evaluate the impact on v_n from varying the track selection cuts and thus the efficiencies.

To evaluate the impact of track selection cuts, the tracking efficiency is evaluated as a function of p_{T} for each choice of track selection cuts as discussed in Section IV.2.2 and then the analysis is repeated by wieghting each track with the inverse of this tracking efficiency while constructing the single and pair distributions. Figure A.12 shows the v_2 and v_3 values as a function of $N_{ch}rec$ for the four choices of track selection cuts listed in Section IV.2.2. The v_n values are identical between the different cuts, supporting the expectation that v_n are less sensitive to change in tracking efficiency.

Figure A.13 shows the v_2 and v_3 values as a function of $p_{\mathrm{T}}^{\mathrm{a}}$ for the different track selection cuts. The lowest bin from $0.3 < p_{\mathrm{T}}^{\mathrm{a}} < 0.5$ GeV shows about a 3% difference as the cuts are made stronger, while higher $p_{\mathrm{T}}^{\mathrm{a}}$ bins give consistent values. A 3% uncertainty is included for the lowest bin as a systematic uncertainty. The uncertainty due to material uncertainty evaluated in the previous ridge analysis ([12]) is also included in the systematic uncertainties, as the detector conditions remained mostly the same.

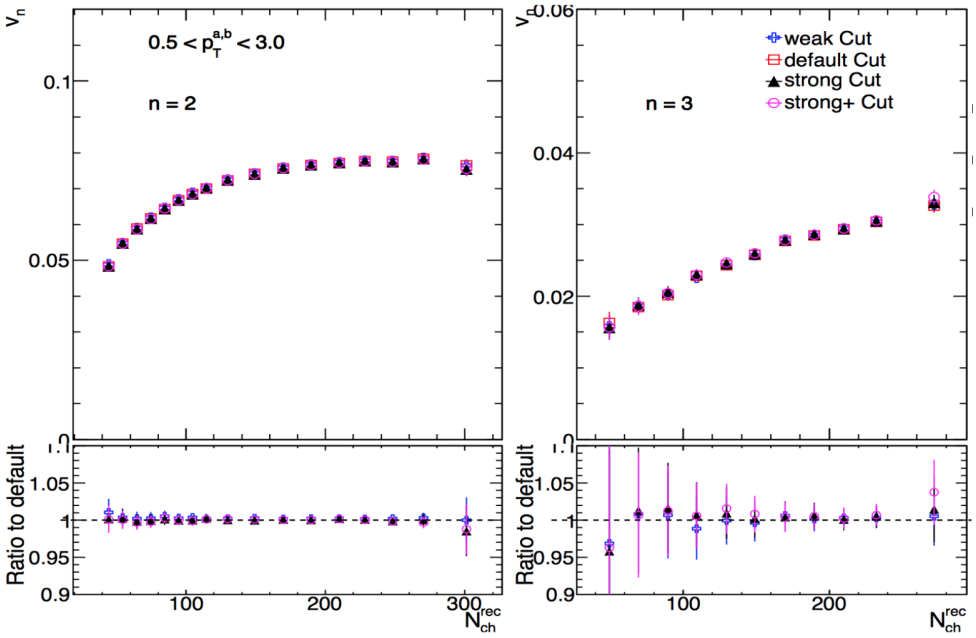

Figure A.12: The v_2 (left) and v_3 (right) values as a function of N_{ch}^{rec} for the four different track selection cuts discussed in Section IV.2.2. The lower panels show the ratio to the values from default choice.

A.3.4 Uncertainty from the ZYAM procedure

As discussed in Section IV.2.3.1, the ZYAM method [188, 189] is used to evaluate the yield above the uncorrelated background, Y^{corr}. Uncertainties in the estimation of b_{ZYAM} therefore would contribute directly to the correlated yield measurements. These uncertainties however have negligible impact on the v_n measurements as they influence the v_n determination only through the recoil subtraction procedure, as an uncertainty on b_{ZYAM} in the peripheral event classes. Since in most cases, the b_{ZYAM} in central event classes is much larger than in the peripheral event class this has negligible impact on the measured v_n values.

The b_{ZYAM} is evaluated by doing a quadratic fit around $\Delta\phi = \pi/2$ to the 1D per-trigger-yield, to determine the point of minimum yield, $\Delta\phi_{ZYAM}$. In the default case, the width of the window in $|\Delta\phi|$ used to do the fit is 0.5 around $\Delta\phi_{ZYAM}$. As systematic cross checks, this width is varied to 0.4 and 0.6. Also a global fit using a Fourier series with up to 6 terms are used to evaluate $\Delta\phi_{ZYAM}$ (This global fit is also used to find the initial estimate of $\Delta\phi_{ZYAM}$, around which the quadratic fits are done). Figure A.14 shows an example of the estimation of $\Delta\phi_{ZYAM}$ using the quadratic fits for a few different event activity classes. Figure A.15 shows the values of b_{ZYAM} estimated with the four different cross-checks along with the default value with the combined systematic uncertainty as the last point in the panels. The systematic variations are small, within 1.5% in most cases. These contribute directly to the uncertainties on the correlated yield measurements

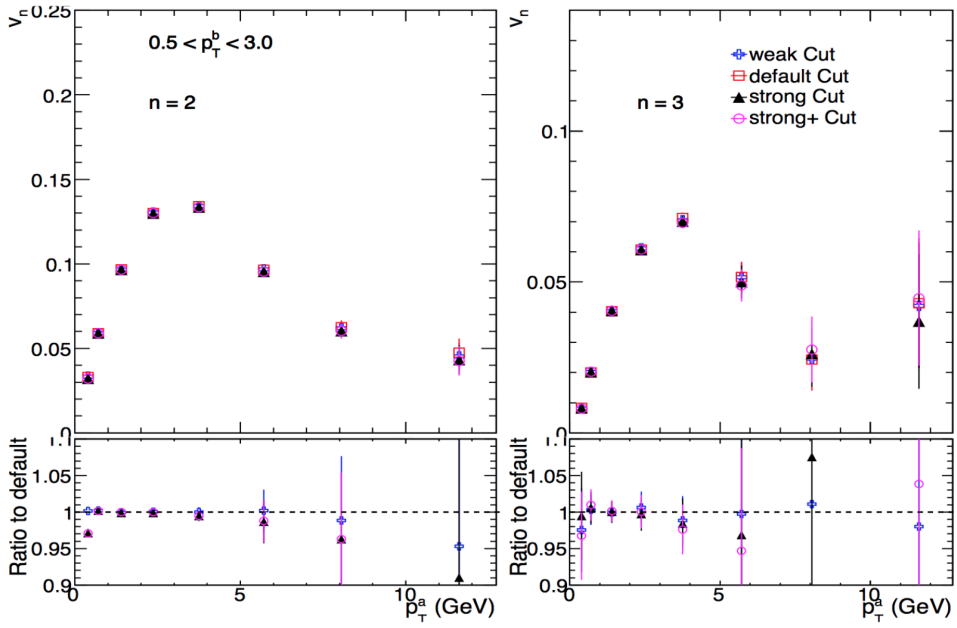

Figure A.13: The v_2 (left) and v_3 (right) values as a function of $p_{\mathrm{T}}^{\mathrm{a}}$ for the four different track selection cuts discussed in Section IV.2.2, for the event class with $N_{\mathrm{ch}}^{\mathrm{rec}} > 200$. The lower panels show the ratio to the values from default choice.

and also are propagated to v_n via the recoil subtraction procedure.

A.3.5 Uncertainty from the scale factor α

The uncertainties in the evaluation of the near-side jet yield, Y^{n-peak}, and thus in the α values, can introduce uncertainties in the final v_n values. These uncertainties are directly evaluated at the v_n level by propagating the uncertainties from the scale factor α depending on the event class and $p_{\mathrm{T}}^{\mathrm{a,b}}$ range. The uncertainty in the evaluation of Y^{n-peak} is estimated by varying the $|\Delta\eta|$ range used to evaluate the long-range pedestal that is subtracted out (second term in Eq. IV.2.6). Figure A.16 shows the variation in Y^{n-peak} from using different $|\Delta\eta|$ ranges for determining the long-range pedestal. The typical variations are small, within 2-4%. The typical uncertainty quoted on α from these variations is 4%. Figures A.17 and $fig : app4_sec4_10$ show the sensitivity of the v_n values to a 4% change in the value of α. The fractional change in v_n in the low p_{T} region (< 4 GeV) is small, within 1–2%, but increases towards high p_{T} where the v_n values are small, and can be up to 10–15% depending on the p_{T} values.

A.3.6 Changing the peripheral bin used for recoil subtraction

The variation in the v_n values from changing the peripheral bin used to do recoil subtraction and the associated systematic uncertainties are discussed in Subsection IV.2.3.4 and are summarized

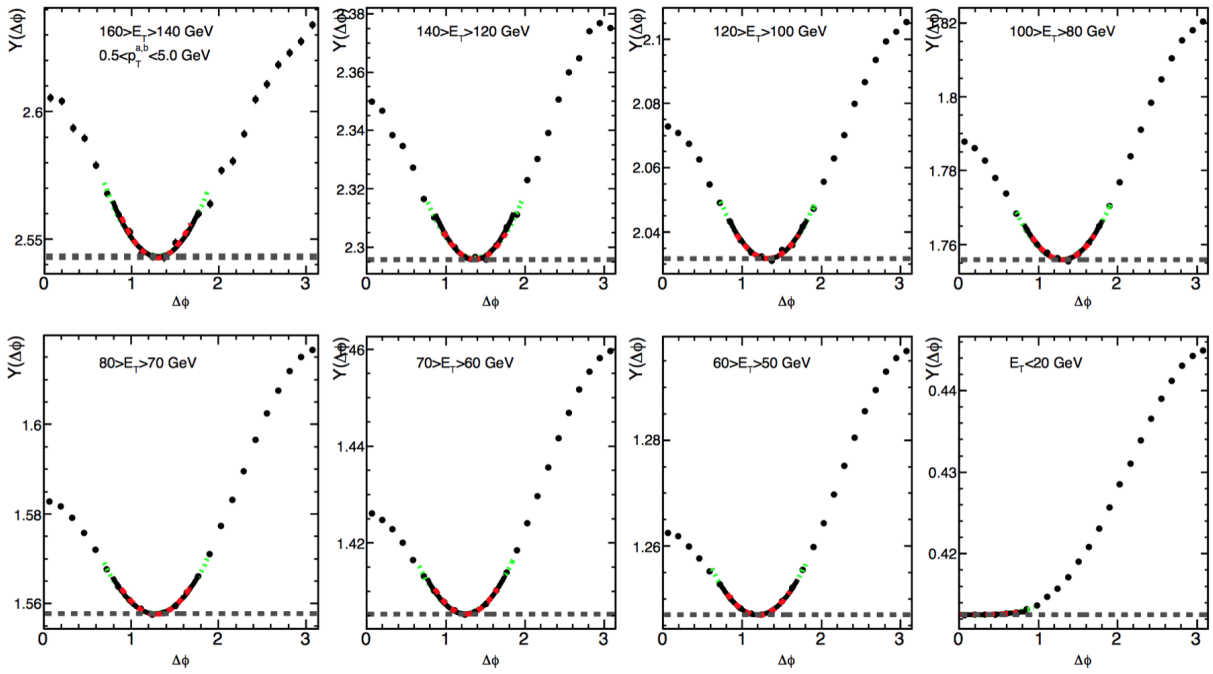

Figure A.14: Figure showing example of estimation of the $\Delta\phi_{ZYAM}$ values using the quadratic fits around $\Delta\phi = \pi/2$, for different $E_{\mathrm{T}}^{\mathrm{Pb}}$ classes. The dotted line indicates the b_{ZYAM} value evaluated with the default choice.

in table IV.2.3.

A.3.7 Monte Carlo closure on correlation function and v_n

The robustness of the analysis methodology, including the influence of tracking efficiency and detector effects, can be evaluated by carrying out the full analysis using simulated events from HIJING [120]. The results obtained at the generated level using truth particles and at the reconstructed level, after passing the events through the detector simulation and reconstructing, using tracks reconstructed can be compared. The detector effects are simulated using the GEANT4 package [185]. HIJING doesn't include any long-range ridge correlations [100]. The generated particles from HIJING are modulated by a separate 'Flow Afterburner' algorithm to have harmonic modulations at the single particle level. v_2, v_3 and v_4 modulations were imparted this way, using the values from the data parametrized as follows (no impact parameter dependence is implemented),

$$v_n(p_{\mathrm{T}}) = a_{0,n} {p_{\mathrm{T}}}^{a_{1,n}} e^{-a_{2,n} p_{\mathrm{T}}}, \tag{A.2}$$

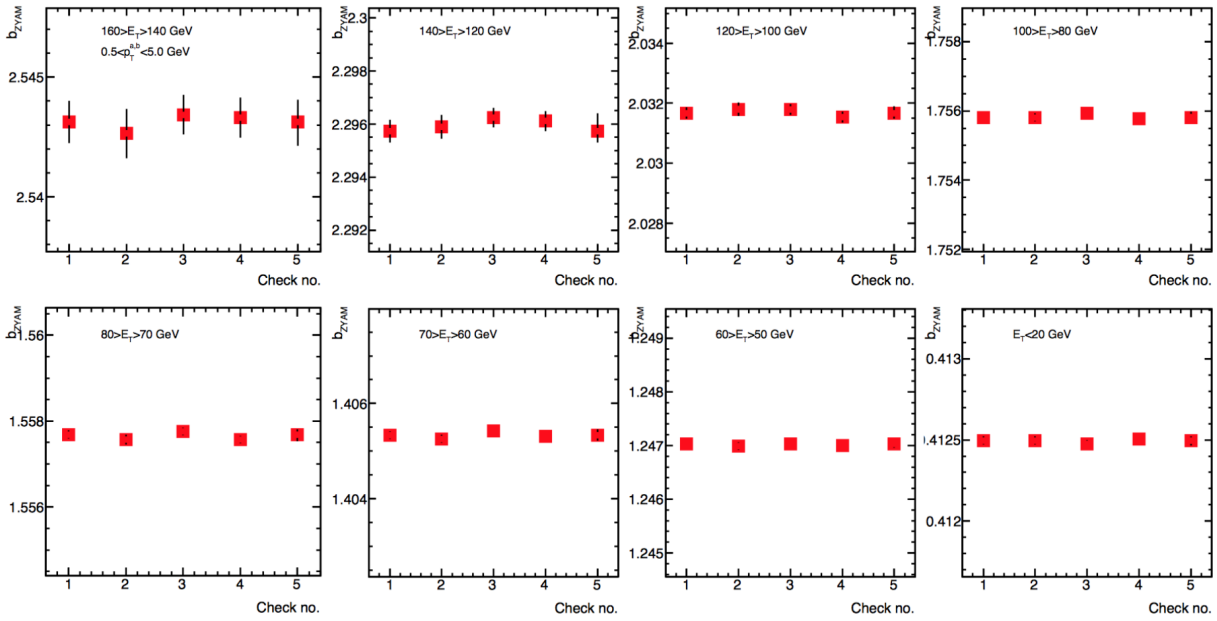

Figure A.15: The b_{ZYAM} values evaluated using the different choices, for different $E_{\mathrm{T}}^{\mathrm{Pb}}$ classes. Check 1 is quadratic fit with width 0.4, 2 is with width 0.5 and 3 with 0.6. Check 4 is the global Fourier fit and Check 5 shows the default value along with the final systematic uncertainties as error bars.

$$a_{0,2} = 0.115, a_{1,2} = 1.181, a_{2,2} = -0.377$$
$$a_{0,3} = 0.498, a_{1,3} = 1.688, a_{2,3} = -0.505$$
$$a_{0,4} = 0.021, a_{1,4} = 2.196, a_{2,4} = -0.626$$

The simulated data used for this study is a 1 million HIJING with flow afterburner sample, with the dataset name, `mc12_5TeV.209000.Hijing_MinBias_pPb_Flow_5TeV.recon.NTUP_HI.e2160_s1825_s1586_r4892_tid01356526_00`

Figure A.19 compares the 1-D correlation functions at the generated and reconstructed levels from the HIJING simulation before the recoil subtraction. The values between the generated and reconstructed levels agree within 0.5% in the p_{T} ranges shown. The recoil subtraction is carried out using the $E_{\mathrm{T}}^{\mathrm{Pb}} < 10$ GeV class, scaled by the near side jet ratio, α. (Since the implemented flow is independent of centrality, the PTY including pedestal in the peripheral class is subtracted, unlike for the data). The recoil subtraction does not introduce any additional biases and a similar level of agreement can be seen between the generated and reconstructed level quantities, as before the subtraction.

Figure A.20 shows the v_2 values as a function of $p_{\mathrm{T}}^{\mathrm{a}}$ at the generated and reconstructed levels before the recoil subtraction, on the left panel. The values agree well at low p_{T} ($0.5 < p_{\mathrm{T}}^{\mathrm{a}} < 3$ GeV) where there is good statistics. The right panel compares the v_2 values at the generated and

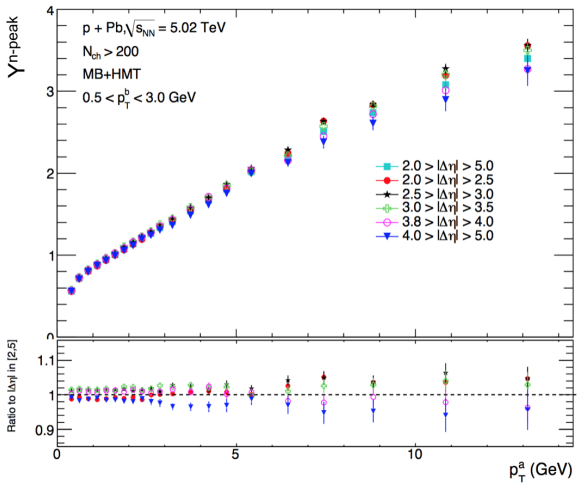

Figure A.16: The Y^{n-peak} values as a function of $p_{\mathrm{T}}^{\mathrm{a}}$ for different choices of $|\Delta\eta|$ ranges to determine the long-range pedestal in Eq. IV.2.6. The lower panel shows the ratios relative to the default choice ($2 < |\Delta\eta| < 5$).

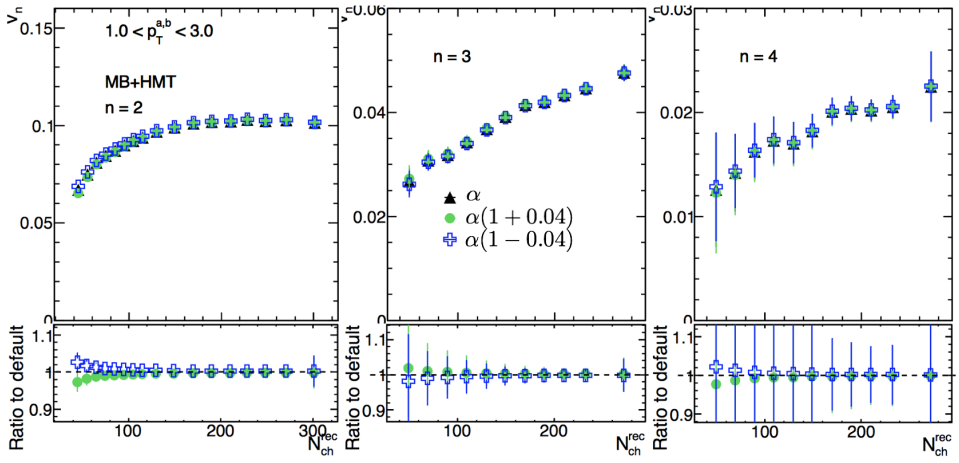

Figure A.17: The v_2 (left), v_3 (middle) and v_4 (right) values as a function of $N_{\mathrm{ch}}^{\mathrm{rec}}$ for a 4% change in the scale factor α. The lower panels show the ratio relative to default.

reconstructed levels after the recoil subtraction. Good consistency can be seen at low p_{T}. However, the statistical uncertainties are very large for the case after recoil subtraction. A 4–8% systematic uncertainty is quoted for th v_n values based on the closure for the case without recoil subtraction, depending on the p_{T} range.

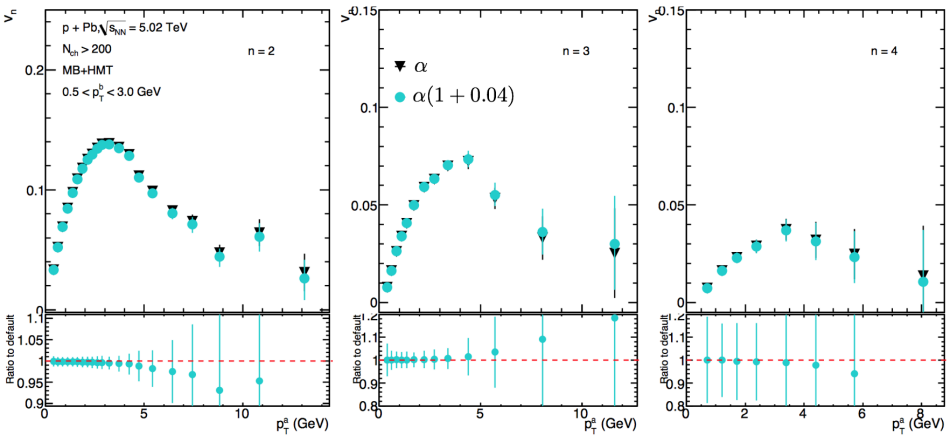

Figure A.18: The variation in v_2 (left), v_3 (middle) and v_4 (right) values for a 4% change in the scale factor α, for an event class with $N_{\mathrm{ch}}^{\mathrm{rec}} > 200$. The lower panels show the ratio relative to default.

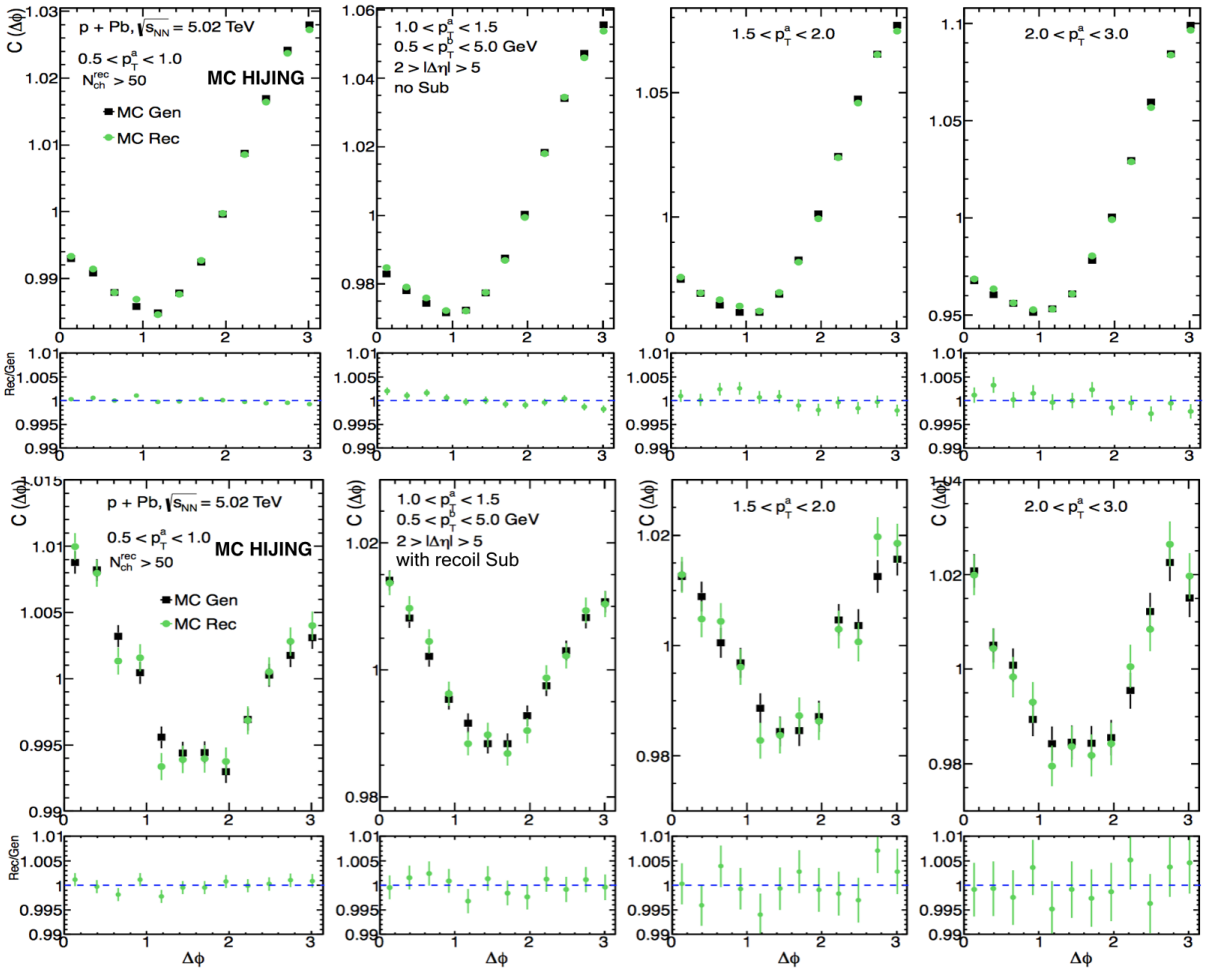

Figure A.19: The 1-D correlation functions (S/B normalized to have average value of 1) compared between the generated and reconstructed levels from HIJING simulation with flow afterburner. The top set of panels show results before doing the recoil subtraction and bottom set of panels show the results after. The smaller panels show the ratio relative to the truth.

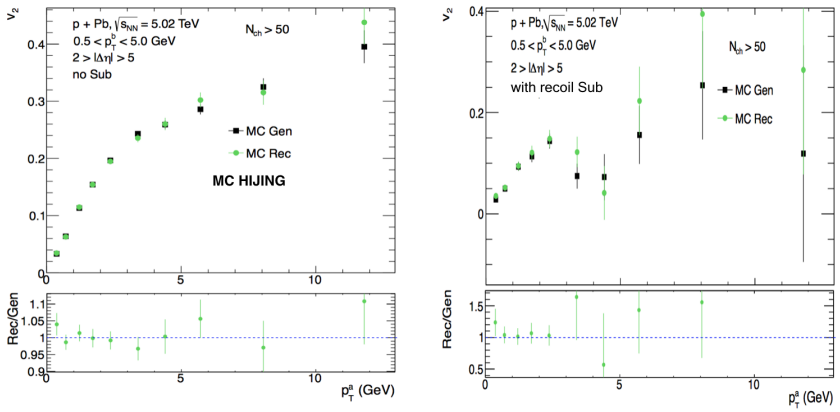

Figure A.20: The v_2 values from HIJING with flow, at the generator and reconstructed levels, before the recoil subtraction (left) and after the recoil subtraction (right). The lower panels show the ratio relative to the truth.

Appendix B

Appendix to Part V

B.1 Systematic uncertainties in measurement of longitudinal correlations in Pb+Pb collisions at $\sqrt{s_{NN}} = 2.76$ TeV

In this part of the Appendix, we detail the evaluation of the systematic uncertainties in the measurement of longitudinal correlations in Pb+Pb collisions at $\sqrt{s_{NN}} = 2.76$ TeV, presented in Chapter V.2 of this thesis. The summary of the systematic uncertainties from the various sources below were presented in Section V.2.3. The systematic uncertainties from the different sources are discussed below.

B.1.1 Track selection and tracking efficiency

Impact of tracking efficiency on the measured quantities

The impact of applying the tracking efficiency correction on the measured $sqrt\langle a_n a_m \rangle$ coefficients are shown in figure B.1 as a function of centrality. After efficiency correction, the $sqrt\langle a_n a_m \rangle$ values decrease about 2% for most of the centrality range and by about 5% in the most central classes. This decrease happens as a result of the p_{T} dependence of the $sqrt\langle a_n a_m \rangle$ coefficients, $sqrt\langle a_n a_m \rangle$ are smaller for lower p_{T} particles. Efficiency correction gives a larger weight to the lower p_{T} particles (as the efficiency is lower at low p_{T}) causing the values to decrease. This can be seen from figure B.2 which shows the $sqrt\langle a_n a_m \rangle$ coefficients as a function of centrality for different narrow p_{T} selections compared between with and without efficiency correction. The $sqrt\langle a_n a_m \rangle$ coefficients show a p_{T} dependence with the value increasing from lower p_{T} to higher p_{T}. But in the differential p_{T} bins, efficiency corrected values are consistent with the values before efficiency correction, showing that the few percent decrease in the inclusive case arises from larger weights for lower p_{T} particles in efficiency corrected results.

The entire deviation from with and without applying the efficiency correction is not quoted as a systematic uncertainty. Instead, the track selection requirements are varied to change the tracking efficiency significantly and the analysis is repeated with the new selection cuts and efficiencies. The deviations from default are then quoted as a systematic uncertainty.

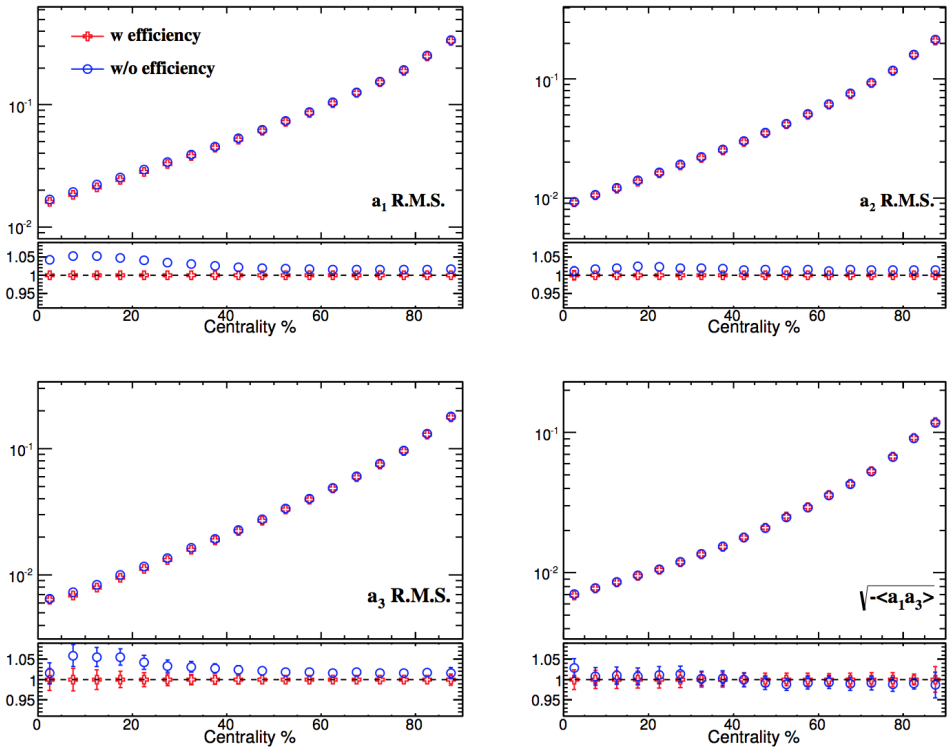

Figure B.1: Comparison of $\sqrt{\langle a_n a_m \rangle}$ values before and after efficiency correction. Smaller panels show ratio relative to the case with efficiency correction.

Impact of varying track selection cuts

The tracking efficiency can be varied considerably by tightening the track pointing cuts on the track impact parameters d_0 and $z_0 sin\theta$. The number of tracks per event in η and the ratios relative to the default (tight) selection are shown in Figure B.3. The default selection requires d_0 and $z_0 sin\theta$ to be within 1.0 mm. This is very close to requiring a cut on the $d_0, z_0 sin\theta$ significance of $< 3\sigma$, i.e requiring $d_0/\sigma_{d_0} < 3$ and $z_0 sin\theta/\sigma_{z_0 sin\theta} < 3$. From tightening the significance to 1.5 σ, the tracking efficiency drops by more than 20%. Figure B.4 shows the correlation functions and their ratios relative to that from the default case for significance cuts of 3σ and 1.5σ. Some structures can be seen in the most central cases which are much smaller than the signal, but otherwise the correlation functions are quite consistent with that from the default selection. Figure B.5 compares the first few $sqrt\langle a_n a_m \rangle$ coefficients between the three selection cuts. The values from the 3σ cuts are consistent with the default selection across all centralities, as expected. Values from 1.5σ cut is also quite consistent, with the maximum deviations being $\approx 5\%$ in the most central cases. The differences between the tight selection and 1.5σ cut are used to quote the systematic uncertainties.

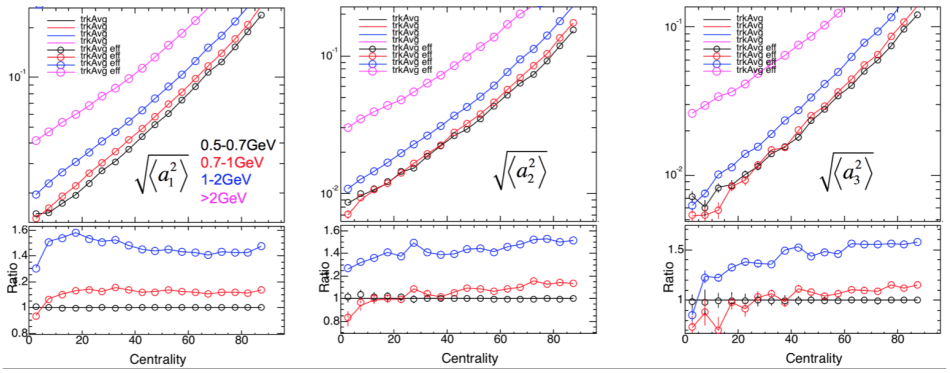

Figure B.2: The $\sqrt{\langle a_n a_m \rangle}$ values before and after efficiency correction in differential p_{T} bins. Solid lines show values before efficiency correction and open circles show values after efficiency correction and different colors indicate the different p_{T} ranges. Smaller panels show ratio relative to the values in $0.5 < p_t < 0.7$ GeV.

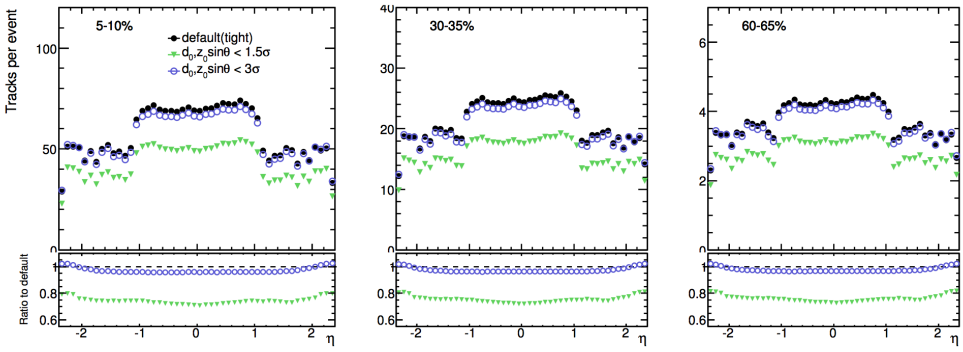

Figure B.3: Multiplicity distribution in η for default (tight) selection and for significance cuts of 3σ and 1.5σ on d_0 and $z_0 sin\theta$, for different centrality intervals. Lower panels show the ratios relative to the tight cut.

Changing z_{vtx} bin width used to evaluate efficiency

The efficiency correction in the default case is evaluated in 10 mm z_{vtx} bins. To check for any potential impact of this choice, the correlation function and $sqrt\langle a_n a_m \rangle$ coefficients are also evaluated by using efficiency correction determined in 4 mm z_{vtx} bins. Figure B.6 shows a comparison of the $sqrt\langle a_n a_m \rangle$ values after efficiency corrections evaluated in 10 mm and 4 mm z_{vtx} bins. The values are very consistent between the two cases, indicating narrowing the z_{vtx} window used for efficiency evaluation does not introduce or remove any features in the correlation.

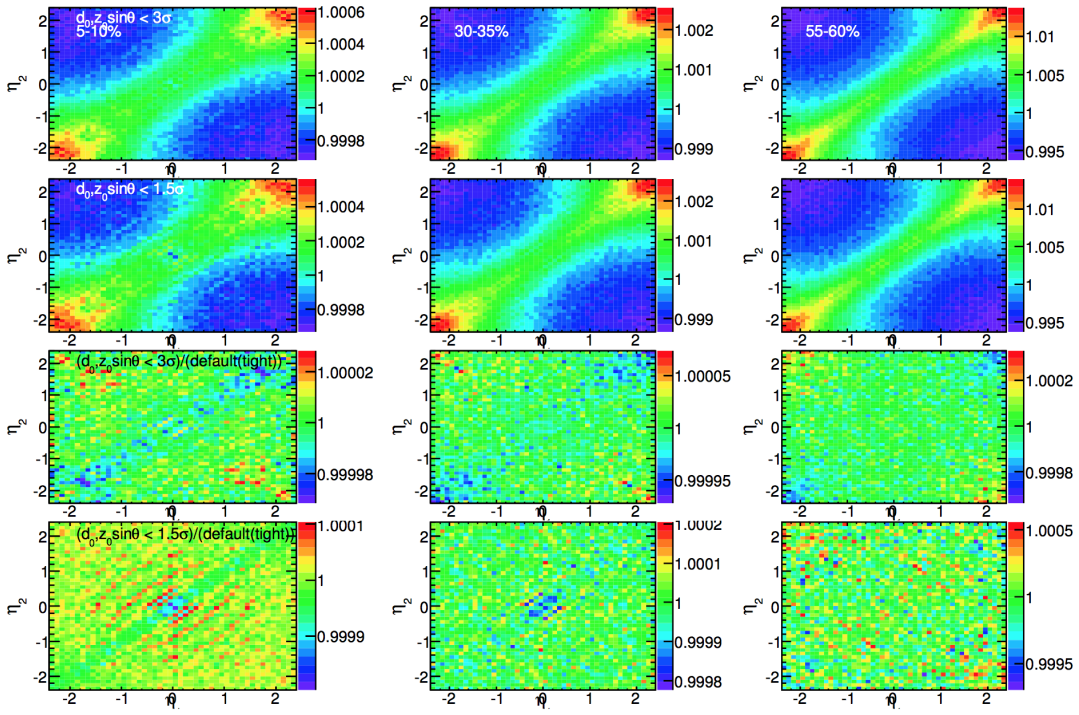

Figure B.4: Correlation functions for the cases with significance cuts of 3σ (first row), 1.5σ (second row) and their ratios relative to that from the tight (default) selection (third and fourth rows respectively), for different centrality intervals.

B.1.2 Event mixing

The sensitivity of the results to the criteria used for matching events used to do event mixing (see Section V.2.2) is evaluated by comparing the results from using $N_{\mathrm{ch}}^{\mathrm{rec}}$ or FCal$\sum E_{\mathrm{T}}$ to match the events in centrality, and by changing the bin widths in $N_{\mathrm{ch}}^{\mathrm{rec}}$ and z_{vtx} used for matching the events.

Centrality matching using $N_{\mathrm{ch}}^{\mathrm{rec}}$ and FCal$\sum E_{\mathrm{T}}$

The correlation functions, $C_N(\eta_1, \eta_2)$, were found to be quite stable between the two mixing schemes, as most of the differences contribute to the residual centrality dependence terms and are removed by the renormalization by the projections (Eq. V.1.13). The $\sqrt{\langle a_n a_m \rangle}$ coefficients as a function of centrality from the two mixing schemes for centrality matching are shown in figure B.7. The values are mostly consistent with each other. A 5% difference in $\sqrt{\langle a_2^2 \rangle}$ for central events can be seen and a variation of 2–5% for peripheral events for the different coefficients can also be seen. For the rest of the centrality bins the differences are within 2%. These will be quoted into the systematic uncertainties.

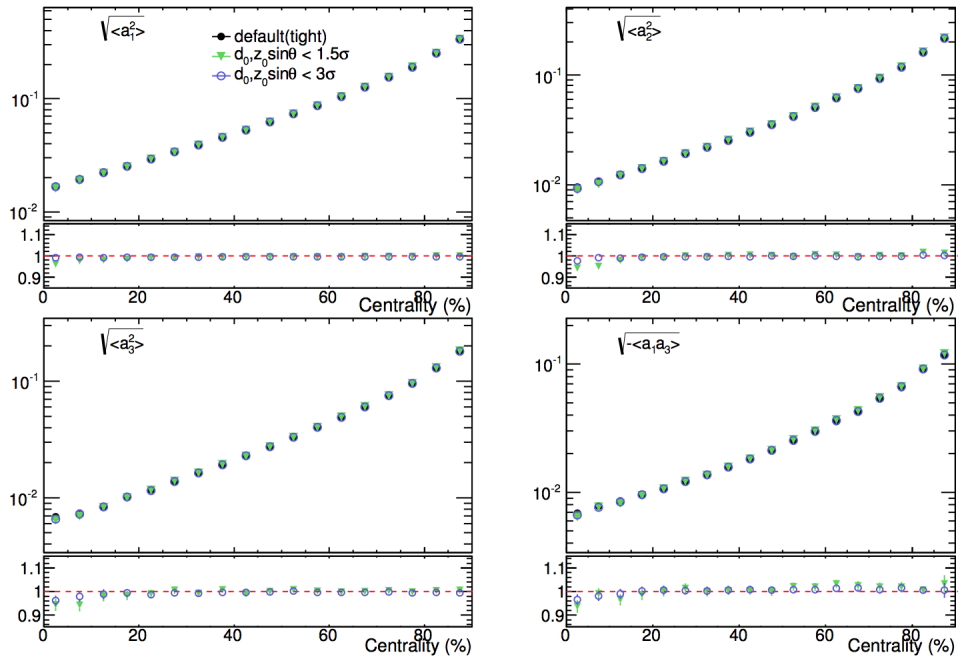

Figure B.5: First few $\sqrt{\langle a_n a_m \rangle}$ coefficients as function of centrality compared between the tight selection and the cases with significance cuts of 3σ and 1.5σ. Smaller panels show the ratio relative to tight selection.

Changing mixing bin width used for centrality matching

In the default case, the mixing bins are defined to contain ∼0.5% of the total statistics. The sensitivity to changing the mixing bin width in $N_{\mathrm{ch}}^{\mathrm{rec}}$ is shown in figure B.8. The results from using the default mixing bin width and bins 10 times larger, containing ∼5% of the total statistics are compared. The values are largely consistent with each other within 1–2%, except for the cases of $sqrt\langle a_2^2 \rangle$ and $sqrt\langle a_3^2 \rangle$, where the differences can be up to 5% in the most central event classes.

Changing mixing bin width used for z_{vtx} matching

The default matching bin width in z_{vtx} used for event mixing is 2.5 mm. The systematic uncertainties from this choice is evaluated by comparing the results from doubling the bin width, to 5 mm. Figure B.9 shows the comparison for $sqrt\langle a_n a_m \rangle$ values between the two choices. The results are mostly consistent, with ∼1% variation seen for most centralities, with up to a 5% variation seen for $sqrt\langle a_2^2 \rangle$ and $sqrt\langle a_3^2 \rangle$ in the case of most central events.

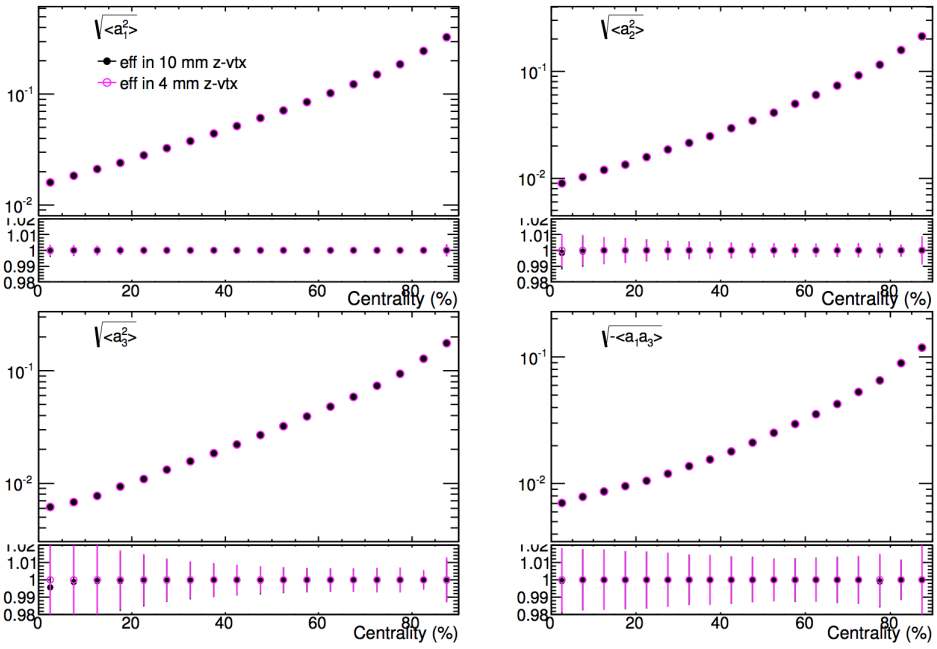

Figure B.6: Comparison of $\sqrt{\langle a_n a_m \rangle}$ values with efficiency corrections evaluated in 10 mm z_{vtx} bins and 4 mm z vertex bins. Smaller panels show ratio relative to the case with efficiency correction from 10 mm z_{vtx} bins.

B.1.3 Comparing events with different z_{vtx} position

The analysis in the default cases uses all events in the range $|z_{vtx}| < 100$ mm. The tracks from events with different z_{vtx} positions could see slightly different parts of the detector for the same η. The influence of the average z_{vtx} position on the results is checked by repeating the analysis separately using events with $|z_{vtx}| < 50$ mm and $50 < |z_{vtx}| < 100$ mm. The comparison of the $sqrt\langle a_n a_m \rangle$ values from these two different choices are shown in figure B.10. The values are mostly consistent with each other with variations of $\sim$5% seen in few cases, mostly in central event classes.

B.1.4 Pair efficiency and pair cuts

Track splitting (incorrect reconstruction of a signal produced by one particle at two tracks) and track merging (reconstructing one track instead of two) can lead to structures in the two-particle correlation functions. The track splitting is usually negligible and track merging leads to loss of track pairs. Figure B.11 shows the pair acceptance in data and reconstructed MC HIJING events in the $\Delta\eta - \Delta\phi$ space. Both data and HIJING show a loss of efficiency in the small $\Delta\eta - \Delta\phi$ region, when the two tracks are close by. (Data also shows an enhancement in larger $\Delta\eta$, which could arise from Bose-Einstein or other short-range correlations). To evaluate the effect these short-range structures on the correlation functions and the derived quantities, the analysis

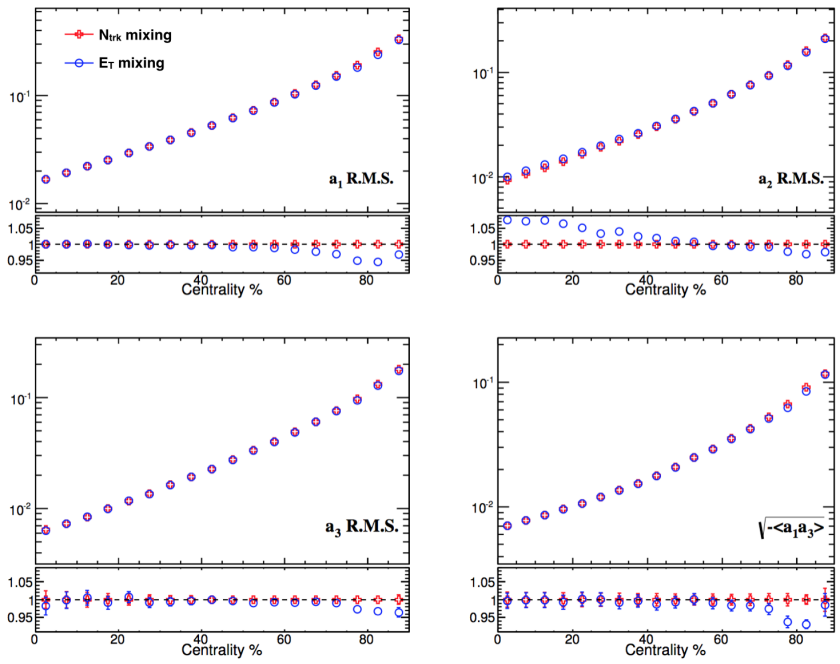

Figure B.7: Comparison of $\sqrt{\langle a_n a_m \rangle}$ values for mixed event distributions constructed by matching events in FCal $\sum E_{\mathrm{T}}$ (denoted as E_{T} in figure) and $N_{\mathrm{ch}}^{\mathrm{rec}}$ (denoted as $\mathrm{N_{trk}}$). The bins for matching in either quantity are required to have ~0.5% of the total statistics. The smaller panels show ratio relative to mixing using $N_{\mathrm{ch}}^{\mathrm{rec}}$.

is repeated by rejecting pairs with very small separation in $|\Delta\eta|$. Three $\Delta\eta$ cuts are studied, by rejecting pairs within $|\Delta\eta| < 0.01$, $|\Delta\eta| < 0.02$ and $|\Delta\eta| < 0.03$. The correlation functions and a_n coefficients are found to be consistent within a few percent for the different cuts. Figure B.12 shows the comparison of the $sqrt\langle a_n a_m \rangle$ values between without applying pair cut and with a pair cut of $|\Delta\eta| < 0.02$. The pair cut only affects the diagonal bins in the correlation function and contributes to a maximum 5% difference in central cases. In the analysis, results are presented without applying pair cuts, but the difference from applying a pair cut of $\Delta\eta < 0.02$ is quoted as a systematic uncertainty.

B.1.5 Higher order coefficients and residual pair acceptance

The Legendre coefficients for n, m values in a wide range of n, from 0 to 19, are shown in figure B.13 for several centrality intervals. The spectrum of coefficients consists of two branches, the diagonal branch $\sqrt{\langle a_n^2 \rangle}$ for $n = 1 - 19$ and the leading mixed branch $\sqrt{-\langle a_n a_{n+2} \rangle}$ for $n = 1 - 17$. The fluctuation patterns seen for large n suggests that these coefficients are not due to physics but rather residual pair acceptance effect. Hence for each centrality interval, a conservative systematic uncertainty band has been estimated based on the fluctuation of $\sqrt{\langle a_n^2 \rangle}$ for $n = 10 - 19$ and

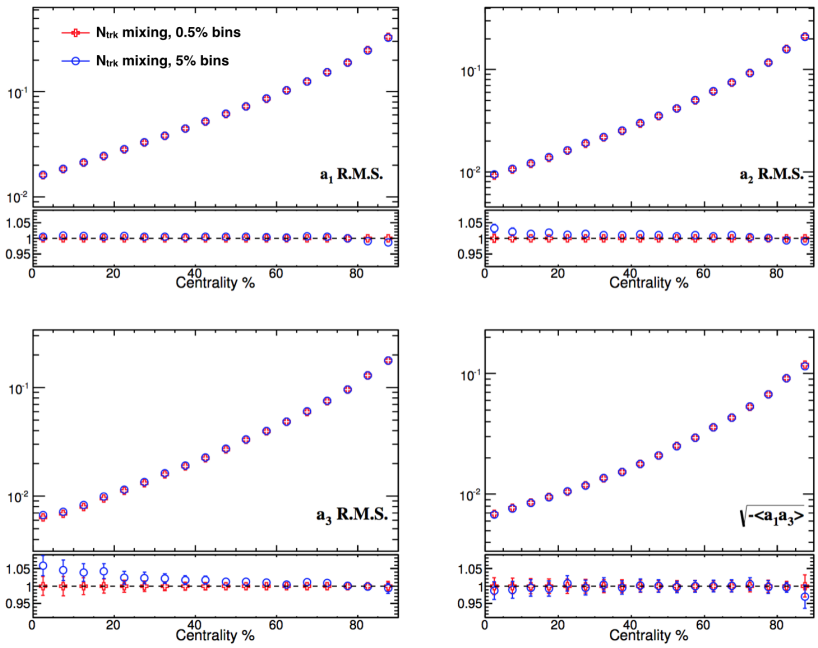

Figure B.8: Comparison of $\sqrt{\langle a_n a_m \rangle}$ values for mixed event distributions constructed by matching events in 0.5% and 5% bins in $N_{\rm ch}^{\rm rec}$ (denoted as $\rm N_{trk}$ in the figure). The smaller panels show ratios relative to the case with 0.5% mixing bins.

$\sqrt{-\langle a_n a_{n+2} \rangle}$ for $n = 6-17$. These bands are shown in the figures as dashed lines. They are about (in absolute value) 0.003 in most central collisions and increase to about 0.02 in most peripheral collisions. As the magnitude of the leading $\sqrt{\langle a_n^2 \rangle}$ values are much larger, these contribute to only small (∼2%) fractional uncertainties, except in central event classes where it can be ∼10% for $\sqrt{\langle a_3^2 \rangle}$ or $\sqrt{\langle a_1 a_3 \rangle}$.

The figure also shows two sets of points. These are obtained from using different bin widths in η_1, η_2 while constructing the correlation function. The default analysis uses 48 bins from -2.4 to 2.4 in both directions. The cross-check (red circles) is done by using 240 bins from -2.4 to 2.4 in both directions. No significant differences, beyond the uncertainty bands quoted from the pair acceptance effects are seen.

B.1.6 Stability across run groups

The stability of the correlation functions and $sqrt\langle a_n a_m \rangle$ values across the time period of data taking are evaluated by comparing them across different 'run groups'. The run groups are defined by including few runs close together in time. Each run group has ≈ similar number of events and the dataset is split into a total of 17 run groups. The correlation functions and $sqrt\langle a_n a_m \rangle$ values are found to be very stable across the run groups, with the maximum difference being ≈ 5% in

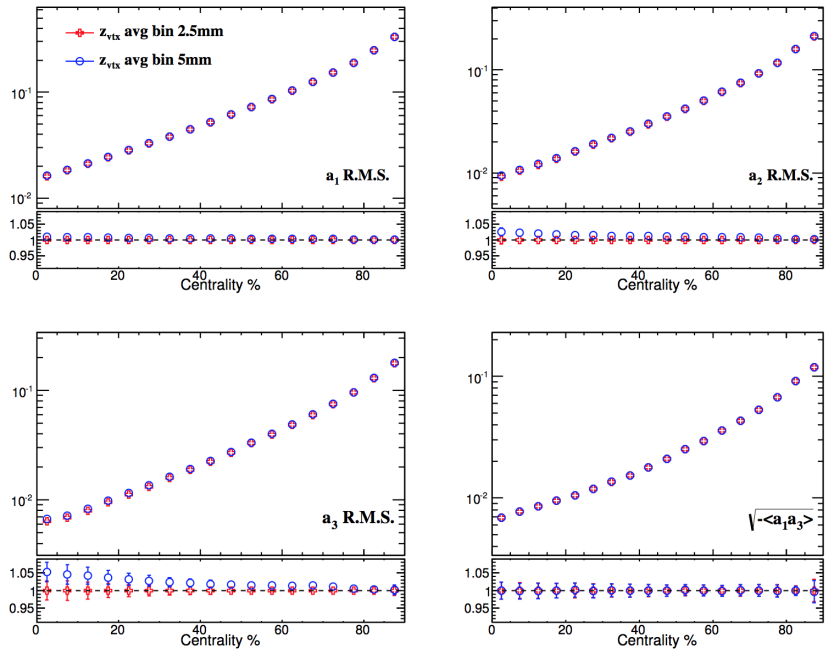

Figure B.9: Comparison of $\sqrt{\langle a_n a_m \rangle}$ values for mixed event distributions constructed by matching events in 2.5 mm (default) and 5 mm z_{vtx} bins. The smaller panels show ratios relative to the case with 2.5 mm mixing bins.

most central classes. The variations in $sqrt\langle a_n a_m \rangle$ for two different centrality intervals across the different run groups are shown in figure B.14. The r.m.s values of these run by run fluctuations are quoted as a systematic uncertainty.

B.1.7 Monte-Carlo consistency

One way to evaluate the stability of the analysis with regard to detector effects and effects from tracking inefficiency and presence of fakes is to compare the correlation functions and the r.m.s values of a_n between the truth (generator) particles and reconstructed tracks from simulated MC HIJING events. The generated HIJING events are passed through the detector simulation using GEANT4 and reconstructed using the same algorithm as that used to reconstruct the data. The dataset used is `mc10_2TeV.119114.Hijing_PbPb_2p75TeV_MinBias_Flow_JJFV6`). HIJING events are found to have an intrinsic correlation at the two-particle level and non-zero r.m.s values for the first few a_n coefficients. At the truth level only charged primary particles are considered. The truth level tracks outside the kinematic boundaries, $|\eta| > 2.4$ and $p_{\mathrm{T}} < 0.5$ are also not considered in the analysis. The track selection cuts for the reconstructed tracks are same as that in the data.

Figure B.15 compares the first few $sqrt\langle a_n a_m \rangle$ coefficients as a function of centrality between the truth, reconstructed tracks and reconstructed with the efficiency correction applied. The

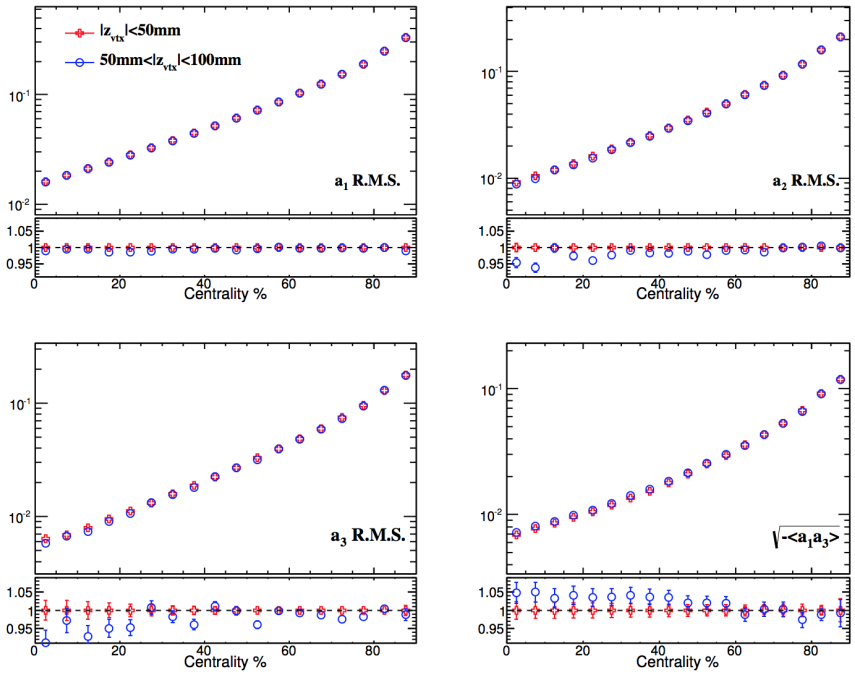

Figure B.10: Comparison of $\sqrt{\langle a_n a_m \rangle}$ values for events with $|z_{vtx}|$ <50mm and $50mm < |z_{vtx}| < 100mm$. The smaller panels show ratio relative to the case with events in $|z_{vtx}| < 50$mm.

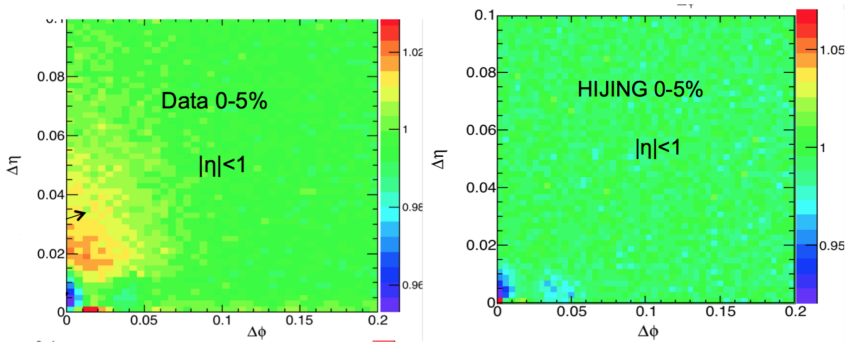

Figure B.11: Pair acceptance in small $\Delta\eta - \Delta\phi$ region for 0-5% most central events in data (left) and reconstructed MC HIJING events (right).

coefficients at the truth and reconstructed level are consistent at the level of $5 - 10\%$. Efficiency correction lowers the value of the coefficients, as the low p_{T} particles get a larger weight. The overall agreement with the truth is better in almost all cases, except for $sqrt\langle a_1 \rangle$ in mid-central collisions, where $\sim$10% variations are seen between truth and reconstructed results after efficiency correction. The difference between the truth and reconstructed a_n after efficiency correction is

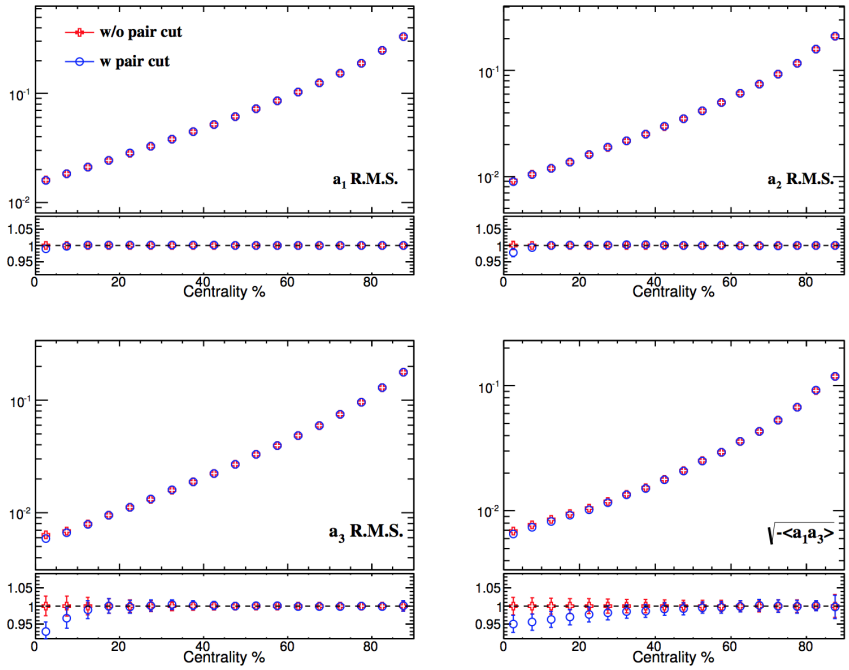

Figure B.12: Comparison of $\sqrt{\langle a_n a_m \rangle}$ values with applying a pair cut of $|\Delta\eta| < 0.02$ and without applying pair cuts.

quoted as a systematic uncertainty.

B.2 Systematic uncertainties in measurement of longitudinal correlations in p+p, p+Pb and peripheral Pb+Pb collisions

In this Section, the details of the evaluation of systematic uncertainties for the analysis presented in Chapter V.2 of the thesis are shown. The summary of the systematic uncertainties from various sources in this measurement is discussed in Section V.3.3. The analysis procedure in Chapter V.2 follows that in Chapter V.1, except for the estimation of the SRC and the separation of the SR and LR components. The evaluation of most sources of systematic uncertainties including those from event mixing, run period dependence, z_{vtx} position etc follow the discussions presented in Appendix B.1. Hence, in this part we focus only on the sources of systematic uncertainties that are new for this analysis or are evaluated following a slightly different procedure than those presented in Appendix B.1. The major new source of systematic uncertainty is the contributions from the short-range subtraction procedure. We also discuss the uncertainties from MC consistency, tracking efficiency and run group dependence (for p+Pb and p+p systems) in this Section. The details of the evaluation of the uncertainties for the individual sources are discussed below.

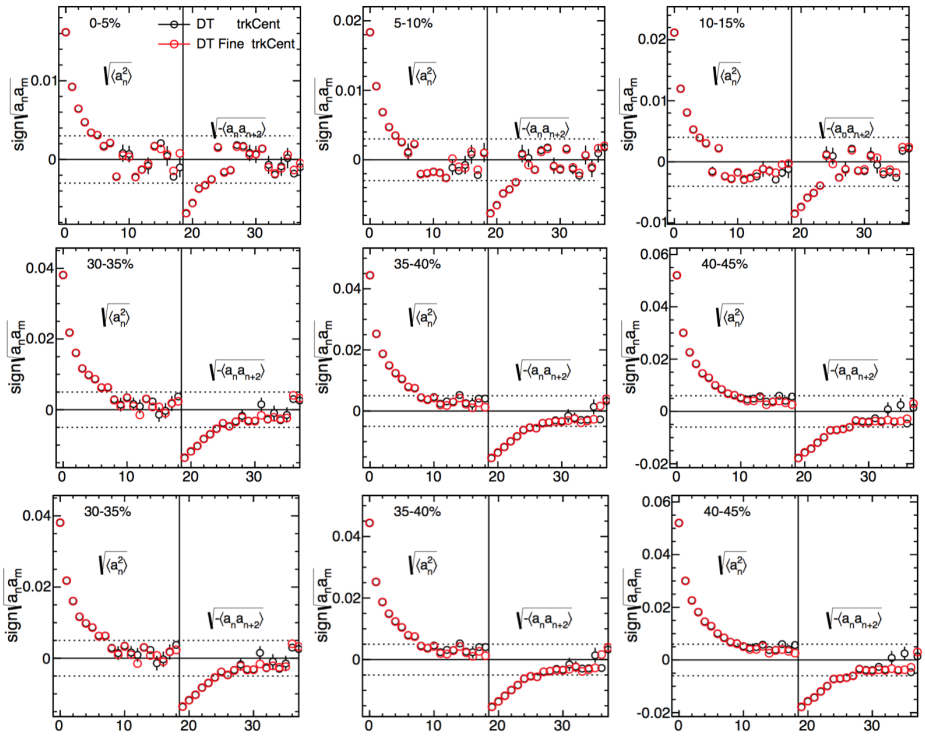

Figure B.13: The values of $\sqrt{\langle a_n^2 \rangle}$ for $n = 10-19$ and $\sqrt{\langle -a_n a_{n+2} \rangle}$ for $n = 1-17$ in nine centrality intervals. The two colored markers indicate values calculated with correlation functions having 48 bins (black symbols) and 240 bins (red symbols) from -2.4 to 2.4 along both η_1 and η_2 directions. The horizontal dotted lines indicate the magnitude of the absolute systematic uncertainties quoted from pair acceptance effects.

B.2.1 Uncertainties from short-range subtraction

Charge dependence after short-range subtraction.

The long-range correlations are expected to be consistent between the same and opposite charge combinations. Since the magnitude of the SRC in the opposite charge combination differ by more than a factor of 2, the difference in the LRC after subtraction of the SRC serves to quantify the robustness of the analysis procedure. The LRC after the short-range subtraction is in fact found to be very consistent between the same and opposite charge combinations, and the difference between the two are included as a source of systematic uncertainty. Figure B.16 shows the $\sqrt{\langle a_1^2 \rangle}$ values as a function of $N_{\rm ch}^{\rm rec}$ compared between the two charge combinations, for the three collision systems. Differences ($\sim$6%) can be seen mainly only in the most peripheral event classes.

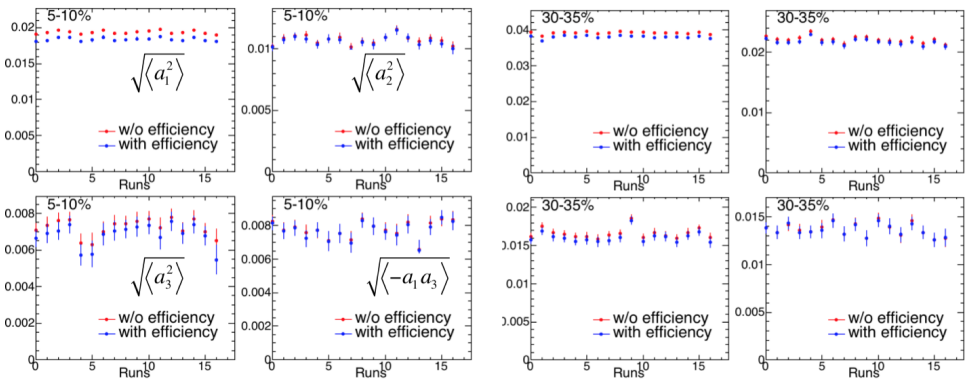

Figure B.14: The $\sqrt{\langle a_n a_m \rangle}$ values from different run groups, for two different centrality intervals. The x-axis correspond to the 17 different run groups.

Varying η_+ range used in the estimation of $g^{\pm\pm}(\eta_-)$

In the analysis, the shape of the short-range correlation in η_- is estimated by using the projection along η_- in the slice with $|\eta_+| < 0.4$. As a cross-check, two other η_+ slices, with $0.4 < \eta_+ < 0.8$ and $0.8 < \eta_+ < 1.2$, were used to do the projections and estimate the short-range. The maximum difference from these choices are quoted as an additional source of systematic uncertainty. Figure B.17 shows the projections along the η_- direction (from the correlation function for same charge combination) at the different η_+ ranges along with the fits in the long-range region (left panel), and the estimated short-range component along η_- (the $g^{\pm\pm}(\eta_-)$ function, see Subsection V.3.2.2) for the different choices. The plots are shown for the Pb+Pb system. The estimated short-range or its shape doesn't vary much with the choice of η_+ slice.

Figure B.18 shows the comparison of the $\sqrt{\langle a_1^2 \rangle}$ the $\sqrt{\Delta_{SRC}}$ values as a function of $N_{\rm ch}^{\rm rec}$, obtained from using the different η_+ ranges. The results are shown for the three collision systems. The deviations are small for both quantities, within 2–4% for most cases, except in the case of a few central bins where ∼10% variation can be seen.

Varying η_- range used for the fit in the estimation of $g^{\pm\pm}(\eta_-)$

The short-range component is estimated by subtracting the long-range pedestal which is estimated from a quadratic fit in the large $|\eta_-|$ region. In the default case this range is chosen to be $|\eta_-| > 1.5$, which corresponds to approximately 2 times the width of the short-range peak along η_- direction. As a cross-check, the range is varied between $|\eta_-| > 1$ and $|\eta_-| > 2.0$. Figure B.19 shows the projections along the η_- direction, with the fits using the default and the two $|\eta_-|$ ranges, for the Pb+Pb system. Changing the fitting range doesn't change the results much.

Figure B.20 shows the comparison of the $\sqrt{\langle a_1^2 \rangle}$ the $\sqrt{\Delta_{SRC}}$ values as a function of $N_{\rm ch}^{\rm rec}$, obtained from using the different choices of η_- to do the fit. The results are shown for the three collision systems. The deviations are small for both quantities, within 2–4% across the centrality

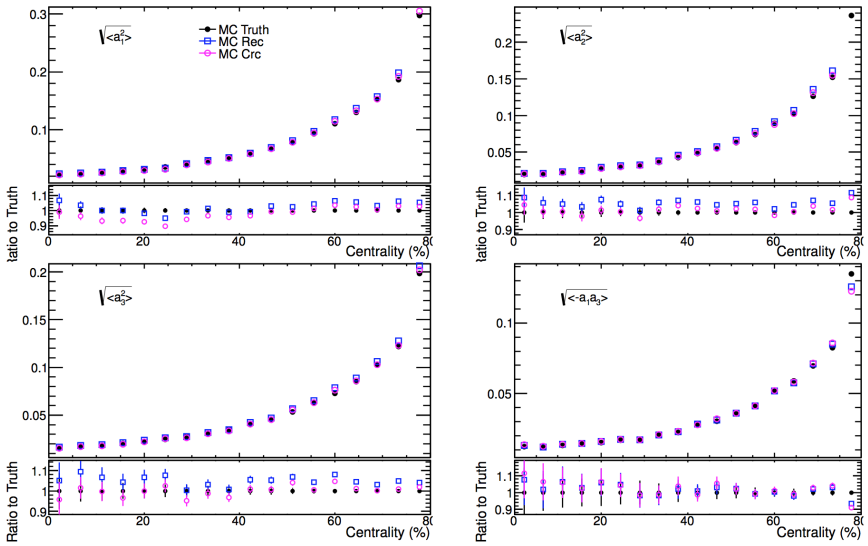

Figure B.15: The $\sqrt{\langle a_n a_m \rangle}$ coefficients as a function of centrality at the truth, reconstructed and reconstructed with efficiency correction for MC HIJING events. The lower panels show ratio to the truth.

range.

B.2.2 Monte-Carlo consistency

The stability of the analysis with regard to detector effects, track reconstruction efficiency, presence of fake tracks etc can be evaluated by comparing the correlation functions and the derived quantities calculated using the truth (generator level) particles and those calculated using the reconstructed tracks, using simulated MC events. For this study we use MC HIJING events reconstructed using the full GEANT4 simulation of the ATLAS detector, for p+Pb and Pythia8 events similarly reconstructed to include detector effects for p+p. Both HIJING and Pythia events are found to have an intrinsic correlation at the two-particle level. Datasets with enough statistics were available only for the p+Pb and p+p systems, but since the tracking efficiency in the p+Pb and peripheral Pb+Pb systems are very similar the systematic uncertainties evaluated for p+Pb is also used for the peripheral Pb+Pb events. The systematic uncertainties are propagated to the other measured quantities by multiplying the correlation function from the default case by the ratio of the correlation function using reconstructed (and efficiency corrected) MC events to that from events at the generated level, and then recalculating all quantities using the modulated correlation function.

At the truth level only primary charged particles are selected. Also particles falling within $p_{\mathrm{T}} < 0.2$ GeV and $|\eta| > 2.4$ are not used. The track selection cuts for the reconstructed tracks are same as those used in the data analysis for the corresponding datasets.

Figure B.21 shows the correlation function $C(\eta_1, \eta_2)$ at the truth and reconstructed levels and

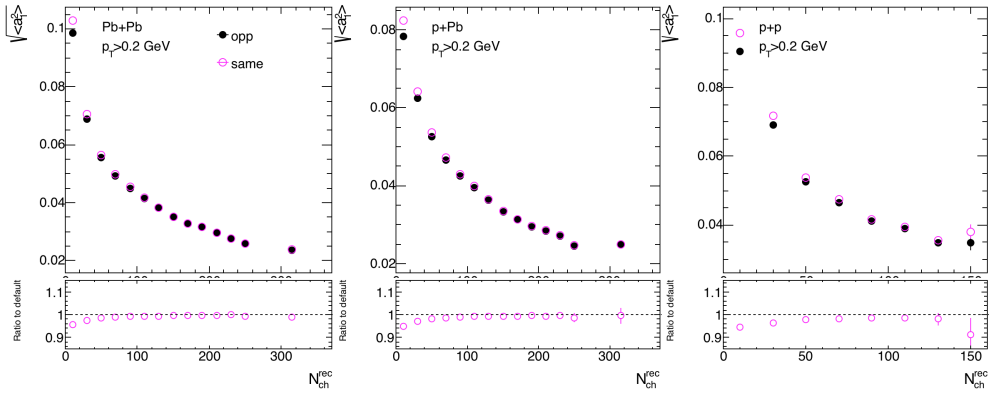

Figure B.16: The $\sqrt{\langle a_1^2 \rangle}$ values as a function of $N_{\mathrm{ch}}^{\mathrm{rec}}$ compared between the opposite and same charged combinations for Pb+Pb (left), p+Pb (middle) and p+p (right) systems. The smaller panels show the ratios relative to the same charge combination.

the ratio of the truth to reconstructed for p+Pb events. The ratio shows that there is some non-closure at the level of the correlation function, which exist mostly along the diagonal in the short-range region. Outside the short range region, no obvious shape can be seen. Figure B.22 shows the $\langle a_n a_m \rangle$ coefficients evaluated from the ratio (solid circles) for different multiplicity intervals. The $\langle a_n a_m \rangle$ coefficients have non-zero values, particularly the $\langle a_1^2 \rangle$ coefficients. But these non-zero values arise primarily from the non-closure along the diagonal direction. This can be seen more clearly from the open circles in the same figure which are calculated from the same ratio in B.22, but with the structure in the short-range region ($|\Delta\eta| < 1$) replaced by the average value in the long-range region ($|\Delta\eta| > 2$). Once the structure in the short-range region is removed, the $\langle a_n a_m \rangle$ coefficients from the ratio are consistent with zero. Since the results for the LRC are with subtraction of the SRC, the expected influence from MC non-closure is small and a few percent deviations are expected for the estimated SRC values.

Figure B.23 shows the comparison of the $\sqrt{\langle a_1^2 \rangle}$ the $\sqrt{\Delta_{SRC}}$ values as a function of $N_{\mathrm{ch}}^{\mathrm{rec}}$, obtained from the default case and with the correlation function in the default case modulated by the ratio of MC correlation function at the reconstructed level to that at the truth level. The deviations are small, 2–4% for the $\sqrt{\langle a_1^2 \rangle}$ values and within 5–10% for the $\sqrt{\Delta_{SRC}}$ values.

B.2.3 Consistency across run-groups

The p+Pb run at the LHC in 2013 were conducted with two orientations for the proton and Pb beams. The first period of the run had protons traveling towards the "C"-side ("beam 1"), while the Pb ions were traveling towards "A"-side ("beam 2"). Nearly half the statistics were collected with this orientation. The other half of the run period had the protons in beam 2 and Pb ions in beam 1. In the analysis, the proton going direction is always taken as the positive η direction, but as far as the detector geometry is concerned, this flips between the two run periods. The results obtained from the two run periods separately, can be compared to evaluate for any

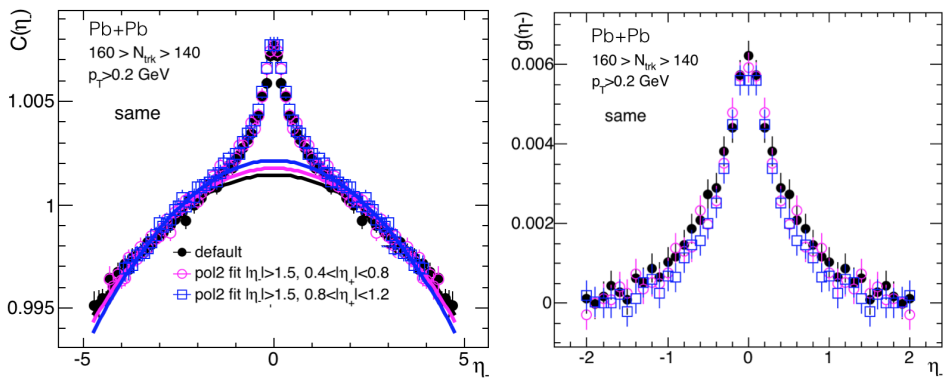

Figure B.17: (Left) Projections of the correlation function along η_- ($C_N(\eta_-)$) for different η_+ ranges along with the quadratic fit in the large η_- region. (Right) The $g^{\pm\pm}(\eta_-)$ function for the three cases. Results shown are for the Pb+Pb system.

possible systematic deviations arising from this flip. Figure B.24 shows the $\sqrt{\langle a_1^2 \rangle}$ the $\sqrt{\Delta_{SRC}}$ values as a function of $N_{\rm ch}^{\rm rec}$ from the two run periods. No significant deviations can be seen for both quantities.

The p+p data from June and August of 2015 have different μ values (average number of collisions per bunch crossing) with the average μ in the August run being about 10 times larger than in the June run. The μ value was between 0.002 and 0.04 for p+p data from June 2015 and between 0.05 and 0.6 for the p+p data from August 2015. The results calculated separately from the two runs can therefore be used to evaluate the effects of residual pileup in the data. Figure B.25 shows the $\sqrt{\langle a_1^2 \rangle}$ the $\sqrt{\Delta_{SRC}}$ values as a function of $N_{\rm ch}^{\rm rec}$ from the two run periods. No systematic deviations are seen for both quantities.

B.2.4 Impact of tracking efficiency correction

The impact of applying the tracking efficiency correction on the measured $\sqrt{\langle a_1^2 \rangle}$ the $\sqrt{\Delta_{SRC}}$ values are shown in figure B.26, as a function of $N_{\rm ch}^{\rm rec}$ for the three collision systems. A small, $\sim$1%, increase ($\sim$2% in the case of p+p) is seen in the case of $\sqrt{\langle a_1^2 \rangle}$ values if the efficiency correction is not applied. The values are expected to increase slightly as the $\sqrt{\langle a_1^2 \rangle}$ values were found to increase with $p_{\rm T}$ and since the tracking efficiency is lower at low $p_{\rm T}$. No noticeable deviations are seen for the case of $\sqrt{\Delta_{SRC}}$ in all the three systems. Since the observed deviations from not applying the tracking efficiency correction at all is very small, this deviation is quoted as a conservative error associated with the uncertainties in tracking efficiency.

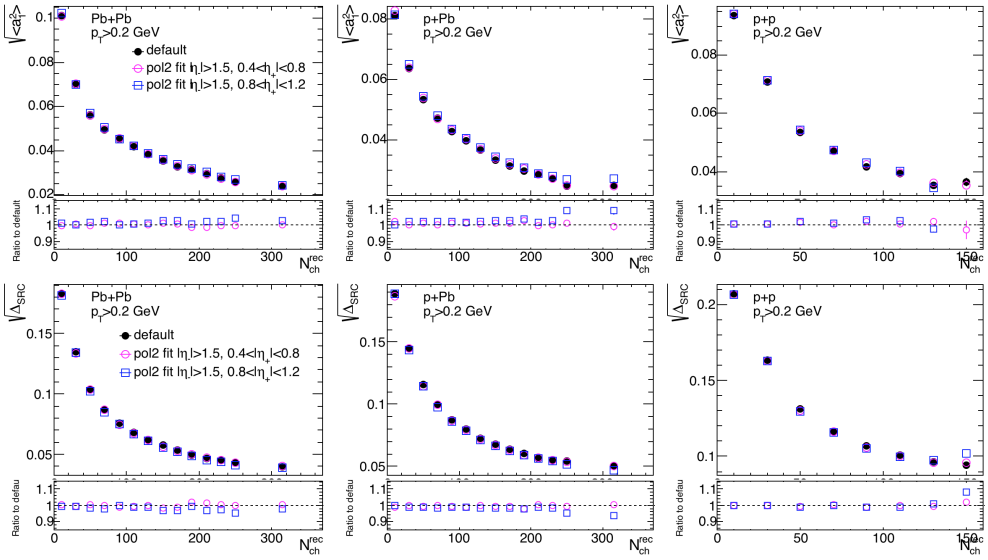

Figure B.18: The $\sqrt{\langle a_1^2 \rangle}$ (top panels) and the $\sqrt{\Delta_{SRC}}$ (bottom panels) values as a function of $N_{\rm ch}^{\rm rec}$ compared between the three choices of $|\eta_+|$ ranges used to determine $g^{\pm\pm}(\eta_-)$, for Pb+Pb (left), p+Pb (middle) and p+p (right) systems. The smaller panels show the ratios relative to the default choice.

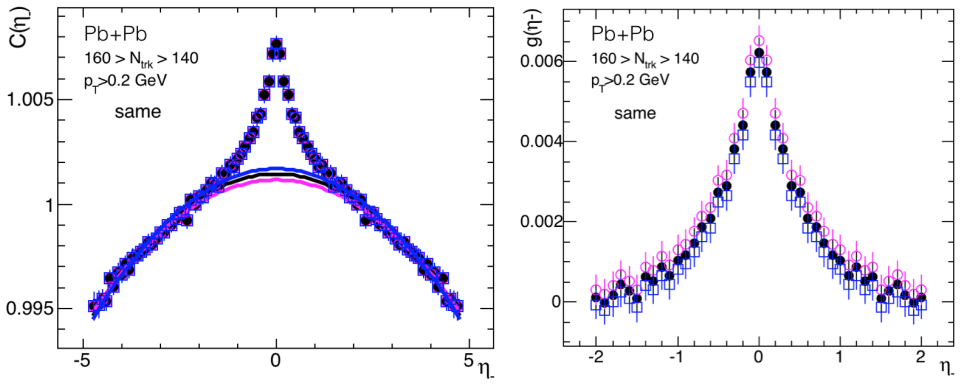

Figure B.19: (Left) Projections of the correlation function along η_- ($C_N(\eta_-)$) along with the quadratic fit in the large η_- region, for different choices of $|\eta_-|$ regions to do the fit. (Right) The $g^{\pm\pm}(\eta_-)$ function for the three cases. Results shown are for the Pb+Pb system.

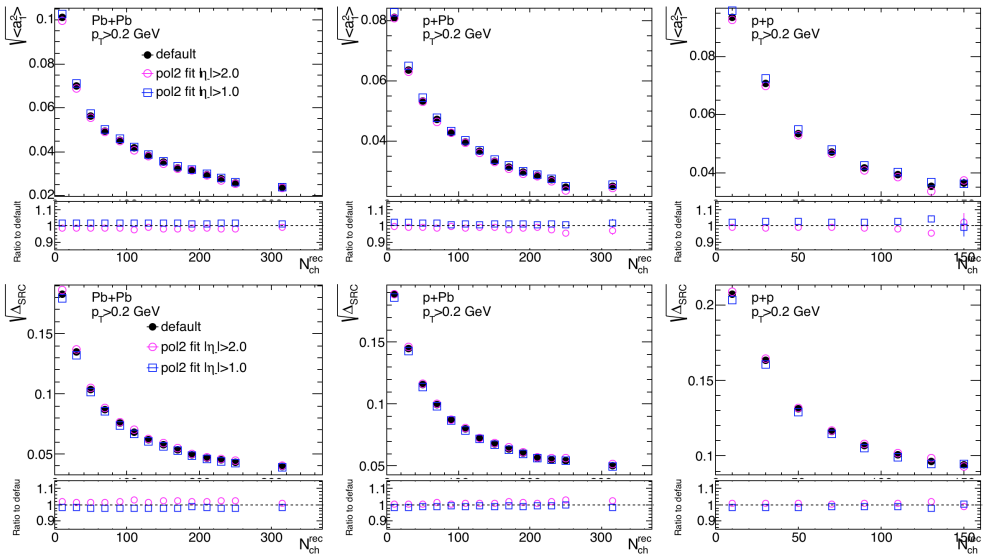

Figure B.20: The $\sqrt{\langle a_1^2 \rangle}$ (top panels) and the $\sqrt{\Delta_{SRC}}$ (bottom panels) values as a function of $N_{\mathrm{ch}}^{\mathrm{rec}}$ compared between the three choices of $|\eta_-|$ ranges used to determine $g^{\pm\pm}(\eta_-)$, for Pb+Pb (left), p+Pb (middle) and p+p (right) systems. The smaller panels show the ratios relative to the default choice.

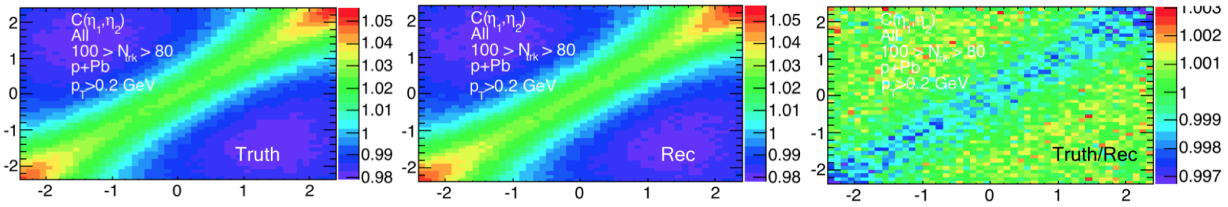

Figure B.21: Correlation function from MC HIJING events at truth (left) and reconstructed levels (middle) and the ratio truth/reconstructed (right) for p+Pb collisions with $100 > N_{\mathrm{ch}}^{\mathrm{rec}} > 80$.

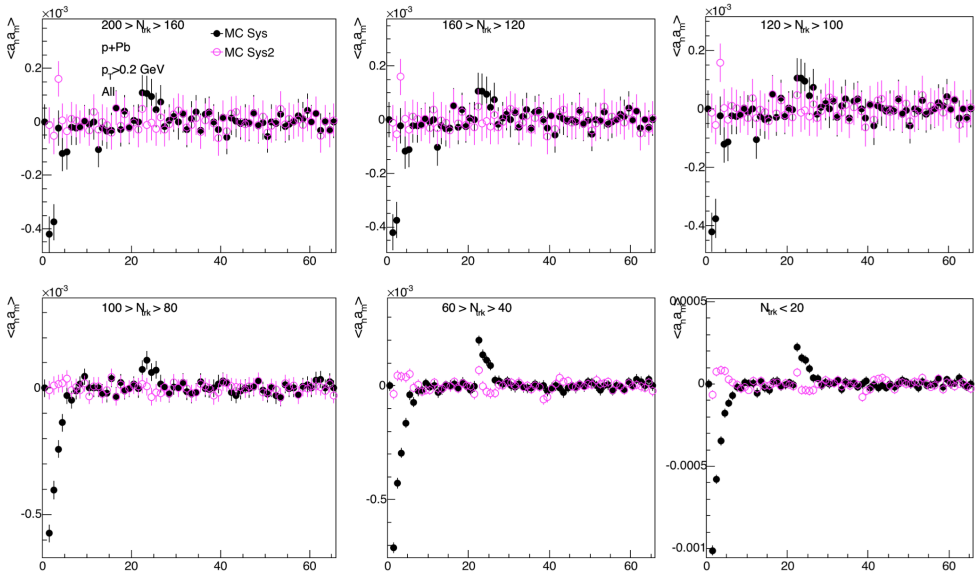

Figure B.22: The $\langle a_n a_m \rangle$ coefficients from the truth/reconstructed ratio for MC HIJING events with $100 > N_{\rm ch}^{\rm rec} > 80$ (solid circles), and from the ratio with the values in the range with $|\Delta\eta| < 1.0$ replaced with the average value from $|\Delta\eta| > 2$ (open circles) for p+Pb collisions. The $\langle a_n a_m \rangle$ are plot in the following order, first 10 points show $\langle a_n a_n \rangle$, next 9 show $\langle a_n a_{n+1} \rangle$, next 8 show $\langle a_n a_{n+2} \rangle$ and so on.

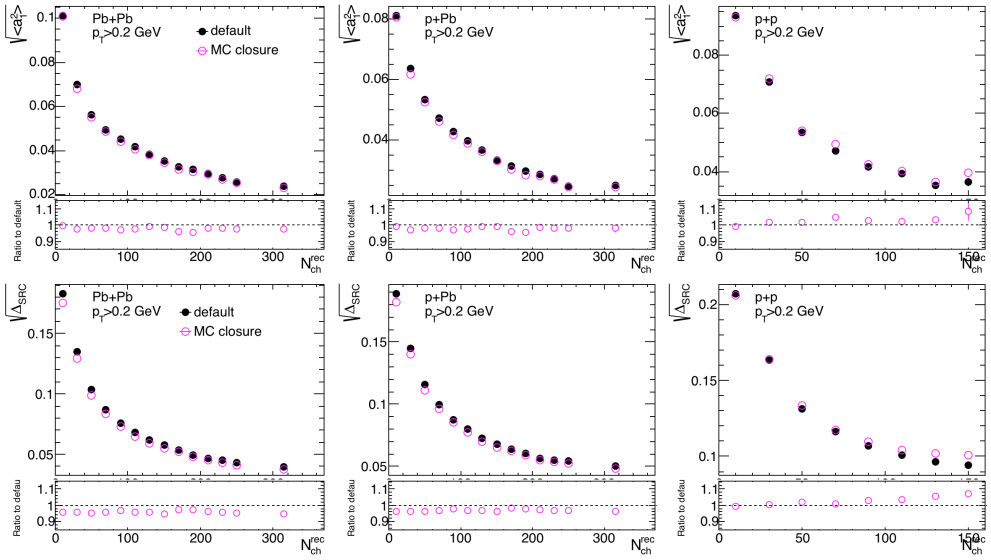

Figure B.23: The $\sqrt{\langle a_1^2 \rangle}$ (top panels) and the $\sqrt{\Delta_{SRC}}$ (bottom panels) values as a function of $N_{\mathrm{ch}}^{\mathrm{rec}}$ compared between the default case and with the correlation function in the default case modulated by the ratio of MC correlation function at the reconstructed level to that at the truth level, for Pb+Pb (left), p+Pb (middle) and p+p (right) systems. The smaller panels show the ratios relative to the default choice.

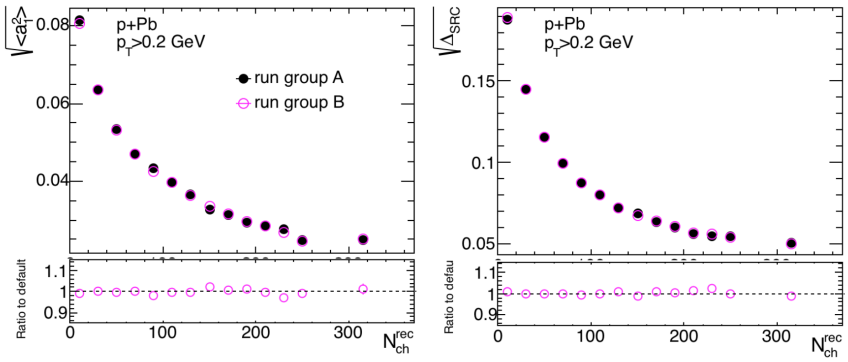

Figure B.24: The $\sqrt{\langle a_1^2 \rangle}$ (left) and the $\sqrt{\Delta_{SRC}}$ (right) values as a function of $N_{\mathrm{ch}}^{\mathrm{rec}}$ compared between the two run periods for the p+Pb dataset. The 'run group A' corresponds to the orientation with protons in beam 1 and 'run group B' has protons in beam2. The smaller panels show the ratios relative to the default choice.

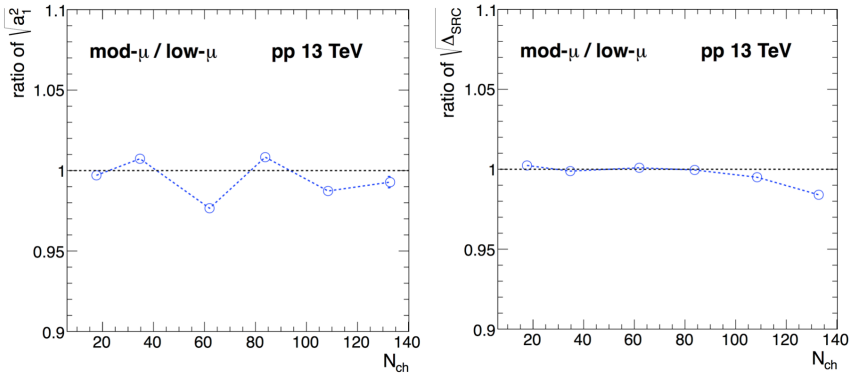

Figure B.25: The $\sqrt{\langle a_1^2 \rangle}$ (left) and the $\sqrt{\Delta_{SRC}}$ (right) values as a function of $N_{\mathrm{ch}}^{\mathrm{rec}}$ compared between the two run periods for the p+p dataset. The 'low-μ' corresponds to the dataset from June and 'mod-μ' to that from August.

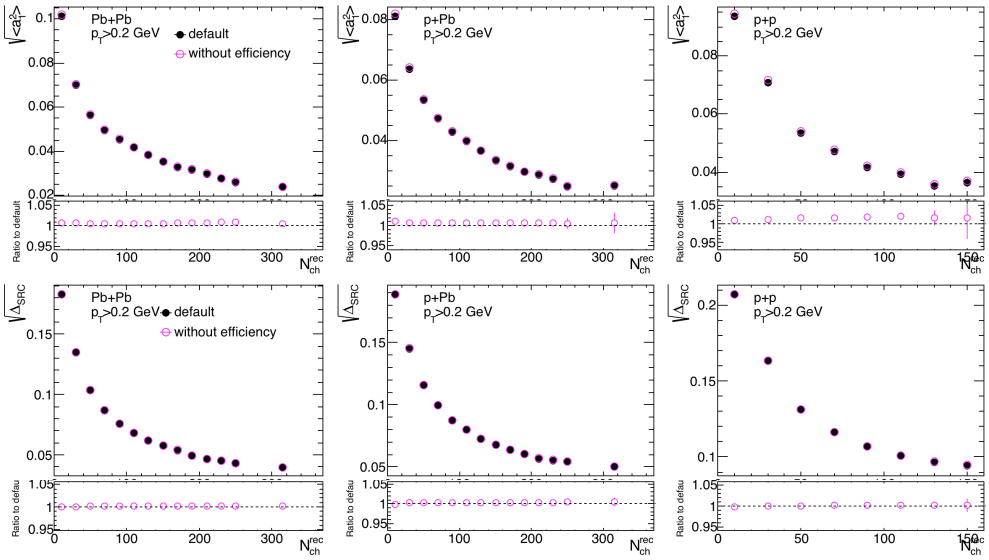

Figure B.26: The $\sqrt{\langle a_1^2 \rangle}$ (top panels) and the $\sqrt{\Delta_{SRC}}$ (bottom panels) values as a function of $N_{\mathrm{ch}}^{\mathrm{rec}}$ compared between the cases with efficiency correction applied (default) and without it being applied, for Pb+Pb (left), p+Pb (middle) and p+p (right) systems. The smaller panels show the ratios relative to the default choice.